Investigation of Microwave Absorption Properties of Nanocomposite: M-type Hexagonal Ferrites, Calcium Copper Titanate (CCTO) and Reduced Graphene Oxide (RGO)

A

Thesis

Submitted to

For the award of the degree of

Doctor of Philosophy (Ph.D)

in

Physics

By

Jibrin Mohammed

(11617660)

Supervised by:

Dr. A. K. Srivastava

(Professor)

Lovely Faculty of Technology and Sciences

Lovely Professional University

July, 2019

Declaration

I hereby declare that the thesis titled "**Investigation of Microwave Absorption Properties of Nanocomposite: M-type Hexagonal Ferrites, Calcium Copper Titanate (CCTO) and Reduced Graphene Oxide (RGO)**" submitted for the award of PhD degree in physics is entirely my original work and all the ideas and references have been duly acknowledged. It does not contain any work for the award of any other degree of diploma from any other university.

Author: **Jibrin Mohammed**

Reg. number: 11617660

Supervisor: **Dr. A. K. Srivastava (Professor)**

Lovely Professional University

Phagwara-144411

Punjab, India.

Certificate

This is to certify that Jibrin Mohammed has completed the thesis titled "**Investigation of Microwave Absorption Properties of Nanocomposite: M-type Hexagonal Ferrites, Calcium Copper Titanate (CCTO) and Reduced Graphene Oxide (RGO)**" under my guidance and supervision. To the best of knowledge, the present work is the result of his original investigation and study. No part of the thesis has ever been submitted for any other degree or diploma at any university. The thesis is fit for submission and partial fulfilment for the award of PhD degree in Physics.

Supervisor: **Dr. A. K. Srivastava (Professor)**

Lovely Professional University

Phagwara-144411

Punjab, India.

Acknowledgments

In the name of Allah, most beneficent, most merciful. All praise and glory be to the Allah (the lord of worlds) for giving me the health and financial capability to successfully carry out my PhD research. I would like to express my sincere gratitude to my PhD supervisor **Dr. A. K. Srivastava (Professor)** for accepting me as his student and giving me all the necessary scientific guidance and financial support required to complete my PhD research. Once again, thank you sir. My mother has been a vital part of my life right from the moment I came into this world. She has been more than a mother for me, sacrificing her comfort so that I can achieve greatness in the academic world. No amount of words could express my appreciation to you. I just pray that Allah give us more time to spend together so that I can do my best in putting some endless smile on your face. My sisters and entire family have been very supportive throughout my entire PhD endeavour, thank you all. I would like to express my sincere gratitude to DSC Kabir Garba for always supporting me in all my endeavours, may Allah reward you with Jannat firdaus.

I would like to express my sincere and profound appreciation to my colleagues, Prof. Chifu E. Ndikilar, Dr. A. B. Suleiman, Dr. Hafeez Y. Hafeez, Bala I. Adamu, S. S. Abdullahi, Khamisu U. Yerima, Ibrahim Murtala, Ibrahim Sa'adu, Y. S. Wudil, and Ibrahim Khalil, all of Department of Physics, Faculty of Science, Federal University Dutse, Jigawa State, Nigeria.

I would like to say a very big thank you to the entire staffs of Department of Physics, Lovely Professional University for always giving words of encouragement. I would like to mention the Dr. Kailash Juglan (HOD), Dr Ramesh Thakur (HOS), and Dr. Niti Kant for their sincere support and encouragement. I would like to express my sincere appreciation to Mr Parminder Pal Singh for always providing me the necessary equipment and chemicals that I may need for my experiments. Also, Mr Manoj Kumar and Mr Bhawneet Singh Kharbanda of Department of Chemistry have been more than helpful during my research activities, thank you all. My sincere gratitude goes Dr. Deepak Basandrai and Dr. Jyoti Sharma for their support and help during the three years of my PhD research. My sincere appreciation goes to Prof. S. B. Narang (Department of Electronics and Communication, Guru Nanak Dev University, Amritsar, India), Dr. Pradip K. Maji (Department of Polymer and Processing Engineering, Indian Institute of Technology Roorkee, Saharanpur Campus, Saharanpur, U. P., India), Dr. Sachin Kumar Godara (Department of Chemistry, Guru Nanak Dev University,

Amritsar, India), Gopala Ram Bhadu (Analytic Division and Centralised Instrument Facility, CSIR-Central Salt and Marine Chemicals Research Institute, Bhavnagar, India) for providing various support in characterization.

Author: **Jibrin Mohammed**

Registration number: 11617660

List of symbols

Symbol	Description
ε^*	Complex permittivity
ε'	Real part of complex permittivity (Dielectric constant)
ε''	Imaginary part of complex permittivity (Dielectric loss)
$tan\,\delta_\varepsilon$	Dielectric loss tangent
δ_ε	Dielectric loss angle
μ^*	Complex permeability
μ'	Real part of complex permeability
μ''	Imaginary part of complex permeability
$tan\,\delta_\mu$	Magnetic loss tangent
δ_μ	Magnetic loss angle
$tan\,\delta_T$	Total loss tangent
Z^*	Complex impedance
Z'	Real part of complex impedance
Z''	Imaginary part of complex impedance
Z_{in}	Normalised input impedance
Z_0	Vacuum impedance
c	Velocity of EM wave in vacuum
ε_0	Permittivity of vacuum
μ_0	Permeability of vacuum
f	Frequency of electric field
ω	Angular frequency
R_L	Reflection loss
σ_t	Total conductivity
σ_{AC}	Frequency dependent part of total conductivity (AC conductivity)
σ_{DC}	Frequency independent part of total conductivity (DC conductivity)
SE_T	Total shielding effectiveness
SE_A	Shielding effectiveness for absorption
SE_R	Shielding effectiveness for reflection
A_{eff}	Effective absorption of the EM wave absorber

T	Transmission coefficient
R	Reflection coefficient
I_i	Incident wave
I_r	Reflected wave
H_c	Coercivity
M_s	Saturation magnetization
M_r	Remnant magnetization
T_c	Curie temperature
λ	X-ray wavelength
hkl	Miller indices
β	Full width at half maximum
β_o	Width observed from the X-ray peaks
β_i	Width as a result of instrumental effects
d_{hkl}	Spacing between the lattices
θ	Angle of diffraction (Braggs angle)
a	Lattice constant
c	Lattice constant
V_{cell}	Volume of unit cell
D	Crystallite size
k	Shape factor
R_p	Profile R-factor
R_{wp}	Weighted profile R-factor
R_{exp}	Expected R-factor
χ^2	Goodness of fit (chi-squared)
C	Capacitance
R	Resistance
E_g	Band gap
α	Absorption coefficient
υ	Frequency of incident photon
R_{gb}	Grain boundary resistance
R_g	Grain resistance

Γ	Line width
δ	Isomer-shift
Δ	Quadrupole splitting
H_{hf}	Hyperfine field
R_A	Relative area

List of figures

List of tables

Abstract

The problem of Electromagnetic interference (EMI) and the quest for efficient and reliable radar absorbing nanocomposites has prompted scientist to synthesize and characterize different nanocomposites. There is still the need to carry out more research in this field due to the observed shortcomings of proper impedance matching, absorber weight and thickness. Generally, excellent magnetic and dielectric properties are required for good impedance matching. However, most of the materials used as EMI shielding and radar absorbing materials show either good magnetic properties or good dielectric properties, but not both. On one hand, M-type hexagonal ferrites exhibit excellent magnetic properties whereas calcium copper titanate shows a remarkable and unusual giant dielectric constant even though it does not show ferroelectric transition. On the other hand, reduced graphene oxide (rGO) shows properties that most materials cannot compete with, these properties include light weight, flexibility, low specific gravity, resistant to heat, high thermal conductivity and good chemical resistance. Hence, in this research, we synthesize and characterise nanocomposites comprising of M-type hexaferrites, CCTO and rGO giving much emphasis to the EMI shielding performance and radar absorbing capability. Also, properties such as structural, dielectric, optical, magnetic and cation distribution have been investigated for various compositions. Sol-gel method was employed to prepare M-type hexaferrites and calcium copper titanate, rGO was prepared using improved Hummer's method, and the preparation of polyaniline (PANI) was done using oxidative polymerization method. The following series of samples have been synthesized.

- $Ca_{1-x}Ni_xCu_{3-x}La_xTi_4O_{12}$ (x=0.1)
- $Ca_{1-x}Pr_xCu_{3-y}Co_yTi_4O_{12}$ (x=0.0, 0.1, 0.2, 0.3 and y=0.0, 0.4, 0.5, 0.6)
- $Ca_{1-x}Ce_xCu_3Ti_{4-y}Ni_yO_{12}$ (x=0.0, 0.25, 0.45, 0.65 and y=0.0, 0.3, 0.5, 0.7)
- $Sr_{1-x}Al_xFe_{12-y}Mn_yO_{19}$ (x=0.3 and y=0.6)
- $Sr_{1-x}Al_xFe_{11.4}Mn_{0.6}O_{19}$ (x=0.0, 0.1, 0.2)
- $Ba_{1-x}Dy_xFe_{12-y}Cr_yO_{19}$ (x=0.0, 0.1, 0.2, and y=0.0, 0.4, 0.5)
- $Sr_{1-x}Cu_xFe_{12-y}Er_yO_{19}$ (x=0.0, 0.1, 0.2, and y=0.0, 0.4, 0.5)
- $Sr_{1-x}Pr_xFe_{12-y}Co_yO_{19}$ (x=0.0, 0.2, 0.4 and y=0.00, 0.15, 0.35)
- $Ba_xCo_xFe_{12-x-y}Dy_xLa_yO_{19}$ (x=0.0, 0.1, 0.2, 0.3 and y=0.0, 0.4, 0.5, 0.6)
- $Ca_{1-x}Er_xCu_3Ti_{4-y}Mn_yO_{12}$ (x=0.0, 0.1, 0.2, 0.3 and y=0.0, 0.4, 0.5, 0.6)
- $SrFe_{12-x}Cs_xO_{19}$ (x=0.0, 0.05, 0.10)

- $CaCu_3Ti_{4-y}Al_yO_{12}$ (y=0.0, 0.1, 0.2)
- $Ca_{1-x}Ce_xCu_3Ti_{4-y}Ni_yO_{12}$ (x=0.0, 0.25, 0.45 and y=0.0, 0.3, 0.5).
- $SrFe_{12-x}Co_xO_{19}$ (x=0.0, 0.1, 0.2)
- $CaCu_{3-x}Y_xTi_4O_{12}$ (x=0.0, 0.1, 0.2)

The samples were characterised using X-ray diffraction (XRD), Fourier transform infrared (FTIR) spectrometer, micro-Raman spectrometer, simultaneous thermal analyser (TGA/DTA/DTG), field emission scanning electron microscope (FESEM), transmission electron microscope (TEM), UV-Vis-NIR spectrometer, impedance analyser, vibrating sample magnetometer (VSM), and vector network analyser (VNA), these characterizations enable proper investigation of the structural, thermal, morphological, optical, dielectric, magnetic, EMI shielding properties, and microwave absorption of the prepared samples.

It is well known that the structural evolution of ceramics depends on the method of synthesis, calcination, and sintering temperature. Sol-gel method happens to be one of the facile cost effective methods of preparation of ceramics. Additionally, it ensure homogeneity of the ceramic sample and pure phase of the ceramic can be attained at low temperature and sintering time in comparison with solid state reaction method. Hence, one of our objectives is to study the effect of temperature on the crystal structure evolution of calcium copper titanate with chemical composition $Ca_{1-x}Ni_xCu_{3-x}La_xTi_4O_{12}$ (x=0.1). The morphology, optical, and dielectric properties were studied in addition. Initially, the prepared ceramic is pre-calcinated in a digital controlled muffle furnace at 800 °C for 6 hours. The pre-calcinated powder was divided into four parts and labelled *T1*, *T2*, *T3* and *T4*. Furthermore, *T2*, *T3* and *T4* were further heated at 800 °C, 900 °C, and 1000 °C for 6 hours respectively. The sample labelled *T1*, *T2*, and *T3* show some traces of $CaTiO_3$, CuO, and TiO_2 (anatase phase) secondary phases whereas *T4* exhibit pure crystalline phase of CCTO ceramic. This indicates that at 6 hour duration, pure phase of CCTO ceramic can be obtained at 1000 °C. The obtained lattice constant and volume of unit cell are in agreement with what was reported earlier in literature. The morphology of the prepared Ni^{2+}-La^{3+} substituted CCTO ceramic tend to evolve with temperature as observed in FESEM micrographs, the known cubic shape of CCTO ceramic evolves with increase in temperature and becomes dominant in the sample with *T4*. The observed inter planar spacing in the HRTEM support the values observed from XRD analysis whereas the SAED pattern indicate that the Ni^{2+}-La^{3+} substituted CCTO ceramic is polycrystalline in nature. The plot of band gap against changes in sintering temperature shows a decreasing behaviour with increase in sintering temperature which ascribe to changes

in the local atomic lattice of the Ni^{2+}-La^{3+} substituted CCTO ceramic. The dielectric properties were explained according to internal barrier layer capacitance (IBLC) model. Dielectric analysis shows that the sample with *T4* has the highest values of dielectric constant (40400) at low frequency which we assumed to be a consequence of space charge polarization.

The XRD patterns of the CCTO ceramic with chemical composition $Ca_{1-x}Pr_xCu_{3-y}Co_yTi_4O_{12}$ (x=0.0, 0.1, 0.2, 0.3 and y=0.0, 0.4, 0.5, 0.6) indicate that the prepared CCTO ceramic exhibit pure phase, secondary phases such as $CaTiO_3$, CuO, and TiO_2 have not been observed. Similarly, these secondary phases have not been observed in the obtained spectra of Raman spectroscopy, this further supports the findings of the XRD analysis. The observed weight losses in the TGA graph stops at 895 °C, this is an indication of the formation of the final CCTO ceramic product. The FESEM micrographs show closely dense arranged faceted grains, agglomeration as a result of formation of liquid oxide phase has not been observed. The stoichiometry of the CCTO ceramic is confirmed in the EDX spectra. The values of the optical band gap (E_g) was observe to show an increasing behaviour with increase in the concentration of Pr^{3+}-Co^{2+}. Maxwell-Wagner relaxation process was used to explain the dielectric response of the prepared CCTO ceramic. The highest value of dielectric constant (4920) at a frequency of 100 Hz was observed in the sample J1 (x=0.0 and y=0.0) whereas the sample J2 (x=0.1 and y=0.4) has the lowest value of dielectric loss tangent (0.194) at 100 Hz. The contribution from grains and grain boundary was analysed using Cole-Cole plot, it was observed that grain boundary resistance (R_{gb}) contribute most to the dielectric response of the CCTO ceramics

XRD patterns of $Ca_{1-x}Ce_xCu_3Ti_{4-y}Ni_yO_{12}$ (x=0.0, 0.25, 0.45, 0.65 and y=0.0, 0.3, 0.5, 0.7) reveals the formation of CCTO ceramics along with small amount of secondary phases ($CaTiO_3$ and CuO). Also, the intensity of these secondary phases increases with increase in Ce^{3+}-Ni^{2+} concentration. Large grains with regular and polyhedral shape and size in the range 902.4-1.562 μm were observed in the HRSEM micrographs and the stoichiometry of the CCTO ceramic is clearly observed in the EDX spectra. A dielectric constant of 16,000 was observed at 100 Hz in the sample K2 (x=0.25 and y=0.3). The lowest dielectric loss (0.189) was observed in the sample K4 (x=0.65 and y=0.7). Similarly, Cole-Cole plot dominance behaviour of grain boundary resistance (R_{gb}) on the dielectric properties.

The influence of temperature variation on the structural, magnetic, and optical properties of strontium hexaferrite having chemical composition $Sr_{1-x}Al_xFe_{12-y}Mn_yO_{19}$(x=0.3 and y=0.6) was investigated. The XRD analysis shows the formation of small quantity of α-Fe_2O_3 in the prepared samples. FTIR spectra show the characteristics peaks of hexaferrite between 400 cm^{-1} and 600 cm^{-1}. Grains with plate-like hexagonal structure were observed in the FESEM micrograph and the confirmation of the stoichiometry of the prepared sample is clearly observed by the presence of the substituted and host cations. TGA analysis shows proof of recrystallization process at 650 °C in the prepared; this temperature is also determined to be the formation temperature. The band gap of the prepared samples tends to decrease with increase in calcination temperature. Koop's phenomenological theory and Maxwell-Wagner theory were used to explain the dielectric properties. Highest dielectric constant was observed in the sample heated at 750 °C, whereas the sample heated at 1050 °C shows the lowest dielectric loss. M-H hysteresis loop was used to determine the magnetic parameters. It was found that the sample heated at 850 °C exhibits the highest value of coercivity (6750 Oe). Also, the values of remanent and saturation magnetization drops as the temperature was increased.

The effect of variation in the concentration of Al^{3+}-Mn^{2+} on the structural, dielectric and magnetic properties of $Sr_{1-x}Al_xFe_{11.4}Mn_{0.6}O_{19}$ (x=0.0, 0.1, 0.2) was investigated. XRD patterns show the formation of crystalline M-type hexagonal ferrites with traces of α-Fe_2O_3. FTIR gives the idea of the formation of M-type hexagonal ferrites by showing the presence of characteristics peaks at 438.94 cm^{-1} and 600.17 cm^{-1}. FESEM shows that the sample exhibit platelet-like structure. The dielectric analysis was done in the frequency range 1 KHz to 5 MHz and discussed on the basis of Koop's phenomenological theory and Maxwell Wagner theory. The sample with x=0.0 exhibits the highest dielectric constant (1410) whereas that with x=0.1 shows the low dielectric loss (0.829). The magnetic parameters show an increasing behaviour with increase in the concentration of Al^{3+}-Mn^{2+}. The sample with x=0.2 shows the highest value of coercivity (4597.58 Oe)

The structural, dielectric, optical, magnetic, and cation distribution of $Ba_{1-x}Dy_xFe_{12-y}Cr_yO_{19}$ (x=0.0, 0.1, 0.2, and y=0.0, 0.4, 0.5) were investigated. Confirmation of the formation of single phase hexaferrites was observed in the XRD pattern. Furthermore, no secondary phase was observed in the pattern with the absence of secondary phase. The formation of two peaks at 438 and 589 cm^{-1} at the lower wavenumber range of the FTIR spectra indicate the presence of M-type hexaferrite. The observed grains in the FESEM micrographs consist of shapes

close to hexagonal platelet-like as well as rice or rod-like shapes. EDX and elemental analysis gives proof of the stoichiometry of the prepared samples. The band gap shows a decreasing trend as the concentration of Dy^{3+}-Cr^{3+} is increased. Maxwell-Wagner model was employed in the discussion of the dielectric properties. All the samples shows increase of dielectric constant at higher frequencies and the dielectric loss observed is reasonably low. Cole-Cole plot analysis indicates that the dielectric properties are mostly influenced by the grain boundary resistance (R_{gb}). The coercivity of the prepared samples was found to increase with change in the concentration of Dy^{3+}-Cr^{3+}. Saturation and remnant magnetization does not show regular variation with increase in Dy^{3+}-Cr^{3+} concentration. The distribution of cation and their site preference were also evaluated. The Raman active modes observed in the Raman shift are consistent with literature. Our analysis of Mössbauer spectra shows that the prepared samples comprise of the high spin Fe^{3+} valence state. Also, Cr^{3+} ion was found to occupy the octahedral 12k, 2a, and $4f_2$ sites, as well as bipyramidal 2b site.

XRD patterns indicate that the prepared samples having chemical composition $Sr_{1-x}Cu_xFe_{12-y}Er_yO_{19}$ (x=0.0, 0.1, 0.2, and y=0.0, 0.4, 0.5) consist of single phase and crystalline structure, secondary phase such as magnetite (α-Fe_2O_3) have not been observed. The two prominent peaks at 454 and 591 cm^{-1} observed in the FTIR spectra suggest the formation of M-type hexaferrites. The observed Raman peaks are consistent with those of single phase hexaferrites, this further supports the XRD analysis. Agglomeration of grains due to magnetic interaction with neighbouring grains is observed in the FESEM micrographs. The band gap exhibits an increasing behaviour with increase in the amount of Cu^{2+}-Er^{3+}. Maxwell-Wagner model and Koop's phenomenological were used to analyse the dielectric properties. Magnetic analysis shows the possibility of the occurrence of spin canting effect, magnetic dilution and the collapsed of the magnetic collinearity as a result of substitution of Er^{3+} ions; this scenario causes the observed decrease in magnetization. Additionally, the prepared samples tend to transition from ferromagnetic towards paramagnetic behaviour. In the Mössbauer spectra, critical analysis of the values of relative area indicate that Er^{3+} occupy the 12k, $4f_2$, 2a, and 2b crystallographic sites.

Structural, optical, magnetic, EMI shielding and microwave absorption properties of $Sr_{1-x}Pr_xFe_{12-y}Co_yO_{19}$ (x=0.0, 0.2, 0.4 and y=0.00, 0.15, 0.35) have been investigated. It was observed from the XRD patterns that the samples are of single crystalline phase without any secondary phase such as α-Fe_2O_3. FTIR spectra shows three peaks at 434, 543, and 586 cm^{-1}, these peaks are signatures of hexaferrite phase. Hence, we can assume the formation of

hexaferrite phase. FESEM micrographs show that the hexaferrite grains are agglomerated as a result of magnetic interaction between the grains while the EDX spectra confirm the stoichiometry of the prepared samples. The observed band gap was found to decrease with variation in Pr^{3+}-Co^{2+} concentration. VNA analysis shows that the sample S2 exhibits a total EMI shielding effectiveness of 27.40 dB at 18 GHz.

Barium hexaferrites (BaM) and calcium copper titanate (CCTO) with chemical composition $Ba_{1-x}Co_xFe_{12-x-y}Dy_xLa_yO_{19}$ (x=0.0, 0.1, 0.2, 0.3 and y=0.0, 0.4, 0.5, 0.6) and $Ca_{1-x}Er_xCu_3Ti_{4-y}Mn_yO_{12}$ (x=0.0, 0.1, 0.2, 0.3 and y=0.0, 0.4, 0.5, 0.6) have been synthesized using sol-gel method respectively., the composite of BaM and CCTO have been prepare by facile mechanical blending in the ratio 1:1. Single crystalline phase of BaM and CCTO have been observed in the XRD patterns. Also, Raman spectra show peaks that are consistent with single crystalline phase of BaM and CCTO. This supports the observation made in the XRD pattern. The spectra of FTIR show peaks of both BaM and CCTO at 439 and 592 cm^{-1}; these peaks are signatures of both BaM and CCTO phase and they give the possibility of formation of BaM and CCTO phase in the nanocomposites. Hence, the XRD patterns, Raman spectra, and FTIR indicate the successful incorporation of both BaM and CCTO phase in the nanocomposite. Uneven distribution of grains of BaM nanoparticles with morphology close to hexagonal structure and homogenous distribution of CCTO nanoparticles with cubic-like grains are observed in the FESEM micrographs. EDX spectra show the chemical composition of the prepared samples; this confirms the stoichiometry of the nanocomposite. Optical analysis show that the band-gap increases with grain sizes. The coercivity was found to increase as a result of the presence of CCTO phase. The calculated maximum reflection loss (RL) of -27.9 dB (99.83 % absorption) at 16.5 GHz and matching thickness of 3 mm was observed in the sample BaMCCTO4. Also, an effective absorption ($RL < 10$ dB) bandwidth of 1.7 GHz between 15.7 and 17.4 was observed in the same sample. The EMI shielding performance of the BaMCCTO4 nanocomposite shows a total shielding effectiveness of 41.8 dB at 16.5 GHz, this values corresponds to 99.99 % shielding of EM waves with effective shielding ($SE_T > 20\ dB$) bandwidth of 4.2GHz.

A composite consisting of M-type strontium hexaferrites (SrM), calcium copper titanate (CCTO) and reduced graphene oxide (rGO) have been prepared in the ratio 1:1:1: using facile in situ method. The chemical composition of the M-type SrM and CCTO are respectively $SrFe_{12-x}Cs_xO_{19}$ (x=0.0, 0.05, 0.10) and $CaCu_3Ti_{4-y}Al_yO_{12}$ (y=0.0, 0.1, 0.2). The XRD pattern show peaks identical to SrM and CCTO that are consistent with single phase, this is further

supported by the Raman and FTIR spectra. Secondary phases such as α-Fe_2O_3, $CaTiO_3$, CuO, TiO_2 have not been observed. FTIR spectra show bands at 446, 551 and 605 cm^{-1}, these bands are characteristics of SrM and CCTO phase. The Raman shift observed at 1358 and 1604 cm^{-1} are respectively that of the D and G bands of GO. Similarly, the Raman shift at 1351 and 1595 cm^{-1} respectively signify the D and G bands of rGO. The FESEM micrographs show the successful incorporation of SrM nanoparticles, CCTO nanoparticles and rGO sheets. The surface energy reduction and magnetic dipolar interaction force the SrM nanoparticles to surround the CCTO nanoparticles and settle at the surface of the rGO sheets. Optical analysis shows that the obtained band gap makes the nanocomposite useful in UV-blue LED application. A maximum reflection loss of −16.0 dB at 18.0 GHz and matching thickness of 2 mm was observed in the sample SCR3. All the samples show SE_T values above 20 dB, the values of SE_T for the sample SCR1, SCR2, and SCR3 was found to be 23.8 dB at 16.2 GHz, 25.9 dB at 15.3 GHz, and 36.8 dB at 18.0 GHz. The values of SE_T for the sample SCR3 was found to be the highest, this value is higher than other composites. The obtained reflection loss and EMI shielding performance could be attributed to multiple absorption mechanism as a result of improved impedance matching between the dielectric and magnetic loss absorbents.

Reduced graphene oxide (rGO) stabilised by chitosan (biodegradable polymer), polyaniline (PANI) and calcium copper titanate (CCTO) nanocomposites have been prepared. The chemical composition of the CCTO ceramic is $Ca_{1-x}Ce_xCu_3Ti_{4-y}Ni_yO_{12}$ (x=0.0, 0.25, 0.45, and y=0.0, 0.3, 0.5). The presence of chitosan ensures that the RGO sheets do not restack into graphite. The dielectric properties were explained on the basis of Maxwell-Wagner relaxation model and Koop's phenomenological theory. The rGO/PANI/$CaCu_3Ti_4O_{12}$ nanocomposite shows the highest dielectric constant (7244).

Nanocomposite of chitosan (biopolymer) stabilised reduced graphene oxide (RGO), sol-gel derived hexaferrites with chemical composition $SrFe_{12-x}Co_xO_{19}$ (x=0.0, 0.1, 0.2), and calcium copper titanate (CCTO) having chemical composition $CaCu_{3-x}Y_xTi_4O_{12}$ (x=0.0, 0.1, 0.2). Chitosan helps to ensure that the rGO sheets do not restack into graphite. The idea of the formation of hexagonal ferrites was observed in FTIR spectra by the occurrence of two prominent peaks between 400 and 600 cm^{-1}. XRD analysis shows that hexagonal ferrites and calcium copper titanate exhibit pure crystalline structure with the absence of secondary phase. Raman spectra show the presence of rGO by the characteristics D and G band at 1350

and 1592 cm^{-1} respectively. Reasonably high values of dielectric constant and low dielectric loss were observed in the nanocomposites.

This thesis is divided into five chapters. Chapter one give the introduction to the research, analysis of the unit cell and crystal structure coupled with the theory behind microwave absorption have been given in details. Chapter two presents a critical review of literatures whereas the research methodology used in the research is discussed in chapter three. Chapter four presents the extensive discussion of the experimental data for each of the compositions. The summary and conclusion have been presented in chapter five.

Table of Contents

Dedicated to my mother

Hajiya Hama Jibrin Mohammed

May Allah (SWT) reward you with Jannatul Firdaus

Chapter 1

1. Introduction

1.1 Preamble

The advancement in telecommunication and other electronic gadgets have resulted in the problem of electromagnetic interference (EMI) and effect on biological tissue [1][2][3][4]. The performance of military equipment and our daily electronics devices are affected by this problem, the resolution of this problem requires the precise design and engineering of reliable and efficient EMI shielding and radar absorbing materials which will offer advantages such as high absorption, wide bandwidth, low density, light weight, antioxidant capability, and excellent thermal stability [5][6]. However, traditional EMI shielding and radar absorbing materials fail to meet this requirements [7]. Hence, there is a dire need to synthesize and characterize EMI shielding and radar materials that will eliminate or reduce the problem. Several attempts have been made in order to design materials that could ensure better performance when it comes to EMI shielding and radar absorbing materials, composites and nanocomposites comprising of Fe_3O_4/graphene [8], TiO_2/polyaniline/graphene oxide [9], graphene foam [10], Fe_3O_2/SiO_2 [11], $CoFe_2O_4@TiO_2$ [12], polypyrrole/graphene [13], Fe_3O_4/Fe-phthalocyanine/graphene oxide [14], conducting polymers/$NiFe_2O_4$/reduced graphene oxide [15], Fe_3O_4/reduced graphene oxide [16], $NiFe_2O_4@MnO_2$ [17], graphene@$CoFe_2O_4$@polyaniline [18], graphene/poly(3,4-ethylenedioxythiophene)/Fe_3O_4 [19], graphene@NiO@PANI decorated with Ag particles [20], graphene/polypyrrole composites with Fe_3O_4 [21], RGO@hematite core–shell nanostructure/PVDF [22], conductive epoxy/graphene/carbonyl iron [23], Ni@C nanocapsules decorated on $SrFe_{12}O_{19}$ hexagonal nanoflakes [24], RGO/$CoFe_2O_4$ [25], RGO/Fe_3O_4/Ag particles [26], RGO/NiO [27], $NiFe_2O_4$/poly-(3,4-ethylenedioxythiophene)/reduced graphene oxide [28], FeCo@SnO_2-nanoparticles/graphene/polyaniline [29], and Reduced graphene oxide/$CoFe_2O4$ [30]. These materials have shown promising properties even though they may not combine the entire necessary requirement for excellent EMI shielding and microwave absorption. For efficient absorption, material for EMI shielding and microwave absorption should possess excellent conductivity, magnetic and dielectric properties. M-type hexaferrites exhibit excellent magnetic properties and calcium copper titanate (CCTO) shows an unusual giant dielectric constant. M-type hexaferrites possesses high saturation magnetization which is vital for EMI shielding and microwave absorption [31]. Additionally, they exhibit high microwave

magnetic loss, high electrical resistivity, high coercivity and anisotropy field coupled with good chemical stability as well as high curie temperature [32][33][34]. CCTO is a non-ferroelectric electroceramic with chemical formula $CaCu_3Ti_4O_{12}$ having low loss at lower frequencies and room temperature, good stability from 100-600 K, and giant room temperature dielectric constant greater than 10^4 for bulk material and 10^5 for single crystals [35][36]. Reduced graphene oxide (rGO) shows high conductivity coupled with good chemical stability, lightweight, and tunable surface properties [37]. Thus, a composite comprising of M-type, CCTO, and rGO could make an excellent lightweight EMI shielding and microwave absorber material.

Generally, solid state reaction method has been extensively used as the traditional method for the synthesis of oxide materials. However, this method is marred by many disadvantages such as high calcination temperature, longer duration of calcination, and appearance of secondary phases as a result of inhomogeneity of the sample, other methods such as co-precipitation method and hydrothermal synthesis suffer from one disadvantage or the other. Sol-gel autocombustion technique ensures the formation of single phase at much lower calcination temperature and duration [38][39][33]. Furthermore, sol-gel autocombustion method utilizes the heat given off during the during the oxidation reaction of the hydrocarbons species to decrease the formation temperature [40]. Hummer's method has been extensively used in the synthesis rGO because of its ability to produce large quantities of rGO [41][42][43].

Hence, this research employed sol-gel autocombustion method to synthesize M-type hexaferrites and CCTO. The dopants were selected after careful review of literatures keeping in mind the need to improve the magnetic and dielectric properties. For the hexaferrites, properties such as structural, magnetic, cation distribution, and microwave absorption properties will be studied whereas dielectric properties of cation-substituted and heat-treated CCTO ceramic will be investigated. Graphene oxide (GO) will be prepared using Hummer's method and subsequently reduced to rGO using different reducing agents. Nanocomposite of hexaferrites, CCTO, and rGO will be synthesized and subjected to structural, morphological, magnetic, and Raman spectroscopic studies as well as EMI shielding and microwave absorption properties will be studied in details.

1.2 Motivation and background (Research gap)

Over the years, high frequency electromagnetic wave has attracted the attention of scientist as a result of its technological application in telecommunication, electronic and military application. Electronic devices such as calculators, printers, computers, mobile phones, and digital circuitry have the ability of emitting electromagnetic radiation which giving rise to a problem called electromagnetic interference (EMI). Electromagnetic radiation is also emitted by telecommunication mast which can damage biological tissue thereby resulting in cancer. Hence, there is a dire need to develop EMI shielding and microwave absorption. EM wave absorption materials have been developed using spinel and garnet ferrites in order to resolve these problems [44][45][46][47].

Although spinel ferrites have been the one of the earliest microwave absorber material, they still have certain disadvantages as electromagnetic (EM) wave absorption material. Spinel ferrites possess relatively small magnetocrystalline anisotropy field (H_A) due to their cubic structure. This causes the zero field ferromagnetic resonance (FMR) frequency of spinel ferrites falls close to or below 1GHz since the FMR frequency strongly rely on H_A. Hence, devices made from spinel ferrites are limited to operate in C-band, S-band, and X-band. Although garnet ferrites exhibit good structural and chemical stability coupled with a small FMR line width, they still have limit of application as EMI shielding and microwave absorption material. Additionally, high values of saturation magnetisation is needed for good EMI shielding and microwave absorption, but garnets show low saturation magnetisation as compared to spinel and hexagonal ferrites. Thus, This devices made from garnet ferrites are limited to operate between 1 GHz to 10 GHz [48][49].

Hexagonal ferrites possesses magnetoplumbite structure with space group $P6_3/mmc$, they are known to show excellent magnetic properties suitable for high frequency EM absorption at and several other applications that may require such properties. The structure of M-type hexaferrites is such that an atomic plane having strontium (Sr) or barium (Ba) atoms separates the spinel blocks (S) which are rotated at 180° with respect to one another. This causes the crystal symmetry to be broken by the plane of atoms, and as a result, a hexagonal structure is formed and large values of H_A which result from single ion anisotropy and dipole-dipole interaction [50][51][52][32]. The H_A of M-type hexaferrites is almost 17,500 Oe; this is almost a 1000 times more than that of spinel ferrites. Additionally, the zero field FMR frequency of hexaferrites is almost 36 GHz and the magnitude of the externally applied

magnetic field required to sufficiently move the FMR frequency of hexaferrites to higher frequency is reasonably low due to this large value of H_A. This results in the construction of electronics devices based on hexaferrites that operates at higher frequencies such as K_u and K_A band [48][45][53][54][55].

1.3 Microwave absorption theory

Microwave absorber generally comprise of a filler material embedded in a matrix material. The filler is composed of one or more material that absorbs the electromagnetic wave. The matrix material is usually selected for its physical properties such as flexibility, and resistance to weather. Microwave absorbers are usually characterized by their electric permittivity and magnetic permeability. By definition, permittivity is a measure of the effect of the material on the electric field within the EM wave and the permeability is a measure of the effect of the material on the magnetic field in the EM wave. When an electromagnetic wave is incident on a certain material, the wave is attenuated and energy is lost due to dissipation of heat. The extent of energy lost greatly relies on the frequency of the wave and the value of dielectric constant of the material. Electromagnetic absorber material can affect the dielectric and magnetic properties of the material in different proportions over different frequency ranges**.**

A dielectric material can be defined as an electrical insulator which does not contain any free charge carriers for conduction. Usually, it is polarised by the application of an external electric field. When a dielectric material is placed in an electric field, the flow of electric charges is restricted unlike in a conductor. The electric charges only shift slightly from their average equilibrium positions there by causing dielectric polarization. Positive charges are shifted towards the electric field whereas negative charges are shifted in the opposite direction as a result of dielectric polarization. This results in the creation of an internal electric field that reduces the total field within the dielectric itself. If a dielectric material comprise of weakly bonded molecules, the molecules within the material become polarized and also reorient themselves so that their axes of symmetry align with the field. Generally, the analysis of dielectric properties of materials involves the storage and dissipation of electric and magnetic energy (field) in materials.

The electric complex permittivity (ε^*) can be defined as the ability of a material to store electrical potential energy under the influence of an electric field. It is measured by the ratio of the capacitance of a capacitor with the dielectric material to its capacitance with vacuum as

dielectric which is called the dielectric constant. The permittivity arises from the dielectric polarization of the material. The permittivity is a complex quantity and is generally written as

$$\varepsilon^* = \varepsilon' - j\varepsilon'' \tag{1.1}$$

Where ε' is the dielectric constant and ε'' is the dielectric loss or a measure of the attenuation of the electric field cause by the material, the dielectric loss tangent of a material is written as

$$\tan\delta_\varepsilon = \frac{\varepsilon''}{\varepsilon'} \tag{1.2}$$

Where δ_ε is the dielectric loss angle, high value of dielectric loss tangent implies high attenuation of the wave as it moves through the material.

The magnetic complex permeability (μ^*) can be defined as the ability of a material to respond to how much electromagnetic flux it can support to pass through itself within an applied electromagnetic field. The permeability arises from the magnetic polarization of the material. The permeability is a complex quantity and is generally written as

$$\mu^* = \mu' - j\mu'' \tag{1.3}$$

Where μ' is the permeability and μ'' is the magnetic loss or a measure of the attenuation of the magnetic field cause by the material, the magnetic loss tangent of a material is written as

$$\tan\delta_\mu = \frac{\mu''}{\mu'} \tag{1.4}$$

Where δ_μ is the magnetic loss angle, similarly, high value of magnetic loss tangent implies high attenuation of the wave as it moves through the material.

Both ε^* and μ^* contribute to the compression of the EM wave inside the material. Furthermore, loss in either the magnetic or electric field will attenuate the energy in the wave as result of coupled nature of EM wave. In general ε', ε'', μ', and μ'' in most absorbers are functions of frequency and may change significantly over even a small range of frequency. If ε^* and μ^* are known over a certain range of frequency then the effect of the material on the wave may be known completely. The actual values of ε' and μ' for most materials can be tiresome in calculation. For this reason they are usually compared to the permittivity and permeability of a vacuum which are $\varepsilon_0 = 8.854 \times 10^{-12}$ *F/m* and $\mu_0 = 4\pi \times 10^{-7}$ H/m. Since ε' depend on the dielectric polarization which always counter the electric field, the ε' for all materials is more than that of free space, and thus, is always greater than 1.

The normalised input impedance (Z_{in}) at the interface of a metal backed layer of microwave absorber can be expressed according to the transmission line theory as [56][57]

$$Z_{in} = Z_0(\mu_0/\varepsilon_0)^{1/2} \tanh\left[j\frac{2\pi ft(\mu_0/\varepsilon_0)^{1/2}}{c} \right] \quad (1.5)$$

Where $Z_0 = \sqrt{(\mu_0/\varepsilon_0)}$ is the vacuum impedance having a value of 377 Ω, μ_0 is permeability of vacuum, ε_0 is permittivity of vacuum, f is the frequency of the incident EM wave, t is the thickness of the pellet sample, and c is the velocity of EM wave in vacuum. The reflection loss (R_L) of an EM wave absorber having certain thickness can be calculated from the using the equation

$$R_L(dB) = 20\log\left|\frac{Z_{in} - Z_0}{Z_{in} + Z_0}\right| \quad (1.6)$$

The effects of eddy current on the appearance of resonance peaks in the plot of magnetic loss tangent ($\tan\delta_\mu$) are described by the relation

$$C_0 = \mu''(\mu')^{-2} f^{-1} = 2\pi\mu_0\sigma t \quad (1.7)$$

where μ_0 is the permeability of vacuum, σ is the conductivity, and t is the thickness of the absorber. Based on the classical theory of electromagnetism, the shielding effectiveness for an EM wave absorber can be expressed as [58]

$$SE = 20\sqrt{\frac{\omega\mu\sigma_{AC}}{2}}\log e \quad (1.8)$$

Generally, shielding effectiveness for reflection (SE_R) and shielding effectiveness for absorption (SE_A) are the parameters describing the shielding effectiveness of an EM wave absorber, they are respectively given in (1.9) and (1.10)

$$SE_R = -10\log(1-R) \quad (1.9)$$

$$SE_A = -10\log(1-A_{eff}) \quad (1.10)$$

Where A_{eff} is the effective absorption of the EM wave absorber. The relation describing A_{eff} is given in terms of reflection coefficient (R) and transmission coefficient (T)

$$A_{eff} = \frac{1-R-T}{1-R} \quad (1.11)$$

Both R and T are usually determined from S parameters (S_{11} or S_{22} and S_{12} or S_{21}) as in equation (1.12) and (1.13) respectively

$$R = |S_{11}|^2 = |S_{22}|^2 \quad (1.12)$$

$$T = |S_{12}|^2 = |S_{21}|^2 \quad (1.13)$$

1.4 Magnetism and magnetic materials

Modern theories suggested that magnetic properties in materials arises as a result of orbital and spin motion of electrons as well as spins of the nuclei. The magnetic effects are produced by the motion of electrons which is equivalent to an electric current. The spin of the unpaired valence electrons which produces the permanent electronic magnetic moments gives the major contribution. These magnetic moments may align themselves in different directions to generate a net non-zero magnetic moment. Hence, the number of unpaired valence electrons presents in the atoms of the material and the relative orientation of the neighbouring magnetic moments determines the nature of magnetism present in the material. All matter is magnetic; the difference lies in the fact that some materials are far more magnetic than others. This is because in some materials, there is no collective interaction between magnetic moments while there is a strong collective interaction between magnetic moments in other materials. Magnetism in materials is classified into five types; they are diamagnetism, paramagnetism, ferromagnetism, antiferromagnetism, and ferrimagnetism.

Diamagnetism is a very weak effect which is observed in materials that do not contain any permanent magnetic moments. It is a fundamental property of all matter. Diamagnetism in materials occurs as a result of changes in the atomic orbital states induced by an applied magnetic field. The magnetic moment in these materials is always in a direction opposite to the applied magnetic field. An electron revolving in an orbit constitutes an electric current. When a magnetic flux linked with such an electric circuit is changed, an induced current is set up in such a direction as to oppose the change in flux in accordance with Lenz's law. The magnetic field of the induced current is opposite to the applied field and produces the diamagnetic effect. The occurrence of diamagnetism is manifested by a very small and negative value of magnetic susceptibility. Diamagnetism exist in all materials, but it is usually suppressed by the presence of other stronger effects such as Paramagnetism, ferromagnetism etc. Diamagnetism is explained by Langevin's theory of diamagnetism.

Paramagnetic behaviour is observed in atoms, ions and molecules which have permanent magnetic moments. For a paramagnetic material, the magnetic moments are randomly oriented and no net magnetization is produced in the absence of applied magnetic field. Paramagnetism is observed in metals, atoms and molecules having odd number of electrons (e.g. free sodium atoms and gaseous nitric oxide), some compounds having even number of electrons (e.g. oxygen molecule), free atoms and ions having partially filled inner shell (e.g.

rare-earth metals, actinide metals and some transition metals such as manganese). When a magnetic field is applied, the magnetic moments orient themselves in the direction of the applied magnetic field thereby leading to some net magnetization in a direction parallel to the applied field. Paramagnetic materials have small, positive and temperature dependent value of susceptibility. For example, the magnetic susceptibility of manganese is 66.10×10^{-6}. The permanent magnetic moments of a paramagnetic material are as a result of spin of the electrons, orbital motion of the electron and spin of the nucleus. Paramagnetism is explained by Langevin's theory of paramagnetism.

Similar to paramagnetism, ferromagnetism is also associated with the existence of permanent magnetic moments. But unlike paramagnetism, the magnetic moments of adjacent ions in a ferromagnetic material are aligned in a particular direction even in the absence of applied magnetic field. Hence, a ferromagnetic material has magnetic moments even in the absence of an applied magnetic field. The magnetization existing in a ferromagnetic material in the absence of an applied field is called spontaneous magnetisation. It exists below a certain critical temperature called Curie temperature (T_c). The exchange interaction between the magnetic ions is the main reason behind the alignment of magnetic moments below the Curie temperature. Above Curie temperature, the spin alignment is altered by thermal effects and the ferromagnetic material exhibit paramagnetic behaviour. Ferromagnetic material acquires large magnetization even in the presence of a weak magnetic field. They possess large and positive value of susceptibility which is generally not constant but varies with the strength of the magnetic field. The well-known hysteresis curve display the variation of magnetization with applied magnetic field. Examples of ferromagnetic material include iron (Fe), nickel (Ni), cobalt (Co), gadolinium (Gd), dysprosium (Dy) and a number of alloys and oxides such as MnAs, MnBi and CrO_2. Ferromagnetism is explained by Weiss theory of ferromagnetism.

Antiferromagnetism occur when the spin moments of the neighbouring atoms are ordered in an antiparallel manner or when the exchange integral is negative. A crystal exhibiting antiferromagnetism may be considered to be consisting of two interpenetrating sub-lattices A and B, one of which is spontaneously magnetized in one direction and the other is spontaneously magnetised in the opposite direction. This type of magnetism is first observed in the crystals of MnO. In the absence of an external magnetic field, the neighbouring magnetic moments cancel each other and the material as whole exhibit no net magnetization. However, when an external magnetic field is applied, a small magnetization appears in the direction of the applied magnetic field which increases with temperature. Such behaviour is a

property of an antiferromagnetic material. The magnetization become maximum at a critical temperature called Neel temperature (T_N) which is analogous to the Curie temperature in paramagnetic or ferromagnetic substances. Above the Neel temperature, the magnetization decreases continuously which is an indication of the paramagnetic state of the material.

Ferrimagnetism is similar to antiferromagnetism except that the magnetization of the two sub-lattices has distinct magnitude which results in a non-zero value of net magnetization. This type of magnetism is found in materials such as ferrites which are basically the oxides of several metallic elements. An example of a ferromagnetic material is Fe_3O_4, one of the Fe^{3+} ion of this ferromagnetic material is in tetrahedral coordination with four oxygen anions (i.e. occupies a tetrahedral site or A-site) whereas the other Fe^{3+} ion and Fe^{2+} ion is in octahedral coordination with six oxygen anions (i.e. occupies a octahedral site or B-site). The ions present at A and B site have opposite magnetization.

Soft ferromagnetic materials possess high relative permeability, low coercive force, easily magnetized and demagnetized and have extremely small hysteresis. Soft ferromagnetic materials are iron and its various alloys with materials like nickel, cobalt, tungsten and aluminium. Ease of magnetization and demagnetization makes them highly suitable for applications involving changing magnetic flux as in electromagnets, electric motors, generators, transformers, inductors, telephone receivers, and relays. They are also useful for magnetic screening. Their properties may be greatly enhanced through careful manufacturing and by heating and slow annealing so as to achieve a high degree of crystal purity. Large magnetic moment at room temperature makes soft ferromagnetic materials extremely useful for magnetic circuits but ferromagnetic materials are very good conductors and suffer energy loss from eddy current produced within them. There is additional energy loss due to the fact that magnetization does not proceed smoothly but in minute jumps. This loss is called magnetic residual loss and it depends purely on the frequency of the changing flux density and not on its magnitude. Examples of soft ferromagnetic material include spinel ferrites and Y-type barium and strontium hexagonal ferrites .Hard ferromagnetic materials possess relatively low permeability, and very high coercive force. These are difficult o magnetize and demagnetize. Typical hard ferromagnetic materials include cobalt steel and various ferromagnetic alloys of cobalt, aluminium and nickel. They retain high percentage of their magnetization and have relatively high hysteresis loss. They are highly suited for use as permanent magnet as speakers, measuring instruments. Examples of hard ferromagnetic material include M-type barium and strontium hexagonal ferrites.

1.4.1 Hexagonal ferrites

Hexagonal ferrites have witnessed an increasing exploration since their discovery in 1950 by Philips laboratory. This is as a result of their excellent magnetic properties with coercivity (H_c) of 6700 Oe, saturation magnetization (M_s) of 72 emu/g and Curie temperature (T_c) of 502 °C. This excellent magnetic properties make them suitable for application as magnetic storage and recording media, electronic components operating at microwave (MW) and gigahertz (GHz) frequency, magnetoelctric and multiferroic application, radar absorbing material (RAM), aircraft (stealth technology), low-power spintronics devices, circulators and phase shifters [39][59]. Ferrite are classified into three types which are spinel, garnet and hexagonal ferrites. Further, hexagonal ferrites are classified into six types according to their chemical composition and crystalline structure; they are M-type, Y-type, U-type, W-type, X-type and Z-type. M-type hexagonal ferrite display better properties such as coercivity and high Curie temperature as compared to the other types. Hence, we select M-type hexagonal ferrite as the required magnetic material to provide the necessary magnetic losses required for excellent absorption of microwaves.

1.4.2 Crystal structure of M-type hexaferrites

The structure of a three dimensional unit cell of calcium M-type hexaferrites is shown in (**Fig. 1.1**). M-type hexagonal ferrites possess magnetoplumbite structure and belong to the space group P63/mmc. The structure of M-type hexaferrites is a superposition of R and S blocks along the hexagonal c-axis with stacking sequence describing the unit cell as RSR*S*, where R is a block of three layers of oxygen ions (O_4-BaO_3-O_4) with composition $BaFe_6O_{11}$ and S is a spinel block of two layers of oxygen ions with composition (O_4-O_4). The asterisk indicates that the corresponding block is rotated 180° around the hexagonal c-axis. There are 38 O^{2-} ions, 2 Ba^{2+} ions, 24 Fe^{3+} ions in a unit cell of hexagonal ferrite. Fe^{3+} ions occupy five sites in the structure which are trigonal bi-pyramidal site (2b), tetrahedral site (4f1) and octahedral sites (12k, 2a and 4f2). Two out of the five sites (4f1 and 4f2) have spin-down ferric ions which results in the reduction of average magnetic moment of the molecule. In order to enhance the magnetic properties of the hexaferrites, appropriate cations with spin up such as rare-earth or transition metals are substituted at spin-down site. Single, two or even more cations can be substituted, but electronegativity should be maintain.

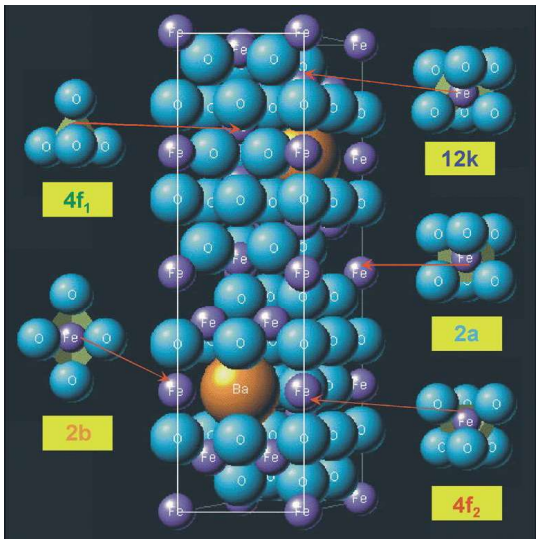

Fig. 1.1 Crystal structure of M-type hexagonal ferrites

1.5 Electroceramics

Electroceramics are a group of ceramic materials that possess good electrical properties and as such, are widely used in electronics devices. Electroceramics have found considerable application in transducers, capacitors, actuators, and devices for data storage. Ferroelectric materials such as barium titanate ($BaTiO_3$) are applied as actuators and capacitors. Magnetic materials such as ferrites (hexagonal, spinel and garnet) are used in magnetic data storage and calcium copper titanate ($CaCu_3Ti_4O_{12}$) is used as circuit protection materials (varistor). Most of these materials have giant dielectric constant. Calcium copper titanate is found to exhibit giant dielectric constant even though it is not a ferroelectric material. Barium titanate is a ferroelectric material but it has certain drawbacks such as temperature and high voltage stability. Calcium copper titanate possesses giant dielectric constant which shows less temperature dependence between ambient temperature and 200 °C [60]. In this proposal, we select calcium copper titanate (CCTO) as the required dielectric material to provide the necessary dielectric losses required for excellent absorption of microwaves.

1.5.1 Calcium copper titanate (CCTO)

In 1967, Alfred Deschanvres and his co-workers for the first time synthesized the cubic perovskite calcium copper titanate (CCTO) [61]. In 1979, B. Bochu and his colleagues determined the crystal structure of calcium copper titanate and in the year 2000, M. A. Subramanian and his colleagues observed an unusual giant dielectric constant of CCTO ceramics at DuPont Central research and development [62][63]. Since then, CCTO has

attracted much interest owing to its potential application as a result of its giant dielectric constant and the fact that it is not ferroelectric. CCTO with chemical formula $CaCu_3Ti_4O_{12}$ has attracted much attention as a result of its giant room temperature dielectric constant of more than 10,000 for bulk material and 100,000 for single crystals. Aside the giant dielectric constant, this electroceramic which is not ferroelectric also exhibit low loss at low frequency and room temperature with good stability from 100-600 K. This novel electroceramic is hoped to play great role in the miniaturisation of electronic devices because the giant dielectric constant will pave the way for smaller electronic components such as ceramic capacitors, ceramic resonators, microwave devices, dynamic random access memory (DRAM), and varistor [38][36][64][35].

In most dielectric materials, the dielectric constant appears as inherent/intrinsic properties of the material, but this is not the case with CCTO ceramics. The origin and nature of this unusual high dielectric constant is not yet fully understood because of the lack of direct evidence of electronic or intrinsic origin. Several mechanisms have been developed in order to explain the nature and origin of this unusual giant dielectric constant. Internal barrier layer capacitor (IBLC) is the most widely accepted mechanism that is used to explain the unusual high dielectric constant of CCTO ceramics. It was proposed that during the processing of calcium copper titanate, insulating surface is formed on the semiconducting grains thereby creating a material that is electronically heterogeneous [60][65]. The occurrence of two dielectric relaxations in the spectra of the dielectric property has forced scientists to assume a second mechanism apart from IBLC mechanism. This second mechanism is the Maxwell-Wagner relaxation present at the interfacial layer of grain and domain boundaries. B. Rivas-murias et al. attributed the giant dielectric constant of this material to the fact that up to a very low temperature, it does not experience ferroelectric distortion [66].

1.5.2 Crystal structure of calcium copper titanate (CCTO)

The determination of the crystal structure of CCTO was done by the French scientist B. Bochu and his colleagues in 1979 [63]. CCTO belongs to the family of double perovskite with general formula $ACu_3Ti_4O_{12}$ (A = Ca or Sr). It possess centro-symmetric structure, space group Im-3 and lattice parameter of 7.391 Å [66][67]. The structure of a three dimensional unit cell of CCTO is presented in **Fig. 1.2**. In this structure, calcium atoms (big light blue balls) are situated at the extreme corners and centre of the unit cell, copper atoms (small blue balls) are situated at the centre of the edges and facial planes of the unit cell.

Titanium atoms (small light blue balls) are situated at the centre of each octahedron forming TiO_6 octahedron. Oxygen atoms (big red balls) are situated at the edges of the TiO_6 octahedron. In the crystal structure of CCTO, the calcium ions (Ca^{2+}) are coordinated by oxygen ions (O^{2-}) in a dodecahedral manner whereas copper ions (Cu^{2+}) are in square planar coordination with oxygen ions (O^{2-}) as the nearest neighbours. Six oxygen ions (O^{2-}) are coordinated by one titanium ions (Ti^{4+}) in a slightly distorted TiO_6 octahedron which is tilted at 20 ° with respect to the axis of the unit cell.

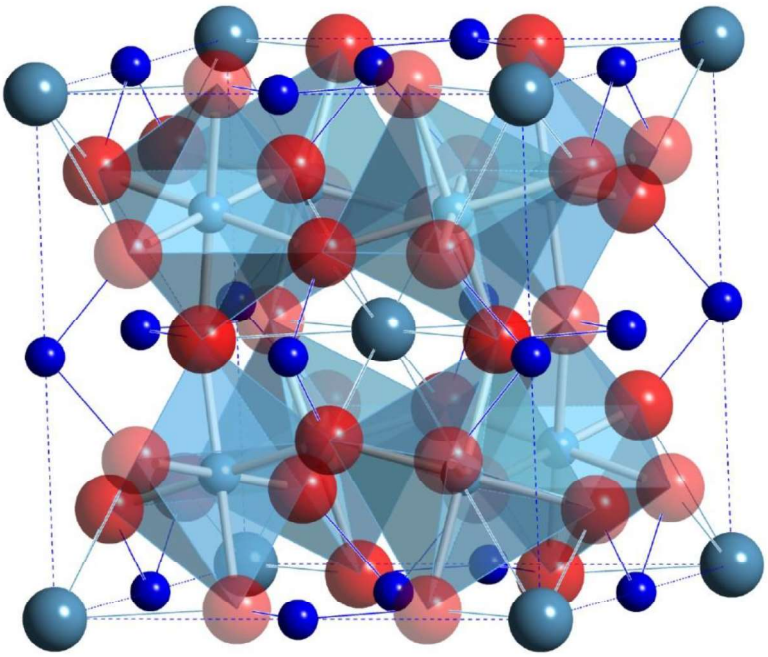

Fig. 1.2 Structure of a three dimensional unit cell of calcium copper titanate (CCTO).

1.6 Reduced graphene oxide (rGO)

Graphite occurs naturally as the most stable three dimensional crystalline form of carbon, it is found in metamorphic and igneous rocks. Due to its excellent qualities such as softness, low specific gravity, resistant to heat, high thermal conductivity and good chemical resistance, it is extensively used in manufacturing and metallurgy [68]. Graphene can be thought of as a two dimensional single atomic layer of graphite or sp^2 carbon atoms densely packed into benzene ring structure [69]. Just like graphite, graphene possess excellent electrical, optical, thermal and mechanical properties which makes it a goldmine of research [70]. Applications

of graphene include nanocomposite materials, solar cells, transparent conducting films, gas storage and electronic devices [71][72][73].

In 2004, graphene was successfully synthesized and characterized by Andre K. Geim and Konstantin S. Novoselov of University of Manchester, UK [74]. Since then, much progress have been recorded in terms the method of synthesis, characterisation and technological application of graphene. The basic methods for the synthesis of graphene include dispersion of graphite in organic solvent, epitaxial growth on silicon carbide, chemical vapour deposition (CVD) of hydrocarbons on the surfaces of transition metals and micromechanical cleavage of graphite. These methods are not cost effective and the yield using any of these methods is low; these factors made researchers to seek for a method that will ensure production of graphene in large quantities. Recently, reduction of graphene oxide (GO) has been used to produce large quantity of graphene at low cost. However, graphene oxide (GO) contains some functional group as compared to pristine graphene (**Fig. 1.3**). These attached functional groups degrade the qualities of graphene oxide (GO).

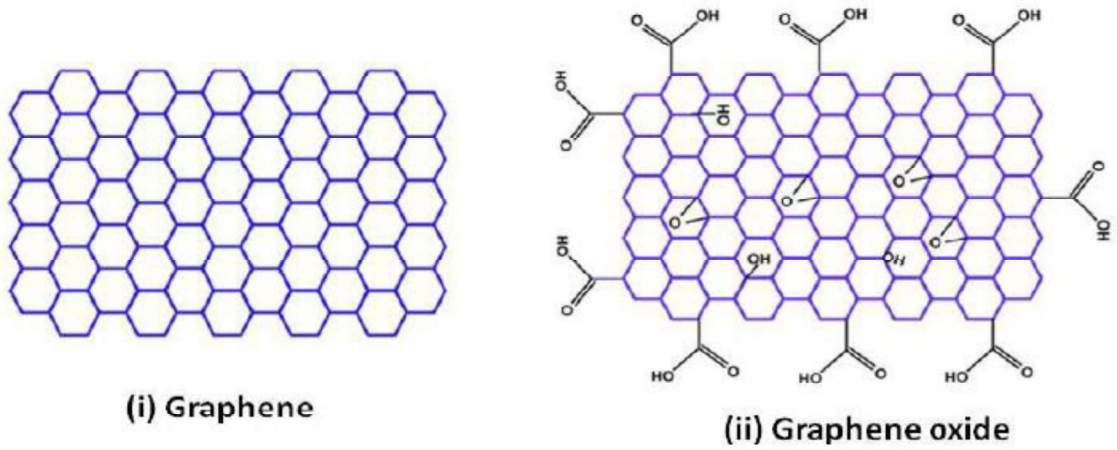

Fig. 1.3 Structure of graphene and graphene oxide (GO)

The basic method employed in the synthesis of graphene oxide (GO) is called Hummers method. Over the years, the method has seen some modification, but a greater part of the original method still remains the same [75][76][77]. The process of producing reduced graphene oxide (rGO) from graphene oxide (GO) entails the subjection of graphite powder or flakes to oxidation process using potassium permanganate ($KMnO_4$) and sodium nitrate ($NaNO_3$), produced graphene oxide (GO) is reduced using hydrazine or other reducing agents to obtain what is called reduced graphene oxide (rGO) (**Fig. 1.4**) [78][79][80]. The obtained

graphene oxide is still not the same as pristine graphene as a result of the presence of some defects and oxygen functional groups as stated earlier (**Fig. 1.3**). Even though the conductivity of reduced graphene oxide (rGO) is more than that of graphene oxide (GO) by 4 orders of magnitude, it is still less than that of pristine graphene by a factor of 10 to 100. The low value of conductivity observed in reduced graphene oxide (rGO) is attributed to the presence of residual oxygen functional groups after reduction [81]. The methods used in reducing graphene oxide include thermal reduction (thermal annealing, microwave and photo irradiation) and chemical reduction (chemical reagent reduction, photo-catalyst reduction, electrochemical reduction, and solvothermal reduction). The carbon to oxygen ratio strongly depends on the reducing agent or method of reduction employed [78].

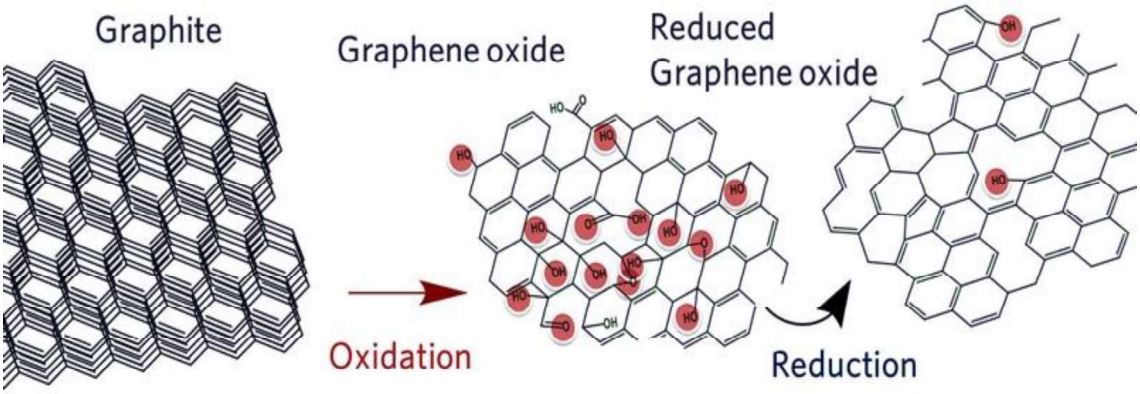

Fig. 1.4 Synthesis of graphene oxide (GO) and reduced graphene oxide (rGO)

The detailed atomic structure of graphene oxide (GO) and reduced graphene oxide (rGO) is still a subject of debate in spite of several microscopic and spectroscopic investigation. Out of the many models that try to explain the atomic structure of graphene oxide (GO) and reduced graphene oxide (rGO), the most accepted describe graphene oxide (GO) as a random distribution of oxidized regions bearing the oxygen functional groups connected with non-oxidized areas where most of the carbon atoms preserve the sp^2 hybridization similar to other 2D nanostructure such as fullerenes and carbon nanotube (CNT) [81].

1.7 Objectives of the study

The aims and objectives of the present research are to synthesize and characterise hexagonal ferrites, calcium copper titanate and reduced graphene oxide (rGO) nanocomposite for high frequency microwave absorption.

1. To study the effect of **cation substitution** on structural, magnetic and microwave absorption properties of rare-earth/ transition metal substituted **hexagonal ferrites.**
2. To study the effect of **calcination temperature** on structural, dielectric properties of **calcium copper titanate.**
3. To study the effect of **cation substitution** on structural, dielectric properties of **calcium copper titanate.**
4. To synthesize and investigate the microwave absorption properties of **hexagonal ferrites and calcium copper titanate nanocomposite.**
5. To synthesize and characterised **graphene oxide (GO)** which is an insulator using Hummer's method and thereafter reduced it to **reduced graphene oxide (rGO)** in order to make it conducting.
6. To synthesize and investigate the microwave absorption properties of **hexagonal ferrites, calcium copper titanate and reduced graphene oxide (rGO) nanocomposite.**

1.8 Scope of the study (Hypothesis)

It is a well-known fact that electromagnetic (EM) wave consist of magnetic and electric field vector. In order to effectively absorb electromagnetic wave such as microwave, a material having good magnetic and dielectric properties is needed. Usually, the magnetic properties of the material ensure the absorption of the magnetic field vector whereas the dielectric properties of the material ensure the absorption of the electric field vector since the absorption of electromagnetic wave (EM) is greatly associated permittivity and permeability. Most materials usually show good magnetic properties and poor dielectric properties or good dielectric properties and poor magnetic properties. Materials such as spinel, garnet and hexagonal exhibit excellent magnetic properties while barium titanate and calcium copper titanate exhibit excellent dielectric properties. Hence, for excellent absorption of electromagnetic wave (EM) wave, a nanocomposite of a material with excellent magnetic properties and another material with excellent dielectric properties is required. Also, a material with good conducting properties is needed in order to improve charge carrier drift, achieve good impedance matching, reduce the thickness of the absorber material and the dielectric properties of the nanocomposite material (because the dielectric properties of the dielectric material is reduced at higher frequencies) [53][54].

Hexagonal ferrites and CCTO respectively exhibit an excellent magnetic and dielectric property which makes them suitable as the required magnetic and dielectric filler material. The attractive conducting properties of rGO make it a suitable candidate as our conducting material and matrix. In this research, we shall attempt to synthesize nanocomposite of hexagonal ferrites, calcium copper titanate and reduced graphene oxide (rGO). Rare-earth and transition metals cation ion will be used to tailor the magnetic and dielectric properties.

1.9 Expected outcome

The need for high frequency microwave absorber material will strongly be addressed by this research. The synthesize material will have positive impact on current technological application such as microwave electronics devices and stealth technology. Also, the problem of electromagnetic interference will be addressed by this research.

Chapter 2

Literature review

2.1 Literature review

Extensive review of literature has been carried out in order to understand the method of synthesis and properties of hexaferrites, CCTO, and rGO. Also, different nanocomposites of rGO with other nanomaterials have been reviewed in details.

N. Adeela et al. (2016) investigated the effect of Mn-substitution on Co_2Y barium hexagonal ferrites with chemical composition $Ba_2Co_{2-x}Mn_xFe_{12}O_{22}$ (x = 0.0, 0.1, 0.3, 0.5, 0.7, 0.9) synthesized by hydrothermal method. The prepared sample was sintered at 950 ℃ for 3 hours. The prepared sample was characterised using FT-IR, XRD, EDX, and SEM. The grain size of the sample increases from few nanometres to micrometres with increase in Mn-concentration. The magnetic properties of prepared sample was improved as a result of substitution of Co^{2+} ions by Mn^{2+} ions which is due to the large values of magnetic moment of Mn^{2+} ions in comparison with that of Co^{2+} ions. The enhanced magnetics properties of the sample were found to be suitable candidate for perpendicular magnetic recording and high frequency application [82].

M. Ahmad et al. (2013) synthesized Co-substituted Mn_2Y barium hexagonal ferries with chemical composition $Ba_2Mn_{2-x}Co_xFe_{12}O_{22}$ (x = 0.0, 0.5, 1.0, 1.5, 2.0) by sol-gel auto-combustion method. Sintering of the prepared powdered sample and pellets was done at 1000 ℃ for 5 hours. The prepared sample was characterised using FT-IR, XRD, EDX FESEM, and DTA/TGA. Within the temperature range 30-100℃, DC electrical resistivity increases with increase in Co-substitution while dielectric constant decreases with increase in Co-substitution. The prepared samples shows high electrical resistivity as well as dielectric constant which make the prepared sample a suitable candidate for microwave device application. FESEM images show densification of the sample with increase in Co-substitution, this property is suitable for high frequency application [83].

M. Awawdeh et al. (2014) conducted magnetic and Mossbauer studies of M-type barium hexagonal ferrites with chemical composition $BaFe_{12-x}M_xO_{19}$ where M represents Gallium (Ga), Aluminium (Al) or Chromium (Cr). The sample is prepared via ball milling method, calcination was done at 1100 ℃ and characterisation was done using XRD, EDX, VSM, SEM

and Mossbauer spectroscopy. Analysis of the characterisation result shows that coercive field increase whereas saturation magnetisation decreases with variation in the concentration of the dopants (Al, Cr and Ga). The high coercivity of the sample makes it suitable for production of low cost permanent magnet [84].

I. Ali et al. (2013) employ sol-gel method and synthesized La-substituted Co_2Y strontium hexagonal ferrites with chemical composition $Sr_2Co_2La_xFe_{12-x}O_{22}$ (x = 0.00, 0.05, 0.10, 0.15, 0.20) and study the influence of La^{3+} ions substitution on the magnetic and structural properties of the prepared sample. The prepared sample was sintered at 1100 ℃ for 5 hours at the rate of 3 ℃/min. The prepared sample was characterised using FT-IR, XRD, DTA/TGA, FESEM, and VSM. Magnetic properties such as coercivity and retentivity increase whereas saturation magnetization decreases with the variation in the concentration of La^{3+}. Since the coercivity of the prepared sample is a few hundred oersteds (Oe), then it may be useful in applications such as security, sensing, switching, high frequency and microwave devices [85].

T. Kaur et al. (2015) synthesized and studied the influence of calcination temperature on the microstructure, dielectric, magnetic and optical properties of M-type barium hexagonal ferrites with chemical composition $Ba_{0.7}La_{0.3}Fe_{11.7}Co_{0.3}O_{19}$ (T = 700 ℃, 900 ℃, 1100 ℃, 1200 ℃). The sample was synthesized via sol-gel auto combustion method and the techniques employed to characterise the prepared sample include FT-IR, XRD, VSM, TGA, UV–visible NIR spectroscopy FESEM. VSM analysis indicates that the increase in temperature increases properties such as saturation magnetization, remnant magnetisation and squareness ratio. It was observed that the sample calcinated at 900 ℃ have higher coercivity and anisotropy constant as compared to those calcinated at 700 ℃, 1100 ℃ and 1200 ℃. Optical studies show that the band gap of the prepared sample increases with La-Co substitution [86].

I. Ali et al. (2014) investigated the influence of calcination temperature on the microstructure, dielectric, magnetic and optical properties of M-type barium hexagonal ferrites with chemical composition $BaCr_xGa_xFe_{12-2x}O_{19}$ (T = 700 ℃, 800 ℃, 900 ℃, 1000 ℃). Synthesis of the sample was done using sol-gel auto combustion method and the techniques employed for the characterisation of the prepared sample are XRD, FESEM, EDX, TGA, DSC, and impedance analyser. The formation of single-phase M-type barium hexagonal ferrites was confirmed by XRD analysis in sample heat treated at 1000 ℃. With increase in

applied frequency, the dielectric constant and dielectric loss tangent decreases while AC conductivity increases. Hence, the prepared sample can be useful in applications such as radar absorbing waves and reduction of eddy current in high frequency application [87].

Y. Bai et al. (2008) studied the dielectric and magnetic properties of Bi-Zn substituted Y-type hexagonal ferrites with chemical composition $Ba_{2-x}Bi_xZn_{0.8+x}Co_{0.8}Cu_{0.4}Fe_{12-x}O_{22}$ (x = 0.0-0.4). The sample was synthesized by solid-state reaction method and sintered at 900 ℃ for. Characterization of the sample was done using FT-IR, XRD, Impedance analyser, pA meter/dc voltage source and FESEM. Within the temperature range 30-100 ℃, DC electrical resistivity increases with Co-substitution while dielectric constant decreases with Co-substitution. Substitution of small amount of Bi reduces the formation temperature significantly and also enhances resistivity. Permittivity and permeability was observed to be stable in the measured range of frequency. The synthesized material can be used for hyper frequency application [88].

I. Ali et al. (2015) synthesize Sr-Co substituted Y-type strontium hexagonal ferrites with chemical composition $Sr_2Co_{2-x}Mn_xTb_yFe_{12-y}O_{22}$ (x=0.0 to 1.0 and y=0.0 to 0.1) via micro-emulsion method and sintered the prepared sample at 1050 ℃ for 8 hours. The influence of Tb-Mn substitution on the electrical properties of the prepared sample was investigated. The prepared sample was characterized via X-ray diffraction (XRD), impedance analyser and two probe. It was observed that with increase in Tb-Mn substitution, the activation energy and the crystallite size increases. The increase in crystallite size is as a result of grain growth occurring at high temperatures. Resistivity of the prepared sample increases with temperature which indicates semiconductor behaviour of the prepared sample. Initially, there is a sharp decrease in dielectric constant with increase in frequency while it decreases at higher frequency. It was observed that with increase in frequency, dielectric loss and tan δ decreases. The prepared material can be suitable for application in multi-layer chip conductor as a result of small dielectric loss and enhanced resistivity [89].

I. Ali et al. (2015) synthesize and studied the magnetic properties of Y-type hexagonal ferrite with chemical composition $Sr_2Co_{2-x}Ni_xEu_yFe_{12-y}O_{22}$ (x=0.0 to 1.0 and y=0.0 to 0.1) via surfactant assisted co-precipitation technique. Sintering of the sample was done for 8 hours at 1050℃. The prepared sample was characterised using FESEM and VSM. The high coercivity value (2300 Oe) of the prepared sample makes the sample potential candidate for perpendicular recording media (PRM) and high frequency application [90].

I. Ali et al. (2014) investigated the effect of Tb-Mn doping on the magnetic properties of Y-type hexagonal ferrites. The prepared sample having chemical composition $Sr_2Co_{2-x}Mn_xTb_yFe_{12-y}O_{22}$ (x=0.0 to 1.0 and y= 0.0 to 0.1) was synthesize via micro-emulsion technique and sintered at 1050℃ for 8 hours. The sample was characterised using VSM, EDX and FESEM. EDXS investigation indicate that the presence of Tb^{3+} and Mn^{2+} ensures the creation of more space in the T-block so as to incorporate Sr^{2+} ions and FESEM images show that the grain exhibit plate-like shape which is required for microwave absorbance application. It was observed from VSM analysis that both saturation magnetisation (M_s) and remanent magnetisation (M_r) decrease whereas coercivity (H_c) increases. The high value of the coercivity 3170Oe and 3195Oe for in-plane and out-plane respectively makes the prepared sample a suitable candidate for perpendicular recording media (PRM) [91].

I. Odeh et al. (2016) use sol-gel auto combustion method and prepared Zn-doped Y-type hexagonal ferrite. The prepared material with chemical composition $Ba_2Co_{2-x}Zn_xFe_{12}O_{22}$ (x=0, 1, 2) was heated-treated at 1100℃ for 4 hours. The sample was characterised using XRD, impedance analyser, FESEM and VSM. At room temperature, a decrease in the imaginary part of the impedance (Z') was observed at higher frequency whereas at lower frequency, an increase was observed with increase in zinc content. An increase in relative dielectric permittivity (ε' and ε") with increase in frequency was observed and high dielectric constant was observed at lower frequency. Cole-Cole plot obtained at different temperatures show a transition from behaviour of semiconductor for samples having x=0 and x=1 to behaviour of insulator for sample having x=2 [92].

Y. Bai et al. (2009) studied the role of Mn substitution on the properties of Y-type hexagonal ferrite. The sample with chemical composition $Ba_2Zn_{0.8}Co_{0.8}Cu_{0.4}Fe_{12-x}Mn_xO_{22}$ was synthesized via solid-state reaction method and sintered at 1050℃. XRD results show that varying the content of manganese does not destroy the formation of Y-type hexagonal ferrite and FESEM micrographs indicate that the samples have dense microstructure and plate-like grains with homogenous size. Also, varying the amount of manganese does not change the permeability of the sample. From VSM analysis, it was observed that varying the amount of manganese does not change the coercivity and saturation magnetisation. However, the prepared samples show good frequency stability with no dielectric resonance in the frequency test range. The sample with manganese doping of x=0.4 can be used for multi-layer chip inductor (MLCI) [93].

I. Sadiq et al. (2014) employ sol-gel technique and synthesized nano-sized Ce-Zn doped X-type and investigated its microwave absorbance characteristics in X-band. The prepared sample was sintered at 1250℃ for 6 hours. XRD and FTIR analysis of all the samples indicate single phase hexagonal ferrites structure. FESEM micrographs show that the prepared samples exhibit hexagonal plate-like grains. The grains orient in such a way that high permeability is observed and consequently results in improved microwave absorbance characteristics. An increase in saturation magnetisation with increase in amount of doping was observed in VSM analysis. This is as a result of replacement of Sr^{2+} by Ce^{3+} which improves magnetic interaction by producing internal stress. Electrical resistivity analysis indicates that the resistivity of Ce-Zn substituted sample is greater than that of the pure sample, as high as $\approx 10^{9} \Omega cm$ value of resistivity was observed. The prepared sample can be used in multi-layer chip inductor (MLCI) and microwave absorbance application, and also in reducing eddy current losses [94].

Z. Yang et al. (2013) synthesized calcium copper titanate using sol-gel method. The prepared sample was characterized using XRD, FESEM, and impedance analyser. The role of sintering in air and in oxygen atmosphere on the dielectric and electrical properties of calcium copper titanate was investigated. Enhancement of activation energy for in grain electrical conduction results in reduced leakage, grain conductivity and the dielectric constant at low frequency for the sample sintered in oxygen atmosphere. The observed improvement of leakage under the influence of higher fields shows that the energy barrier for electrical transport is compensated by the strong electrical field [95].

J. Liu et al. (2007) used combustion and pyrolysis method to synthesize CCTO. The prepared samples were heat-treated at 600 °C, 700 °C, 750 °C and 800 °C for 1 hour and afterwards calcinated at 1030 °C and 1040 °C for 4 hours. The samples heat-treated at 600 °C, 700 °C and 750 °C show traces of TiO_2 (rutile), CuO and $CaTiO_3$. For the combustion method, the sample heat treated at 800 °C exhibit pure phase. FESEM images of the sample calcinated at 1030 °C shows grain sizes in the range 0.4 μm to 1.0 μm whereas the sample calcinated at 1040 °C show SEM images with large grain size (20 μm). For the pyrolysis method, the sample heat-treated at 800 °C exhibit some impurities which become absent after heat-treating the sample for another 1 hour. FESEM images of the sample calcinated at 1030 °C shows grain sizes in the range 0.5 μm to 1.5 μm whereas the sample calcinated at 1040 °C shows FESEM image with grain size of 3 μm. The dielectric constant of the sample prepared

using combustion method was found to be 159330 while that of the sample prepared by pyrolysis was found to be 39008. The difference in dielectric constant for the two different methods does not indicate that one method is better than the other because the dielectric constant of calcium copper titanate depends on the microstructure of prepared sample [96].

M. Wang et al. (2014) synthesized CCTO using non-hydrolytic sol-gel method. The method was developed to overcome the limitation of the traditional sol-gel method such as uncontrolled amount of water used during hydrolysis and dependence of quality of the prepared sample on pH. The sample was heat treated at 400 °C, 600 °C and 800 °C for 2 hours, the sample calcinated at 800 °C exhibit pure phase with no impurity. The synthesized sample was characterised using FT-IR, XRD, TGA/DSC, FESEM and LCR meter. No weight loss was observed after 350 °C in TG graph. FESEM micrograph shows particle size in the between 350 nm t0 450 nm. The maximum value of dielectric constant at 1 kHz is 1.40×10^5 whereas the maximum value of dielectric constant at 10 kHz is 1.39×10^5. The maximum value of dielectric loss is 0.1 for 1 kHz and 0.092. The temperature range considered is 30 °C to 110 °C [97].

A. K. Rai et al. (2012) study the effect of substitution of tantalum on the microstructures and dielectric properties of $CaCu_3Ti_4O_{12}$. The sample was sintered at 900 °C for 6 hours. XRD patterns confirmed the formation of CCTO with little traces of TiO_2 and CuO. FESEM micrograph shows morphology with faceted grain-packed, the grain size vary from 150 nm to 1 μm. EDX spectrum confirm the substitution of tantalum. Capacitance, resistance and dielectric constant increases with tantalum substitution [98].

A. K. Rai et al. (2011) doped calcium copper titanate with iron and studied its dielectric properties. The sample was prepared using semi-wet method. The sample was calcinated at 800 °C and afterwards sintered at 900 °C. XRD patterns of the sample calcinated at 800 °C show traces of CuO whereas that sintered at 900 °C exhibit pure phase. SEM images show dense non-homogenous microstructure comprising of many small grains having size in the range 1 μm to 5 μm and little large grains separated by fine grains. The doping of Fe^{3+} at Cu site significantly reduces the dielectric constant [99].

L. Liu et al. (2008) prepared CCTO ceramics using sol-gel method. The samples were cold pressed into pellets and sintered at relatively low temperature and short sintering time as compared to solid state reaction method. The samples were first calcinated at 900 °C and then

sintered at 1040 °C for 3 hours and 30 hours. Three samples were studied, they are (1) sample A: calcinated at 900 °C only, (2) sample B: calcinated at 900 °C and sintered at 1040 °C for 3 hours and (3) sample C: calcinated at 900 °C and sintered at 1040 °C for 30 hours. XRD patterns show pure phase of CCTO in sample B and C whereas sample A shows TiO_2, CuO and $CaTiO_3$ phases. FESEM micrograph of sample B shows duplex microstructure with grain size of 30 μm and isolated regions of fine grains with size less than 3 μm while that of sample C show uniform microstructure grain size approximately 22 μm and some bigger grains of 40 μm. Both sample B and C show similar dielectric properties. The permittivity of sample B is approximately 30,000 whereas that of sample C is approximately 60,000. This improvement in permittivity is attributed to the difference in microstructure and lattice parameters of the samples [100].

L. Liu et al. (2007) studied the heterogeneity of electrical properties of undoped calcium copper titanate prepared by sol-gel method. The sample was pre-sintered at 900 °C for 2 hours. Sintering of the sample was done at 1060 °C for 48 hours. XRD pattern of the sample sintered at 1060 °C for 48 hours exhibit pure phase of CCTO ceramics. FESEM micrograph of the sample sintered at 1060 °C for 48 hours indicate that grain growth with duplex microstructure comprising of large grains of size 100 μm. The isolated regions show fine grains of size less than 10 μm. Dielectric measurement show that the dielectric constant is greater than 28.000 over the frequency range 100 Hz to 100 kHz. This giant dielectric constant is attributed to the presence of thin re-oxidized grain boundaries on the outer surface of large semiconducting grains of the sample or possibly to a secondary phase at the grain boundary region [101].

S. Chang et al. (2012) substituted cerium in M-type hexagonal ferrites and studied its microwave absorption properties. Two samples ($BaFe_{12}O_{19}$ and $BaCe_{0.05}Fe_{11.95}O_{19}$) were prepared by sol-gel method. The samples were calcinated at 800 °C and characterised using XRD and VNA. XRD patterns show the formation of pure M-type hexagonal ferrites with proper substitution of the dopant. The lattice constant of $BaCe_{0.05}Fe_{11.95}O_{19}$ was found to be $a = 5.8947$ Å and $c = 23.2943$ Å which is a little bit larger than that of $BaFe_{12}O_{19}$. The variation was attributed to the difference in ionic radius of Ce^{3+} and Fe^{3+} which is 1.034 Å and 0.645 Å respectively. Microwave absorption studies were carried out in the frequency range 8 to 13 GHz. The real part of permittivity (ε') of $BaCe_{0.05}Fe_{11.95}O_{19}$ was found to increase with increase in frequency whereas a broad peak of value 1.73 at 12 GHz was

observed in the curve of ε′′. The values of μ′ of $BaCe_{0.05}Fe_{11.95}O_{19}$ shows an increase behaviour with frequency whereas the values of μ′′ increases up to 0.969 at 9.9 GHz and then decreases. A minimum reflection loss of -37.4 dB at a frequency of 12.8 GHz and matching thickness of 3.5 mm was observed. This shows that $BaCe_{0.05}Fe_{11.95}O_{19}$ is a good microwave absorber material [102].

N. Zhang et al. (2016) employ facile temperature-free solvothermal approach coupled with thermal treatment procedure and synthesized nanocomposite consisting of hollow microspheres of $ZnFe_2O_4$, SiO_2 and reduced graphene oxide. The microwave absorption studies were carried out in the frequency range 2-18 GHz. Four different sample of the composite was prepared; they are $ZnFe_2O_4$, $ZnFe_2O_4/SiO_2$, $RGO/ZnFe_2O_4$, and $RGO/ZnFe_2O_4/SiO_2$. All the components of the composite were observed in the XRD patterns. SEM images show the hollow structure of the $ZnFe_2O_4$ with an irregular size of about 1μm. EDX spectra indicate the growth of SiO_2 on the surface of the hollow microspheres of $ZnFe_2O_4$ and the presence of Zn, Fe, C, Si and O in the prepared sample. Raman spectra show the two characteristics peaks at 1340 cm^{-1} (D-band) and 1590 cm^{-1} (G-band). $RGO/ZnFe_2O_4/SiO_2$ composites exhibit the highest reflection loss of -45.8 dB at a frequency of 7.6 GHz and absorber thickness of 3.7 mm. Below -10 dB, the reflection loss of $RGO/ZnFe_2O_4/SiO_2$ composites covers the frequency range 3.5-18 GHz. Hence, the material can be used from S to K_u band. It was also observed that the dielectric losses are dominant at high frequency whereas the magnetic losses are dominant at low frequency [5].

Chapter 3

Research methodology

3.1 Introduction

In this research, we intend to use sol-gel method to synthesize and characterise hexaferrites and CCTO. Graphene oxide (GO) which is an insulator will be synthesized via the improved Hummer's method and subsequently reduced to reduced graphene oxide (rGO) to make it conducting. A suitable reducing method will be used for the reduction process. Structural, magnetic, and microwave absorption properties of hexagonal ferrites will be studied whereas structural and dielectric properties of cation-substituted and heat-treated CCTO will be investigated. Nanocomposite of pure and cation-substituted hexagonal ferrites, pure and cation-substituted and CCTO and rGO will be synthesized and characterized in order to study the microwave absorption properties.

3.2 Method of synthesis

3.2.1 Sol-gel autocombustion method

Sol-gel autocombustion method is a wet chemical method that is widely used in synthesizing nanomaterial. The popularity and wide acceptance of this method is attributed to its great advantages over other methods of synthesis such as solid state reaction method, co-precipitation and hydrothermal method. The advantages of sol-gel autocombustion method includes better control of particle size and porosity, it is performed at a low temperature, complicated equipment are not required thereby making it a cheap method, high homogeneity and it can be used to synthesize thin film. The raw materials which are usually metal nitrates or alkoxides are usually dissolved in a liquid medium such as water, ethylene glycol or a suitable acid to form a colloidal suspension called the "sol" followed by aging and subsequent heating of the sol to get what is termed as the "gel", further heating or drying of the gel at higher temperatures evaporates the liquid medium and transform the gel into a "precursor". A sol is a colloid suspended in a liquid whereas a gel is a suspension that keeps its shape; Hence the name "sol-gel".

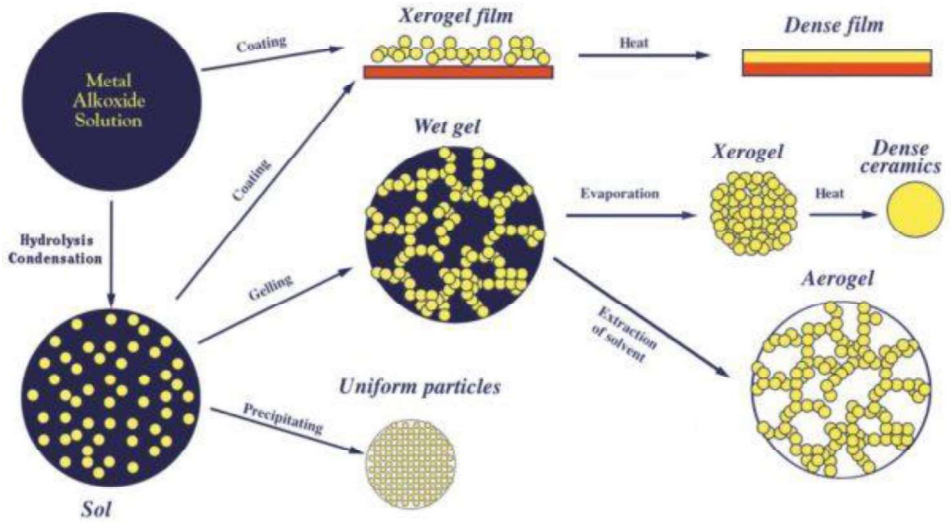

Fig. 3.1 Illustration of sol-gel auto-combustion technique

Sol-gel autocombustion method basically constitute of hydrolysis, condensation and polymerisation of monomers to form particles which later agglomerate followed by the formation of networks that extend throughout the liquid medium. This results in the formation of the solution which forms the gel (**Fig. 3.1**). Hydrolysis is the chemical breakdown of a compound as a result of reaction with water whereas condensation is the conversion of a gas or vapour to liquid. The description of hydrolysis and condensation is given below

Hydrolysis

$$MOR + H_2O \rightarrow MOH + ROH \qquad (3.1)$$

Condensation

$$MOH + ROM \rightarrow M{-}O{-}M + ROH \qquad (3.2)$$

3.2.2 Hummers method

GO is usually synthesized from graphite flakes or powder using Hummers method. Over the years, this method has witness some modifications (**Fig. 3.2**). The traditional Hummers method entails dissolving appropriate amount of graphite flakes in concentrated sulfuric acid (H_2SO_4) that is cooled to 0 °C in an ice bath as a measure of safety. While maintaining

vigorous stirring, appropriate amount of sodium nitrate ($NaNO_3$) and potassium permanganate ($KMnO_4$) is carefully added to the above solution in order to avoid raising the temperature of the solution above 20 °C. At this point, the solution is removed from the ice bath and heat is applied to the solution for 30 minutes at a temperature of 32 or 38 °C. The mixture gradually becomes thick and at the end of 20 minutes, the solution becomes brownish grey gel-like with the evolution of little amount of gas. Appropriate amount of water is slowly added to the brownish grey gel-like, the solution becomes brown with effervescence and increase in temperature to 98 °C. The solution is maintained at 98 °C for 15 minutes and then diluted with warm water to 14 litres and subsequently treated with 30% of hydrogen peroxide (H_2O_2) so as to reduce the residual permanganate and manganese dioxide to colourless and soluble manganese sulphate, the solution now turns light yellow. Filtering the solution gives a yellow-brown cake; the filtering is carried out while the solution is still warm so as to avoid precipitation of the metallic acid salt which is slightly soluble.

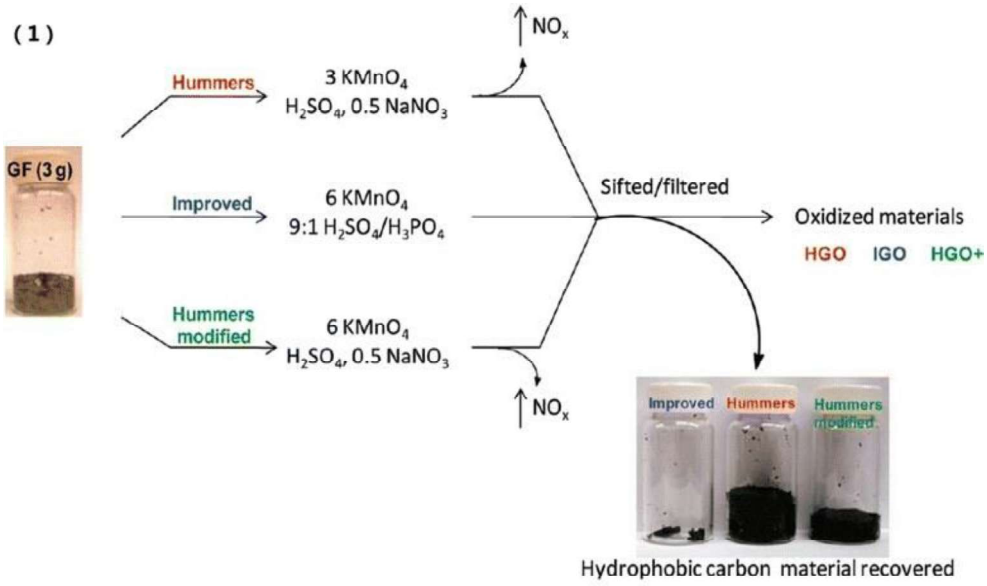

Fig. 3.2 Hummers' method, modified Hummers' method and improved Hummers' method

The yellow-brown cake is washed three times with 14 litres of warm water to obtain the graphene oxide and subsequent treatment with resinous cation and anion exchangers. Centrifugation and heating in vacuum at a temperature of 40 °C in the presence of phosphorus pentoxide give the dry graphene oxide [75]. Although the Hummers method has witness some modification over the years, but much of the original method is still retained. In the modified Hummers method, an additional process of oxidation was added in order to

facilitate complete oxidation of the graphite-core/graphene-oxide-shell particles to avoid its occurrence in the final product. Typically, an appropriate amount of graphite flake is dissolved in concentrated sulphuric acid (H_2SO_4) at a temperature of 80 °C followed by the addition of potassium persulfate ($K_2S_2O_8$) and phosphorus pentoxide (P_2O_5) thereby forming a dark-blue solution. Further, the solution is thermally isolated and allowed to cool at room temperature for duration of 6 hours. The solution is then diluted, filtered, and washed until the pH of the rinse water becomes neutral followed by drying at room temperature over night to form preoxidizes graphite powder which is subjected to Hummers method discussed above [76][77].

In 2010, D. C. Marcano et al. proposed an improved method of synthesis of graphene oxide (GO) which is called the "improved Hummers' method" [103]. The improved Hummers' method differs from both the traditional Hummers method and modified Hummers method in that it exclude sodium nitrate ($NaNO_3$), increases the amount of potassium permanganate ($KMnO_4$), introduce phosphoric acid (H_3PO_4) and mix it with concentrated sulfuric acid (H_2SO_4) in a ratio of 9:1. The main reason for this improvement is to improve the efficiency of the oxidation process. The following are the advantages of this method [104][105][106].

- The Graphene oxide (GO) produced with this method has more regular structure with fewer defects in the basal plane in comparison with graphene oxide (GO) synthesized using Hummers' method.
- It offers greater amount of hydrophilic oxidized graphene oxide (GO) in comparison to Hummers' method and modified Hummers' method.
- This method is simpler with high yield and no toxic gas evolution during synthesis.
- The Graphene oxide (GO) produced with this method show similar conductivity with that synthesized using Hummers' method after reduction.
- Possibility of good performance in technological application.

3.2.3 Synthesis of Ni^{2+}-La^{3+} substituted calcium copper titanate (CCTO)

Analytic reagent (AR) grade calcium nitrate [$Ca(NO_3)_2 \cdot 4H_2O$] was obtained from Central Drug House (CDH) whereas nickel nitrate [$Ni(NO_3)_2 \cdot 6H_2O$], cupric nitrate [$Cu(NO_3)_2 \cdot 3H_2O$], lanthanum nitrate [$La(NO_3)_3 \cdot 6H_2O$], titanium dioxide (TiO_2) and citric acid ($C_6H_8O_7$) were purchased from Loba Chemie. All chemicals have 99%-99.5% purity. CCTO ceramic with chemical composition $Ca_{0.9}Ni_{0.1}Cu_{2.9}La_{0.1}Ti_4O_{12}$ have been successfully synthesized using sol-gel technique. Appropriate amount of the chemicals were dissolved in

double distilled water in stoichiometric ratios to form an aqueous solution. The molar ratio of citric acid to cation was maintained at 1:1. The prepared solution was heated at a temperature of 80-100 °C. The solution was stirred using constant and continuous magnetic stirring in order to evaporate water; a light blue gel obtained which was transferred to a hot plate and heated at a temperature of 280-300 °C. This gives a black precursor material which was grounded with mortar and pestle to obtain a fine CCTO precursor which was pre-calcinated in a digital controlled muffle furnace at 800°C for 6 hours. The pre-calcinated powder was divided into four parts and labelled *T1*, *T2*, *T3* and *T4*. Furthermore, *T2*, *T3* and *T4* were further heated at 800°C, 900°C, and 1000°C for 6 hours respectively. The obtained product was crushed using mortar and pestle to obtain the fine CCTO ceramic powder followed by various characterizations. The Sample composition, heat treatment temperature, and sample composition of $Ca_{0.9}Ni_{0.1}Cu_{2.9}La_{0.1}Ti_4O_{12}$ are presented in **Table 3.1**.

Table 3.1 Sample composition, heat treatment temperature, and sample composition of $Ca_{0.9}Ni_{0.1}Cu_{2.9}La_{0.1}Ti_4O_{12}$

Sample code	Heat treatment temperature (°C)	Sample composition
T1	800	$Ca_{0.9}Ni_{0.1}Cu_{2.9}La_{0.1}Ti_4O_{12}$
T2	800/800	$Ca_{0.9}Ni_{0.1}Cu_{2.9}La_{0.1}Ti_4O_{12}$
T3	800/900	$Ca_{0.9}Ni_{0.1}Cu_{2.9}La_{0.1}Ti_4O_{12}$
T4	800/1000	$Ca_{0.9}Ni_{0.1}Cu_{2.9}La_{0.1}Ti_4O_{12}$

3.2.4 Synthesis of Pr^{3+}-Co^{2+} substituted calcium copper titanate (CCTO)

CCTO with chemical composition $Ca_{1-x}Pr_xCu_{3-y}Co_yTi_4O_{12}$ (x=0.0, 0.1, 0.2, 0.3 and y=0.0, 0.4, 0.5, 0.6) have been successfully synthesized via sol-gel method as presented in **Table 2**. Analytic reagent (AR) grade starting material such as calcium nitrate ($Ca(NO_3)_2{\cdot}4H_2O$, CDH), praseodymium nitrate ($Pr(NO_3)_3{\cdot}xH_2O$, CDH), cupric nitrate ($Cu(NO_3)_2{\cdot}3H_2O$, Loba Chemie), cobalt nitrate ($Co(NO_3)_2{\cdot}6H_2O$, Loba Chemie), titanium dioxide (TiO_2, Loba Chemie) and citric acid ($C_6H_8O_7$, Loba Chemie) with 99%-99.5% purity were used in the experiment. Stoichiometric amount of the starting materials were dissolved in double distilled water to form an aqueous solution. Citric acid was added to the aqueous solution with cations to citric acid molar ratio of 1:1. The prepared solution was heated at a temperature of 80-100 °C using constant and continuous magnetic stirring so as to evaporate water. After the

evaporation of the water, a light blue gel was formed which upon further heating at a temperature of 280-300 °C gives a black CCTO precursor material. Mortar and pestle was used to grind the precursor material into fine CCTO powder which was subjected to pre-sintering at a temperature of 800 °C for 6 hours in order to remove organic matter and impurities. Sintering of the prepared sample was carried out at 900 °C for 6 hours. The obtained product was crushed using mortar and pestle to obtain the fine CCTO ceramic powder. The sample composition and code of $Ca_{1-x}Pr_xCu_{3-y}Co_yTi_4O_{12}$ (x=0.0, 0.1, 0.2, 0.3 and y=0.0, 0.4, 0.5, 0.6) are presented in **Table 3.2**.

Table 3.2 Sample composition and code of $Ca_{1-x}Pr_xCu_{3-y}Co_yTi_4O_{12}$ (x=0.0, 0.1, 0.2, 0.3 and y=0.0, 0.4, 0.5, 0.6)

x	y	Sample composition	Sample code
0.0	0.0	$CaCu_3Ti_4O_{12}$	J1
0.1	0.4	$Ca_{0.9}Pr_{0.1}Cu_{2.6}Co_{0.4}Ti_4O_{12}$	J2
0.2	0.5	$Ca_{0.8}Pr_{0.2}Cu_{2.5}Co_{0.5}Ti_4O_{12}$	J3
0.3	0.6	$Ca_{0.7}Pr_{0.3}Cu_{2.4}Co_{0.6}Ti_4O_{12}$	J4

3.2.5 Synthesis of Ce^{3+}-Ni^{2+} substituted calcium copper titanate (CCTO)

Analytic reagent (AR) grade chemicals with high purity (99%-99.5%) are used as raw material for sol-gel synthesis of polycrystalline calcium copper titanate with chemical composition $Ca_{1-x}Ce_xCu_3Ti_{4-y}Ni_yO_{12}$ (x=0.0, 0.25, 0.45, 0.65 and y=0.0, 0.3, 0.5, 0.7). Stoichiometric amount of the raw materials such as $Ca(NO_3)_2{\cdot}4H_2O$ (CDH), $Ce(NO_3)_3{\cdot}xH_2O$ (CDH), $Cu(NO_3)_2{\cdot}3H_2O$ (Loba Chemie), $Ni(NO_3)_2{\cdot}6H_2O$ (Loba Chemie) and TiO_2 (Loba Chemie) were dissolved in 100 ml of double distilled to form an aqueous solution. Thereafter, citric acid was added to the aqueous solution with cations to citric acid molar ratio of 1:1. The prepared solution was placed on a hot plate and subjected to constant heating at a temperature of 80-100°C using continuous magnetic stirring in order to evaporate water. A light blue gel was formed which upon further heating at a temperature of 280-300°C gives a black precursor material. The precursor material was ground with mortar and pestle so as to obtain fine CCTO powder. Pre-sintering of the fine CCTO powder was carried out at a temperature of 800°C for 6 hours so as to remove organic matter and impurities. Furthermore, the sample

was sintered at 900°C for 6 hours. The sample composition and code of $Ca_{1-x}Ce_xCu_3Ti_{4-y}Ni_yO_{12}$ (x=0.0, 0.25, 0.45, 0.65 and y=0.0, 0.3, 0.5, 0.7) are presented in **Table 3.3**.

Table 3.3 Sample composition and code of $Ca_{1-x}Ce_xCu_3Ti_{4-y}Ni_yO_{12}$ (x=0.0, 0.25, 0.45, 0.65 and y=0.0, 0.3, 0.5, 0.7)

x	y	Sample composition	Sample code
0.0	0.0	$CaCu_3Ti_4O_{12}$	K1
0.25	0.3	$Ca_{0.75}Ce_{0.25}Cu_{2.6}Ni_{0.3}Ti_4O_{12}$	K2
0.45	0.5	$Ca_{0.55}Ce_{0.45}Cu_{2.5}Ni_{0.5}Ti_4O_{12}$	K3
0.65	0.7	$Ca_{0.35}Ce_{0.65}Cu_{2.3}Ni_{0.7}Ti_4O_{12}$	K4

3.2.6 Synthesis of Al^{3+}-Mn^{2+} substituted M-type strontium hexaferrites (heat-treatment)

We synthesized M-type strontium hexaferrites having chemical composition $Sr_{1-x}Al_xFe_{12-y}Mn_yO_{19}$(x=0.3 and y=0.6) using sol-gel auto combustion technique as in eqn. 3. The starting AR grade chemicals were $Sr(NO_3)_2$ (Loba Chemie; 99%), $Al(NO_3)_3{\cdot}9H_2O$ (Loba Chemie; 98%), $Fe(NO_3)_3{\cdot}9H_2O$ (Loba Chemie; 98%), $Mn(NO_3)_2{\cdot}xH_2O$ (Sigma Aldrich; 98%)and citric acid ($C_6H_8O_7{\cdot}H_2O$) (Loba Chemie; 99.5% purity). Appropriate amount of the chemicals were weighed separately in stoichiometric ratios and dissolved in distilled water. Citric acid was added taking care to ensure that cation to citric acid molar ratio stands at 1:1.5. Afterwards ammonia solution was added in drop wise manner to maintain a pH value of 7.00. The mixture was placed on a hot plate with constant and continuous magnetic stirring at 80-86℃ for 3-4 hours to evaporate the water and obtain the brown gel (viscous solution). The gel was place on a hot plate (at 280-300 °C) for 2 hours to completely remove the water and obtain the precursor material. Then the precursor material was heat-treated at varying temperatures (750 °C, 850 °C, 950 °C and 1050 °C).

$$(1-x)Sr(NO_3)_2 + xAl(NO_3)_3{\cdot}9H_2O + (12-y)Fe(NO_3)_3{\cdot}9H_2O + yMn(NO) + NH_4OH + heat \rightarrow Sr_{1-x}Al_xFe_{12-y}Mn_yO_{19} \quad (3.3)$$

3.2.7 Synthesis of Al^{3+}-Mn^{2+} substituted M-type strontium hexaferrites

We have successfully used high purity analytic grade reagent and synthesized M-type strontium hexagonal ferrites $Sr_{1-x}Al_xFe_{11.4}Mn_{0.6}O_{19}$ (x=0.0, 0.1, 0.2) using sol-gel auto

combustion technique. The starting materials include strontium nitrate ($Sr(NO_3)_2$, LOBA Chemie), aluminium nitrate ($Al(NO_3)_3{\cdot}9H_2O$, LOBA Chemie), ferric nitrate ($Fe(NO_3)_3{\cdot}9H_2O$, LOBA Chemie), manganese nitrate ($Mn(NO_3)_2{\cdot}xH_2O$, Sigma Aldrich), and citric acid ($C_6H_8O_7$, LOBA Chemie). The starting materials are used without further purification. Appropriate amount of the starting materials was weighed in stoichiometric ratios and dissolved in distilled water to form the salt solution. Required amount of citric acid was added to the salt solution with molar ratio of cations to citric acid maintained at 1:1.5. Ammonia was added drop wise until the pH of the salt solution reached 7.00. The solution was placed on a hot plate and subjected to heating and constant and continuous magnetic stirring at 80-100 °C in order to evaporate the water. The solution turned into brown gel which is then placed on another hot plate and heated at temperature of 280-300℃ so as to evaporate the water completely and obtain the precursor material. The precursor material was pre-sintered at 300 for 2 and then sintered at heat-treated at four different temperatures 950 °C for 5 hours.

3.2.8 Synthesis of Dy^{3+}-Cr^{3+} substituted M-type barium hexaferrites

Sol-gel method was used to synthesize M-type barium hexaferrites with chemical composition $Ba_{1-x}Dy_xFe_{12-y}Cr_yO_{19}$ (x=0.0, 0.1, 0.2, and y=0.0, 0.4, 0.5) as presented in **Table 3.4**. The starting materials used were of analytic reagent grade such as $Ba(NO_3)_2$ (Loba Chemie),$Cr(NO_3)_3{\cdot}9H_2O$ (Loba Chemie), $Fe(NO_3)_3{\cdot}9H_2O$ (Loba Chemie), $DyN_3O_9{\cdot}xH_2O$ (Sigma-Aldrich), and citric acid (Loba Chemie) having 98-99% purity. Stoichiometric amount of the starting were weighed and dissolved in water to form the salt solution, required amount of citric acid was added to the salt solution with cations to citric acid molar ratio maintained at 1:1.5 respectively. Ammonia solution was added drop wise to adjust the pH of the salt solution to 7.00. The solution was placed on a magnetic stirrer and stirred at 80-100 °C, much of the water was evaporated and a brown gel was formed which upon further heating at 280-300 °C gives the precursor material. The precursor material was pre-sintered at 400 ℃ for 3 hours and sintered at 950 ℃ for 5 hours.

Table 3.4 Sample composition and code for $Ba_{1-x}Dy_xFe_{12-y}Cr_yO_{19}$ (x=0.0, 0.1, 0.2, and y=0.0, 0.4, 0.5)

x	y	Sample composition	Sample code
0.0	0.0	$BaFe_{12}O_{19}$	B1

0.1	0.4	$Ba_{0.9}Dy_{0.1}Fe_{11.6}Cr_{0.4}O_{19}$	B2
0.2	0.5	$Ba_{0.8}Dy_{0.2}Fe_{11.5}Cr_{0.5}O_{19}$	B3

3.2.9 Synthesis of Cu^{2+}-Er^{3+} substituted M-type strontium hexaferrites

The starting materials include analytical grade chemicals such as strontium nitrate [$Sr(NO_3)_2$, LOBA Chemie], cupric nitrate [$Cu(NO_3)_2.3H_2O$, LOBA Chemie], ferric nitrate [$Fe(NO_3)_3.9H_2O$, LOBA Chemie], erbium nitrate [$Er(NO_3)_3.5H_2O$, CDH], and citric acid [$C_6H_8O_7$, LOBA Chemie] with 99%-99.5% purity. Nanocrystalline M-type strontium hexaferrites with chemical composition $Sr_{1-x}Cu_xFe_{12-y}Er_yO_{19}$ (x=0.0, 0.1, 0.2, and y=0.0, 0.4, 0.5) have been synthesized via sol-gel autocombustion technique as presented in **Table 3.5**. Required amount of the starting materials were weighed in stoichiometric ratios and dissolved in a beaker containing distilled water to form the aqueous solution, citric acid was added to the aqueous solution keeping the molar ratio of cation to citric acid at 1:1.5 respectively. The pH of the aqueous solution was adjusted to 7.00 by the addition ammonia solution followed by magnetic stirring at 80-100 °C so as to evaporate the water. After sometime, the water was evaporated and a brown gel was formed which upon further heating at 280-300 °C results in autocombustion thereby giving the precursor material which was pre-sintered at 400 ℃ for 3 hours and sintered at 950 ℃ for 5 hours.

Table 3.5 Sample code and composition for $Sr_{1-x}Cu_xFe_{12-y}Er_yO_{19}$ (x=0.0, 0.1, 0.2, and y=0.0, 0.4, 0.5)

x	y	Sample composition	Sample code
0.0	0.0	$SrFe_{12}O_{19}$	H1
0.1	0.4	$Sr_{0.9}Cu_{0.1}Fe_{11.6}Er_{0.4}O_{19}$	H2
0.2	0.5	$Sr_{0.8}Cu_{0.2}Fe_{11.5}Er_{0.5}O_{19}$	H3

3.2.10 Synthesis of Pr^{3+}-Co^{2+} substituted M-type strontium hexaferrites

The starting materials include analytic reagent grade chemicals such as strontium nitrate ($Sr(NO_3)_2$, LOBA Chemie), praseodymium nitrate ($Pr(NO_3)_3{\cdot}6H_2O$, Sigma Aldrich), ferric nitrate ($Fe(NO_3)_3{\cdot}9H_2O$, LOBA Chemie), cobalt nitrate ($Co(NO_3)_2{\cdot}6H_2O$, LOBA Chemie), and citric acid ($C_6H_8O_7$, LOBA Chemie) with purity between 99% to 99.5%. Nano-sized M-

type strontium hexaferrites having chemical composition $Sr_{1-x}Pr_xFe_{12-y}Co_yO_{19}$ (x=0.0, 0.2, 0.4 and y=0.00, 0.15, 0.35) have been synthesized using sol-gel autocombustion technique [107]. Stoichiometric amount of the starting materials were weighed and dissolved in a beaker containing double distilled water to form the aqueous solution, citric acid was added to the aqueous solution keeping the molar ratio of cation to citric acid at 1:1.5 respectively. The pH of the aqueous solution was adjusted to 7.00 using ammonia solution. The resulting solution was placed on a magnetic stirrer at 80-100 °C in order to evaporate water and form a viscous brown gel. Furthermore, the brown gel was transferred to a hot-plate and heated at 280-300 °C until the occurrence of autocombustion coupled with the emission of volatile gases such as NH_3, HNCO, and N_2 to give the precursor material. The precursor material was pre-sintered at 400 ℃ for 3 hours and sintered at 950 ℃ for 5 hours. **Table 3.6** shows the sample composition and their codes. The assumed chemical reaction is written below as

$$(1-x)Sr(NO_3)_2 + xPr(NO_3)_3{\cdot}6H_2O + (12-y)Fe(NO_3)_3{\cdot}9H_2O + yCo(NO_3)_2{\cdot}6H_2O + NH_4OH + heat \rightarrow Sr_{1-x}Pr_xFe_{12-y}Co_yO_{19} \quad (3.4)$$

Table 3.6 Sample composition and code for $Sr_{1-x}Pr_xFe_{12-y}Co_yO_{19}$ (x=0.0, 0.2, 0.4 and y=0.00, 0.15, 0.35)

x	y	Sample composition	Sample code
0.00	0.00	$SrFe_{12}O_{19}$	S1
0.20	0.15	$Sr_{0.8}Pr_{0.2}Fe_{11.85}Co_{0.15}O_{19}$	S2
0.40	0.35	$Sr_{0.6}Pr_{0.4}Fe_{11.65}Co_{0.35}O_{19}$	S3

3.2.11 Synthesis of barium hexaferrites and calcium copper titanate (BaM/CCTO) nanocomposites

The reagents are of analytic grade and include barium nitrate [$Ba(NO_3)_2$, LOBA Chemie], cobalt nitrate [$Co(NO_3)_2{\cdot}6H_2O$ LOBA Chemie], ferric nitrate [$Fe(NO_3)_3{\cdot}9H_2O$, LOBA Chemie], dysprosium nitrate [$DyN_3O_9{\cdot}xH_2O$, Sigma Aldrich], lanthanum nitrate [$La(NO_3)_3{\cdot}6H_2O$, Sigma Aldrich], calcium nitrate [$Ca(NO_3)_2{\cdot}4H_2O$, CDH], erbium nitrate [$Er(NO_3)_3{\cdot}5H_2O$, CDH], cupric nitrate [$Cu(NO_3)_2{\cdot}3H_2O$, LOBA Chemie], titanium dioxide (TiO_2, LOBA Chemie), manganese nitrate [$Mn(NO_3)_2.xH_2O$, Sigma Aldrich], ethylene glycol

[$C_2H_6O_2$, LOBA Chemie], and citric acid [$C_6H_8O_7$, LOBA Chemie] with purity in the range 99 to 99.5%.

AR grade reagents were used to synthesize Co^{+2}-Dy^{+3}-La^{+3} substituted BaM with chemical composition $Ba_{1-x}Co_xFe_{12-x-y}Dy_xLa_yO_{19}$ (x=0.0, 0.1, 0.2, 0.3 and y=0.0, 0.4, 0.5, 0.6) using sol-gel autocombustion method (**Table 3.7**). Stoichiometric amount of the reagents were weighed and poured in a beaker containing ethylene glycol, appropriate amount of citric acid was weighed and added to the beaker. The molar ratio of cations to citric acid kept at 1:1.5. Ammonia was added drop wise until the pH of the salt solution reached 7.00. The solution was heated on a hot plate at constant and continuous magnetic stirring at 80-100 °C; brown gel was formed after 3 hours which upon further heating at 280-300 °C gives the BaM precursor which was calcinated at 1000 °C for 7 hours.

Table 3.7 Sample code of Co^{2+}-Dy^{3+}-La^{3+} substituted BaM nanoparticles

x	y	Sample composition	Sample code
0.0	0.0	$BaFe_{12}O_{19}$	BaM1
0.1	0.4	$Ba_{0.9}Co_{0.1}Fe_{11.5}Dy_{0.1}La_{0.4}O_{19}$	BaM2
0.2	0.5	$Ba_{0.8}Co_{0.2}Fe_{11.3}Dy_{0.2}La_{0.5}O_{19}$	BaM3
0.3	0.6	$Ba_{0.7}Co_{0.3}Fe_{11.1}Dy_{0.3}La_{0.6}O_{19}$	BaM4

Similarly, Er^{+3}-Mn^{+2} substituted CCTO with chemical composition $Ca_{1-x}Er_xCu_3Ti_{4-y}Mn_yO_{12}$ (x=0.0, 0.1, 0.2, 0.3 and y=0.0, 0.4, 0.5, 0.6) was successfully synthesized using sol-gel auto combustion technique. Stoichiometric amount of the reagents were dissolved in double distilled water to form the salt solution. Required amount of citric acid was added to the aqueous solution with 1:1 molar ratio of cations to citric acid. The salt solution was heated at 80-100°C on a hot plate magnetic stirrer so as to evaporate water and obtained a light blue gel which upon further heating at a temperature of 280-300°C ignite and undergo auto-combustion thereby producing a black CCTO precursor. Fine CCTO powder was obtained by grinding the CCTO precursor with mortar and pestle and pre-sintered at 800 °C for 7 hours and sintered at 1000 °C for 7 hours.

Table 3.8 Sample code of Er^{3+}-Mn^{2+} CCTO microparticles

x	y	Sample composition	Sample code

0.0	0.0	$CaCu_3Ti_4O_{12}$	CCTO1
0.1	0.4	$Ca_{0.9}Er_{0.1}Cu_3Ti_{3.6}Mn_{0.4}O_{12}$	CCTO2
0.2	0.5	$Ca_{0.8}Er_{0.2}Cu_3Ti_{3.5}Mn_{0.5}O_{12}$	CCTO3
0.3	0.6	$Ca_{0.7}Er_{0.3}Cu_3Ti_{3.4}Mn_{0.6}O_{12}$	CCTO4

Required amount of BaM and CCTO nanoparticle were measured in the ratio 1:1 and mixed using mortar and pestle. The mixture was thoroughly blended for 15 minutes so as to obtain a homogeneous mixture of BaM/CCTO nanocomposite. The chemical compositions of the prepared BaM/CCTO nanocomposite are shown in **Table 3.9**.

Table 3.9 Sample code of BaM/CCTO nanocomposite

Sample code	Sample composition
BaMCCTO1	$BaFe_{12}O_{19}/CaCu_3Ti_4O_{12}$
BaMCCTO2	$Ba_{0.9}Co_{0.1}Fe_{11.5}Dy_{0.1}La_{0.4}O_{19}/Ca_{0.9}Er_{0.1}Cu_3Ti_{3.6}Mn_{0.4}O_{12}$
BaMCCTO3	$Ba_{0.8}Co_{0.2}Fe_{11.3}Dy_{0.2}La_{0.5}O_{19}/Ca_{0.8}Er_{0.2}Cu_3Ti_{3.5}Mn_{0.5}O_{12}$
BaMCCTO4	$Ba_{0.7}Co_{0.3}Fe_{11.1}Dy_{0.3}La_{0.6}O_{19}/Ca_{0.7}Er_{0.3}Cu_3Ti_{3.4}Mn_{0.6}O_{12}$

3.2.12 Synthesis of strontium hexaferrites, calcium copper titanate, and reduced graphene oxide (SrM/CCTO/rGO) nanocomposite

M-type strontium hexagonal ferrites $SrFe_{12-x}Cs_xO_{19}$ (x=0.0, 0.05, 0.10) have been successfully synthesized using sol-gel auto combustion technique as presented in **Table 3.10**. The starting materials include high purity strontium nitrate ($Sr(NO_3)_2$, LOBA Chemie), ferric nitrate ($Fe(NO_3)_3.9H_2O$, LOBA Chemie), cesium nitrate ($CsNO_3$, LOBA Chemie), and citric acid ($C_6H_8O_7$, LOBA Chemie). Required amount of the starting materials were weighed in stoichiometric ratios and dissolved in ethylene glycol to form the salt solution. The molar ratio of citric acid to metal nitrates was maintained at 1:1.5. Ammonia was added drop wise to adjust the pH of the solution to 7.00. The solution was heated on a hot plate with constant and continuous magnetic stirring at 80-100 °C for 3 hours in order to evaporate the water. A brown gel viscous solution was obtained which turned to fluffy precursor powder upon further heating at 280-300℃ for 30 minutes. The precursor material was calcinated at 1000 °C for 5 hours to obtain the desired hexagonal phase.

Table 3.10 Sample code of Cs^{3+}-substituted SrM nanoparticles

x	Sample composition	Sample code
0.00	$SrFe_{12}O_{19}$	SrM1
0.05	$SrFe_{11.95}Cs_{0.05}O_{19}$	SrM2
0.10	$SrFe_{11.90}Cs_{0.10}O_{19}$	SrM3

Sol-gel technique was used to synthesized calcium copper titanate $CaCu_3Ti_{4-y}Al_yO_{12}$ (y=0.0, 0.1, 0.2) using high purity AR grade starting material such as calcium nitrate ($Ca(NO_3)_2.4H_2O$), cupric nitrate ($Cu(NO_3)_2.3H_2O$, LOBA Chemie), aluminium nitrate ($Al(NO_3)_3.9H_2O$, LOBA Chemie) and titanium dioxide (TiO_2, LOBA Chemie) (**Table 3.11**). Stoichiometric amount of the starting materials were dissolved in double distilled water to form an aqueous solution. Citric acid ($C_6H_8O_7$, LOBA Chemie) was added to the aqueous solution with cations to citric acid molar ratio of 1:2. The prepared solution was subjected to constant heating and magnetic stirring on a hot plate at a temperature of 80-100 °C for approximately 3 hours in order to evaporate water. A light blue gel was formed which upon further heating at a temperature of 280-300 °C for 30 minutes to give a black CCTO precursor material. Mortar pestle was used to grind the CCTO precursor material into fine CCTO powder which was pre-sintered at temperature of 800 °C for 6 hours in order to remove organic matter and impurities. Furthermore, the obtained product was sintered at 1000 °C for 6 hours to give the final product.

Table 3.11 Sample code of Al^{3+}-substituted CCTO microparticles

x	Sample composition	Sample code
0.0	$CaCu_3Ti_4O_{12}$	CCT1
0.1	$CaCu_3Ti_{3.9}Al_{0.1}O_{12}$	CCT2
0.2	$CaCu_3Ti_{3.8}Al_{0.2}O_{12}$	CCT3

Graphite oxide was synthesized via improved Hummer's method [75][76]. Typically, Concentrated sulfuric acid (H_2SO_4, RANKEM) (300ml) was poured into a beaker containing a mixture of natural graphite powder (LOBA Chemie) (20 gm), potassium persulfate ($K_2S_2O_8$, MOLYCHEM) (10 gm), and phosphorus pentoxide (P_2O_5, CDH) (10 gm) at 80°C under vigorous magnetic stirring. The dark blue mixture obtained was thermally isolated and

allowed to cool to room temperature followed by dilution with double distilled water. The resulting mixture was filtered and washed with double distilled water. The product was left to dry at room temperature, this gives the pre-oxidized graphite powder [76][77]. The pre-oxidized graphite (20 gm) was poured into a beaker containing concentrated sulfuric acid (H_2SO_4) (400 ml) in an ice bath under continuous magnetic stirring. Potassium permanganate ($KMnO_4$) (60 gm) was gradually added to the mixture under continuous magnetic stirring while keeping the temperature below 10°C, a thick viscous mixture was obtained. Additional sulfuric acid (H_2SO_4) (200 ml) was added to enable constant and continuous magnetic stirring, thereafter, the mixture was stirred for 2 hours. The resulting mixture was then heated to 40°C in a hot water bath and maintained at this temperature for 1 hour. The mixture was diluted with double distilled water and hydrogen peroxide (H_2O_2, LOBA Chemie) (60 ml) was added drop wise to the mixture under vigorous magnetic stirring. With the gradual addition of H_2O_2, the colour of the mixture gradually turned from dark brown into brilliant yellow which is as a result of the reduction of the residual permanganate and manganese dioxide to colourless soluble manganese sulphate [108]. The mixture was filtered and washed with a 5 litres solution of double distilled water and hydrochloric acid (HCl) in the ratio 1:10 so as to remove metal ions. The resulting product was dispersed in double distilled water (24 ml) and sonicated for 1 hours in order to exfoliate the residual graphite into sheets of graphene oxide (GO) [75][109]. The solution was filtered and dried in air at room temperature for 5 days.

Appropriate amount of GO was dispersed in double distilled water followed by the addition of ammonia solution to adjust the pH to 10, equivalent amount of Sodium dodecyl benzene sulfonate (SDBS) which is an anion surfactant was added to the GO dispersion. The GO dispersion was stirred for 15 minutes in order to obtain a homogeneous GO dispersion. Hydrazine monohydrate was added to the GO dispersion, the mixture was stirred for 1 hour to obtain the black reduced graphene oxide (rGO) dispersion. Required amount of SrM and CCTO were added to the rGO dispersion and stirred for 30 minutes. The mixture was subjected to sonication for 1 hour in order to exfoliate the any residual graphite and GO into sheets of rGO. The mixture was filtered and dried in air for 7 days. The sample composition and code of the SrM/CCTO/rGO nanocomposite are presented in **Table 3.12**

Table 3.12 Sample composition and code of SrM/CCTO/rGO nanocomposites

Sample code	Sample composition

SCR1	$SrFe_{12}O_{19}$/ $CaCu_3Ti_4O_{12}$/rGO
SCR2	$SrFe_{11.95}Cs_{0.05}O_{19}$/ $CaCu_3Ti_{3.9}Al_{0.1}O_{12}$/rGO
SCR3	$SrFe_{11.90}Cs_{0.10}O_{19}$/ $CaCu_3Ti_{3.8}Al_{0.2}O_{12}$/rGO

3.2.13 Synthesis of reduced graphene oxide, polyaniline, calcium copper titanate (rGO/PANI/CCTO) nanocomposites

High purity AR grade starting materials are used for sol-gel synthesis of CCTO with chemical composition $Ca_{1-x}Ce_xCu_3Ti_{4-y}Ni_yO_{12}$ (x=0.0, 0.25, 0.45 and y=0.0, 0.3, 0.5). Stoichiometric amount of the starting materials such as calcium nitrate, cerium nitrate, copper nitrate, nickel nitrate and titanium dioxide were dissolved in 100 ml of double distilled to form an aqueous solution. Thereafter, citric acid was added to the aqueous solution with cations to citric acid molar ratio of 1:1. The prepared solution heated on a hot plate (magnetic stirrer) at 80-100°C in order to evaporate water. A light blue gel was formed which upon further heating at a temperature of 280-300°C gives a black precursor material. The precursor material was grounded with mortar and pestle so as to obtain fine CCTO powder. Pre-sintering of the fine CCTO powder was carried out at a temperature of 800°C for 6 hours so as to remove organic matter and impurities. Furthermore, the samples were sintered at 900°C for 6 hours.

Polyaniline was synthesized via oxidative polymerization method. In this method, 23.28 gm of aniline monomer was gradually poured into 91. 15 ml of hydrochloric acid at 0 °C in an ice bath followed by addition of 40.47 gm ammonium persulphate dissolved in water. The solution was stirred for 1 hour after which distilled water was added. The solution was filtered and washed with distilled water and methanol. The sample was dried in an oven at 60 °C for 48 hours.

GO was synthesized using Hummer's method. Briefly, 10 gm of graphite powder was gradually poured into 260 ml of H_2SO_4 at 0 °C in an ice bath. 10 gm $NaNO_3$ and 30 gm $KMnO_4$ were gradually added and the mixture was stirred for 2 hours. The mixture was transferred to a hot water bath and warm at 40 °C for 1 hour. The mixture was then transferred to an ice bath and diluted with distilled water. H_2O_2 (30%) was gradually added and the mixture turned to bright yellow. The mixture was filtered and washed with HCl (10%) and dried at 40 °C in an oven. GO (4.4 g) was dispersed in double distilled water and

stirred for 10 minutes. Ammonia was added to adjust the pH of the solution to 10; this is labelled as solution A. Chitosan (4.4 g) was added into 500 ml beaker containing 250 ml of glacial acetic acid. The mixture was subjected to constant heating and magnetic stirring for 15 minutes at 100 °C. Thereafter, 150 ml of double distilled water was added to the mixture and stirred for 30 minutes; this is labelled as solution B. Now, solution B was added to solution A and the mixture was stirred for 30 minutes to obtain a homogenous mixture followed by the addition of hydrazine. The mixture was heated for 30 minutes at 100 °C. Thereafter, the mixture was filtered and dried for 24 hours at 60 °C. The rGO/PANI/CCTO nanocomposite was prepared via mechanical blending (**Table 3.13**). Briefly, the rGO, PANI and CCTO were mixed in a mortar and pestle in the ratio 1:1:1 respectively.

Table 3.13 Sample composition and code of rGO/PANI/CCTO nanocomposites

Sample code	Sample composition
RPC1	rGO/PANI/$CaCu_3Ti_4O_{12}$
RPC2	rGO/PANI/$Ca_{0.75}Ce_{0.25}Cu_3Ti_{3.7}Ni_{0.3}O_{12}$
RPC3	rGO/PANI$Ca_{0.55}Ce_{0.45}Cu_3Ti_{3.5}Ni_{0.5}O_{12}$

3.2.14 Synthesis of strontium hexaferrites, calcium copper titanate, and reduced graphene oxide rGO/SrM/CCTO nanocomposites

Co-substituted SrM with chemical composition $SrFe_{12-x}Co_xO_{19}$ (x=0.0, 0.1, 0.2) was synthesized using sol-gel autocombustion method. AR grade starting materials such as strontium nitrate, ferric nitrate, cobalt nitrate and citric acid have been used in the synthesis process without further purification. Briefly, stoichiometric amount of the starting materials were weighed and dissolved in ethylene glycol to form the salt solution, citric acid was added with cations to citric acid molar ratio as 1:1.5 respectively. Ammonia was added drop wise to adjust the pH of the salt solution to 7.00. The solution was heated on a hot plate with magnetic stirring at 80-100 °C to evaporate the water. A brown gel was obtained which was heated at 280-300 °C to give the precursor material. The precursor material was calcinated at 1000 °C for 7 hours.

Y-substituted CCTO with chemical composition $CaCu_{3-x}Y_xTi_4O_{12}$ (x=0.0, 0.1, 0.2) via sol-gel technique. Required amount of the starting materials such as AR grade calcium nitrate,

copper nitrate, yttrium nitrate and titanium dioxide were dissolved in double distilled to form the salt solution, citric acid was added to the salt solution with cations to citric acid molar ratio of 1:1 respectively. The salt solution was heated on a magnetic stirrer at 80-100°C so as to evaporate water. A light blue gel was obtained which upon further heating at 280-300°C gives a black CCTO precursor which was grounded with mortar and pestle. The precursor was pre-calcinated for 6 hours at 800°C followed by calcination for 6 hours at 900°C.

Graphene oxide (GO) was prepared via Hummer's method using graphite powder. The graphite powder (10 gm) was slowly poured into sulfuric acid (260 ml) at 0 °C in an ice bath. Sodium nitrate (10 gm) and potassium permanganate (30 gm) were carefully into the mixture, the mixture was stirred for 2 hours while maintaining the ice bath. The mixture was warmed at 40 °C for 1 hour in a hot water bath. Thereafter, the mixture was diluted with distilled water in an ice bath. Hydrogen peroxide (30%) was slowly added and the colour of the mixture turned to bright yellow. The mixture was filtered and washed with hydrochloric acid (10%) and dried at 40 °C in an oven.

GO (4.4 g) was poured into a 500 ml beaker containing double distilled water and stirred for 10 minutes. Ammonia solution was added to alter the pH of the solution to 10; this is labelled as solution 1. Chitosan (4.4 g) was poured into a 500 ml beaker containing 250 ml of glacial acetic acid. After 15 minutes of stirring at 100 °C, 150 ml of double distilled water was added to the mixture and stirred for 30 minutes; this is labelled as solution 2. Both solutions 1 and 2 were slowly mixed in a 1000 ml beaker and stirred for 30 minutes to obtain a homogenous. Hydrazine was slowly added to the mixture and heated for 30 minutes at 100 °C. The mixture was filtered and dried for 24 hours at 60 °C. Required amount of rGO, hexaferrites and CCTO in the ratio 1:1:1 respectively, were mechanically blended using mortar to obtain the rGO/SrM/CCTO nanocomposite (**Table 3.14**).

Table 3.14 Sample composition and sample code of rGO/SrM/CCTO nanocomposites

Sample code	Sample composition
R1	rGO/$SrFe_{12}O_{19}$/ $CaCu_3Ti_4O_{12}$
R2	rGO/$SrFe_{11.9}Co_{0.1}O_{19}$/ $CaCu_{2.9}Y_{0.1}Ti_4O_{12}$
R3	rGO/$SrFe_{11.8}Co_{0.2}O_{19}$/ $CaCu_{2.8}Y_{0.2}Ti_4O_{12}$

3.3 Characterisation techniques

In order to understand how the cation substitutions affect the properties of the prepared samples, we carry out different characterizations using various characterisation tools such as XRD, FTIR, Raman spectroscopy, FE-SEM, EDX, TEM, TGA/DTA/DTG, UV-vis NIR spectroscopy, Impedance analyser, VSM, VNA.

3.3.1 X-ray diffraction (XRD)

In 1912, Max von Laue observed that materials that are crystalline act as three-dimensional diffraction gratings for X-ray wavelengths analogous to the spacing between the planes of a crystal lattice. This gave birth to the study of structure of crystals and atomic spacing using X-rays in a process called X-ray powder diffraction (XRD). Additionally, XRD is basically used for identification of phase of a crystalline material coupled with information on dimensions of unit cell. XRD technique is based on the principle of constructive interference of cathode ray tube generated monochromatic X-rays and a crystalline sample (**Fig. 3.3**). These X-rays consist of different components with the most common being K_α and K_β. K_α partly consists of $K_{\alpha1}$ and $K_{\alpha2}$ with $K_{\alpha1}$ having double the intensity as $K_{\alpha2}$ and a slight shorter wavelength, the specific wavelengths are unique to a particular target material (Cu, Fe, Mo, Cr). Monochromatic X-rays required for diffraction are produced by filtering using foils or crystal monochrometers. The components $K_{\alpha1}$ and $K_{\alpha2}$ are very close in wavelength such that a weighted average of the two components is used. To record the spectra, these X-rays are collimated to concentrate at a certain spot and then focused on the sample to be studied. The sample interacted with the incident X-rays thereby producing constructive interference and a diffracted X-ray when Bragg's law (**Eqn. 3.5**) is satisfied

$$n\lambda = 2d\sin\theta \tag{3.5}$$

Where λ is the X-ray wavelength, d is the spacing between the lattices, and θ is the angle of diffraction. The diffracted X-rays are detected, counted and processed by the X-ray detector into signal to count rate and then output to a computer monitor. All possible diffraction directions of the lattice are attained by scanning the sample through a range of 2θ angles; this result in the recording of the XRD spectra which shows diffraction peaks representing specific hkl values. These diffraction peaks are converted to d-spacing and compared standard XRD patterns thereby enabling the identification of the sample since each mineral has a set of unique d-spacing. In this research, the XRD patterns of the synthesized samples

were obtained in the range 20°-80° using Cu-Kα radiation operating at 40 kV and 35 mA with step size 0.02° (Bruker AXS D8 advance diffractometer).

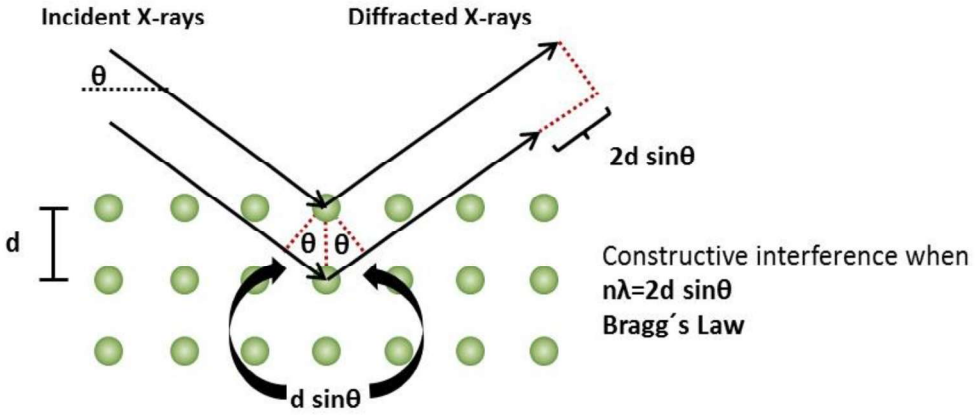

Fig. 3.3 Principle of X-ray diffractometer

3.3.2 Fourier transforms infrared spectroscopy (FTIR)

FTIR is a characterization technique used mostly for identifying compounds that are either organic or inorganic. The illustration of the principle behind this technique is presented in **Fig 3.4.** It can be used to determined and quantify some components of an unknown compound in the solid or liquid state. Depending on the range of wavelength, the infrared spectrum (IR) is divided into three region, namely near-infrared (14000 to 4000 cm^{-1}), mid-infrared (4000 to 400 cm^{-1}), and far-infrared (400 to 10 cm^{-1}). The low energy of the far-infrared can be used in the study of rotational vibrations, fundamental vibrations and associated rotations coupled with vibrational structure are studied via mid-infrared whereas the high energy of the near-infrared can be used to excite overtone or harmonic vibrations in experiments. FTIR utilise the mid-infrared (4000 to 400 cm^{-1}) spectrum. The interferometer used in FTIR has the capability to measure the entire mid-infrared frequencies in some seconds. It consists of a beam splitter that splits the incident IR radiation into two. One of the beams is made to remain at fixed path length in order to introduce a path difference in the other beam which is a function of a moving mirror position. The two beams undergo interference and a resultant beam known as interferogram is emitted from the interferometer. The interferogram entails all the information of the entire signal that comes out of the interferometer. This information is extracted from individual frequencies and decoded using software that comprises of a mathematical technique called Fourier transformation. In this research, Fourier transform

infrared (FTIR) spectrometer (Nicolet FTIR interferometer IR prestige-21(model-8400S)) was used to study the room temperature FTIR spectra which was recorded in the wavenumber range 4000 cm^{-1} and 400 cm^{-1} by making thin pellets of a mixture of KBr with the prepared sample in the ratio 10:1 respectively

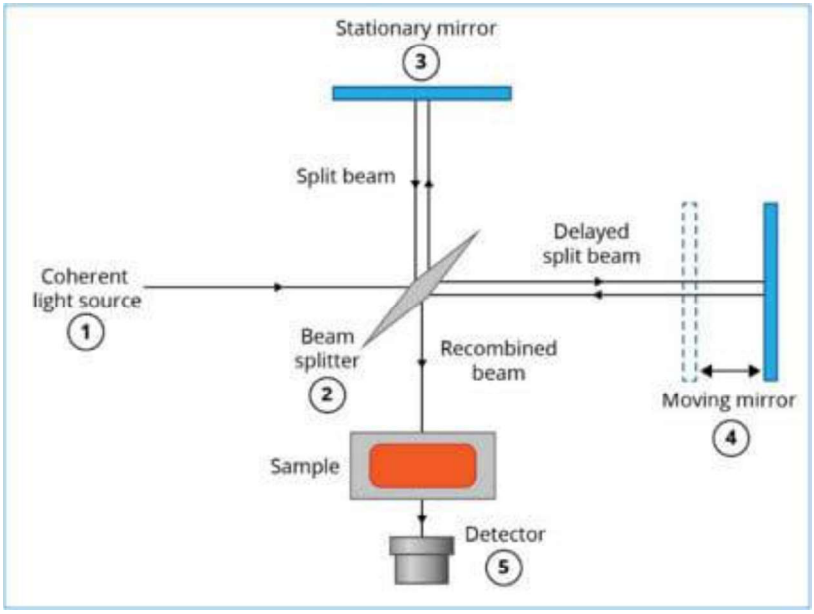

Fig 3.4 Principle of FTIR spectrometer

3.3.3 Raman spectroscopy

Raman spectroscopy is a type of molecular spectroscopy based on the Raman effect; this effect is observed via inelastic scattering of light. Additionally, Raman spectroscopy is based on the principle of Raman scattering which is defined as the absorption of photons having a specific frequency followed by scattering at a higher or lower frequency. Raman scattering is always accompanied by Rayleigh scattering which is defined as the scattering of light without change in frequency arising from scattering centres such as molecules (**Fig. 3.5**). This scattering process permits the interrogation, probing, and identification of vibrational states (phonon) of. Hence, Raman spectroscopy provides an indispensable analytical technique for identification of finger print and monitoring changes in molecular bond structure of atoms and molecules. Raman spectroscopy is advantageous compare to many other vibrational spectroscopy techniques such as FTIR. These advantages originate from the fact that the Raman effect establish itself when light is scattered off a sample as opposed to when light is absorbed by a sample as in FTIR. Therefore, Raman spectroscopy is not sensitive to aqueous

absorption bands and demand little to no preparation of sample prior to commencement of the experiment. This characteristic of Raman spectroscopy permit the direct analysis of solid, liquid, and gas through containers that is transparent such as quartz, glass, and plastic. The high selectivity of Raman spectroscopy allows it to detect and distinguish between molecules and chemical species that are very much similar in nature.

Raman spectrophotometer comprises of three main components, these include an apparatus for sampling, a source for excitation, and a detector. Even though these components have come in different form over the years, advanced Raman spectrophotometers uses a microscope or fibre optic as the apparatus for sampling, a laser as the excitation source, and a spectrometer as the detector. In this research, the Raman spectra were obtained on the STR 500 Confocal Micro-Raman spectrometer, AIRIS Japan (excitation wavelength: 532 nm).

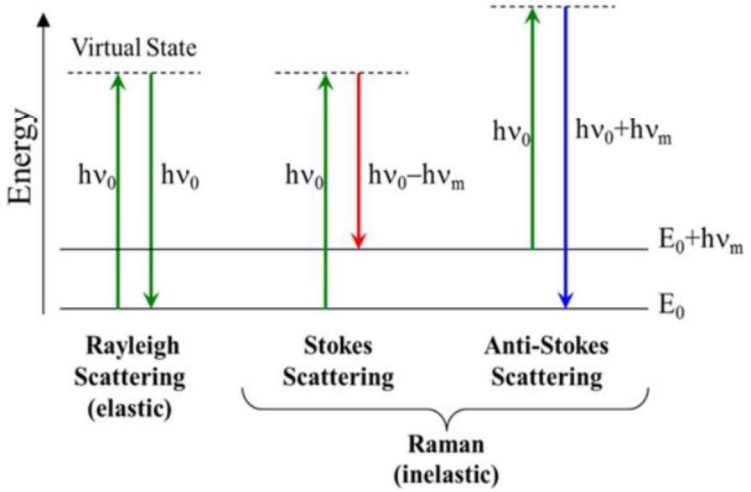

Fig. 3.5 Jablonski diagram of quantum energy transitions for Rayleigh and Raman scattering

3.3.4 UV-vis NIR spectroscopy

In atoms and molecules, the absorption of ultraviolet (UV) and visible radiation causes the excitation of electrons from lower to higher energy levels. The quantized nature of the energy levels in matter dictates that only radiation with specific amount of energy can be absorbed and consequently prompt the transition from one energy level to another. The larger the gap between the energy levels, the more the energy required to cause the transition. According to

Beer-Lambert's law (**Eqn. 3.6**), the absorbance (α) is directly proportional to the amount of the sample (c) and the path length of the absorbing medium (b)

$$\alpha = \log_{10}\left(\frac{I_0}{I}\right) = \varepsilon bc \tag{3.6}$$

Where I_0 is the intensity of the reference beam which should have experience little or no light absorption, I intensity of the sample beam, and ε is a constant of proportionality. The energy associated with UV radiation (200 to 400 nm) is enough to cause electronic excitations between molecular orbitals (ΔE). Generally, it is the energy difference between the highest occupied molecular orbital (HOMO) to the lowest unoccupied molecular orbital (LUMO). The smaller the ΔE, the lower the energy required to excite an electron. Naturally, frequency of incident quanta need to be lower or the wavelength required need to be longer. When the energy of the incident photon ≥ ΔE, the photon gets absorbed and an electron from an occupied level jumps from its ground state to an empty state.

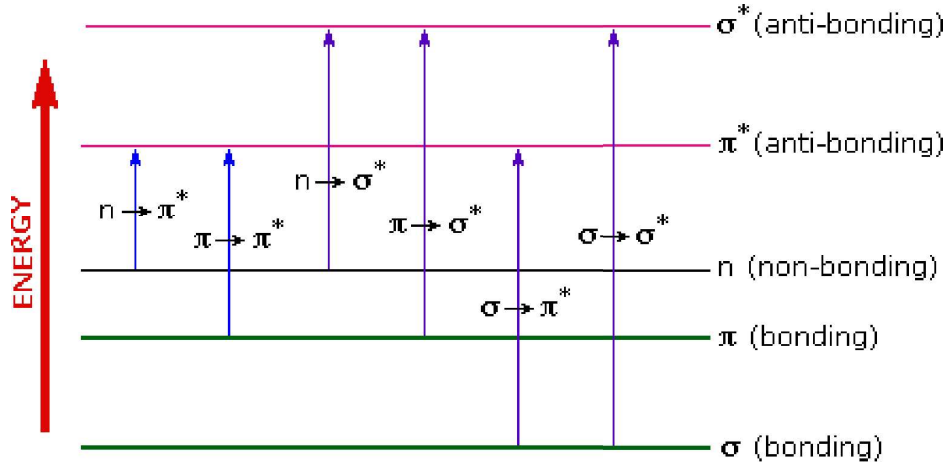

Fig 3.6 Electrons transitions in an atom or molecule

When light falls on a sample, it may be completely absorbed or reflected. However, only a part of the incident light is absorbed and the remaining is reflected. It is observed that the colour of a substance has a direct relationship with the electronic structure of the material. Hence, if UV or visible light causes electronic transition in an atom or molecule, a part of the energy of the incident light is absorbed. This absorption by an atom or molecule results in an electronic state of the atom or molecule of the material. The energy absorbed is responsible for promoting electrons from ground state to excited state orbitals or anti-bonding orbitals.

The following transitions are possible $\sigma - \sigma^*$, $\pi - \pi^*$, $\pi - \sigma^*$, $\sigma - \pi^*$, $n - \sigma^*$, and $n - \pi^*$ when light is absorbed as shown in **Fig. 3.6**. However, the possible transitions that can occur in UV-Vis spectroscopy are $\sigma - \sigma^*$, $n - \sigma^*$, $\pi - \pi^*$, and $n - \pi^*$ transitions. Of these transitions, $\sigma - \sigma^*$ and $n - \sigma^*$ transitions requires lot of energy and is therefore possible in the far UV region (lower wavelength region). Transitions from $\pi - \pi^*$ and $n - \pi^*$ occur in molecules with unsaturated centres as these requires less energy, hence, they occur at lower energy (higher wavelength region). In this research, the absorption spectra was recorded with UV-Vis-NIR Spectrophotometer (Varian, Cary 5000 with spectral range of 175 – 3300 nm)

3.3.5 Field emission scanning electron microscope (FE-SEM)

FE-SEM gives topographical and elemental information at magnifications of 10 times to 300,000 times with unlimited depth of field. In comparison with convention scanning electron microscopy (SEM), FE-SEM provides clearer images which are less electrostatically distorted and with spatial resolution which is three to six times better than conventional SEM. Furthermore, areas with smaller contamination spots can be examined at electron accelerating voltages compatible with Energy Dispersive X-ray Spectroscopy (EDX). The interaction of beams of electrons with a sample target results in a variety of emission of radiation such as X-rays. An EDX detector is used to distinguish the characteristic X-rays of various elements into an energy spectrum which is analysed using software so as to determine the amount of specific elements in the sample. In principle, an FE-SEM scans the sample under study with electrons instead of light. Under high vacuum, electrons are generated by a field emission source (electron gun) and accelerated via a field gradient (**Fig 3.7**). The beams pass through electromagnetic lenses and are focused onto the sample. As result of this focussing, various types of electrons are emitted from the sample. The secondary electrons are caught by a detector and an image of the surface of the sample is created by comparing the intensity of the secondary electrons to that of the scanning primary electron beam. Finally, the created image is displayed on a computer monitor. In this research, Field emission scanning electron microscope (FESEM) (JOEL, Model-JSM 7100F) used to study the morphology and elemental analysis.

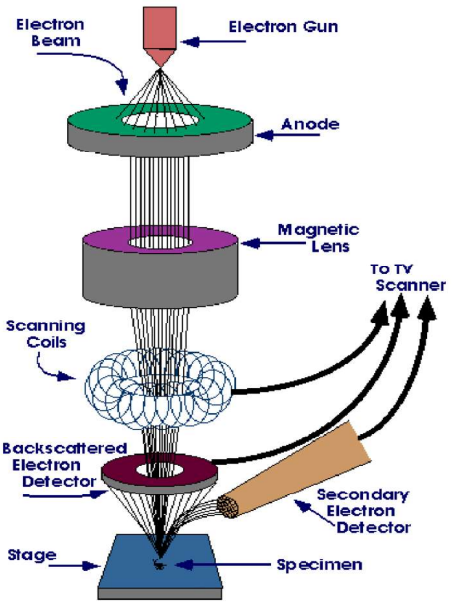

Fig 3.7 Working principle of field emission scanning electron microscope (FE-SEM)

3.3.6 Transmission electron microscope (TEM)

TEM is much similar to typical optical microscope. In TEM, a heated tungsten filament emits a beam of electrons which are then focussed on a very thin optically opaque specimen; some electrons are deflected while others pass through the specimen using electromagnetic lenses (**Fig 3.8**). After the electrons passes through the specimen, both the electrons that were deflected and those that were not are focussed again on the specimen by another set of electromagnetic lenses to produce an image on a fluorescent screen at the bottom of the TEM instrument. Advantages of TEM include high depth of field, high resolution, high magnification and diffraction pattern of micro constituents. In this research, transmission electron microscope (TEM) (JEOL, Model-JEM 2100) was used to study the surface features.

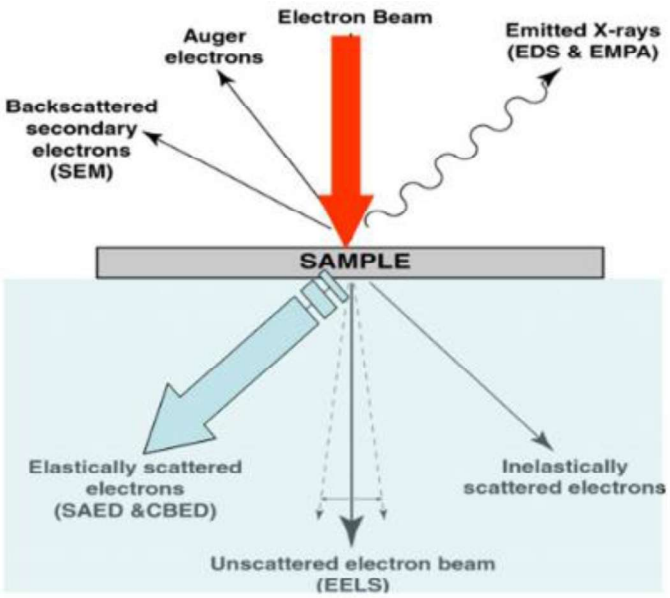

Fig 3.8 Working principle of transmission electron microscope (TEM)

3.3.7 Thermal Characterization

Thermal characterization techniques include thermo gravimetric analysis (TGA), differential thermal analysis (DTA), and derivative thermogravimetry (DTG). TGA is a technique that monitors the rate of change of a mass of a specimen as a function of temperature or isothermally as a function of time (**Fig 3.9**). The observed curve of the weight loss provides information thermal stability of the sample, changes in the composition of the sample, and chemical kinematics of the samples. Additionally, the point where weight loss occurs most and where it ceases to occur can be clearly observed in the curve. Weight loss occur when chemical bonds breaks apart (decomposition), volatile materials are evaporated at elevated temperatures (evaporation), sample interacts with an atmosphere that is reducing (reduction), and when absorbed substances are release from the sample (desorption or dying). Weight gain can also occur due to the interaction of the sample with an oxidizing atmosphere (oxidation) and when the sample holds molecules of liquid, gas, or solid in the form of a thin film (adsorption or absorption). DTA is technique in which a reference material and the sample under study are subjected to identical thermal cycles while observing any difference in temperature between the sample and the reference material against temperature or time, a graph of the differential temperature versus temperature is plotted from the obtained data. When the sample experiences change in energy as a result of certain chemical or physical phenomenon, a variation in the temperature profile of the sample and the reference material is

observed and subsequently this transition in temperature is identified. As an example, the temperature of the sample will lag behind the temperature of the reference materials when the sample undergoes melting. Endothermic and exothermic processes can be clearly observed relative to the inert reference. On one hand, physical phenomenon that my result in changes in heat and temperature as a result of exothermic processes include adsorption and crystallization whereas those that may result from endothermic processes include desorption, vaporization, melting, and sublimation. On the other hand, chemical phenomenon that my result in changes in heat and temperature as a result of exothermic processes include oxidation and chemisorption while endothermic processes causes reduction. Furthermore, changes in crystal structure, solid-state reaction and break-down reactions could result from endothermic or exothermic processes. DTG technique is also called differential scanning calorimetry (DSC). In this technique, the difference in the amount of heat required to raise the temperature of the sample and a reference sample are recorded. This technique can measure glass transition, heat of fusion and reaction, percentage crystallinity, melting and boiling point, crystallization temperature and time, purity of the sample, reaction kinetic, specific heat capacity, and oxidation and thermal stability. The heating can be carried (5, 10, or 15 °C) and maximum temperature could reach 1500 °C depending on the capacity of the furnace. The weight of the sample ranges from 1 to 150 mg although 10 mg is usually preferred. The thermal analysis was performed with simultaneous thermal analyser (STA 6000, Perkin Elmer) with minimum temperature 15 °C and maximum temperature 1000 °C.

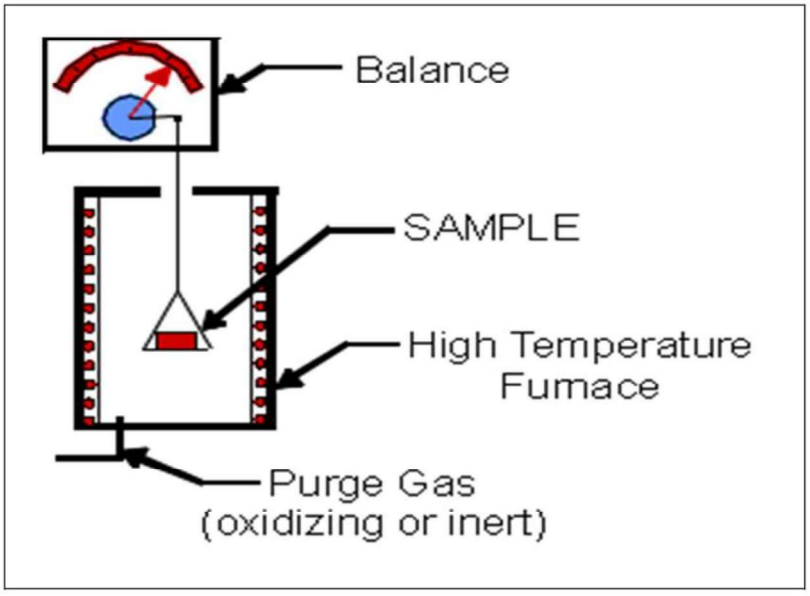

Fig 3.9 Working principle of thermal analysis instrument

3.3.8 Impedance analyser

An impedance analyser is an electronic instrument used in the measurement of impedance and admittance. The total opposition offered to the flow of periodic current (AC test signal) when voltage is applied to a circuit or device is called impedance. The periodic current consists of real and imaginary parts. When the connection is done in series, the impedance can be written as

$$Z = R + jX \tag{3.7}$$

Where j is an imaginary number, R is the resistance (i.e. real part of impedance) and X is the reactance (i.e. imaginary part of impedance). The measurement plane of the impedance can be taken with the resistance on the x-axis and the reactance on the y-axis. In general, AC voltage is applied to the device under test (DUT), the response of the DUT is measured in the form of impedance (Z), and capacitance (C). Also, the angle (θ) which the impedance (Z) make with the x-axis is measured. The obtained data such as impedance (Z), capacitance (C), and angle (θ) can be used to calculate various dielectric parameters such as real part of permittivity (ε'), imaginary part of permittivity (ε''), dielectric tangent loss ($\tan\delta$), and AC conductivity.

3.3.9 Vibrating sample magnetometer (VSM)

VSM is a device used to measure magnetic response of materials based on Faraday's law of electromagnetic induction which states that a changing magnetic field produces an electric field. The sample under study is placed in a sample holder which is then placed in between two sets of pick up coils that are attached to an electromagnet (**Fig 3.8**). A magnetization will be induced in the sample as a result of the uniformity of the magnetic field of the electromagnet. The sample holder with the sample inside it is made to mechanically undergo sinusoidal vibration. An electric field which is proportional to the magnetization is generated according to Faraday's law of electromagnetic induction when the vibrating component induces a change in the magnetic field of the sample. Variations in the magnetic flux induce a voltage in the pickup coils which is directly proportional to the magnetization of the sample. Software in a computer attached to the VSM equipment convert these changes into graph of magnetization (M) against the applied magnetic field (H).

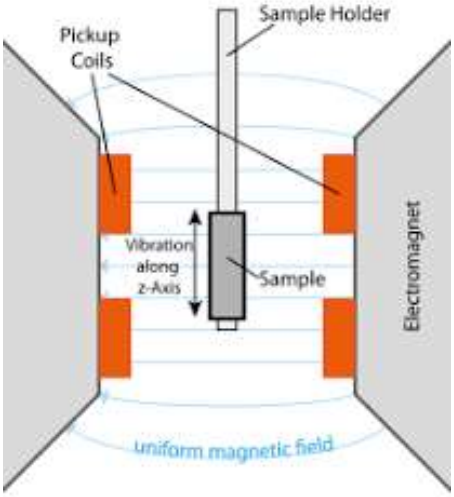

Fig. 3.10 Principle of vibrating sample magnetometer (VSM)

3.3.10 Mössbauer spectroscopy

Mössbauer spectroscopy is a spectroscopic technique that is based on the Mössbauer effect which is a recoil free emission and absorption gamma ray by atomic nuclei in a solid sample. A gamma ray can be absorbed by a nuclei when its energy is exactly the energy the difference between the ground state and the excite state of the nuclei since the nuclei exist only in certain definite energy levels, this is called resonance absorption.

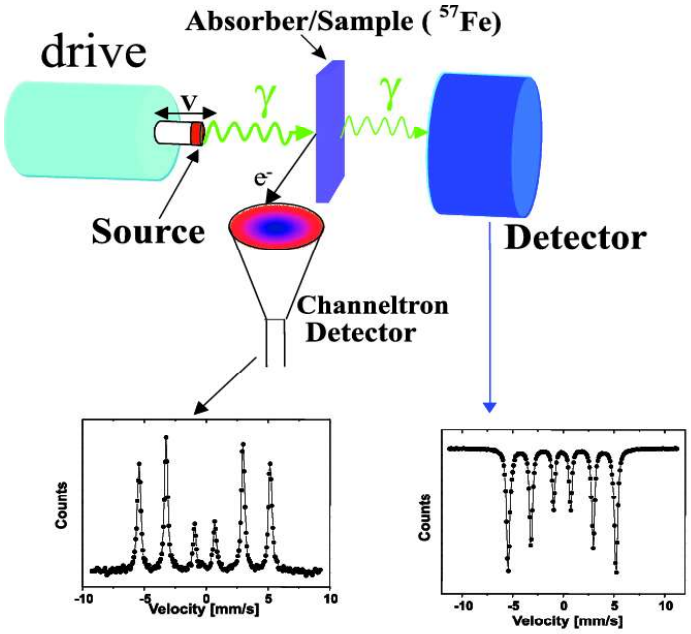

Fig. 3.11 Principle of Mössbauer spectroscopy

A Mössbauer spectroscopy setup consists of a gamma source, the sample, and the detector (**Fig 3.11**). In general, the gamma ray source is ^{57}Co (Cobalt nuclei) which is unstable, this cobalt nuclei usually decay to ^{57}Fe (Iron nuclei) which in turn decay to ground state by giving off a gamma ray that get absorbed by the sample in a resonant manner. The source of the gamma ray is usually made to undergo acceleration through varying velocities using a linear motor so that Doppler Effect is observed. A fraction of the gamma ray is absorbed when the source velocity corresponds to the resonant energy level of the sample and this result in the decreases in the intensity of the gamma ray. This situation is observed as a dip in the Mössbauer spectrum. The gamma ray produced is then scan through a given range of velocities for ^{57}Fe which is then detected by a detector. A computer attached to the detector provides a plot of the gamma ray intensity versus velocity of the source.

3.3.11 Vector network analyser (VNA)

Vector network analyser (VNA) is a device used to analyse different circuits in radio frequency (RF) engineering. When a VNA device is combined with one or more antennas, it can used as a radar system. To carry out radar analysis, the incident wave (I_i) must propagate from the analyser to the device under test (DUT). Since some of the wave is reflected, the reflected wave (I_r) travels in a direction opposite to the DUT and then back to the analyser. The reflection coefficient (R) is given as ratio of I_i and I_r (**Eqn. 3.8**)

$$R = \frac{I_i}{I_r} \tag{3.8}$$

Also, since R is in general a complex quantity, it can be calculated from complex impedance (Z)

$$R = \frac{Z-1}{Z+1} \tag{3.7}$$

Apart from the I_R, there is also the possibility of a transmitted wave (I_t) in both the forward and reverse directions. The scattering parameters which are also called the S parameters (S_{11}, S_{22}, S_{12}, S_{21}), can be thought of as the ratio of the respective wave quantities, these parameters can be used to calculate the reflection loss and determine the electromagnetic Shielding performance of the DUT.

Chapter 4

Results and discussion

4.1 Ni^{2+}-La^{3+} substituted calcium copper titanate (CCTO)

4.1.1 XRD analysis

XRD spectra of $Ca_{0.9}Ni_{0.1}Cu_{2.9}La_{0.1}Ti_4O_{12}$ CCTO ceramic are presented in **Fig. 4.1**. The observed diffraction peaks for the samples with *T1*, *T2*, and *T3* shows presence of $CaTiO_3$, CuO, and TiO_2 (anatase phase) secondary phase.

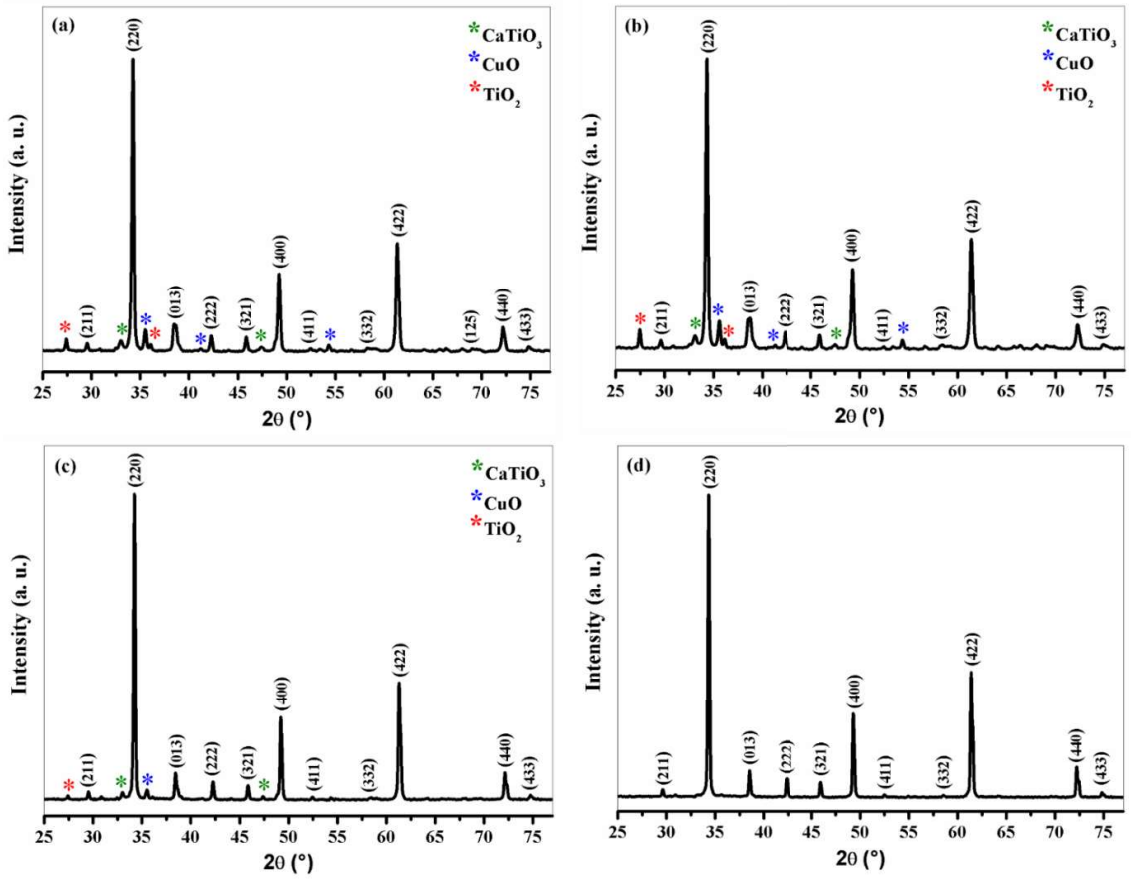

Fig. 4.1 XRD spectra of $Ca_{0.9}Ni_{0.1}Cu_{2.9}La_{0.1}Ti_4O_{12}$ (a) T1 (b) T2, (c) T3, and (d) T4

The lattice constant (a) and volume of the unit cell (V_{cell}) are respectively calculated using (4.1) and (4.2) and tabulated in **Table 4.1**.

$$a = d\sqrt{h^2 + k^2 + l^2} \tag{4.1}$$

$$V_{cell} = a^3 \quad (4.2)$$

where d is the inter planer spacing, *hkl* represents the miller indices. The full width at half maximum denoted by β (in radian) can be written as $\beta = (\beta_o^2 - \beta_i^2)^{1/2}$ where β_o is the width observed from the X-ray peaks and β_i is the width as a result of instrumental effects. Both the values of a and V_{cell} were found to increase with increase in calcination temperature (**Table 4.1, Fig. 4.3**), these values are in agreement with literatures [110]. Rietveld refinement using Fullproof software has been performed in order to refine the lattice parameters of the prepared samples. The peaks of the observed secondary phases were also observed in the Ritveld refined spectra (**Fig. 4.2**). Strikingly enough, the sample with *T4* exhibit the lowest R_p, R_{wp}, R_{exp}, and χ^2 value (**Table 4.1**), this is an indication of the level of ordered crystal structure in this sample as compare to the samples with *T1*, *T2*, and *T3*.

Table 4.1 Values of lattice constant (a), volume of unit cell (V_{cell}) *R*-factors (R_p, R_{wp}, and R_{exp}), and chi-square (χ^2) of $Ca_{0.9}Ni_{0.1}Cu_{2.9}La_{0.1}Ti_4O_{12}$ at different temperature

Sample code	*T1*	*T2*	*T3*	*T4*
$\boldsymbol{T}$ (°$\boldsymbol{C}$)	800	800/800	800/900	800/1000
$2\boldsymbol{\theta}$ *(°)*	49.259	49.209	49.159	49.109
d (Å)	1.8483	1.8501	1.8518	1.8536
$\boldsymbol{\beta}$ *(°)*	0.212	0.224	0.155	0.148
a (Å) (Eqn. 4.1)	7.3935	7.4005	7.4075	7.4146
a (Å) (Rietveld)	7.3953	7.3945	7.4002	7.4007
$\boldsymbol{V_{cell}}$ *(Å^3) (Eqn. 4.2)*	404.1538	405.3028	406.4606	407.6272
$\boldsymbol{V_{cell}}$ *(Å^3) (Rietveld)*	404.4524	404.3211	405.2569	405.3390
$\boldsymbol{R_p}$ (%)	19.10	15.90	9.34	7.58
$\boldsymbol{R_{wp}}$ (%)	23.1	21.5	12.4	8.75
$\boldsymbol{R_{exp}}$ (%)	7.60	6.02	5.95	5.76
$\boldsymbol{\chi^2}$	9.228	12.750	4.345	2.298
Observed Phase	CCTO $CaTiO_3$ CuO TiO_2	CCTO $CaTiO_3$ CuO TiO_2	CCTO $CaTiO_3$ CuO TiO_2	CCTO

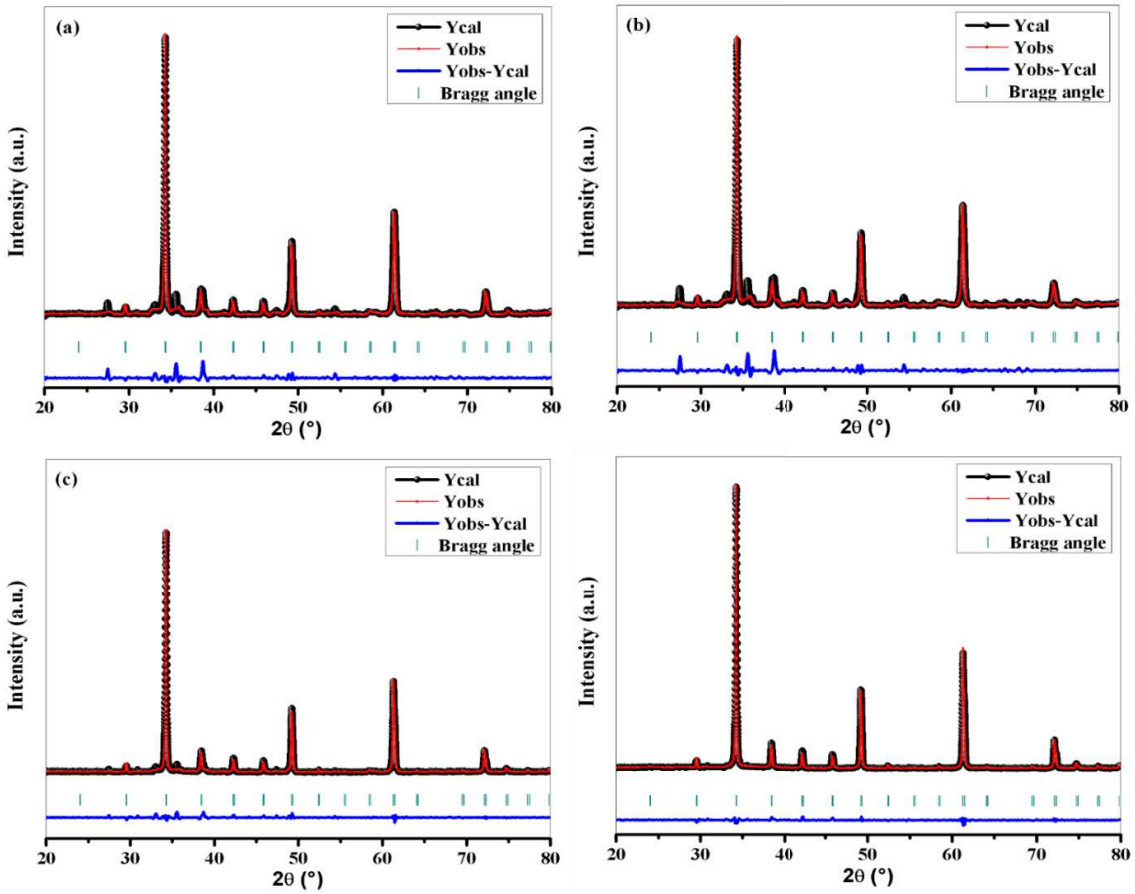

Fig. 4.2 Rietveld refinement of $Ca_{0.9}Ni_{0.1}Cu_{2.9}La_{0.1}Ti_4O_{12}$ (a) T1 (b) T2, (c) T3, and (d) T4

This observation is no surprise to us as the XRD spectra shows that the samples with *T1*, *T2*, and *T3* contain varying amount of these secondary phases which alter the structure these samples. As compared to *T1*, the intensity of the peaks of these secondary phases increases for the sample with *T2*. However, the peaks of these secondary phases start to decrease for the sample with *T3* and finally disappear for the sample with *T4*. This shows that a single phase of the prepared sample have been obtained at *T4*. The diffraction peaks for the sample with *T4* appear to be less broad as compared to the samples with *T1*, *T2*, and *T3*, this shows that the sample with *T4* is more crystalline in nature as compared to the samples with *T1*, *T2*, and *T3*. Hence, we can assume that increasing the calcination temperature enhances the purity and crystallinity of the prepared sample. The peaks of the sample with *T4* were found to match with the standard patterns of unsubstituted single phase CCTO ceramic (JCPDS 75-2188) having cubic perovskite structure with space group *Im*3 and *hkl* planes (211), (220), (013), (222), (321), (400), (411), (332), (422), (125), (440), and (433). Ritveld refinement analysis also confirms that the sample with *T4* exhibit cubic perovskite structure and belong

to the space group *Im*3. Thus, we can conclude that *T4* is the maximum temperature for the formation of pure crystalline CCTO phase via sol-gel autocombustion method using TiO_2 as source for Ti^{4+} ions. A. K. Rai et al. reported that the appearance of secondary phase in CCTO ceramics could be attributed to shortening of ion diffusion displacement in the sol-gel autocombustion method, presence of surplus Ti^{4+} ions in the sample since 4 Ti^{4+} ions are linked to 12 O^{2-} ions, absence of electronic compensation as a result of not ensuring charge neutrality during substitution of ions, slight decrease in the content of Cu^{2+} ions, and lack of solubility of the substituted ions [111][112]. However, since in our research the secondary phases disappear as the calcination temperature is increased, we suggest that the secondary phases appear as a result of inhomogeneity of the mixture of the started materials and/or incomplete crystallization reaction as a result of lack of sufficient calcination temperature [113]. Clearly, the XRD spectra show that the increase in calcination temperature enhances crystallinity and phase formation of the prepared samples.

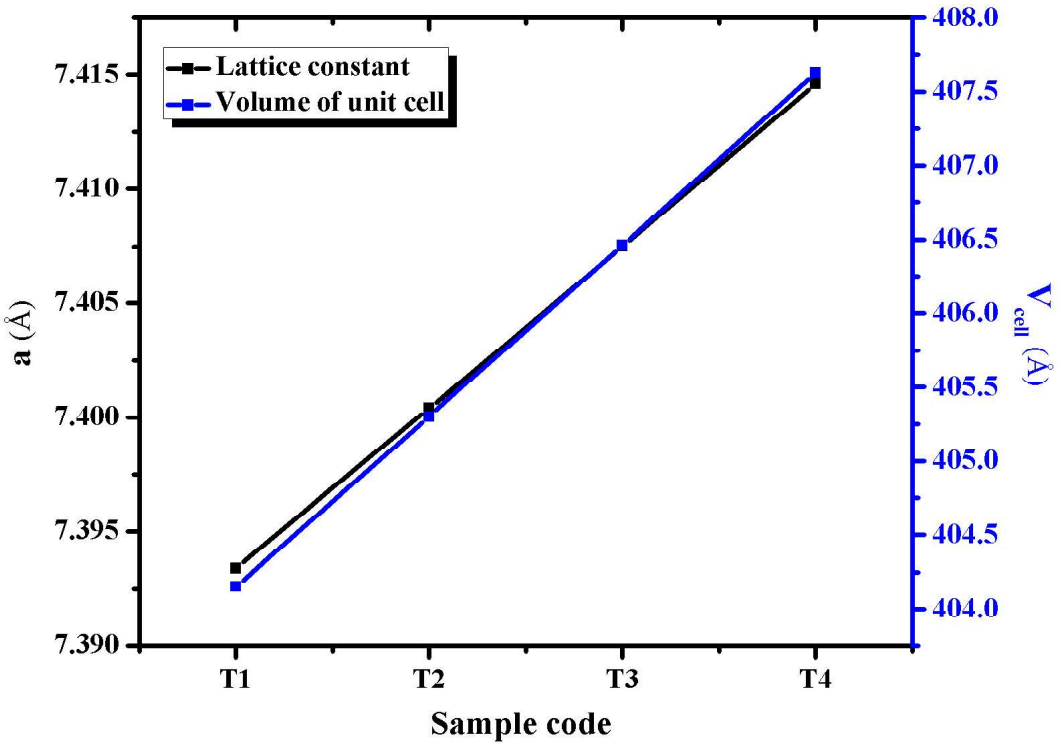

Fig. 4.3 Variation of lattice constant (a) and volume of unit cell (V_{cell}) with heat treatment temperature (T)

4.1.2 Thermal analysis

In order to determine the response of the un-heated precursor of $Ca_{0.9}Ni_{0.1}Cu_{2.9}La_{0.1}Ti_4O_{12}$ to variation in temperature, we carry out simultaneous thermo gravimetric analysis (TGA), differential thermal analysis (DTA) and derivative thermogravimetry (DTG) analysis from room temperature to 950 °C. The simultaneous TGA plot of the un-heated precursor of $Ca_{0.9}Ni_{0.1}Cu_{2.9}La_{0.1}Ti_4O_{12}$ is presented in **Fig. 4.4**, four stages of weight loss have been observed in the TGA plot. The first weight loss of 0.37 % observed between room temperature and 362 °C could be attributed to exothermic reaction as a result of removal of residual water and dehydration of hydrated water in the precursor material [114][115].

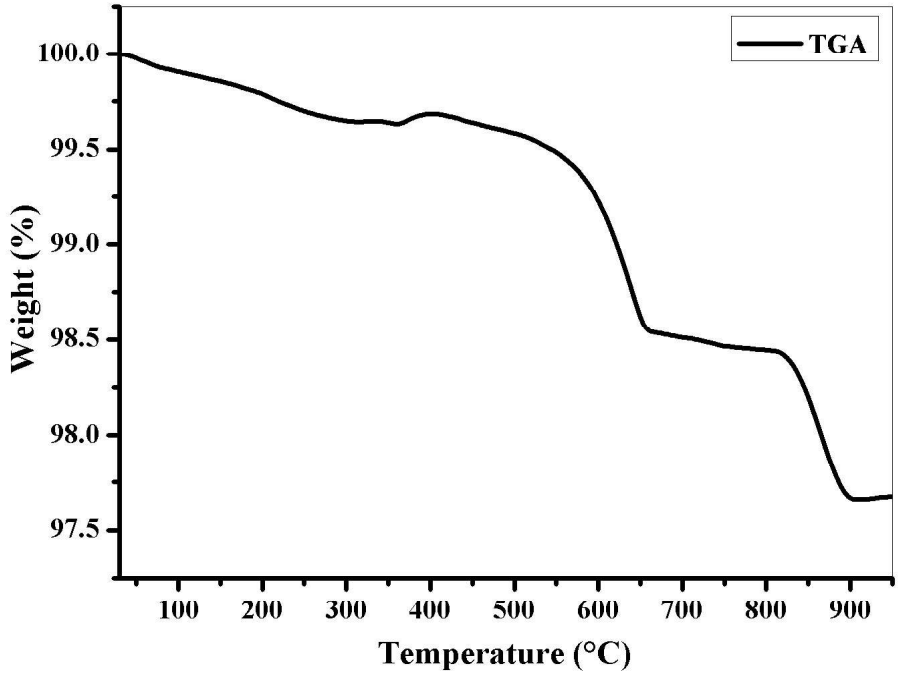

Fig. 4.4 Simultaneous TGA plot of the un-heated precursor of $Ca_{0.9}Ni_{0.1}Cu_{2.9}La_{0.1}Ti_4O_{12}$

The second weight loss of 1.09 % was observed between 406 and 661 °C, this could be as a result of participation of citric acid in the exothermic reaction and combustion of nitrates [116]. The third weight loss of 0.13 % observed between 661 and 821 °C could be due to formation of an intermediate compound ($Ca_{0.9}Ni_{0.1}Cu_{2.9}La_{0.1}O_4$) [117]. The fourth weight loss of 0.76 % observed between 821 and 900 °C is due to exothermic reaction between $Ca_{0.9}Ni_{0.1}Cu_{2.9}La_{0.1}O_4$ and TiO_2 to form the final CCTO product [118]. No further weight loss

was observed beyond 900 °C i. e. the mass becomes constant; this indicates that the final CCTO phase has been formed. The total observed weight loss in the TGA plot is 2.35 %.

The simultaneous DTA and DTG plot of the un-heated precursor of $Ca_{0.9}Ni_{0.1}Cu_{2.9}La_{0.1}Ti_4O_{12}$ is presented in **Fig. 4.5**. The DTG plot shows four endothermic peaks with varying extent. The first endothermic peak occurred between room temperature and 323 °C and the second endothermic peak occurred between 323 and 373 °C. The third endothermic peak occurred between 373 and 667 °C whereas the fourth endothermic peak occurred between 810 and 906 °C. Each of the observed endothermic peaks corresponds to the exothermic peaks observed at each stage of the TGA plot. Hence, the DTG plot support the result obtained in the TGA plot. Similar endothermic peaks were observed in the DTG plot, this further support the results obtained in the DTA and TGA plot. The process of the formation of final CCTO product from the starting materials may be explained as thus, TiO_2 will not form any complex with citric acid since it will directly react with the intermediate compound at higher temperatures during the process of combustion [119].

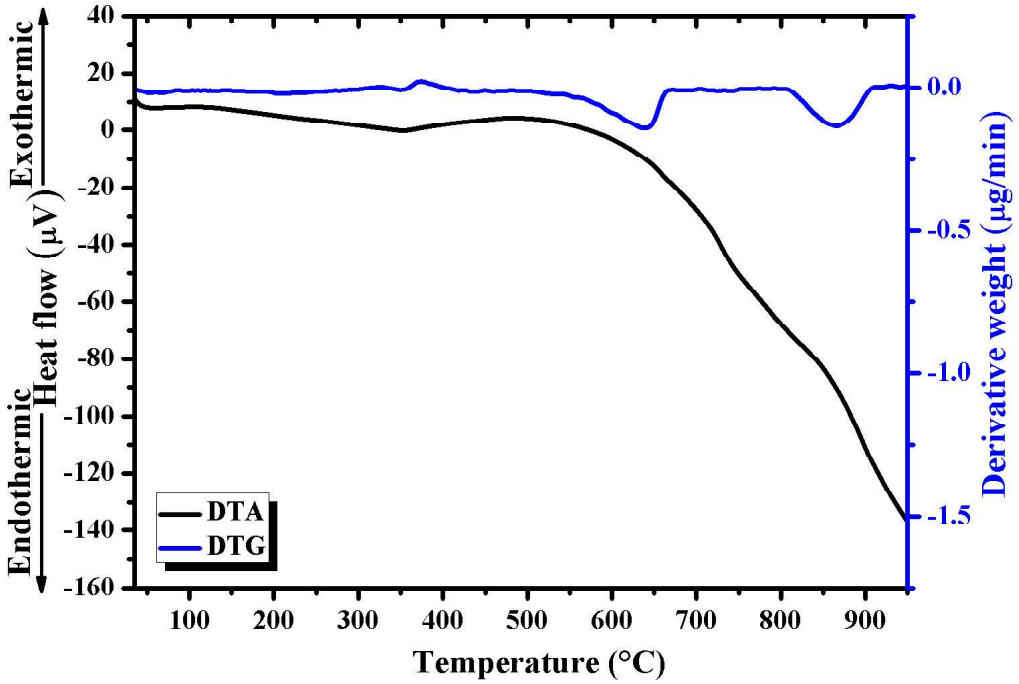

Fig. 4.5 Simultaneous DTA and DTG plot of the unsintered precursor of $Ca_{0.9}Ni_{0.1}Cu_{2.9}La_{0.1}Ti_4O_{12}$

4.1.3 Raman spectroscopy

Raman spectroscopy was carried out in order to effect of phonon vibration on the crystal structure and the dielectric properties of the prepared samples. The Raman spectra of $Ca_{0.9}Ni_{0.1}Cu_{2.9}La_{0.1}Ti_4O_{12}$ recorded in the range 200 to 800 cm^{-1} are presented in **Fig. 4.6**.

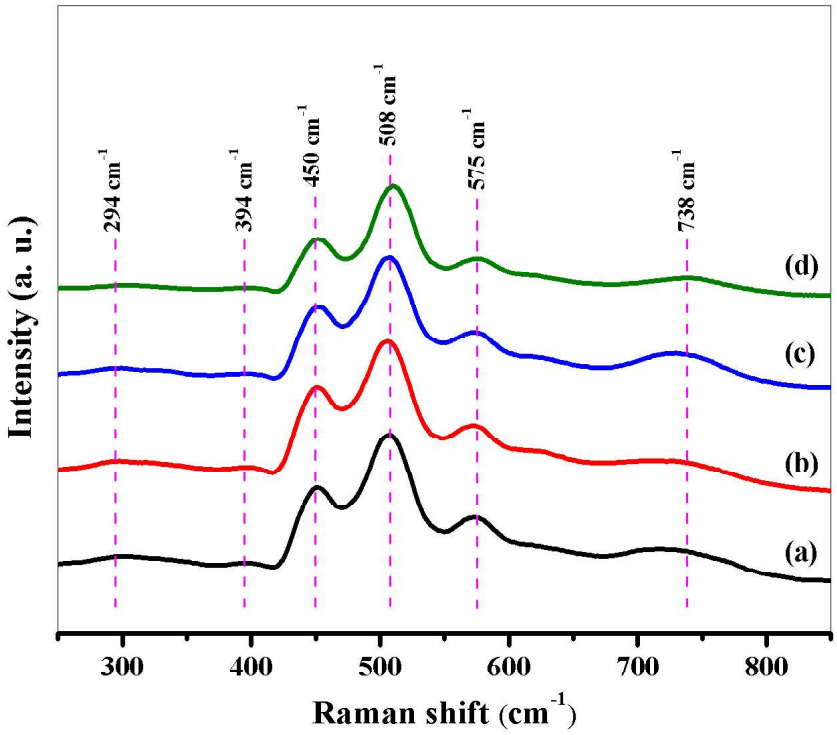

Fig. 4.6 Raman spectra of $Ca_{0.9}Ni_{0.1}Cu_{2.9}La_{0.1}Ti_4O_{12}$ (a) T1 (b) T2, (c) T3, and (d) T4

Group theory analysis of CCTO ceramics predicts eight Raman active modes as $2A_g + 2E_g + 4F_g$. However, only five Raman active mode corresponds to vibrational mode of TiO_6 octahedron [120]. Three intense Raman active modes were observed at 450, 508, and 575 cm^{-1}, these Raman active modes are characteristics modes of CCTO phase [114]. The Raman active mode at 450 and 508 cm^{-1} are respectively associated with TiO_6 rotation like A_g (1) and A_g (2) symmetry whereas that observed at 575 cm^{-1} is attributed to O-Ti-O anti-stretching F_g (3) symmetry [121][122][123][124]. First principle studies have predicted the occurrence of Raman active mode at 739 cm^{-1} which could be associated with symmetric stretching breathing F_g (4) symmetry of TiO_6 (O-Ti-O) [125][126]. However, this Raman

active mode was observed at 738 cm^{-1} in our case. Furthermore, C. Mu et al. reported that the appearance of the Raman active

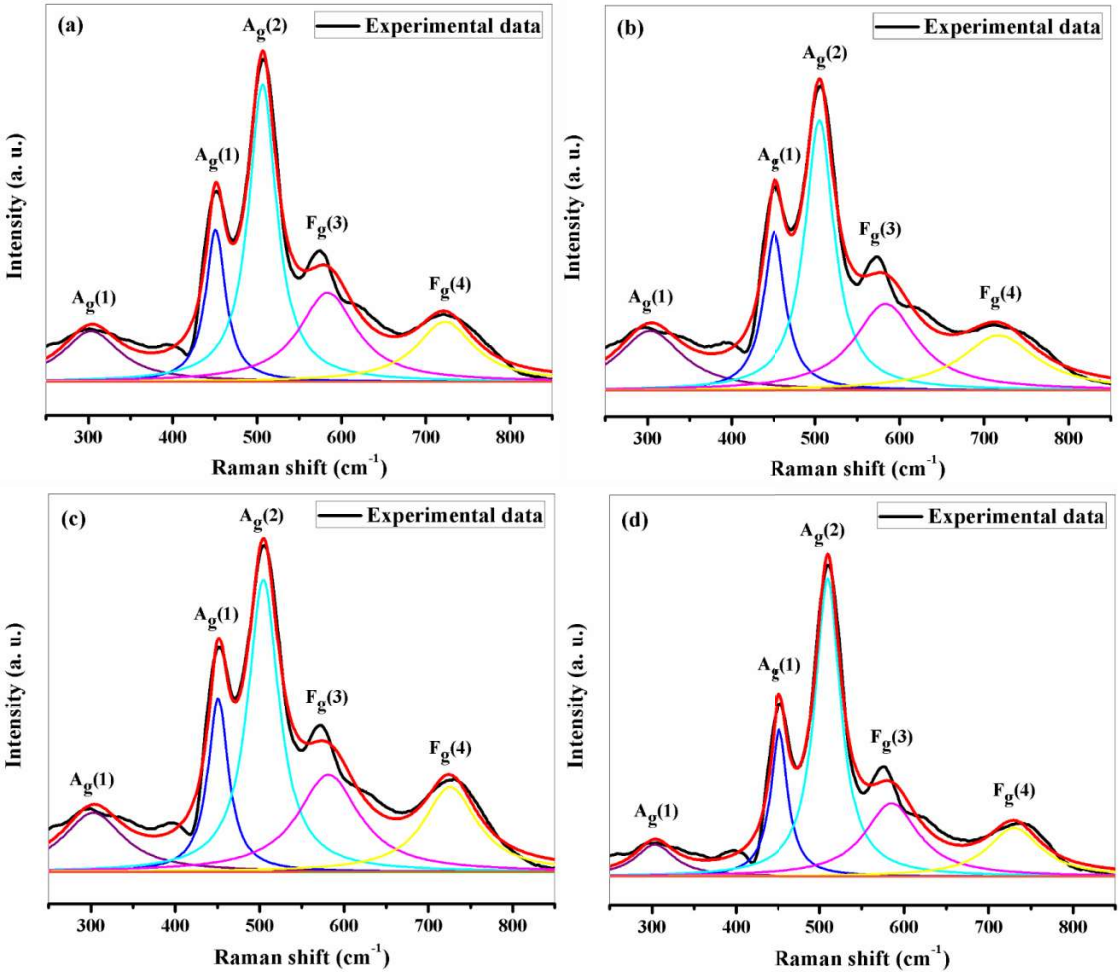

Fig. 4.7 De-convoluted first order Raman modes of $Ca_{0.9}Ni_{0.1}Cu_{2.9}La_{0.1}Ti_4O_{12}$ (a) T1 (b) T2, (c) T3, and (d) T4, the red line shows the Gaussian fitted curve

mode at 739 cm^{-1} could be ascribed to the presence of $CaTiO_3$ [124]. Since the XRD spectra shows the presence of $CaTiO_3$ in all the synthesized samples except the sample with *T4* and that Raman spectroscopy is more sensitive to XRD, we may accept that this mode occur as result of $CaTiO_3$. The weak Raman active mode observed at 294 as a result of A_g (1) symmetry of CuO whereas that observed at 394 cm^{-1} could be ascribed to A_g (1) symmetry of TiO_2 (anatase phase) [127][128]. Hence, Raman analysis shows the presence of $CaTiO_3$, CuO and TiO_2 secondary phase in all the samples (*T1*, *T2*, *T3* and *T4*). However, XRD analysis rules out the presence of $CaTiO_3$, CuO and TiO_2 secondary phase in the sample with *T4*. This

contradiction arises because Raman spectroscopy is more sensitive than XRD, similar observation has been made by S. Rhouma *et al.* [129]. Additionally, the fact that there is no observed shift in the position of the observed peaks is an indication that the Ti-shift within the TiO_6 octahedron or charge redistribution is not affected. The de-convoluted first order Raman modes of $Ca_{0.9}Ni_{0.1}Cu_{2.9}La_{0.1}Ti_4O_{12}$ fitted using Gaussian fitting is presented in **Fig. 4.7**. The fitting vividly shows that Raman spectroscopy is insensitive to changes in sintering temperature since all the Raman spectra looks identical.

4.1.4 Morphology analysis

The FESEM micrographs, particle size distribution and EDX spectra of $Ca_{0.9}Ni_{0.1}Cu_{2.9}La_{0.1}Ti_4O_{12}$ sintered at different temperatures (*T1*, *T2*, *T3*, and *T4*) are presented in **Fig. 4.8**, **4.9** and **4.10** respectively. Clearly, the shapes and sizes of the grains become more cubic with increase in calcination temperature. This shows that the increase in calcination temperature inhibit grain growth and enhances the formation of pure cubic CCTO

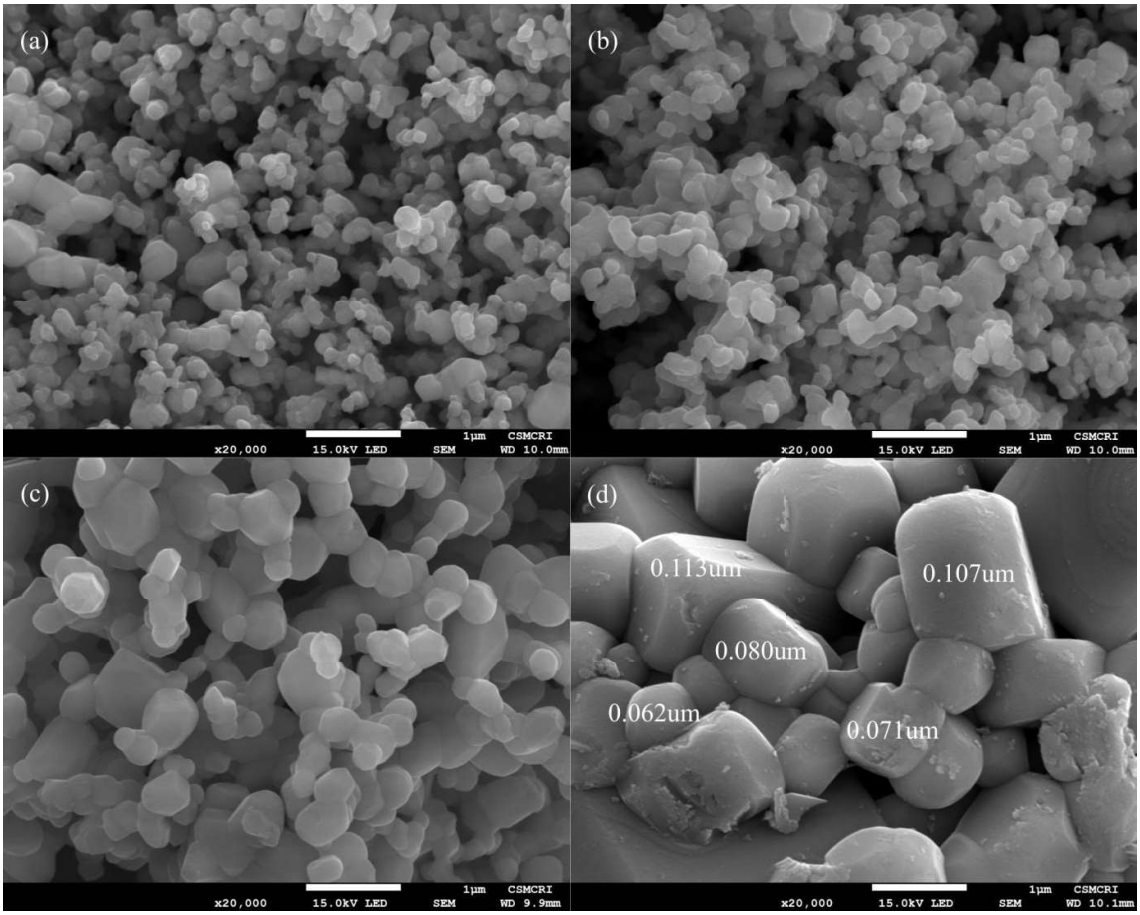

Fig. 4.8 FESEM micrograph of $Ca_{0.9}Ni_{0.1}Cu_{2.9}La_{0.1}Ti_4O_{12}$ (a) T1 (b) T2, (c) T3, and (d) T4

phase; this scenario coupled with clear grain boundaries is most notable in the sample with *T4*. The samples with *T1*, *T2*, and *T3* do not show CCTO grains with cubic shape and the grain boundaries are not clearly visible even though the micrographs were taken at same resolution with the sample with *T4*, this may be because of the presence of different phases such as $CaTiO_3$, CuO, and TiO_2 in the samples. We assume that the presence of secondary phases promote the formation of pure cubic CCTO phase, this is also evident in XRD spectra. W. Li et al. reported that the presence of CuO phase at the grain boundary of CCTO ceramic increase the rate of diffusion of ions during sintering process and enhance the formation of pure CCTO phase [130]. The average particle size was found to be 0.027, 0.025, 0.039, and 0.117 μm for *T1*, *T2*, *T3* and *T4* respectively (**Fig. 4.9**). Furthermore, individual particle sizes

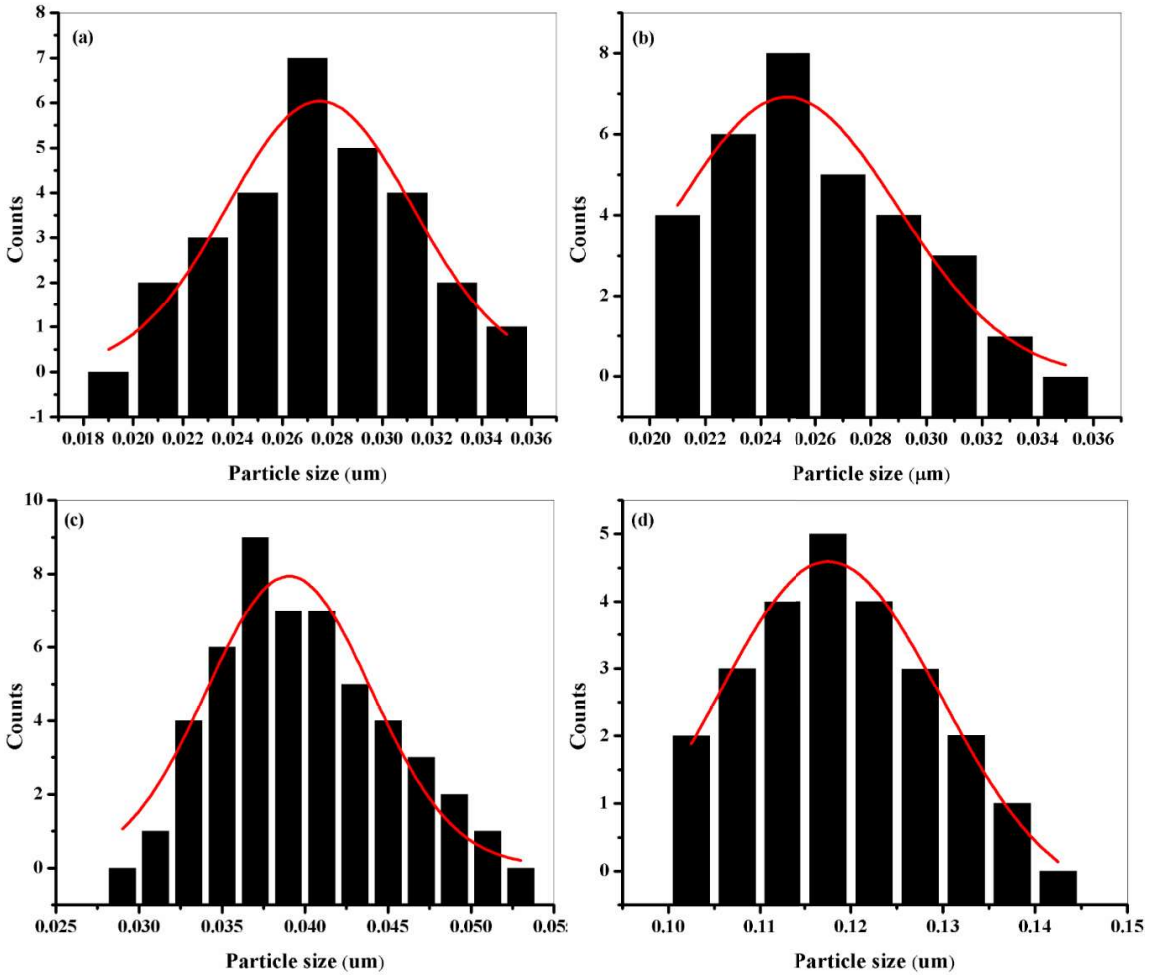

Fig. 4.9 Particle size distribution of $Ca_{0.9}Ni_{0.1}Cu_{2.9}La_{0.1}Ti_4O_{12}$ (a) T1 (b) T2, (c) T3, and (d) T4

of the sample with T4 were found to be in the range 0.062-0.113 μm. It can be observed that changes in sintering temperature affect the particle size of the prepared sample. At lower sintering temperatures (*T1*, *T2*, and *T3*), the particle sizes were much closer to nm range. However, the grain sizes attain μm range at high sintering temperatures (*T4*). Careful analysis of literatures shows that single phase CCTO ceramic has particle size in μm range [131][132], this further supports the single phase Ni^{2+}-La^{3+} substituted CCTO ceramic observed at *T4*. EDX analysis shows the host (Ca^{2+}, Cu^{2+}, and Ti^{4+}) and substituted cation (Ni^{2+} and La^{3+}) (**Fig. 4.10**), this confirms the stoichiometry of the prepared Ni^{2+}-La^{3+} substituted CCTO ceramic.

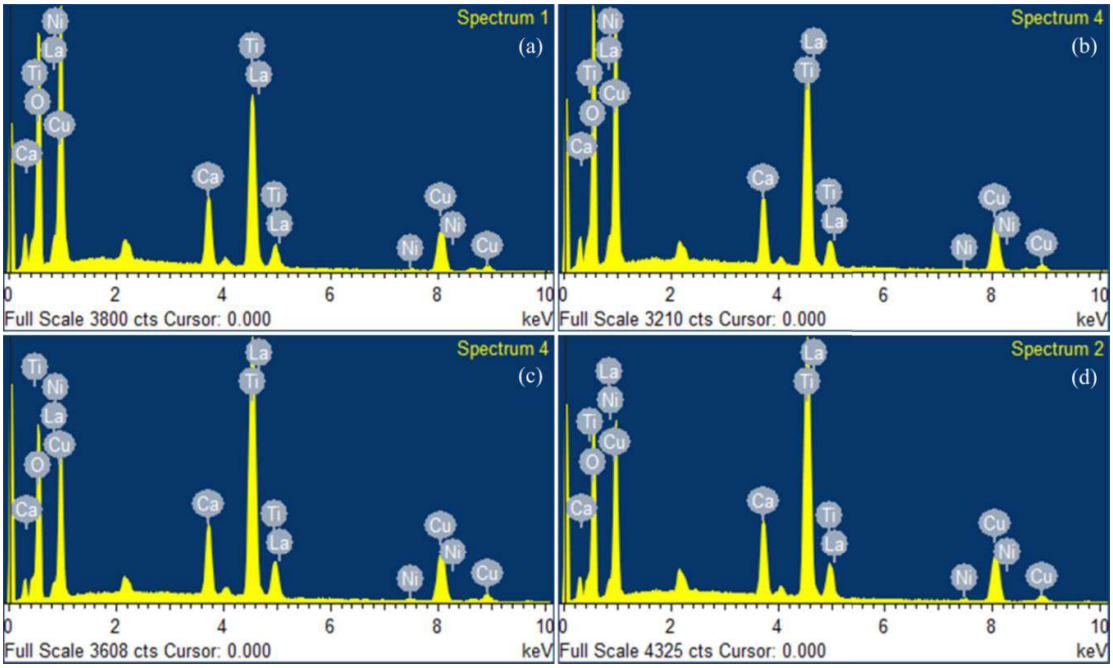

Fig. 4.10 EDX spectra of $Ca_{0.9}Ni_{0.1}Cu_{2.9}La_{0.1}Ti_4O_{12}$ (a) T1 (b) T2, (c) T3, and (d) T4

The TEM micrographs, HRTEM micrographs and SAED pattern of $Ca_{0.9}Ni_{0.1}Cu_{2.9}La_{0.1}Ti_4O_{12}$ for the samples with *T3* and *T4* are presented in **Fig. 4.11**. The inter-planar spacing for (400) *hkl* plane measured from HRTEM support the values observed from XRD analysis. Bright diffraction spots with three distinct rings corresponding to (220), (400), and (422) *hkl* planes can be observed in the SAED pattern, this observation also supports the XRD analysis and confirms the polycrystalline nature of the prepared Ni^{2+}-La^{3+} substituted CCTO ceramic.

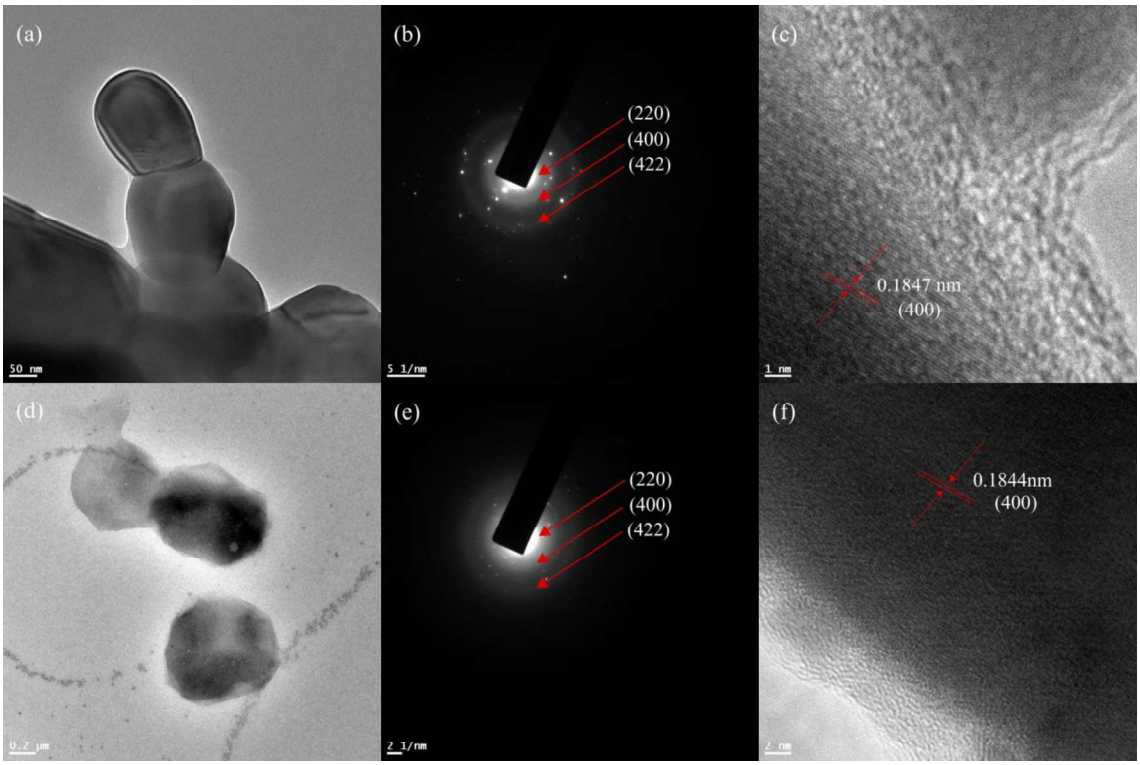

Fig. 4.11 TEM micrographs, HRTEM micrographs and SAED pattern of $Ca_{0.9}Ni_{0.1}Cu_{2.9}La_{0.1}Ti_4O_{12}$ (a-c) T3 and (d-f) T4

4.1.5 Optical analysis

UV-vis NIR spectroscopy was used to study the optical properties of $Ca_{0.9}Ni_{0.1}Cu_{2.9}La_{0.1}Ti_4O_{12}$ in the range 200-900 nm. The variation of absorbance with wavelength for $CaCu_{2.6}Ni_{0.2}Co_{0.2}Ti_4O_{12}$ is presented in **Fig. 4.12**. The optical band gap (E_g) was determined using the relation

$$(\alpha h\upsilon)^m = K\left(h\upsilon - E_g\right) \tag{4.3}$$

where α is the absorption coefficient, h is the planks constant ($6.6260 \times 10^{-34}\, J.s$), υ is incident photon's frequency and m is a constant having values of 1/2, 2, 3/2, and 3 respectively corresponding to allowed direct, allowed indirect, forbidden direct, and forbidden indirect transitions [133][134]. From **Fig. 4.12**, we can observed that all the prepared samples shows $\sigma - \sigma^*$, $n - \sigma^*$, and $n - \pi^*$ transition respectively at 243, 289, and 682 nm absorption peaks. The $\pi - \pi^*$ transition for the sample with *T2*, *T3*, and *T4* were observed at 370, 427, and 494 nm, this clearly shows the shifting of the absorption peak towards higher wavelengths region i. e. bathochromic (red) shift. Three reflection peaks were

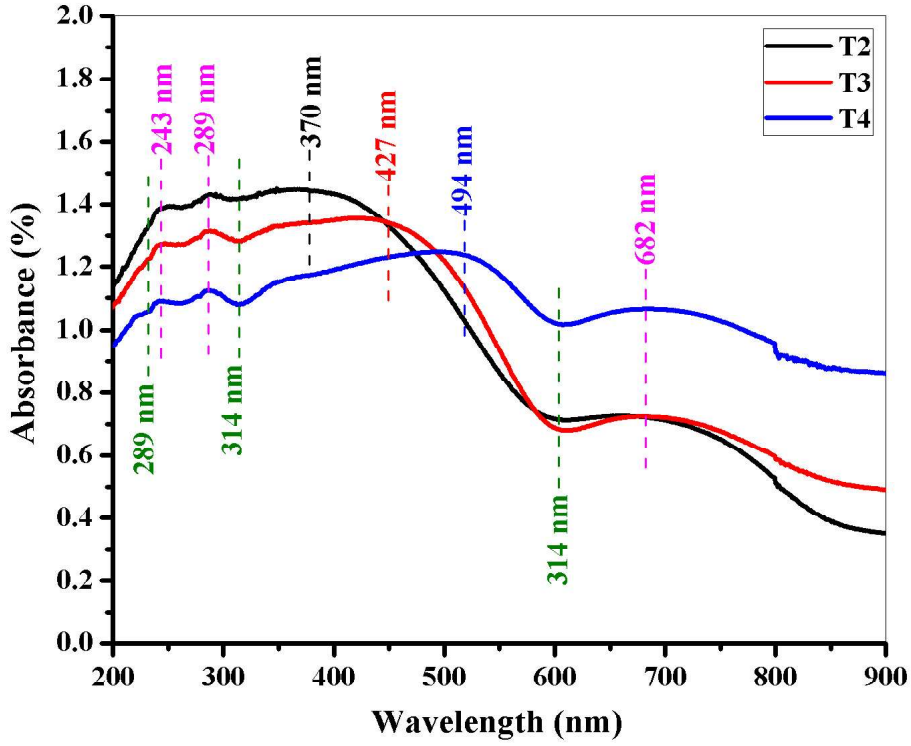

Fig. 4.12 Variation of absorbance against wavelength for $CaCu_{2.6}Ni_{0.2}Co_{0.2}Ti_4O_{12}$

observed at 289, 314 and 611 nm; the reflection peaks observed at 289 and 314 nm appear to be more intense as the calcination temperature is increased, this corresponds to hypochromic shift. The reflection peak observed at 611 nm first experiences a hypochromic shift when the calcination temperature was increased from *T2* to *T3*, and upon increasing the calcination temperature from *T3* to *T4*, a hyperchromic shift was observed. Evidence of hypsochromic (blue) shift was not observed in all the prepared samples. **Fig. 4.13** shows the graph of $(\alpha h\upsilon)^2$ against E_g, the value of E_g for the sample with *T2*, *T3*, and *T4* was evaluated by linear extrapolation of the graph of $(\alpha h\upsilon)^2$ against E_g and were found to be 1.71, 1.63, and 1.42 eV respectively. A plot of the variation of E_g against sintering temperature shows that E_g decreases with increase in calcination temperature, this could be attributed to changes in the local atomic lattice (**Fig. 4.14)** [135].

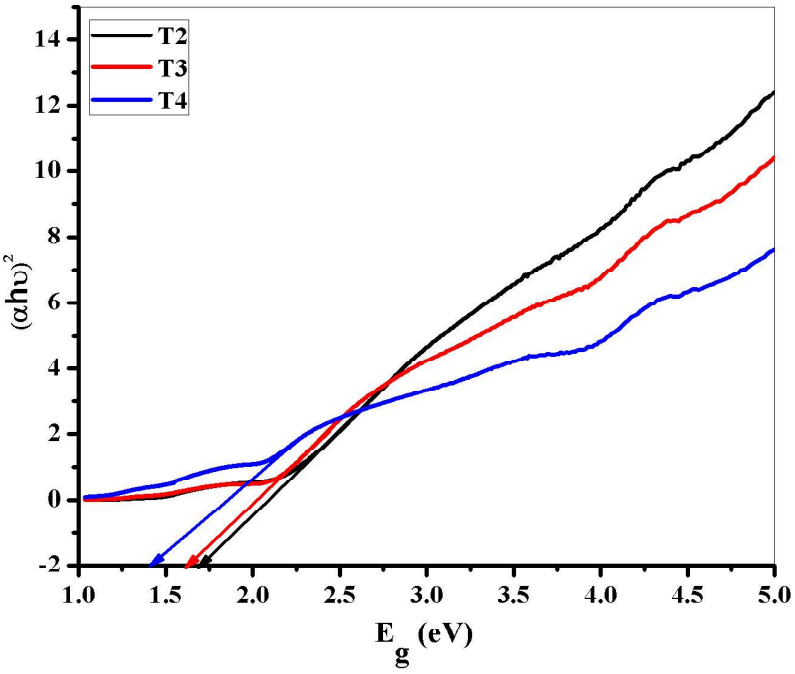

Fig. 4.13 Band gap of $CaCu_{2.6}Ni_{0.2}Co_{0.2}Ti_4O_{12}$

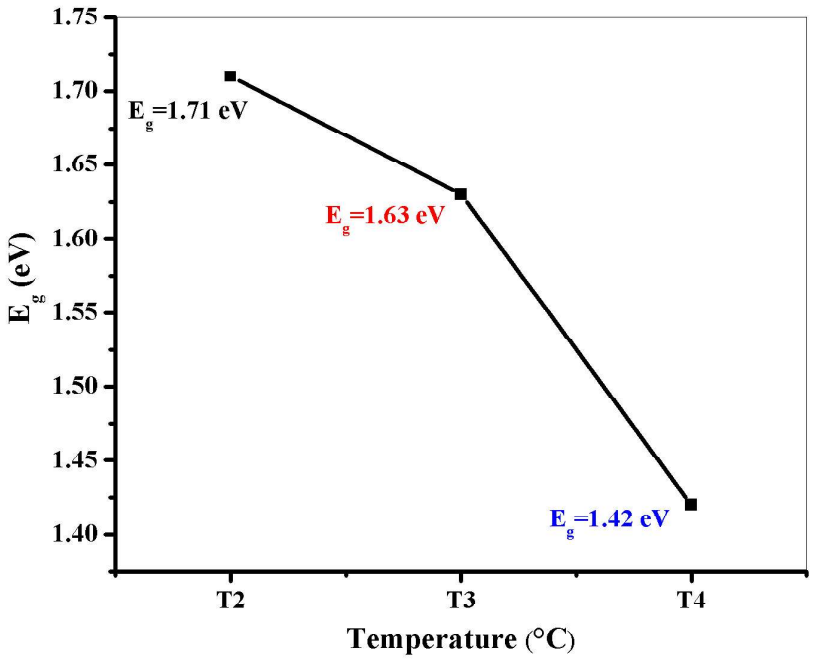

Fig. 4.14 Variation of band gap against calcination temperature (*T*)

4.1.6 Dielectric and impedance spectroscopy

The complex permittivity (ε^*) defined the dielectric response of material and can be expressed by the following equation [136][137]

$$\varepsilon^* = \varepsilon' - j\varepsilon'' \tag{4.4}$$

Where ε' is the real part of complex impedance and ε'' is the imaginary part of complex impedance and they are expressed as

$$\varepsilon' = \frac{Z''}{2\pi\omega C_0 Z^2} \tag{4.5}$$

$$\varepsilon'' = \frac{Z'}{2\pi\omega C_0 Z^2} \tag{4.6}$$

Where Z' is the real part of complex impedance, Z'' is the imaginary part of complex impedance, ω is the frequency and C_0 is the geometrical capacitance. The dielectric loss can be expressed as ratio of ε'' and ε'

$$\tan\delta = \frac{\varepsilon''}{\varepsilon'} \tag{4.7}$$

According to Jonscher's law, total conductivity (σ_t) of solids can be expressed as a function of AC conductivity (σ_{AC}) and DC conductivity (σ_{DC}) as described in the relation

$$\sigma_t = \sigma_{AC} + \sigma_{DC} \tag{4.8}$$

$$\sigma_{AC} = A\omega^S \tag{4.9}$$

Where σ_{AC} is the frequency dependent part of total conductivity, σ_{DC} is the frequency independent part of total conductivity, A is a constant which depends on temperature and it estimate the amount of dispersion at high temperature, ω is the frequency, and S is the exponential term having value from 0 to 1 and it represents the rate of interaction between mobile ions. The electrical conducting nature of the material is frequency independent when $S = 0$ and frequency dependent when $S = 1$.

The measurement of the dielectric response was recorded at room temperature from 100 Hz to 120 MHz. The room temperature dependence of dielectric constant (ε') on frequency for $Ca_{0.9}Ni_{0.1}Cu_{2.9}La_{0.1}Ti_4O_{12}$ is presented in **Fig. 4.15**. The net polarization which comprises of space charge (interfacial) polarization, dipolar (orientation) polarization, atomic (ionic)

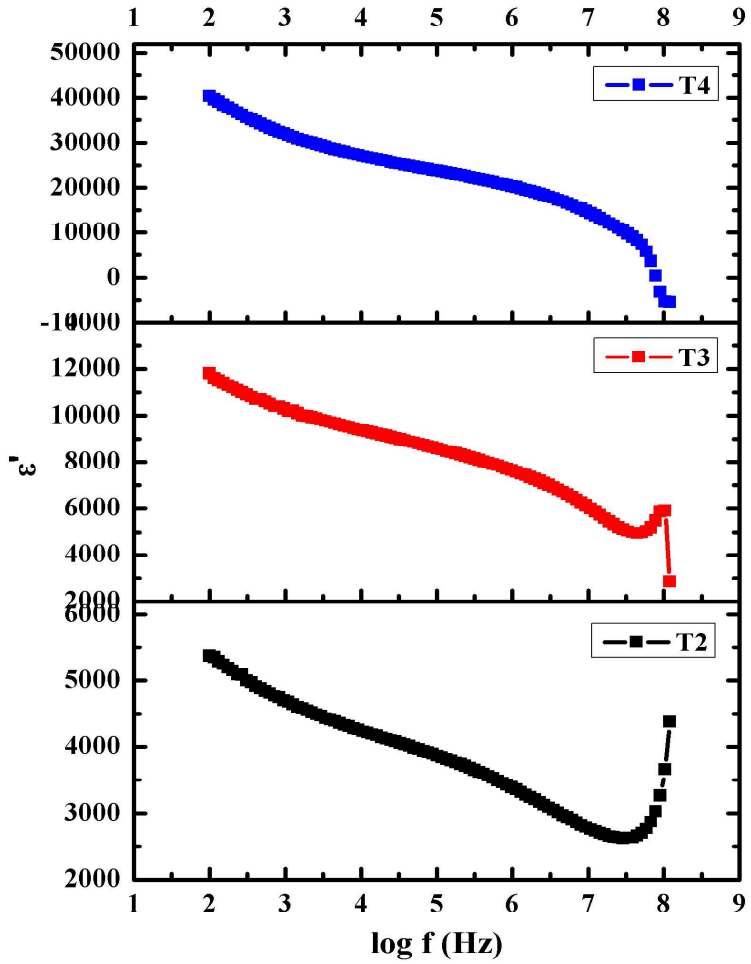

Fig. 4.15 Variation of room temperature dielectric constant with frequency for $Ca_{0.9}Ni_{0.1}Cu_{2.9}La_{0.1}Ti_4O_{12}$

polarization, and electronic polarization defines the response of a dielectric material in the presence of applied electric field [138]. Space charge polarization and electronic polarization occurs at lower and higher frequencies respectively whereas dipolar (orientation) polarization and atomic or ionic polarization occurs at intermediate frequencies. The values of ε' at lower frequencies (100 Hz) were found to be 5370, 11800, and 40400 for the samples with *T2*, *T3*, and *T4* respectively, these high values could be attributed to accumulation of charge carriers at the interface of insulating grain boundary and semiconducting grains which causes space charge polarization as a result of the presence of micro heterogeneities which result from random occupation of equivalent crystallographic sites by Cu^{2+} and La^{3+} ions [139][140][99].

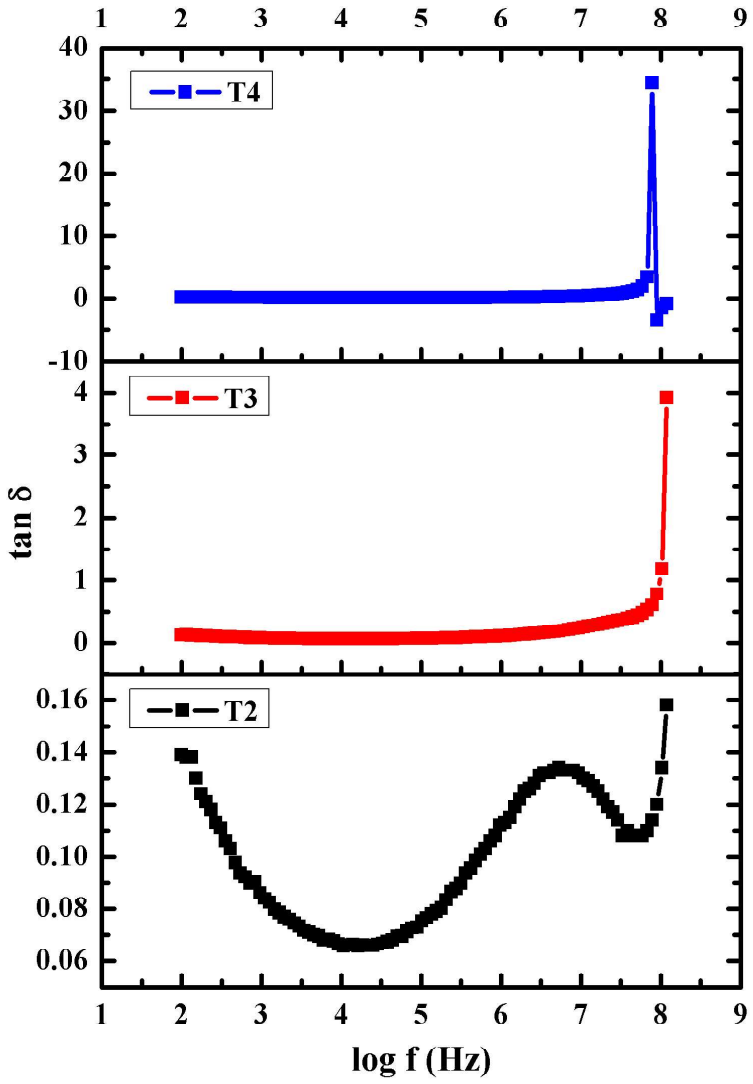

Fig. 4.16 Variation of room temperature dielectric loss tangent with frequency for $Ca_{0.9}Ni_{0.1}Cu_{2.9}La_{0.1}Ti_4O_{12}$

The difference in electrical conductivity of the prepared samples between insulating grain boundary and semiconducting grains increases with increase in calcination temperature which in turn increases the accumulation of charge carriers and consequently increases space charge polarization, this causes increase in the values of ε' (5370, 11800, and 40400) with increase in calcination temperature (*T2*, *T3*, and *T4*) [141]. The values of ε' for all samples decrease almost uniformly with increase in frequency up to higher frequencies where a sudden increase in ε' were observed for the sample with *T2* and *T3*, this sudden increase in ε'

observed at higher frequencies is caused by electronic polarization [116]. A relaxation peak was observed at higher frequencies for the samples with *T3*; the presence of dielectric relaxation peak in the samples with *T3* could attributed to the occurrence of Debye-like relaxation process [142].

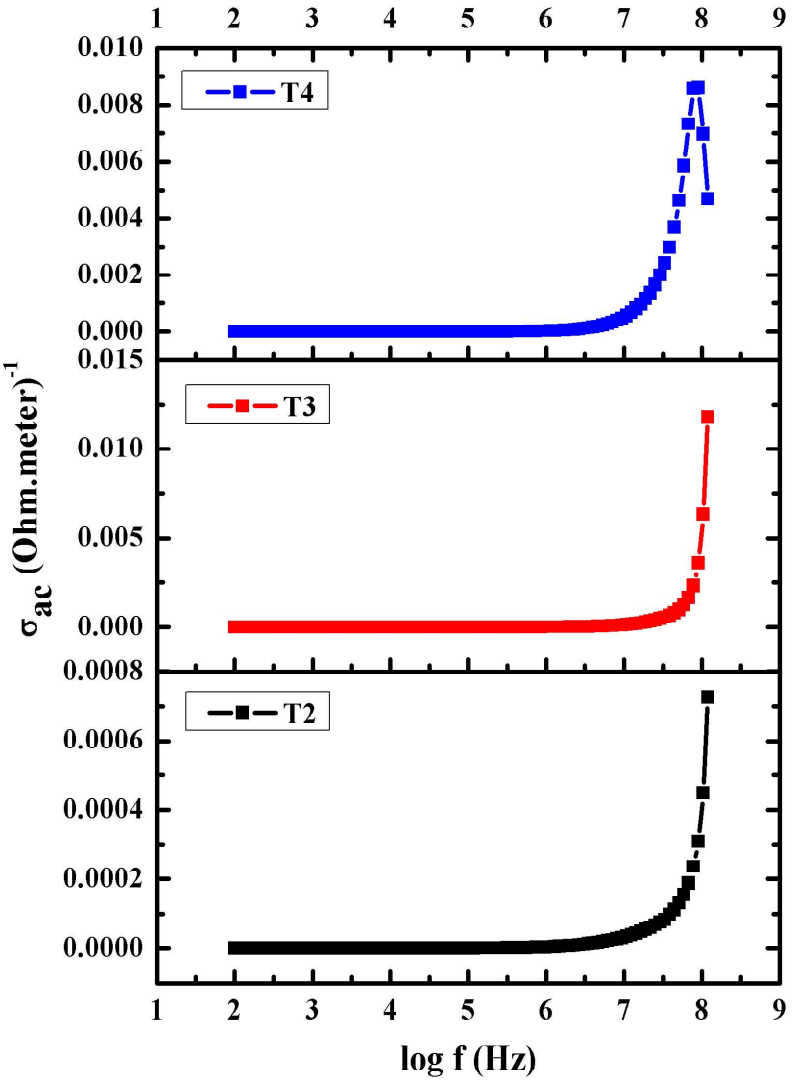

Fig. 4.17 Variation of room temperature Ac conductivity with frequency for $Ca_{0.9}Ni_{0.1}Cu_{2.9}La_{0.1}Ti_4O_{12}$

The room temperature dielectric loss tangent $(\tan\delta)$ of $Ca_{0.9}Ni_{0.1}Cu_{2.9}La_{0.1}Ti_4O_{12}$ is presented in **Fig. 4.16**. It can be observed that increase in calcination temperature causes the increase in $\tan\delta$, this is expected as similar behaviour was observed for ε'. According to

internal barrier layer capacitance (IBLC) model, the presence of semiconducting grains induce high values of ε' and high grain boundary resistance result in low $\tan\delta$ at lower frequencies [143]. It is a well-known fact that the substitution of cation with larger ionic radius causes lattice distortion, this scenario have been observed to enhance the formation of Cu^{2+}-rich and Ti^{4+}-poor layer of grain boundary with high resistance reduced leaky current [144][143]. On the basis of the above discussion, we can conclude that the substitution of Cu^{2+} (0.730 Å) by La^{3+} (1.061 Å) would induce lattice distortion and create Cu^{2+}-rich and Ti^{4+}-poor layer of grain boundary with high resistance and consequently low values of $\tan\delta$ was observed in the sample with *T2*. Additionally, P. Liu et al. reported that $\tan\delta$ in CCTO ceramic may originate from defects in the CCTO structure which include oxygen vacancies, change in valency of cation, and pores [145].

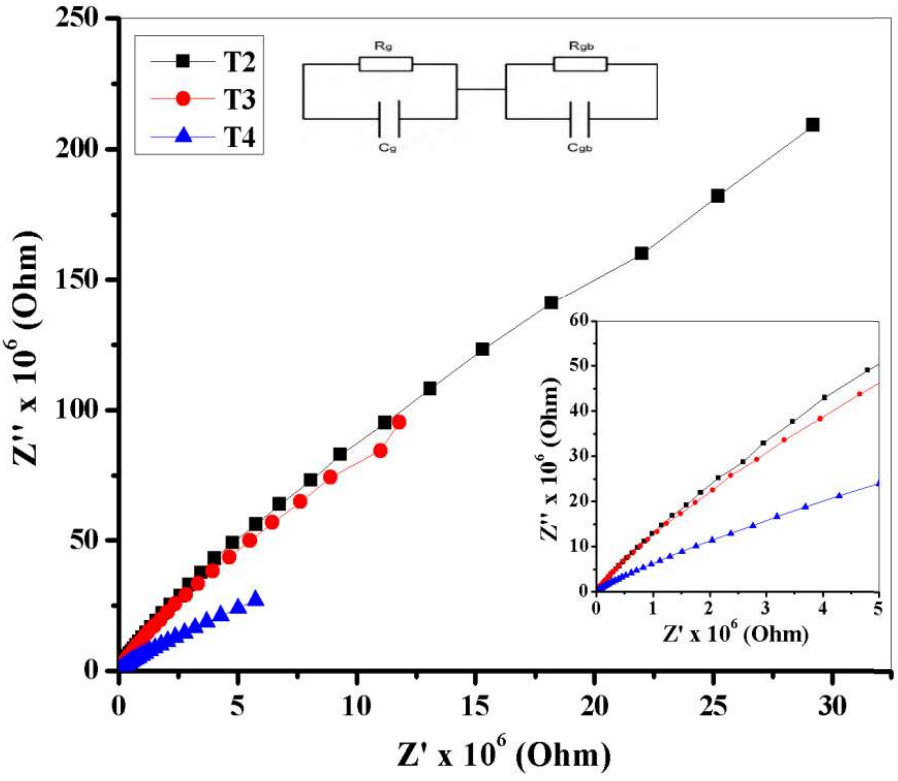

Fig. 4.18 Cole-Cole plot of $Ca_{0.9}Ni_{0.1}Cu_{2.9}La_{0.1}Ti_4O_{12}$ at room temperature

The room temperature AC conductivity (σ_{ac}) of $Ca_{0.9}Ni_{0.1}Cu_{2.9}La_{0.1}Ti_4O_{12}$ is presented in **Fig. 4.17**. The values of σ_{ac} remains constant at lower and intermediate frequencies, this

frequency independent behaviour could be attributed to non-equilibrium occupancy of trap charges [146]. At higher frequencies, an abrupt and sudden increase in σ_{ac} was observed as a result of increased forced experience by trap charges which result in their release from the trapping centres, hence, the observed increase in σ_{ac}. The Cole-Cole plot of $Ca_{0.9}Ni_{0.1}Cu_{2.9}La_{0.1}Ti_4O_{12}$ is presented in **Fig. 4.18**. Clearly, we can see semicircles with different intercepts due to the effects of grain boundary resistance (R_{gb}) and grain resistance (R_g) which can be described by an equivalent electric circuit model consisting of series arrangements of two parallel RC elements (**Fig. 4.18**) [145]. The contribution of the R_{gb} to the dielectric properties give rise to the appearance of the semicircle arc in the low frequency region of the Cole-Cole plot while that of the R_g give rise to the semicircle arc in the high frequency region [147]. Hence, our samples exhibit more R_{gb} compared to R_g since the semicircle arc at the high frequency region is not observed (**Fig. 13**). From the foregoing, we can conclude that most of the dielectric properties of the prepared samples come from R_{gb}. This conclusion is further supported by the fact that for CCTO ceramic, R_g is negligible compared to R_{gb} [148]. Since our sample is more resistive at the low frequency region, we can assume an intrinsic grain boundary relaxation that is dominated by grain boundary thereby stopping the charge carriers close to the grain boundary as a result of the insulating nature of the grain boundary. The presence of CuO at the grain boundaries could enhance R_{gb} by acting as a layer of insulating barrier; this claim could be validated by close examination of **Fig. 13**. Clearly, the samples with CuO phase (*T2* and *T3*) shows much larger semicircle as compared to the sample without CuO phase (*T4*), similar observation was made by W. X. Yuan et al. [149].

4.2 Pr^{3+}-Co^{2+} substituted calcium copper titanate (CCTO)

4.2.1 XRD analysis

XRD diffraction patterns of polycrystalline $Ca_{1-x}Pr_xCu_{3-y}Co_yTi_4O_{12}$ (x=0.0, 0.1, 0.2, 0.3 and y=0.0, 0.4, 0.5, 0.6) ceramic are shown in **Fig. 4.19**. The diffraction peaks were compared with standard powder diffraction database file (JCPDS 75-2188) and found to be identical to pure undoped CCTO ceramic. The major *hkl* planes in the diffraction patterns are (211), (220), (310), (222), (321), (400), (422), (440), and (620) which were found to match with that of single phase crystalline CCTO ceramic having cubic perovskite structure and space group *Im*-3. The lattice constant (a) and volume of the unit cell (V_{cell}) are calculated using

$$a = d\sqrt{h^2 + k^2 + l^2} \tag{4.10}$$

$$V_{cell} = a^3 \tag{4.11}$$

where d is the inter planer spacing, hkl are the miller indices, the full width at half maximum denoted by β (in radian) is given by $\beta = (\beta_o^2 - \beta_i^2)^{1/2}$ where β_o is the width from the observed XRD peaks and β_i is the width due to instrumental effects. The values of lattice

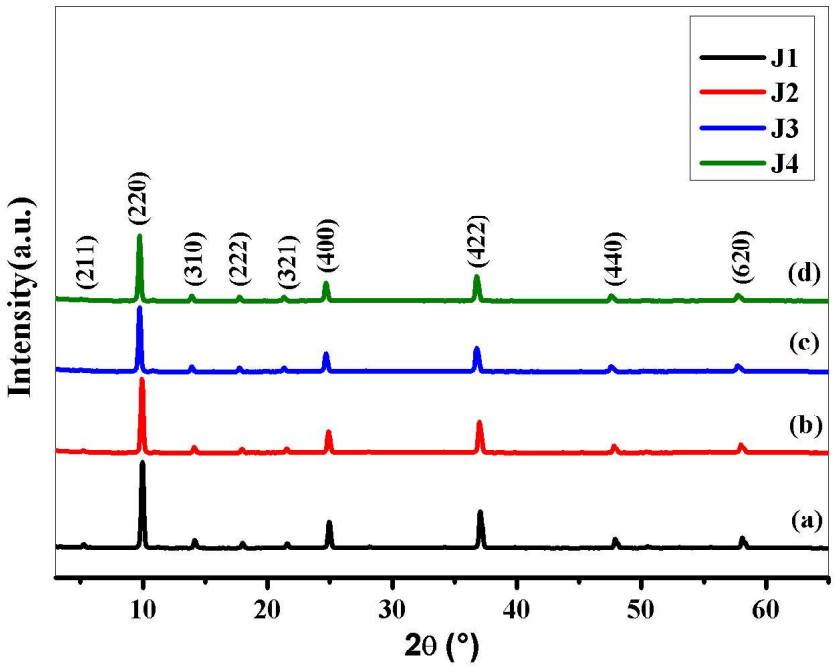

Fig. 4.19 XRD pattern of $Ca_{1-x}Pr_xCu_{3-y}Co_yTi_4O_{12}$ (x=0.0, 0.1, 0.2, 0.3 and y=0.0, 0.4, 0.5, 0.6)

constant (a) and volume of unit cell (V_{cell}) are given in **Table 4.2.** The lattice constant is found to increase with increase in Pr^{3+}-Co^{2+} concentration (**Fig. 4.20**). Similarly, the volume of unit cell increase with increase in Pr^{3+}-Co^{2+} concentration (**Fig. 4.20**). This may be due lattice distortion induced when the ions of the host ($r_{Ca^{2+}} = 0.990$ Å and $r_{Cu^{2+}} = 0.730$ Å) are replaced by ions with larger ionic radius ($r_{Pr^{3+}} = 1.013$ Å and $r_{Co^{2+}} = 0.745$ Å) respectively [141][150]. The calculated lattice parameters are in agreement with literature [140].

Table 4.2 Values of lattice constant (a) and volume of unit cell (V_{cell}) of $Ca_{1-x}Pr_xCu_{3-y}Co_yTi_4O_{12}$ (x=0.0, 0.1, 0.2, 0.3 and y=0.0, 0.4, 0.5, 0.6)

Sample code	2θ (°)	d (Å)	β (°)	a (Å)	V_{cell} (Å^3)
J1	38.601	1.8477	0.170	7.391	403.747
J2	38.575	1.8480	0.163	7.392	403.911
J3	38.521	1.8485	0.154	7.394	404.239
J4	38.462	1.8487	0.149	7.395	404.403

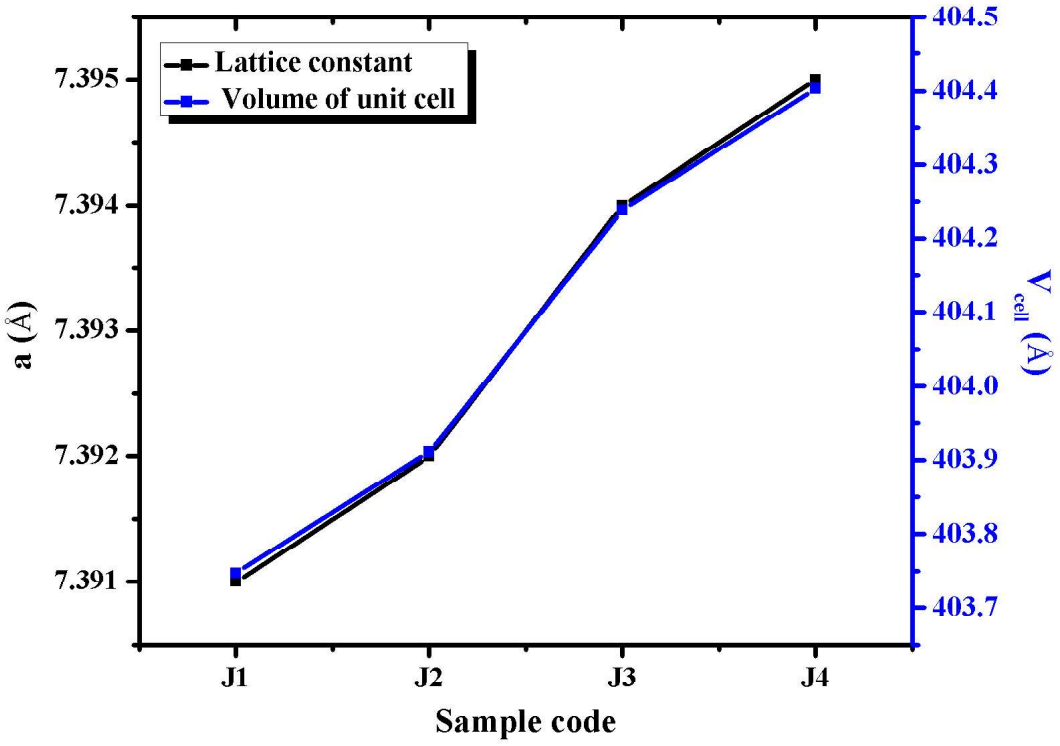

Fig. 4.20 Variation of lattice constant and volume of unit cell with Pr^{3+}-Co^{2+} substitution

4.2.2 Thermal analysis

Thermal gravimetric analysis (TGA) was carried out in order to understand the processes of thermal decomposition and phase transition of the prepared sample. **Fig. 21** presents the simultaneous TGA plot of the unsintered precursor $Ca_{1-x}Pr_xCu_{3-y}Co_yTi_4O_{12}$ (x=0.0 and

y=0.0). The TGA curve shows a total weight loss of about 6.49 % from room temperature to

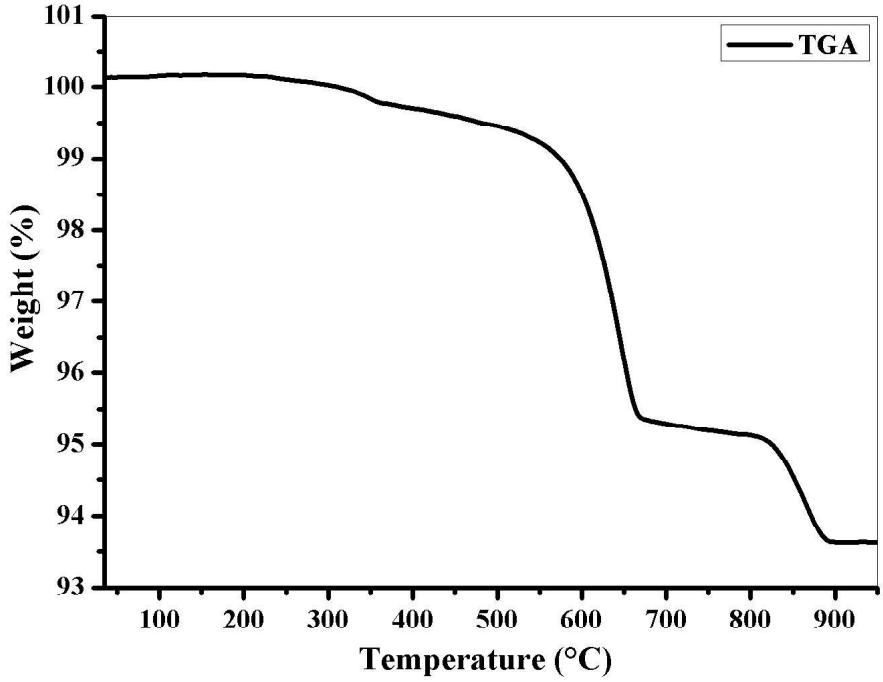

Fig. 4.21 Simultaneous TGA plot of the unsintered precursor (J1)

892 °C. It can be observed from the plot that the weight loss occurs at different temperatures during the heating process. At the initial stage, a slight weight gain has been observed from room temperature to 313 °C as a result of the interaction of the sample with an oxidizing atmosphere (oxidation) and presence of molecules of liquid in the form of thin film (adsorption or absorption). Further still, a slight weight loss started to occur at 313 °C and extends up to 561 °C; this could be attributed to exothermic reaction as a result of the removal of residual water [151].There is a major and sudden weight loss between 561 °C and 813 °C as a result of combustion of citric acid and organic matter [118]. Thereafter, an abrupt weight loss ensued from 813 °C to 889 °C; this may be as a result of exothermic addition reaction of an intermediate compound with TiO_2 [117]. Weight losses cease to occur at 895 °C, this signifies the formation of the final CCTO ceramic product.

Differential thermal analysis (DTA) and derivative thermal gravimetric (DTG) were done in order to observe how the prepared sample respond to endothermic and exothermic transitions i. e. melting and crystallization temperatures respectively**. Fig. 4.22** shows the simultaneous

DTA and DTG plot of unsintered precursor (J1) i. e. $Ca_{1-x}Pr_xCu_{3-y}Co_yTi_4O_{12}$ (x=0.0 and y=0.0).

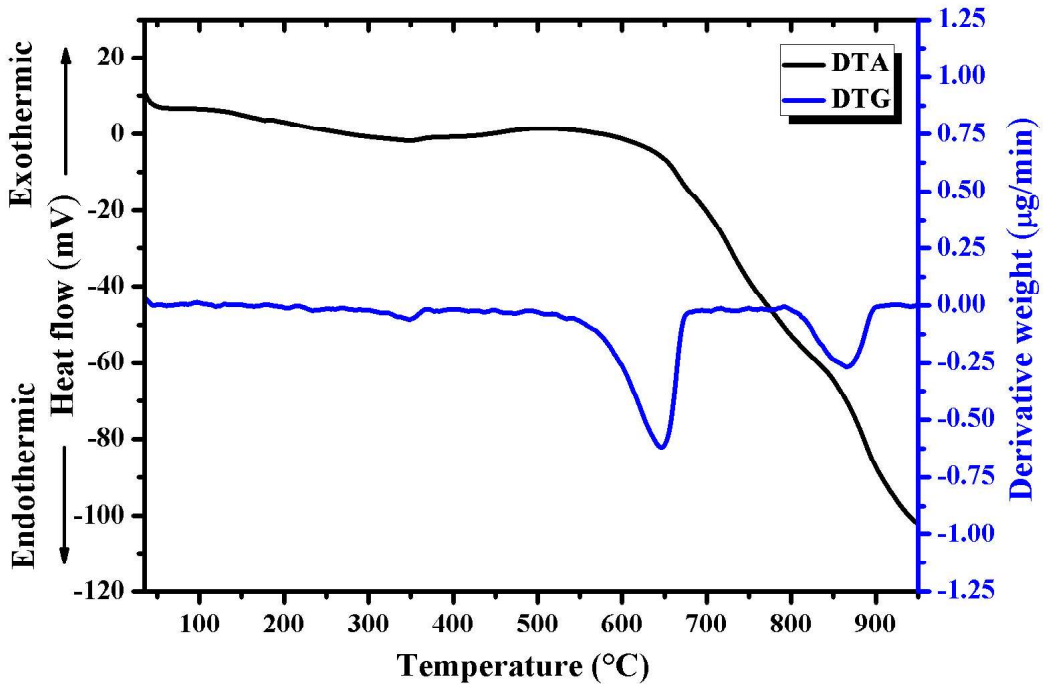

Fig. 4.22 Simultaneous DTA/DTG plot of the unsintered precursor (J1).

The DTA curve shows slight and broad endothermic peak at 345 °C and broad exothermic peak at 507 °C. Also, there is a slight exothermic peak at around 877 °C, this could be attributed to the combination of the intermediate compound formed during the autocombustion process with TiO_2 to form the final CCTO ceramic product [116]; this is further supported by TGA curve. There are three endothermic peaks in the DTG curve, the first one at 345 °C corresponds to similar endothermic peak observed in the DTA curve. The second and third endothermic peaks were observed at 646 °C and 867 °C respectively. The endothermic peak at 646 °C could be due to citric acid and organic matter whereas that at 867 °C could signify the melting point of the prepared sample.

4.2.3 Raman spectroscopy

Raman spectroscopy was carried out in order to understand the modes of polarization and how the Raman modes changes with Pr-Co substitution. **Fig. 4.23** shows the Raman spectra

of $Ca_{1-x}Pr_xCu_{3-y}Co_yTi_4O_{12}$ (x=0.0, 0.1, 0.2, 0.3 and y=0.0, 0.4, 0.5, 0.6) in the range 400 to 1000 cm^{-1}. The Raman active modes 446, 509, 575, and 733 cm^{-1} have been observed from the Raman spectra. Also, the Raman active modes at 446, 509, and 575 cm^{-1} tend to shift towards lower Raman shift. It can be seen that the intensity of the peaks decreases with Pr^{3+}-Co^{2+} substitution. The intense Raman active modes at 446 and 509 cm^{-1} correspond to TiO_6 rotation-like modes whereas the weak Raman active mode at 575 cm^{-1} could be attributed to Ti-O-Ti anti-stretching mode of the octahedron, these three peaks are characteristics peaks of CCTO ceramic phase [152]. The broad Raman active mode at 733 cm^{-1} could be ascribed to

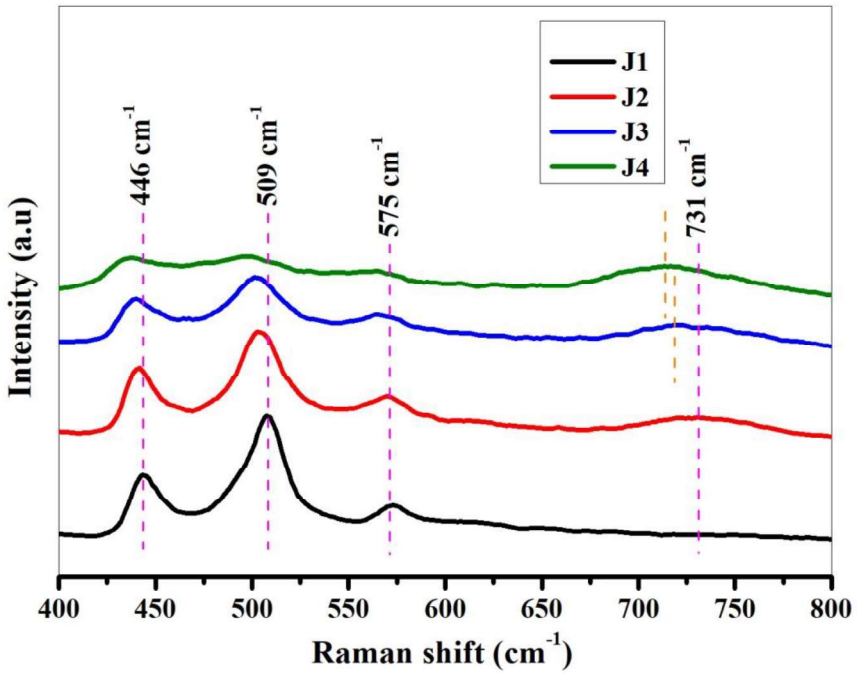

Fig. 4.23 Raman spectra of $Ca_{1-x}Pr_xCu_{3-y}Co_yTi_4O_{12}$ (x=0.0, 0.1, 0.2, 0.3 and y=0.0, 0.4, 0.5, 0.6)

the presence of $CaTiO_3$. Since the purity of the prepared sample has been confirmed from XRD result, we can rule out the possibility of this Raman active mode originating from the secondary phase $CaTiO_3$. However, this mode can be ascribed to Co-O-Ti or Co-O-Co stretching mode as a result of occupation of Co^{2+} at Ti^{4+} sites [153]. This is further supported by the observation of the fact that the Raman active mode at 733 cm^{-1} appear only after the initiation of Pr-Co substitution (**Fig. 4.23**).Additionally, this peak shifted to lower Raman

shift as a result of successful incorporation of Pr^{3+}-Co^{2+} into the CCTO lattice. Raman active mode at 610 cm^{-1} which signify the presence of rutile phase of TiO_2 was not observed [154]. Hence, Raman analysis supports the single phase structure observed in XRD spectra.

4.2.4 Morphology analysis

The morphology of the prepared sample was investigated using FESEM. **Fig. 6** presents the FESEM micrograph and particle distribution of $Ca_{1-x}Pr_xCu_{3-y}Co_yTi_4O_{12}$ (x=0.0, 0.1 and y=0.0, 0.4) The CCTO ceramic shows a wide range of well-defined almost cubic grain with grain size in μm. It can be observed from **Fig. 4.24** that the small grains were embedded in

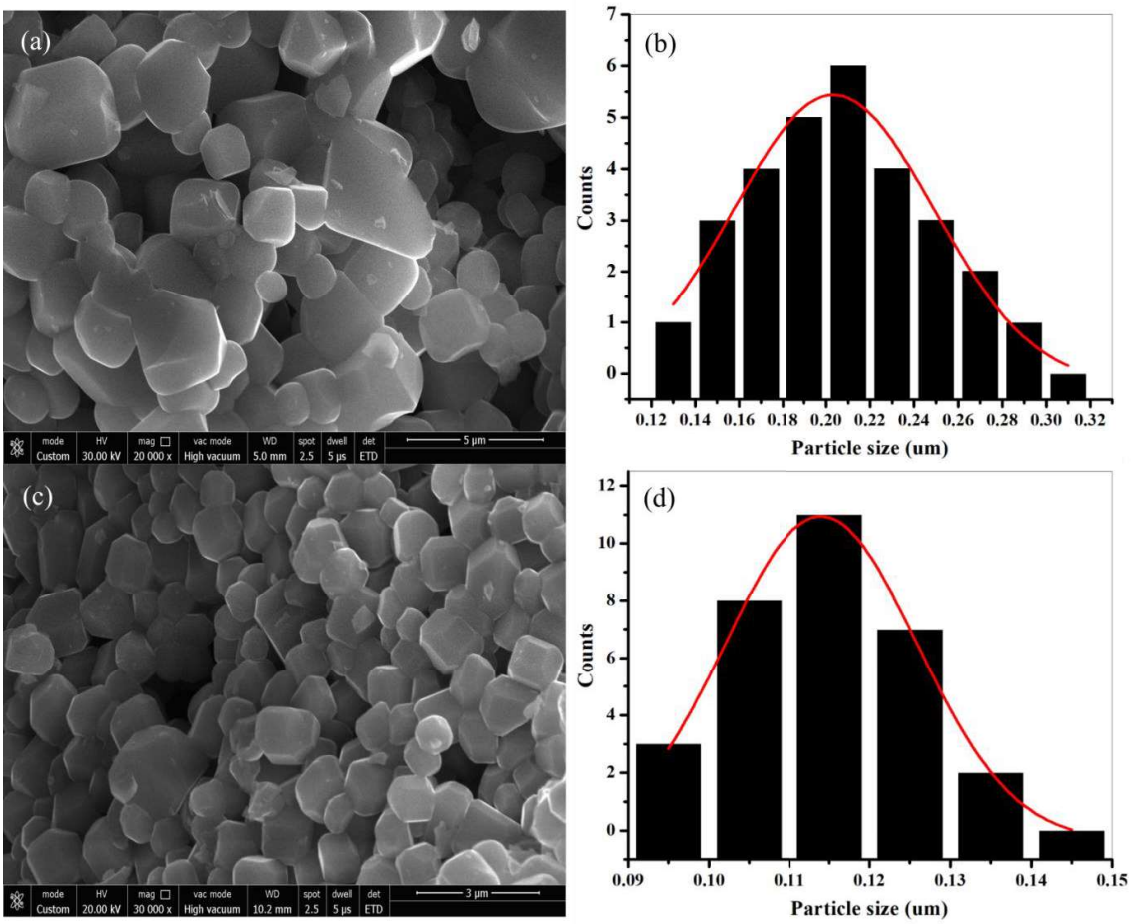

Fig. 4.24 FESEM micrograph and particle distribution of $Ca_{1-x}Pr_xCu_{3-y}Co_yTi_4O_{12}$ (x=0.0, 0.1 and y=0.0, 0.4) (a-b) J1 and (c-d) J2

between the large grains. The microstructure of the synthesized sample shows dense and closely arranged faceted grains and the absence of agglomeration. It has been reported that the dielectric properties of CCTO ceramic greatly depend on the microstructure

[151][155][156]. CCTO ceramic with dense microstructure usually exhibit high dielectric constant. The appearance of liquid oxide phase of the dopants as a result of high temperature sintering process was not observed in the samples [157].

The elemental composition of the prepared sample was studied via EDX spectroscopy. **Fig. 4.25** (b) and (d) presents the EDX spectra of $Ca_{1-x}Pr_xCu_{3-y}Co_yTi_4O_{12}$ (x=0.0, 0.1 and y=0.0, 0.4). The entire substituted elements have been observed in the EDX spectra. From the EDX analysis, we conclude that the stoichiometry of the prepared samples has been maintained. The fact that no impurity is observed in the EDX spectra further supported the results obtained from XRD and Raman spectroscopy.

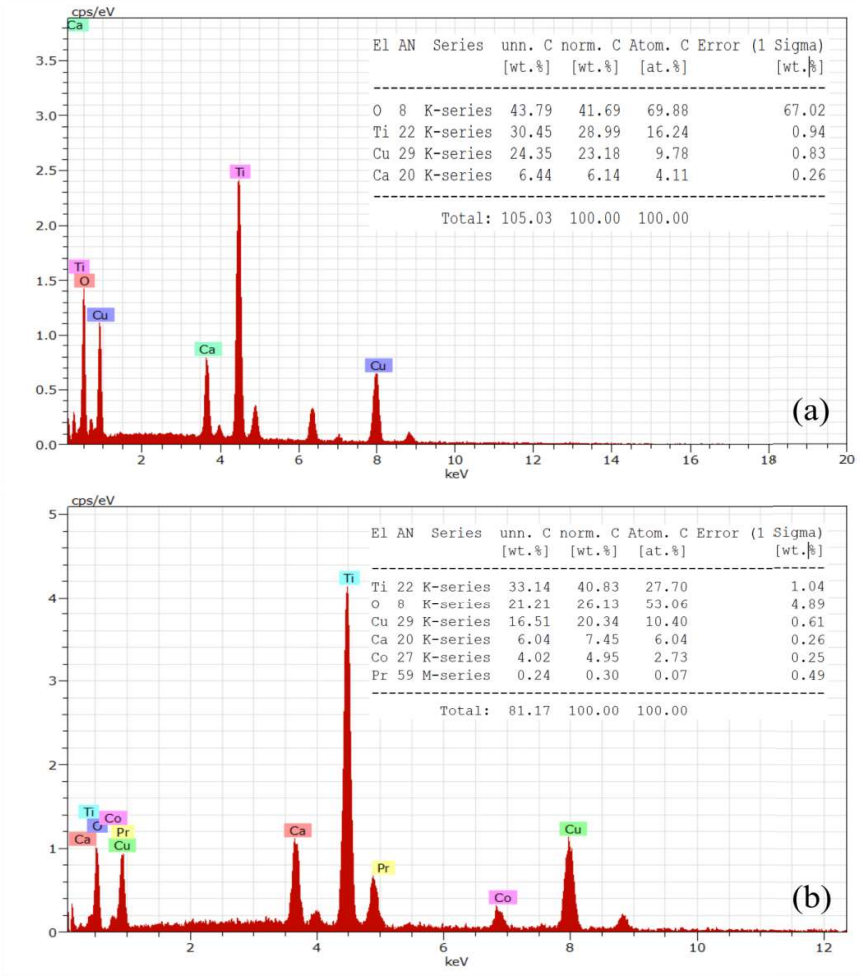

Fig. 4.25 EDX spectra of $Ca_{1-x}Pr_xCu_{3-y}Co_yTi_4O_{12}$ (x=0.0, 0.1 and y=0.0, 0.4) for (a) J1 and (b) J2

4.2.5 Optical analysis

The mechanism of UV-vis spectroscopy involves the absorption of photons by nanomaterials thereby using the energy of the photon to excite electrons from the valence to conduction band. The optical properties of $Ca_{1-x}Pr_xCu_{3-y}Co_yTi_4O_{12}$ (x=0.0, 0.1, 0.2, 0.3 and y=0.0, 0.4, 0.5, 0.6) have been examined using UV-vis spectroscopy in the range 234-766 nm. The optical band gap (E_g) was calculated from the following formula [158].

$$(\alpha h\upsilon)^m = K\left(h\upsilon - E_g\right) \tag{4.12}$$

Where α is the absorption coefficient, h is the planks constant ($6.6260 \times 10^{-34}\, J.s$), υ is incident photon's frequency and m is a constant having values of 1/2, 2, 3/2, and 3 for allowed direct, allowed indirect, forbidden direct, and forbidden indirect transitions respectively [159][160]. The graph of transmittance against wavelength is shown in **Fig. 4.26**.

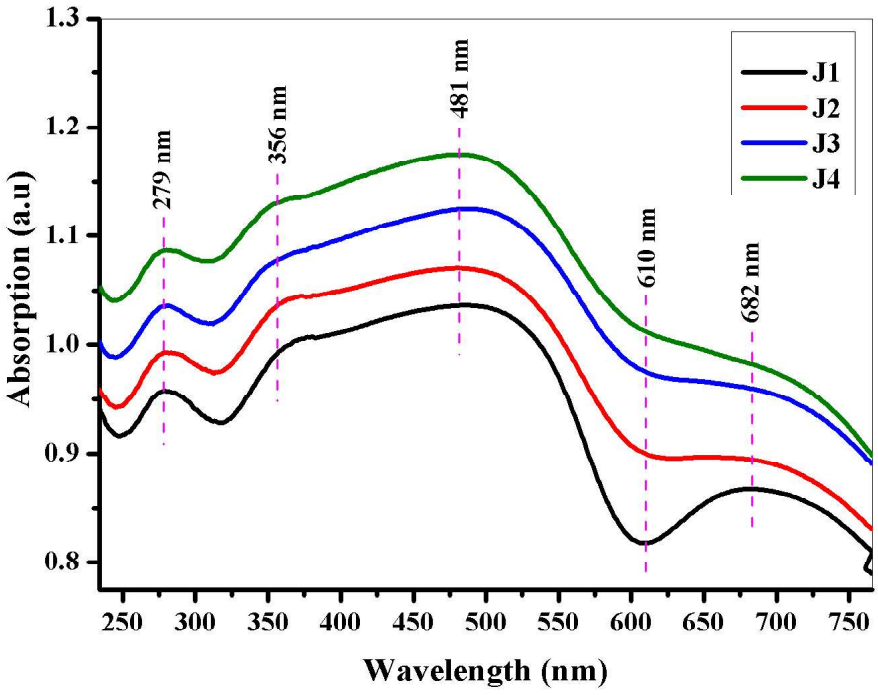

Fig. 4.26 Variation of transmittance with wavelength for $Ca_{1-x}Pr_xCu_{3-y}Co_yTi_4O_{12}$ (x=0.0, 0.1, 0.2, 0.3 and y=0.0, 0.4, 0.5, 0.6)

The synthesized material shows absorption peaks at 279, 356, 481 and 682 nm which corresponds to $\sigma - \sigma^*$, $n - \sigma^*$, $\pi - \pi^*$, and $n - \pi^*$ transition respectively. The absorption peak at 279 nm shows a slight red (bathochromic) shift of about 7 nm. A wide reflection peak was observed at 610 nm, this peak slowly merges with the absorption peaks at 680 nm as Pr-Co substitution is increased. This observed merger of absorption and reflection peaks signify that Pr-Co substitution enhances absorption by the prepared samples. The plots of $(\alpha h\upsilon)^2$ against E_g are presented in **Fig. 4.27**, the value of E_g for each of the prepared sample was determined by extrapolation of the linear part of plot up to x-axis. The values of E_g were found to be 3.88, 3.63, 3.55 and 3.49 eV for J1, J2, J3, and J4 respectively, these observed values of $E_g$are higher than those reported by Turky *et al.* [161]. From **Fig. 4.28**, we observe that E_g shows a decreasing trend with increase in Pr^{3+}-Co^{2+} substitution, this could be attributed to structural defects which results from symmetry breaking of TiO_6 octahedral as a result of cation substitution [161][162]. The observed values of E_g are within the range of that obtained for UV-blue light emitting diodes (LEDs) application [163].

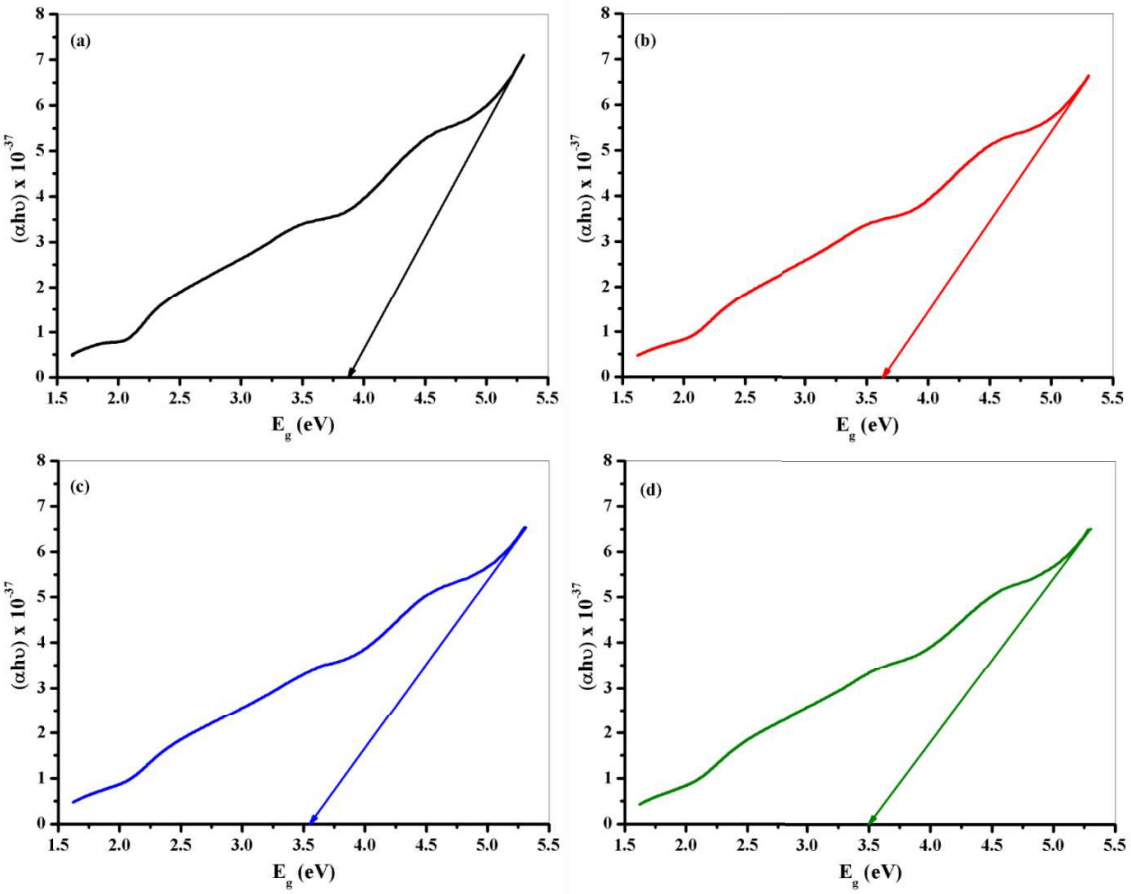

Fig. 4.27 Optical band gap of $Ca_{1-x}Pr_xCu_{3-y}Co_yTi_4O_{12}$ (x=0.0, 0.1, 0.2, 0.3 and y=0.0, 0.4, 0.5, 0.6) (a) J1, (b) J2, (c) J3 and (d) J4

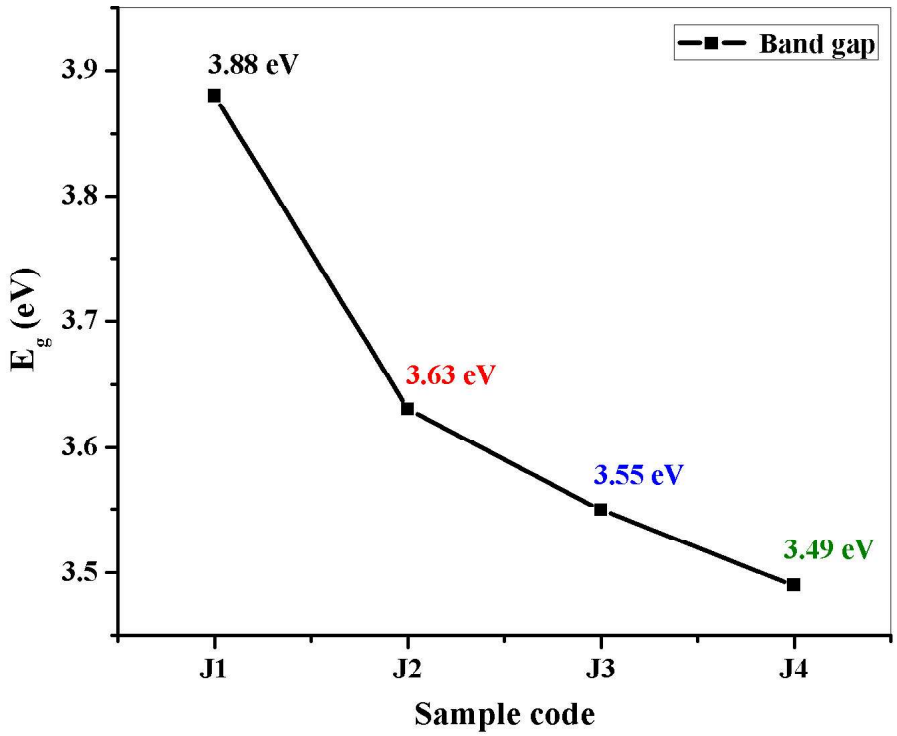

Fig. 4.28 Variation of band gap with Pr^{3+}-Co^{2+} substitution

4.2.6 Dielectric and impedance spectroscopy

The room temperature real part of dielectric permittivity (ε') was calculated so as to understand the energy storage behaviour of the prepared samples. **Fig. 4.29** presents the room temperature plot of ε' for $Ca_{1-x}Pr_xCu_{3-y}Co_yTi_4O_{12}$ (x=0.0, 0.1, 0.2, 0.3 and y=0.0, 0.4, 0.5, 0.6) over the frequency range 100 Hz to 120 MHz. The values of ε' for the prepared samples were estimated using the formula [164].

$$\varepsilon' = \frac{Z''}{2\pi\omega C_0 Z^2} \tag{4.13}$$

Where Z'' is the imaginary part of impedance, ω is the frequency, C_0 is the geometrical capacitance and Z is the impedance. The value of ε' for all the synthesized samples decrease with increase in frequency throughout the frequency range except at higher frequencies where

a relaxation peak was observed. The values of ε' for the synthesized samples at room temperature and frequency of 100 Hz are 4920, 2030, 1920, and 3560 for the samples J1, J2, J3, and J4 respectively. The values of ε' for all the samples decrease with increase in Pr-Co concentration. Furthermore, the sample J4 shows high value of ε' at higher frequencies followed by a relaxation process (**Fig. 4.29**). All the samples show high values of ε' at low frequencies; this could be attributed to charges being accumulated at the sample-electrode interface and interfacial space charge polarization [116][165].

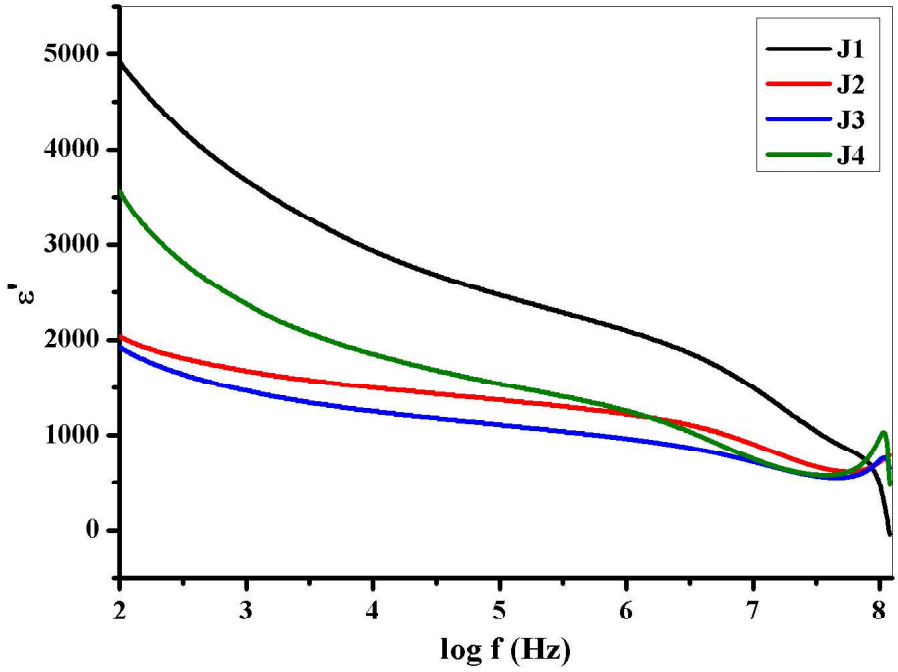

Fig. 4.29 Room temperature real part of dielectric permittivity (ε') for $Ca_{1-x}Pr_xCu_{3-y}Co_yTi_4O_{12}$ (x=0.0, 0.1, 0.2, 0.3 and y=0.0, 0.4, 0.5, 0.6)

The observation of high values of ε' at low frequency could mean that charge carriers are accumulated at the semiconducting and insulating grain boundary interface. The prepared samples will differ in relative density of grain boundaries since they are polycrystalline in nature, this gives the possibility of boundary layer mechanism which eventually affects the ε' [150][166][167]. At higher frequency, a relaxation peak was observed in the sample J4; this can be explained on the basis of Maxwell-Wagner relaxation process associated with the depletion layer created between the grain and grain boundary interface [141]. The absence of

relaxation peak at low frequency which is associated with depletion layers at the interface of electrode-bulk was observed [168]. From **Fig. 4.29**, we can see that the ε' of all the Pr-Co substituted samples is less that of the un-substituted sample, this could be attributed to the absence of segregation of impurity phase ($CaTiO_3$ and CuO) at grain boundaries and lower calcination temperature [169].

The room temperature imaginary part of dielectric permittivity (ε'') is determined in order to understand the interfacial relaxation processes in the prepared samples. **Fig. 4.30** presents the room temperature plot of ε'' against frequency (log f) for $Ca_{1-x}Pr_xCu_{3-y}Co_yTi_4O_{12}$ (x=0.0, 0.1, 0.2, 0.3 and y=0.0, 0.4, 0.5, 0.6). The values of ε'' for the prepared samples were calculated from [163].

$$\varepsilon'' = \frac{Z'}{2\pi\omega C_0 Z^2} \tag{4.14}$$

Where Z' is the real part of impedance, the values of room temperature ε'' for the prepared samples J1, J2, J3, and J4 at frequency of 100 Hz are respectively 1490, 395, 526, and 1460.

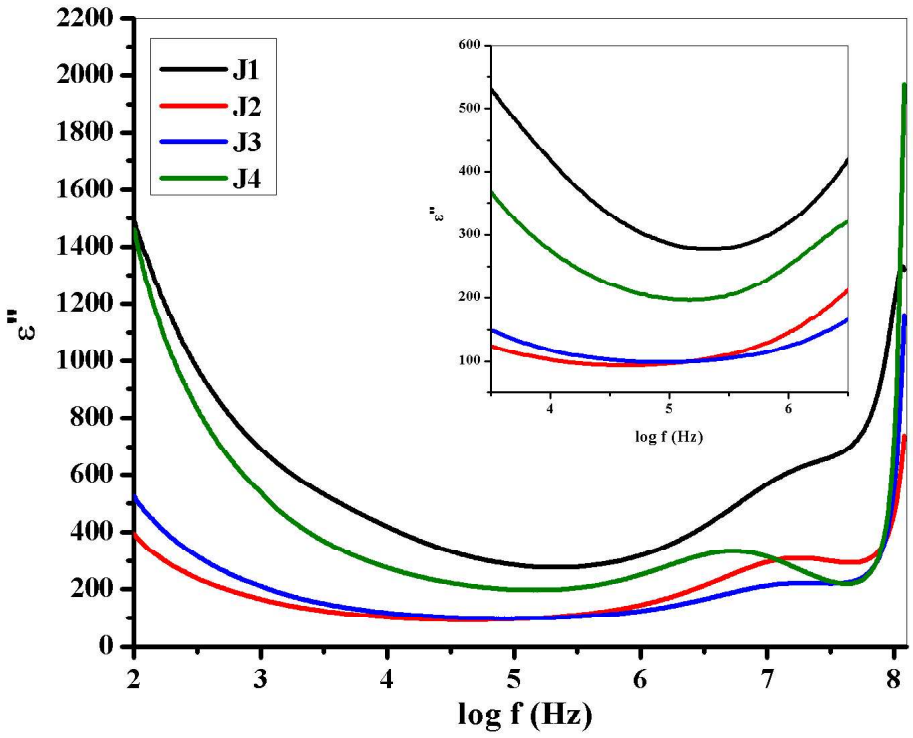

Fig. 4.30 Room temperature imaginary part of dielectric permittivity (ε'') for $Ca_{1-x}Pr_xCu_{3-y}Co_yTi_4O_{12}$ (x=0.0, 0.1, 0.2, 0.3 and y=0.0, 0.4, 0.5, 0.6)

The values of ε'' shows a decreasing trend at low frequencies and exhibit frequency independent behaviour at intermediate frequencies. At higher frequencies, there is an increase in ε'' with relaxation peaks in all the samples except in the sample with x=0.2/y=0.5. At higher frequencies, a Debye-like relaxation peak is observed in all the samples with the most intense peak in the sample with J4. This phenomenon usually arises due to dipolar relaxation process between semiconducting grains separated by insulating grain boundaries [116].

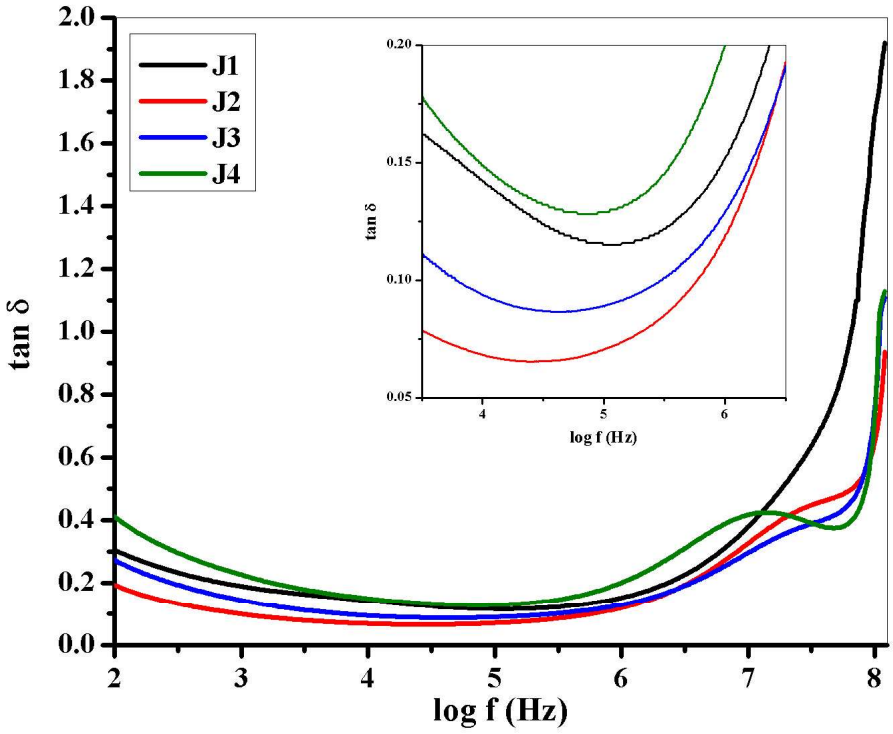

Fig. 4.31 Room temperature dielectric loss tangent of $Ca_{1-x}Pr_xCu_{3-y}Co_yTi_4O_{12}$ (x=0.0, 0.1, 0.2, 0.3 and y=0.0, 0.4, 0.5, 0.6)

The room temperature dielectric loss (tan δ) is determined in order to understand the energy loss behaviour of the prepared samples. **Fig. 4.31** presents the plot of tan δ against frequency (log f) for $Ca_{1-x}Pr_xCu_{3-y}Co_yTi_4O_{12}$ (x=0.0, 0.1, 0.2, 0.3 and y=0.0, 0.4, 0.5, 0.6) at room temperature. The values of tan δ for the prepared samples were calculated from [170].

$$\tan \delta = \frac{\varepsilon''}{\varepsilon'} \quad (4.15)$$

The values of tan δ for the synthesized samples J1, J2, J3, and J4 at 100 Hz are respectively 0.304, 0.194, 0.273 and 0.411. The tan δ decreases with increase in Pr-Co concentration and then increases (**Fig. 4.31**). The values of tan δ for all the synthesized samples initially decreases with frequency at much lower frequency and then becomes almost constant (i.e. independent of frequency) at intermediate frequencies. At much higher frequencies, the values of tan δ shows a steady increase except for the sample J4 where a relaxation peak was observed; this could be due to orientation polarization resulting from oxygen defects in the sample [171]. The absence of relaxation peak at lower frequency which is usually as a result of space charge polarisation was observed. Space charge polarization occurs due to contact between two phases having different electrical conductivity [172].

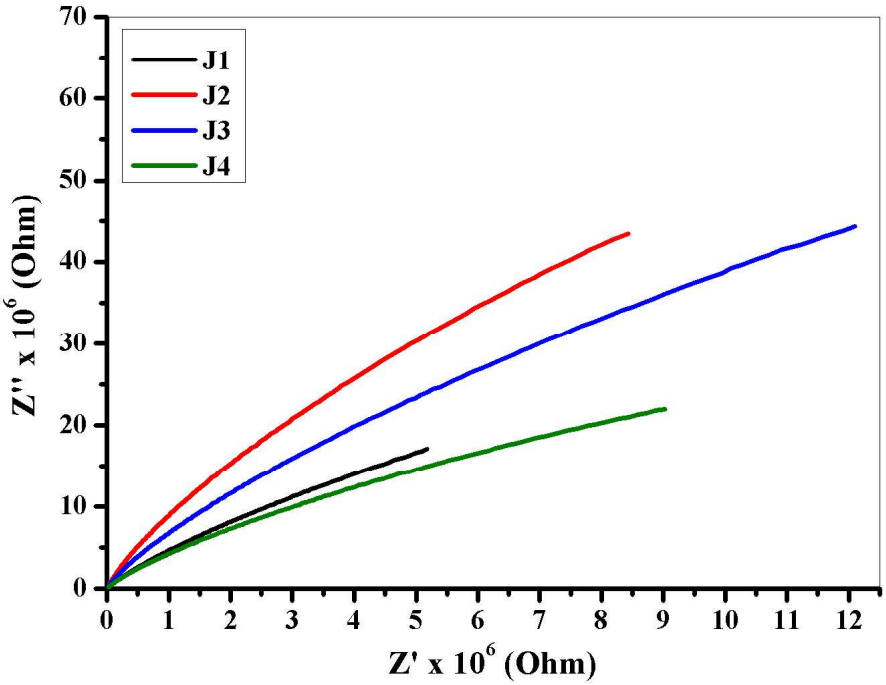

Fig. 4.32 Cole-Cole plot of $Ca_{1-x}Pr_xCu_{3-y}Co_yTi_4O_{12}$ (x=0.0, 0.1, 0.2, 0.3 and y=0.0, 0.4, 0.5, 0.6)

The Cole-Cole plot reveals the nature of the grain and grain boundary resistance of the synthesized samples which is determined from the nature of the curve observed from plotting

the imaginary part (Z'') versus real part (Z') of complex impedance (Z^*). **Fig. 4.32** presents Cole-Cole plot of $Ca_{1-x}Pr_xCu_{3-y}Co_yTi_4O_{12}$ (x=0.0, 0.1, 0.2, 0.3 and y=0.0, 0.4, 0.5, 0.6) at room temperature. The complex impedance can be expressed as [137]

$$Z^* = Z' - jZ'' \tag{4.16}$$

Where $j = \sqrt{-1}$ is an imaginary number, Z' is the real part and Z'' is the imaginary part of the complex impedance (Z^*). Usually, a semi-circle arc results from the plot of Z'' versus Z'. The part of the semi-circle at the higher frequency region (away from the origin) of the Cole-Cole plot display contribution from the grains also called the grain resistance (R_g) whereas the semi-circle arc in the lower frequency region (near the origin) display contribution of the grain boundaries also called grain boundary resistance (R_{gb}) [151]. The values of R_g can be retrieved from the intercept of the semi-circle arc at the higher frequency region with Z'-axis whereas the values of R_{gb} can be retrieved from the intercept of the semi-circle arc at the lower frequency region with Z'-axis. Hence, most of the contributions to dielectric constant of the CCTO ceramics originate from R_{gb}. **Fig. 4.29** show high dielectric constant at lower frequencies; hence we can ascribe this behaviour to high R_{gb} of the prepared sample [141].

The room temperature conductivity of the sample has been determined by calculating the AC conductivity (σ_{ac}). **Fig. 4.33** presents plot of AC conductivity against frequency (log f) for $Ca_{1-x}Pr_xCu_{3-y}Co_yTi_4O_{12}$ (x=0.0, 0.1, 0.2, 0.3 and y=0.0, 0.4, 0.5, 0.6). Variation of conductivity with frequency can be explained on the basis of the following equation [173]

$$\sigma_t = \sigma_{AC} + \sigma_{DC} \tag{4.17}$$

Where σ_{DC} is the frequency independent part of conductivity, $\sigma_{AC} = A\omega^s$ is the frequency dependent part of conductivity, A is the temperature dependent constant and s is a numerical constant. The conductivity for all the prepared samples shows similar behaviour. The conductivity remains constant at lower frequencies showing frequency independent behaviour up to intermediate frequencies. At higher frequencies, there is an abrupt and steady increase in conductivity; this could be attributed to different conduction mechanism such as hopping, tunnelling or free band conduction [174]. There is no evidence of conductivity of the grain boundaries which occur at intermediate frequencies [168].

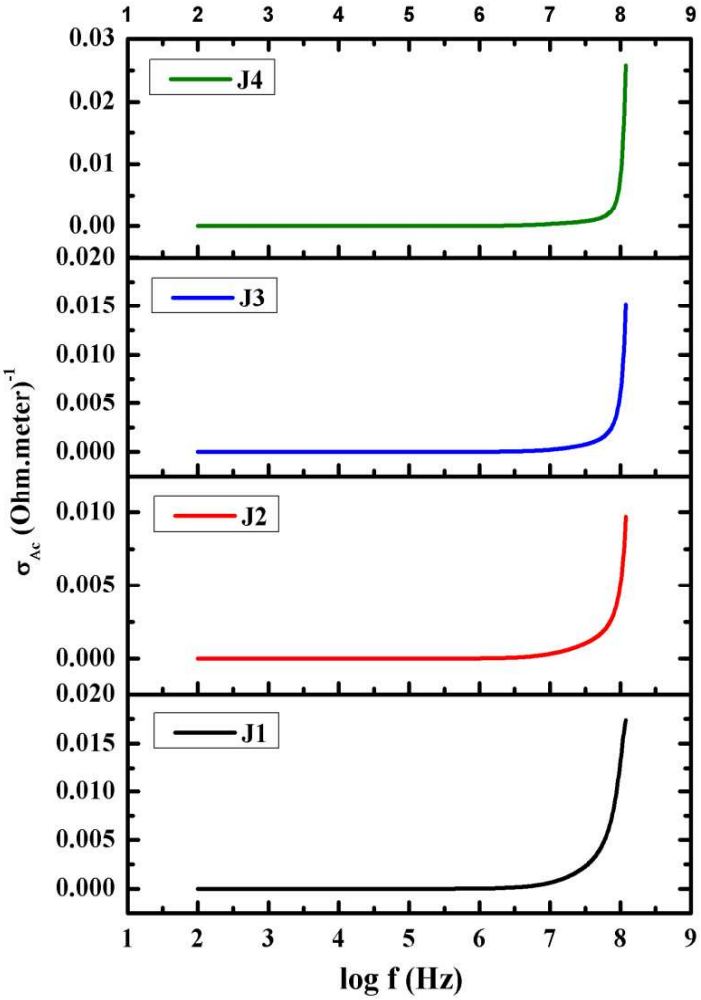

Fig. 4.33 Room temperature Ac conductivity of $Ca_{1-x}Pr_xCu_{3-y}Co_yTi_4O_{12}$ (x=0.0, 0.1, 0.2, 0.3 and y=0.0, 0.4, 0.5, 0.6)

4.3 Ce^{3+}-Ni^{2+} substituted calcium copper titanate (CCTO)

4.3.1 XRD analysis

Fig. 4.34 presents X-ray diffraction (XRD) patterns of $Ca_{1-x}Ce_xCu_3Ti_{4-y}Ni_yO_{12}$ (x=0.0, 0.25, 0.45, 0.65 and y=0.0, 0.3, 0.5, 0.7) prepared by sol-gel method and calcinated at 900 °C. It has been confirmed from X-powder that the prepared sample exhibit crystalline structure of calcium copper titanate ($CaCu_3Ti_4O_{12}$). Traces of secondary phases of calcium titanate ($CaTiO_3$) and copper oxide (CuO) are observed in the prepared samples. A fairly single perovskite structure of the material is formed in the absence of Ce^{3+}-Ni^{3+} substitution. The

lattice parameters are calculated and presented in table 1. From **Fig. 4.34**, it can be seen that the intensity of the peaks of the secondary phases increases with Ce^{3+}-Ni^{3+} substitution. The XRD patterns are indexed using JCPDS card number 75-2188. The lattice constant (a) is calculated using the formula

$$a = d\sqrt{h^2 + k^2 + l^2} \tag{4.18}$$

where d is the inter planer spacing and hkl are the miller indices. The volume of the unit cell is calculated using

$$V_{cell} = a^3 \tag{4.19}$$

Both the lattice constant and volume of unit cell increases with Ce^{3+}-Ni^{2+} substitution (**Fig. 4.35**). This could be attributed to the fact the ionic radius of Ce^{3+} (1.034 Å) and Ni^{2+} (0.690 Å) are larger than those of Ca^{2+} (0.990 Å) and Ti^{4+} (0.605 Å) respectively [141]. The calculated lattice constant and volume of unit cell are in agreement with literature.

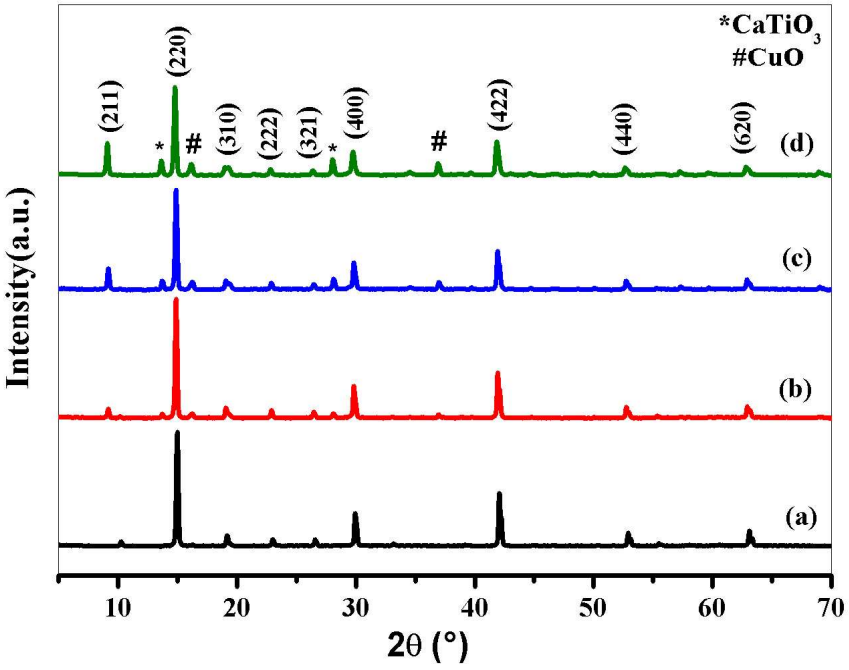

Fig. 4.34 XRD spectra of $Ca_{1-x}Ce_xCu_3Ti_{4-y}Ni_yO_{12}$ (x=0.0, 0.25, 0.45, 0.65 and y=0.0, 0.3, 0.5, 0.7) for (a) K1, (b) K2, (c) K3, and (d) K4.

Table 4.3 Values of lattice constant (a) and volume of unit cell (V_{cell}) of $Ca_{1-x}Ce_xCu_3Ti_{4-y}Ni_yO_{12}$ (x=0.0, 0.25, 0.45, 0.65 and y=0.0, 0.3, 0.5, 0.7)

Sample code	2θ (°)	d (Å)	β (°)	a (Å)	V_{cell} (Å^3)
K1	29.968	2.9792	0.199	7.390	403.583
K2	29.872	2.9886	0.196	7.392	403.911
K3	29.823	2.9935	0.216	7.393	404.075
K4	29.774	2.9982	0.256	7.394	404.239

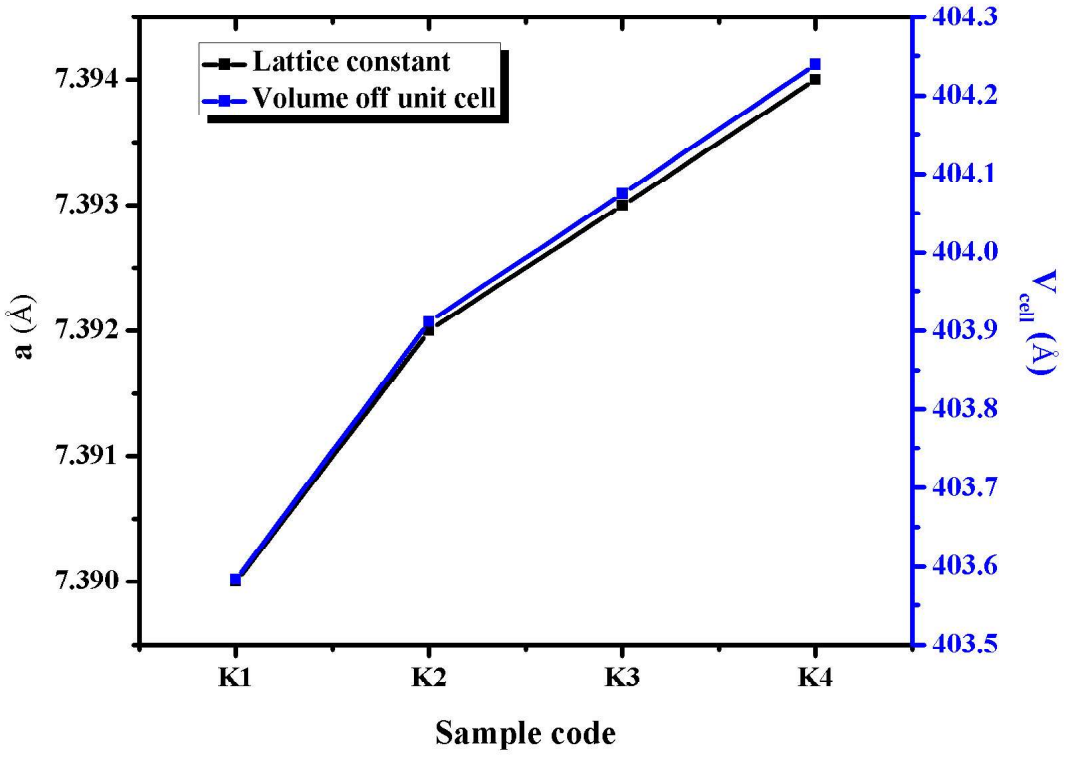

Fig. 4.35 Variation of lattice constant and volume of unit cell with sample composition

4.3.2 Morphology analysis

Fig. 4.36 presents the FESEM micrographs and EDX of the sample K2 at different resolution. Large, regular and polyhedral grains of sizes between 902.4 nm to 1.562 μm were observed. It is clear from the micrographs that the prepared sample exhibit bi-modal distribution of grains, this shows that the prepared sample are agglomerated which upon

calcination forms larger grains [175]. The energy dispersive X-ray (EDX) spectra show clearly the presence of Ca, Ce, Cu, Ti, Ni and O, this result is as per the stoichiometry of the prepared sample.

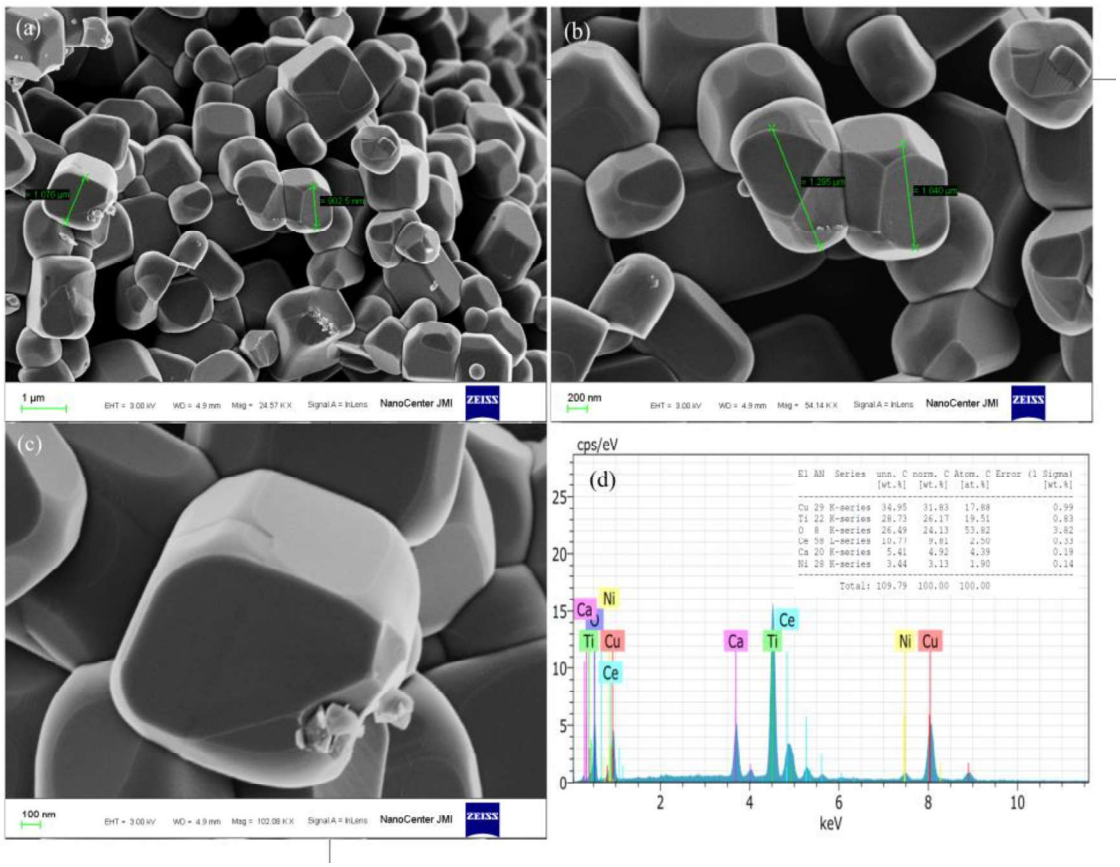

Fig. 4.36 FESEM micrographs and EDX spectra of $Ca_{1-x}Ce_xCu_3Ti_{4-y}Ni_yO_{12}$ (x=0.25 and y=0.3) at (a) 1 μm, (b) 200 nm, (c) 100 nm, and (d) EDX spectra

4.3.3 Dielectric and impedance spectroscopy

Room temperature dielectric constant (ε') and as a function of frequency (log f) for the sample prepared are presented in **Fig. 4.37**. The values of ε' of the prepared samples were calculated from

$$\varepsilon' = \frac{Z''}{2\pi\omega C_0 Z^2} \tag{4.20}$$

Where Z'' is the imaginary part of impedance, ω is the frequency, C_0 is the geometrical capacitance and Z is the impedance. Four series of sample were synthesized $Ca_{1-x}Ce_xCu_3Ti_{4-y}Ni_yO_{12}$ (x=0.0, 0.25, 0.45, 0.65 and y=0.0, 0.3, 0.5, 0.7). The dielectric constant of the

prepared sample at 100 Hz are 4590, 16000, 2130 and 2750 for the corresponding Ce-Ni substitution $_yNi_yO_{12}$ (x=0.0, 0.25, 0.45, 0.65 and y=0.0, 0.3, 0.5, 0.7). The dielectric constant of the prepared sample first increases with Ce-Ni substitution and then decreases We observed high dielectric constant (of value 16000 at 100 Hz) in the sample $Ca_{1-x}Ce_xCu_3Ti_{4-y}Ni_yO_{12}$ (x=0.25 and y=0.3), this high dielectric constant could be attributed to the presence of thin re-oxidized grain boundary regions on the surfaces of grains with large sizes [176].

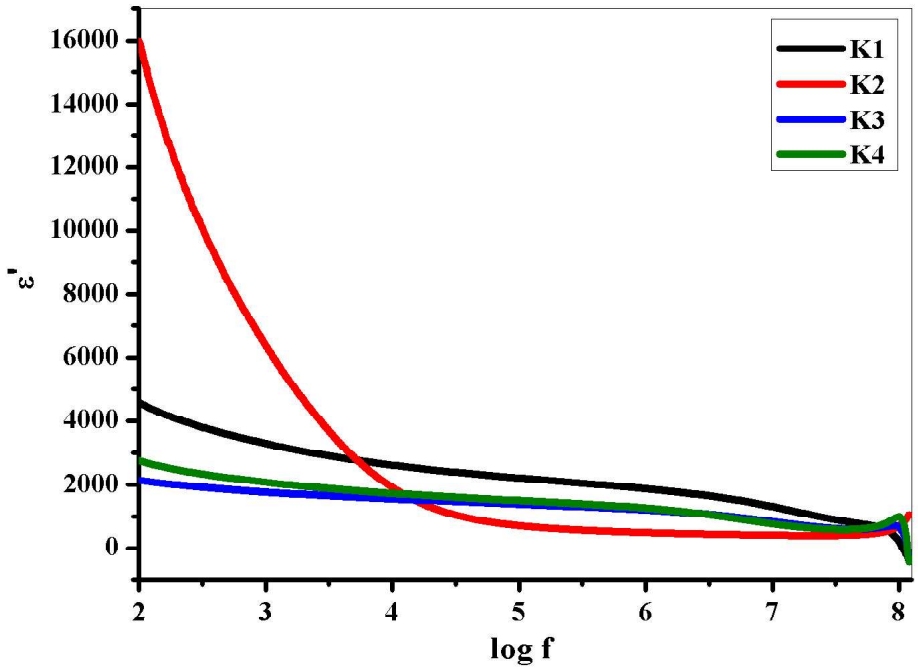

Fig. 4.37 Dielectric constant of $Ca_{1-x}Ce_xCu_3Ti_{4-y}Ni_yO_{12}$ (x=0.0, 0.25, 0.45, 0.65 and y=0.0, 0.3, 0.5, 0.7) at room temperature

This is in agreement with HRSEM micrograph as they show grains having large sizes. Also, this high dielectric constant could be explained in terms of barrier layer formation which is due to the differences in conductivity of the grain and grain boundaries [151]. The decreasing behaviour of the dielectric constant in the samples with higher Ce-Ni substitution (x= 0.45, 0.65 and y= 0.5, 0.7) could be related to the presence of secondary phase ($CaTiO_3$ and CuO) at the grain boundaries of the prepared sample [177]. At higher frequencies, the dielectric constant for the undoped sample shows frequency independent behaviour, this could be ascribed to different sizes in the grain [178]. A Debye-type relaxation peak is observed in the

sample $Ca_{1-x}Ce_xCu_3Ti_{4-y}Ni_yO_{12}$ (x=0.65 and y=0.7) at higher frequency, this can be explained on the basis of Maxwell-Wagner relaxation between the grain and grain boundary [179].

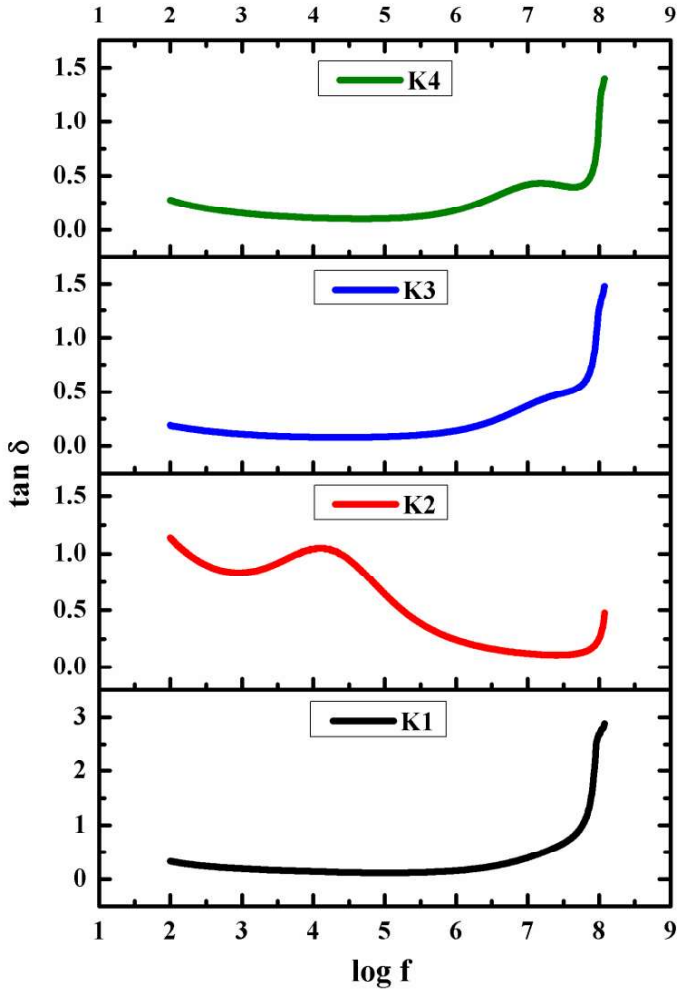

Fig. 4.38 Dielectric loss of $Ca_{1-x}Ce_xCu_3Ti_{4-y}Ni_yO_{12}$ (x=0.0, 0.25, 0.45, 0.65 and y=0.0, 0.3, 0.5, 0.7) at room temperature

Fig. 4.38 present room temperature dielectric loss (tan δ) versus frequency (log f) for the synthesized sample. The values of tan δ for the prepared samples were calculated from [170].

$$\tan\delta = \frac{\varepsilon''}{\varepsilon'} \tag{4.21}$$

Where ε'' is the imaginary part of permittivity. The dielectric tangent loss of the samples are 0.330, 1.140, 0.189, 0.227 for the sample $Ca_{1-x}Ce_xCu_3Ti_{4-y}Ni_yO_{12}$ (x=0.0, 0.25, 0.45, 0.65 and

y=0.0, 0.3, 0.5, 0.7) respectively (Fig. 9). All the samples show decrease in dielectric loss at low frequency and an increase as the frequency increases. At much higher frequencies (63.9 MHz), the dielectric loss increase rapidly. This rapid increase in dielectric loss might be due to resonance effect resulting from stray conductance of the contacts and leads [151]. The sample with the highest dielectric constant exhibits a relaxation peak at a frequency of 11.7 kHz. The sample $Ca_{1-x}Ce_xCu_3Ti_{4-y}Ni_yO_{12}$ (x=0.65 and y=0.7) exhibit the lowest dielectric tangent loss (0.189). All the prepared samples show low dielectric loss tangent.

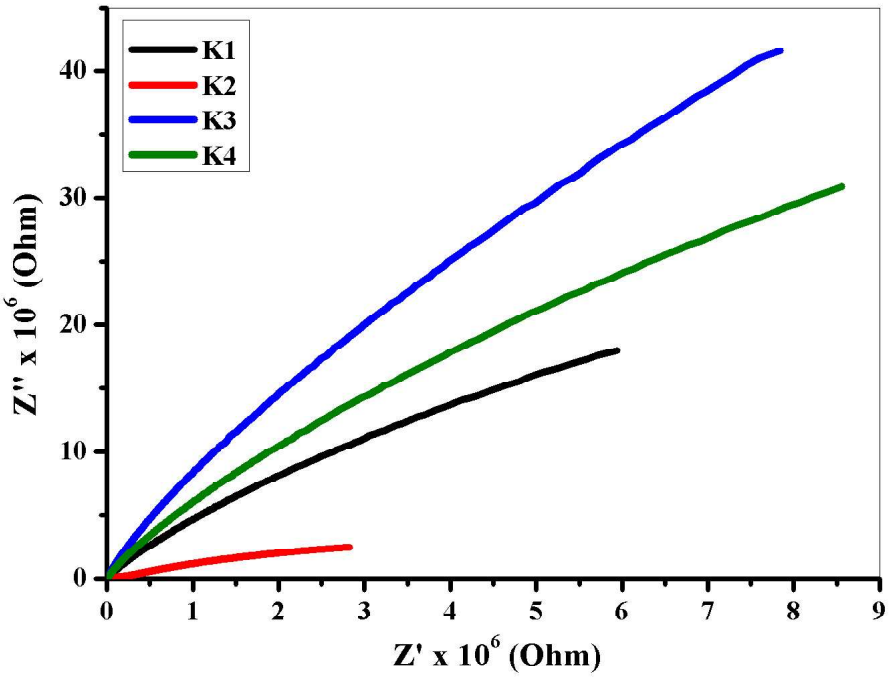

Fig. 4.39 Cole-Cole plot of $Ca_{1-x}Ce_xCu_3Ti_{4-y}Ni_yO_{12}$ (x=0.0, 0.25, 0.45, 0.65 and y=0.0, 0.3, 0.5, 0.7)

The complex impedance plot also known as the Cole-Cole plot is presented in **Fig. 4.39**. We carry out impedance studies in order to understand the nature of grain boundary resistance of the prepared sample. The nature of the grain boundary resistance is determined by the nature of curve resulting from plotting Z'' against Z'. The samples $Ca_{1-x}Ce_xCu_3Ti_{4-y}Ni_yO_{12}$ (x= 0.45, 0.65 and y= 0.5, 0.7) show high grain boundary resistance. These are also the samples with low dielectric tangent loss and their XRD peak show increasing intensity of secondary phases ($CaTiO_3$ and CuO). Li et al. reported the sample with high grain boundary resistance usually

have low dielectric loss as a result of existence of secondary phases in the prepared sample [177]. The semi-circle arc at the higher frequency part of the complex impedance plot represents contribution from the grain while that in the lower frequency part represents contributions from grain boundary [151]. Hence, the dielectric properties of the prepared sample can be ascribed to grain boundary resistance.

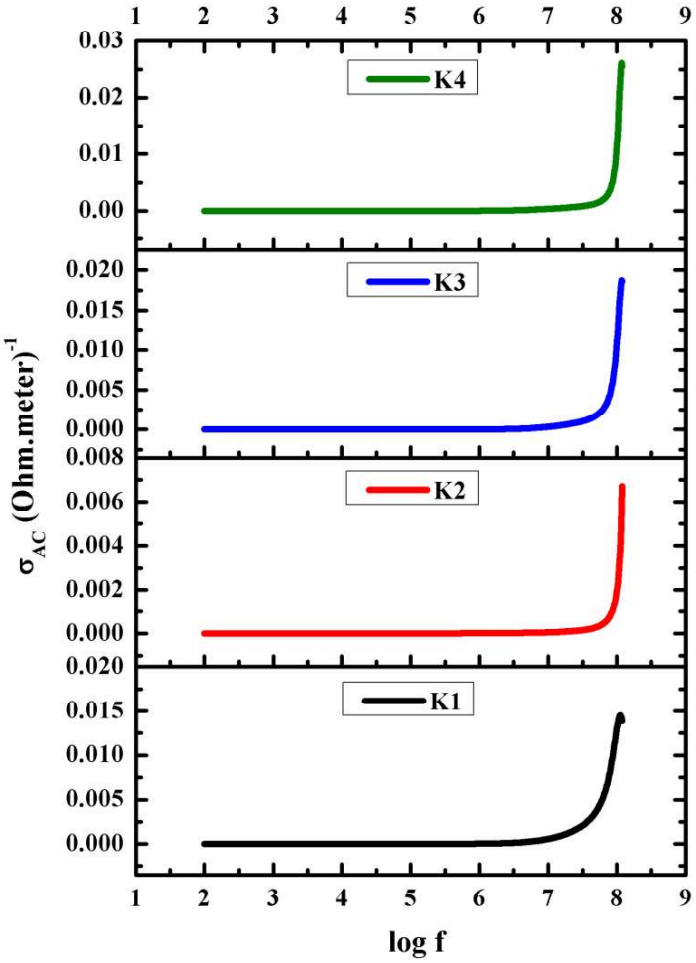

Fig. 4.40 AC conductivity of $Ca_{1-x}Ce_xCu_3Ti_{4-y}Ni_yO_{12}$ (x=0.0, 0.25, 0.45, 0.65 and y=0.0, 0.3, 0.5, 0.7) at room temperature

Fig. 4.40 presents the room temperature variation of AC conductivity with frequency (log f) of the prepared sample. The recorded AC conductivity of the prepared at a frequency of 100 Hz are 1.66×10^{-8}, 1.99×10^{-7}, 4.38×10^{-9}, and 8.33×10^{-9} (Ohm.meter)$^{-1}$ for $Ca_{1-x}Ce_xCu_3Ti_{4-y}Ni_yO_{12}$ (x=0.0, 0.25, 0.45, 0.65 and y=0.0, 0.3, 0.5, 0.7) respectively. All the

prepared samples show similar behaviour of conductivity. The variation of the conductivity of the prepared sample with frequency can be understood using the equations [180]

$$\sigma_t = \sigma_{AC} + \sigma_{DC} \quad (4.22)$$

where σ_{AC} is the frequency dependent part of the conductivity and σ_{DC} is the frequency independent part of the conductivity. From **Fig. 4.40**, we can see that the conductivity first decrease and then later increases with increase in frequency. Also, it can be seen that the conductivity show frequency independent behaviour at low frequency, this corresponds to σ_{DC}. At higher frequencies, the conductivity increases in all the prepared samples showing that the prepared sample exhibit frequency dependent behaviour, this corresponds to σ_{AC} [181]. The transition from σ_{DC} at lower frequencies to σ_{AC} at higher frequencies started to occur after the σ_{DC} reaches a certain frequency called the cross over frequency.

4.4 Al^{3+}-Mn^{2+} substituted M-type strontium hexaferrites (heat treatment)

4.4.1 XRD analysis

Fig. 4.41 presents the XRD pattern of $Sr_{0.7}Al_{0.3}Fe_{11.4}Mn_{0.6}O_{19}$ at room temperature. The prepared samples exhibit crystalline phases. The presence of α-Fe_2O_3 (JCPDS-010862368) at an angle of 33.80° was observed in all the samples, this can be attributed to incomplete crystallization reaction and the inhomogeneity of the mixture of starting materials or high level of substituted cations [86][182][87]. The emergence of α-Fe_2O_3 may be avoided by ensuring complete reaction of the starting materials and substituting small amount of cations. The presence of peaks (006), (110), (107), (114), (200), (203), (205), (206), (209), (217), (304), (2011), (220), and (2014) confirm the formation of hexagonal structure of the prepared samples which are similar to standard pattern of hexagonal ferrites of JCPDS-391433. Lattice parameters (*a* and *c*) were calculated using the following formula [183].

$$\frac{1}{d_{hkl}^2} = \frac{4}{3}\left(\frac{h^2+hk+k^2}{a^2}\right) + \frac{l^2}{c^2} \quad (4.23)$$

Here d_{hkl} is the *d* spacing value and *hkl* represent the miller indices for the peaks in XRD spectra. The values of lattice parameters (*a* and *c*), crystallite size (*D*) and unit cell volume (V_{cell}) are calculated and presented in **Table 4.4**. The lattice constant *c* shows variation with temperature (**Table 4.4**). The sample calcinated at 850 °C have the lowest lattice constant

(a=5.8570 Å) whereas those calcinated at 750 °C, 950 °C and 1050 °C have the almost same

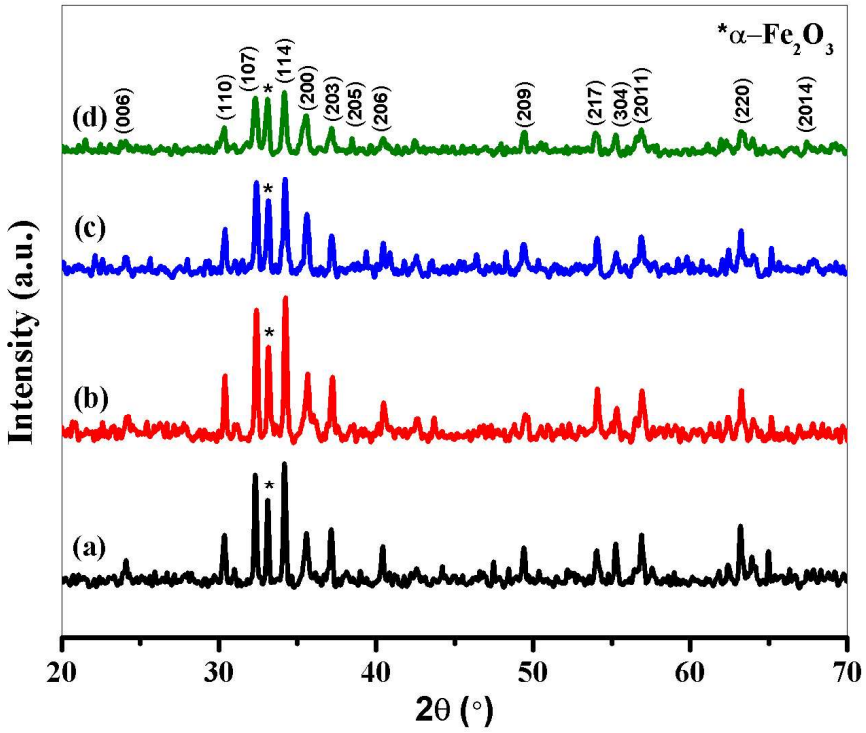

Fig. 4.41 XRD spectra of $Sr_{0.7}Al_{0.3}Fe_{11.4}Mn_{0.6}O_{19}$ at (a) T=1050 °C, (b) T=950 °C, (c) T=850 °C, and (d) T=750 °C

lattice constant. This variation in lattice constant may be attributed to microstructural defects, strain and interaction between substituted cations in the sample [184]. The crystallite size and volume of unit cell of the prepared sample were calculated using the formula [86].

$$D = \frac{k\lambda}{\beta cos\theta} \tag{4.24}$$

$$V_{cell} = 0.8666a^2c \tag{4.25}$$

where λ=1.54056 Å and it is the X-ray wavelength, θ is the Braggs angle, k is the shape factor ($k = 1$ for hexagonal ferrites) and β (in radian) is the full width at half maximum. The crystallite size first increase as the temperature is increased up to 850 °C, and then decreases (**Table 4.4**). The sample calcinated at 850 °C show high value of unit cell volume (707.13 $Å^3$) as compared to the other samples.

Table 4.4 Values of lattice parameters (a and c), crystallite size (D) and volume of unit cell (V_{cell}) for $Sr_{0.7}Al_{0.3}Fe_{11.4}Mn_{0.6}O_{19}$.

T (°C)	2θ (°)	d (Å)	β (°)	a (Å)	c (Å)	D (nm)	V_{cell} (Å^3)
1050	34.18	2.6212	0.732	5.8872	23.0418	12.62	692.07
950	34.26	2.6153	0.246	5.8872	22.7945	37.55	695.34
850	34.10	2.6272	0.726	5.8570	23.7864	12.72	707.13
750	34.28	2.6138	0.809	5.8872	22.7326	11.42	682.79

4.4.2 FTIR analysis

FTIR was carried out in the range 400 to 4000 cm^{-1} in order to get an idea of the formation of M-type hexagonal ferrites and to check for the presence of residual groups in the prepared samples. The plot of the FTIR spectra is shown in **Fig. 4.42**. Prior to the measurement of the

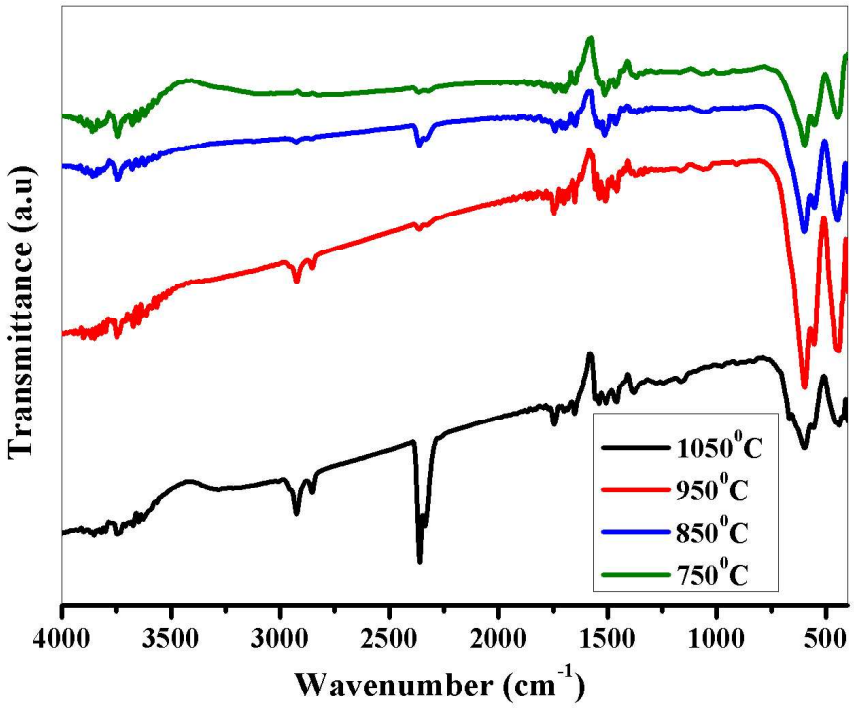

Fig. 4.42 FTIR spectra of $Sr_{0.7}Al_{0.3}Fe_{11.4}Mn_{0.6}O_{19}$

FTIR spectra, anhydrous KBr was mixed with the prepared sample in the ratio 1:10 and pressed into pellets. The occurrence of two peaks between 400 cm^{-1} and 600 cm^{-1} which are common characteristics of hexagonal ferrites. The presence of these peaks gives an idea of the formation of hexagonal ferrites. These peaks are formed as a result of stretching vibration of metal oxygen bond [184]. The absorption bands in the range 446 to 439 $cm^{-1}(\upsilon_2)$ are attributed to Fe-O bending in $Fe\text{-}O_4$ and while the absorption bands in the range 596 to 598 $cm^{-1}(\upsilon_1)$ are due to Fe-O stretching in $Fe\text{-}O_6$ [32][185]. This indicates that the Al^{3+} and Mn^{2+} ions have been substituted in strontium hexaferrite and thereby modifying Fe^{3+} ions distribution. The presence of nitrate ions in the prepared sample was observed as a result of the band at 1381 cm^{-1} [186]. The bands that appear in the range 1148-1464 cm^{-1} occur as a result of Metal-Oxygen-Metal (M-O-M) such as Fe-O-Fe and Co-O-Co [187].The presence of CO_2 is evident by the observation of the band at 2363 cm^{-1} [188][185]. The broad band that appear at 3463 cm^{-1} corresponding to O-H stretching could be attributed to the presence of moisture in the sample [189].

4.4.3 Thermal analysis

In order to comprehend the effect of heat on the mass of the prepared sample, we carry out thermal analysis of the prepared sample. In thermogravimetry analysis (TGA) graph (**Fig. 4.43**), decomposition of the residual organic matter is observed between 0-324°C.This is as a result oxidation-reduction reaction linking metal nitrates with citric acid. The weight loss observed between 324 and 650 °C is as a result of decomposition of the precursor and the fact that hematite is converted to hexagonal ferrites structure. After 650 °C, the weight loss becomes constant and this signify the formation of $Sr_{0.7}Al_{0.3}Fe_{12.4}Mn_{0.6}O_{19}$ [184]. Differential thermal analysis (DTA) and derivative thermo gravimetric (DTG) of $Sr_{0.7}Al_{0.3}Fe_{11.4}Mn_{0.6}O_{19}$ are shown in **Fig. 4.44**. An endothermic peak observed in the DTA curve as well as DTG curve at 358 °C is as a result of loss of water whereas the peak observed 357 °C indicates the recrystallization of the sample and nitrate complex decomposition [188][186].

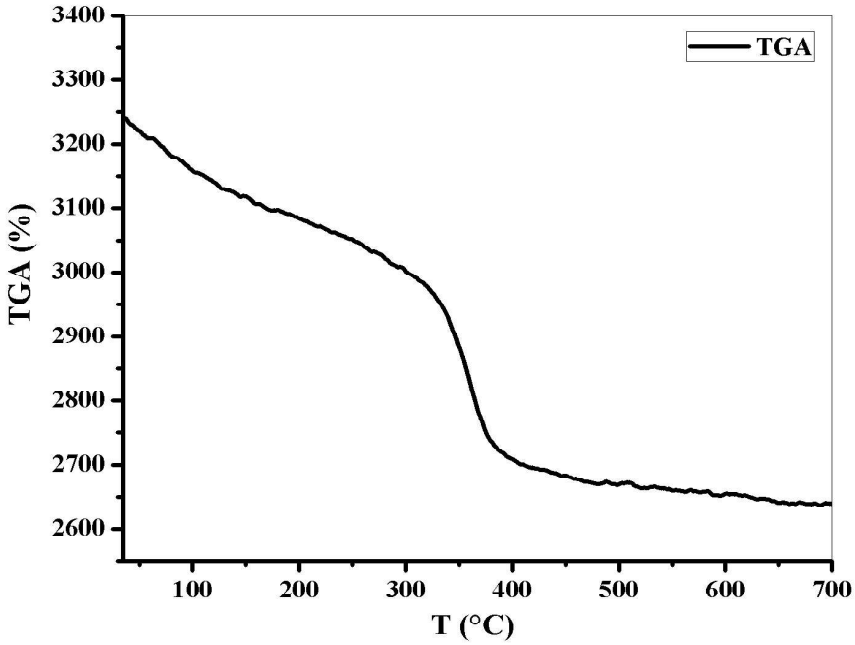

Fig. 4.43 TGA graph for $Sr_{0.7}Al_{0.3}Fe_{11.4}Mn_{0.6}O_{19}$ precursor

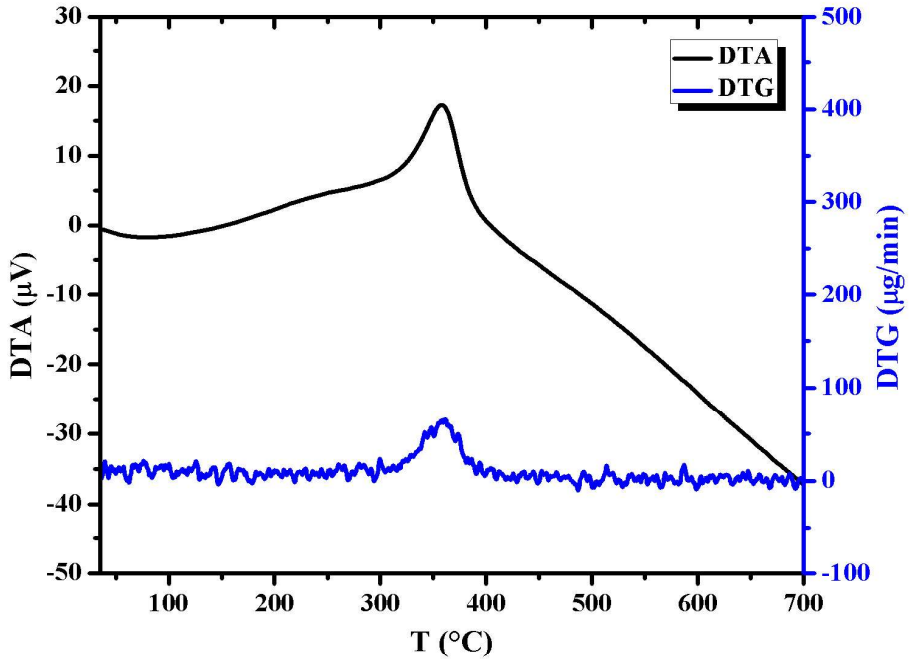

Fig. 4.44 DTA/DTG graph for $Sr_{0.7}Al_{0.3}Fe_{11.4}Mn_{0.6}O_{19}$ precursor

4.4.4 Morphology analysis

FESEM micrographs of $Sr_{0.7}Al_{0.3}Fe_{11.4}Mn_{0.6}O_{19}$ calcinated at 1050 °C are presented in **Fig. 4.45** (a), (b), and (c). From the FESEM images, we can see that the grains of the prepared sample exhibit hexagonal plate like structure. The grains seems to be agglomerated which could be as a result of magnetic interaction between the grains [190]. The atomic ratios obtained from EDX spectra are in agreement with the expected stoichiometry of the prepared sample (**Fig. 4.45** (d)). Peaks representing strontium, manganese, iron, aluminium and oxygen can be seen in the spectra of EDS, this confirms the stoichiometry of the prepared sample.

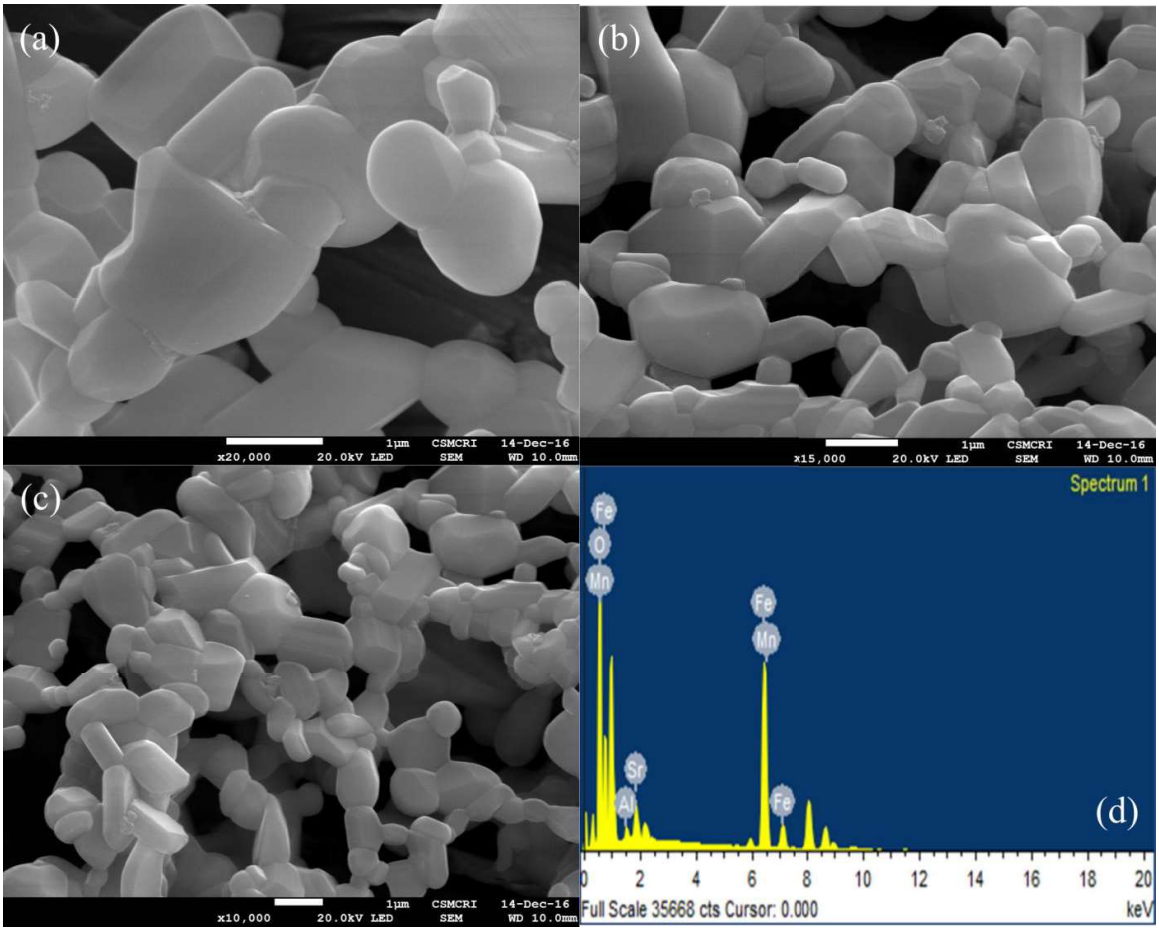

Fig. 4.45 FESEM micrograph for $Sr_{0.7}Al_{0.3}Fe_{11.4}Mn_{0.6}O_{19}$ at 1050 °C and resolution of (a) x20000, (b) x15000, (c) x10000, and (d) EDX spectra.

4.4.5 Optical analysis

The optical properties of the prepared sample were calculated from UV-visible absorption spectra. The energy level of electrons in the valence band is raised when they absorb energy from an incident source of energy such as electromagnetic waves. The band gap can be calculated from the following relation [86].

$$\alpha = \frac{A(h\upsilon - E_g)^{1/2}}{h\upsilon} \tag{4.26}$$

Where A is a constant, E_g is the band gap and h is the Planck's constant. The band gap is calculated from fundamental absorption edges. **Fig. 4.46** presents the plot of band gap of

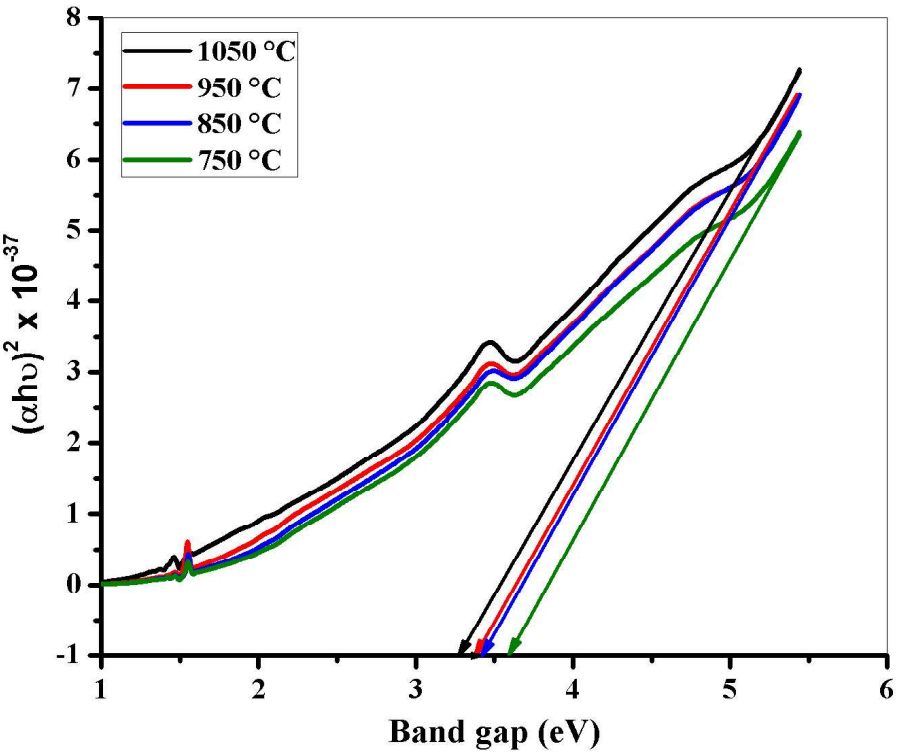

Fig. 4.46 Optical band gap for $Sr_{0.7}Al_{0.3}Fe_{11.4}Mn_{0.6}O_{19}$

$Sr_{0.7}Al_{0.3}Fe_{11.4}Mn_{0.6}O_{19}$. From the plot, we can see that band gap decreases with sintering temperature, it has been reported that quantum confinement and grain size affects the band gap [186][191]. Variation of band gap with temperature is presented in **Fig. 4.47**, the highest value of band gap (3.58 eV) was obtained at 750 °C, this value is by contrast lower than that

obtained for $Mg(OH)_2$-rGO nanocomposites (5.03 eV) [174]. Z. Zhong et al. reported that a band gap that a band of 3.5 eV could be used for UV-blue light emitting diodes (LEDs) [163]. Hence, the synthesized sample could be used for UV-blue LED application.

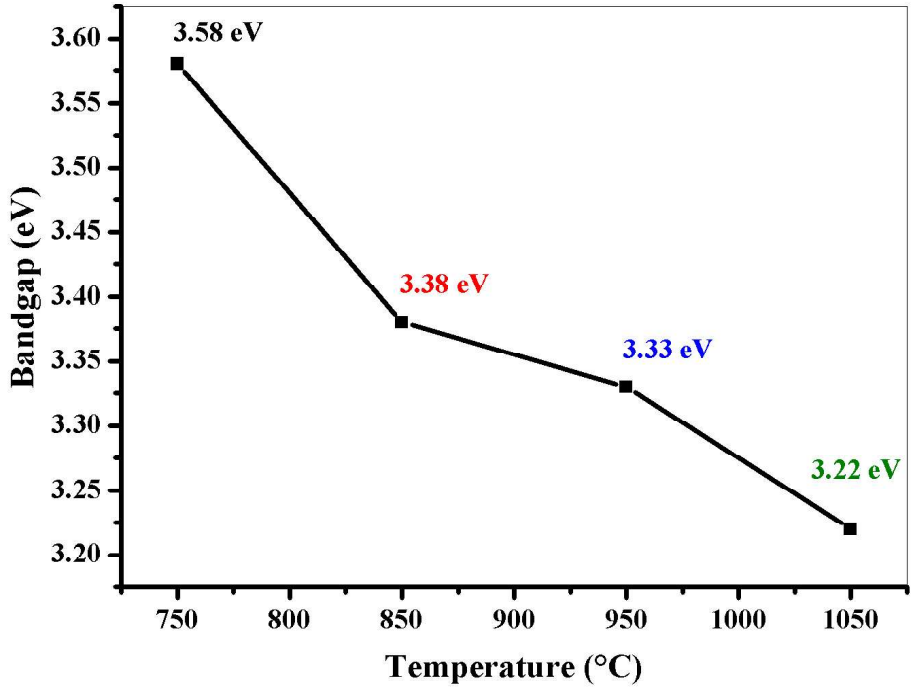

Fig. 4.47 Variation of optical band gap with temperature for $Sr_{0.7}Al_{0.3}Fe_{11.4}Mn_{0.6}O_{19}$

4.4.6 Dielectric and impedance spectroscopy

The room temperature impedance analysis was carried out using impedance analyser in the frequency range 1 KHz to 5MHz. The prepared sample was pressed into pellets of diameter 1cm and thickness 4mm. Equation (4.27) and (4.28) are used to calculate the room temperature real and imaginary part of impedance respectively [92].

$$Z' = |Z| \cos\theta \tag{4.27}$$

$$Z'' = |Z| \sin\theta \tag{4.28}$$

Where Z is the impedance and θ is the phase angle, the complex impedance can be expressed in terms of the real and imaginary part of complex impedance as

$$Z^* = Z' - jZ'' \tag{4.29}$$

Where $j = \sqrt{-1}$. The dielectric parameters were calculated from the impedance parameters. Equation (4.30) and (4.31) are used to calculate the room temperature dielectric constant and dielectric loss respectively [164].

$$\varepsilon' = \frac{Z''}{2\pi f C_0 Z^2} \tag{4.30}$$

$$\varepsilon'' = \frac{Z'}{2\pi f C_0 Z^2} \tag{4.31}$$

Where C_0 is the geometrical capacitance, Z is the impedance, and f is the frequency, the complex permittivity can be expressed in terms of the dielectric constant and dielectric loss as

$$\varepsilon^* = \varepsilon' - j\varepsilon'' \tag{4.32}$$

The dielectric loss tangent of the prepared sample can be expressed as ratio of dielectric loss and dielectric constant as

$$\tan \delta_e = \frac{\varepsilon''}{\varepsilon'} \tag{4.33}$$

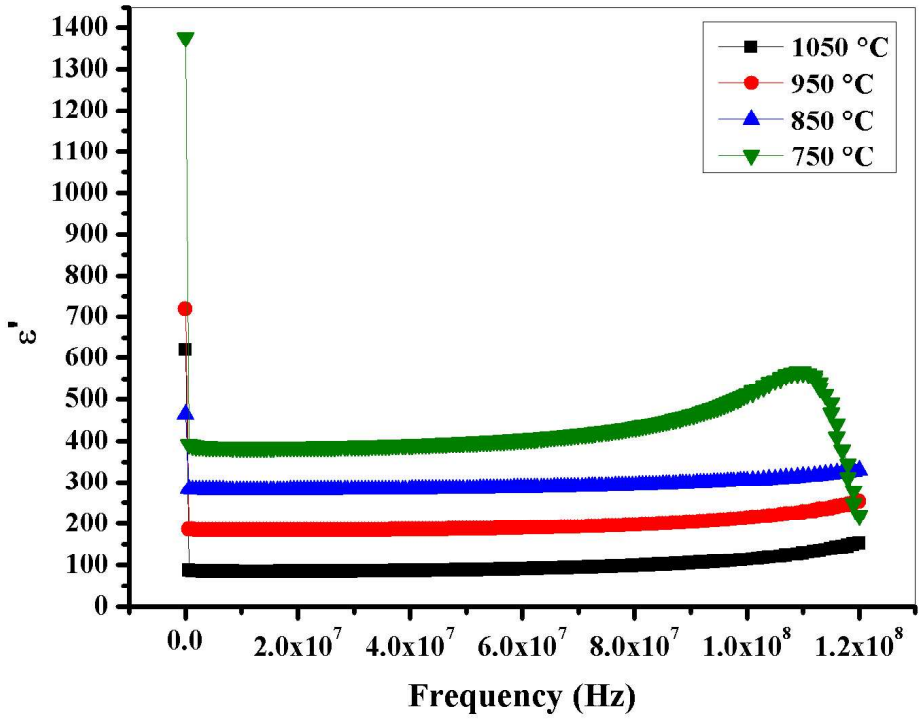

Fig. 4.48 Room temperature dielectric constant (ε') of $Sr_{0.7}Al_{0.3}Fe_{11.4}Mn_{0.6}O_{19}$

Room temperature spectra of real part of permittivity (ε'), imaginary part of permittivity (ε''), and dielectric loss tangent ($\tan\delta$) are respectively presented in **Fig. 4.48, 4.49,** and **4.50**. The dielectric response of the prepared sample is typical of a ferrite material. This dielectric behaviour can be explained on the basis of Koop's phenomenological theory and Maxwell Wagner theory. It can be seen that the dielectric constant (ε') and dielectric loss (ε'') decreases with frequency and became constant for the frequency range 0-80 MHz and 0-70 MHz respectively, a slight increases is observed thereafter. This behaviour is observed for the

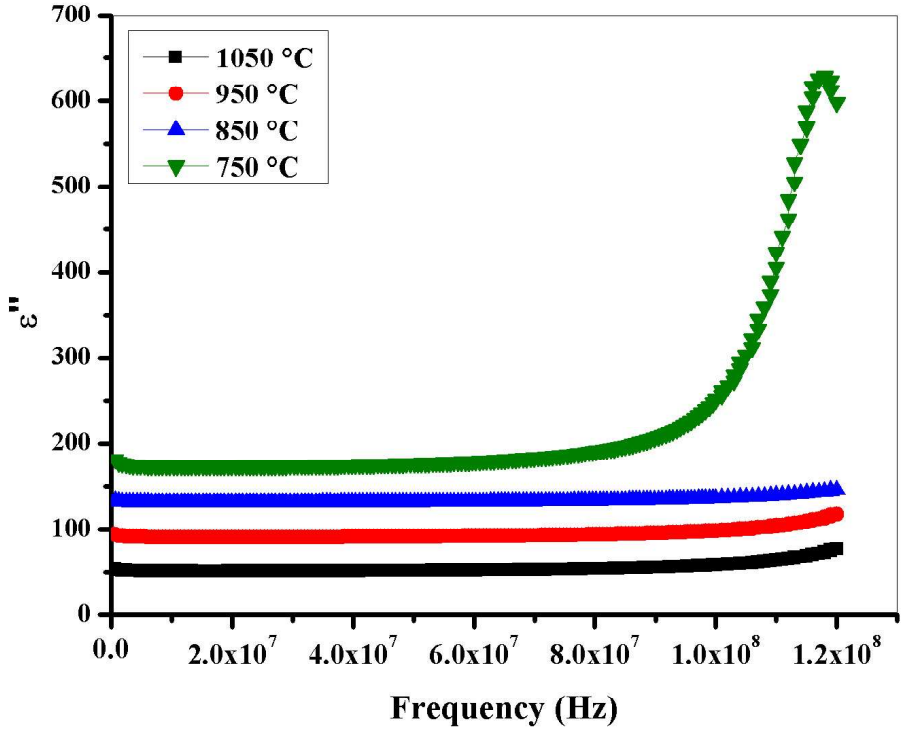

Fig. 4.49 Room temperature dielectric loss (ε'') of $Sr_{0.7}Al_{0.3}Fe_{11.4}Mn_{0.6}O_{19}$

sample calcinated at 1050°C, 950°C and 850°C. The sample calcinated at 750°C shows constant dielectric constant (ε') and dielectric loss (ε'') in the frequency range 0-60 MHz and 0-70 MHz respectively, and increases thereafter. Dielectric resonance is observed at 1.1 MHz for the dielectric constant (ε') and 1.18 MHz for the dielectric loss (ε''). The sample calcinated at 750°C shows the highest value of dielectric constant, this is as a result of smaller crystallite size as compared to the samples calcinated at1050°C, 950°C and 850°C. This high dielectric constant is attributed to large surface area as a result of small crystallite size. Larger surface area results in high space-charge polarisation and consequently high

dielectric constant. The electron hopping between Fe^{3+} and Fe^{2-} resulted in the displacement of ionic charges thereby causing the space-charge polarisation [186][192]. The dielectric loss tangent ($\tan\delta$) increases steadily with temperature **Fig. 13**. The energy loss in the synthesized sample is given by the dielectric loss tangent ($\tan\delta$) which occurs as a result of the polarisation lagging behind the AC electric field, this may be attributed to defects and/or impurities in the prepared sample [183].

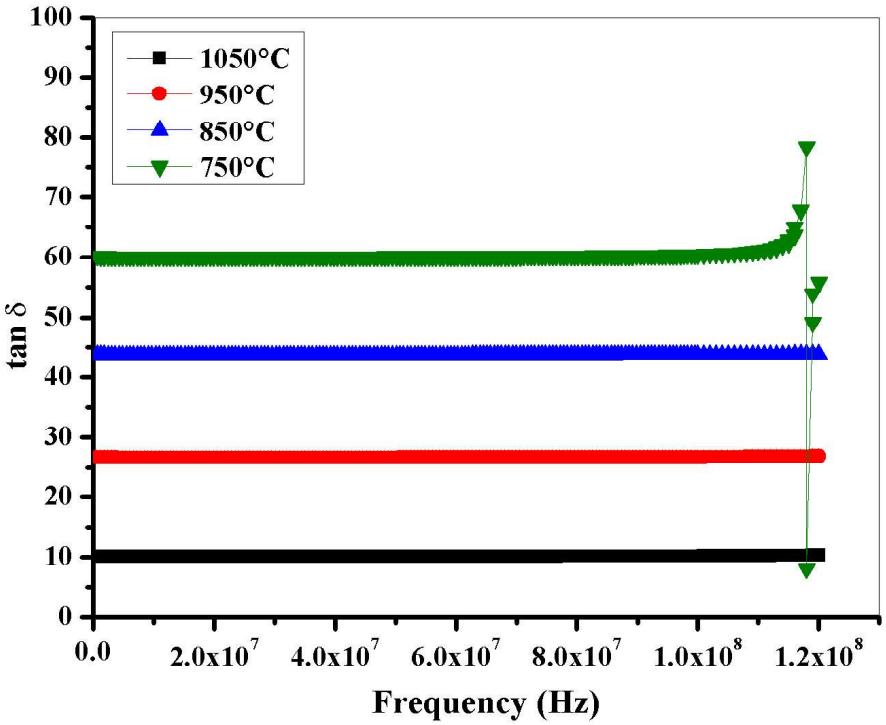

Fig. 4.50 Room temperature dielectric loss ($\tan\delta$) of $Sr_{0.7}Al_{0.3}Fe_{11.4}Mn_{0.6}O_{19}$

The room temperature AC conducting properties of the prepared sample was calculated using the equation below

$$\sigma_{AC} = 2\pi f \varepsilon'' C_0 \tag{4.34}$$

The variation of room temperature AC conductivity (σ_{AC}) with frequency is presented in **Fig. 4.51**, the real and imaginary part of impedance shows the possibility of increasing AC conductivity with frequency. The sample calcinated at 750°C have the highest value of AC conductivity (76.1×10^{-3} Ω cm^{-1}).

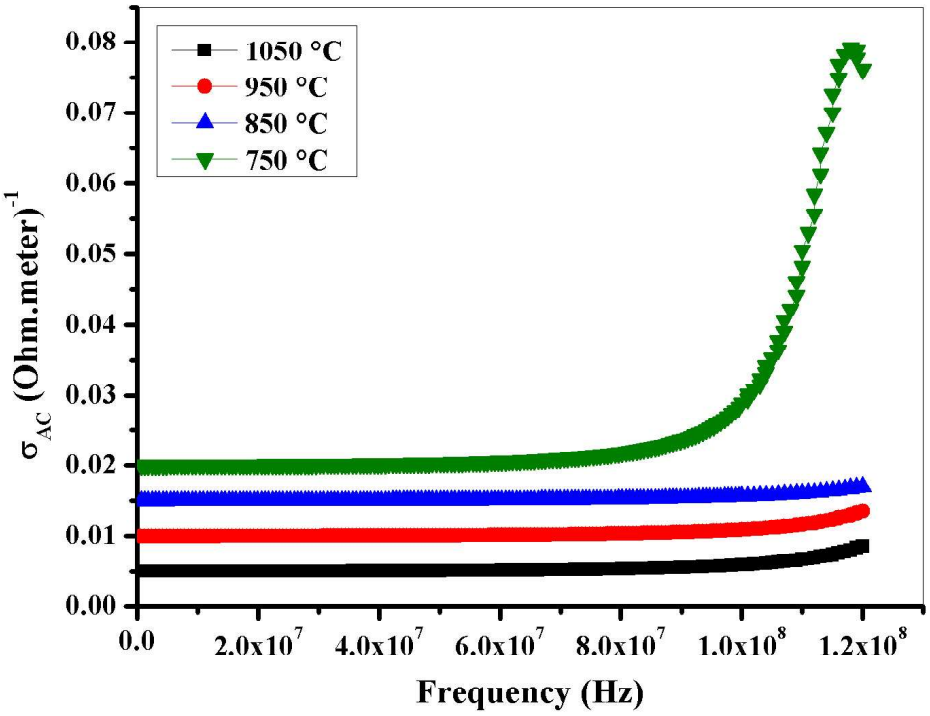

Fig. 4.51 Room temperature AC conductivity (σ_{AC}) of $Sr_{0.7}Al_{0.3}Fe_{11.4}Mn_{0.6}O_{19}$

The variation of real part of impedance (Z') and imaginary part of impedance (Z'') with frequency at room temperature are respectively given in **Fig. 4.52 and 4.53**. It can be observed from the figures that both the real and imaginary part of impedance increases with frequency and becomes independent at higher frequencies. The impedance values at the high frequency side of the impedance spectrum shows the possibility of releasing space charge and reduction in barrier properties of the material [92][87].

Col-Cole plots of the prepared sample are presented in **Fig. 4.54**, black line with dots represents experimental data while the red line represents fitted curve. Usually, the Cole-Cole plots are semi-circle or semi-circle arc. The left side of the semi-circle represents grain resistance whereas the right side represents whole resistance of the grain and grain boundary. There is no the grain resistance as a result of deficiency in cation but significant increase in grain boundary resistance is observed [193].

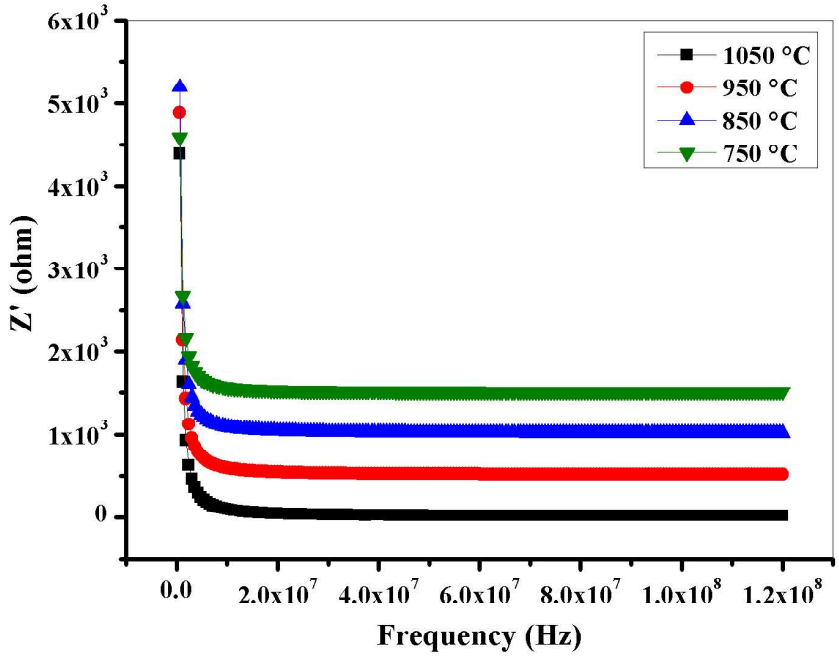

Fig. 4.52 Real part of impedance for $Sr_{0.7}Al_{0.3}Fe_{11.4}Mn_{0.6}O_{19}$ at room temperature

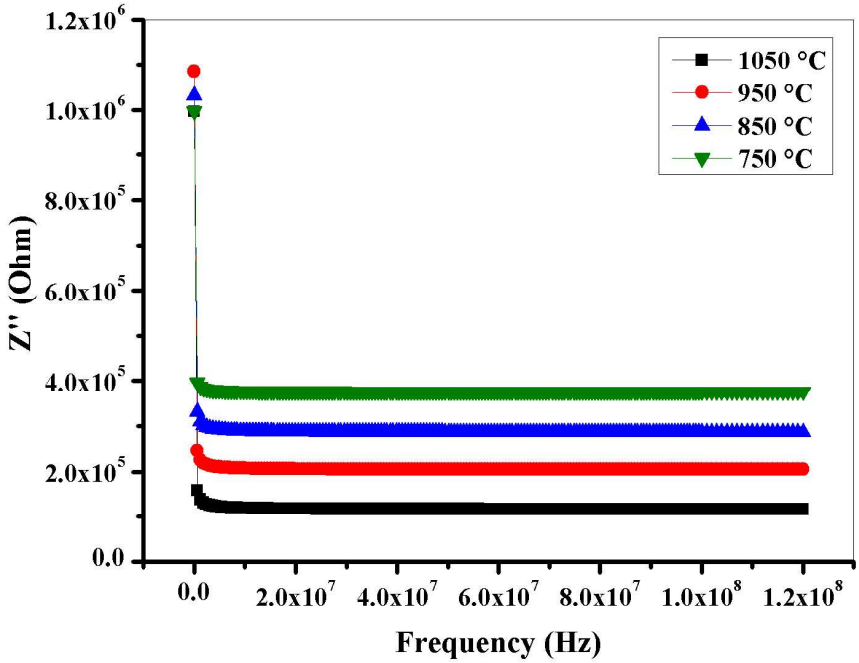

Fig. 4.53 Imaginary part of impedance of $Sr_{0.7}Al_{0.3}Fe_{11.4}Mn_{0.6}O_{19}$ at room temperature

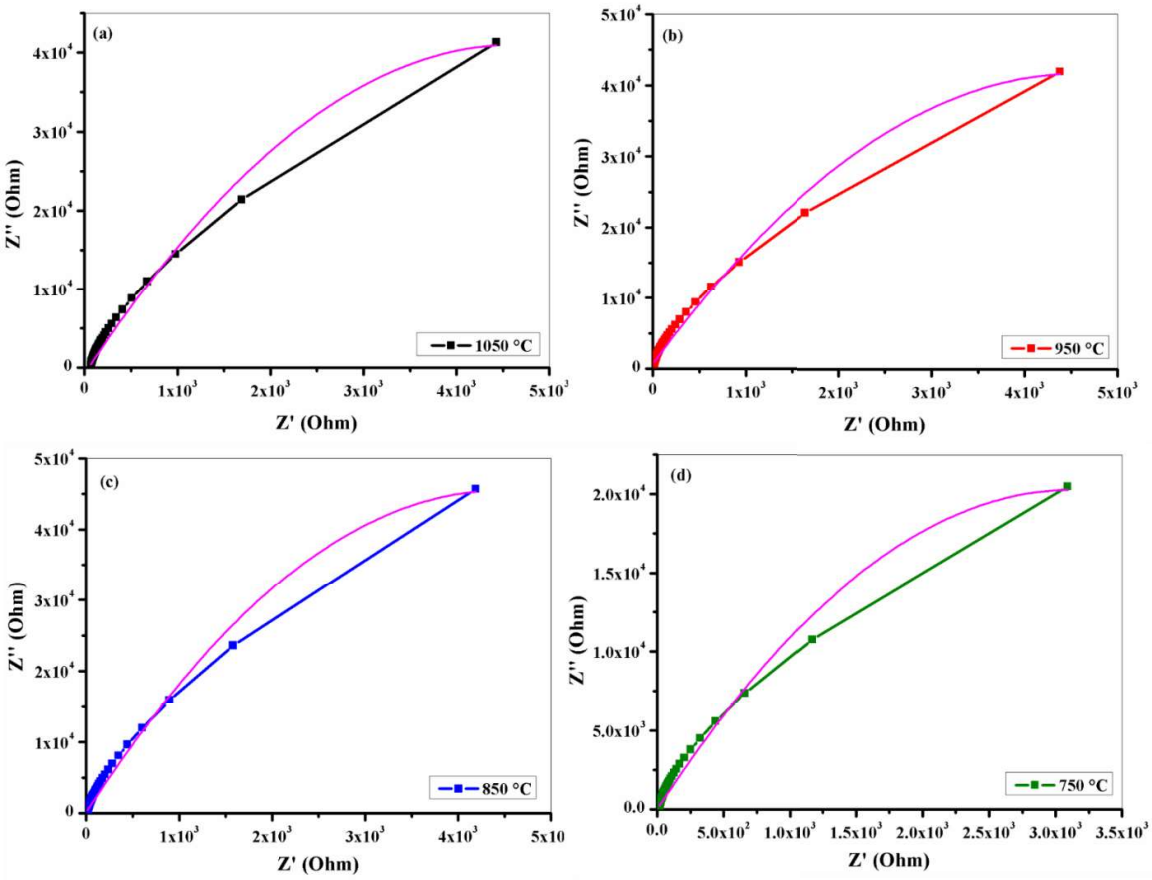

Fig. 4.54 Cole-Cole plots of $Sr_{0.7}Al_{0.3}Fe_{11.4}Mn_{0.6}O_{19}$ at (a) T=1050 °C, (b) T=950 °C, (c) T=850 °C, and (d) T=750 °C (Magenta coloured line represents fitted curve)

4.4.7 Magnetic analysis

The M-H hysteresis loops of the synthesized samples are presented in **Fig. 4.55**. Remanent magnetisation (M_r), saturation magnetisation (M_s) as well as coercivity (H_c) were calculated from the M-H hysteresis loop and presented in **Table 4.5**. Anisotropy constant (K) was calculated using the following formula [86].

$$K = \frac{\mu_0 M_s H_c}{2} \tag{4.35}$$

Where $\mu_0 = 4\pi \times 10^7\, H/m$ is the permeability in vacuum, M_s is the saturation magnetisation, and H_c is the coercivity. The magneton number was calculated from the following formula [189].

$$\mu_B = \frac{Molecularweight \times M_s}{5585} \tag{4.36}$$

It has been observed that remanent as well as saturation magnetization decreases with increase in heat-treatment temperature (**Table 4.5**), the nonmagnetic Al^{3+} ion could be

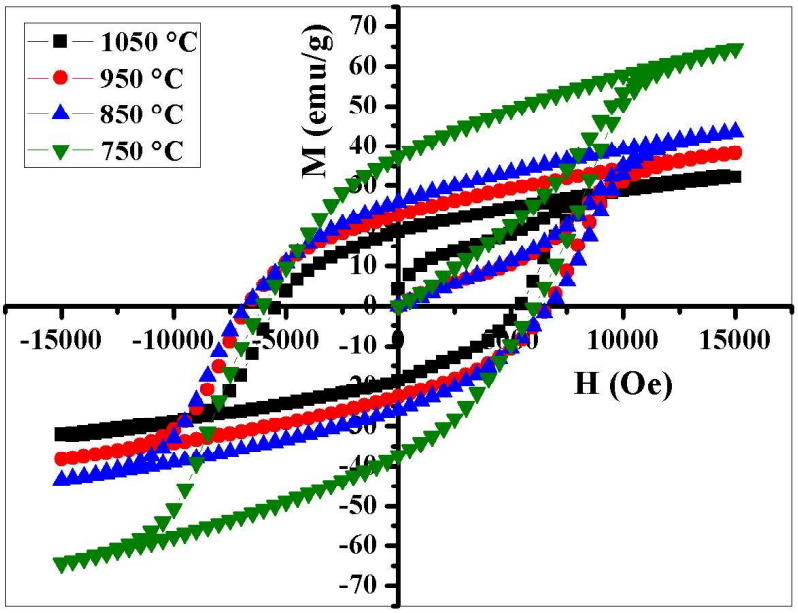

Fig. 4.55 M-H hysteresis loop for $Sr_{0.7}Al_{0.3}Fe_{11.4}Mn_{0.6}O_{19}$

responsible for the low saturation magnetization observed and this can be ascribed to the greater enhancement of the super-exchange interaction between Fe^{3+}-O-Fe^{3+} as a result of smaller grain sizes which is observed in XRD analysis and increase coercivity [113][189]. Similar studies was carried out for manganese ferrites in which the highest value of saturation magnetization obtained is 27.05 emu/g for the sample heat treated at 400 °C [194]. In contrast, the sample heat treated at 750 °C shows a saturation magnetization value of 64.33 emu/g. Y. Wu *et al.* reported that high value of saturation magnetization is beneficial for magnetic data storage devices [195]. Hence the synthesized samples could be useful for magnetic storage of data. All the prepared samples exhibit high values of coercivity, the sample sintered at 850 °C exhibit high value of coercivity (6750 Oe) (**Table 4.5**) which is a little more than the theoretical value of coercivity for hexaferrites (6700 Oe) [190]. The coercivity decrease in the temperature range 850 to 1050 °C. If the value of coercivity is than 1200 Oe, then the material can be used for application in perpendicular recording medium

(PRM). Also since $H_c > M_r/2$, then the material is considered as hard magnet, this type of material can be used in high frequency application [82]. Anisotropy constant (K) shows an increasing behaviour with temperature (**Table 4.5**). The squareness ratio (SR) is almost constant for both the samples sintered at 850 °C and 1050 °C, and the magneton number (μ_B) was found to continuously reduce as the temperature increased (**Table 4.5**).

Table 4.5 Values of Remanent magnetisation (M_r), saturation magnetisation (M_s) as well as coercivity (H_c), squareness ratio (SR), anisotropy constant (K) and magnetic moment (μ_B) parameters for $Sr_{0.7}Al_{0.3}Fe_{11.4}Mn_{0.6}O_{19}$.

T (°C)	$\boldsymbol{M_r}$ (emu/g)	$\boldsymbol{M_s}$ (emu/g)	$\boldsymbol{H_c}$ (Oe)	SR ($\boldsymbol{M_r/M_s}$)	K (HA^2/kg)	$\boldsymbol{\mu_B}$
1050	19.38	32.43	5931.22	0.5976	9.61	6.06
950	22.69	38.25	6673.11	0.5932	12.76	7.14
850	25.98	43.51	6750.39	0.5971	14.68	8.13
750	37.33	64.33	6047.14	0.5803	19.45	12.01

4.5 Al^{3+}-Mn^{2+} substituted M-type strontium hexaferrites

4.5.1 XRD analysis

Fig. 5.56 presents the XRD spectra of $Sr_{1-x}Al_xFe_{11.4}Mn_{0.6}O_{19}$ (x=0.0, 0.1, 0.2) synthesized by sol-gel method. The peaks in the XRD spectra are identical to those in the standard pattern (JCPDS-391433). Single phase M-type hexagonal ferrites was obtained when x=0.0 and y=0.6. The other samples show the formation of M-type hexagonal ferrites with traces of α-Fe_2O_3. The intensity of the peaks increases with Al^{+3}-Mn^{+2} substitutions. **Table 4.6** gives the lattice parameters, crystallite size and volume of unit cell which are calculated using [196].

$$\frac{1}{d_{hkl}^2} = \frac{4}{3}\left(\frac{h^2+hk+l^2}{a^2}\right) + \frac{l^2}{c^2} \tag{4.37}$$

$$D = \frac{k\lambda}{\beta \cos\theta} \tag{4.38}$$

$$V_{cell} = 0.8666a^2c \tag{4.39}$$

Where d_{hkl} is the value of d spacing, hkl are the miller indices, β (in radian) is the full width at half maximum, θ is the Braggs angle, k is the shape factor which has a value of 1 for hexagonal ferrites, λ is the X-ray wavelength having a value of 1.54056Å. The lattice

parameter (a) first increases and then later decrease with Al^{+3}-Mn^{+2} substitution. The volume of the unit cell decreases with increase in Al^{+3}-Mn^{+2} substitutions whereas the crystallite size increases with Al^{+3}-Mn^{+2} substitution (**Table 4.6**). This variation in lattice parameters could be attributed to strain (stress) induced by the Al^{+3}-Mn^{+2} substitution [183][197].

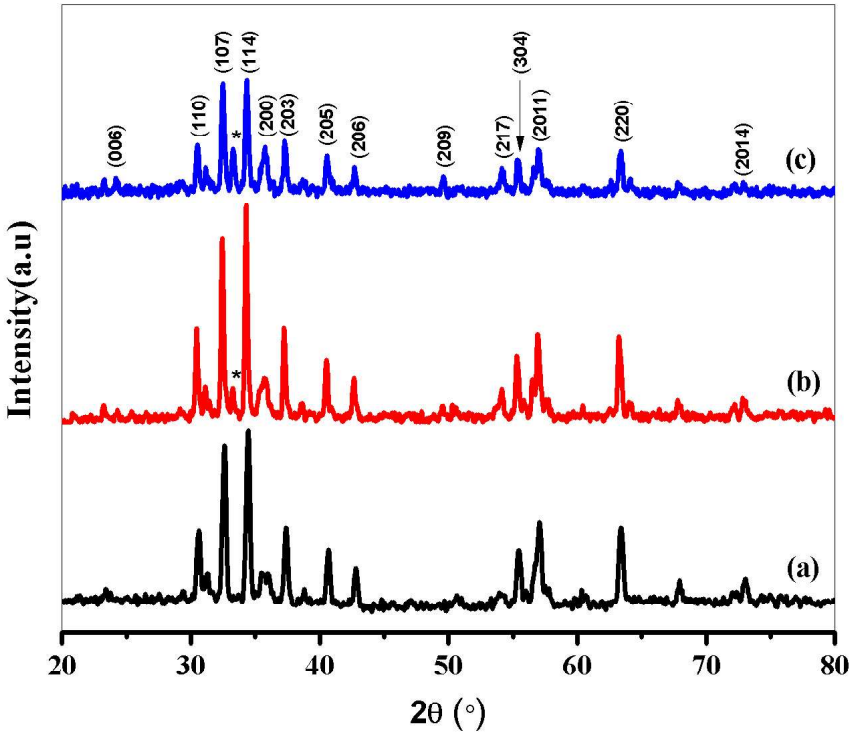

Fig. 5.56 XRD spectra of $Sr_{1-x}Al_xFe_{11.4}Mn_{0.6}O_{19}$ (x=0.0, 0.1, 0.2) for (a) x=0.0, (b) x=0.1, and (c) x=0.2

Table 4.6 Values of lattice parameters (a and c), volume of unit cell (V_{cell}), crystallite size (D) and strain (η) for $Sr_{1-x}Al_xFe_{11.4}Mn_{0.6}O_{19}$ (x=0.0, 0.1, 0.2)

x	2θ (°)	d (Å)	β (°)	a (Å)	c (Å)	V_{cell} (Å^3)	D (nm)	$\eta \times 10^{-4}$
0.0	30.31	2.9463	0.356	5.8925	23.3440	702.41	25.684	11.453
0.1	30.23	2.9542	0.170	5.9084	23.1472	700.25	53.787	5.4777
0.2	30.31	2.9463	0.257	5.8726	23.3886	699.01	53.786	5.4779

4.5.2 FTIR analysis

Fig. 4.57 presents the FTIR spectra of $Sr_{1-x}Al_xFe_{11.4}Mn_{0.6}O_{19}$ (x=0.0, 0.1, 0.2) with varying contents of Al^{3+}-Mn^{2+}. The idea of the formation of M-type hexagonal ferrites is proven by the presence of two peaks at 438.94 cm^{-1} and 600.17 cm^{-1}, this could be attributed to vibration of octahedral and tetrahedral sites in the crystal structure [86][198]. The peak at 2365 cm^{-1} is due to presence of CO_2 [199][186]. A broad band is observed at 3423 cm^{-1} which is due to O-H stretching band, this could be ascribed to the presence of water molecules in the prepared sample [189].

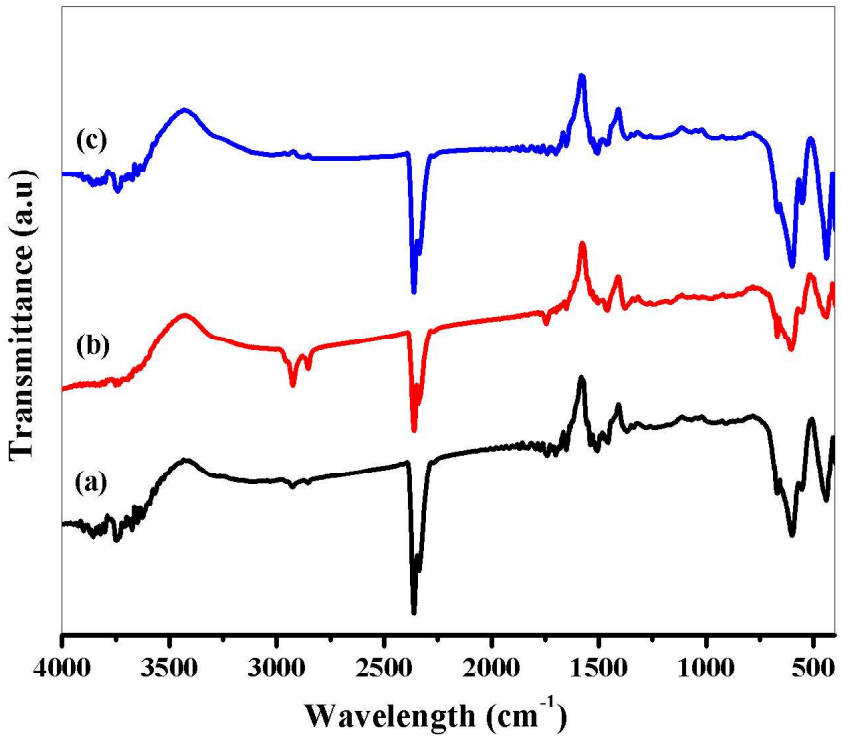

Fig. 4.57 FTIR spectra of $Sr_{1-x}Al_xFe_{11.4}Mn_{0.6}O_{19}$ (x=0.0, 0.1, 0.2) for (a) x=0.0, (b) x=0.1, and (c) x=0.2

4.5.3 Morphology analysis

Fig. 4.58 (a) and **(c)** shows the FESEM micrographs and **Fig. 4.58 (b)** and **(d)** presents the particle size distribution of $Sr_{1-x}Al_xFe_{11.4}Mn_{0.6}O_{19}$ (x=0.0, 0.1) nanoparticles. The surface features of the prepared samples shows the formation of aggregates as a result of

agglomeration of the nanoparticle. This is common observation in magnetic nanoparticles as they interact with each other due to the magnetic dipole interaction [200]. Also, the FESEM micrograph shows that the nanoparticles exhibit hexagonal platelet-like structure with smooth surfaces and sharp edges. The platelet-like structure is necessary for good high frequency application [201].

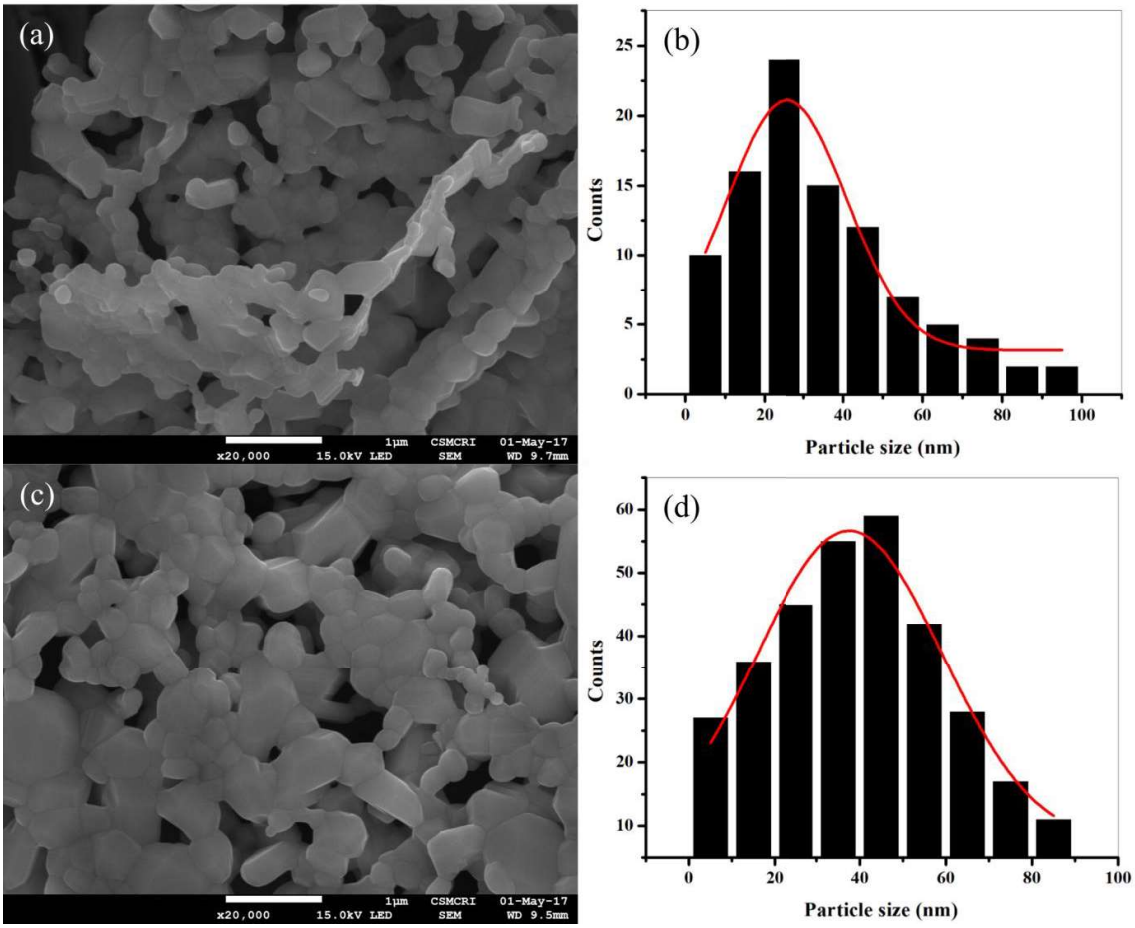

Fig. 4.58 FESEM micrographs and particle distribution of $Sr_{1-x}Al_xFe_{11.4}Mn_{0.6}O_{19}$ (x=0.0, 0.1) for (a-b) x=0.0 and (c-d) x=0.1

4.5.4 Dielectric and impedance spectroscopy

The room temperature variation of dielectric constant with frequency for $Sr_{1-x}Al_xFe_{11.4}Mn_{0.6}O_{19}$ (x=0.0, 0.1, 0.2) is presented in **Fig. 4.59**. The behaviour of the dielectric properties can be explained on the basis of the assumption that the process of the dielectric polarization is identical to that of electrical conduction. The value of the dielectric constant at frequency of 100 Hz was found to be 1410, 600 and 266 for x=0.0, x=0.1, and x=0.2

respectively. Hence, we see that the value of the dielectric constant decrease with increase in Al^{3+}-Mn^{2+} substitution, this is due to reduction of Fe^{2+} ions at the octahedral sites [189]. The dielectric constant of the sample with x=0.0 shows frequency independent behaviour at higher frequency. The dielectric constant of the sample with x=0.1 show a resonance peak at higher frequency, this could be attributed to resonance of frequencies of electron hopping with the externally applied electric field [202]. The sample with the sample with x=0.2 shows increase in dielectric constant at much higher frequency.

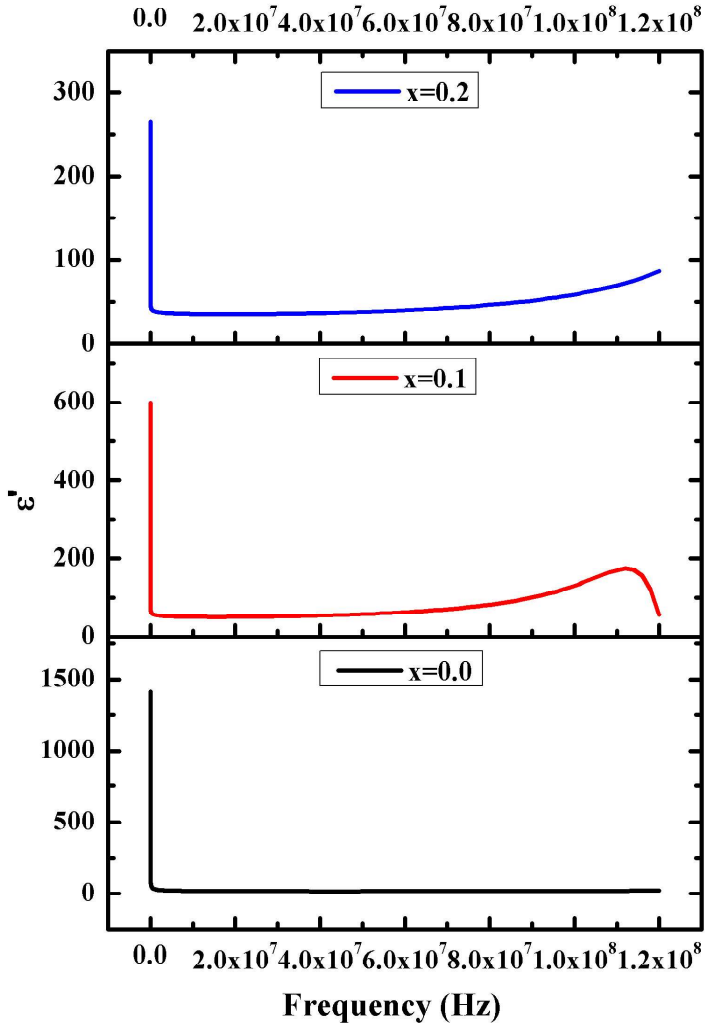

Fig. 4.59 Variation of dielectric constant with frequency for $Sr_{1-x}Al_xFe_{11.4}Mn_{0.6}O_{19}$ (x=0.0, 0.1, 0.2)

Fig. 4.60 presents the room temperature variation of dielectric lose with frequency for $Sr_{1-x}Al_xFe_{11.4}Mn_{0.6}O_{19}$ (x=0.0, 0.1, 0.2). The material losses energy via the mechanism of dielectric loss during conduction of electrons [189]. Dielectric loss was found to have a value of 2.040, 0.829, and 0.883 at a frequency of 100 Hz for x=0.0, x=0.1, and x=0.2 respectively. The dielectric loss shows frequency independent behaviour at higher frequency for the sample with x=0.0. The sample with x=0.1 and x=0.2 show frequency independent behaviour at intermediate frequencies and then the behaviour changes to frequency dependent at much higher frequency.

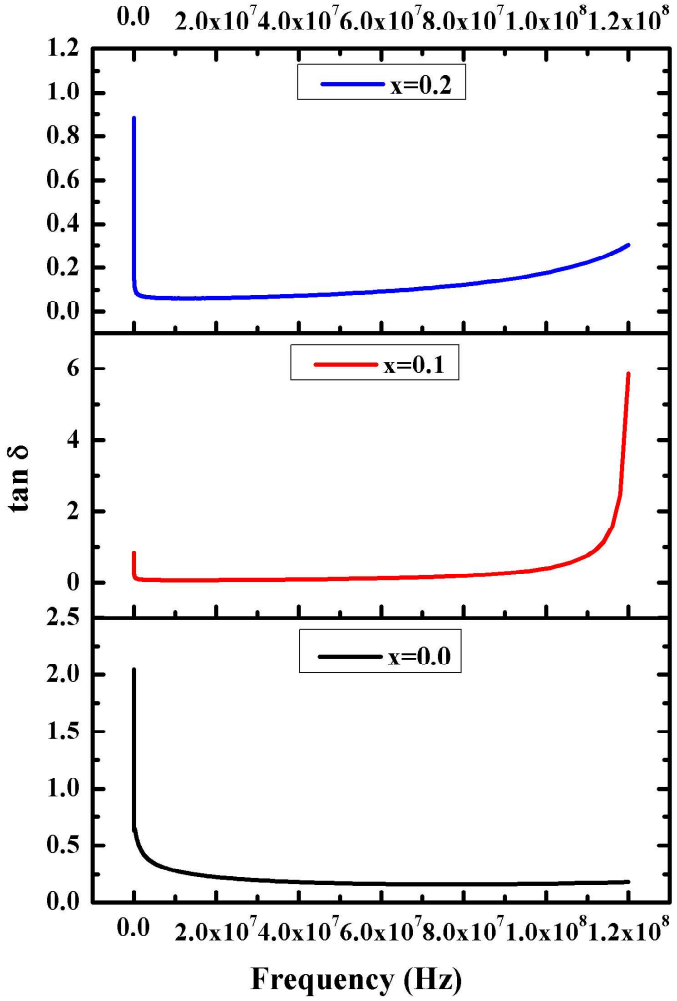

Fig. 4.60 Variation of dielectric lose with frequency for $Sr_{1-x}Al_xFe_{11.4}Mn_{0.6}O_{19}$ (x=0.0, 0.1, 0.2)

Fig. 4.61 shows the room temperature variation of AC conductivity with frequency for $Sr_{1-x}Al_xFe_{11.4}Mn_{0.6}O_{19}$ (x=0.0, 0.1, 0.2). All the prepared samples show frequency independent behaviour. Based on Maxwell-Wagner model, the AC conductivity at lower frequencies explain the grain boundary behaviour whereas the dispersion that occur at higher frequencies may be due to grain conductivity and hopping of electrons Fe^{3+} and Fe^{2+} ions [189].

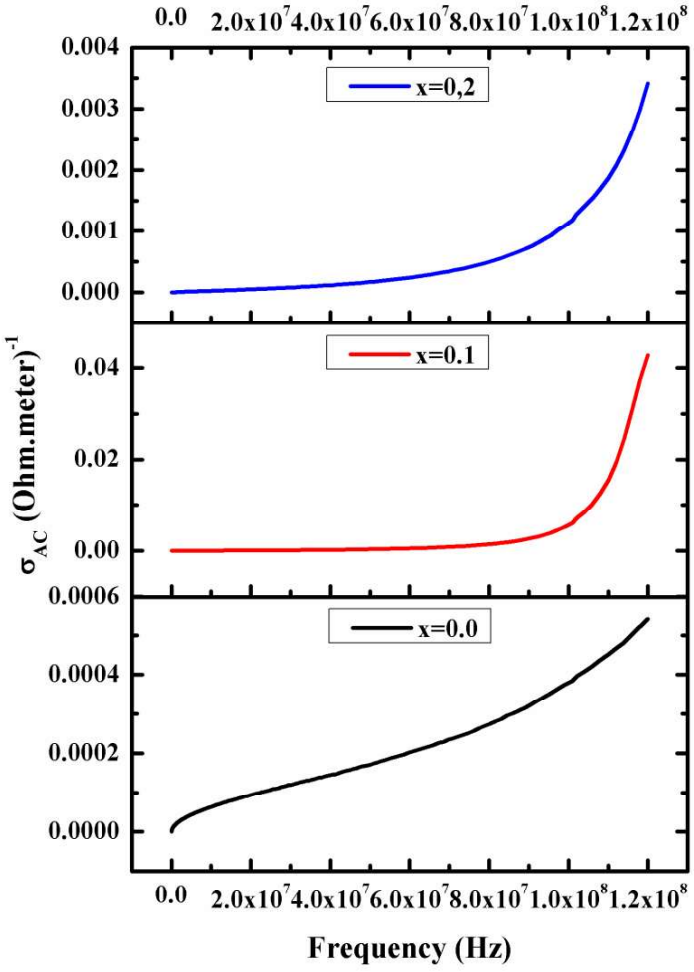

Fig. 4.61 Variation of Ac conductivity with frequency for $Sr_{1-x}Al_xFe_{11.4}Mn_{0.6}O_{19}$ (x=0.0, 0.1, 0.2)

4.5.5 Magnetic analysis

Fig. 4.62 presents the room temperature plot of M-H hysteresis loop of $Sr_{1-x}Al_xFe_{11.4}Mn_{0.6}O_{19}$ (x=0.0, 0.1, 0.2). The values of coercivity (H_c), remnant magnetization (M_r) and saturation magnetization (M_s) were determined from this plot and presented in **Table 4.7**. From these

values, the anisotropy constant (K), magneton number (μ_B) and squareness ratio (SR) were evaluated from the following equations [86][189].

$$K = \frac{\mu_0 M_S H_c}{2} \tag{4.40}$$

$$\mu_B = \frac{Molecularweight \times M_s}{5585} \tag{4.41}$$

$$SR = \frac{M_r}{M_s} \tag{4.42}$$

Where $\mu_0 = 4\pi \times 10^7\, H/m$ is the permeability in vacuum, M_s is the saturation magnetisation, and H_c is the coercivity. The effect of increasing the concentration of Al^{3+}-Mn^{2+} can be clearly observed on the values of H_c, M_r, and M_s. The values of H_c increases with increase in Al^{3+}-Mn^{2+} concentration whereas the anisotropy constant (K) decreases with

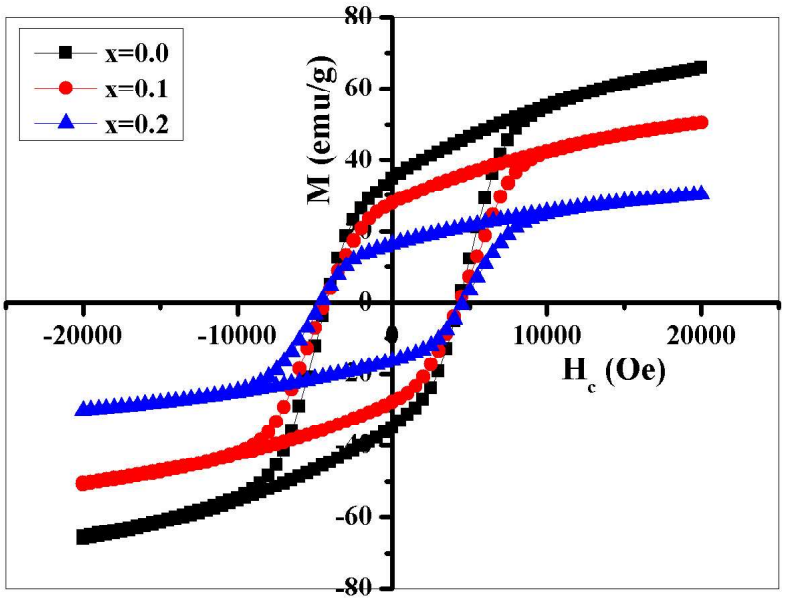

Fig. 4.62 M-H hysteresis loop of $Sr_{1-x}Al_xFe_{11.4}Mn_{0.6}O_{19}$ (x=0.0, 0.1, 0.2)

increase in Al^{3+}-Mn^{2+} substitution. El-Sayed et al. investigated the effect of aluminium substitution on the properties of barium hexaferrite, the values of H_c was found to increase with increase in Al^{3+}-Mn^{2+} substitution, the highest value of H_c (2119.8 Oe) observed was in the sample with x=3.5 [189]. In our case, the highest value of H_c (4597.58 Oe) was observed

in the sample with x=0.2. This high value of H_c may be attributed to size of the grains and magnetocrystalline anisotropy of the prepared sample [203]. Also, the high value of H_c in our sample could be due to the presence of magnetic Mn^{2+}. It has been reported that high value of H_c may be useful for magnetic recording media [199]. The increase in H_c with increase in Al^{3+}-Mn^{2+} concentration has been reported in literatures [189][204]. Similarly, the sample with x=0.0 exhibits the highest K. Both the values of M_r and M_s decrease with increase in the concentration of Al^{3+}-Mn^{2+} (**Table 4.7**). This decrease is as a result of the replacement of the Fe^{3+} by the nonmagnetic Al^{3+} [205]. The sample with x=0.2 exhibit the lowest value of M_s (16.27 emu/g) and M_r (30.23 emu/g), this could be ascribed to the presence of secondary phase (α-Fe_2O_3) in the material as seen in the XRD plot and the weakening of the super exchange interaction Fe^{3+}-O-Fe^{3+} [189][205][186]. The squareness ratio (SR) does not follow a regular pattern whereas the magneton number decreases with increase in Al^{3+}-Mn^{2+} substitution.

Table 4.7 Values of coercivity (H_c), remnant magnetization (M_r), saturation magnetization (M_s), squareness ratio (SR), anisotropy constant (K) and magnetic moment (μ_B) for $Sr_{1-x}Al_xFe_{11.4}Mn_{0.6}O_{19}$ (x=0.0, 0.1, 0.2)

x	H_c (Oe)	M_r (emu/g)	M_s (emu/g)	SR (M_r/M_s)	K (HA^2/kg)	μ_B
0.0	4305.49	65.77	34.67	1.8970	7.46	6.47
0.1	4348.76	50.54	27.88	1.8127	6.06	5.20
0.2	4597.58	30.23	16.27	1.8580	3.74	3.03

4.6 Dy^{3+}-Cr^{3+} substituted M-type barium hexaferrites

4.6.1 XRD analysis

Fig. 4.63 presents the XRD spectra of M-type barium hexagonal ferrites with chemical composition $Ba_{1-x}Dy_xFe_{12-y}Cr_yO_{19}$ (x=0.0, 0.1, 0.2, and y=0.0, 0.4, 0.5). The XRD spectra shows well defined intense and sharp peaks with *hkl* values (006), (110), (008), (107), (114), (200), (203), (109), (205), (206), (1011), (209), (217), (304), (2011), (2012), (220), (2014) and (317), this indicates the formation of a crystalline hexagonal ferrites phase with no secondary phase such as α-Fe_2O_3 and the successful substitution of Dy^{3+} and Cr^{3+} in the M-type hexagonal structure. The XRD spectra were indexed according to standard JCPDS Card

no. 39-1433 and were found to be identical to unsubstituted $BaFe_{12}O_{19}$ with space group *P6₃/mmc*. The values of lattice parameters (a and c),crystallite size (D), volume of unit cell (V_{cell}) and strain (η) were calculated from equation (4.43), (4.44), (4.45), and (4.46) respectively, and presented in **Table 4.8**.

$$\frac{1}{d_{hkl}^2} = \frac{4}{3}\left(\frac{h^2+hk+l^2}{a^2}\right) + \frac{l^2}{c^2} \tag{4.43}$$

$$D = \frac{k\lambda}{\beta \cos\theta} \tag{4.44}$$

$$V_{cell} = 0.8666a^2c \tag{4.45}$$

$$\eta = \frac{\beta \cos\theta - \frac{0.9\lambda}{D}}{2 \sin\theta} \tag{4.46}$$

Where d_{hkl} is the value of d spacing, hkl are the miller indices, β (in radian) is the full width at half maximum, θ is the Braggs angle, k is the shape factor which having value of 1 for hexagonal ferrites, λ is the X-ray wavelength having a value of 1.54056Å. From **Table 4.8**, it

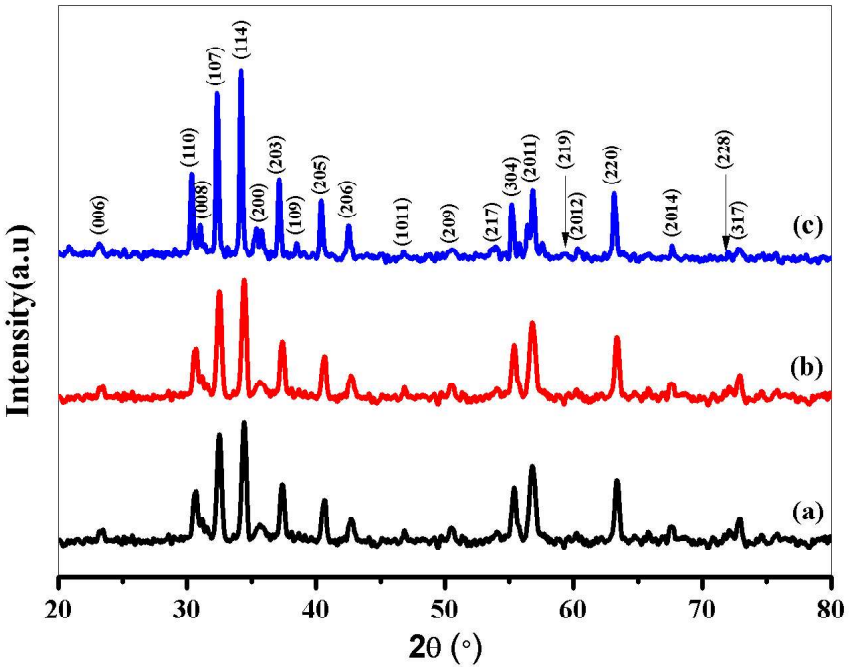

Fig. 4.63 XRD patterns of $Ba_{1-x}Dy_xFe_{12-y}Cr_yO_{19}$ (x=0.0, 0.1, 0.2, and y=0.0, 0.4, 0.5) for (a) B1, (b) B2, and (c) B3

can be seen that a, c and V_{cell} decreases with Dy^{3+}-Cr^{3+} substitution, this could be explained on the basis of the ionic radius of the substituted ions. It has been reported that the values of a, c and V_{cell} may decrease if the ionic radii of the substituted ions is smaller than that of the host ions and vice versa. The ionic radius of Dy^{3+} (1.03Å) is smaller than that of Ba^{2+} (1.35 Å); similarly, the ionic radius of Cr^{3+} (0.52 Å) is also smaller than that of Fe^{3+} (0.64 Å) [206][207][208][209][205]. This scenario prompt the distortion of the unit cell thereby causing microstructural defects and strain, consequently resulting in the observed decreased$a$,c and V_{cell} values. The c/a ratio varies slightly with Dy^{3+}-Cr^{3+} substitution and maintained an approximate value of 3.94 for all samples (**Table 4.8**). It has been reported that if the c/a ratio is below 3.98, then the prepared sample can be assumed to exhibit hexagonal structure [210][32]. Since the c/a ratio is less than 3.98 for all samples, we can assume that the prepared samples exhibit hexagonal structure. The values crystallite size does not follow a regular pattern with Dy^{3+}-Cr^{3+} substitution (**Table 4.8**), it increases at B2 and decreases at B3. The unsubstituted sample i.e. B1 exhibits the lowest crystallite size (22.91 nm). The strain (η) which is a distortion induced during synthesis process shows a decreasing behaviour with Dy^{3+}-Cr^{3+}substitution, this may be due to enhancement towards pure phase of hexaferrites [86].

Table 4.8 Values of lattice parameters (a and c),crystallite size (D), volume of unit cell (V_{cell}) and strain (η) for $Ba_{1-x}Dy_xFe_{12-y}Cr_yO_{19}$ (x=0.0, 0.1, 0.2, and y=0.0, 0.4, 0.5).

Sample code	2θ (°)	d (Å)	β (°)	a (Å)	c (Å)	c/a	V_{cell} ($Å^3$)	D (nm)	$\eta \times 10^{-4}$
B1	30.23	2.9541	0.399	5.90	23.27	3.9440	703.92	22.91	12.89
B2	30.31	2.9464	0.174	5.89	23.21	3.9405	698.51	52.54	5.60
B3	30.39	2.9015	0.235	5.87	23.15	3.9437	693.16	38.91	7.55

4.6.2 FTIR analysis

Fig. 4.64 shows the room temperature FTIR spectra of $Ba_{1-x}Dy_xFe_{12-y}Cr_yO_{19}$ (x=0.0, 0.1, 0.2, and y=0.0, 0.4, 0.5) in the range 4000 to 400 cm^{-1}. The presence of two absorption bands at 438 and 589 cm^{-1} which are characteristics bands of hexaferrites gives an idea of the formation of the hexaferrite structure [184]. These band are due to metal-oxygen stretching vibrations (such as Fe-O, Cu-O, Mg-O, and Zr-O) at the octahedral and tetrahedral sites in the

hexagonal lattice [56]. The band at 438 cm^{-1} occur in the octahedral site whereas the band at 598 cm^{-1} occur at the tetrahedral site, the variation in Fe^{3+}-O^{2-} distances at octahedral and tetrahedral sites cause shifting of the position of the absorption bands towards low frequency side [211]. The shifts in these absorption bands towards low frequency occur as a result of the occupation of the substituted cations in the Fe^{3+} site, the un-substituted sample (i.e. B1) exhibit these bands due to stretching vibration of Ba-O. The absorption bands in the range 1100 to 1500 cm^{-1} observed in all the samples could be attributed to metal-oxygen-metal (M-O-M) bonds such Fe-O-Fe and Co-O-Co bonds [212]. The observed absorption band at 1649 cm^{-1} results from H-O-H bending vibration of H_2O [187]. A broad absorption band was observed at 3459 cm^{-1} as a result of –OH stretching vibration, this is due to the presence of water molecules absorbed by the samples [212].

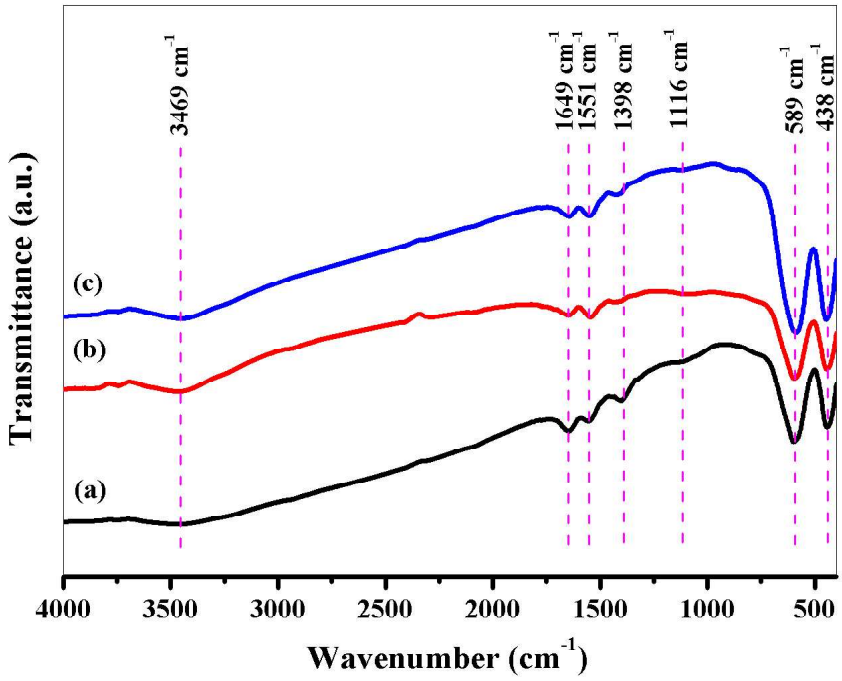

Fig. 4.64 FTIR spectra of $Ba_{1-x}Dy_xFe_{12-y}Cr_yO_{19}$ (x=0.0, 0.1, 0.2, and y=0.0, 0.4, 0.5) for (a) B1 (b) B2 and (c) B3

4.6.3 Raman spectroscopy

Raman spectroscopy is carried out in order to understand cation disorder in the prepared samples and vibrational/rotational energy states which appear when the derivative of the

polarizability is non-zero [213]. According to group theory treatment of hexaferrites based on the D_{6h} symmetry, there are 30 IR active modes ($13A_{2u} + 17E_{1u}$), 42 Raman active modes ($11A_{1g} + 14E_{1g} + 17E_{2g}$), and 54 modes ($3A_{1u} + 4A_{2g} + 13B_{1g} + 4B_{1u} + 3B_{2g} + 12B_{2u} + 15E_{2u}$) [214][215]. **Fig. 4.65** presents the room temperature Raman spectra of $Ba_{1-x}Dy_xFe_{12-y}Cr_yO_{19}$ (x=0.0, 0.1, 0.2, and y=0.0, 0.4, 0.5) in the range 150 to 800 cm^{-1}. The Raman spectra show a combination of weak and intense Raman active modes at 175, 197, 287, 320, 405, 516, 615, 675, and 733 cm^{-1} (**Table 4.9**), these modes are in good agreement with pure M-type hexaferrites. At lower Raman shift, two modes at 175 and 197 cm^{-1} corresponding to vibrational mode of the whole spinel block due to E_{1g} symmetry was observed [216][217]. The extremely weak

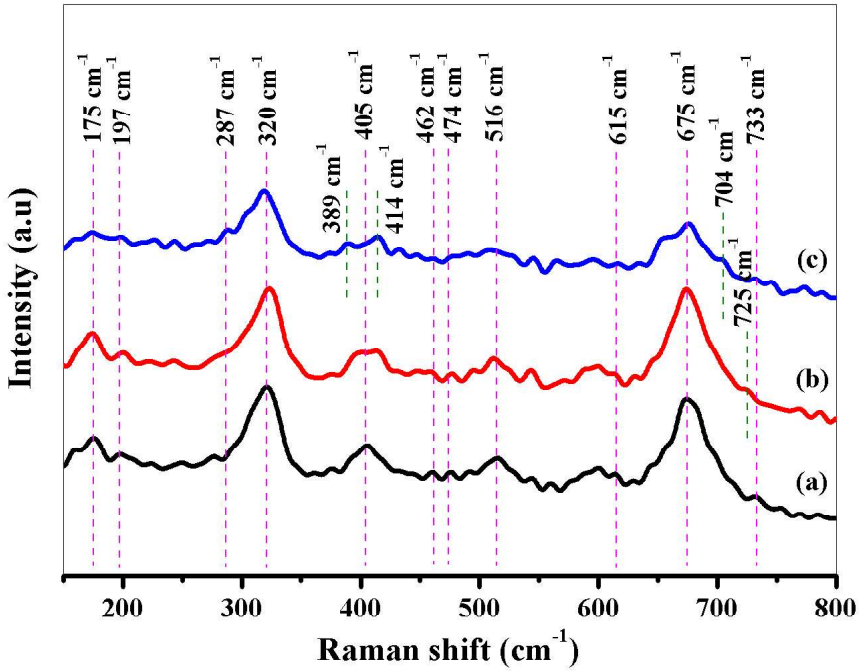

Fig. 4.65 Raman shift of $Ba_{1-x}Dy_xFe_{12-y}Cr_yO_{19}$ (x=0.0, 0.1, 0.2, and y=0.0, 0.4, 0.5) for (a) B1 (b) B2 and (c) B3

Raman active mode observed at 287 cm^{-1} is a signature of the vibration of octahedral 2a site as a due to A_{1g} symmetry [218]. Raman active mode at 405 and 320 cm^{-1} respectively arise due to E_{1g} and E_{2g} symmetry, these modes could be attributed to vibration of octahedral 12k site [219][220]. This mode split to distinct modes, one on the lower Raman shift (389 cm^{-1}) and the other on the higher Raman shift (414 cm^{-1}). Clearly, this Raman mode appeared as a

singled mode in the sample B1, it began splitting in the sample B2 and finally well-defined two distinct Raman active modes at 389 and 414 cm^{-1} can be observed. A moderately intense Raman active mode can be observed at 516 cm^{-1}, the occurrence of this mode could be ascribed to vibration of metal oxide bonds in the octahedral 12k and 2a site (mixed mode) as a result of E_{1g} symmetry [221][222]. Similarly, vibration of metal oxide bonds in the octahedral 12k and 2a site give rise to the appearance of another weak Raman active mode at 474 cm^{-1} which could be attributed to A_{1g} symmetry, the same symmetry is responsible for the appearance of 462 cm^{-1} Raman active mode at octahedral 12k site [218][223][224]. The appearance of the weak Raman active mode at 615 cm^{-1} stretching vibration of Fe-O bond at octahedral ($4f_2$) site as a result of A_{1g} symmetry [225][191][226], whereas intense Raman active mode observed at 675 cm^{-1} as a result of A_{1g} symmetry corresponds to vibrational mode of Bipyramidal (2b) site which differentiate the hexagonal ferrite structure from that of the spinel structure [227][228][229]. The weak Raman active mode that appear at 733 cm^{-1} is ascribed to vibrations of tetrahedral ($4f_1$) site as a result of A_{1g} symmetry [224]. Additionally, this mode tend to shift towards the lower frequency side of the spectra as the concentration of Dy^{3+}-Cr^{+3} is increased for the sample B2 (this mode shift to 725 cm^{-1}) and B3 (this mode shift to 704 cm^{-1}) as indicated by a green dotted line.

Table 4.9 Raman active modes of $Ba_{1-x}Dy_xFe_{12-y}Cr_yO_{19}$ (x=0.0, 0.1, 0.2, and y=0.0, 0.4, 0.5,)

Raman active mode (cm^{-1})	Symmetry	Mode assignment	Reference
175	E_{1g}	Whole spinel block	[216]
197	E_{1g}	Whole spinel block	[217]
287	A_{1g}	Octahedral (2a)	[218]
320	E_{2g}	Octahedral (12k)	[219][220]
405	E_{1g}	Octahedral (12k dominated)	[219][220]
462	A_{1g}	Octahedral (12k)	[223][224]
474	A_{1g}	Octahedral (12k and 2a)	[218]
516	E_{1g}	Octahedral (12k and 2a)	[221][222]
615	A_{1g}	Octahedral ($4f_2$)	[225][191]
675	A_{1g}	Bipyramidal (2b)	[227][228]
733	A_{1g}	Tetrahedral ($4f_1$)	[224][230]

4.6.4 Morphology analysis

The FESEM micrographs of $Ba_{1-x}Dy_xFe_{12-y}Cr_yO_{19}$ (x=0.0, 0.1, 0.2, and y=0.0, 0.4, 0.5) is presented in **Fig. 4.66**.The average grain sizes for all the samples are around 0.1 to 0.2μm as estimated from the micrographs. Since the grain sizes obtained from XRD is much smaller than that observed in FESEM, we can assume that the grains agglomerate to form larger ones

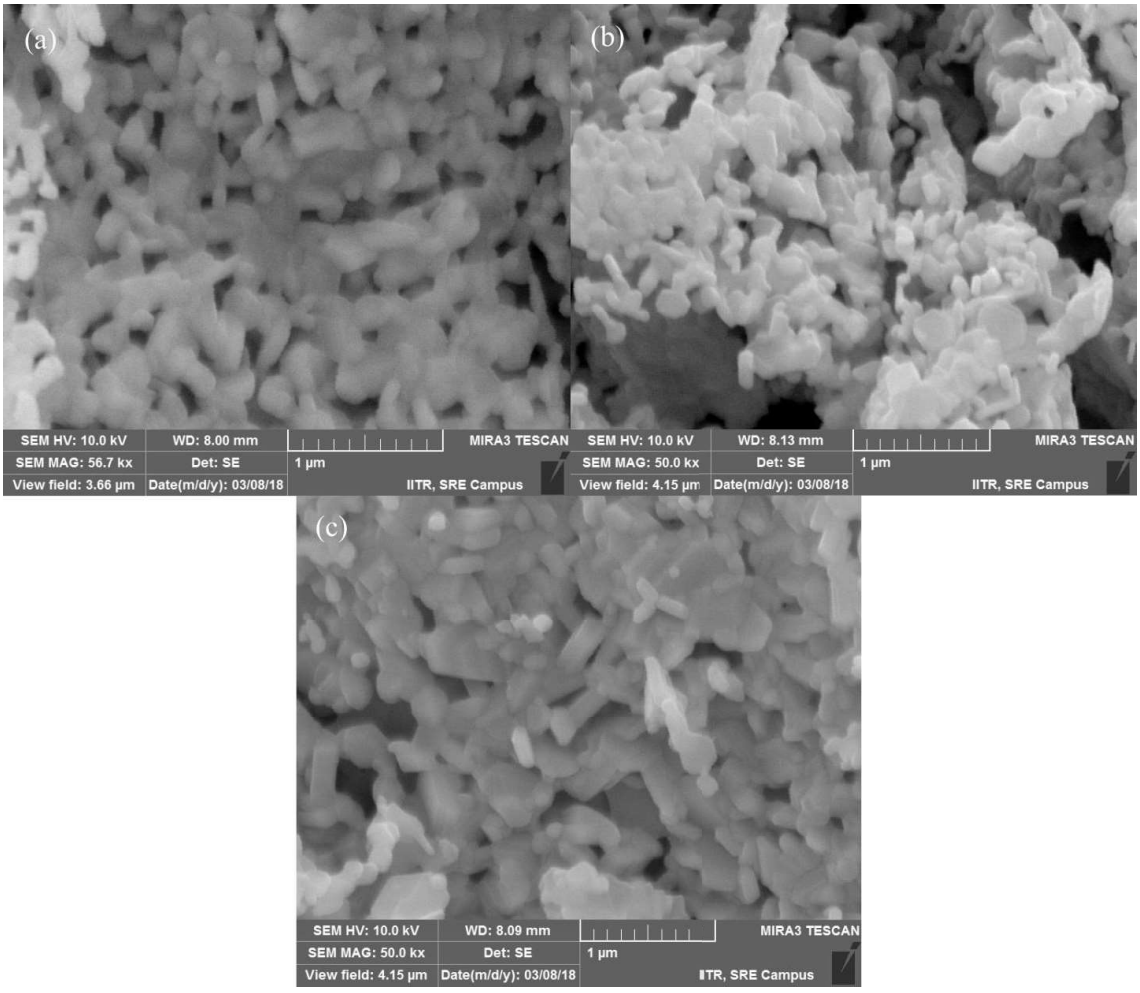

Fig. 4.66 FESEM micrograph of $Ba_{1-x}Dy_xFe_{12-y}Cr_yO_{19}$ (x=0.0, 0.1, 0.2, and y=0.0, 0.4, 0.5) for (a) B1 (b) B2 and (c) B3

in all the prepared samples. Clearly, agglomeration is observed in all the samples, this could be attributed to magnetic interaction with other neighbouring grains [200]. The micrographs show some crystallites with large shapes close to hexagonal platelet-like and others with rice or rod-like shapes. The shapes of the crystallites is vital for various applications, crystallites

with large hexagonal platelet-like shapes are useful as radar absorber materials [231][232]. The crystallites with rice or rod-like shapes may find application in data storage, catalysis, imaging, sensing and surface enhance Raman scattering [85]. The EDX and elemental analysis for the sample B2 and B3 are shown in **Fig. 4.67**. Both the EDX spectra and elemental micrographs confirm the stoichiometry of the prepared samples.

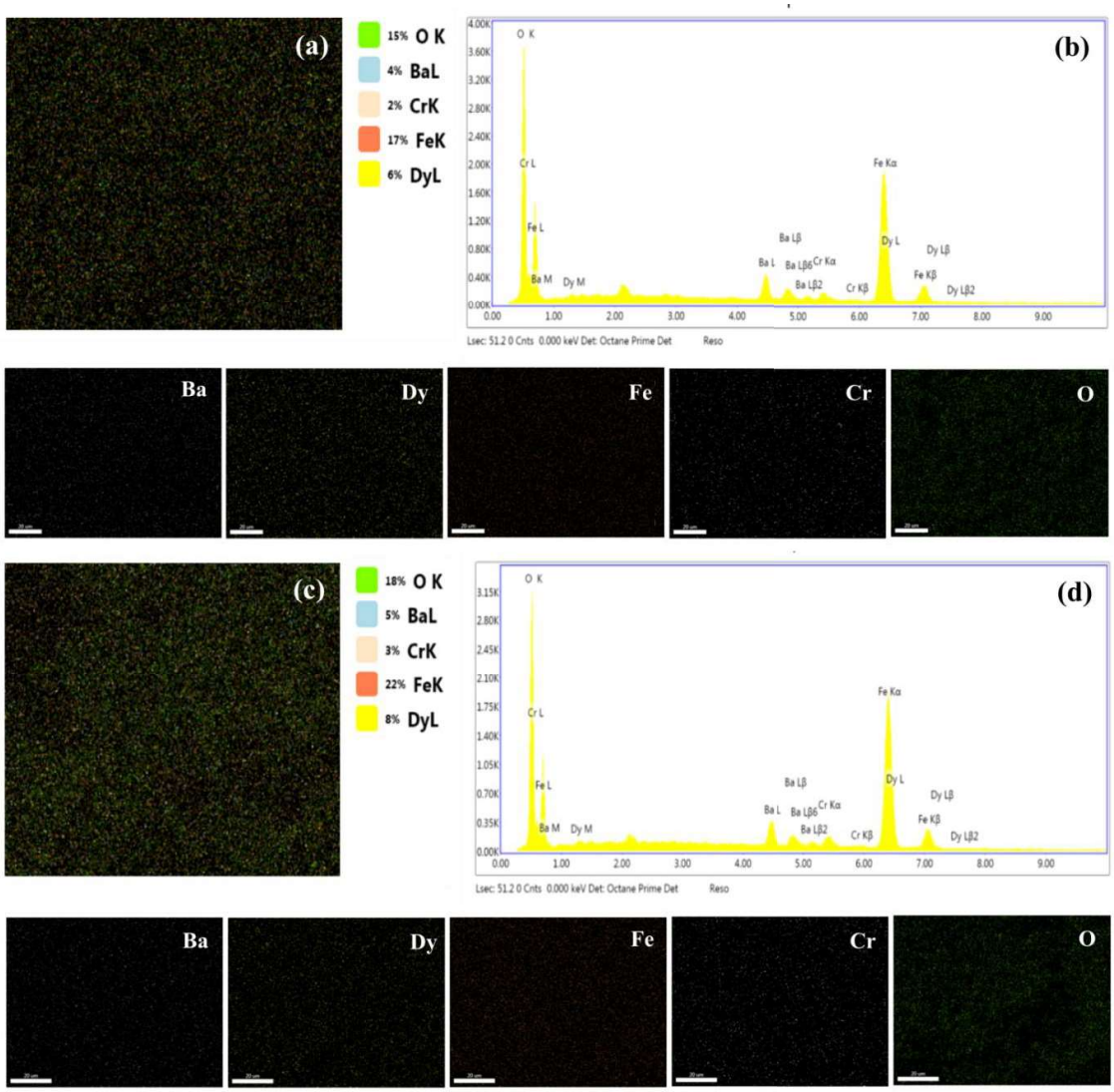

Fig. 4.67 EDX spectra and elemental mapping of $Ba_{1-x}Dy_xFe_{12-y}Cr_yO_{19}$ (x=0.1, 0.2, and y=0.0, 0.4, 0.5) for (a-b) B1 and (c-d) B2

4.6.5 Optical analysis

In UV-vis NIR spectroscopy, the energy of incident photons is absorbed by electrons in the sample followed by their excitation from the valence band to the conduction band. The

optical properties of$Ba_{1-x}Dy_xFe_{12-y}Cr_yO_{19}$(x=0.0, 0.1, 0.2, and y=0.0, 0.4, 0.5) have been investigated using UV-vis spectroscopy in the range 234-766 nm. The spectra of absorbance

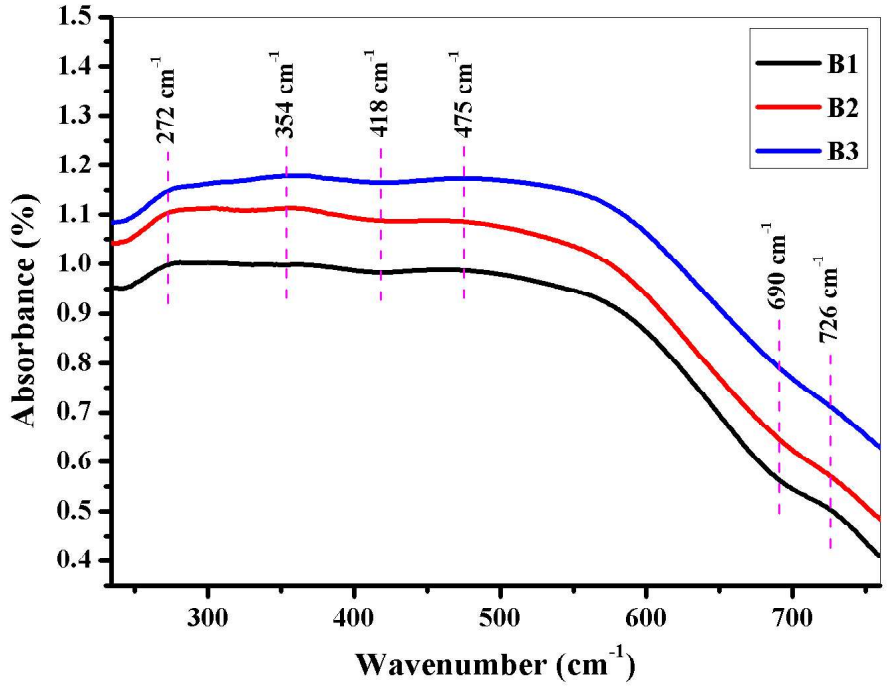

Fig. 4.68 Variation of absorbance versus wavelength for $Ba_{1-x}Dy_xFe_{12-y}Cr_yO_{19}$ (x=0.0, 0.1, 0.2, and y=0.0, 0.4, 0.5)

as a function of wavelength are presented in **Fig. 4.68**. The spectra shows absorption peaks at 272, 354, 475 and 726 nm which results from $\sigma - \sigma^*$, $n - \sigma^*$, $\pi - \pi^*$, and $n - \pi^*$ transition. Also, there were two reflection peaks observed at 418 and 690 nm. The reflection peak at 418 nm corresponds to hypochromic shift whereas that at 690 nm corresponds to hyperchromic shift. There is no observation of hypsochromic (blue) shift and bathochromic (red) shift in the spectra. The absorption peak at 726 nm and the reflection peak at 690 nm merge together as Dy^{3+}-Cr^{3+} is substituted, this shows that the substitution of Dy^{3+}-Cr^{3+} enhances absorption by the prepared samples. The optical band gap (E_g) was determined using Tauc relation [174].

$$\alpha h\upsilon = A\left(h\upsilon - E_g\right)^n \tag{4.47}$$

Where α is the absorbance, h is the planks constant ($6.6260 \times 10^{-34}\, J.s$), υ is the frequency of incident photon and A is a characteristics constant that depends on n. The values of n are

respectively 1/2, 3/2, 2 and 3 for allowed direct, forbidden direct, allowed indirect and forbidden indirect transitions. **Fig. 4.69** shows the plots of E_g for the synthesized samples.

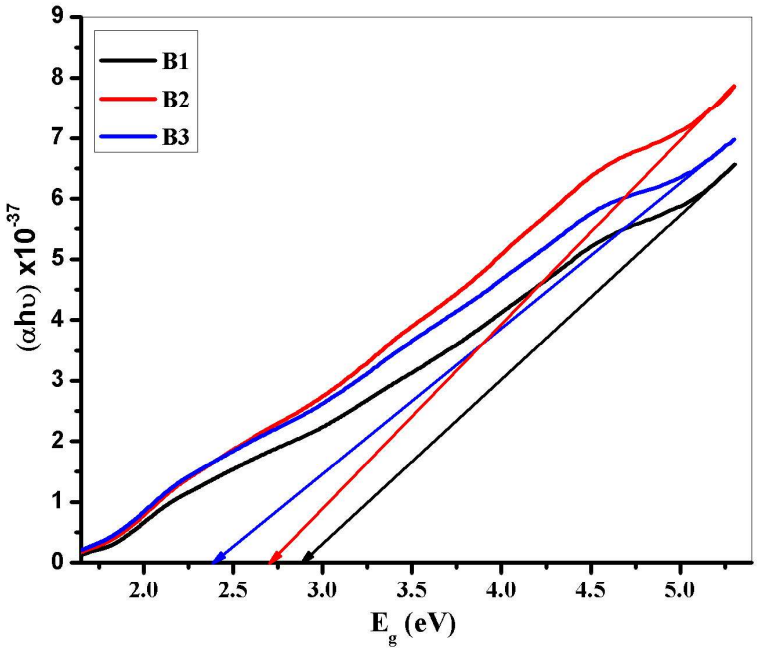

Fig. 4.69 Optical band gap for $Ba_{1-x}Dy_xFe_{12-y}Cr_yO_{19}$ (x=0.0, 0.1, 0.2, and y=0.0, 0.4, 0.5)

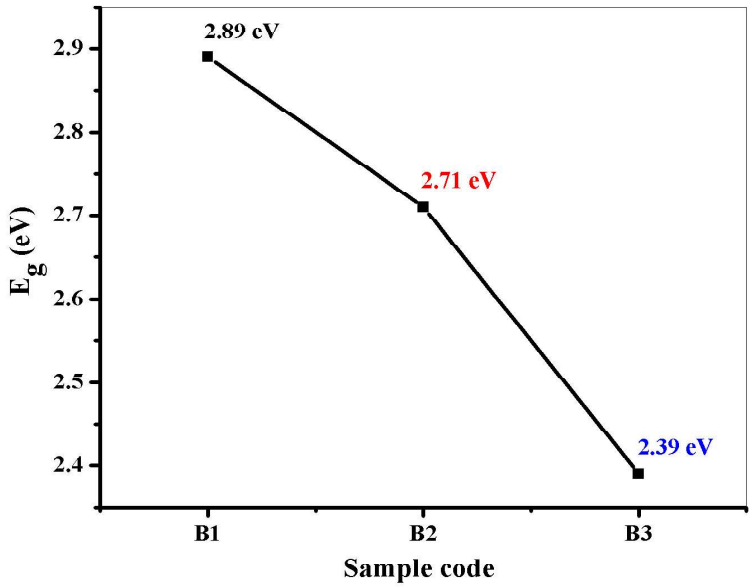

Fig. 4.70 Variation of band gap with Dy^{3+}-Cr^{3+} substitution

The value of E_g for all the samples was evaluated by extrapolation of the linear part of the graph of $(\alpha h\upsilon)^2$ against E_g. The values of E_g for the sample B1, B2 and B3 were found to be 2.89, 2.71 and 2.39 eV respectively. From **Fig. 4.69** and **4.60**, we can observe that E_g decreases with increase in Dy^{3+}-Cr^{3+} substitution. Kaur *et al.* observed that the variation of E_g relies on factors such as quantum confinement and crystallite sizes [186]. The $E_g$observed are higher than those obtained for strontium hexaferrites thin films prepared laser ablation method [233].

4.6.6 Dielectric and impedance spectroscopy

The response of nanomaterial to an applied electric field is better understood using impedance spectroscopy; this may present us with vital information regarding conduction mechanism involving ionic, electronic, and interfacial polarization. The parameters calculated from the impedance spectroscopy are complex permittivity (ε^*), real part of complex permittivity (ε'), and the imaginary part of complex permittivity (ε'') which are expressed in equation (4.48), (4.47), and (4.48) respectively [164].

$$\varepsilon^* = \varepsilon' - j\varepsilon'' \tag{4.48}$$

$$\varepsilon' = \frac{Z''}{2\pi\omega C_0 Z^2} \tag{4.49}$$

$$\varepsilon'' = \frac{Z'}{2\pi\omega C_0 Z^2} \tag{4.50}$$

where $j = \sqrt{-1}$ is an imaginary number, Z' is the real part of complex impedance, Z'' is the imaginary part of complex impedance, $\omega = 2\pi f$ is the frequency and C_0 is the geometrical capacitance. The complex impedance(Z^*), real part of complex impedance (Z'), and the imaginary part of complex impedance (Z'') are respectively given in equation (4.51), (4.52), and (4.53) [92].

$$Z^* = Z' - jZ'' \tag{4.51}$$

$$Z' = |Z| \cos\theta \tag{4.52}$$

$$Z'' = |Z| \sin\theta \tag{4.53}$$

where θ is the phase angle. The ratio of ε'' and ε'represents the dielectric loss tangent ($\tan\delta$) or energy dissipation factor of the nanomaterial [137].

$$\tan \delta = \frac{\varepsilon''}{\varepsilon'} \tag{4.54}$$

The conducting properties of a nanomaterial can be explained on the basis of the following equation [180].

$$\sigma_t = \sigma_{AC} + \sigma_{DC} \tag{4.55}$$

Where σ_{DC} is the frequency independent part of conductivity, $\sigma_{AC} = A\omega^s$ is the frequency dependent part of conductivity, A is the temperature dependent constant and s is a numerical constant. AC conductivity can be expressed by the following relation [234].

$$\sigma_{AC} = \omega \varepsilon_0 \varepsilon' \tan \delta \tag{4.56}$$

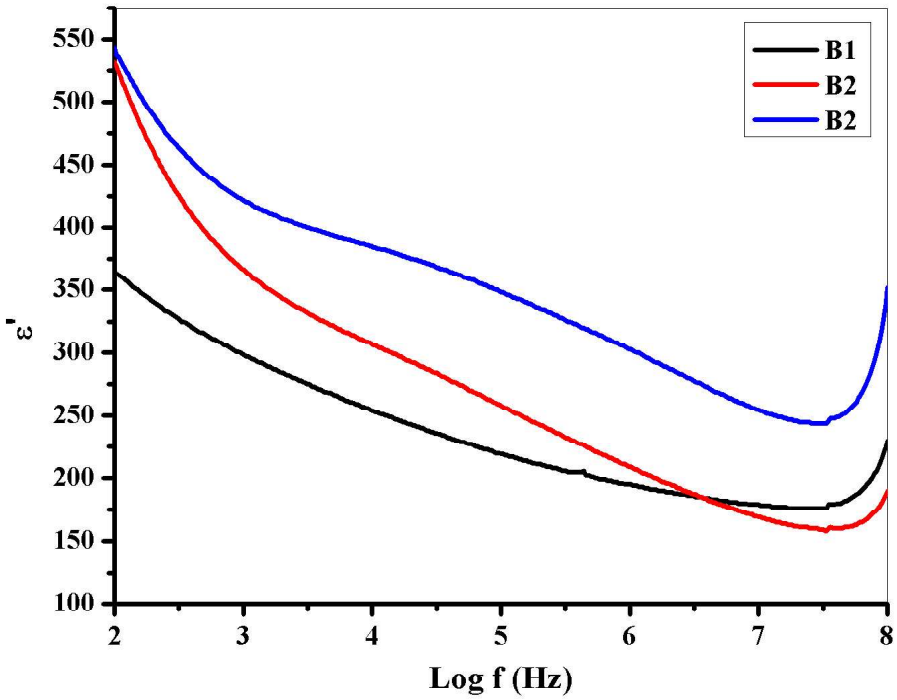

Fig. 4.71 Variation of room temperature real part of dielectric permittivity (ε') with frequency for $Ba_{1-x}Dy_xFe_{12-y}Cr_yO_{19}$ (x=0.0, 0.1, 0.2, and y=0.0, 0.4, 0.5)

The energy storage ability of hexaferrites is better understood by analysing ε'. **Fig. 4.71** represents the room temperature frequency dependent ε' for $Ba_{1-x}Dy_xFe_{12-y}Cr_yO_{19}$ (x=0.0, 0.1, 0.2, and y=0.0, 0.4, 0.5). The dielectric properties of hexaferrites can be explained on the basis of Maxwell-Wagner model. In accordance with this model, the layers of conducting

grains in ferrites is surrounded by layers of poorly conducting grain boundaries [174]. When electric field is applied at lower frequencies, charge carriers easily migrate through the grains and accumulate at the grain boundaries which result in high interfacial polarization owing to high resistivity and consequently high values of ε' whereas at higher frequencies, the interfacial polarization drastically decreases to negligible values. At this point, only electronic and dipolar polarization contribute to the values of ε' [235]. All the samples exhibit high value of ε' at lower frequencies as compared with intermediate and higher frequencies. The substitution of Dy^{3+} at Ba^{2+} site and Cr^{3+} at Fe^{3+} site forces the hopping of electrons from Fe^{3+} ion to Fe^{2+}ion on octahedral 2a sites in order to maintain charge neutrality. The accumulation of Fe^{2+}, space charge polarization, oxygen vacancies and grain boundary defects are the reason behind the high value of ε' at lower frequencies [209].

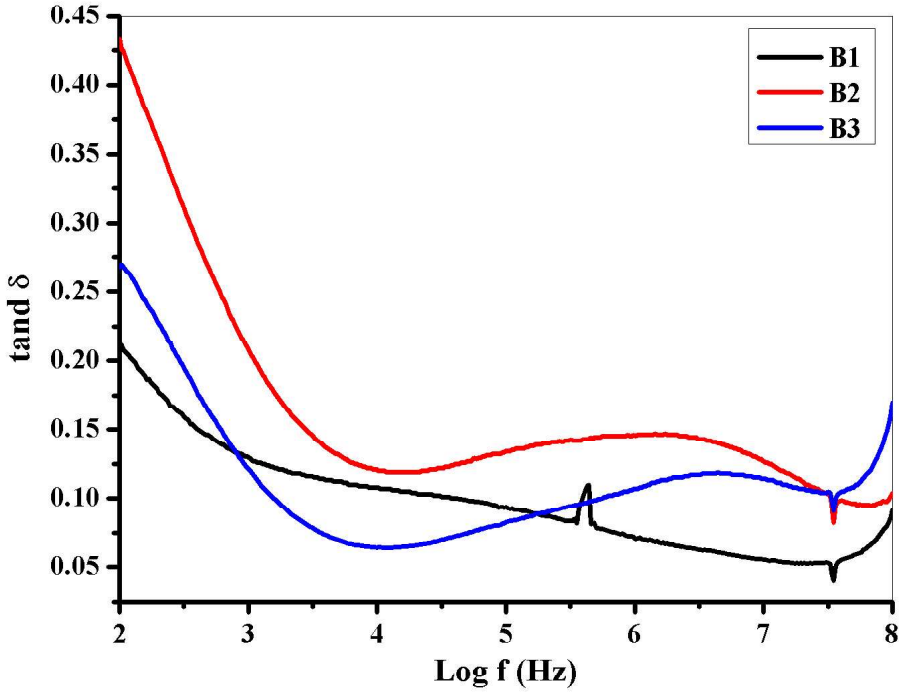

Fig. 4.72 Variation of dielectric loss tangent ($\tan\delta$) with frequency for $Ba_{1-x}Dy_xFe_{12-y}Cr_yO_{19}$ (x=0.0, 0.1, 0.2, and y=0.0, 0.4, 0.5)

From **Fig. 4.71**, it can be observed that ε' increases with increase in Dy^{3+}-Cr^{3+} substitution for all the samples, this could be attributed to increased space charge polarization as a result enhancement in electron hopping. [236]. Clearly, ε' shows a decreasing trend with increase in

frequency both at lower and intermediate frequencies for all samples. At higher frequencies, there is an abrupt increase in ε', this indicates thatε' is enhanced by Dy^{3+}-Cr^{3+} substitution at higher frequencies. The increasing behaviour of ε' reduces the penetration depth of EM waves by increasing the skin effect, this means that lower values of ε' observed in hexagonal ferrites as compared with the ε' of calcium copper titanate ($> 9 \times 10^3$at 10^6 Hz) makes them useful for high frequency application [237][238].

The dielectric loss ($\tan\delta$) shows the nature of energy dissipation of the hexaferrite nanomaterial during the conduction of electrons in the dielectric system. Variation of $\tan\delta$ with frequency at room temperature for $Ba_{1-x}Dy_xFe_{12-y}Cr_yO_{19}$ (x=0.0, 0.1, 0.2, and y=0.0, 0.4, 0.5) is presented in **Fig. 4.72**. Electron hopping produces polarization which varies with the ac electric field; when the polarization lags behind the applied ac electric field above a certain critical frequency, $\tan\delta$ appears [183]. This is justified by the presence of defects (vacancies and interstitials), impurities and structural imperfections in the material as a result of substitutions of cation with different valency [208][189]. The prepared samples exhibit high $\tan\delta$at lower frequencies; this corresponds to loss of energy. There is high resistivity at lower frequencies as a result of grain boundaries; this scenario prompt the need for more energy in order for electron hopping between Fe^{3+} and Fe^{2+} ions to occur. Hence, high $\tan\delta$ (or loss of energy) is observed at lower frequencies. Less resistivity is observed at higher frequencies as a result of conducting grains and consequently less energy is required for electron hopping between Fe^{3+} and Fe^{2+} ions to occur. Thus, small $\tan\delta$ (or loss of energy) is observed at higher frequencies [237][209]. The contribution to $\tan\delta$ at lower frequencies could be attributed to hopping conduction of electrons whereas the observed $\tan\delta$ at higher frequencies could be due to the response of defect dipoles to the applied electric field, the defect dipoles arise during the process of calcination as a result of the transition of Fe^{3+} ions to Fe^{2+} ions [239]. Resonance or Debye-like relaxation peaks are observed in the samples B2 as well as that with B3 at higher frequencies, these peaks occur when the frequency of electron jumping during electron exchange between Fe^{3+} and Fe^{2+} ions equals the frequency of the applied electric field [234]. The observed decrease in $\tan\delta$ after the occurrence of the Debye-like relaxation peaks in the samples B2 as well as that with B3 at higher frequencies can be explained on the basis of relaxation of the defects dipoles, under the influence of applied electric field the relaxation of these defects dipoles display a decreasing behaviour with increase in frequency and subsequently decreases the $\tan\delta$ in the higher frequencies side [240].

The understanding of the nature of the grain and grain boundary resistance of the synthesized samples is observed from the behaviour of the curve observed in Cole-Cole plot (also called the Nyquist plots) which is a plot of the imaginary part (Z'') versus real part (Z') of complex impedance (Z^*). **Fig. 4.73** presents the Cole-Cole plot of $Ba_{1-x}Dy_xFe_{12-y}Cr_yO_{19}$ (x=0.0, 0.1, 0.2, and y=0.0, 0.4, 0.5) at room temperature. The analysis of Cole-Cole plots gives vital parameters which characterized non Debye-like relaxation behaviour [241]. A polycrystalline

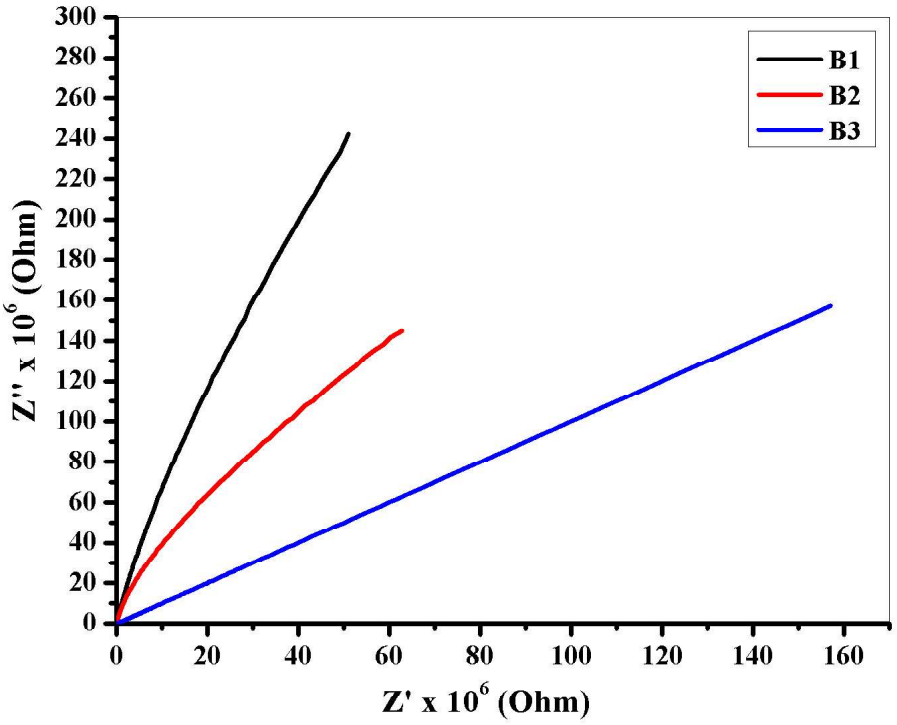

Fig. 4.73 Cole-Cole plot of $Ba_{1-x}Dy_xFe_{12-y}Cr_yO_{19}$ (x=0.0, 0.1, 0.2, and y=0.0, 0.4, 0.5)

hexagonal ferrite sample can be thought to consist of grains (or parallel conducting plates) separated by grain boundaries (or resistive plates). A Cole-Cole plot consists of a semi-circle arc starting from the lower frequencies side to the higher frequencies side. The part of the semi-circle at the lower frequency side represents contribution of the grain boundaries (or grain boundary resistance (R_{gb}) while the part of the semi-circle at the higher frequency side of the Cole-Cole plot represents contribution from the grains (or grain resistance (R_g) [242]. From **Fig. 4.73**, we can observe that there is no higher frequency arc for the samples with B1 as well as that with B2. Hence, we can conclude that there is no or less contribution from R_g towards the dielectric properties for these samples. The arc for the sample with x=0.2 and y=0.5 extend to the higher frequency side of the plot; this is an indication that there is

contribution from R_g towards the dielectric properties for this sample and that the quantity of grains has increased. With the foregoing, we can expect the sample with B3 to be more conducting than the samples with B1 as well as that with B2 since grain boundaries are less conducting than grains. From the forgoing discussion, we can assume that R_{gb} contribute most to the dielectric properties of the synthesized samples.

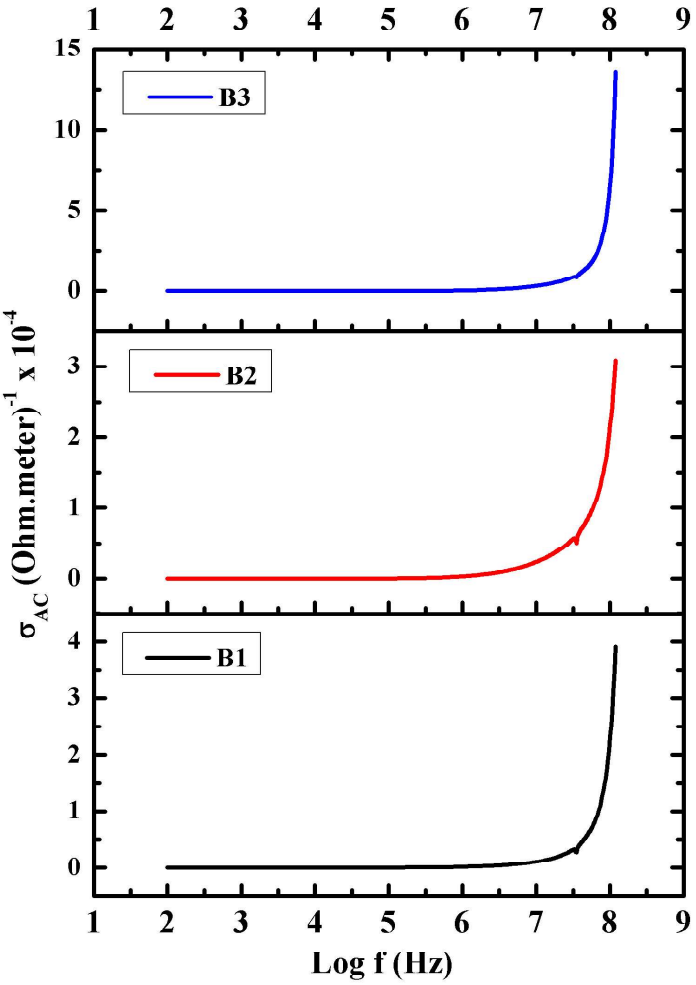

Fig. 4.74 AC conductivity of $Ba_{1-x}Dy_xFe_{12-y}Cr_yO_{19}$ (x=0.0, 0.1, 0.2, and y=0.0, 0.4, 0.5)

The AC conductivity (σ_{AC}) of $Ba_{1-x}Dy_xFe_{12-y}Cr_yO_{19}$ (x=0.0, 0.1, 0.2, and y=0.0, 0.4, 0.5) is presented in **Fig. 4.74.** From lower to intermediate frequencies, σ_{AC} exhibit frequency independent behaviour, this could be attributed to the presence of random distribution of charge carriers through activated electron hopping [183]. At higher frequencies, there is a sudden and abrupt rise in σ_{AC} of the prepared samples; this behaviour correlates with the

increase in ε' at higher frequencies (**Fig. 9**). Similar to the behaviour of ε', the behaviour of σ_{AC} of hexaferrites depends on electron hopping between Fe^{3+} and Fe^{2+} ions at octahedral site. As the frequency of the applied field is varied, electron hopping between Fe^{3+} and Fe^{2+} ions at octahedral site increases thereby resulting in increased conductivity [243]. The conduction mechanism in hexaferrites have been explained by assuming the process of polarization in hexaferrites to be similar to the process of conduction, in this manner, electron hopping between Fe^{3+} and Fe^{2+} ions at octahedral site results in the occurrence of local displacement and the subsequent generation of polarization which is responsible for conduction in hexaferrites [244][192]. Similar to ε', we can conclude that Dy^{3+}-Cr^{3+} substitution enhances σ_{AC} at higher frequencies.

4.6.7 Magnetic analysis

Fig. 4.75 shows the room temperature M-H hysteresis loops of the $Ba_{1-x}Dy_xFe_{12-y}Cr_yO_{19}$ (x=0.0, 0.1, 0.2, and y=0.0, 0.4, 0.5) where the maximum applied magnetic field is 15 kOe. Coercivity (H_c), remanent (M_r) and saturation magnetisation (M_s) were obtained from the M-H hysteresis loop and presented in **Table 4.10**. Anisotropy constant (K), magneton number (μ_B) and squareness ratio (SR) were calculated using equation (4.57), (4.58), and (4.59) (respectively [86][189].

$$K = \frac{\mu_0 M_s H_c}{2} \tag{4.57}$$

$$\mu_B = \frac{Molecularweight \times M_s}{5585} \tag{4.58}$$

$$SR = \frac{M_r}{M_s} \tag{4.59}$$

Where $\mu_0 = 4\pi \times 10^7\, H/m$ is the permeability in vacuum, M_s is the saturation magnetisation, and H_c is the coercivity. It has been observed that the width and shape of the hysteresis loop is dependent upon parameters such as grain size, nature of dopants, porosity and cation distribution [245]. Specifically, cation substitution results in the weakening of the super exchange interaction of the type $Fe_A^{3+} - O - Fe_B^{3+}$ thereby causing the collapse of magnetic collinearity of the lattice [246]. The values of H_c, M_s and M_s were found to be in the range 5050.81 to 6047.68 Oe, 20.57 to 34.02 emu/g and 36.00 to 60.69 emu/g respectively (**Table 4.10**). It was observed that H_c increases with increase in Dy^{3+}-Cr^{3+} Substitution whereas K initially decreases and then increase for the sample B3 (**Table 4.10, Fig. 4.76**). All samples show high values of H_c, the value of H_c for the sample with x=0.2

and y=0.5 is 6356.52 Oe; this value is close to the theoretical value of H_c (6700 Oe) for hexagonal ferrites. It has been reported that hexaferrites having H_c greater than 1200 Oe can be used for high density perpendicular recording media. Also, hexaferrites with $H_c > M_r/2$ are considered as hard magnets, hard magnets are useful in high frequency application [82][247].

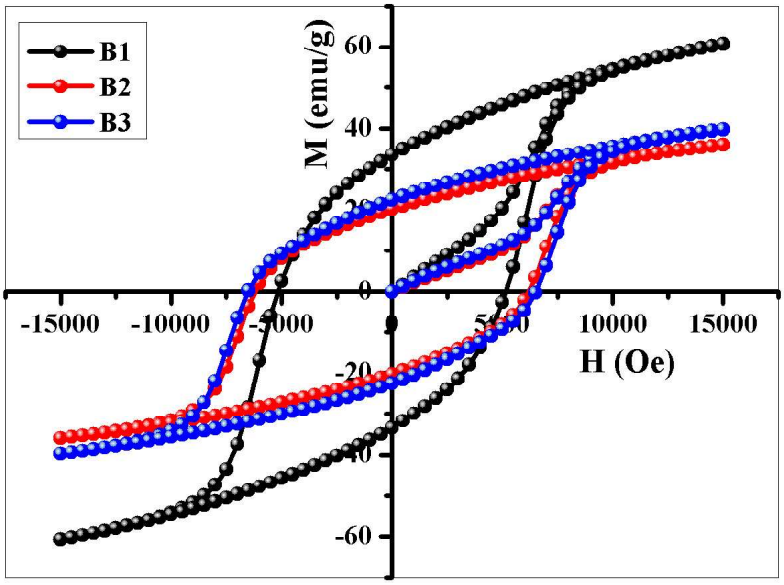

Fig. 4.75 M-H hysteresis loop of $Ba_{1-x}Dy_xFe_{12-y}Cr_yO_{19}$ (x=0.0, 0.1, 0.2, and y=0.0, 0.4, 0.5)

The variation of M_r and M_s does not follow a regular pattern, there in an initially decrease in the sample B2 followed by an increase for the sample B3 (**Table 4.10, Fig. 4.77**). The sample B1 shows M_s value of 60.69 emu/g, this value is also close to the theoretical value of M_s (74.30 emu/g) for hexagonal ferrites [248].The observed increase in H_c could be attributed to increase in magnetocrystalline anisotropy with anisotropic Fe^{2+} ions located at 2*a* crystallographic site [249]. The observed increase in M_s and M_r for the sample B3 can be explained on the basis of site occupation by Cr^{3+} substitution. In the hexagonal sub-lattice, there are 64 ions per unit cell on 11 sites having distinct symmetry, 24 Fe^{3+} ions are distributed over five crystallographic sites (2*a*, 2*b*, 4f_1, 4f_2, and 12*k*) out of which 2*a*, 4f_2, and 12*k* is octahedral sites, 4f_1 is tetrahedral site and 2*b* is trigonal pyramidal site. There are 2 Fe^{3+} ions at 4f_1 and another 2 Fe^{3+} ions at 4f_2 crystallographic sites having spin down electrons, 6 Fe^{3+} ions at 12*k* crystallographic site having spin up electrons, 1 Fe^{3+} ion at 2*a*

crystallographic site having spin up electron and another 1 Fe^{3+} ion at 2*b* crystallographic site having spin up electrons. In total, there are 4 Fe^{3+} ions with spin down electrons and eight with spin up electrons, this result in a net 4 Fe^{3+} ions with spin up electrons. Since the μ_B for each Fe^{3+} ion is 5 μ_B as a result of the unpaired electrons, then the total net μ_B would be 20 μ_B [250]. It has been reported that when Fe^{3+} ions are substituted with Cr^{3+} ions, the Cr^{3+}ions

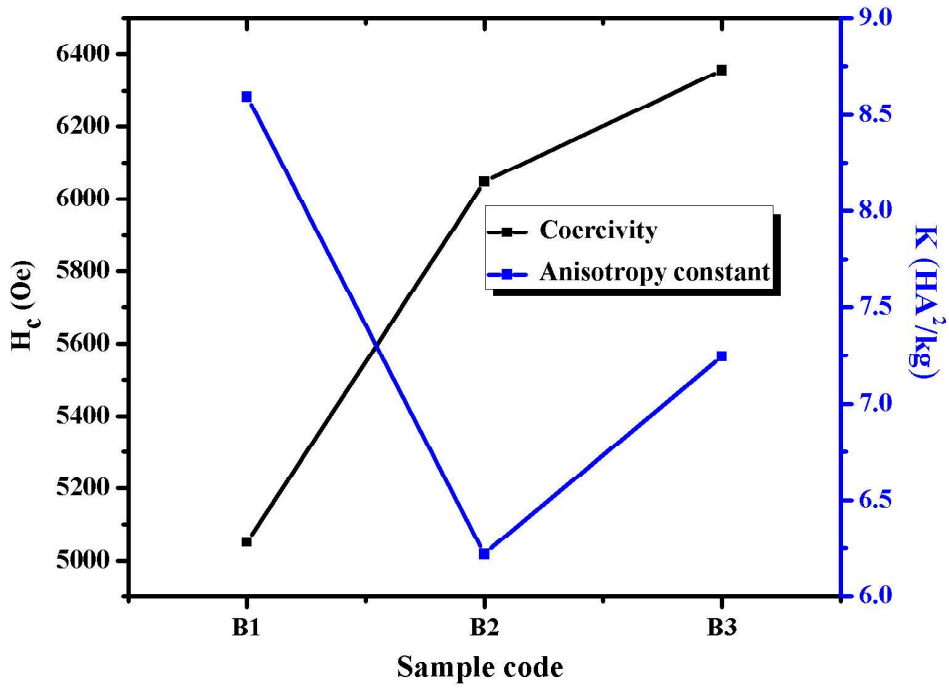

Fig. 4.76 Variation of coercivity and anisotropy constant with Dy^{3+}-Cr^{3+} substitution

having 3 μ_B display greater preference to occupy 12*k*, 2*a*, and 4f_2 crystallographic site [251][252]. Taking this into account, we can infer that the number of Cr^{3+} ions occupying 4f_2 crystallographic site is greater than those occupying 12*k* and 2*a* crystallographic sites thereby resulting in increased M_s and M_r and we observed a decrease when they replace Fe^{3+} ions in 12*k* and 2*a* because the net magnetic moment of Cr^{3+} (3 μ_B) is less than that of Fe^{3+} (5 μ_B) [245][253][246]. Furthermore, it has been theoretically shown that the Fe^{3+} ion at 4f_2 and 2b site are responsible for the uniaxial anisotropy and that a decrease in the values of anisotropy constant (*K*) may be ascribed to the substitution of Fe^{3+} ion by the substituting ion [254][255]. Our analysis of magnetic properties shows that K decreases with increase in the

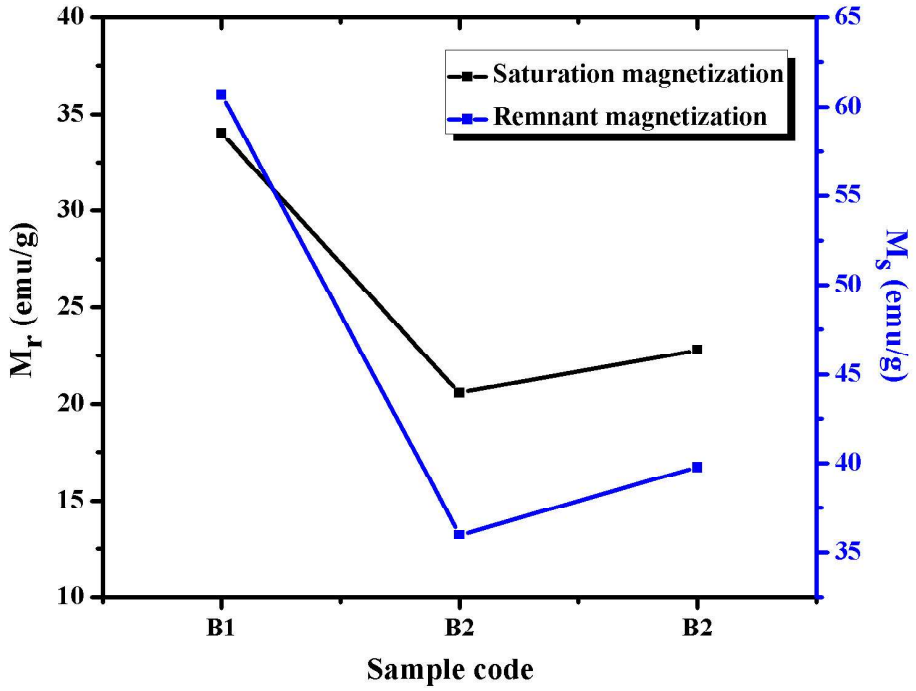

Fig. 4.77 Variation of remnant and saturation magnetization with Dy^{3+}-Cr^{3+} substitution

Table 4.10 Values of coercivity (H_c), remnant magnetization (M_r), saturation magnetization (M_s), squareness ratio (SR), anisotropy constant (K) and magnetic moment (μ_B) for $Ba_{1-x}Dy_xFe_{12-y}Cr_yO_{19}$ (x=0.0, 0.1, 0.2, and y=0.0, 0.4, 0.5,)

Sample code	H_c (Oe)	M_r (emu/g)	M_s (emu/g)	SR (M_r/M_s)	K (HA^2/kg)	μ_B
B1	5050.81	34.02	60.69	0.5606	8.59	6.77
B2	6047.68	20.57	36.00	0.5712	6.22	4.09
B3	6356.52	22.80	39.78	0.5731	7.25	4.55

concentration of Dy^{3+}-Cr^{3+}; this could mean that Cr^{3+} ions replaces Fe^{3+} ions at octahedral $4f_2$ and bipyramidal 2b site. Hence, this further supports the occupancy of octahedral $4f_2$ site by Cr^{3+} ions. The values of SR for the samples B1, B2, and B3 are respectively 1.78, 1.75 and 1.74, it has been reported that the hexaferrites with SR greater than 0.5 exhibit single domain structure [32][248]. Hence, we can conclude that the prepared samples are of single domain structure.

4.6.8 Mössbauer spectroscopy

^{57}Fe Mössbauer spectroscopy was carried out in order understand the site preference of the cations and their distribution. The Mössbauer spectra of $Ba_{1-x}Dy_xFe_{12-y}Cr_yO_{19}$ (x=0.0, 0.1, 0.2, and y=0.0, 0.4, 0.5) is presented **Fig. 4.78**. The Mössbauer parameters such as line width (Γ), isomer-shift (δ), quadrupole splitting (Δ), hyperfine field (H_{hf}), and relative area (R_A) are fitted according to the five sexets which were respectively assigned to 12k, $4f_2$, $4f_1$, 2a, and 2b crystallographic sites (**Table 4.11**). The variation of δ, Δ, H_{hf}, and R_A with concentration of Dy-Cr is presented in **Fig. Fig. 4.79 (a)**, **(b)**, **(c)**, and **(d).** It has been reported that the

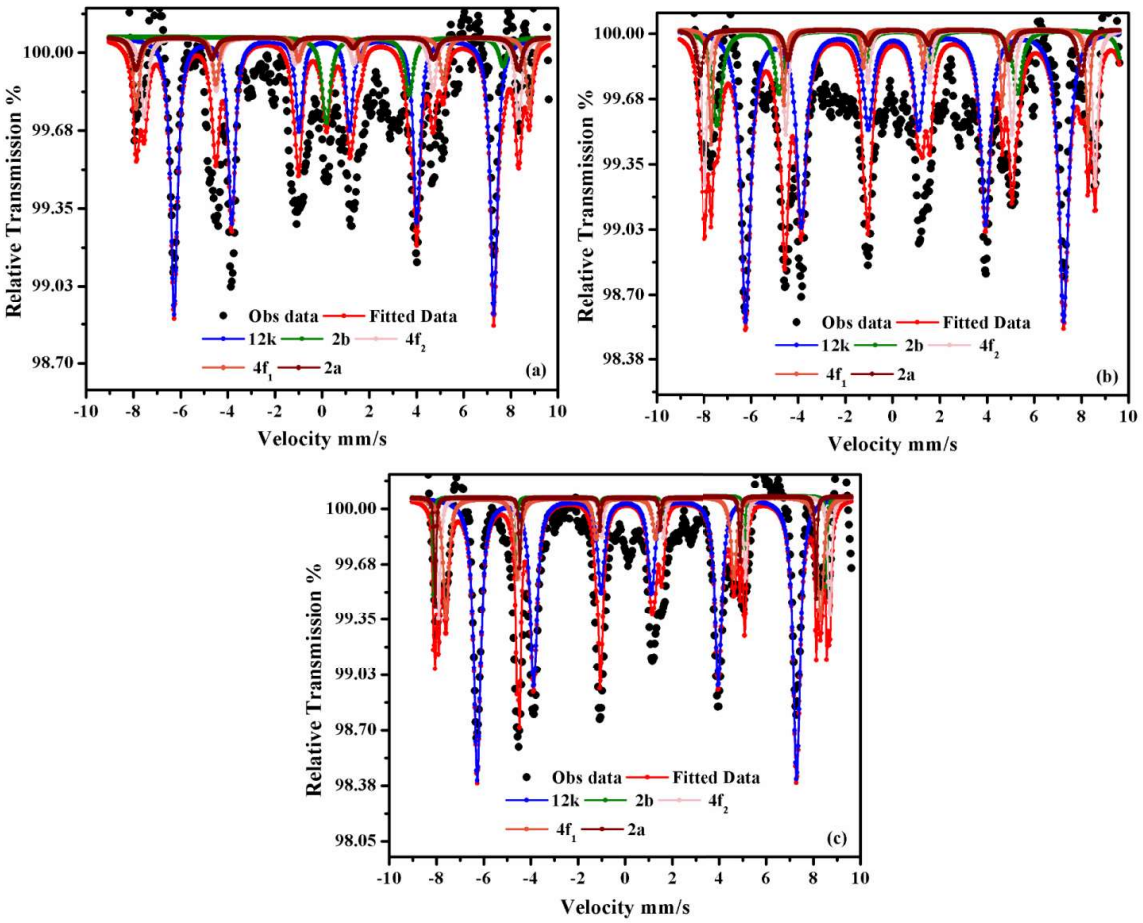

Fig. 4.78 Mössbauer spectra of $Ba_{1-x}Dy_xFe_{12-y}Cr_yO_{19}$ (x=0.0, 0.1, 0.2, and y=0.0, 0.4, 0.5) for (a) B1 (b) B2 and (c) B3

values of δ determines the nature of chemical bonding and the valence state of Fe in a magnetically ordered material, δ should be in the range -0.15 to 0.05 mm/s, 0.05 to 0.5 mm/s,

and 0.6 to 1.7 mm/s for Fe^{4+}, Fe^{3+}, and Fe^{2+} respectively [256]. In our research, the values of δ ranges from 0.11 to 0.56 mm/s (**Fig. 4.79 (a)**), hence we can conclude that the samples comprises of the high spin Fe^{3+} valence state. The values of δ show variation for each of the sexets, this show that the electronic distribution is influenced by Ba^{2+}, Dy^{3+}, and Cr^{3+}.The values of Δ for the $4f_2$ site shows a decreasing behaviour with increase in the concentration of Dy^{3+}-Cr^{3+} (**Fig. 4.79 (b)**), this could be ascribed to increase in the strength of the positive charge density as a result of replacement of Fe^{3+} ions by Cr^{3+} ions [257].The values of H_{hf} at octahedral (12k) and bipyramidal (2b) sites increases with increase in the concentration of Dy^{3+}-Cr^{3+} (**Fig. 4.79 (c)**), this could be explained as thus. The lattice constant c decreases with increase in substitution of Dy^{3+}-Cr^{3+} as reported in our previous research (c=23.27, 23.21, and 23.15 Å for B1, B2, and B3 respectively) [133], this scenario causes an alteration

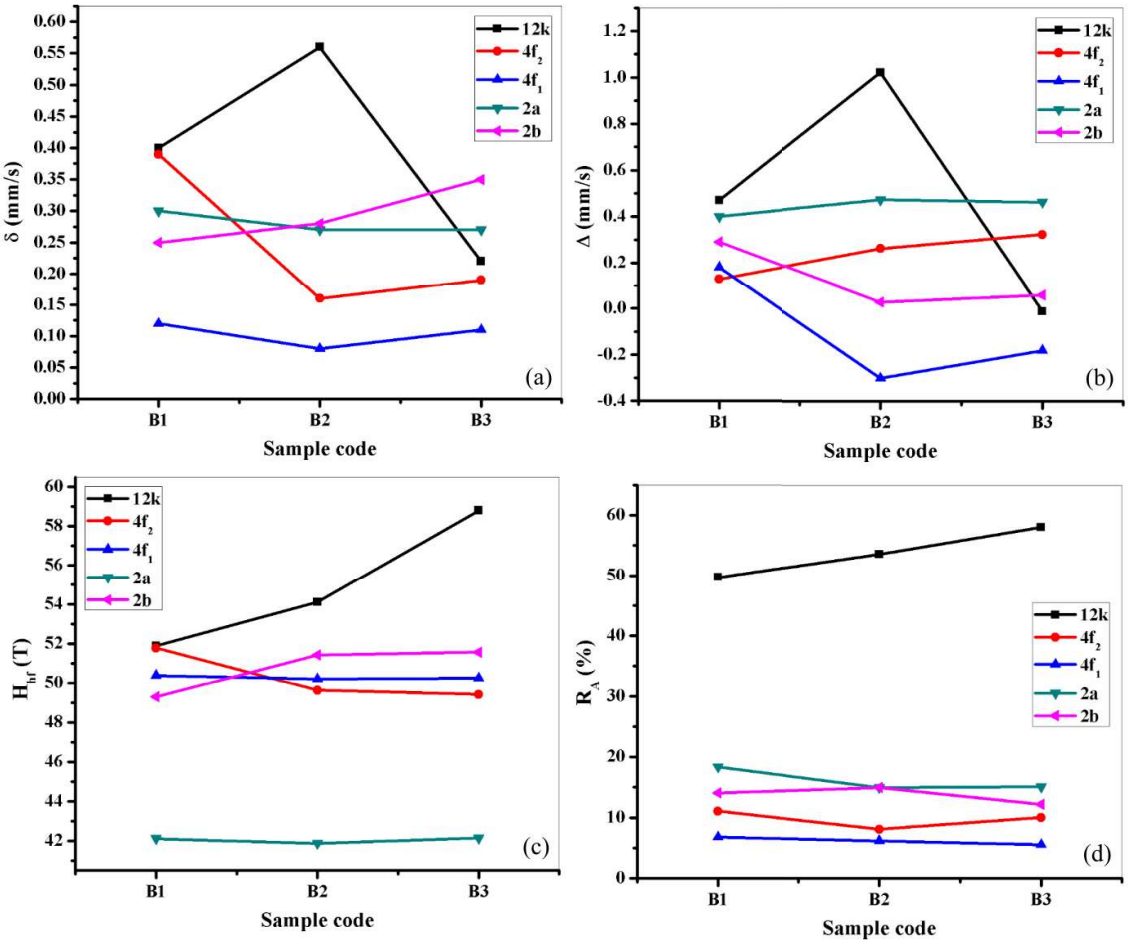

Fig. 4.79 Mössbauer parameters for $Ba_{1-x}Dy_xFe_{12-y}Cr_yO_{19}$ (x=0.0, 0.1, 0.2, and y=0.0, 0.4, 0.5) (a) isomer-shift (δ), (b) quadrupole splitting (Δ), (c) hyperfine field (H_{hf}), and (d) relative area (R_A)

of the bond angles of the super-exchange paths and a decrease in the Fe-O distance thereby influencing the exchange interaction between the five Fe^{3+} crystallographic sites and this usually result in an increase in the values of H_{hf} [258]. The 12k, $4f_2$, and 2b are the sites usually affected by this situation. Hence, Cr^{3+} ion replaces Fe^{3+} ion at octahedral 12k and $4f_2$ site, as well as bipyramidal (2b) sites. Additionally, the occupancy of the bipyramidal (2b) site could be supported by the Ligand theory which states that ions having d^1, d^2, d^3, and d^4 orbitals prefer to occupy tetrahedral site, ions possessing d^6, d^7, d^8, and d^9 orbitals show

Table 4.11 Values of line width (Γ), isomer-shift (δ), quadrupole splitting (Δ), hyperfine field (H_{hf}), and relative area (R_A) for $Ba_{1-x}Dy_xFe_{12-y}Cr_yO_{19}$ (x=0.0, 0.1, 0.2, and y=0.0, 0.4, 0.5)

Sample code	Fe^{3+} sites	Γ (mm/s)	δ (mm/s)	Δ (mm/s)	H_{hf} (T)	R_A (%)
B1	12k↑	0.41	0.40	0.47	51.89	49.71
	$4f_2$↓	0.30	0.39	0.13	51.78	11.07
	$4f_1$↓	0.40	0.12	0.18	50.39	6.8
	2a↑	0.34	0.30	0.40	42.11	18.36
	2b↑	0.34	0.25	0.29	49.30	14.08
B2	12k↑	0.46	0.56	1.02	54.11	53.56
	$4f_2$↓	0.18	0.16	0.26	49.63	8.10
	$4f_1$↓	0.35	0.08	-0.3	50.21	6.19
	2a↑	0.47	0.27	0.47	41.87	17.18
	2b↑	0.24	0.28	0.03	51.43	14.96
B3	12k↑	0.07	0.22	-0.01	58.80	58.05
	$4f_2$↓	0.28	0.19	0.32	49.42	10.05
	$4f_1$↓	0.08	0.11	-0.18	50.25	5.56
	2a↑	0.35	0.27	0.46	41.14	15.10
	2b↑	0.17	0.35	0.06	51.57	12.24

preference towards octahedral site, and ions with d^0, d^5, and d^{10} orbitals does not show any preference towards a particular site [259]. Since Cr^{3+} possesses d^5 orbital configuration, it could occupy the bipyramidal (2b) site. The area of a particular sexets is directly proportional to the quantity of Fe^{3+} ions in that site. Hence, the crystallographic sites12k, $4f_1$, $4f_2$, 2a, and 2b should respectively occupy an area in the ratio 50:17:17:8:8 in order for the Fe^{3+} ions to

be uniformly distributed [188]. However, several factors such as electronegativity and ionic radius of the substituting cations affect the attainment of this theoretical value by the cations. The observed values of R_A in 12k site are close to the theoretical values (**Fig. 4.79 (d)**). Clearly, R_A decrease with increase in Dy^{3+}-Cr^{3+} concentration, this could be ascribed to the preference of Cr^{3+} ion to occupy octahedral 2a site.

4.7 Cu^{2+}-Er^{3+} substituted M-type strontium hexaferrites

4.7.1 XRD analysis

The structural properties of $Sr_{1-x}Cu_xFe_{12-y}Er_yO_{19}$ (x=0.0, 0.1, 0.2, and y=0.0, 0.4, 0.5) were studied from XRD patterns (**Fig. 4.80**). The values of lattice constants (a and c),crystallite size (D), volume of unit cell (V_{cell}) and strain (η) were calculated and presented in **Table 4.12**. The observed well-defined peaks having hkl values (006), (110), (107), (114), (200), (203), (205), (206), (1011), (209), (217), (304), (2011), (2012), (220), (2014) and (317) are identical to the standard patterns of pure magnetoplumbite phase (JCPDS-391433) with space group $P6_3/mmc$. The absence of magnetite (α-Fe_2O_3) and other secondary phases is evident from the XRD patterns (**Fig. 4.80**). The lattice constants (a and c) were calculated using the equation

$$\frac{1}{d_{hkl}^2} = \frac{4}{3}\left(\frac{h^2+hk+l^2}{a^2}\right) + \frac{l^2}{c^2}, \tag{4.60}$$

where d_{hkl} is the value of d spacing and hkl are the miller indices, the volume of unit cell (V_{cell}) can be expressed as [198].

$$V_{cell} = 0.8666a^2c \tag{4.61}$$

The values of a and c decreases with increase in Cu^{2+}-Er^{3+} substitution. Since V_{cell} depends on a and c, similar trend is observed in the variation of V_{cell} with Cu^{2+}-Er^{3+} substitution. This could be attributed to microstructural defects and interaction between substituted cations [191][260]. Variation in a and c depends on the distance between magnetic ions resulting in change of the exchange interaction and consequently changes in the magnetic properties [208]. This shows that with the increase in Cu^{2+}-Er^{3+} substitution, the changes in easy magnetization of c-axis is greater than a-axis. It has been reported that if the c/a ratio of a hexaferrite material is not greater than 3.98, then the hexaferrite material can be thought to possess hexagonal structure [261][32][210]. Hence, we can assume that all the prepared

samples exhibit hexagonal structure since the c/a ratio is not greater than 3.98. The average particle size (D) were estimated from Scherrer formula

$$D = \frac{k\lambda}{\beta cos\theta} \tag{4.62}$$

where θ is the Braggs angle, k is the shape factor which has a value of 1 for hexagonal ferrites, λ is the X-ray wavelength having a value of 1.54056Å and β (in radian) is the full width at half maximum which can be expressed as $\beta = (\beta_o^2 - \beta_i^2)^{1/2}$, where β_o is the width from the observed X-ray peaks and β_i is the width due to instrumental effects [121]. The values of average crystallite size were calculated from XRD pattern (**Table 4.12**).

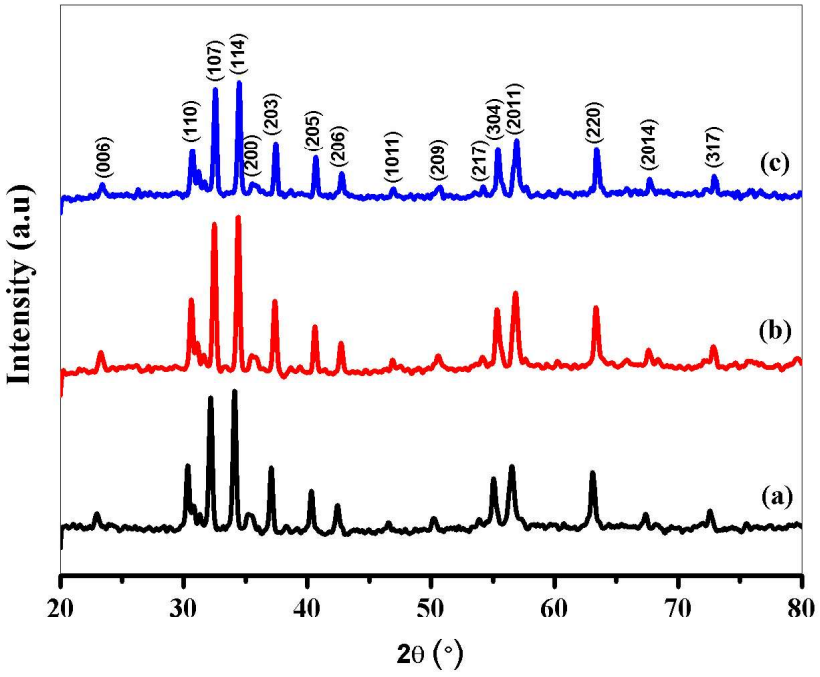

Fig. 4.80 XRD pattern of $Sr_{1-x}Cu_xFe_{12-y}Er_yO_{19}$ (x=0.0, 0.1, 0.2, and y=0.0, 0.4, 0.5) for (a) H1 (b) H2, and (c) H3

The average crystallite sizes are observed to be in the range 35.30-42.33 nm. The average crystallite size remains almost constant initially and then increases with Cu^{2+}-Er^{3+} substitution. A maximum particle size of 42.33 nm was observed in the sample H3. It has been reported that an average crystallites size below 50 nm is required to obtain appropriate

signal to noise ratio in high density recording media [262][192]. The strain (η) in the sample was evaluated from the following relation

$$\eta = \frac{\beta cos\theta - \frac{0.9\lambda}{D}}{2sin\theta} \tag{4.63}$$

The strain (η) observed in the sample occur during synthesis and calcination processes. The variation in the values of the strain (η) with Cu^{2+}-Er^{3+} substitution may be attributed to improvement towards pure hexagonal structure [260][192].

Table 4.12 Values of lattice constants (a and c),crystallite size (D), volume of unit cell (V_{cell}) and strain (η) for $Sr_{1-x}Cu_xFe_{12-y}Er_yO_{19}$ (x=0.0, 0.1, 0.2, and y=0.0, 0.4, 0.5)

Sample code	$2\boldsymbol{\theta}$ (°)	d (Å)	$\boldsymbol{\beta}$ (°)	a (Å)	c (Å)	$\boldsymbol{c/a}$	$\boldsymbol{V_{cell}}$ (Å^3)	D (nm)	$\boldsymbol{\eta \times 10^{-4}}$
H1	30.23	2.9540	0.255	5.91	23.27	3.937	703.92	35.85	8.23
H2	30.31	2.9464	0.259	5.89	23.21	3.940	698.51	35.30	8.34
H3	30.39	2.9388	0.216	5.87	23.15	3.943	693.16	42.33	6.94

4.7.2 FTIR analysis

Attached functional groups and molecular bands of $Sr_{1-x}Cu_xFe_{12-y}Er_yO_{19}$ (x=0.0, 0.1, 0.2, and y=0.0, 0.4, 0.5) have been studied using FTIR in the range 4000-400 cm^{-1}. The FTIR spectra of the synthesized samples are shown in **Fig. 4.81**. The presence of two prominent peaks at 454 and 591 cm^{-1} corresponding to asymmetric stretching and out plane vibrations of octahedral and tetrahedral sites in hexaferrites gives an indication of the formation of hexaferrites [263][264]. These absorption peaks results from metal-oxygen stretching and bending in hexaferrites [237]. The absorption peak at 454 cm^{-1} is due to Fe-O stretching by Fe-O_6 and Fe-O bending by Fe-O_4 while that at 591cm^{-1} is attributed to Fe-O stretching by Fe-O_4 [32]. The successful substitution of Fe^{3+} ions by Er^{3+} ions result in the progressive shifting of these peaks towards the low frequency side. The peak of nitrate ions which usually occur near 1300 cm^{-1} is not observed in the prepared sample [86]. H-O-H bending vibration of H_2O gives rise to the absorption peak at 1615 cm^{-1} [187]. The peak at 2348 cm^{-1} occurs as a result of the presence of CO_2 in the prepared sample [186].

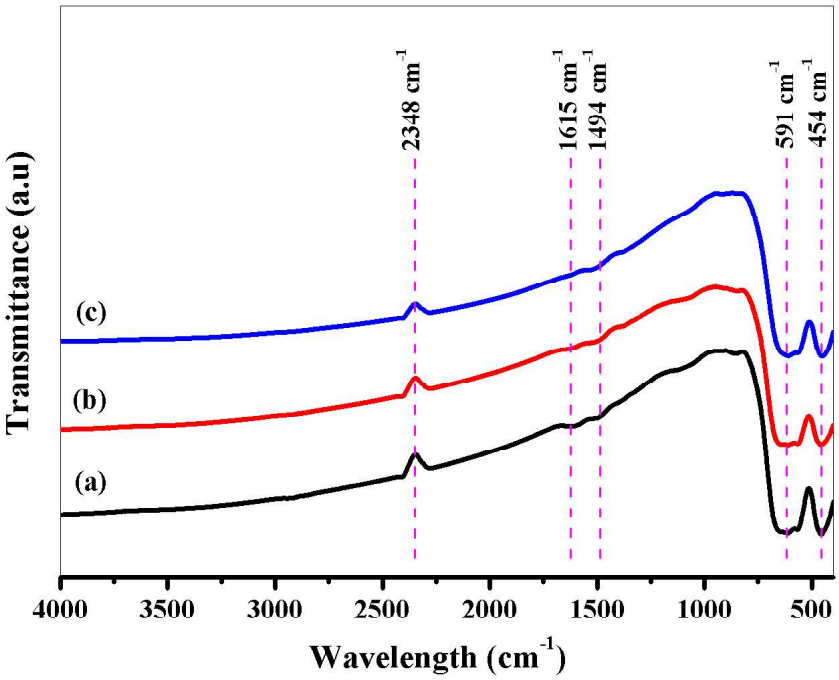

Fig. 4.81 FTIR spectra of $Sr_{1-x}Cu_xFe_{12-y}Er_yO_{19}$ (x=0.0, 0.1, 0.2, and y=0.0, 0.4, 0.5) for (a) H1 (b) H2, and (c) H3

4.7.3 Raman spectroscopy

Raman spectroscopy is a powerful non-destructive technique that gives information regarding lattice modification induced by cation substitution [265][266]. Group theory analysis of hexagonal ferrites based on the D_{6h} symmetry conclude the following symmetry relationships [267][268].

$$\Gamma=13A_{1g} + 3A_{2g} + 10B_{1g} + 5B_{2g} + 18E_{1g} + 13E_{2g} + 4A_{1u} + 14A_{2u} + 5B_{1u} + 10B_{2u} + 20E_{1u} + 13E_{2u} \quad (4.64)$$

Where 42 out of these modes are Raman active modes ($11A_{1g} + 14E_{1g} + 17E_{2g}$), 30 are IR active modes ($13A_{2u} + 17E_{1u}$), the remaining 54 modes are silent modes ($3A_{1u} + 4A_{2g} + 13B_{1g} + 4B_{1u} + 3B_{2g} + 12B_{2u} + 15E_{2u}$). The letters A, B and E represents 1D, 2D, and 3D optical modes, the subscript u and g stands for the anti-symmetry and symmetry with respect to the centre of inversion [225]. The features identical to Raman spectra of the of hexagonal ferrites determined based on the Raman tensor [$Z(XX)\bar{Z}$ and $Z(XY)\bar{Z}$] measured by observing the

polarization of the incident and scattered light fields allow both the A_{1g} and E_{2g} phonon symmetry to be observed in the $Z(XX)\bar{Z}$ configuration whereas only E_{2g} phonon symmetry are allowed to observed in the $Z(XY)\bar{Z}$ configuration [226]. In general, the M-type hexagonal structure consist of Ba^{2+} cations, octahedral FeO_6, tetrahedral FeO_4, and octahedral FeO_5 with each having a different Raman active mode [269].

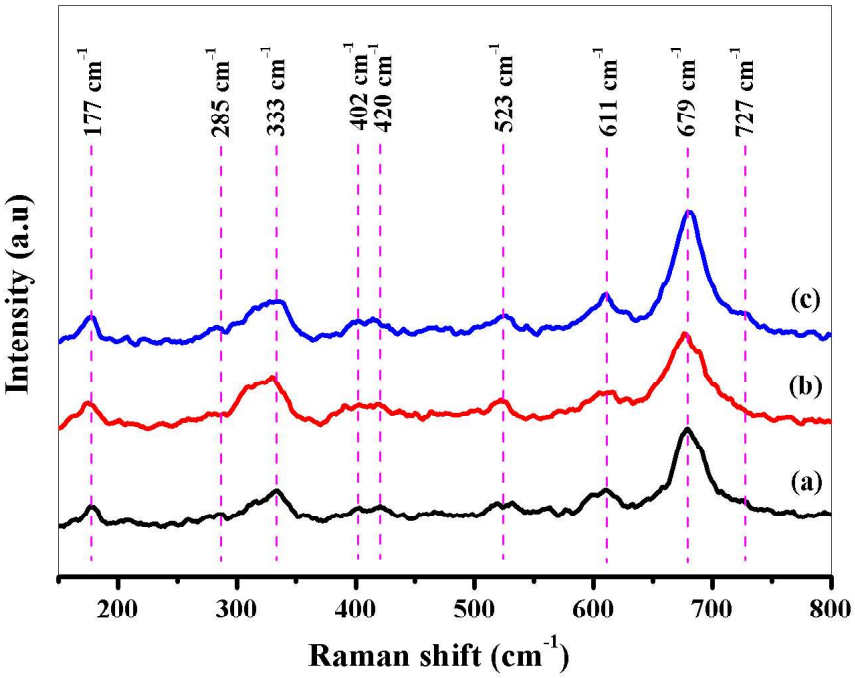

Fig. 4.82 Raman spectra of $Sr_{1-x}Cu_xFe_{12-y}Er_yO_{19}$ (x=0.0, 0.1, 0.2, and y=0.0, 0.4, 0.5) for (a) H1 (b) H2, and (c) H3

Fig. 4.82 shows the room temperature of Raman spectra of $Sr_{1-x}Cu_xFe_{12-y}Er_yO_{19}$ (x=0.0, 0.1, 0.2, and y=0.0, 0.4, 0.5) recorded using 532 nm laser source in the range 150 t0 800 cm^{-1}. Several Raman active modes with varying intensities were observed at 177, 285, 333, 402, 420, 523, 611, 679, and 727 cm^{-1} and presented in **Table 4.13**. The Raman active modes at 177, 285, 333, and 402 cm^{-1} occur due to the vibration of the whole spinel block, octahedral (2a), octahedral (12k), and octahedral (12k dominated) site as a result of E_{1g}, A_{1g}, E_{2g}, and E_{1g} symmetry respectively [218][220]. The Raman active modes at 420 and 523 cm^{-1} are respectively due to E_{2g} and E_{1g} symmetry as a result of the occupation of the octahedral (12k and 2a) site [221][191]. This kind of mixed vibration results from the replacement of Fe^{3+} ion

at octahedral 12k and 2a site, we can assume on this basis that Fe^{3+} ion is replaced by Er^{3+} ion at 12k and 2a sites. The observed Raman active modes at 611, 679, and 727 cm^{-1} are respectively due to vibration of octahedral ($4f_2$), bipyramidal (2b), and tetrahedral ($4f_1$) as a result of A_{1g} symmetry [191][230].

Table 4.13 Raman active modes of $Sr_{1-x}Cu_xFe_{12-y}Er_yO_{19}$ (x=0.0, 0.1, 0.2, and y=0.0, 0.4, 0.5)

Raman active mode (cm^{-1})	Symmetry	Mode assignment	Reference
177	E_{1g}	Whole spinel block	[218]
285	A_{1g}	Octahedral (2a)	[218]
333	E_{2g}	Octahedral (12k)	[220]
402	E_{1g}	Octahedral (12k dominated)	[220]
420	E_{2g}	Octahedral (12k and 2a) site	[221]
523	E_{1g}	Octahedral (12k and 2a) site	[191]
611	A_{1g}	Octahedral ($4f_2$)	[191]
679	A_{1g}	Bipyramidal (2b)	[230]
727	A_{1g}	Tetrahedral ($4f_1$)	[230]

4.7.4 Morphology analysis

Morphological and microstructural investigation of $Sr_{1-x}Cu_xFe_{12-y}Er_yO_{19}$ (x=0.0, 0.1, 0.2, and y=0.0, 0.4, 0.5) was carried out with FESEM and presented in **Fig. 4.83**. The synthesized samples shows surfaces with agglomerated particles, magnetic interaction between individual particles could be the reason for the observed agglomeration which leads to formation of larger particles [200]. The average particle size of the sample H1, H2 and H3 are respectively 47.05, 48.78 and 79.28 nm (**Fig. 4.84**). The average size of the particles observed from FESEM micrograph is larger than that observed in XRD, the larger particle sizes are as a result of formation of agglomerates due to magnetic interaction between neighbouring particles [240]. **Fig. 4.85** and **4.86** respectively presents the EDX spectra and elemental mapping of the samples H2 and H3. All the elements in the prepared samples were observed in EDX spectra, this also confirms the stoichiometry of the prepared samples. Elemental mapping also shows the presence and homogenous distribution of the all the elements in the prepared samples. This further supports the results of the EDX spectra.

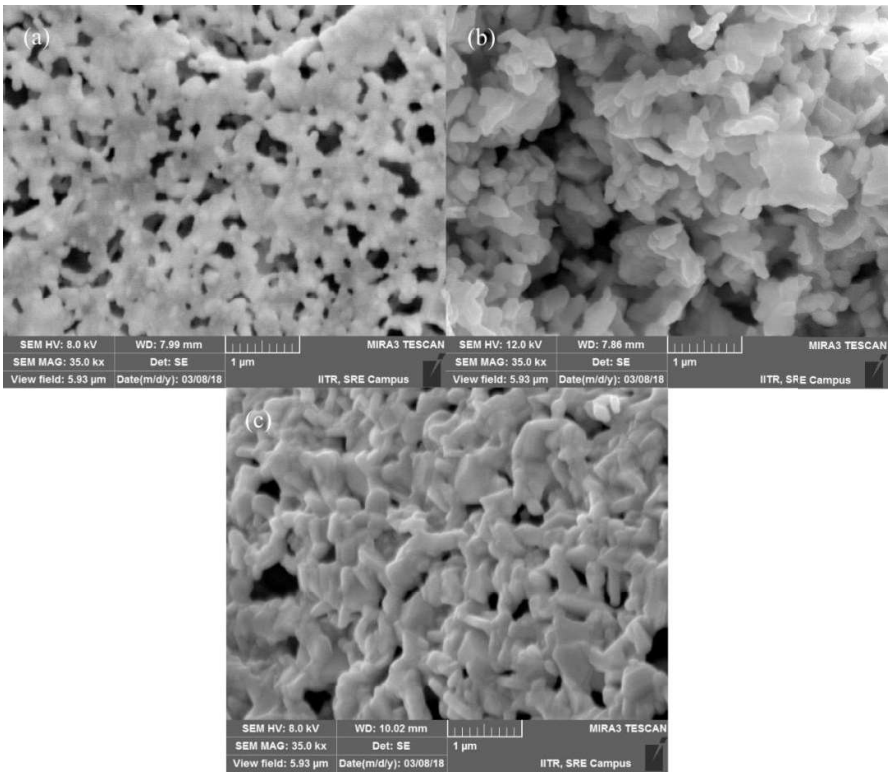

Fig. 4.83 FESEM micrograph of $Sr_{1-x}Cu_xFe_{12-y}Er_yO_{19}$ (x=0.0, 0.1, 0.2, and y=0.0, 0.4, 0.5) for (a) H1 (b) H2 and (c) H3

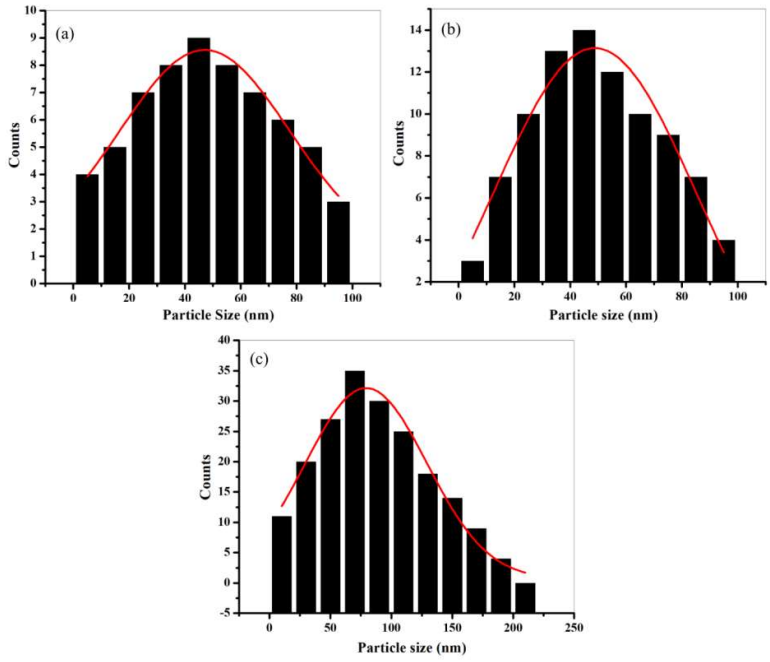

Fig. 4.84 Particle distribution of $Sr_{1-x}Cu_xFe_{12-y}Er_yO_{19}$ (x=0.0, 0.1, 0.2, and y=0.0, 0.4, 0.5) for (a) H1 (b) H2 and (c) H3

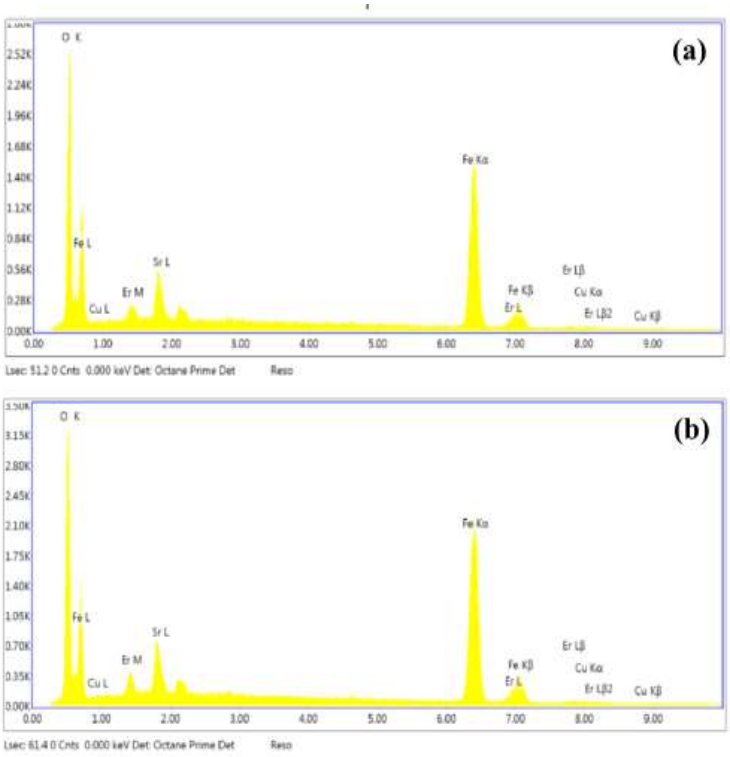

Fig. 4.85 EDX spectra of $Sr_{1-x}Cu_xFe_{12-y}Er_yO_{19}$ (x=0.0, 0.1, 0.2, and y=0.0, 0.4, 0.5) for (b) H2 and (c) H3

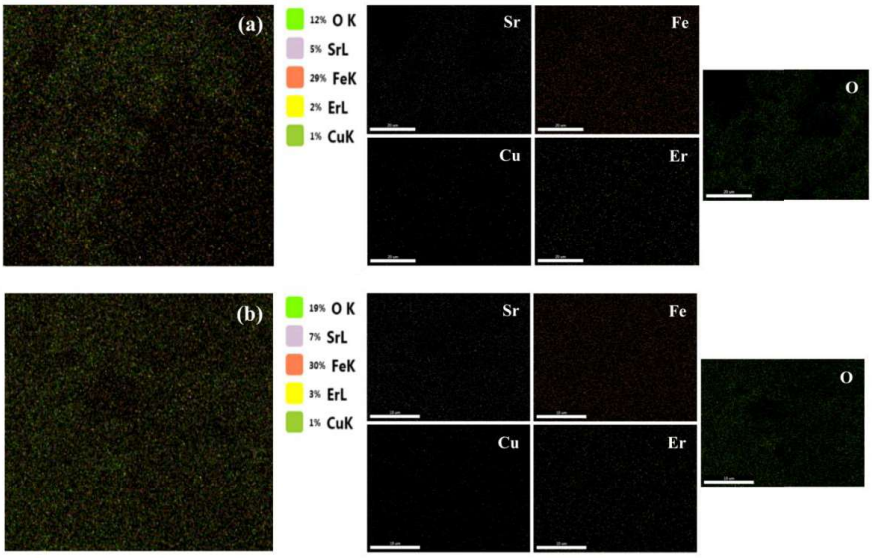

Fig. 4.86 Elemental mapping of $Sr_{1-x}Cu_xFe_{12-y}Er_yO_{19}$ (x=0.0, 0.1, 0.2, and y=0.0, 0.4, 0.5) for (b) H2 and (c) H3

4.7.5 Optical analysis

The optical analysis of $Sr_{1-x}Cu_xFe_{12-y}Er_yO_{19}$ (x=0.0, 0.1, 0.2, and y=0.0, 0.4, 0.5) was carried out via UV-visible-NIR spectroscopy in the wavelength range 234-766 nm. Usually, electrons are excited from valence to conduction band when they absorb the energy of incident photons. The spectra of absorbance versus wavelength are presented in **Fig. 4.87**.

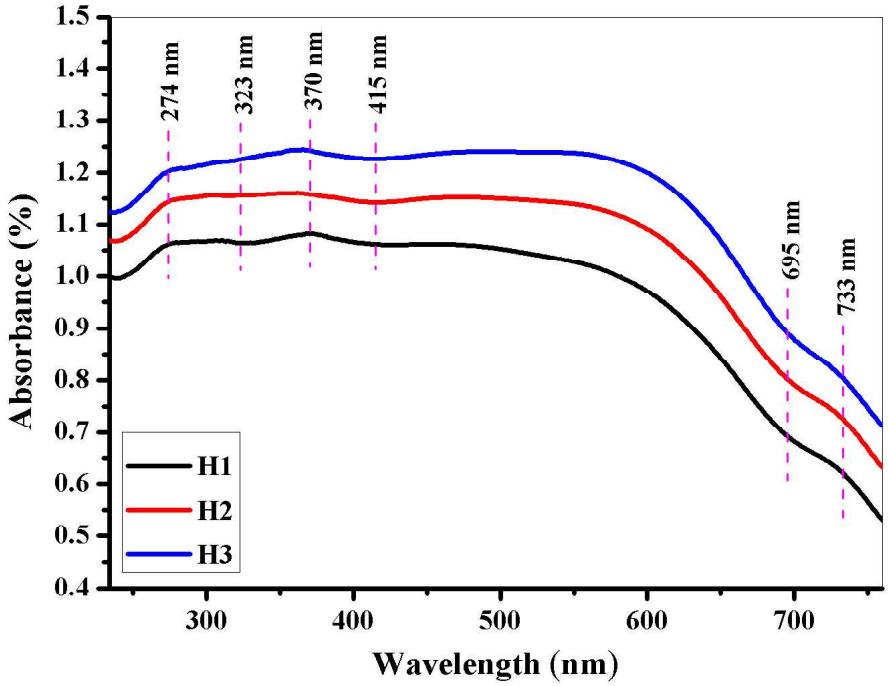

Fig. 4.87 Variation of absorbance versus wavelength of $Sr_{1-x}Cu_xFe_{12-y}Er_yO_{19}$ (x=0.0, 0.1, 0.2, and y=0.0, 0.4, 0.5)

Clearly, absorption peaks at 274 and 370 nm can be observed from the spectra whereas the peaks observed at 323 and 415 nm are reflection peaks. At higher wavelengths, a reflection peak (695 nm) and absorption peak (733 nm) are also observed. The observed absorption peaks (274, 370 and 733 nm) corresponds to hyperchromic shift whereas the reflection peaks (323, 415 and 695 nm) corresponds to hypochromic shift. There is no observation of hypsochromic (blue) shift and bathochromic (red) shift in the spectra. The optical band gap (E_g) was evaluated using the relation

$$\alpha h\upsilon = A\left(h\upsilon - E_g\right)^n \tag{4.65}$$

where α is the coefficient of absorption, h is the planks constant ($6.6260 \times 10^{-34} J.s$), υ is the frequency of incident photon and A is a characteristics constant that depends on n. For allowed direct, forbidden direct, allowed indirect and forbidden indirect transitions, n have the following values 1/2, 3/2, 2 and 3 respectively. The plots of E_g of the prepared samples are shown in **Fig. 4.88 (a), (b)** and **(c)**. Extrapolation of the linear part of the plot of $(\alpha h\upsilon)^2$ against E_g gives the values of E_g for all the synthesized samples. The observed values of E_g for the sample H1, H2 and H3 are respectively 2.62, 268 and 2.75 eV. The observed E_g shows an increasing behaviour as the concentration of Cu^{2+}-Er^{3+} is increased (**Fig. 4.88 (d)**), this could be attributed to quantum confinement effects [199][86][186]. It has been observed that E_g may also be affected by the size of the crystallites, smaller crystallites results in more discrete energy levels and consequently increased E_g [191].

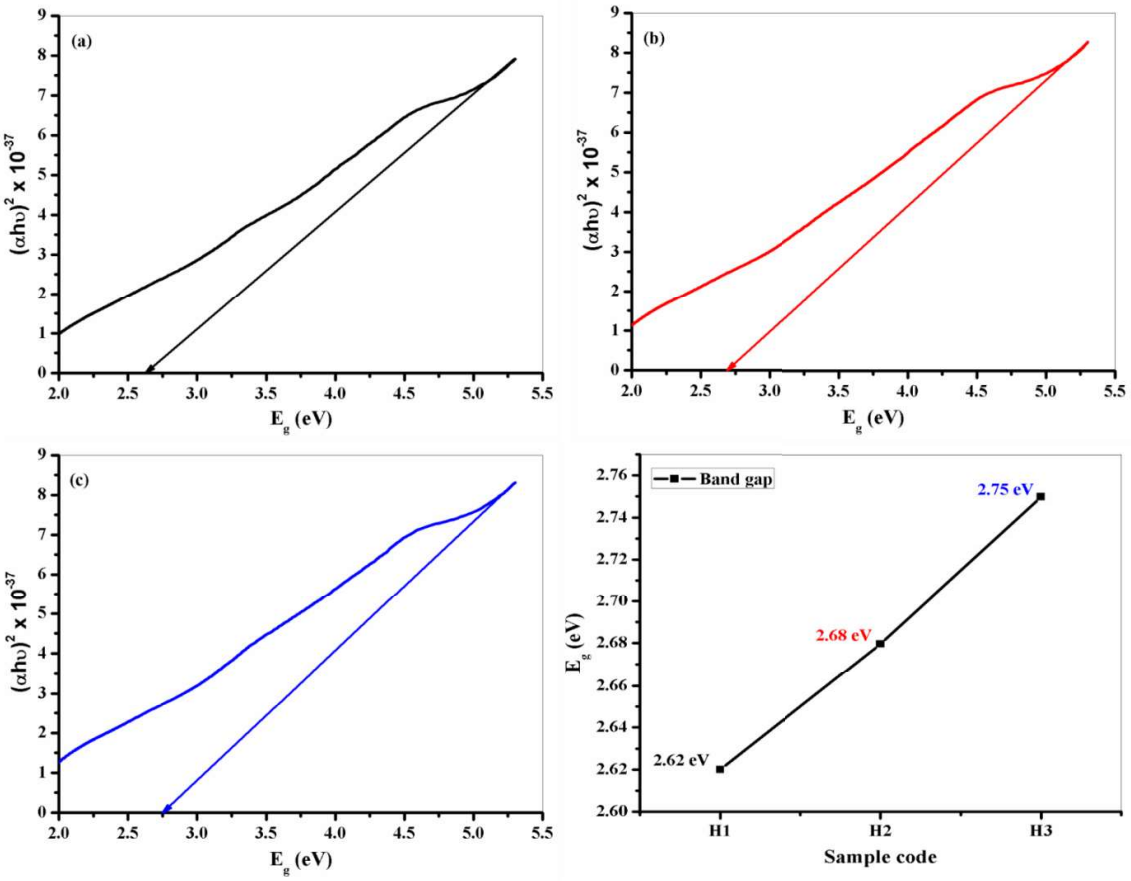

Fig. 4.88 Optical band gap of $Sr_{1-x}Cu_xFe_{12-y}Er_yO_{19}$ (x=0.0, 0.1, 0.2, and y=0.0, 0.4, 0.5) for (a) H1 (b) H2, (c) H3, and (d) Variation of band gap with Cu^{2+}-Er^{3+} substitution

4.7.6 Dielectric and impedance spectroscopy

Impedance spectroscopy and dielectric studies of nanomaterials may provide valuable information regarding the nanoscale conduction processes occurring in the nanomaterial. The complex impedance (Z^*) is a function of real part of impedance (Z') and imaginary part of impedance (Z'') which are represented in the equations below

$$Z^* = Z' - jZ'' \tag{4.66}$$

$$Z' = |Z|cos\theta \tag{4.67}$$

$$Z' = |Z|sin\theta \tag{4.68}$$

where $j = \sqrt{-1}$ is an imaginary number, Z is the modulus of impedance and θ is the phase angles [92]. The complex permittivity (ε^*), real part of permittivity (ε'), and imaginary part of permittivity (ε'') can be represented using the equations below

$$\varepsilon^* = \varepsilon' - j\varepsilon'' \tag{4.69}$$

$$\varepsilon' = \frac{Z''}{2\pi\omega C_0 Z^2} \tag{4.70}$$

$$\varepsilon'' = \frac{Z'}{2\pi\omega C_0 Z^2} \tag{4.71}$$

where $\omega = 2\pi f$ is the frequency and C_0 is the geometrical capacitance [164]. The dielectric loss tangent ($tan\delta$) is a ratio of real and imaginary part of permittivity and it gives the extent of energy dissipation in the nanomaterial whereas the AC conductivity (σ_{ac}) which describes the conducting properties of the nanomaterials is also expressed as a function of real part of permittivity and dielectric loss tangent [270].

$$tan\delta = \frac{\varepsilon''}{\varepsilon'} \tag{4.72}$$

$$\sigma_{ac} = \omega\varepsilon_0\varepsilon' tan\delta \tag{4.73}$$

The room temperature real part of permittivity (dielectric constant) and dielectric loss as a function of frequency for $Sr_{1-x}Cu_xFe_{12-y}Er_yO_{19}$ (x=0.0, 0.1, 0.2, and y=0.0, 0.4, 0.5) are respectively shown in **Fig. 4.89** and **4.90**. The dielectric constant decreases from lower to intermediate frequencies and then suddenly increases at higher frequencies. Koop's phenomenological and Maxwell-Wagner model was used to analyse the dielectric properties

of the prepared samples [271][272]. According to these models, ferrites materials consist of layers of conducting grains which are surrounded by layers of poorly conducting grains. Ferrites materials consist of Fe^{2+} (ferrous) and Fe^{3+} (ferric) ions at octahedral sites. Electrons are continuously exchanged between the ferrous and ferric ions thereby giving rise to local

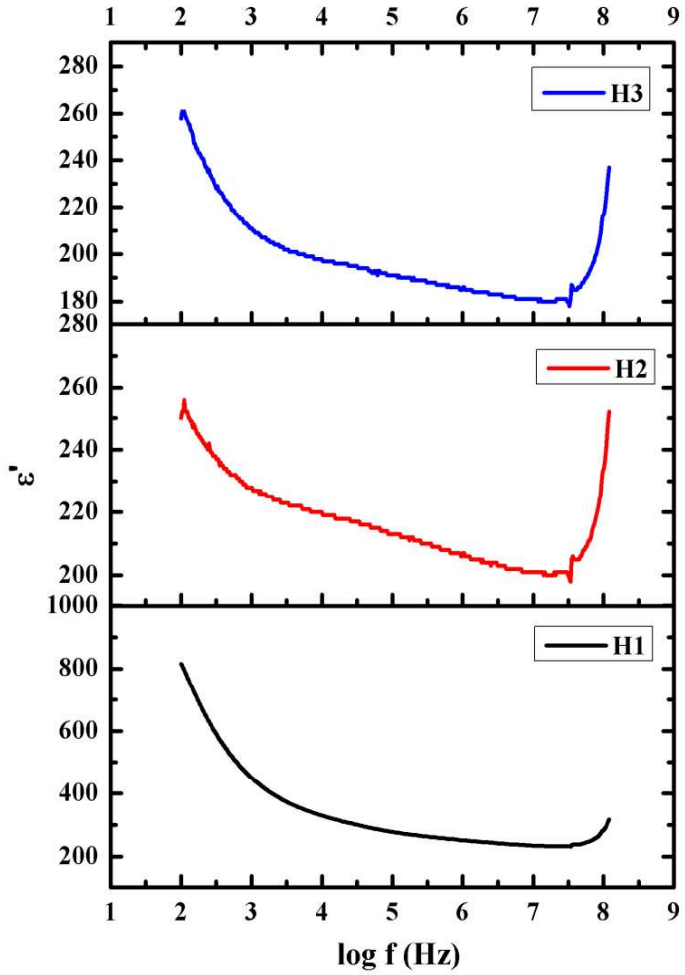

Fig. 4.89 Variation of dielectric constant with frequency of $Sr_{1-x}Cu_xFe_{12-y}Er_yO_{19}$ (x=0.0, 0.1, 0.2, and y=0.0, 0.4, 0.5) for (a) H1 (b) H2, and (c) H3

displacement of charge carriers in the direction of the field which results in appearance of polarization and consequently the dielectric constant [199][236]. The high values of dielectric constant observed at lower frequencies are attributes to of the presence of ionic, electric, interfacial as well as dipolar polarization [273]. The appearance of polarization in ferrites can be explain as thus, high temperature calcination causes ferrites to loose traces of oxygen; this

result in the formation of defects such as oxygen and electron vacancies during cooling via re-oxidation. This re-oxidation process offers the scenario for the variation of grain boundary resistance and grains resistance thereby forming a barrier layer at the interface of the grains and grain boundaries. The grain and grain boundary interface is a conducive environment for charges to build up, and when they do, high polarization appears[242]. Electron hopping between Fe^{3+} and Fe^{2+} ions at octahedral sites occurs in the direction of the applied electric

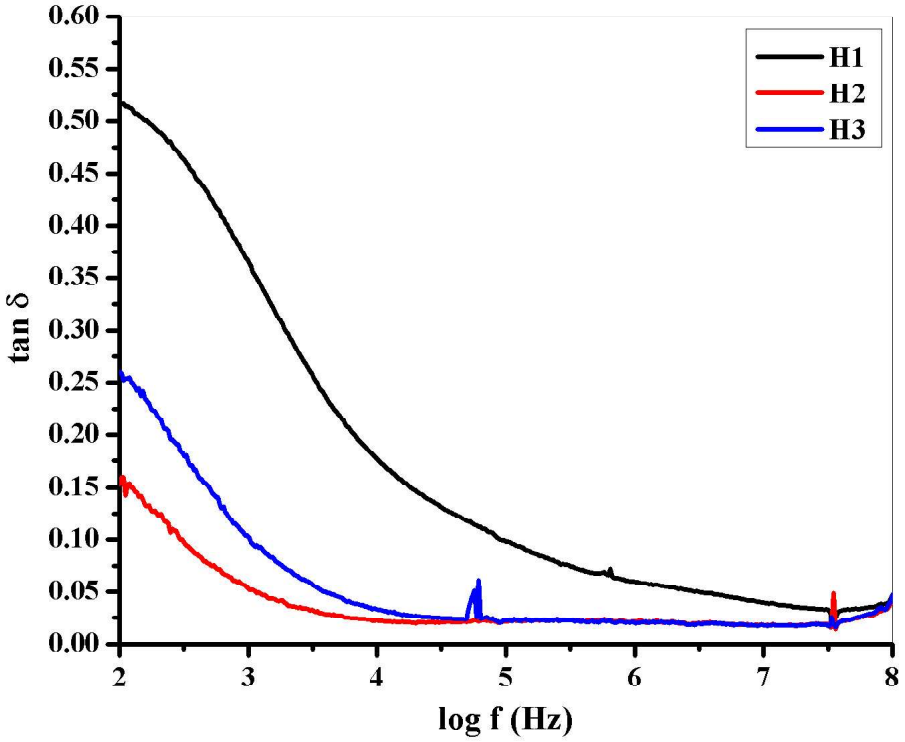

Fig. 4.90 Variation of dielectric loss with frequency of $Sr_{1-x}Cu_xFe_{12-y}Er_yO_{19}$ (x=0.0, 0.1, 0.2, and y=0.0, 0.4, 0.5) for (a) H1 (b) H2, (c) H3

field, if the frequency of electron hopping is less than or lag behind the frequency of the applied electric field, then the dielectric constant decreases [274]. The sudden enhancement of the dielectric constant at higher frequencies could reduce the penetration depth of electromagnetic waves by increasing the skin effect; this shows that the synthesized samples could be useful for high frequency application [237][202]. Materials with dielectric properties usually experience energy losses or dielectric loss as a result of the work done in order to overcome the frictional damping forces that influence the dipoles during their rotation. In

accordance with Koop's model, the dielectric loss is observed when the polarization lags behind the applied electric field [272]. Grain boundary effects are dominant at lower frequencies with high resistivity whereas the effects of grains with low resistivity dominate the higher frequency region [241]. High dielectric loss is observed at lower frequencies as a result of high resistivity of grain boundaries which require high energy for hopping of electrons to occur between Fe^{3+} and Fe^{2+} ions at octahedral sites. At higher frequencies, less energy is required for electron hopping to occur between Fe^{3+} and Fe^{2+} ions at octahedral sites as a result of low resistivity of grains and subsequently low dielectric loss is observed [273][275].

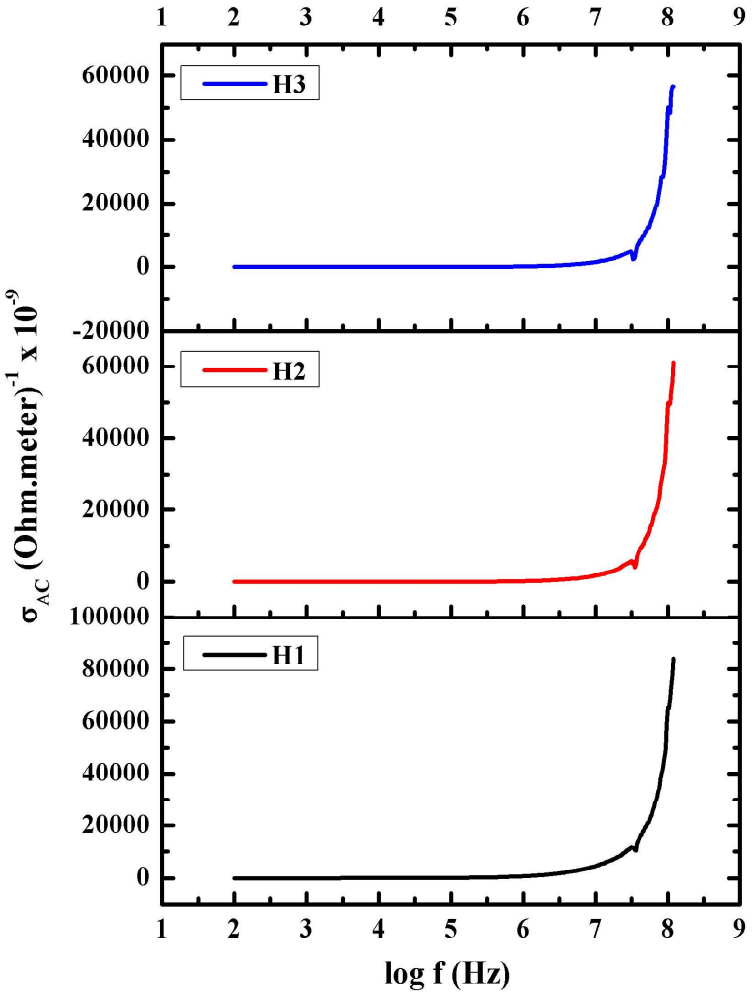

Fig. 4.91 AC conductivity of $Sr_{1-x}Cu_xFe_{12-y}Er_yO_{19}$ (x=0.0, 0.1, 0.2, and y=0.0, 0.4, 0.5) for (a) H1 (b) H2, (c) H3

The room temperature AC conductivity as a function of frequency for $Sr_{1-x}Cu_xFe_{12-y}Er_yO_{19}$ (x=0.0, 0.1, 0.2, and y=0.0, 0.4, 0.5) is presented in **Fig. 4.91**. The AC conductivity of the prepared samples exhibits frequency independent behaviour at lower and intermediate frequencies. At higher frequencies, there is an abrupt and sudden increase in AC conductivity; also, this behaviour could also be explained on the basis of Koop's and Maxwell-Wagner model. In a similar manner, the fact that the grain boundaries dominate the lower frequencies with high resistivity result in restricted hopping of electrons; this scenario cause a significant decrease in conductivity at lower frequencies. Electrons experience less resistance because the grains effects dominates the higher frequencies, this prompt massive hopping of electrons between Fe^{3+} and Fe^{2+} ions at octahedral sites and consequently increase in conductivity with increase in frequency [234][189]. The obtained result of conductivity in our work is in agreement with that obtained by H. Malik *et al.* [276].

4.7.7 Magnetic study

The room temperature magnetization loop for $Sr_{1-x}Cu_xFe_{12-y}Er_yO_{19}$ (x=0.0, 0.1, 0.2, and y=0.0, 0.4, 0.5) have been recorded and presented in **Fig. 4.92**. Magnetic parameters such as coercivity (H_c), remnant magnetization (M_r), and saturation magnetization (M_s) were determined from the magnetization loop and tabulated in **Table 4.14**, squareness ratio (*SR*), anisotropy constant (K) and magnetic moment (μ_B) were calculated from the equations below

$$K = \frac{\mu_0 M_s H_c}{2} \tag{4.74}$$

$$\mu_B = \frac{\text{Molecular weright} \times M_s}{5585} \tag{4.75}$$

$$SR = \frac{M_r}{M_s} \tag{4.76}$$

Where $\mu_0 = 4\pi \times 10^7\ H/m$ is the permeability in vacuum The magnetic properties of hexaferrites is dependent upon how the 12 Fe^{3+} ions in the hexagonal structure are distributed in the five crystallographic sites of the hexagonal structure which include 12k, 2b, 2a, $4f_1$ and $4f_2$. The Fe^{3+} ions with spin up electrons are found at 12k octahedral site with 6 Fe^{3+} ions, 2b trigonal bipyramidal site with 1 Fe^{3+} ion, and 2a octahedral site with 1 Fe^{3+} ion whereas those with spin down electrons are found at $4f_1$ tetrahedral site with 2 Fe^{3+} ions and $4f_2$ octahedral site with 2 Fe^{3+} ions [264]. Hence, there are a total of 8 Fe^{3+} ions with spin up electrons and 4 Fe^{3+} ions with spin down electrons; when 4 Fe^{3+} ions with spin up electrons cancel out 4 Fe^{3+}

ions with spin down electrons, and then there will be a residue of 4 Fe^{3+} ions with spin up electrons which contribute to the total magnetic moment. Since each Fe^{3+} ions has a magnetic moment of 5 μ_B, then the net magnetic moment per unit formula is a total of 20 μ_B [262][234]. Generally, substitution of magnetic cation with magnetic moment less than that of Fe^{3+} or non-magnetic cation at $4f_1$ and $4f_2$ crystallographic sites leads to increase in magnetization whereas substitution at 12k, 2b, and 2a results in decreased magnetization.

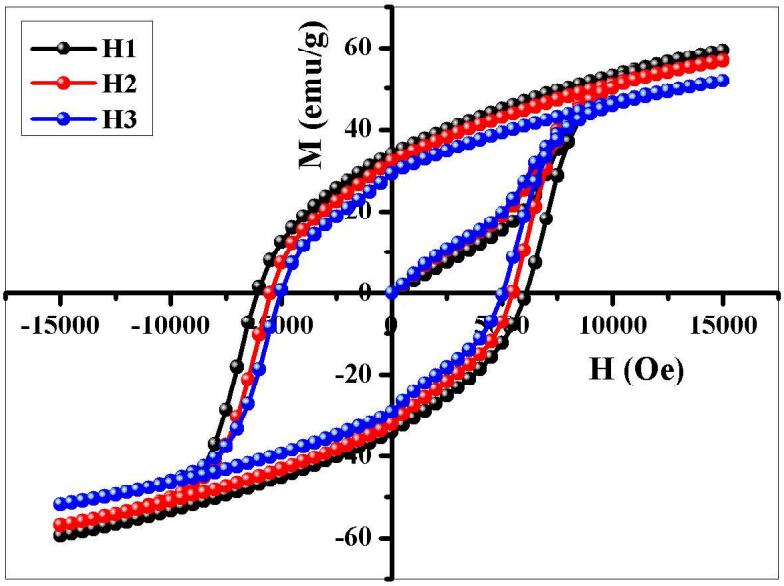

Fig. 4.92 M-H hysteresis loop of $Sr_{1-x}Cu_xFe_{12-y}Er_yO_{19}$ (x=0.0, 0.1, 0.2, and y=0.0, 0.4, 0.5) for (a) H1 (b) H2, (c) H3

However, the probability of a cation to enter a particular site is dependent upon factors such as electronegativity and ionic radius of the substituting and host cation [264]. From **Table 4.14**, it can be seen that H_c, M_r, M_s, SR, K and μ_B decrease with increase in Cu^{2+}-Er^{3+} substitution. This decreasing behaviour of the magnetic parameters can be explained on the basis of the nature of the substituted cations. The observed coercivity in the samples H1, H2, and H3 are respectively 6031.74, 5423.18 and 4962.09. In general, substitution of rare earth ions has been observed to weaken the super exchange interaction thereby leading to reduction in magnetic moment. Also, the difference between the ionic radii of Fe^{3+} ($r_{Fe^{3+}}$= 0.645 Å) and Er^{3+} ($r_{Er^{3+}}$= 0.881 Å) induces local strain which leads to modification and disorder in the

Table 4.14 Values of coercivity (H_c), remnant magnetization (M_r), saturation magnetization (M_s), squareness ratio (SR), anisotropy constant (K) and magnetic moment (μ_B) for $Sr_{1-x}Cu_xFe_{12-y}Er_yO_{19}$ (x=0.0, 0.1, 0.2, and y=0.0, 0.4, 0.5)

Sample code	$\boldsymbol{H_c}$ (Oe)	$\boldsymbol{M_r}$ (emu/g)	$\boldsymbol{M_s}$ (emu/g)	SR ($\boldsymbol{M_r/M_s}$)	$\boldsymbol{K}$ (HA^2/kg)	$\boldsymbol{\mu_B}$
H1	6031.74	34.07	59.41	0.573	17.91	11.29
H2	5423.18	32.25	56.92	0.566	15.43	11.25
H3	4962.09	29.27	51.84	0.564	12.86	10.33

electronic states [247]. Furthermore, Er^{3+} substitution will result in the formation of spin canting effect where the orientation of spins in magnetic ions is aligned by making angles from the preferred direction (this is usually caused by rare earth cations), magnetic dilution and the magnetic collinearity will be broken leading to decrease magnetization, similar scenario was observed by M. J. Iqbal et al. when they synthesized Ce^{3+}-Ni^{2+} substituted strontium hexaferrites [274] Also, it has been reported that hexaferrites with H_c=$M_r/2$ are vital for high frequency application [277]. Hence, we concluded that the synthesized samples may be useful in high density perpendicular magnetic recording media and high frequency application since we respectively observed that H_c=1200 Oe and H_c=$M_r/2$ in the current research. In general, substitution of rare earth ions has been observed to weaken the super exchange interaction thereby leading to reduction in magnetic moment. Also, the difference between the ionic radii of Fe^{3+} ($r_{Fe^{3+}}$= 0.645 Å) and Er^{3+} ($r_{Er^{3+}}$= 0.881 Å) induces local strain which lead modification and disorder in the electronic states [278]. Furthermore, Er^{3+} substitution will result in the formation of spin canting effect where the orientation of spins in magnetic ions is aligned by making angles from the preferred direction (this is usually caused by rare earth cations), magnetic dilution and the magnetic collinearity will be broken leading to decrease magnetization, similar scenario was observed by M. J. Iqbal et al. when they synthesized Ce^{3+}-Ni^{2+} substituted strontium hexaferrites [274]. M. N. Ashiq et al. reported that hexaferrites with SR value greater than or equal to 0.5 exhibit single magnetic domain structure whereas those with SR value less than 0.5 can be thought to exhibit non-interacting multi-domain structure with uniaxial anisotropy. Since the samples synthesized in this work have SR value (0.573, 0.566, and 0.564 for the samples with H1, H2, and H3 respectively) greater than 0.5, then we conclude that the synthesized samples exhibit single domain

structure. Materials with single domain structure are useful as permanent magnets and magnetic recording media [200][262].

4.7.8 Mossbauer spectroscopy

^{57}Fe Mössbauer spectroscopy was carried out in order to determine the Fe^{3+} deficient crystallographic sites, site preference of the cations, magnetic ordering, Fe^{3+} ion symmetry, valence levels, and the relationships between the distributions of cations at different crystallographic sites. Mössbauer spectra of $Sr_{1-x}Cu_xFe_{12-y}Er_yO_{19}$ (x=0.0, 0.1, 0.2, and y=0.0, 0.4, 0.5) is presented in **Fig. 4.93**. The fitted hyperfine parameters such as line width (Γ), isomer-shift (δ), quadrupole splitting (Δ), hyperfine field (H_{hf}), and relative area (R_A) are shown in **Table 4.15**. The recorded Mössbauer spectra were fitted according to five distinct sexets which corresponds to bi-pyramidal (2b), tetrahedral ($4f_1$), and octahedral (12k, $4f_2$, and 2a) crystallographic sites, these sexets are related to the presence of Fe^{3+} ions in the various crystallographic sites of the M-type hexagonal structure [279][280]. In general, these crystallographic sites have different spin orientation, it has been reported that 12k, 2a, and 2b sub-lattices have spin-up orientation whereas $4f_1$ and $4f_2$ sub-lattices have spin-down orientation [281][282][283]. Furthermore, a structure with ferrimagnetic nature consisting of different spin orientation is suggested by Gorter model [259]. These spin orientations are such that $4f_1$ and $4f_2$ sub-lattices exhibit four parallel spin orientation while 12k, 2a, and 2b exhibit anti-parallel orientation of spin and are associated through the oxygen ions (O^{2-}) by the super exchange interaction [32]. According to the ligand theory, ions possessing d^1, d^2, d^3, and d^4 orbitals tend to prefer tetrahedral site, ions having d^6, d^7, d^8, and d^9 orbitals exhibit preference towards octahedral site, and ions with d^0, d^5, and d^{10} orbitals does not show any preference towards a particular site [269][33][284]. The values of M_s , M_r and H_c decreases with increase in the concentration of Cu^{2+}-Er^{3+} as reported in our previous research [136]. The decrease in the values of M_s and M_r can be affected by the fact that Er^{3+} is a rare earth ion since the Fe^{3+}-O-Fe^{3+} super-exchange interaction is weaken by the substitution of rare earth ions [285]. The super-exchange interaction becomes Fe^{3+}-O-Er^{3+} when Er^{3+} replaces Fe^{3+} in the hexagonal structure, this interaction usually occur via the indirect 4f-5d-4f coupling which is weak and consequently results in the decrease in the values of M_s [286]. This scenario shows that the prepared samples tend to transition from ferromagnetic towards paramagnetic behaviour. Similar observation was made by A. Ghasemi et al. in the investigation of magnetic properties and site preference of $SrFe_{12-x}(Sn_{0.5}Zn_{0.5})_xO_{19}$ thin films

[287]. As stated in the magnetic analysis, the probability of a particular cation to occupy a particular site relies on the ionic radius and electronegativity of the substituting and host ions.

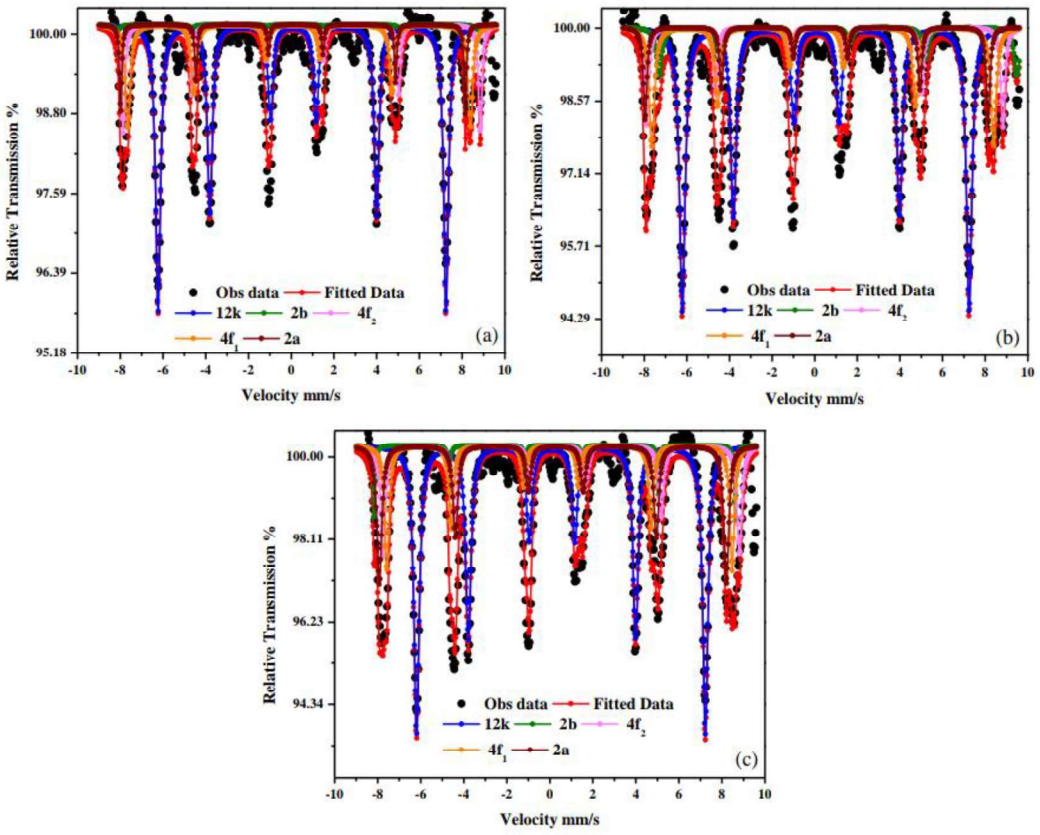

Fig. 4.93 Mossbauer spectra of $Sr_{1-x}Cu_xFe_{12-y}Er_yO_{19}$ (x=0.0, 0.1, 0.2, and y=0.0, 0.4, 0.5) for (a) H1 (b) H2, (c) H3

The electronegativity of Er^{3+} and Fe^{3+} ion are respectively 1.24, and 1.83 (Pauling scale) whereas their ionic radius are respectively 0.881, and 0.645. Å. I. Auwal et al. reported that less electronegative cations shows preference towards $4f_1$ tetrahedral site [284]. Hence, we can assume that on the basis of electronegativity, Er^{3+} ions with the lesser electronegativity as compared with Fe^{3+} would occupy the $4f_1$ tetrahedral site.

The line width (Γ), isomer-shift (δ), quadrupole splitting (Δ), hyperfine field (H_{hf}), and relative area (R_A) of $Sr_{1-x}Cu_xFe_{12-y}Er_yO_{19}$ (x=0.0, 0.1, 0.2, and y=0.0, 0.4, 0.5) are presented in **Fig. 4.94 (a), (b), (c), and (d)** respectively. The values of Γ for 12k site decrease with increase in the concentration of Cu^{2+}-Er^{3+} whereas it increases for the $4f_1$ and 2b site (**Table 2**). Variation in chemical environment, nuclear radius, and the interaction between nuclear

charge density and the surrounding *s* electron cloud is the reason behind the appearance of δ. In general, δ depends on *s* electron density or *p* and *d* electron density, spin states of Fe^{3+}, nature of ligands, and electronegativity of ligands. The values of δ at 12k site decreases with increase in the concentration of Cu^{2+}-Er^{3+} whereas the $4f_2$ and $4f_1$ sites shows an increasing trend with increase in Cu^{2+}-Er^{3+} concentration (**Fig. 4.94 (a)**), this indicates that the density of the *s* electron cloud at the 12k, $4f_2$, and $4f_1$ is affected by Cu^{2+}-Er^{3+} substitution [286]. Decrease in the values of δ is observed as a result of increase in the density of the *s* electron cloud while an increase in δ means that more shielding of the *s* electron cloud by the *d* electrons is taking place. It has been reported that the values of δ ranges from 0.05 to 0.50 mm/s and 0.9 to 1.5 mm/s for Fe ion in the +3 oxidation state and Fe ion in the +2 oxidation state respectively [288][289]. Since the values of δ in this research ranges from 0.15 to 0.45 mm/s, we can assume that all the five sexets originate from Fe^{3+} ion with high spin. Understanding of Δ could provide insight into the variation of local distortion and crystal symmetry of the prepared samples. It is known that Δ appear because of the interaction between the electric field gradient and the electric quadrupole moment of the Fe^{3+} ion. The 12k site shows decreasing behaviour of Δ with increase in the substitution of Cu^{2+}-Er^{3+} cations while it increases for the $4f_2$ and 2b sites (**Fig. 4.94 (b)**). The $4f_1$ and 2a sites shows and initial increase in the values of Δ for the sample H2 and then decreases for the sample H3. The 2a sites shows the highest values of Δ as a result of asymmetric charge distribution character at this site [280]. Additionally, high values of Δ are observed when high electric field gradient are present at the crystallographic site [290]. The H_{hf} arises due to the interaction between the nucleus with the internal magnetic field which comes from the ferromagnetic, antiferromagnetic, or ferrimagnetic properties (i. e. dipole properties of the nucleus) of the prepared sample. The values of H_{hf} remain almost constant for the crystallographic sites except the 2b sites, a decrease with increase in the concentration of Cu^{2+}-Er^{3+} was observed for this crystallographic site and the values was found to be 41.88, 41.83 and 41.72 for H1, H2, and H3 respectively (**Fig. 4.94 (c)**). This could be ascribed to the decrease in the super-transferred field that originate from the magnetic ions surrounding a particular Fe^{3+} ion [291]. The site occupancy of the substituted cations can be evaluated from the curve of R_A from the spectra of Mössbauer. The Plot of R_A against sample composition is presented in **Fig. 4.94 (d)**. The obtained results shows that the values of R_A varies from 55.67-44.37% for 12k site, 20.43-16.20 for $4f_2$ site, 19.74-8.36 for $4f_1$, 9.03-8.37% for 2a site, and 14.30-12.33% for 2b site. For the Fe^{3+} ions to be uniformly distributed in the various

crystallographic sites of the M-type hexagonal structure, the crystallographic sites should occupy an area in the ratio 50:17:17:8:8 respectively for 12k, $4f_2$, $4f_1$, 2a, and 2b crystallographic sites [254]. Clearly, most of the obtained values of R_A are close to the theoretical values. In all the samples, the 2b site is highly populated whereas the 2a site is less

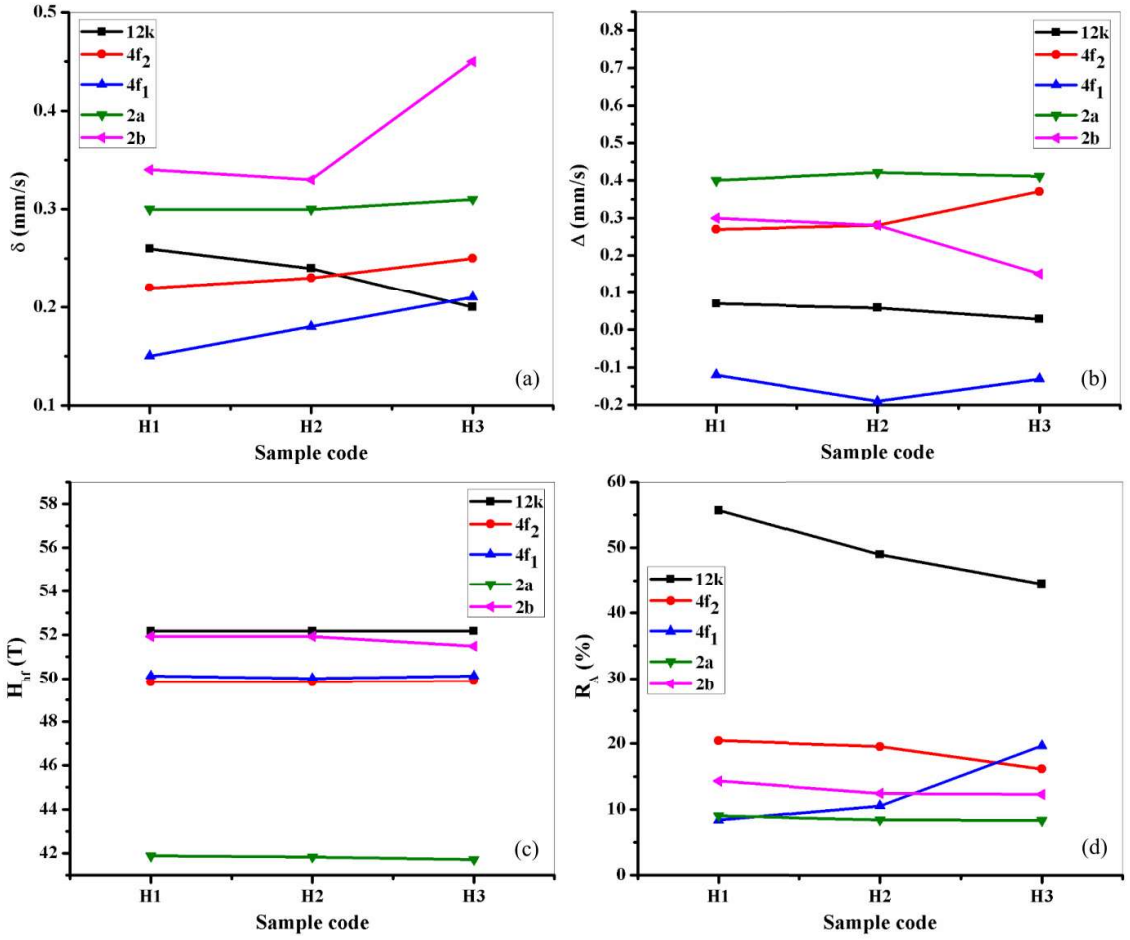

Fig. 4.94 Mössbauer parameters of $Sr_{1-x}Cu_xFe_{12-y}Er_yO_{19}$ (x=0.0, 0.1, 0.2, and y=0.0, 0.4, 0.5) (a) isomer-shift (δ), (b) quadrupole splitting (Δ), (c) hyperfine field (H_{hf}), and (d) relative area (R_A)

populated. With increase in the concentration of Cu^{2+}-Er^{3+}, the values of R_A increase in all the sites (12k, $4f_2$, 2a, and 2b) except in $4f_1$ site where a decrease is observed. Hence, we can conclude that Er^{3+} (with d^{10} orbitals) replaces Fe^{3+} at 12k, $4f_2$, 2a, and 2b site in different proportion. This claim is supported by the Ligand theory as it states that ions with d^{10} orbitals does not show any preference towards a particular site, as such, they are free to occupy any site. This is contrary to our analysis of the occupancy of Er^{3+} based on electronegativity of the ion as we found that it could occupy $4f_1$ site. Since the obtained data of the values of R_A

Table 4.15 Values of line width (Γ), isomer-shift (δ), quadrupole splitting (Δ), hyperfine field (H_{hf}), and relative area (R_A) for $Sr_{1-x}Cu_xFe_{12-y}Er_yO_{19}$ (x=0.0, 0.1, 0.2, and y=0.0, 0.4, 0.5)

Sample code	Fe^{3+} ion sites	Crystallographic site	Γ (mm/s)	δ (mm/s)	Δ (mm/s)	H_{hf} (T)	R_A (%)
H1	12k↑	Octahedral (R-S)	0.32	0.26	0.07	52.17	55.67
	$4f_2$↓	Octahedral (R)	0.27	0.22	0.27	49.83	20.43
	$4f_1$↓	Tetrahedral (S)	0.13	0.15	-0.12	50.12	8.36
	2a↑	Octahedral (S)	0.27	0.30	0.40	41.88	9.03
	2b↑	Bi-pyramidal (R)	0.18	0.34	0.30	51.93	14.30
H2	12k↑	Octahedral (R-S)	0.29	0.24	0.06	52.17	48.86
	$4f_2$↓	Octahedral (R)	0.30	0.23	0.28	49.83	19.61
	$4f_1$↓	Tetrahedral (S)	0.20	0.18	-0.19	50.01	10.57
	2a↑	Octahedral (S)	0.31	0.30	0.42	41.83	8.46
	2b↑	Bi-pyramidal (R)	0.22	0.33	0.28	51.93	12.51
H3	12k↑	Octahedral (R-S)	0.25	0.20	0.03	52.17	44.37
	$4f_2$↓	Octahedral (R)	0.24	0.25	0.37	49.88	16.2
	$4f_1$↓	Tetrahedral (S)	0.27	0.21	-0.13	50.12	19.74
	2a↑	Octahedral (S)	0.29	0.31	0.41	41.72	8.37
	2b↑	Bi-pyramidal (R)	0.26	0.45	0.15	51.48	12.33

is more reliable, we can conclude that Er^{3+} replaces Fe^{3+} at 12k, $4f_2$, 2a, and 2b sites in different proportion and consequently we should observed increase in the values of M_s with increase in Er^{3+} concentration. However, the values of M_s decrease with increase in Er^{3+} concentration. This situation is observed because the substitution of rare earth cation such as Er^{3+} causes the formation of spin canting effect which makes the orientation of spins to be aligned by forming angles from the preferred direction, this results in magnetic dilution and consequently the magnetic collinearity will be broken and hence, a reduction in the values of σ_s is observed [136]. Thus on this basis, we can conclude that Er^{3+} replaces Fe^{3+} at 12k, 2a, and 2b sites in different proportion. This further supports the Raman analysis.

4.8 Pr^{3+}-Co^{2+} substituted M-type strontium hexaferrites

4.8.1 XRD analysis

XRD patterns of M-type strontium hexagonal ferrites with chemical composition $Sr_{1-x}Pr_xFe_{12-y}Co_yO_{19}$ (x=0.0, 0.2, 0.4 and y=0.0, 0.15, 0.35) are presented in **Fig. 4.95**. The XRD patterns were compared with standard patterns of hexaferrites (JCPDS 39-1433), it was observed that the samples are similar to the peaks of pure crystalline hexaferrites with space group *$P6_3/mmc$*. The patterns show well defined pure crystalline peaks of hexaferrites, presences of α-Fe_2O_3 (JCPDS 00-033-664) have not been observed in all the samples [292]. The structural parameters such as lattice parameters (a and c), crystallite size (D), volume of unit cell (V_{cell}) and strain (η) were respectively calculated from the equations below

$$\frac{1}{d_{hkl}^2} = \frac{4}{3}\left(\frac{h^2+hk+l^2}{a^2}\right) + \frac{l^2}{c^2} \tag{4.77}$$

$$D = \frac{k\lambda}{\beta \cos\theta} \tag{4.78}$$

$$V_{cell} = 0.8666a^2c \tag{4.79}$$

$$\eta = \frac{\beta \cos\theta - \frac{0.9\lambda}{D}}{2\sin\theta} \tag{4.80}$$

where d_{hkl} is the value of d spacing, hkl are the miller indices, β (in radian) is the full width at half maximum, k is the shape factor which is having a value of 1 for hexagonal ferrites, θ is the diffraction angle and λ is the X-ray wavelength having a value of 1.54056Å. The values of a, c and V_{cell} decrease with Pr^{3+}-Co^{2+} substitution (**Table 4.16**), this could be attributed to microstructural defects as a result of site occupation by the substituted cations and interaction between substituted cations [260][191]. It has been reported that the hexagonal structure can be ascertain if the c/a falls below 3.98 [236][293]. Since the c/a ratio are 3.93, 3.94, and 3.93 for the samples S1, S2, and S3 respectively, then we assumed that the synthesized samples exhibit the hexagonal structure. The values of D was estimated using Scherer formula. The variation of D with Pr^{3+}-Co^{2+} substitution does not show regular pattern (**Table 2**), the values of D are 49.96, 51.37 and 43.76 nm for the samples S1, S2, and S3 respectively, strain (η) which results from distortion induced during the synthesis process does not show much variation with Pr^{3+}-Co^{2+} substitution.

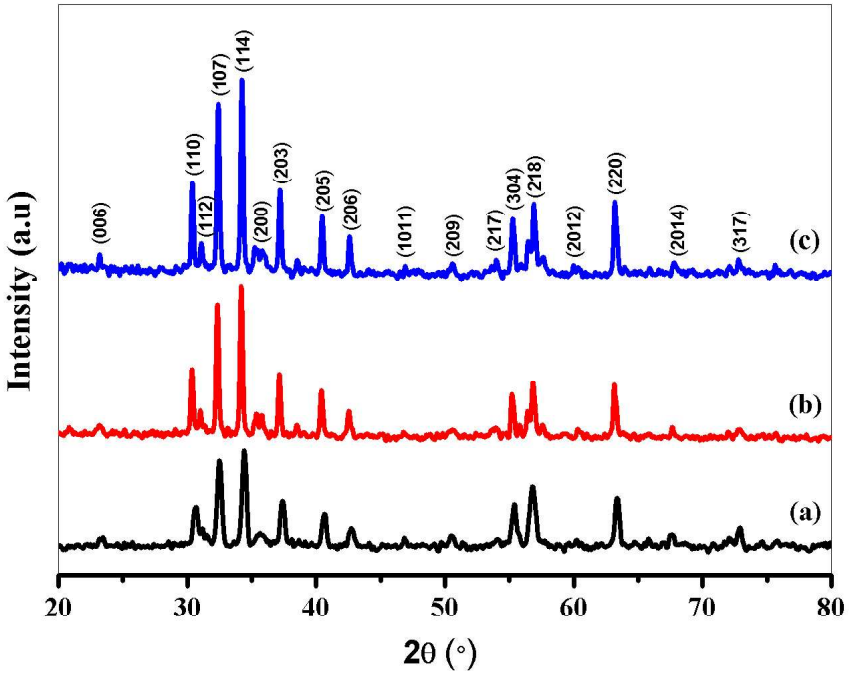

Fig. 4.95 XRD spectra of $Sr_{1-x}Pr_xFe_{12-y}Co_yO_{19}$ (x=0.0, 0.2, 0.4 and y=0.0, 0.15, 0.35) for (a) S1, (b) S2, and (c) S3

Table 4.16 Values of lattice parameters (a and c),crystallite size (D), volume of unit cell (V_{cell}) and strain (η) for $Sr_{1-x}Pr_xFe_{12-y}Co_yO_{19}$ (x=0.0, 0.2, 0.4 and y=0.00, 0.15, 0.35)

Sample code	2θ (°)	d (Å)	β (°)	a (Å)	c (Å)	c/a	V_{cell} (Å^3)	D (nm)	$\eta \times 10^{-4}$
S1	30.23	2.9540	0.183	5.91	23.27	3.93	703.93	49.96	5.91
S2	30.31	2.9464	0.178	5.89	23.21	3.94	698.52	51.37	5.73
S3	30.39	2.9388	0.209	5.88	23.15	3.93	693.16	43.76	6.71

4.8.2 FTIR analysis

Attached functional groups and molecular bands were investigated using FTIR in the range 4000 to 400 cm^{-1}. The FTIR of $Sr_{1-x}Pr_xFe_{12-y}Co_yO_{19}$ (x=0.0, 0.2, 0.4 and y=0.00, 0.15, 0.35) are presented in **Fig. 4.96**. The characteristics bands that appear at 434, 543, and 586 cm^{-1} gives an idea of the formation of hexagonal ferrites structure, the appearance of the band at

434 cm^{-1} may be due to A2u vibration of octahedral Fe^{4+}-O bonds whereas those at 543 and 586 cm^{-1} could be attributed to E1u vibration of octahedral Fe^{3+}-O_4 bonds [250]. The band at 2893 cm^{-1} results from symmetrical stretching CH_2 bonds whereas the broad band observed at 3435 cm^{-1} may be attributed to -OH stretching vibration which are acquired from wet atmosphere [212].

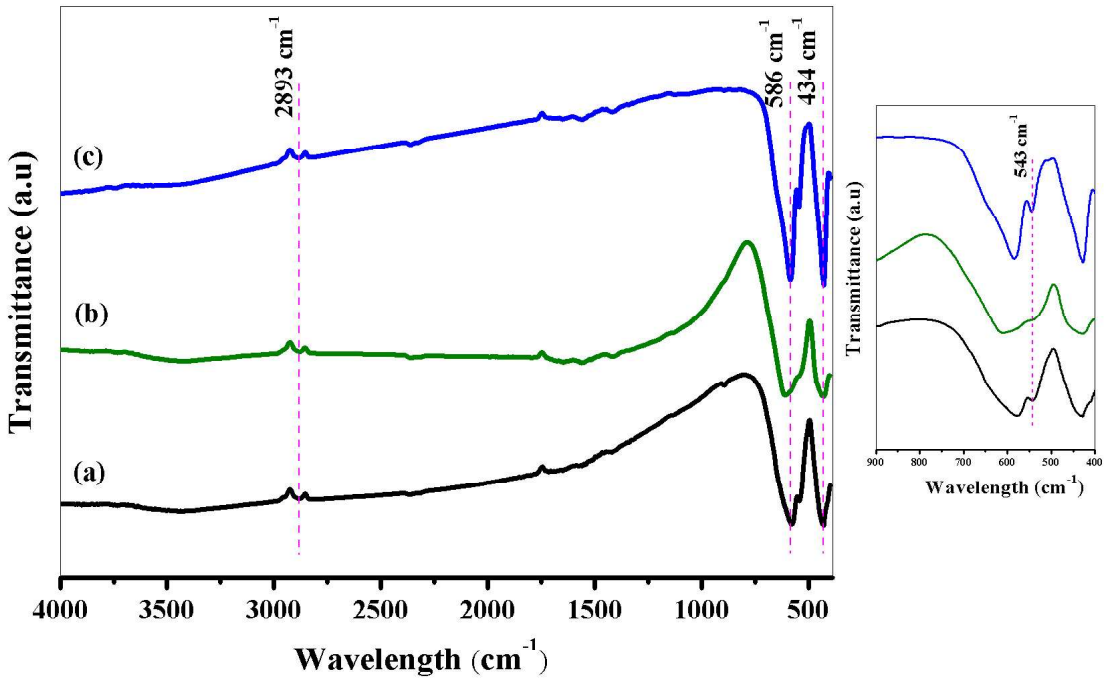

Fig. 4.96 FTIR spectra of $Sr_{1-x}Pr_xFe_{12-y}Co_yO_{19}$ (x=0.0, 0.2, 0.4 and y=0.0, 0.15, 0.35) for (a) S1, (b) S2, and (c) S3

4.8.3 Raman spectroscopy

Raman spectroscopy entails rotational or vibrational motion of crystal lattice which are unique characteristics of a specific material [294]. Group theory analysis of hexaferrites based on the D_{6h} factor group selection rules concluded the existence of 42 Raman active modes ($11A_{1g} + 14E_{1g} + 17E_{2g}$), 30 IR active modes ($13A_{2u} + 17E_{1u}$), and 54 silent modes ($3A_{1u} + 4A_{2g} + 13B_{1g} + 4B_{1u} + 3B_{2g} + 12B_{2u} + 15E_{2u}$) [215][230][267][216][217]. In this presentation, optical modes are denoted by A, B, and E, while symmetry and anti-symmetry with respect to the centre of inversion are denoted by *u* and *g* [225]. The polarization of the incident and scattered radiation allow both the A_{1g} and E_{2g} phonon mode to be observed in the

$Z(XX)\bar{Z}$ configuration of the Raman tensor while only the E_{2g} phonon mode is permitted to observe in the $Z(XY)\bar{Z}$ configuration Raman tensor [295], these phonon modes (rotational or vibrational) are observed only for non-zero derivative of polarizability [213].

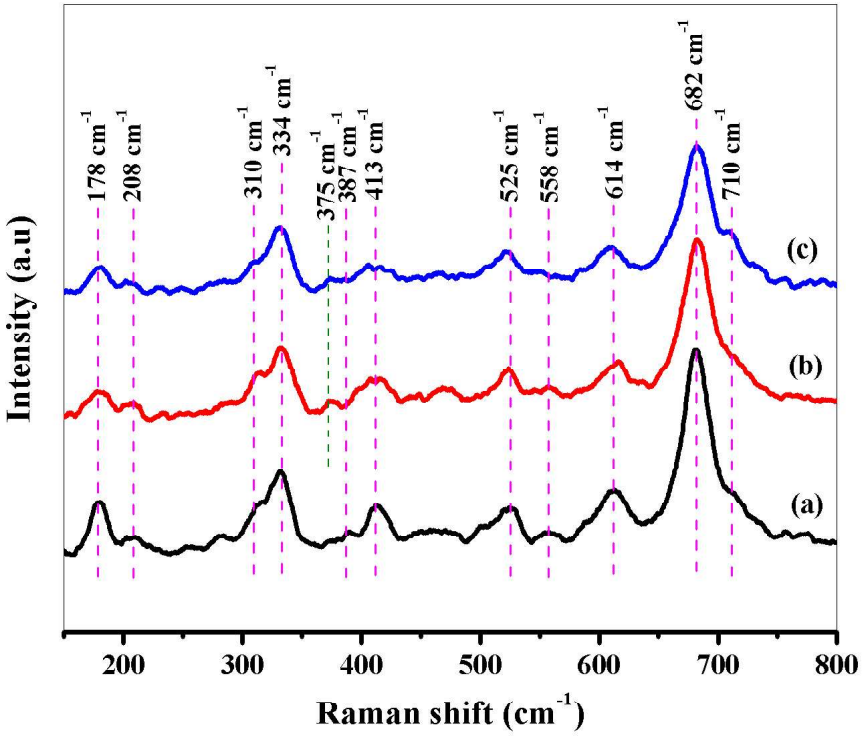

Fig. 4.97 Raman shift of $Sr_{1-x}Pr_xFe_{12-y}Co_yO_{19}$ (x=0.0, 0.2, 0.4 and y=0.0, 0.15, 0.35) for (a) S1 (b) S2 and (c) S3

The room temperature Raman spectra of $Sr_{1-x}Pr_xFe_{12-y}Co_yO_{19}$ (x=0.0, 0.2, 0.4 and y=0.0, 0.15, 0.35) is shown in **Fig. 4.97**. The spectra were recorded in the 150-800 cm^{-1} using 532 semiconductor laser and several peaks of varying intensities were observed from lower to higher Raman shift. Intense and weak Raman active modes were observed at 178, 208, 310, 334, 387, 413, 525, 558, 614, 682, 710 cm^{-1}, these modes are characteristics signatures of single phase M-type hexaferrites and are in agreement with observations made by other research groups [215][230][295][220][218]. The E_{1g} symmetry is responsible for the appearance of the Raman active mode at 178 and 208 cm^{-1} as result of vibration of the whole spinel block and octahedral 2a site [220][296]. At higher Raman shift, the high energy A_{1g} symmetry give rise to Raman active modes at 558, 614, 682, 710 cm^{-1} which respectively

correspond to vibrational motion of octahedral 12k, octahedral $4f_2$, bipyramidal 2b, and tetrahedral $4f_1$ site [218][267][225][227][229][297]. The Raman active modes at 334 and 387 cm^{-1} respectively results from A_{1g} and E_{2g} symmetry vibrations of octahedral (12k), a weak shoulder mode observed at 310 cm^{-1} also occur due to A_{1g} symmetry [296][223][298]. The mode at 387 cm^{-1} shifted to lower Raman shift in the sample S2 and S3, this could be attributed to the replacement of Fe^{3+} ion ($r_{Fe^{3+}} = 0.645$ Å) by the larger Co^{2+} ion ($r_{Co^{2+}} = 0.745$ Å) [298]. The Raman active modes at 413 cm^{-1} arise due to vibrations of octahedral 12k site as a result of A_{1g} whereas the 525 cm^{-1} mode appear because of mixed mode vibrations of metal oxide bond at octahedral 12k and 2a site mediated by E_{1g} symmetry respectively [296][224][223][222].

Table 4.17 Raman active modes of $Sr_{1-x}Pr_xFe_{12-y}Co_yO_{19}$ (x=0.0, 0.2, 0.4 and y=0.0, 0.15, 0.35)

Raman active mode (cm^{-1})	Symmetry	Mode assignment	Reference
178	E_{1g}	Whole spinel block	[220][296]
208	E_{1g}	Octahedral (2a)	[220]
310	A_{1g}	Octahedral (12k)	[223]
334	A_{1g}	Octahedral (12k)	[298]
387	E_{2g}	Octahedral (12k)	[296]
413	A_{1g}	Octahedral (12k)	[296][224][223]
525	E_{1g}	Octahedral (12k and 2a)	[222]
558	A_{1g}	Octahedral (12k)	[218]
614	A_{1g}	Octahedral ($4f_2$)	[218][297]
682	A_{1g}	Bipyramidal (2b)	[267][225][227] [229]
710	A_{1g}	Tetrahedral ($4f_1$)	[297][218]

4.8.4 Morphology analysis

The FESEM micrographs and particle distribution of unsubstituted and Pr^{3+}-Co^{2+} substituted M-type strontium hexaferrites are presented in **Fig. 4.98** and **4.99**. The crystallite size observed from FESEM micrographs is more than 100 nanometre; this result is not consistent with the calculated crystallite size from XRD, this could be attributed to agglomeration and

non-uniform distribution of grains as a result of magnetic interaction with neighbouring grains [134]. The prepared samples exhibit hexagonal plate-like structure, it has been reported that hexagonal plate-like structure is vital for absorption of microwaves and EMI shielding [299]. The difference between the ionic radius of Pr^{3+} and Sr^{2+} could causes disturbance of the locality of atoms thereby resulting in lattice distortion and consequently interfacial dislocation and the occurrence of grain boundary defect, this scenario may prompt the suppression of grain growth [300][301][94]. **Fig. 4.100** shows the EDX spectra of the prepared samples, EDX spectra of the prepared samples were examined by their weight% and atomic%, these ratios were calculated by focusing the beam of electrons at one particle at a time. Weak peaks along with strong peaks are observed for particular metal ions, indicating that dopant ions are incorporated in the crystal lattice of hexaferrite [302][236]. Clearly, all the elemental composition of the prepared samples was observed.

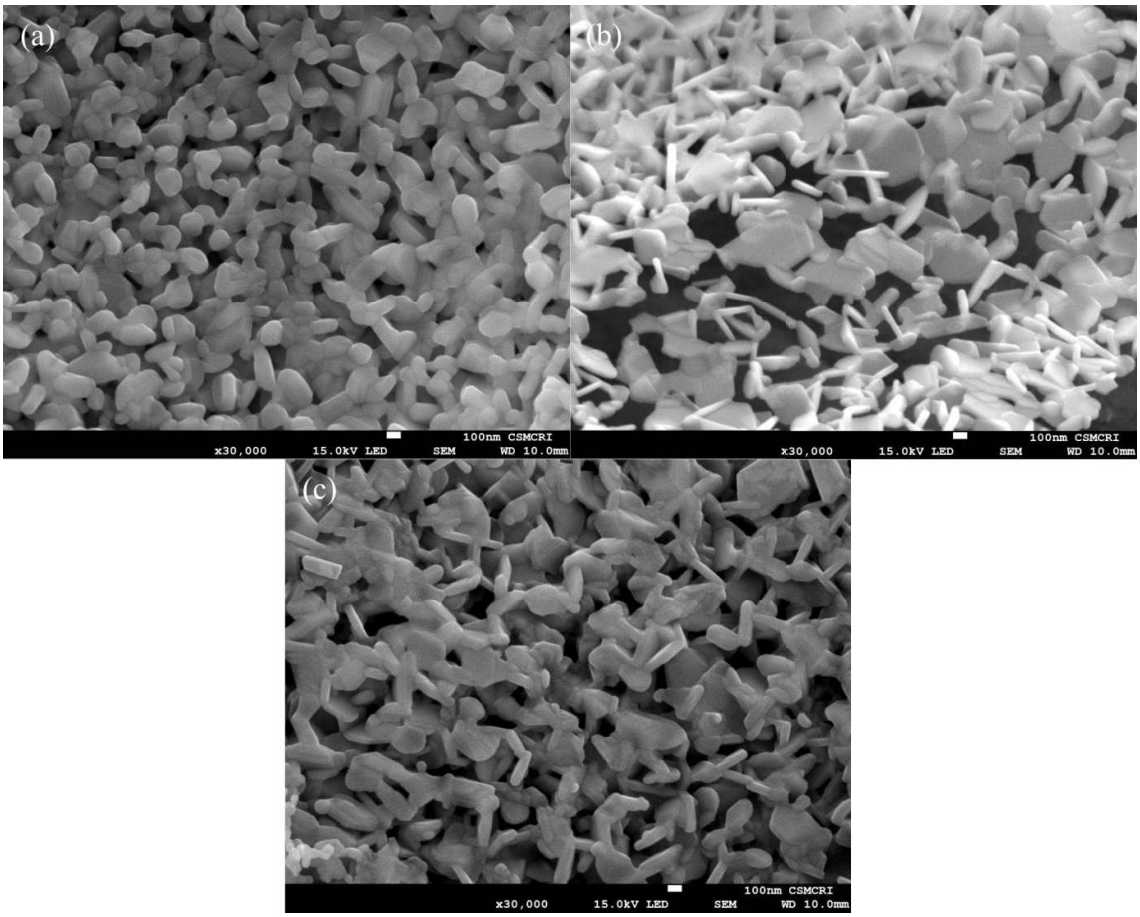

Fig. 4.98 FESEM micrographs of $Sr_{1-x}Pr_xFe_{12-y}Co_yO_{19}$ (x=0.0, 0.2, 0.4 and y=0.0, 0.15, 0.35) for (a) S1, (b) S2, and (c) S3

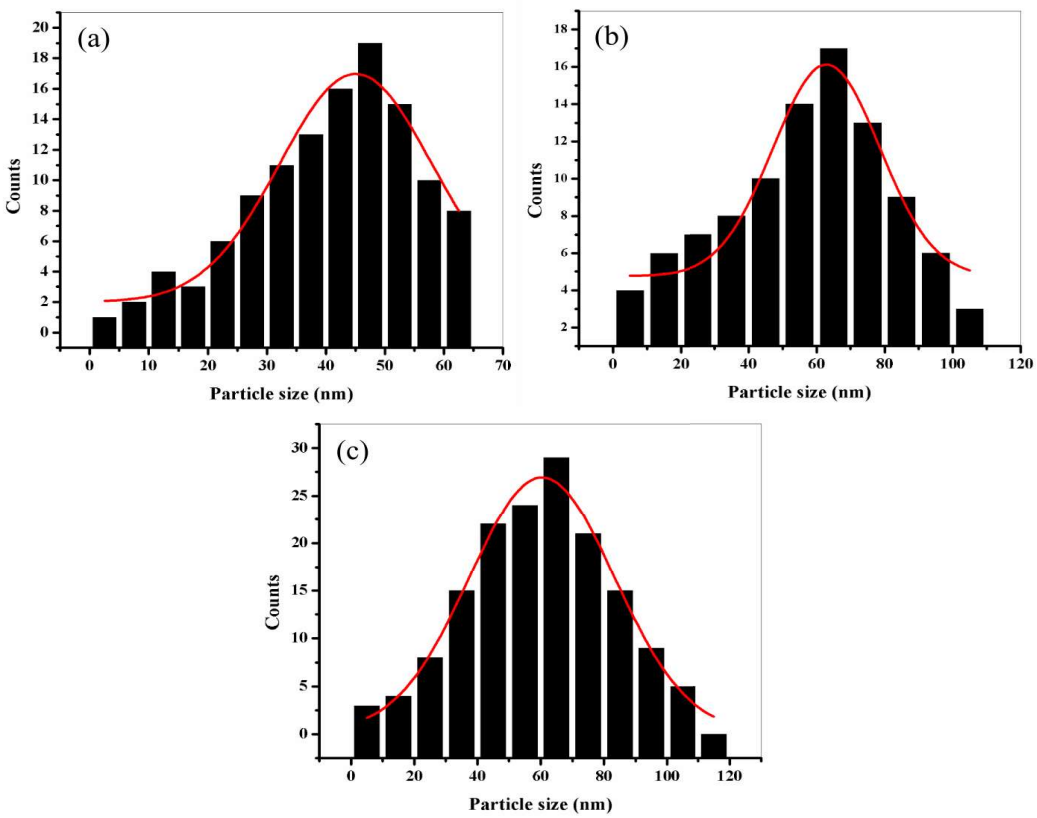

Fig. 4.99 Particle size distribution of $Sr_{1-x}Pr_xFe_{12-y}Co_yO_{19}$ (x=0.0, 0.2, 0.4 and y=0.0, 0.15, 0.35) for (a) S1, (b) S2, and (c) S3

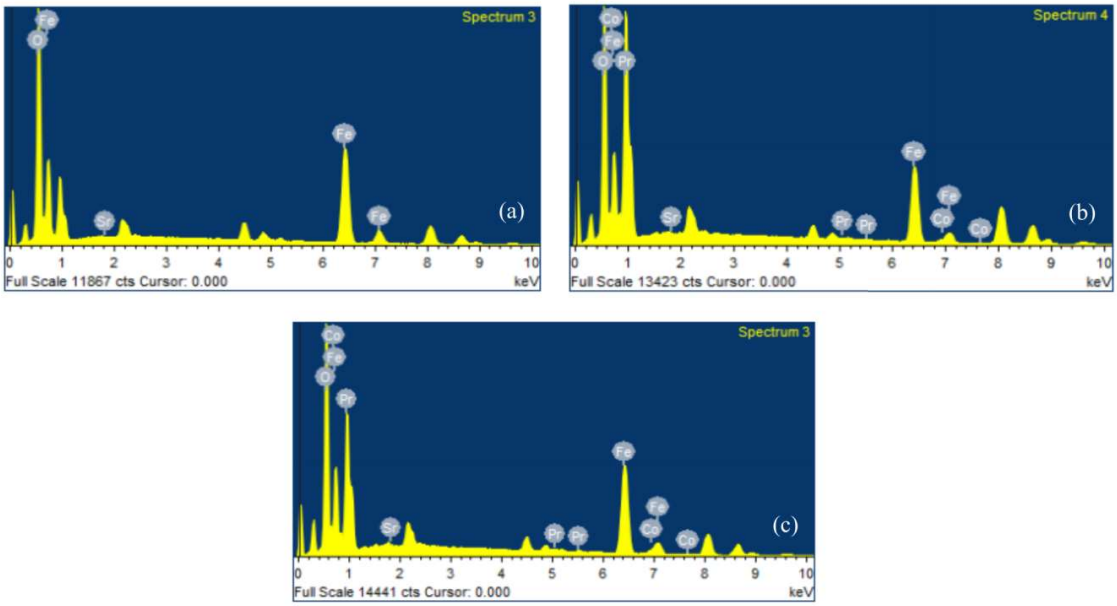

Fig. 4.100 EDX spectra of $Sr_{1-x}Pr_xFe_{12-y}Co_yO_{19}$ (x=0.0, 0.2, 0.4 and y=0.0, 0.15, 0.35) for (a) S1, (b) S2, and (c) S3

4.8.5 Optical analysis

The absorbance spectra of $Sr_{1-x}Pr_xFe_{12-y}Co_yO_{19}$ (x=0.0, 0.2, 0.4 and y=0.0, 0.15, 0.35) were recorded at room temperature in the range 234-766 nm. All the prepared samples absorbs light from 247 to 579 nm, this include part of UV and visible light region. The sample S1 shows a slight reflection peak at 694.7 nm. However, this reflection peak seems to disappear

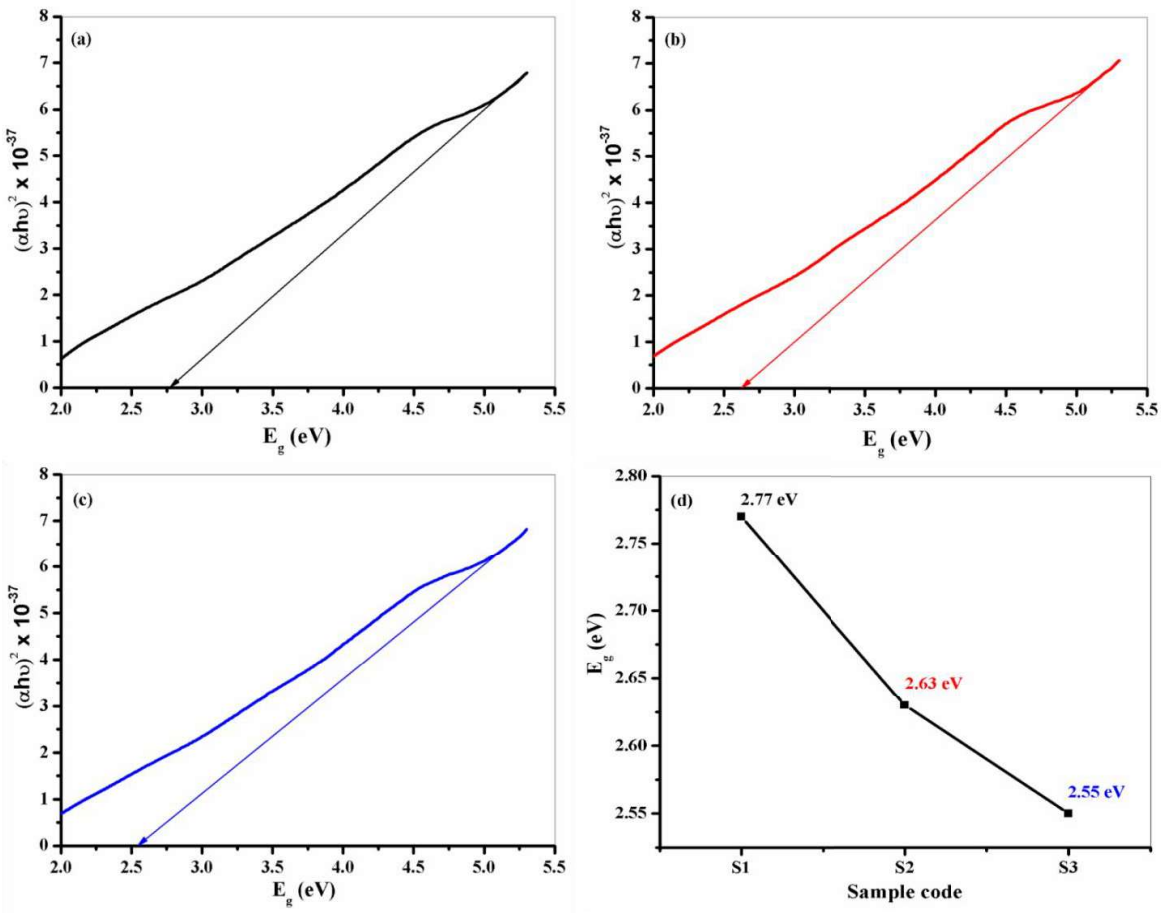

Fig. 4.101 Optical band gap of $Sr_{1-x}Pr_xFe_{12-y}Co_yO_{19}$ (x=0.0, 0.2, 0.4 and y=0.0, 0.15, 0.35) for (a) S1, (b) S2, (c) S3, and (d) variation of band gap with composition

after the initiation of Pr^{3+}-Co^{2+} substitution i. e. the samples S2 and S3 does not show this reflection peak, this phenomenon correspond to hyperchromic shift. Hence, we can conclude that Pr^{3+}-Co^{2+} enhances absorption of light by the prepared samples. The optical band gap (E_g) was calculated from the formula

$$(\alpha h\upsilon)^m = K(h\upsilon - E_g) \tag{4.81}$$

where α is the absorption coefficient, h is the planks constant ($6.6260 \times 10^{-34}\, J.s$), υ is incident photon's frequency and K is a constant that rely on m [303]. The values of m are 1/2, 2, 3/2 and 3 for allowed direct, allowed indirect, forbidden direct and forbidden indirect transition respectively. The plot of E_g of the prepared samples is presented in **Fig. 4.101** (a), (b) and (c). Tauc's plot was used to obtained the values of E_g; typically, the extrapolation of the linear part of the graph of $(\alpha h\upsilon)^2$ versus E_g gives the values of E_g for each of the prepared sample [304]. The values of E_g for S1, S2, and S3 are respectively 2.77, 2.63 and 2.55. It is clearly evident from **Fig. 6** (d) that E_g decreases with increase in Pr^{3+}-Co^{2+} substitution; this could be attributed to factors such as structural defects, crystallite size and quantum confinement [86][162][305]. The obtained values of E_g are higher than those obtained for La-substituted hexaferrites (E_g ranges from 1.34 to1.83 eV) [306] and less than those reported for calcium copper titanate (E_g ranges from 3.8 to 4.2 eV) [305] and Sr-substituted barium titanate (E_g ranges from 3.2 to 3.6 eV) [159].

4.8.6 Magnetic analysis

The M-H hysteresis loop of $Sr_{1-x}Pr_xFe_{12-y}Co_yO_{19}$ (x=0.0, 0.2, 0.4 and y=0.0, 0.15, 0.35) was recorded in room temperature and presented in **Fig. 4.102**. Magnetic parameters such as coercivity (H_c), remanent (M_r) and saturation magnetisation (M_s) were determined from the M-H hysteresis loop and tabulated in **Table 4.18**. The obtained values of H_c, M_r, and M_s were used to calculate the anisotropy constant (K), magneton number (μ_B) and squareness ratio (SR) using equation (4.82), (4.83), and (4.84) respectively

$$K = \frac{\mu_0 M_s H_c}{2} \tag{4.82}$$

$$\mu_B = \frac{\text{molecular weight} \times M_s}{5585} \tag{4.83}$$

$$SR = \frac{M_r}{M_s} \tag{4.84}$$

Where $\mu_0 = 4\pi \times 10^7\, H/m$ is the permeability in vacuum. The values of H_c, M_r, M_s and K, and μ_B decrease after the initiation of Pr^{3+}-Co^{2+} substitution and then increase. This behaviour can be explained on the basis of site preference and occupancy of the Pr^{3+} and Co^{2+} ions. It is well known that the structure of M-type hexagonal ferrite consist of 2 layers having SRS^*R^* stacking. The R and R^* blocks comprises of 3 layers of oxygen having hexagonal

structure with general formula $BaFe_6O_{11}$ while the *S* and S^* blocks is made up of 2 layers of oxygen having spinel structure with general formula Fe_6O_8, the asterisk is an indication of 180° rotation of the block with respect to *R* and *S* blocks around the *c*-axis [199]. A unit cell of M-type hexaferrite comprises of 38 O^{2-} ions, 2 Ba^{2+} ions and 24 Fe^{3+} ions. The 24 Fe^{3+} ions are distributed among trigonal bi-pyramidal (2b), tetrahedral ($4f_1$), octahedral (12k, 2a, and $4f_2$) crystallographic sites [186]. The Fe^{3+} ions situated at 12k, 2a and 2b are having spin

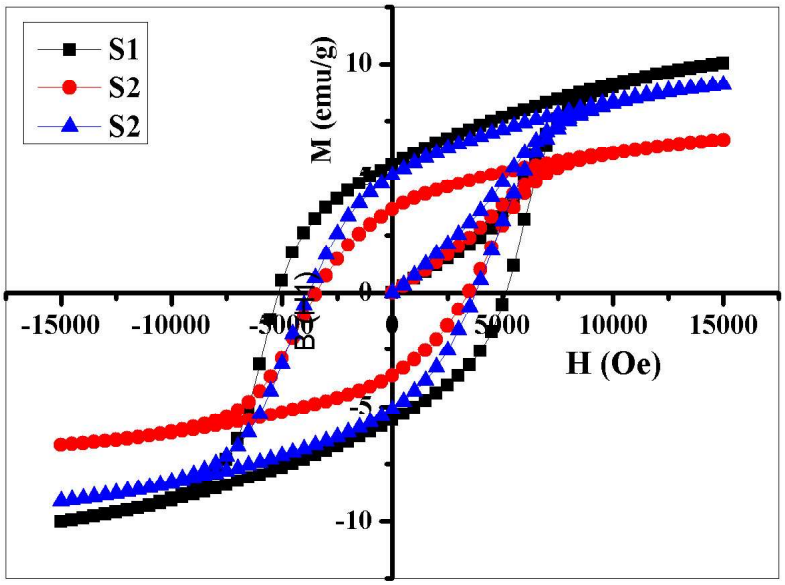

Fig. 4.102 *M-H* hysteresis loop for $Sr_{1-x}Pr_xFe_{12-y}Co_yO_{19}$ (x=0.0, 0.2, 0.4 and y=0.0, 0.15, 0.35)

up whereas those located at $4f_1$ and $4f_2$ are having spin down [307]. In generally, the substitution of magnetic cation with magnetic moment less than that of Fe^{3+} or non-magnetic cation at $4f_1$ and $4f_2$ crystallographic sites should result in increase in magnetization while cation substitution at 12k, 2b, and 2a should lead to decrease in magnetization. However, the possibility of a particular cation occupying a particular crystallographic site depend on factors such as electronegativity and ionic radius of the substituting and host cation [264]. The mechanisms that determine how the substituted cations are distributed among the five crystallographic sites is not fully understood , although it has been observed that the manner

in which each crystallographic site contributes to the magnetic properties differs [254]. The Ligand theory states that the tetrahedral crystallographic site is preferred by ions with d_1, d_2, d_3, and d_4, the octahedral crystallographic site is preferred by ions with d_6, d_7, d_8, and d_9, and there is no preference for ions with d_0, d_5, and d_{10} [308]. The Fe^{3+} ion has a magnetic moment of 5 μ_B as a result of the $3d_5$ configuration of the Fe^{3+} ion [309]. It can be observed that both M_r and M_s decrease for the sample S2, this decrease in M_r and M_s occurs when Pr^{3+} ion substitutes Sr^{2+} ion thereby leading to the conversion of Fe^{3+} ion having $3d_5$ high spin and magnetic moment of 5 μ_B to Fe^{2+} ion having $3d_6$ low spin and magnetic moment of 4 μ_B, this scenario results in the weakening of super exchange interaction between Fe^{3+}-O^{2-}-Fe^{2+}, magnetic dilution and the occurrence of spin canting usually caused by rare earth ion substitution and collapse of magnetic collinearity [264][310][311]. It has been reported that Fe^{3+} ion having a magnetic moment of 5 μ_B is substituted by Co^{2+} ion having a magnetic moment of 3.7 μ_B at $4f_1$, $4f_2$ and 2b crystallographic sites [309][308][312]. For the sample S3; both M_r and M_s increases, this could be attributed to inhibiting and offsetting of the magnetic moment as result of the substitution of spin down Fe^{3+} ion by Co^{2+} ion at $4f_1$ and $4f_2$ crystallographic sites [312][264]. Similarly, increase in K was observed in the sample S3, this could be ascribed to the occurrence of lattice distortion and the lowering symmetry of trigonal bi-pyramidal (2b) crystallographic site when Pr^{3+} ion with smaller ionic radius ($r_{Pr^{3+}}$=1.180 Å) substitutes Sr^{2+} ion with larger ionic radius ($r_{Sr^{2+}}$=1.180 Å) [310]. Consequently, H_c increases because of the direct proportionality relationship of K with H_c (**Eqn. 6**). Also, it has been reported that substitution of Pr^{3+} ion results in increase in the value of K which in turn increase H_c [301]. According to **Eqn. 4.82**, decrease in H_c could also be attributed to decrease in K. It has been reported that if the SR value is greater than or equal to 0.5, then a single magnetic domain structure of the hexaferrite could be established whereas non-interacting multi-domain structure with uniaxial anisotropy can be assumed when the value of SR is less than 0.5. In our case, the SR value of the samples S1, S2, and S3 are respectively 0.55, 0.54, and 0.56. Hence, we conclude that the prepared samples are of single domain structure since the observed SR value is greater than 0.5. It has been reported that magnetic recording media and permanent magnets application require magnetic materials with single domain structured, thus the synthesized samples could be useful in magnetic recording media and as permanent magnets [262][200].

Table 4.18 Values of coercivity (H_c), remnant magnetization (M_r), saturation magnetization (M_s), squareness ratio (SR), anisotropy constant (K) and magnetic moment (μ_B) for $Sr_{1-x}Pr_xFe_{12-y}Co_yO_{19}$ (x=0.0, 0.2, 0.4 and y=0.0, 0.15, 0.35)

Sample code	H_c (Oe)	M_r (emu/g)	M_s (emu/g)	SR (M_r/M_s)	K (HA^2/kg)	μ_B
S1	5149.28	5.58	10.01	0.55	2.57	1.90
S2	3453.05	3.63	6.68	0.54	1.15	1.27
S3	3778.66	5.09	9.08	0.56	1.71	1.74

4.8.8 Electromagnetic interference (EMI) shielding analysis

The complex permittivity (ε^*) of hexaferrites can be evaluated based on the electronic, ionic, interfacial, and intrinsic dielectric polarization; variation of ε^* with frequency for hexaferrites is mostly attributed to interfacial and intrinsic dielectric polarization [94].

$$\varepsilon^* = \varepsilon' - j\varepsilon'' \tag{4.85}$$

Where ε' is the real part of complex permittivity and ε'' is the imaginary part of complex permittivity. The hexagonal lattice structure is such that the positive ions of Ba^{2+} and Fe^{3+} which are surrounded by O^{-2} ions contribute to the ε' and ε'' through contribution via dipolar polarization and dipolar relaxation respectively [264]. The frequency dependent ε' and ε'' for $Sr_{1-x}Pr_xFe_{12-y}Co_yO_{19}$ (x=0.0, 0.2, 0.4 and y=0.00, 0.15, 0.35) are presented in **Fig. 4.103** and **4.104** respectively. Both ε' and ε'' shows variation from 12.4 to 18 GHz with several resonance peaks. In the spectra of ε' and ε'', the samples S2 and S3 show one strong resonance peaks between 13 and 14.5 GHz and two weak resonance peaks between 16 and 18 GHz. The style of doping adopted in this research forces the conversion of Fe^{3+} to Fe^{2+} in order to maintain electronegativity, this scenario resulted in hopping of electrons from Fe^{3+} to Fe^{2+} and consequently more electric dipoles are produced. The occurrence of resonance peaks is a direct consequence of matching of the frequency of electron hopping between Fe^{3+} to Fe^{2+} with that of the applied field [313]. The increase in ε' and ε'' occur at lower frequencies as a result of the emergence of more electric dipoles due to substitution of Sr^{2+} by Pr^{3+} and Fe^{3+} by Co^{2+} [314]. In accordance with Debye relaxation model, the applied electric field varies more slowly compared to the relaxation processes taking place in the synthesized

material. Furthermore, there is a good variation of polarization with electric field at lower frequencies; this scenario causes ε'' to have small values and ε' to tend to be static i. e. static permittivity (ε_s). At much higher frequencies (between 16 and 18 GHz), two resonant peaks

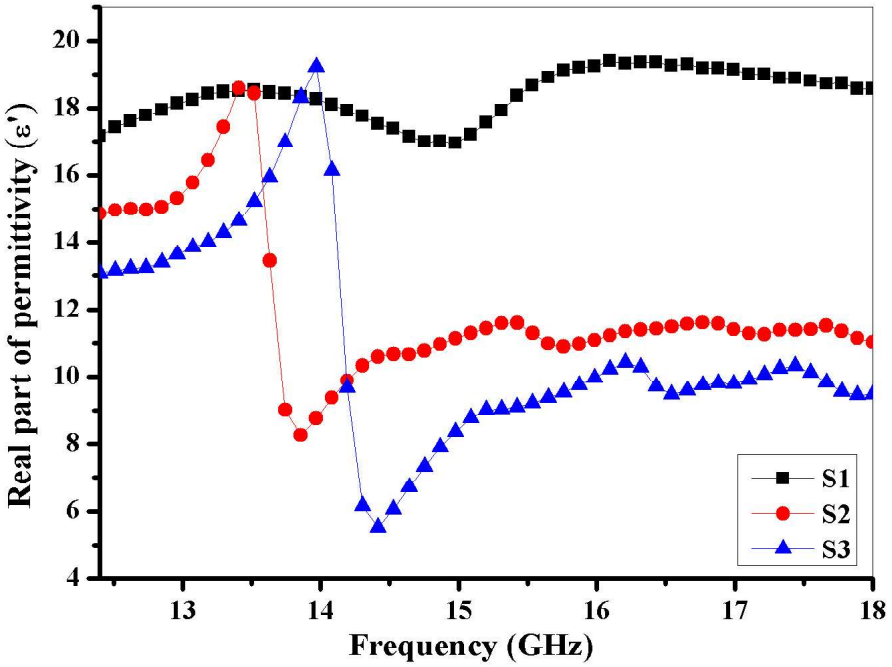

Fig. 4.103 Variation of real part of complex permittivity (ε') with frequency for $Sr_{1-x}Pr_xFe_{12-y}Co_yO_{19}$ (x=0.0, 0.2, 0.4 and y=0.00, 0.15, 0.35)

are clearly observed in the spectra of the samples S2 and S3 (**Fig. 4.103** and **4.104**); this could also be attributed to Debye-like relaxation process which occur when the polarization lag behind the applied electric field [315]. The observed high values of ε' at lower frequencies could be attributed to presence of oxygen vacancies, interfacial polarization, grain boundary defects, and the occurrence of large number of electron hopping between Fe^{3+} to Fe^{2+} whereas the observed low values of ε' at higher frequencies is due to the fact that the frequency of electron hopping between Fe^{3+} to Fe^{2+} lags behind the applied field [316]. The complex permeability (μ^*) of ferrites can be described by analysing magnetic resonance processes present in the synthesized samples.

$$\mu^* = \mu' - j\mu'' \tag{4.86}$$

Where μ' is the real part of complex permeability and μ'' is the imaginary part of complex permeability. **Fig. 4.105** and **4.106** shows the frequency dependent μ' and μ'' for $Sr_{1-x}Pr_xFe_{12-y}Co_yO_{19}$ (x=0.0, 0.2, 0.4 and y=0.00, 0.15, 0.35) respectively. Similarly, we observe an intense resonance peaks between 13 and 14.5 GHz and two less intense resonance peaks between 16 and 18 GHz in the spectra of μ' and μ'' for the samples S2 and S3. The

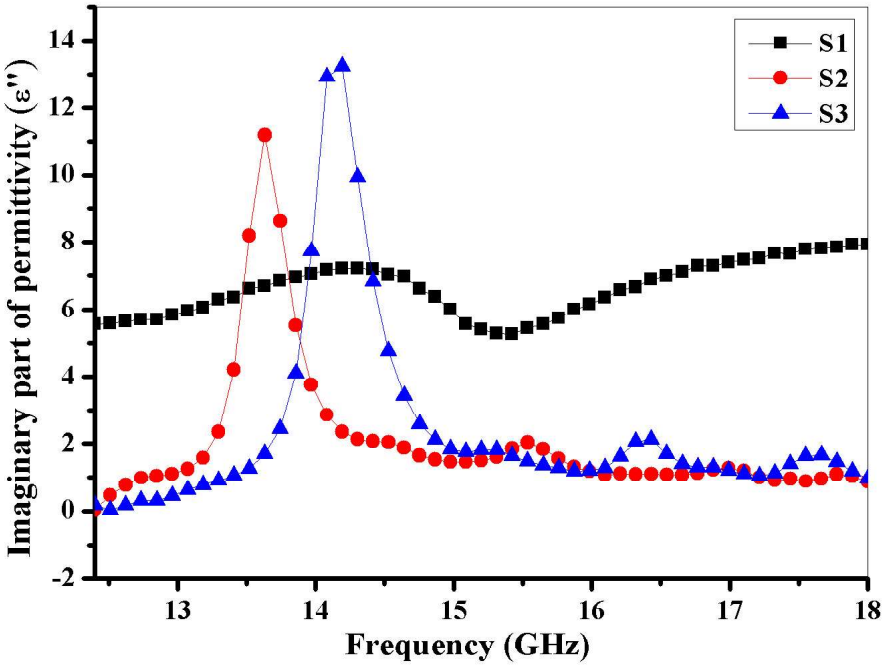

Fig. 4.104 Variation of imaginary part of complex permittivity (ε'') with frequency for $Sr_{1-x}Pr_xFe_{12-y}Co_yO_{19}$ (x=0.0, 0.2, 0.4 and y=0.00, 0.15, 0.35)

permeability spectra of polycrystalline ferrite materials can be described by spin rotation with relaxation type dispersion and domain wall motion with resonance type dispersion [317][318]. Hence, the presence of these resonance peaks could be ascribed to different ferromagnetic processes such as spin or magnetic domain motion and rotation as well as domain wall resonance. The decreasing behaviour observed in the values of μ' and μ'' at some specific frequencies could be attributed to limited speed of spins with resonance type dispersion and domain wall movement with relaxation type dispersion in the prepared samples [232]. The resonance peak at lower frequencies is due to domain wall resonance whereas ferromagnetic resonance (spin rotation) dominates the region of higher frequencies with the appearance of two resonance peaks [94][319].

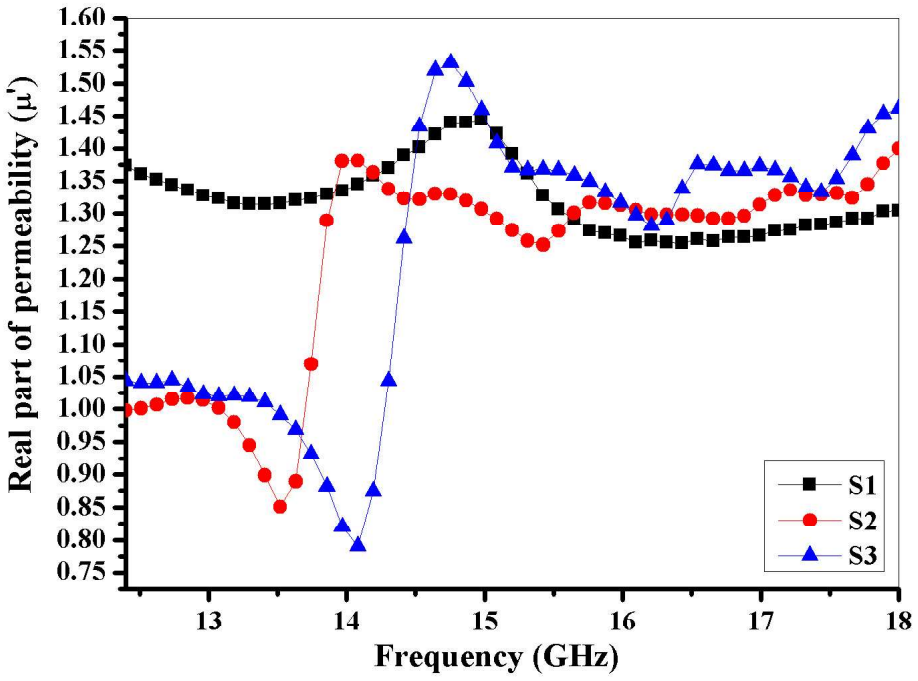

Fig. 4.105 Variation of real part of complex permeability (μ') with frequency for $Sr_{1-x}Pr_xFe_{12-y}Co_yO_{19}$ (x=0.0, 0.2, 0.4 and y=0.00, 0.15, 0.35)

The dielectric tangent loss ($\tan\delta_\varepsilon$) and magnetic tangent loss ($\tan\delta_\mu$) of $Sr_{1-x}Pr_xFe_{12-y}Co_yO_{19}$ (x=0.0, 0.2, 0.4 and y=0.00, 0.15, 0.35) are respectively calculated from (4.87) and (4.88) and presented in **Fig. 4.107** and **4.108.**

$$\tan\delta_\varepsilon = \varepsilon''/\varepsilon' \tag{4.87}$$

$$\tan\delta_\mu = \mu''/\mu' \tag{4.88}$$

The maximum values of $\tan\delta_\varepsilon$ and $\tan\delta_\mu$ are 1.60 and 0.63 respectively. Resonant peaks are observed in both the spectra of $\tan\delta_\varepsilon$ and $\tan\delta_\mu$, this could signify the attainment of impedance matching in the prepared samples [320]. Eddy current losses, domain wall motion, magnetic hysteresis loss, and magnetic resonance (exchange and natural resonance) are the main factors for the appearance of $\tan\delta_\mu$ in hexaferrites. We can debunk contribution from eddy current and magnetic hysteresis loss since hexagonal ferrites are insulator and the field applied is weak. Domain wall motion and magnetic resonance could be the possible factors contributing to the magnetic losses as the prepared samples are multi domain [313][321].

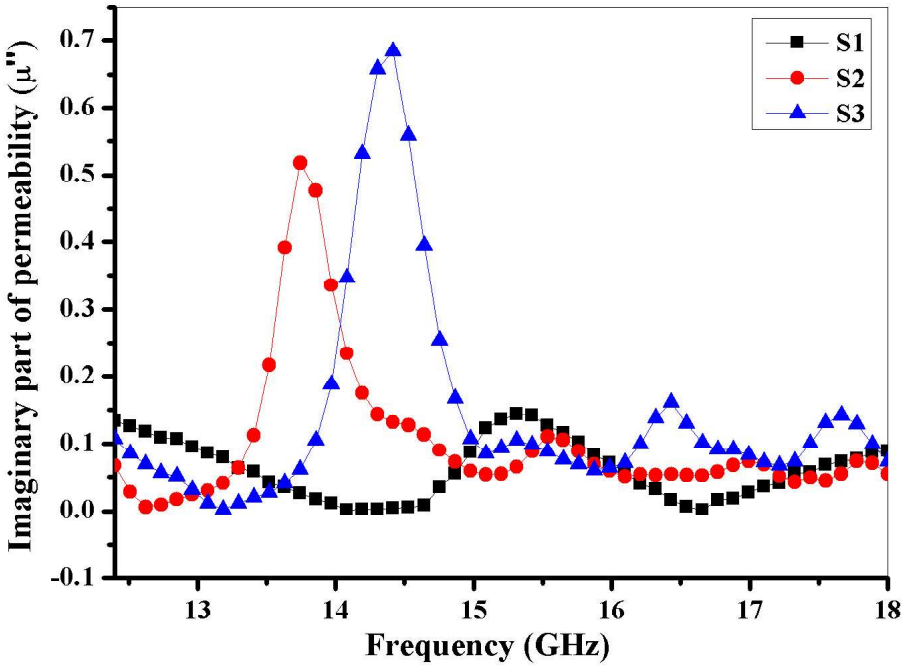

Fig. 4.106 Variation of imaginary part of complex permeability (μ'') with frequency for $Sr_{1-x}Pr_xFe_{12-y}Co_yO_{19}$ (x=0.0, 0.2, 0.4 and y=0.00, 0.15, 0.35)

The presence of resonance peaks at higher and lower frequencies signifies the contribution of magnetic resonance which could be exchange or natural resonance. However, exchange resonances are usually observed at higher frequencies than natural resonance. Since the resonance peaks are more pronounced at lower frequencies, we can assume more contribution from natural resonance than exchange resonance [16][24]. The highest value of $\tan\delta_e$ (1.61) was observed at 14. 30 GHz in the sample with S3, this value is much higher than that of reduced graphene oxide/Mn_3O_4 nanocomposites (1.10) [322].

The shielding effectiveness for absorption (SE_A) and Shielding effectiveness for reflection (SE_R) for $Sr_{1-x}Pr_xFe_{12-y}Co_yO_{19}$ (x=0.0, 0.2, 0.4 and y=0.00, 0.15, 0.35) are presented in **Fig. 4.109** and **4.110**. In general, the parameters describing the shielding effectiveness of a microwave absorber are SE_A and SE_R which are respectively given in the equations below

$$SE_A = -10\log\left(1 - A_{eff}\right) \quad (4.89)$$

$$SE_R = -10log(1 - R) \quad (4.90)$$

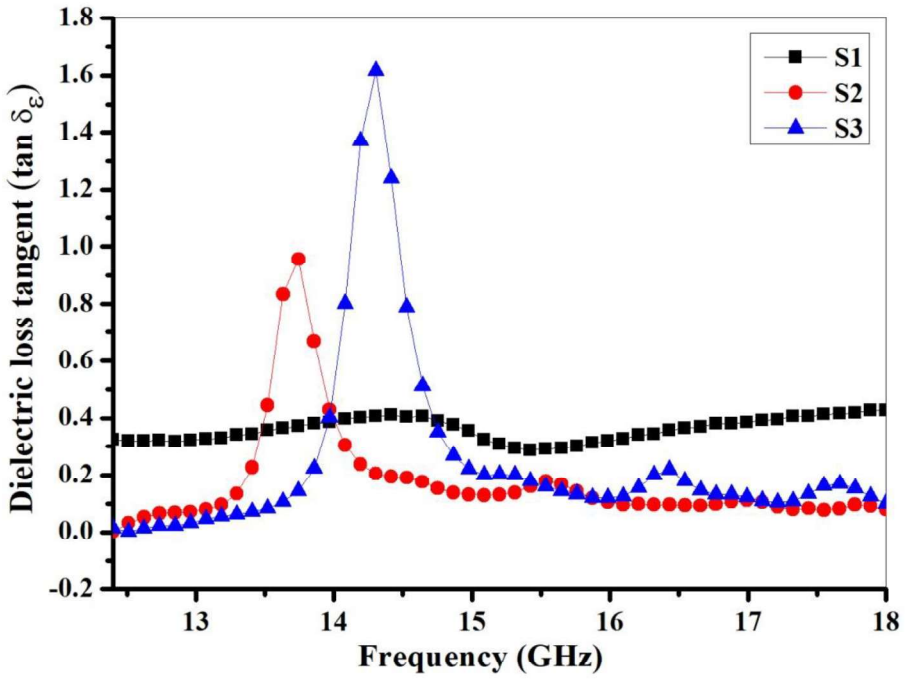

Fig. 4.107 Variation of dielectric tangent loss with frequency for $Sr_{1-x}Pr_xFe_{12-y}Co_yO_{19}$ (x=0.0, 0.2, 0.4 and y=0.00, 0.15, 0.35)

where A_{eff} is the effective absorption of the EM wave absorber. The relation describing A_{eff} is given in terms of reflection coefficient (R) and transmission coefficient (T) as

$$A_{eff} = (1 - R - T)/(1 - R) \quad (4.91)$$

Both R and T are usually determined from S parameters ($S_{11} or\ S_{22}$ and $S_{12}\ or\ S_{21}$) using the equation

$$R = |S_{11}|^2 = |S_{22}|^2 \quad (4.92)$$

$$T = |S_{12}|^2 = |S_{21}|^2 \quad (4.93)$$

The total shielding effectiveness (SE_T) for $Sr_{1-x}Pr_xFe_{12-y}Co_yO_{19}$ (x=0.0, 0.2, 0.4 and y=0.00, 0.15, 0.35) is presented in **Fig. 4.111**. The total shielding effectiveness (SE_T) can be expressed as a sum of shielding effectiveness for absorption (SE_A), shielding effectiveness for reflection (SE_R), and shielding effectiveness for multiple reflection (SE_{MR}) as in the equation below [323].

$$SE_T = SE_A + SE_R + SE_{MR} = 10\log(1/T) \quad (4.94)$$

However, SE_{MR} can be neglected when SE_T is greater than 10 dB [324]. Hence, since in our case SE_T is greater than 10 dB for all samples, then we can neglect SE_{MR}. In general, two conditions must be achieved in order for maximum of the incident waves to be absorbed; firstly, the incident microwave should propagate much more into the pellet samples. Secondly and most importantly for hexagonal ferrites, the pellet samples should be able to attenuate the incident microwave over small thickness of the pellet samples [314]. When microwave is incident on the surface of the prepared sample, unsaturated coordination on the surface of the prepared samples, enhanced surface area and dangling bond atoms causes multiple scattering and consequently absorption of the incident microwave [53]. Frequency matching is achieved as a result of hopping of electrons between Fe^{3+} and Fe^{2+} which also prompt the occurrence of natural resonance [325]. Hence, a greater percentage of the microwave can be absorbed as a result of natural resonance. Generally, μ' contributes to SE_A whereas ε' contributes to SE_R [325]. Furthermore, SE_A contributes most to SE_T, and this contribution become more pronounced at microwave range as a result of high conductivity and skin depth [324][326].

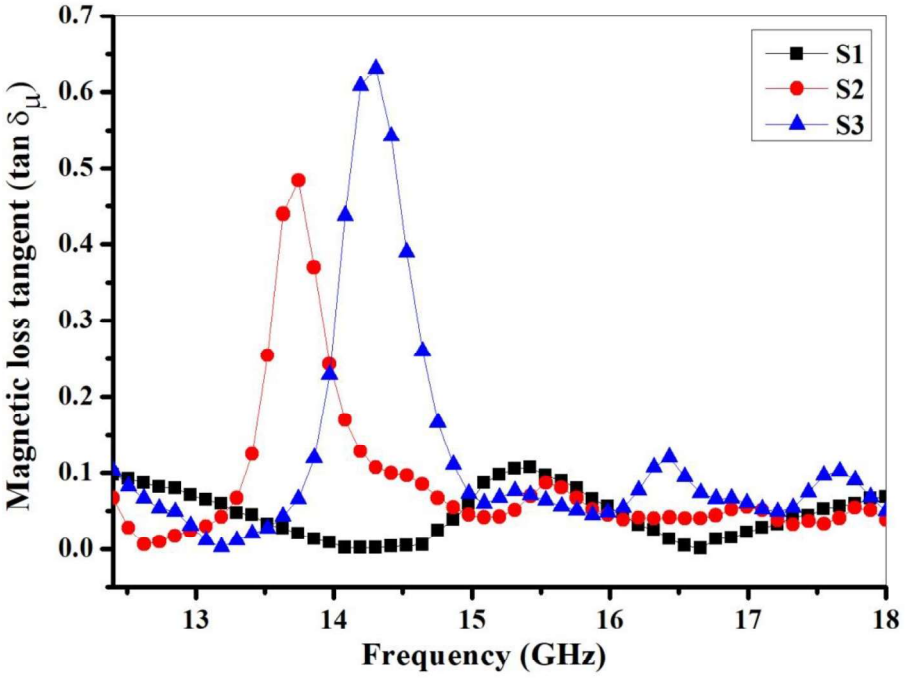

Fig. 4.108 Variation of magnetic tangent loss with frequency for $Sr_{1-x}Pr_xFe_{12-y}Co_yO_{19}$ (x=0.0, 0.2, 0.4 and y=0.00, 0.15, 0.35)

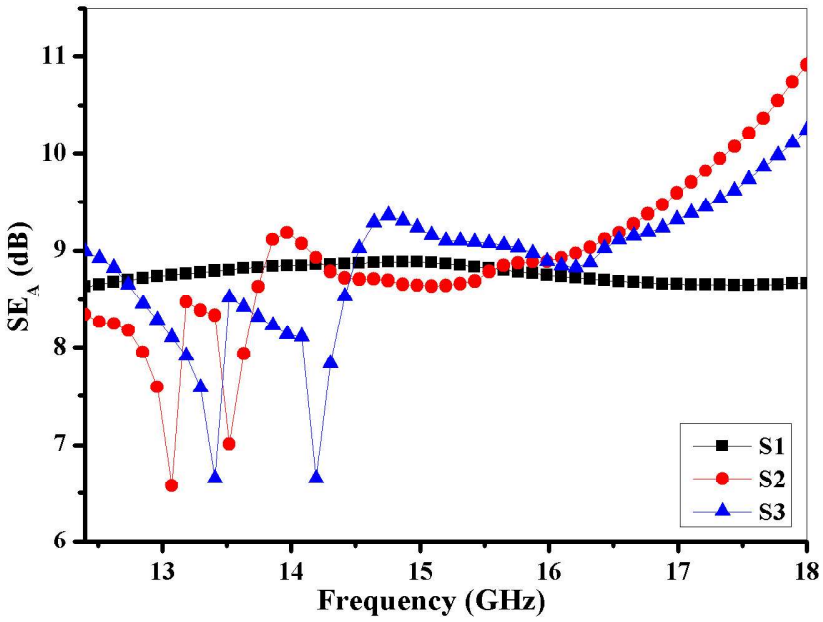

Fig. 4.109 Shielding effectiveness for absorption (SE_A) for $Sr_{1-x}Pr_xFe_{12-y}Co_yO_{19}$ (x=0.0, 0.2, 0.4 and y=0.00, 0.15, 0.35)

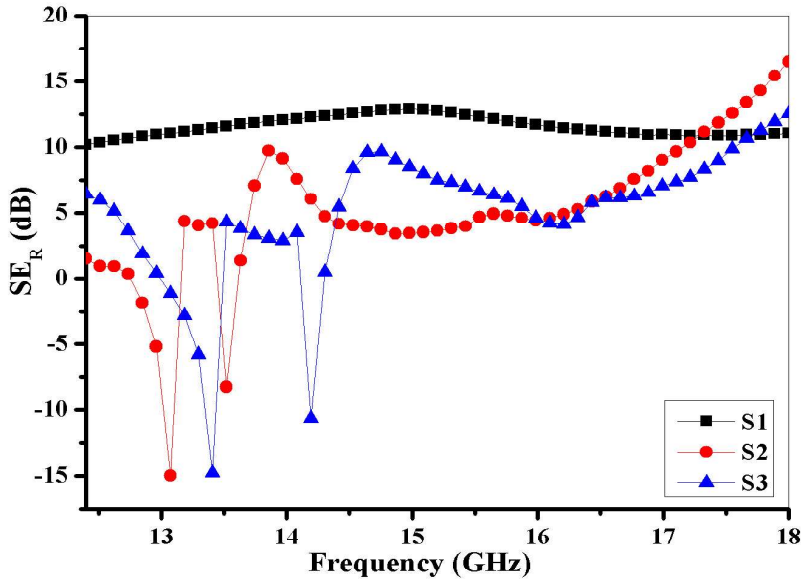

Fig. 4.110 Shielding effectiveness for reflection (SE_R) for $Sr_{1-x}Pr_xFe_{12-y}Co_yO_{19}$ (x=0.0, 0.2, 0.4 and y=0.00, 0.15, 0.35)

Table 4.19 Comparison of maximum values of total shielding effectiveness (SE_T) our S1, S2 and S3 with other samples

Prepared sample	Thickness (mm)	Frequency (GHz)	$\boldsymbol{SE_T}$ (dB)	References
Polypropylene/carbon fibre composite foams	3.2	8-12	25	[327]
Graphene/polymer composite films	0.35	8-12	27	[328]
carbon fibres-reinforced polypropylene matrix composites	1	1.5	16	[329]
Fe_3O_4@reduced graphene oxide/natural rubber composite	1.2	8-12	25	[330]
graphene/texture composites	2	8-12	27	[331]
S1	2	12.4-18	21.80	this work
S2	2	12.4-18	27.40	this work
S3	2	12.4-18	22.82	this work

Both SE_A and SE_R shows multiple resonance peaks from 12.4 to 16 GHz and thereafter a steady increase is observed in all the samples except S1 which remains almost constant. Hence, we can assumed that Pr^{3+}-Co^{2+} substitution causes structural modification in the samples with S2 and S3 which leads to the occurrence of multiple resonances at lower frequencies (<16 GHz) and improvement of EMI shielding at higher frequencies (>16 GHz). The maximum values of SE_T for the samples S1, S2, and S3 were found to be 21.80, 27.40, and 22.82 dB respectively. The value of SE_T obtained in all the samples is above the commercial level of 20 dB. Interestingly, the sample with S2 exhibit SE_T values higher than those obtained for some nanocomposites (**Table 4.19**).

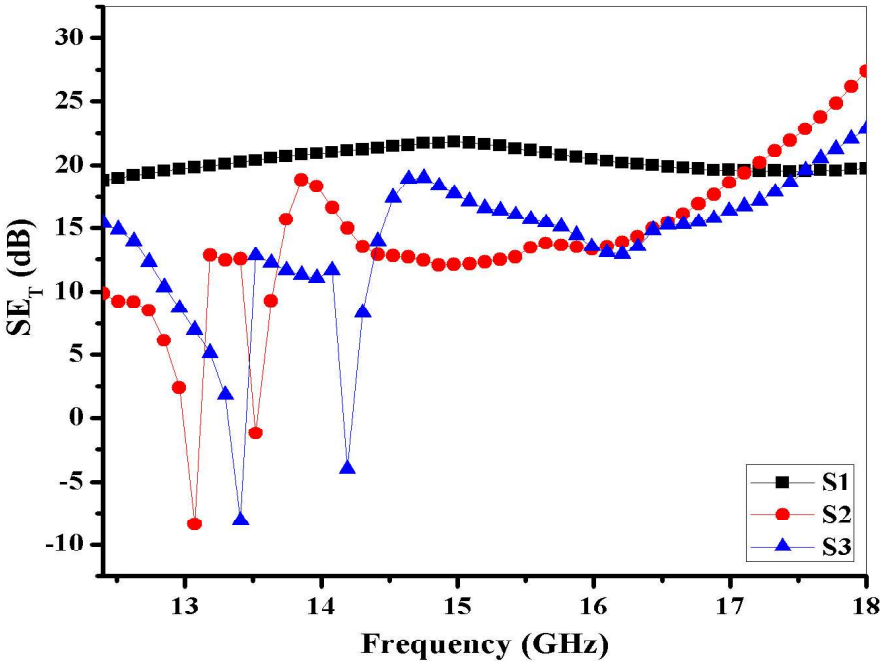

Fig. 4.111 Total shielding effectiveness (SE_T) for $Sr_{1-x}Pr_xFe_{12-y}Co_yO_{19}$ (x=0.0, 0.2, 0.4 and y=0.00, 0.15, 0.35)

4.9 Barium hexaferrites and calcium copper titanate (BaM/CCTO) nanocomposites

4.9.1 XRD analysis

Fig. 4.112 presents the XRD spectra of BaM/CCTO nanocomposite. The presence of well-defined peaks of almost equal intensity indicates the absence of degradation of crystalline structure of the sample [19]. It can be observed from **Fig. 4.112** that the successful formation of BaM/CCTO nanocomposite has been achieved. The major diffraction peaks having *hkl* values (006), (110), (008), (112), (107), (114), (200), (108), (203), (109), (205), (206), (1011), (209) (300), (217), (304), (2011), (220), (2014) and (317) corresponds to hexagonal ferrite. These peaks were compared in accordance with standard JCPDS card number (39-1433) and were found to exhibit single phase crystalline structure of BaM with space group *$P6_3/mmc$*. Traces of secondary phase such a magnetite (α-Fe_2O_3) are completely absent in the sample.

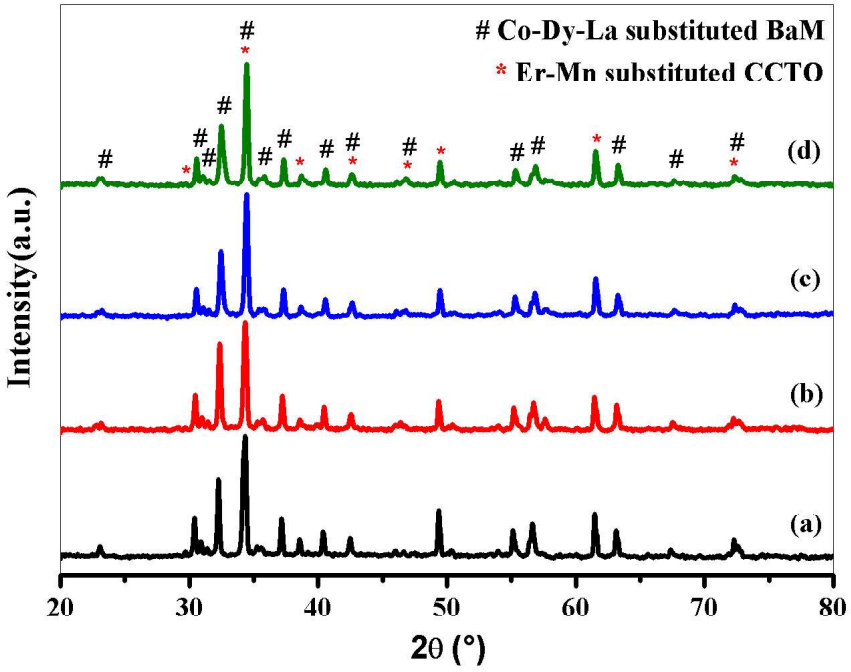

Fig. 4.112 XRD pattern of BaM/CCTO nanocomposite for (a) BaMCCTO1, (b) BaMCCTO2, (c) BaMCCTO3, and (d) BaMCCTO4

The calculation of the lattice parameters was carried out using the XRD pattern, lattice constants (*a* and *c*) were calculated from the following formula

$$\frac{1}{d_{hkl}^2} = \frac{4}{3}\left(\frac{h^2 + hk + k^2}{a^2}\right) + \frac{l^2}{c^2} \tag{4.95}$$

where d_{hkl} is the *d*-spacing between the planes and *hkl* are the miller indices of the peaks in the XRD patterns. The following formula was used to determine the volume of the unit cell (V_{cell}) for the Co-Dy-La substituted BaM

$$V_{cell} = 0.8666\, a^2 c \tag{4.96}$$

In order to calculate the value of the crystallite size (*D*) of the prepared sample from the line broadening of the main peaks, we employ Scherer formula

$$D = \frac{k\lambda}{\beta \cos\theta} \tag{4.97}$$

where, β is the full width at half maximum (in radian), θ is the Braggs angle, k is the shape factor ($k = 1$) and λ is the X-ray wavelength (1.54056 Å). The strain (η) in BaM/CCTO nanocomposite was calculated using the following formula

$$\eta = \frac{\beta\cos\theta - \frac{0.9\lambda}{D}}{2\sin\theta} \tag{4.98}$$

The values of a, c, D, V_{cell} and η for Co^{2+}-Dy^{3+}-La^{3+} substituted BaM are calculated and presented in **Table 4.20**. It can be observed that both the values of a, c, and V_{cell} increases with increase in Co^{2+}-Dy^{3+}-La^{3+} substitution (**Table 4.20**). Variation of a and c depends upon factors such as oxidation state, ionic radii, electron affinity and interaction of atoms with their neighbours [199]. The values of D ranges from 60.14 nm for the undoped sample to 71.45 nm for the doped samples and exhibit a non-uniform behaviour, it first decreases with Co^{2+}-Dy^{3+}-La^{3+} substitution and then increases thereafter (**Table 4.20**). The c/a ratio was found to be in the range 3.942 to 3.950, these values are consistent with the limit set for a sample to exhibit hexagonal structure [188]. Hence, we can assume that the prepared BaM nanoparticles possess hexagonal structure.

Table 4.20 Values of lattice parameters (a and c), crystallite size (D), and volume of unit cell V_{cell} for Co^{2+}-Dy^{3+}-La^{3+} substituted BaM

Sample code	$2\boldsymbol{\theta}$ (°)	d (Å)	$\boldsymbol{\beta}$ (°)	a (Å)	c (Å)	$\boldsymbol{c/a}$	$\boldsymbol{V_{cell}}$ (Å$^{\mathbf{3}}$)	D (nm)	$\boldsymbol{\eta \times 10^{-4}}$
BaM1	30.41	2.936	0.128	5.87	23.15	3.943	692.07	71.45	4.109
BaM2	30.36	2.940	0.166	5.88	23.23	3.950	696.49	55.08	5.338
BaM3	30.31	2.945	0.160	5.89	23.26	3.949	699.83	50.14	7.012
BaM4	30.21	2.955	0.152	5.91	23.30	3.942	705.46	60.14	4.913

Also, the major diffraction peaks having *hkl* values (211), (220), (310), (222), (321), (400), (422), (440), and (620) have been indexed according to JCPDS card number 75-2188 and have been found to exhibit single phase crystalline phase of CCTO having space group *Im-3*. The presence of secondary phases such as CuO and $CaTiO_3$ has not been observed in the sample. The lattice constant (a) and volume of unit cell (V_{cell}) were calculated using

$$a = d_{hkl}\sqrt{h^2 + k^2 + l^2} \quad (4.99)$$

$$V_{cell} = a^3 \quad (4.100)$$

The values of a and V_{cell} for Er^{3+}-Mn^{3+} substituted CCTO are presented in **Table 4.21**. It can be observe that the values of a and V_{cell} increases with increase in Er^{3+}-Mn^{3+} substitution (**Table 4.21**), this could be attributed to increase in concentration of oxygen vacancies in the lattice [332]. The calculated values of a and V_{cell} are in good agreement with literatures [333][99].

Table 4.21 Values of lattice constant (a) and volume of unit cell (V_{cell}) for Er^{3+}-Mn^{2+} substituted CCTO

Sample code	2θ (°)	d (Å)	β (°)	a (Å)	V_{cell} (Å^3)
CCTO1	49.358	1.844	0.147	7.379	401.862
CCTO2	49.308	1.846	0.148	7.386	403.007
CCTO3	49.259	1.848	0.178	7.393	404.158
CCTO4	49.209	1.850	0.172	7.400	405.302

4.9.2 FTIR analysis

FTIR was carried out in order to obtain information regarding the presence of molecular bands and functional groups attached. Typically, transitions between vibrational energy levels of a molecule as a result of absorption of infrared (IR) radiation give rise to the FTIR spectra. **Fig. 4.113** Present the FTIR spectra of BaM/CCTO nanocomposite in the range 400 to 4000 cm^{-1}. The absorption bands at 439 and 592 cm^{-1} are characteristics peaks of both BaM and CCTO and they signify the formation of both BaM and CCTO phase, these bands results from stretching vibration of metal-oxygen bonds [186][332][334][133]. In general, these bands are attributed to vibration of ferric crystallographic sites (octahedral and tetrahedral coordination) in the BaM structure and stretching vibrations of TiO_6 octahedral (Ti-O-Ti) and CuO_4 (Cu-O) in the CCTO structure [335][53]. The absorption band at 1075 cm^{-1} results from the in-plane deformation vibrations of C-H bond [58]. The absorption peak observed at 1447 cm^{-1} could be assigned to medium C-H bending mode [336]. The absorption band at 1656 cm^{-1} could be attributed to OH vibrational mode of absorbed water molecule [337]. A

peak assigned to the presence of CO_2 is observed at 2357 cm^{-1}, this peak result from the asymmetric stretching mode of CO_2 [335]. The –OH stretching vibrational band at 3400 cm^{-1} which usually occur as a result of absorption of moisture from atmosphere was not observed [212].

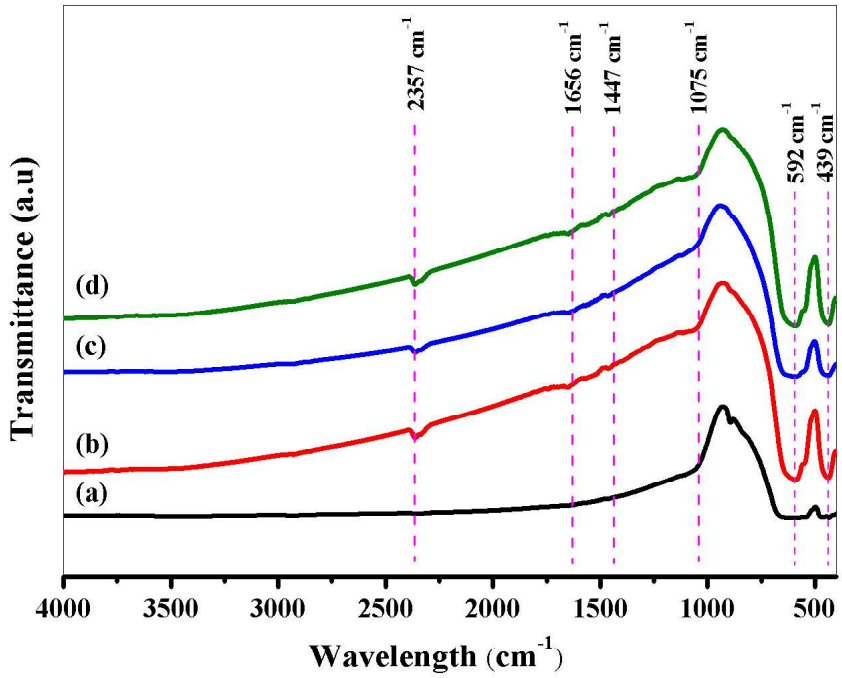

Fig. 4.113 FTIR spectra for BaM/CCTO nanocomposite (a) BaMCCTO1, (b) BaMCCTO2, (c) BaMCCTO3, and (d) BaMCCTO4

4.9.3 Raman spectroscopy

Vibrational transition induced by scattering of light by molecules can be studied using Raman spectroscopy in order to understand compositional structure of nanomaterials. **Fig. 4.114** shows the room temperature Raman spectra for BaM/CCTO nanocomposite in the range 150-800 cm^{-1} using 532 nm laser as the excitation source. Group theory analysis of BaM on the basis of D_{6h} symmetry give rise to 42 Raman active modes [214]. It has been predicted from group theory that the Raman active modes of hexaferrites are distributed in the form of irreducible representation as $11A_{1g} + 14E_{1g} + 17E_{2g}$ [221]. The Raman active modes at 176, 325, 406, 610 and 680 cm^{-1} are characteristics Raman active modes of hexaferrite phase whereas those at 450, 513 and 749 cm^{-1} are for CCTO phase. The Raman active modes at 176

and 325 cm^{-1} are associated with the vibration of S-block as a result of E_{1g} and E_{2g} symmetry. The 406, 610, and 680 cm^{-1} Raman active modes are respectively assigned to vibrations of *12k* octahedral site, *4f2* octahedral site and *2b* bi-pyramidal site as a result of A_{1g} symmetry [191]. The observed Raman active modes further support the XRD analysis by confirming the magnetoplumbite structure of the hexaferrites phase in the BaM/CCTO nanocomposites.

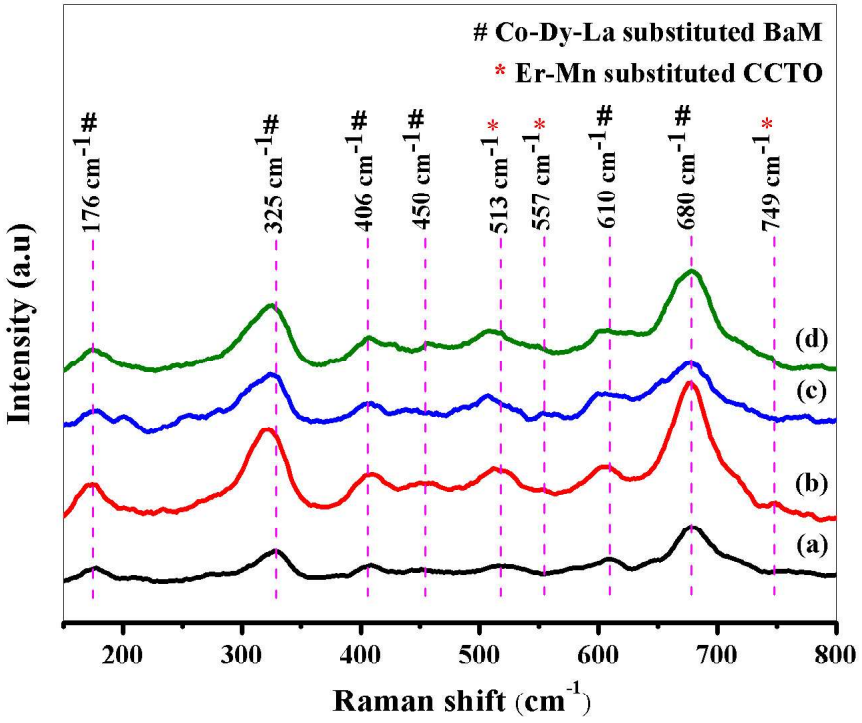

Fig. 4.114 Raman spectra for BaM/CCTO nanocomposite (a) BaMCCTO1, (b) BaMCCTO2, (c) BaMCCTO3, and (d) BaMCCTO4

Similarly, analysis using group theory predicted that Raman active modes of CCTO are distributed as $2A_g + 2E_g + 4F_g$ in the form of irreducible representation [338]. The Raman active mode at 450 and 513 cm^{-1} are associated with TiO_6 rotation-like mode as a result of A_{1g} and A_{2g} symmetry respectively [154][166]. Raman active mode at 575 cm^{-1} associated with F_{3g} symmetry Ti-O-Ti anti-stretching vibration mode of the TiO_6 octahedron was not observed [339][340][166][121]. Raman active modes observed at 749 cm^{-1} is associated with stretching breathing of TiO_6 octahedron as a result of F_{4g} symmetry, this mode may also result from Mn-O-Ti or Mn-O-Mn stretching vibration after the replacement of Ti^{4+} ion by Mn^{2+} ion [338][153], this is further supported by the fact this Raman active mode does not

appear in the un-substituted sample . Raman active modes at 144 cm^{-1} and 249 cm^{-1} corresponding to TiO_2 and CuO secondary phase respectively were not observed [125][341], this further supports the purity of the CCTO phase observed by the XRD analysis in the BaM/CCTO nanocomposites. The effect of the substitution of cation is observed in 325 and 610 cm^{-1} Raman active modes of hexaferrites as well as in 513 cm^{-1} Raman active mode of CCTO. Clearly, these Raman active modes tend to shift towards lower wave number with increase in cation substitution.

4.9.4 Morphology analysis

The surface features and elemental analysis were studied with FESEM, HRTEM, TEM, SAED and EDX. The FESEM images, particle distribution, and EDX spectra of the BaM nanoparticles are shown in **Fig. 4.115**, **4.116**, and **4.117**. The average particle size was found to be 117.98, 110.91, 115.14, and 113.09 nm for the sample BaM1, BaM2, BaM3, and BaM4 respectively; these particles are larger than those calculated from The XRD data. Hence, this contradicts the average particle size calculated from XRD data. This contradiction could be explained as thus, magnetic interaction between the BaM nanoparticles cause them to

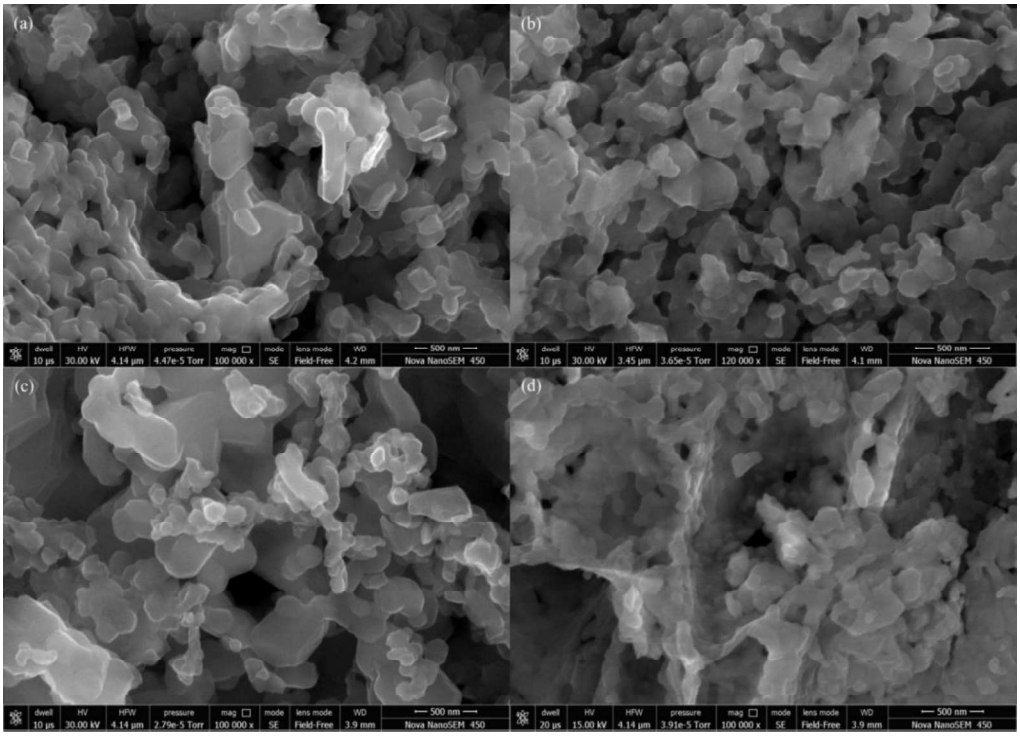

Fig. 4.115 FESEM micrographs of BaM nanoparticles for (a) BaM1, (b) BaM2, (c) BaM3, and (d) BaM4

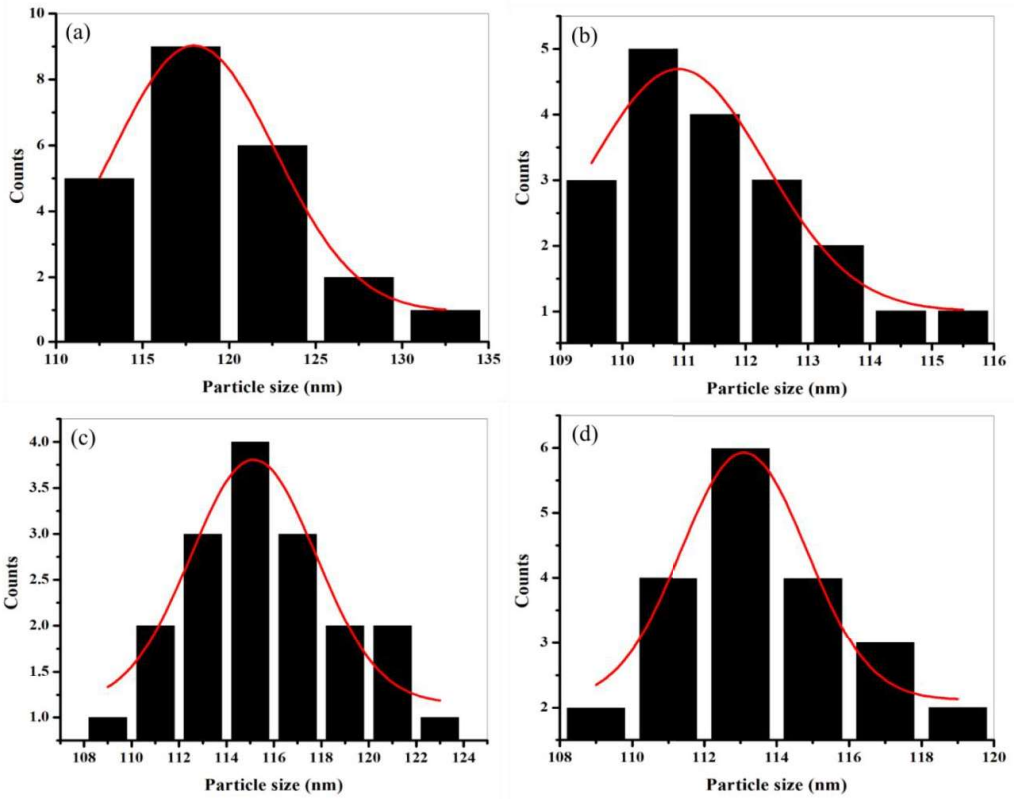

Fig. 4.116 Particle distribution of BaM nanoparticles for (a) BaM1, (b) BaM2, (c) BaM3, and (d) BaM4

agglomerate and form larger aggregate which is clearly evident in the FESEM micrographs (**Fig. 4.115**). Similar observation was made by S. Asiri et al. [200]. The substituted and host cations are clearly observed in the EDX spectra (**Fig. 4.117**); this confirms the stoichiometry and purity of the prepared BaM nanoparticles. The FESEM images, particle distribution, and EDX spectra of the CCTO microparticles are shown in **Fig. 4.118**, **4.119**, and **4.120**. Well defined cubic-shaped particles with the absence of agglomeration can be clearly seen from the FESEM micrographs. The average particle size for the sample CCTO1, CCTO2, CCTO3, and CCTO4 are respectively found to be 0.1485, 0.1564, 0.1541, 0.1482 μm. All the substituted cations and host cations are observed in the EDX spectra (**Fig. 4.120**), this confirms the stoichiometry and purity of the CCTO microparticles.

The FESEM images and EDX spectra of the BaM/CCTO microparticles are shown in **Fig. 4.121** and **4.122**. The sizes of the grains of CCTO nanoparticles are larger than those of BaM nanoparticles as observed from the images. The grains of the BaM nanoparticles exhibit uneven distribution with hexagonal like morphology whereas the CCTO ceramics shows

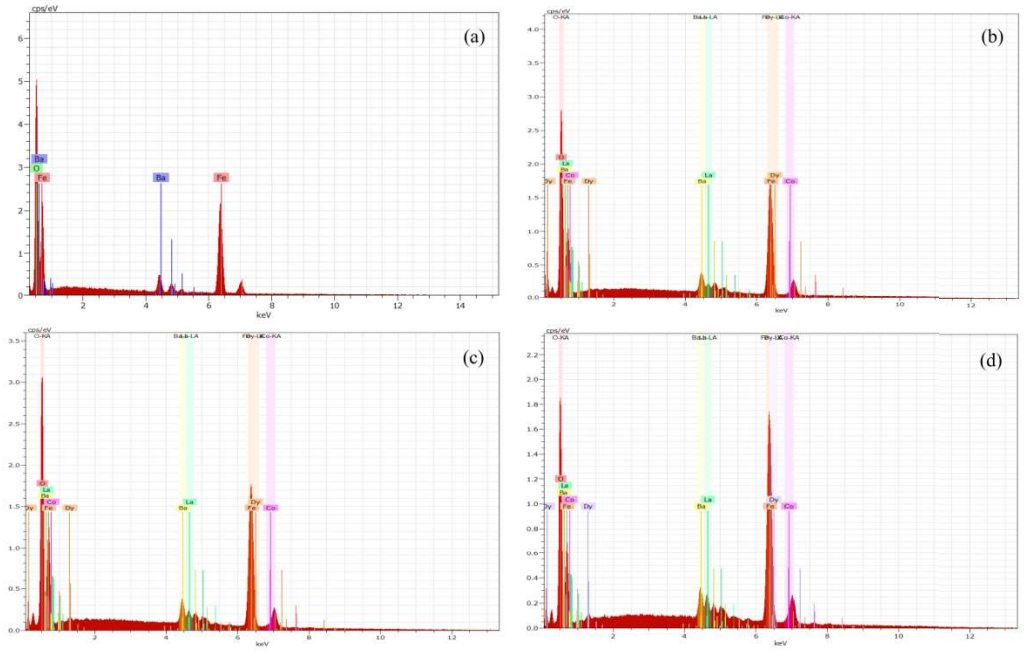

Fig. 4.117 EDX spectra of BaM nanoparticles for (a) BaM1, (b) BaM2, (c) BaM3, and (d) BaM4

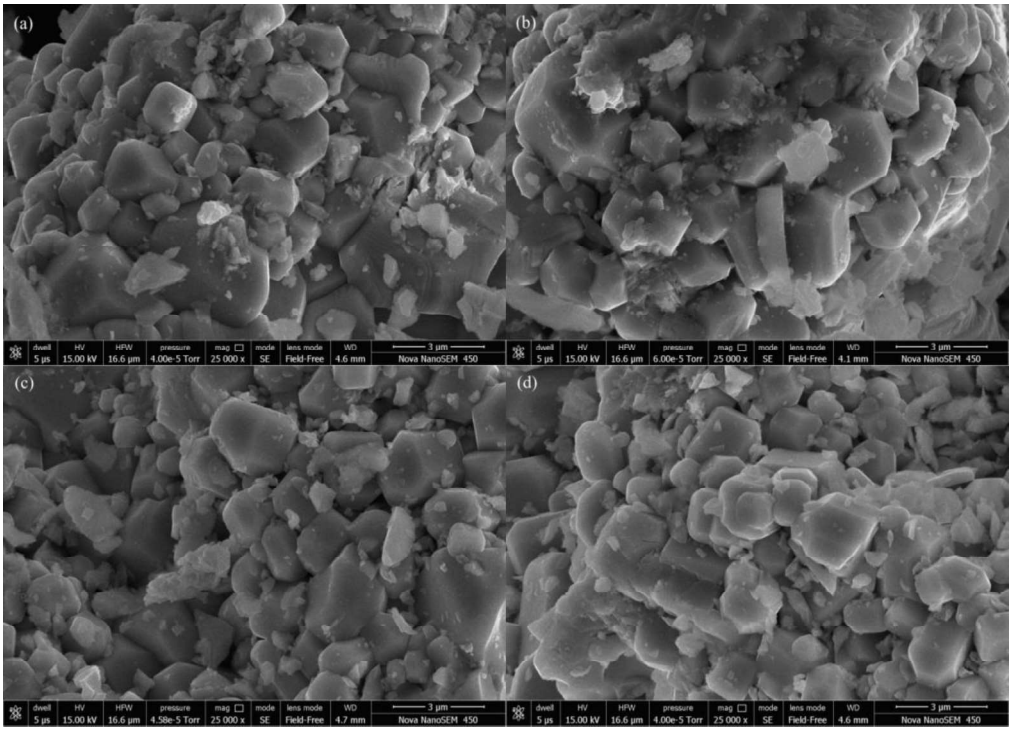

Fig. 4.118 FESEM micrograph of CCTO microparticles for (a) CCTO1, (b) CCTO2, (c) CCTO3, and (d) CCTO4

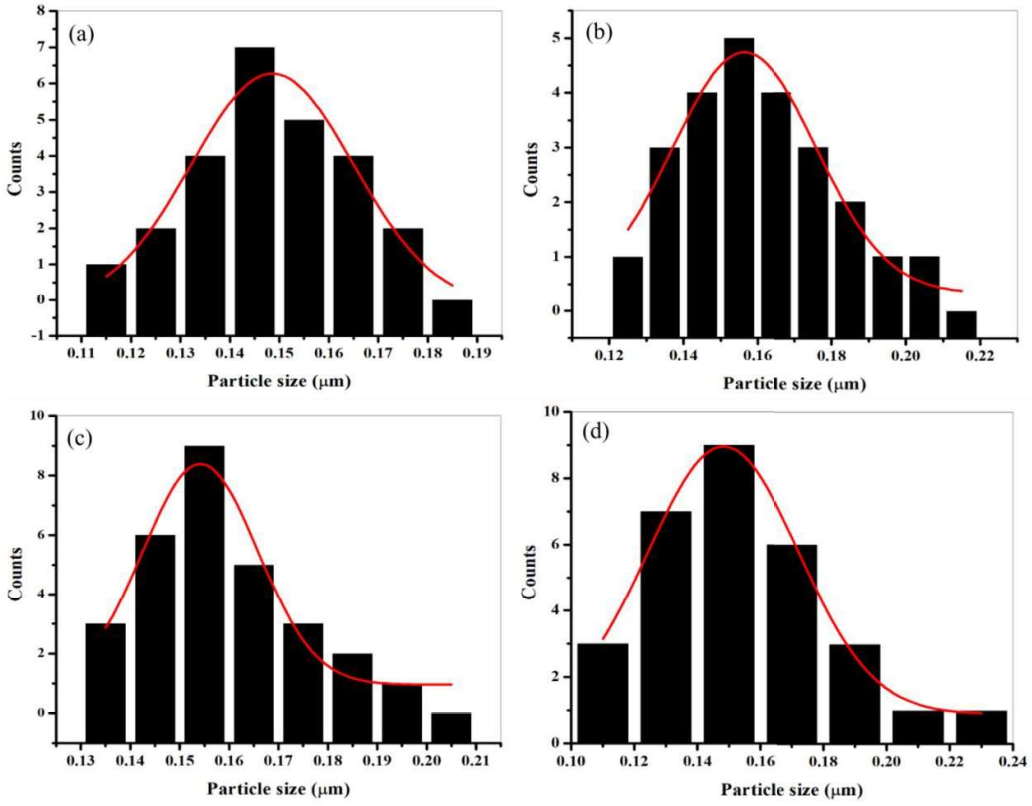

Fig. 4.119 Particle distribution of CCTO microparticles for (a) CCTO1, (b) CCTO2, (c) CCTO3, and (d) CCTO4

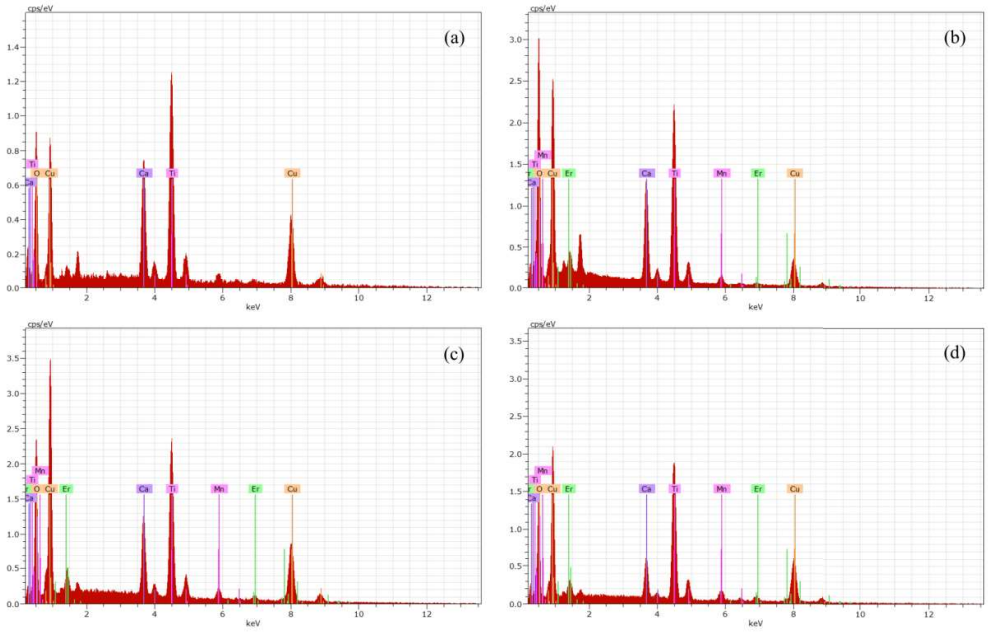

Fig. 4.120 EDX spectra of CCTO microparticles for (a) CCTO1, (b) CCTO2, (c) CCTO3, and (d) CCTO4

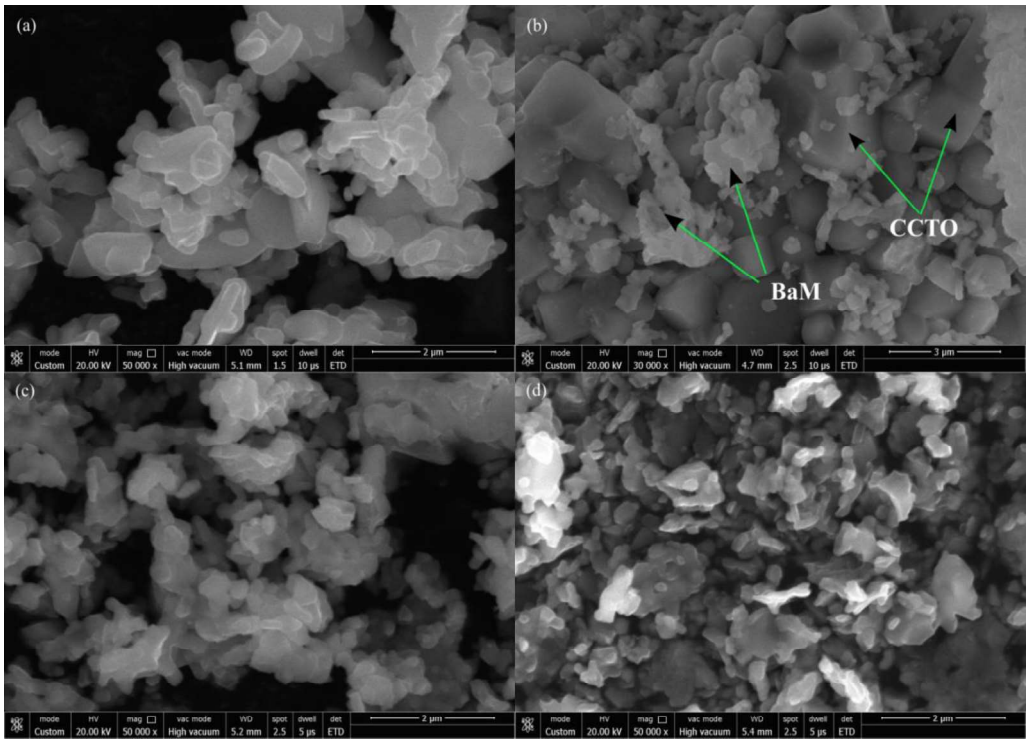

Fig. 4.121 FESEM micrograph of BaM/CCTO nanocomposite (a) BaMCCTO1, (b) BaMCCTO2, (c) BaMCCTO3, and (d) BaMCCTO4

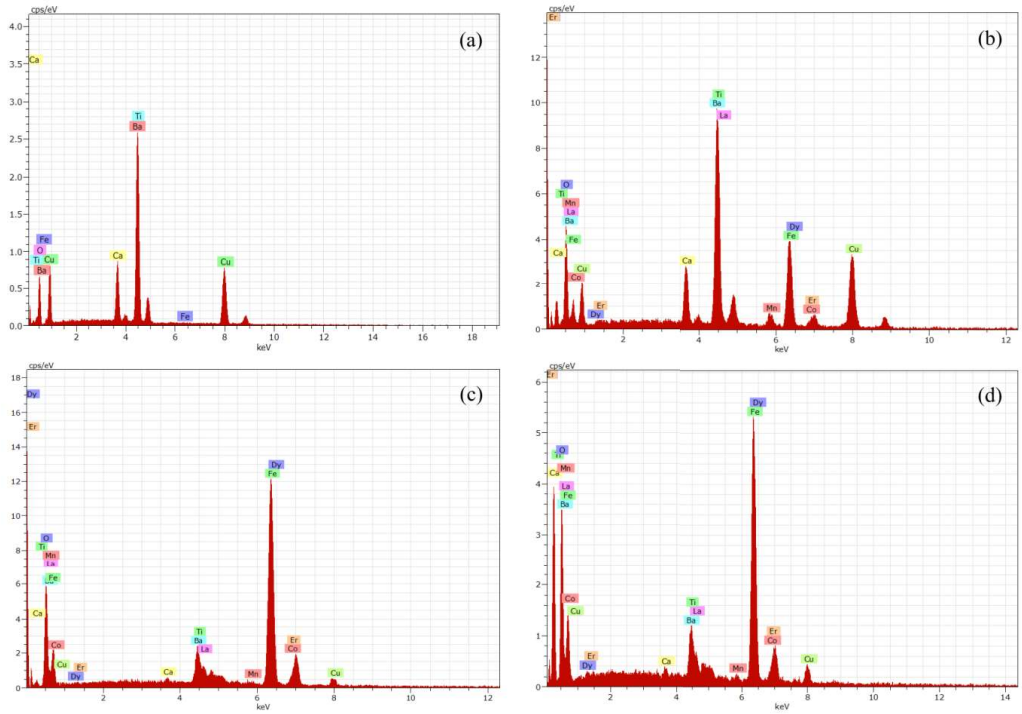

Fig. 4.122 EDX spectra of BaM/CCTO nanocomposite (a) BaMCCTO1, (b) BaMCCTO2, (c) BaMCCTO3, and (d) BaMCCTO4

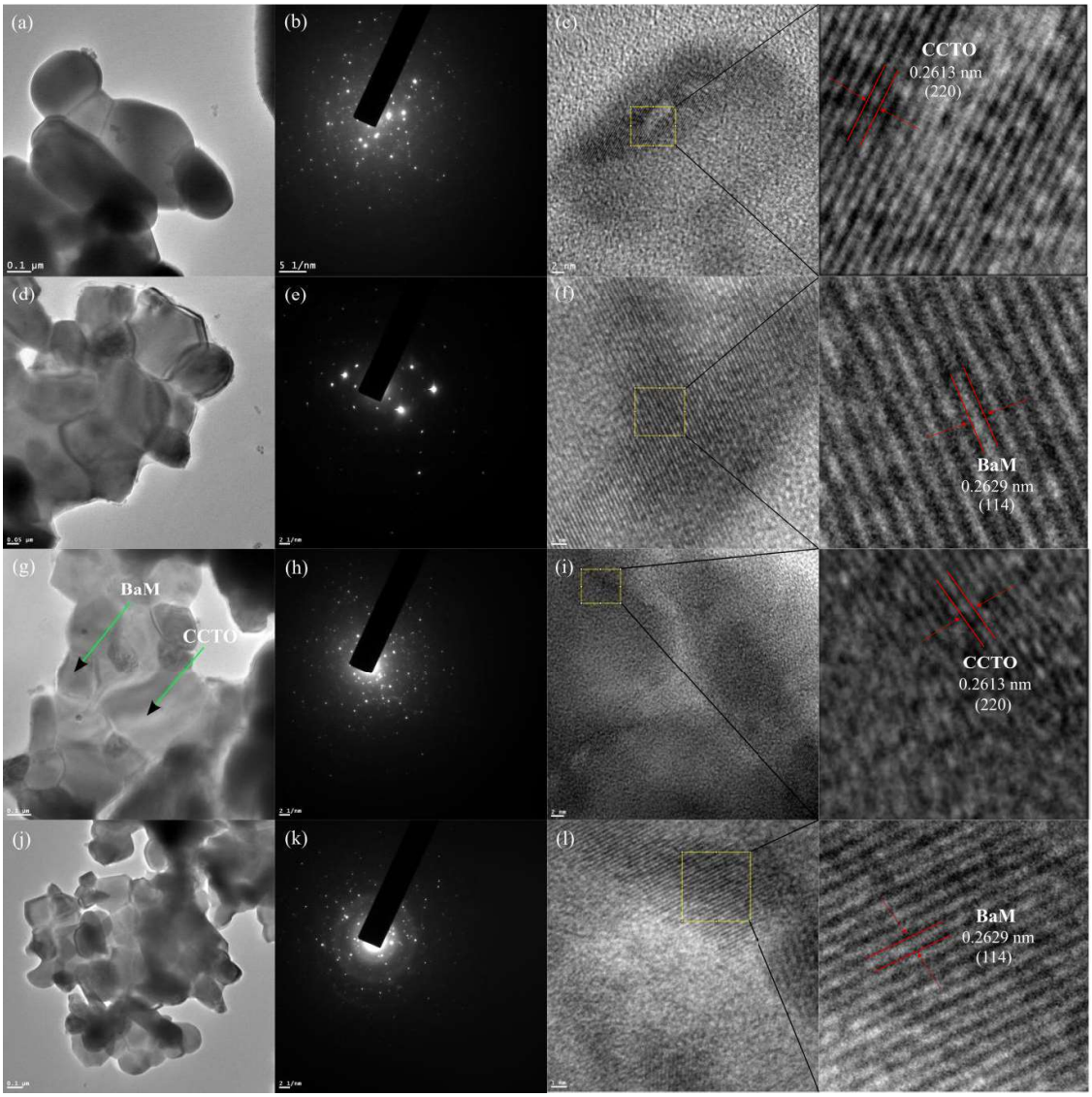

Fig. 4.123 TEM images, SAED patterns, and HRTEM images of BaM/CCTO nanocomposite (a, b, and c) BaMCCTO1, (d, e, and f) BaMCCTO2, (g, h, and i) BaMCCTO3, and (j, k, and l) BaMCCTO4

cubic like grains with homogenous distribution [306]. The process of reduction in surface energy and dipolar interactions between the BaM nanoparticles results in the incorporation of the BaM nanoparticles around the CCTO nanoparticles [332][342].

TEM, HRTEM images and SAED patterns of BaM/CCTO/ nanocomposites are shown in **Fig. 4.123** (a-g). It can be clearly observed that the particles exhibit hexagonal shape and cubic shape corresponding to BaM and CCTO nanoparticles respectively. The HRTEM images shows lattice fringes of BaM and CCTO nanoparticles with size of 0.2629 and 0.2613

nm corresponding to (114) and (220) hkl planes respectively [343]. The polycrystalline nature of the prepared samples is supported by the appearance of bright diffraction spots in the SAED pattern even though individual diffraction rings of BaM and CCTO nanoparticles are not observed as a result of inter-particles interaction. As seen from the EDX spectra, all the substituted elements are observed in the BaM/CCTO nanocomposite. This further confirms the purity of the BaM/CCTO nanocomposite.

4.9.5 Optical analysis

UV-vis spectroscopy utilises the energy of a photon of an incident radiation to excite an electron from the valence to conduction band. The optical analysis of BaM/CCTO nanocomposite was carried out via UV-visible-NIR spectroscopy in the wavelength region 200-800 nm. The optical band gap (E_g) was evaluated using the following relation [186]

$$\alpha h\upsilon = A\left(h\upsilon - E_g\right)^n \tag{4.101}$$

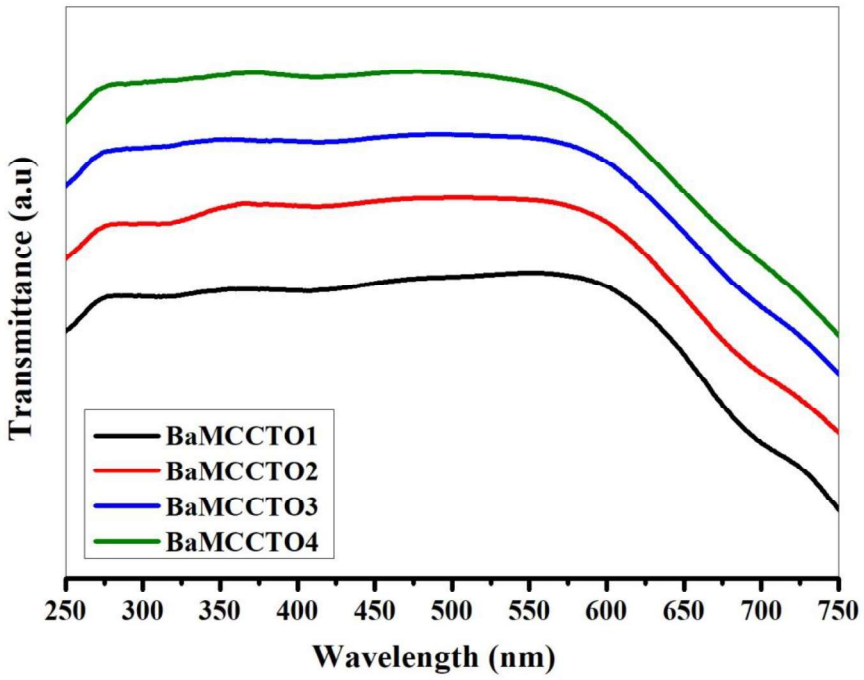

Fig. 4.124 Variation of transmittance versus wavelength for BaM/CCTO nanocomposite

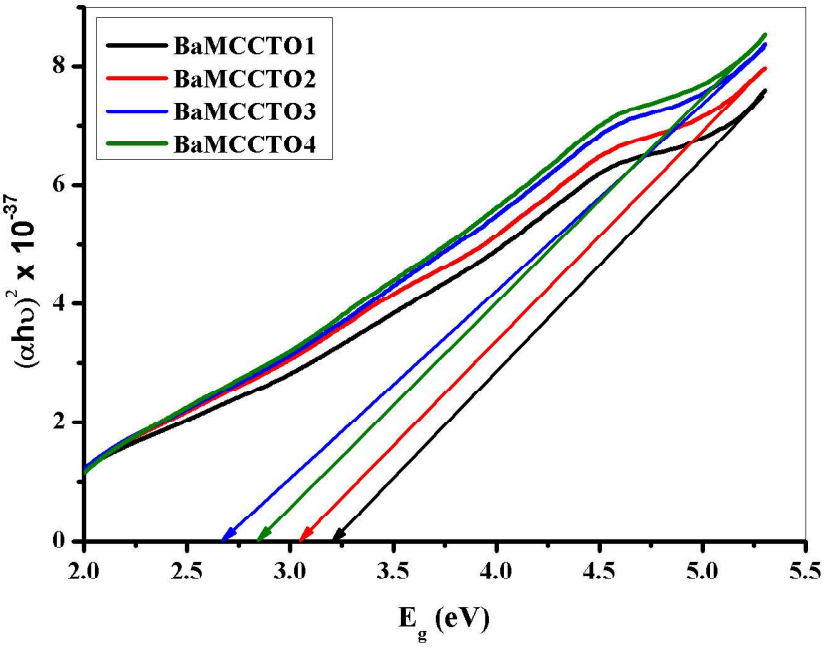

Fig. 4.125 Optical band-gap for BaM/CCTO nanocomposite

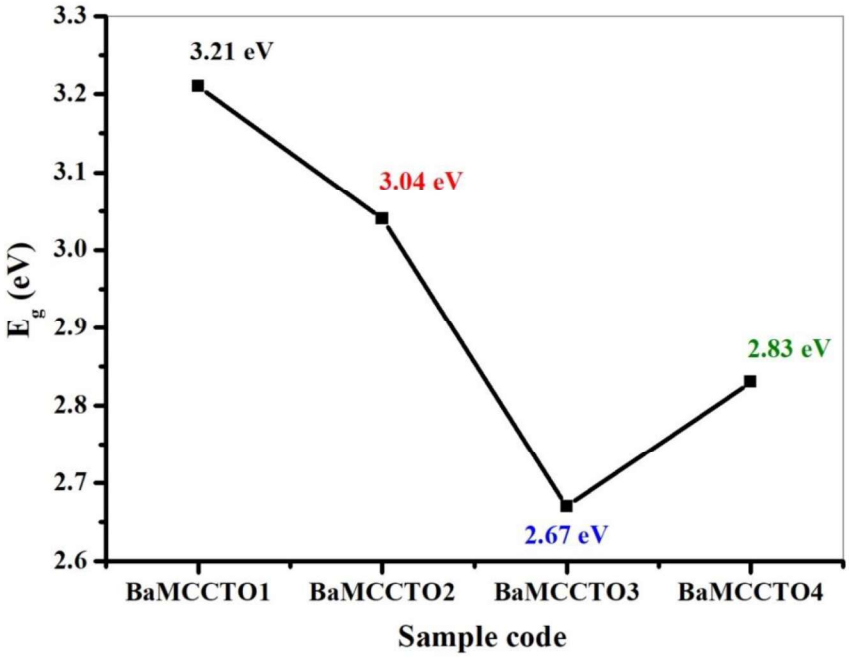

Fig. 4.126 Variation of optical band-gap with composition

Where α is the absorption coefficient, h is the planks constant ($6.6260 \times 10^{-34}\ J.s$), υ is the frequency of incident photon and A is a characteristics constant that depends on n. For allowed direct, forbidden direct, allowed indirect and forbidden indirect transitions, the values of n are respectively 1/2, 3/2, 2 and 3. Hence, the band-gap in this case is direct band-gap since $n = 1/2$. The prepared BaM/CCTO nanocomposite shows absorption in UV and visible region (**Fig. 4.124**); it can be observed that the absorption region of the BaM/CCTO nanocomposite is from 275 to 600 nm. Similar absorption region was obtained for Nd-Co doped hexaferrite [199]. **Fig. 4.125** shows the graph of E_g of the BaM/CCTO nanocomposite; the values of E_g of each of the BaM/CCTO nanocomposites were evaluated by extrapolating the linear part of **Fig. 4.125**. The observed values of E_g were found to be 3.21, 3.04, 2.67 and 2.83 eV. Clearly, E_g decreases with variation in composition (**Fig. 4.126**), it has been observed that E_g rely on the size of the crystallites. In actuality, E_g is directly proportional to the sizes of the crystallite [162], this claim had been verified in our analysis of the structural and optical properties of the BaM/CCTO nanocomposites. A closer look at **Fig. 4.126**, **Table 4.20** and **4.21** reveals that E_g and crystallite size show similar behaviour with variation in composition of the BaM/CCTO nanocomposites i. e. they both decrease with composition from BaMCCTO1 to BaMCCTO3 and increases at BaMCCTO4. Hence, the calculated values of crystallite size support the values of the obtained band-gap. S. Asiri *et al.* reported that reduction in quantum confinement as a result of large crystallite sizes are the reason for variation of E_g in hexaferrites [200]. The obtained values of E_g are within the range of those obtained for light sensor in camera and satellite technology [344].

4.9.6 Magnetic analysis

Fig. 4.127 presents the *M-H* hysteresis loop for BaM/CCTO nanocomposite at room temperature. The values of coercivity (H_c), remnant magnetization (M_r), saturation magnetisation (M_s) and anisotropy constant (K) were calculated from the M-H hysteresis loop and presented in **Table 4.22**. As stated in Stoner-Wohlfarth single domain theory, the magnetocrystalline anisotropy energy of a single domain nanocrystalline material can be express as [185]

$$E_A = KVsin^2\theta \tag{4.102}$$

Where V is the volume of the nanocrystal, θ is the angle between the easy axis and the direction of magnetization induced by the applied field, and K is the anisotropy constant which is expressed as

$$K = \frac{\mu_0 M_s H_c}{2} \tag{4.103}$$

Where $\mu_0 = 4\pi \times 10^7\, H/m$ is the permeability in vacuum, M_s is the saturation magnetisation, and H_c is the coercivity. It has been observed that CCTO influences the magnetic properties although it is nonmagnetic in nature. The observed values of magnetic parameters for the BaM/CCTO nanocomposites are lower than those obtained for BaM [186]. BaMCCTO2 exhibit the highest values of M_r and M_s, i.e. 15.936 and 25.687 emu/g

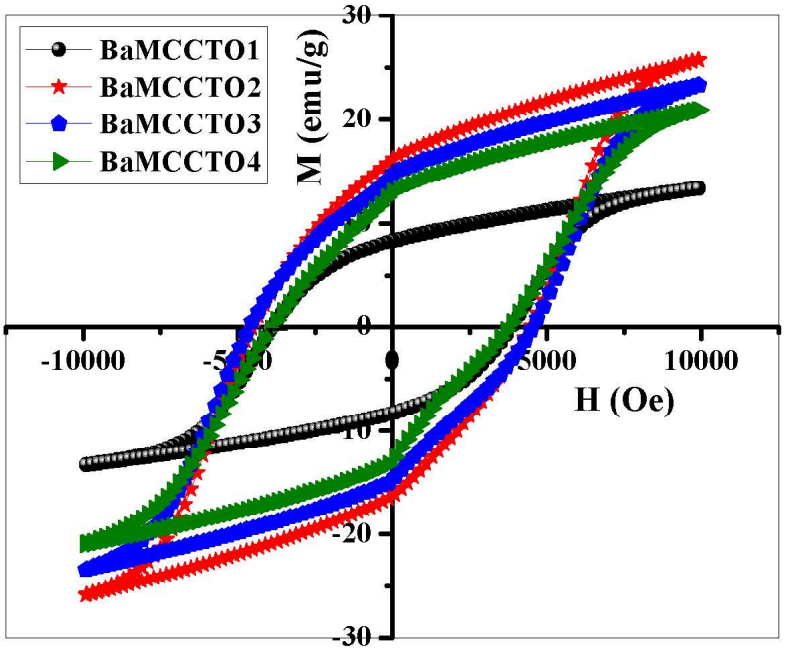

Fig. 4.127 *M-H* hysteresis loop for BaM/CCTO nanocomposite

respectively. Both M_r and M_s initially increase initially up to BaMCCTO2 but later decreases for the rest of the samples. Spin canting, cation distribution and tangled surface layer have been observed to be influenced by particle size and consequently influenced M_s. Hence, the decreased in M_s could be attributed to reduced particle size [345]. Coercivity

shows and increasing trend up to BaMCCTO3 and reduces thereafter. It has been reported that the domain wall motion might be altered by the area of grain boundary having disordered arrangement of atoms thereby increasing the coercivity of the prepared samples [346]. The presence of CCTO phase may also hinder the domain wall motion resulting in increased coercivity [332].

Table 4.22 Coercivity (H_c), remnant magnetization (M_r), saturation magnetization (M_S), squareness ratio (SR), anisotropy constant (K) for BaM/CCTO nanocomposite

Sample code	$\boldsymbol{H_c}$ (Oe)	$\boldsymbol{M_r}$ (emu/g)	$\boldsymbol{M_s}$ (emu/g)	$\boldsymbol{SR}$ ($\boldsymbol{M_r}$ /$\boldsymbol{M_s}$)	$\boldsymbol{K}$ (HA^2/kg)
BaMCCTO1	3986.854	8.202	13.302	0.617	2.652
BaMCCTO2	4564.972	15.936	25.687	0.620	5.863
BaMCCTO3	4646.755	14.391	23.337	0.639	5.422
BaMCCTO4	3892.179	12.746	20.941	0.609	4.075

4.9.7 Microwave absorption analysis

In accordance with the EM energy conversion principle, the attenuation and reflection properties of EM wave absorbers are determined from the complex permittivity (ε^*), complex permeability (μ^*) which are given in equation (11) and (12) respectively [347]

$$\varepsilon^* = \varepsilon' - j\varepsilon'' \tag{4.104}$$

$$\mu^* = \mu' - j\mu'' \tag{4.105}$$

where $j = -1$ is a complex number, ε' is the real part of complex permittivity, ε'' is the imaginary part of complex permittivity, μ' is the real part of complex permeability and μ'' is the imaginary part of complex permeability. The dielectric loss tangent ($\tan\delta_\varepsilon$) and magnetic loss tangent ($\tan\delta_\mu$) which respectively measures the attenuation of the electric field and magnetic field by the EM wave absorber is written as

$$\tan\delta_\varepsilon = \frac{\varepsilon''}{\varepsilon'} \tag{4.106}$$

$$\tan\delta_\mu = \frac{\mu''}{\mu'} \tag{4.107}$$

Where δ_ε is the dielectric loss angle and δ_μ is the magnetic loss angle, high value of δ_ε and δ_μ implies high attenuation of the wave as it moves through the EM wave absorber. Hence,

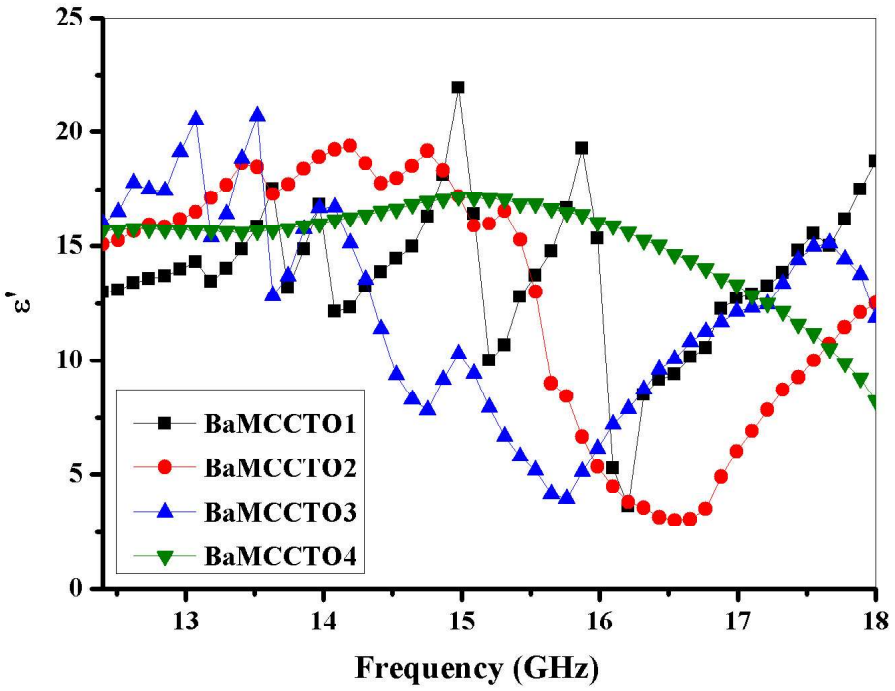

Fig. 4.128 Real part of complex permittivity against frequency for BaM/CCTO nanocomposite

both components of ε^* and μ^* contribute to the compression of EM wave inside the material. Additionally, due to the coupled EM wave, loss in either the magnetic or electric field will attenuate the energy of the EM wave. In most absorbers, both ε^* and μ^* are functions of frequency and can vary significantly over even a small frequency range. Hence, if ε^* and μ^* are known over a certain frequency range, then the effect of the EM wave absorber on the EM wave can be quantified. Also, the overall attenuation ability of material can be determine from the nature of the total loss tangent ($\tan\delta_T$) which is given as

$$\tan\delta_T = \tan\delta_\varepsilon + \tan\delta_\mu \qquad (4.108)$$

The electric energy storage ability and dissipation of the prepared nanocomposites are respectively determined by the nature of ε' and ε'' [348]. **Fig. 4.128** and **4.129** respectively represents ε' and ε'' as a function of frequency. Regular pattern of variation in ε' and ε'' with frequency have not been observed in all the plots. Several resonance peaks have been observed at lower and intermediate frequencies in the plot of ε' for all the nanocomposites.

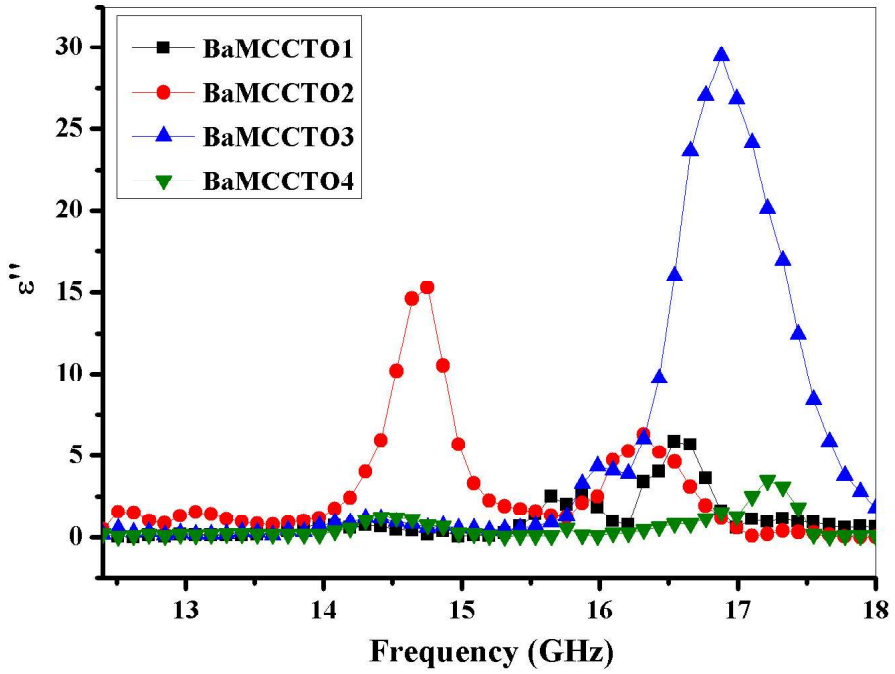

Fig. 4.129 Imaginary part of complex permittivity against frequency for BaM/CCTO nanocomposite

Usually, electrical conductivity and polarization in a dielectric material are associated with the nature of ε' and ε'' [349]. High values of ε' are observed in all the nanocomposites which seems to fluctuate with increase in frequency. All the nanocomposites shows increase in ε' at higher frequencies (above 16.5 GHz) except for the sample BaMCCTO4 which seems to decrease from 16 to 18 GHz. The decrease in the values of ε' at higher frequencies results when the induced charges in the nanocomposites lag behind the applied EM field [350]. In the BaM/CCTO nanocomposites, low resistive grains are separated by highly resistive grains boundaries; this scenario induces interfacial polarization and thus increased the values of ε' are observed [58]. The ability of the prepared nanocomposites to store and dissipate magnetic energy is determined by μ' and μ'' respectively. **Fig. 4.130** and **4.131** shows the plot of μ' and μ'' as a function of frequency respectively. The graphs show no regular pattern with some resonance peaks which mostly appear at intermediate and higher frequencies. The decreasing manner of μ' and μ'' after the relaxation at higher frequencies could be attributed to skin effect as a result of eddy current effects [351].

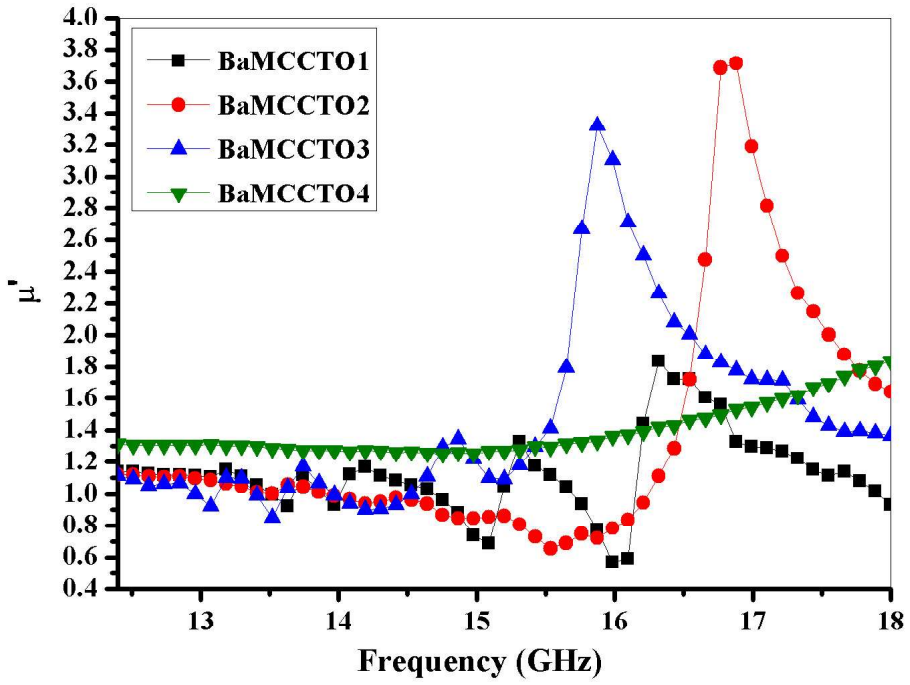

Fig. 4.130 Real part of complex permeability against frequency for BaM/CCTO nanocomposite

Variation of tan δ_ε and tan δ_μ as a function of frequency are respectively given in **Fig. 4.132** and **4.133**. Both the graph of tan δ_ε and tan δ_μ exhibit resonance peaks, the resonance peaks observed in the graph of tan δ_μ could be attributed to surface effect, small size effect and spin wave excitation of the BaM nanoparticles [352]. The most intense of tan δ_ε resonance peak occur in the sample BaMCCTO3 whereas that of tan δ_μ can be observed in the sample BaMCCTO4. It can be observed that in the frequency range 14.5 to 18 GHz, the values of tan δ_ε are greater than those of tan δ_μ, this statement is further supported by the observation from **Fig. 4.129** and **4.131** where the values of ε'' are much greater than those of μ''. Additionally, it is worthy to note that by comparing **4.128** and **4.130**, we can observe that the values of ε' are much greater than the values of μ', this is as a result of the excellent dielectric properties of CCTO nanoparticles. Hence, it is safe to conclude that most of the microwave absorption properties of the nanocomposites mainly occur due to dielectric losses [353][354]. The total tangent loss (tan δ_T) of the BaM/CCTO nanocomposite shows similar behaviour to

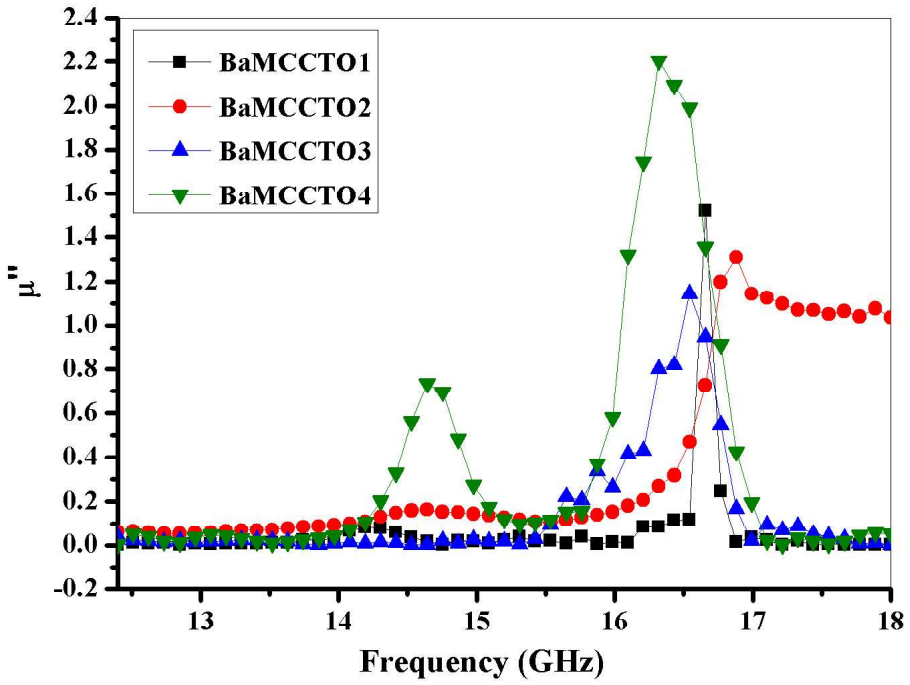

Fig. 4.131 Imaginary part of complex permeability against frequency for BaM/CCTO nanocomposite

$\tan \delta_\varepsilon$ and $\tan \delta_\mu$ i. e. several resonance peaks evolve over the whole frequency range (**Fig. 4.134**). The theory of polarization by Maxwell-Wagner propose that interfacial polarization prompt the appearance of virtual charges at the interface of the prepared sample which may comprise of materials having different conductivity and permittivity [355]. In our case, the nanoparticles of BaM and CCTO exhibit difference conductivity and permittivity, hence, interfacial polarization occurs. Generally, factors such as resonance of domain wall, magnetic hysteresis losses, effect of eddy current, exchange resonance and natural resonance are the main reason behind the appearance of magnetic loses. Domain wall resonance of hexaferrites usually appears at lower frequencies (< 1 GHz) and in multi-domain materials only, therefore no magnetic loss arise from this effect in our case. Magnetic hysteresis loss results basically when the applied EM field vector moves ahead of the magnetization vector, this is negligible for hexaferrites in the frequency range 2 to 18 GHz. Similarly, we can rule out contribution from magnetic hysteresis loss [321].

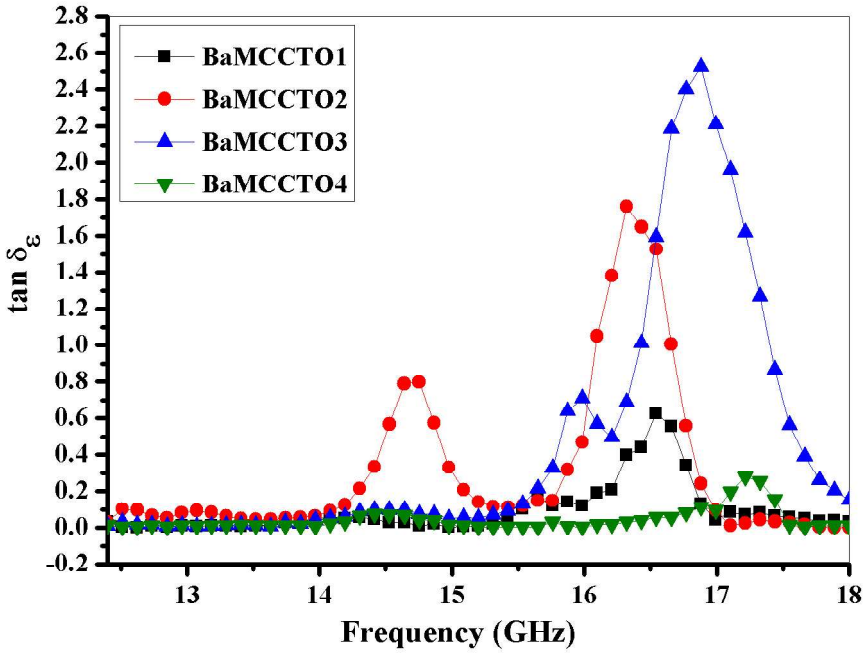

Fig. 4.132 Dielectric tangent loss against frequency for BaM/CCTO nanocomposite

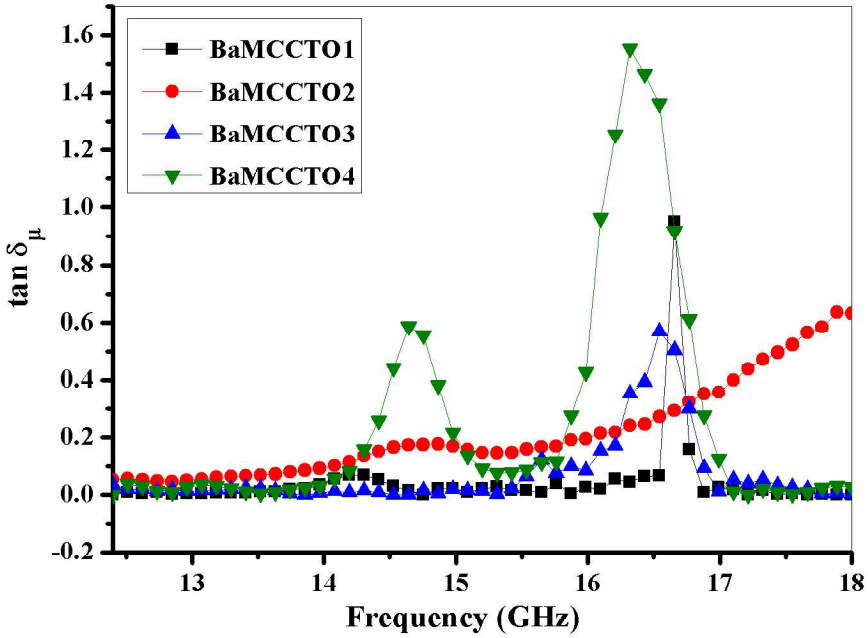

Fig. 4.133 Magnetic tangent loss against frequency for BaM/CCTO nanocomposite

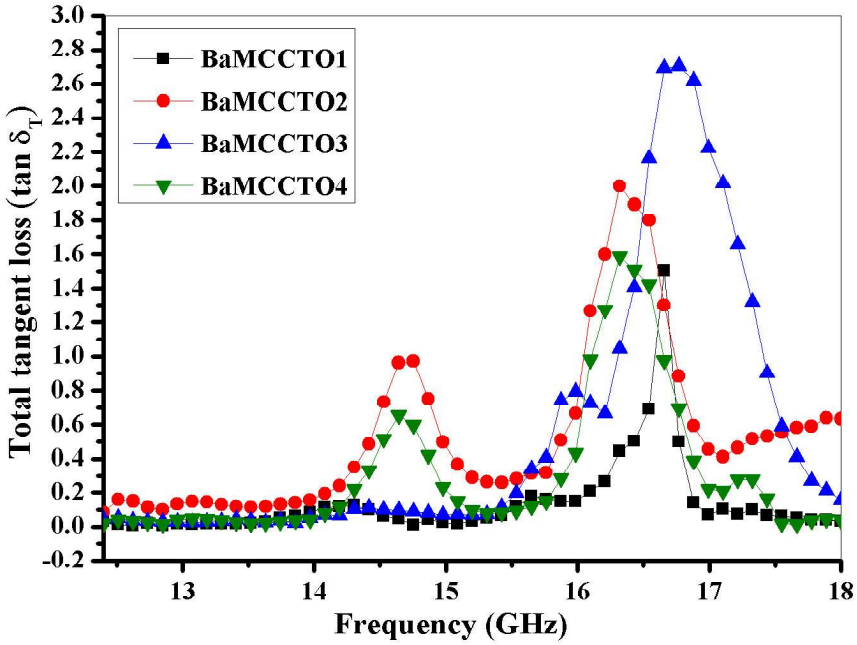

Fig. 4.134 Variation of total tangent loss against frequency for BaM/CCTO nanocomposite

The magnetic loss as a result of eddy current effect is described by the relation [356]

$$C_0 = \mu''(\mu')^{-2} f^{-1} = 2\pi\mu_0\sigma t \qquad (4.109)$$

Where μ_μ is the permeability of vacuum, σ is the conductivity and t is the thickness of the absorber. According to the skin-effect criterion, the plot of C_0 versus frequency (**Fig. 4.135**) should be constant and independent of frequency if the magnetic losses only occur as a result of eddy current effects [349][357]. However, C_0 remain almost constant at lower, intermediate and much higher frequencies for all the nanocomposites except for the nanocomposite with code BaMCCTO2. Hence, the contribution from eddy current effect to the magnetic losses exists in the said regions. At higher frequencies (between 16 and 17 GHz), resonance peaks are observed in all the nanocomposites. This resonance peaks could be exchange resonance or natural resonance. However, exchange resonances are usually observed at higher frequencies than natural resonance in accordance with Aharoni's theory. Hence, the resonance peaks observed between 16 and 17 GHz in all the nanocomposites could be ascribed to exchange resonance [24][16]. Thus, it is safe to conclude that the overall magnetic losses of the BaM/CCTO nanocomposites arise from both eddy current effect and exchange resonance.

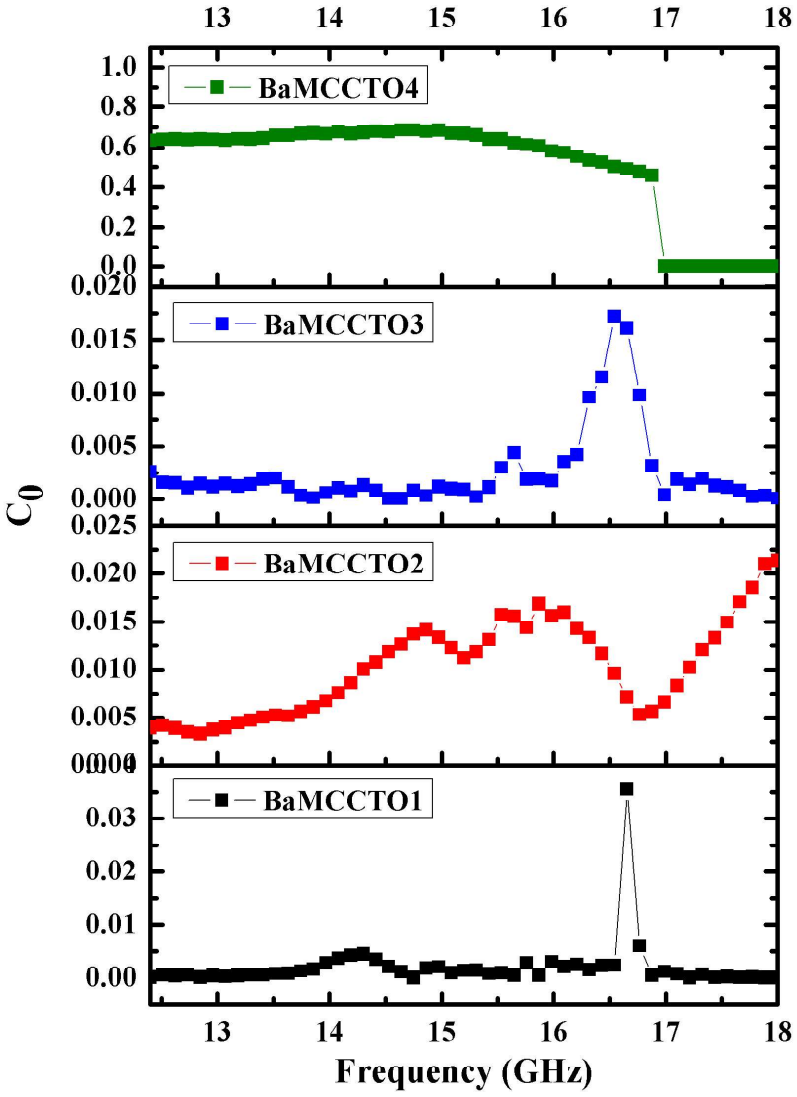

Fig. 4.135 Variation of C_0 against frequency for BaM/CCTO nanocomposite

According to the transmission line theory, the reflection loss (RL) of an EM wave absorber can be calculated from the parameters of the EM wave at a given frequency and thickness of the absorber material via the following relation [358]

$$RL(dB) = 20\log\left|\frac{Z_{in} - Z_0}{Z_{in} + Z_0}\right| \tag{4.110}$$

Where Z_{in} is the input impedance at the materials interface and Z_0 is the characteristics impedance of free space which are respectively given in equation (4.111) and (4.112)

$$Z_{in} = Z_0\sqrt{\frac{\mu^*}{\varepsilon^*}}\tanh\left(j\frac{2\pi ft}{c}\right)\sqrt{\mu^*\varepsilon^*} \quad (4.111)$$

$$Z_0 = \sqrt{\frac{\mu_0}{\varepsilon_0}} \quad (4.112)$$

Where t is the measure of the thickness of the prepared rectangular pellet sample, f is the frequency of the incident EM wave, c is the velocity of EM wave in free space. The best microwave absorbance properties can be achieved when the impedance matching condition ($Z_0 = Z_{in}$) is satisfied [359]. The impedance matching condition is an important function of t and RL usually changes with change in t [231], thus t is a determining factor for the microwave absorption properties of an EM wave absorber. **Fig. 4.136** represents the RL of BaM/CCTO nanocomposite in the frequency range 12.4 to 18 GHz (K_u band) with matching thickness of 3 mm. Distinct patterns of RL can be observed at varying frequencies in all the synthesized samples with the highest RL (-27.9 dB) observed in BaMCCTO4. Comparison of this reflection loss with those obtained for different nanocomposites is presented in **Table 4.23**; we can see that the BaM/CCTO nanocomposite is a better EM wave absorber. The proper matching between ε' and μ' as a result of interaction between BaM and CCTO nanoparticles coupled with enhanced dielectric losses of CCTO are the main reason for the observed highest RL in the BaM/CCTO nanocomposites [332]. Magnetic losses as a result of eddy current effect and exchange resonance also contribute to the RL. Also, when an EM wave is incident on the surface of an EM wave absorber, standing waves appear on the air-absorber interface as a result of phase matching between the incident and reflected EM waves thereby increasing the RL [342]. **Table 4.24** gives the summary of the values of the RL observed in all the samples, all the synthesized samples shows at least one reflection peak with RL less than -10 dB. Generally, a microwave absorber is considered to be efficient and for possible practical application if its reflection loss is less than -10 dB [16][360]. In all the prepared samples, the sample BaMCCTO4 shows maximum reflection loss of -27.9 dB (99.83 % absorption) at a frequency of 16.5 GHz and matching thickness of 3 mm. For the same sample, the bandwidth of effective absorption (reflection loss less than -10 dB) is 1.7 GHz (between 15.7 and 17.4). Also, the sample BaMCCTO1 exhibits a maximum reflection

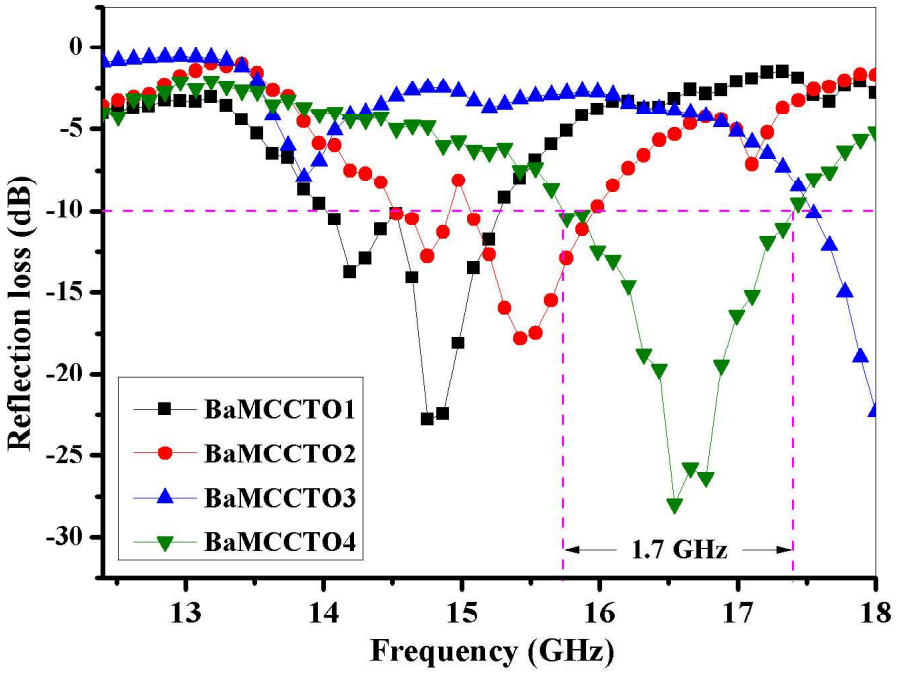

Fig. 4.136 Variation of reflection loss with frequency for BaM/CCTO nanocomposite

Table 4.23 Reflection loss (RL), effective absorption ($RL \leq -10\ dB$), and bandwidth of effective absorption of BaMCCTO1, BaMCCTO2, BaMCCTO3, and BaMCCTO4

Sample code	Frequency (GHz)	Reflection loss ($\boldsymbol{RL}$) (dB)	Effective absorption ($\boldsymbol{RL \leq -10\ dB}$)	Bandwidth of effective absorption (GHz)
BaMCCTO1	14.7	−22.8	−22.8	0.7
	14.1	−13.7	−13.7	0.5
	17.6	−3.3	–	–
BaMCCTO2	14.7	−12.7	−12.7	0.4
	14.4	−17.7	−17.7	0.9
	17.1	−7.1	–	–
BaMCCTO3	13.8	−7.9	–	–
	15.2	−3.6	–	–
	18.0	−22.3	−22.3	0.6
BaMCCTO4	16.5	−27.9	−27.9	1.7

Table 4.24 Comparison of the maximum reflection loss (RL_{max}) with thickness (t) of some microwave absorbers

Composites	Pellet thickness ($\boldsymbol{t}$) (mm)	Maximum reflection loss ($\boldsymbol{RL_{max}}$) (dB)	Frequency (GHz)	Ref.
Barium hexaferrite and polyaniline nanocomposites	2	−23.10	17.9	[53]
Barium hexaferrite, barium titanate and polypyrrole nanocomposites	2	−14.23	16.09	[58]
Polypyrrole and cobalt nanocomposites	3	−20.0	13.8	[359]
CoNi/nitrogen-doped graphene nanocomposites	2	−22.0	12.6	[361]
Fe_3O_4/polypyrrole/carbon nanotube nanocomposites	3	−25.9	10.2	[362]
Hollow glass microspheres coated with $CoFe_2O_4$	1.5	−8.3	18.0	[363]
Fe_3O_4/graphene nanocomposites	5	−23.0	4.0	[351]
SrM/CCTO/rGO nanocomposites	2	−16.0	18.0	[364]
Multi-walled carbon nanotube/doped barium hexaferrite nanocomposites	2.1	−23.1	6	[56]
Multi dopant barium hexaferrite nanoparticles	3.3	−14.4	8.5	[365]
BaM/CCTO nanocomposites (BaMCCTO1)	3	−22.8	14.7	This work
BaM/CCTO nanocomposites (BaMCCTO3)	3	−22.3	18.0	This work
BaM/CCTO nanocomposites (BaMCCTO4)	3	−27.9	16.5	This work

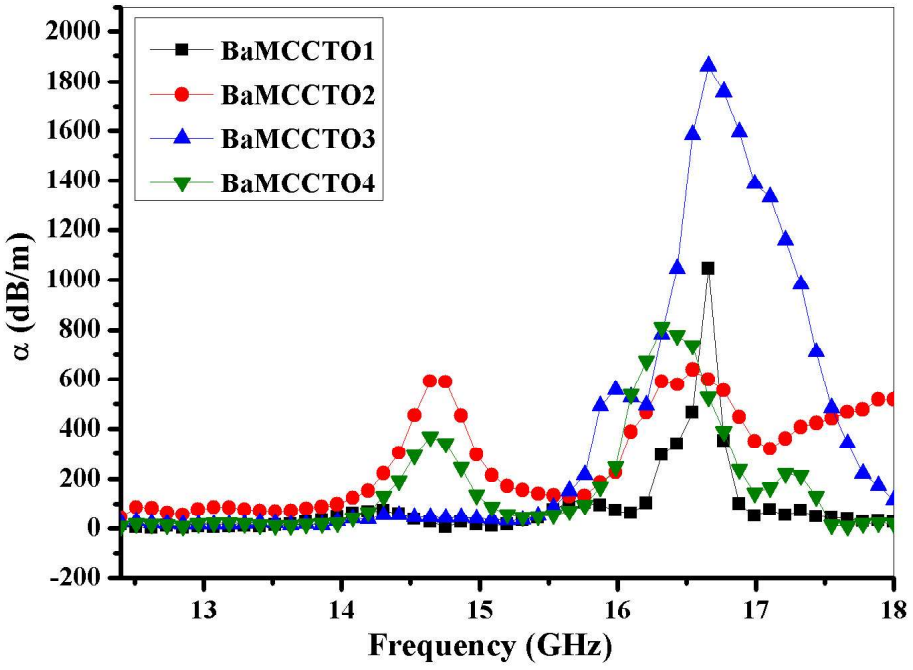

Fig. 4.137 Variation of attenuation coefficient with frequency for BaM/CCTO nanocomposite

loss of −22.8 dB (99.47 % absorption) at a frequency of 14.7 GHz with bandwidth of effective absorption (reflection loss less than −10 dB) of 0.7 GHz (between 14.0 and 15.2). The percentage absorption of EM wave was calculated from the following relation [366]

$$Absorption(\%) = 100 - \left(10^{(RL/10)} \times 100\right) \tag{4.113}$$

The plot of attenuation coefficient (α) against frequency is given in **4.137**. The attenuation properties of the EM wave absorber or the extent of the reduction of the intensity and power of the EM wave as it travel through the EM wave absorber is determined by the values of α and is given by [16].

$$\alpha = \frac{\pi f}{c}\left(2\left(\mu''\varepsilon'' - \mu'\varepsilon' + \left(\left(\mu''^2 + \mu'^2\right)\left(\varepsilon''^2 + \varepsilon'^2\right)\right)^{1/2}\right)\right)^{1/2} \tag{4.114}$$

The larger the values of α, the greater the extent of attenuation of the EM wave as it passes through the EM wave absorber whereas smaller values of α shows that the EM wave absorber is relatively transparent to the EM wave. It can be seen that the highest values of α are obtained at higher frequencies. All the samples shows good attenuation properties, the

highest value of α (214.15) was observed in the sample BaMCCTO3 at frequency of 16.6 GHz.

4.9.8 EMI shielding performance

Shielding of EM wave occurs as a result of reflection, absorption and multiple internal reflection losses at the interface of the EM wave absorber [367]. In accordance with classical theory of electromagnetism, the shielding effectiveness for an EM wave absorber can be written as [58]

$$SE = 20\sqrt{\frac{\omega\mu\sigma_{AC}}{2}}\log e \tag{4.115}$$

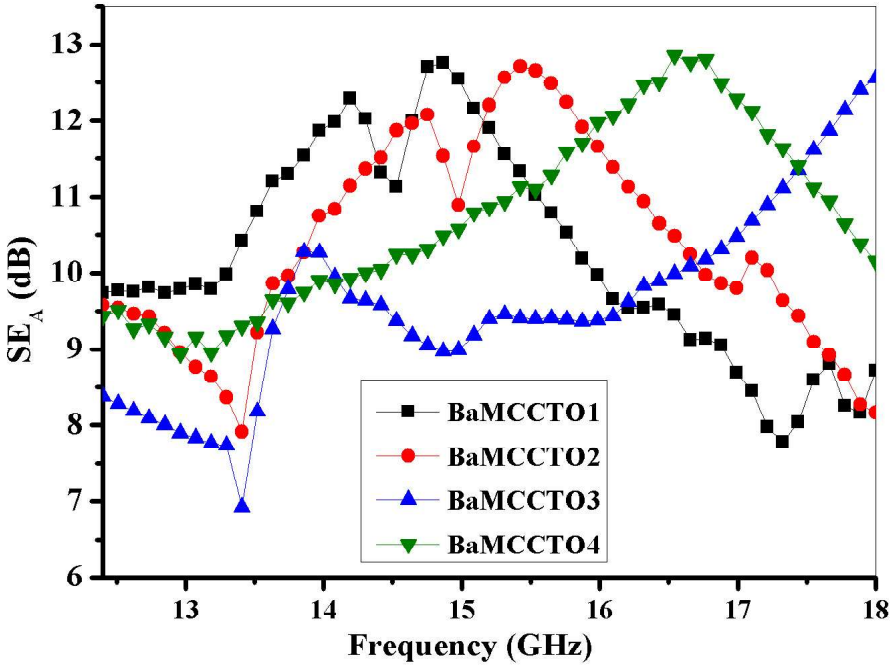

Fig. 4.138 Variation of shielding effectiveness for absorption with frequency for BaM/CCTO nanocomposite

In general, the parameters describing the shielding effectiveness of an EM wave absorber are shielding effectiveness for reflection (SE_R) and shielding effectiveness for absorption (SE_A) which are respectively given in equation (4.116) and (4.117)

$$SE_R = -10\log(1-R) \tag{4.116}$$

$$SE_A = -10\log(1-A_{eff}) \tag{4.117}$$

Where A_{eff} is the effective absorption of the EM wave absorber, the relation describing A_{eff} is given in terms of reflection coefficient (R) and transmission coefficient (T)

$$A_{eff} = \frac{1-R-T}{1-R} \tag{4.118}$$

Both R and T are usually determined from S parameters ($S_{11} or\ S_{22}$ and $S_{12} or\ S_{21}$) as in equation (4.119) and (4.120) respectively

$$R = |S_{11}|^2 = |S_{22}|^2 \tag{4.119}$$

$$T = |S_{12}|^2 = |S_{21}|^2 \tag{4.120}$$

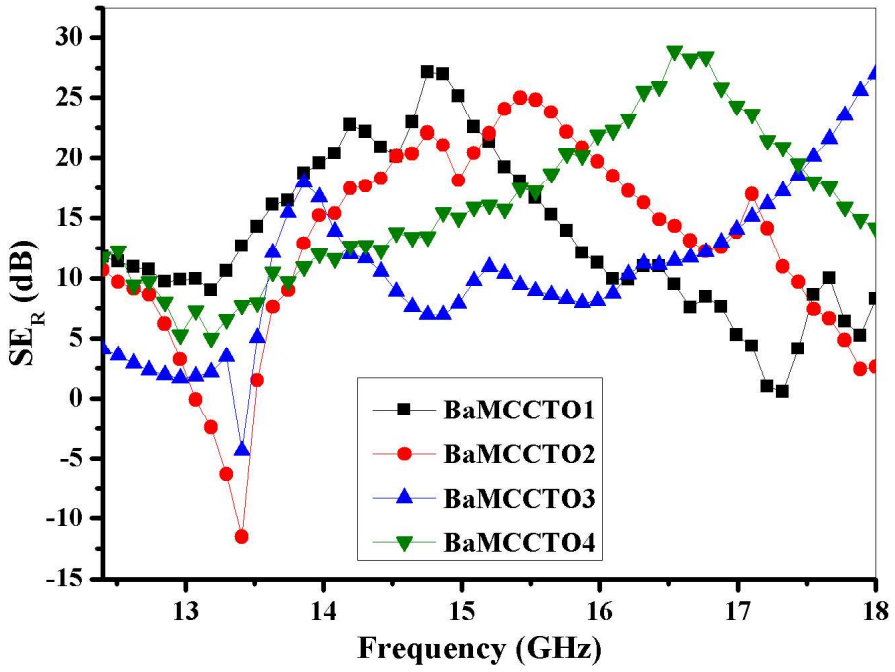

Fig. 4.139 Variation of shielding effectiveness for reflection with frequency for BaM/CCTO nanocomposite

Fig. 4.138, **4.139**, and **4.140** respectively shows the shielding effectiveness for absorption (SE_A), shielding effectiveness for reflection (SE_R), and total shielding effectiveness (SE_T) for BaM/CCTO nanocomposite. It has been reported that μ' contribute to SE_A whereas ε' contributes to SE_R [58]. The observed maximum SE_A are 12.7 dB at 14.9 GHz, 12.7 dB at 15.4 GHz, 12.5 dB at 18.0 GHz and 12.8 dB at 16.5 GHz for BaMCCTO1, BaMCCTO2, BaMCCTO3 and BaMCCTO4 nanocomposites respectively. Similarly, BaMCCTO1,

BaMCCTO2, BaMCCTO3 and BaMCCTO4 nanocomposites respectively shows maximum SE_R of 27.1 dB at 14.7 GHz, 24.9 dB at 15.4 GHz, 26.9 dB at 18.0 GHz and 28.9 dB at 16.5 GHz. All the nanocomposites exhibit good SE_R and SE_A which could be as a result of the matching between μ' and ε'. **Table 4.25** presents the values of SE_T, effective shielding ($SE_T > 20\ dB$), and bandwidth of effective shielding for BaMCCTO1, BaMCCTO2, BaMCCTO3, and BaMCCTO4. Clearly, all the samples show values of effective above 20 dB which is the limit for commercial application. **Table 4.26** presents a comparison of EMI shielding effectiveness of our prepared nanocomposites with other nanocomposites reported recently in literature. Interestingly, our nanocomposites out-perform all these nanocomposites in terms of EMI shielding performance. This excellence performance the prepared BaM /CCTO nanocomposites could be attributed to high $\tan\delta_{\mu}$ of BaM nanoparticles, high $\tan\delta_{\varepsilon}$ of CCTO nanoparticles and remarkable impedance matching. This is also evident in **Fig. 4.134** where the values of $\tan\delta_T$ reach as high as ≈2.8, this is greater than that obtained for

Table 4.25 Total shielding effectiveness (SE_T), effective shielding ($SE_T > 20\ dB$), and bandwidth of effective shielding of BaMCCTO1, BaMCCTO2, BaMCCTO3, and BaMCCTO4

Sample code	Frequency (GHz)	Total shielding effectiveness ($\boldsymbol{SE_T}$) (dB)	Effective shielding ($\boldsymbol{SE_T > 20\ dB}$)	Bandwidth of effective shielding (GHz)
BaMCCTO1	12.4	21.5	21.5	–
	14.1	35.0	35.0	2.8
	14.7	39.9	39.9	2.8
	16.4	20.6	20.6	2.8
BaMCCTO2	14.7	34.3	34.3	–
	15.4	37.7	37.7	3.6
	17.1	27.4	27.4	–
BaMCCTO3	13.9	28.1	28.1	0.8
	15.2	20.4	20.4	–
	18.0	39.5	39.5	1.8
BaMCCTO4	12.5	21.8	21.8	–
	16.5	41.8	41.8	4.2

Table 4.26 Comparison of EMI shielding effectiveness with other nanocomposite

Composites	Pellet thickness ($\boldsymbol{t}$) (mm)	Maximum total shielding effectiveness ($\boldsymbol{SE_T}$) (dB)	Frequency (GHz)	Ref.
polypropylene/carbon fibre composite foams	3.2	24.9	8-12	[327]
Porous super-hydrophobic polymer/carbon composites	2	28.5	8-12	[368]
core-shell non-woven fabrics covered by reduced graphene oxide	0.27	32.0	8-12	[369]
polystyrene/graphene composites with magnetic Fe_3O_4 nanoparticles	–	36.0	11.95	[370]
PDMS/ferrous ferric oxide decorated RGO–SWCNH composite	10	35.8	14-20	[355]
carbon nanotube–reduced graphene oxide composites	2	37.0	12.4-18	[326]
BaM/CCTO nanocomposites (BaMCCTO1)	3	39.9	14.7	this work
BaM/CCTO nanocomposites (BaMCCTO2)	3	37.7	15.4	this work
BaM/CCTO nanocomposites (BaMCCTO3)	3	39.5	18.0	this work
BaM/CCTO nanocomposites (BaMCCTO4)	3	41.8	16.5	this work

PDMS/ferrous ferric oxide decorated RGO–SWCNH composite which also has a lower value of SE_T compared to our nanocomposites [355]. The EMI shielding capacity of the BaMCCTO4 nanocomposites shows a total shielding effectiveness of 41.8 dB at 16.5 GHz

and bandwidth of 4.2GHz, this value corresponds to 99.99 % shielding of EM waves and is above the limit ($SE_T > 20\ dB$).

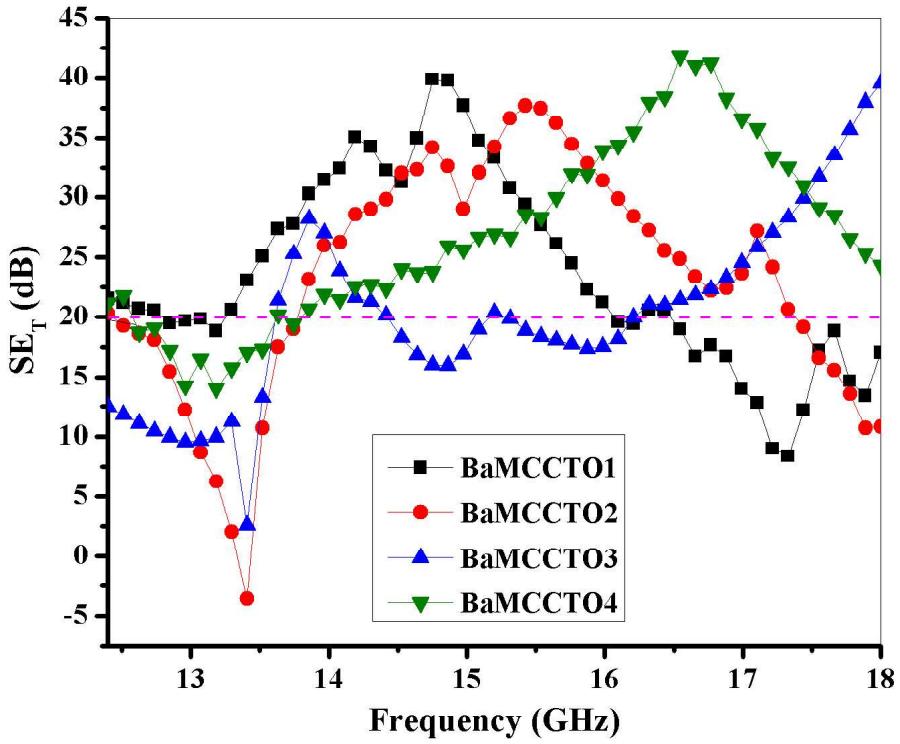

Fig. 4.140 Variation of total shielding effectiveness with frequency for BaM/CCTO nanocomposite

4.10 Strontium hexaferrites, calcium copper titanate, and reduced graphene oxide (SrM/CCTO/rGO) nanocomposite

4.10.1 XRD analysis

The XRD patterns of SrM/CCTO/rGO nanocomposites are presented in **Fig. 4.141**. According to the JCPDS card 39-1433, the diffraction peaks at $2\theta = 23.04°$, 30.36°, 30.81°, 32.21°, 34.20°, 35.10°, 37.09°, 38.74°, 40.28°, 42.33°, 46.51°, 53.89°, 54.99°, 56.63°, 63.01°, 68.05°, and 72.58° corresponds to the (006), (110), (008), (107), (114), (200), (203), (0010), (205), (206), (1011), (300), (217), (2011), (220), (226), and (317) hkl planes of pure SrM hexaferrites phase with space group $P6_3/mmc$ respectively. Similarly, the JCPDS card

number 75-2188 shows that the diffraction peaks at $2\theta = 34.30°$, 38.54°, 42.38°, 45.96°, 49.30°, 61.47°, and 72.28° respectively corresponds to the (211), (220), (013), (222), (321), (400), (422), and (440) hkl planes of pure CCTO crystal structure with space group Im-3. The broad diffraction peak at around $2\theta = 25°$ shows the presence of rGO in the nanocomposites.

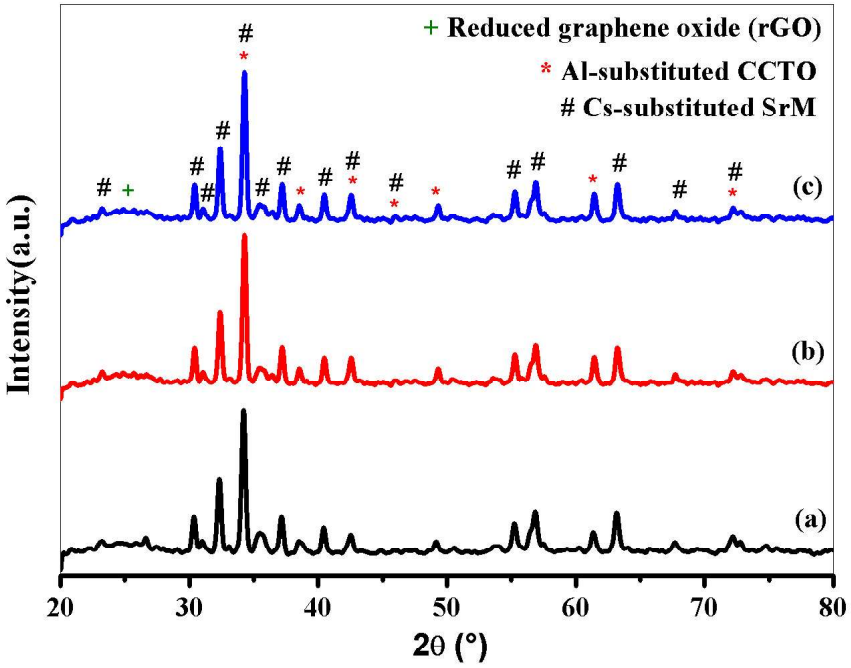

Fig. 4.141 XRD patterns of SrM/CCTO/rGO nanocomposites (a) SCR1, (b) SCR2, and (c) SCR3

The lattice constants (a and c), volume of the unit cell (V_{cell}), crystallite size (D) and strain (η) of the Cs-substituted SrM hexaferrites phase were determined from the following equation

$$\frac{1}{d_{hkl}} = \frac{4}{3}\left(\frac{h^2 + hk + k^2}{a^2}\right) + \frac{l^2}{c^2} \tag{4.121}$$

$$V_{cell} = 0.8666\, a^2 c \tag{4.122}$$

$$D = \frac{0.89\lambda}{\beta \cos\theta} \tag{4.123}$$

$$\eta = \frac{\beta\cos\theta - \frac{0.9\lambda}{D}}{2\sin\theta} \tag{4.124}$$

Where d_{hkl} is the d spacing between the planes, hkl are the miller indices, β is the full width at half maximum (in radian), θ is the Braggs angle and λ is the X-ray wavelength (1.54056 Å). **Table 4.27** presents the calculated values of lattice parameters (a and c), volume of the unit cell (V_{cell}), crystallite size (D) and strain (η) of the Cs^{3+}-substituted SrM hexaferrites phase. The values of a, c, V_{cell}, D and η increases with increase in Cs^{3+}-substitution (Table **4.27**). The increase in a, c, and V_{cell} could be attributed to the fact that the ionic radius of Cs^{3+} ($r_{Cs^{3+}} = 1.67$ Å) is larger than that of Fe^{3+} ($r_{Fe^{3+}} = 0.645$ Å) [264][371][50]. The larger ionic radius causes distortion in the unit cell and subsequently increases the a and c, this fact could be further supported by the calculated values of η which also increase with Cs^{3+}-substitution as a result of the distortion induced by the large ionic radius of Cs^{3+}. Furthermore, it has been reported that the lattice parameters might be affected by change in exchange energy after cation substitution [211][251]. It has been reported that the M-type hexagonal structure can be ascertained if the c/a ratio is not greater than 3.98 [32][372][373]. Since all the calculated values the c/a ratio was found to less than 3.98, we can conclude that the sample exhibit the M-type hexagonal structure. The values of D was estimated from Scherer formula (**Eqn. 4.123**). It can be observed that the values of D also decreases with Cs^{3+}-substitution, this is further supported by the slight broadening of some XRD peaks as a result of decrease in D [374]. The decrease in D could be attributed to segregation effect of rare earth ions [191].

Table 4.27 Values of lattice constants lattice constants (a and c), volume of the unit cell (V_{cell}), crystallite size (D) and strain (η) of Cs-substituted SrM hexaferrites phase.

Sample code	2θ (°)	d (Å)	β (°)	a (Å)	c (Å)	c/a	V_{cell} (Å^3)	D (nm)	$\eta \times 10^{-4}$
SrM1	30.36	2.940	0.264	5.88	23.12	3.93	693.187	34.639	8.489
SrM2	30.31	2.945	0.275	5.89	23.19	3.93	697.623	33.250	8.859
SrM3	30.26	2.950	0.311	5.90	23.26	3.94	702.081	29.397	10.036

Similarly, the lattice constant (a) and volume of the unit cell (V_{cell}) of the Al^{3+}-substituted CCTO phase were calculated using following equation

$$a = d_{hkl}\sqrt{h^2 + k^2 + l^2} \tag{4.125}$$

$$V_{cell} = a^3 \tag{4.126}$$

Table 4.28 shows the calculated values of a and V_{cell} of the Al^{3+}-substituted CCTO phase. Both the values of a and V_{cell} shows a decreasing trend with increase in Al^{3+}-substitution (**Table 4.28**). This could be explained on the basis of the ionic radius of the cations. The ionic radius of Al^{3+} ($r_{Al^{3+}} = 0.535$ Å) is small compared to that of Ti^{4+} ($r_{Ti^{4+}} = 0.605$ Å), this scenario results in the shrinkage of the unit cell since the site occupied by Ti^{4+} ion is big for the Al^{3+} ion [155][141].

Table 4.28 Values of lattice constant (a) and volume of the unit cell (V_{cell}) of Al^{3+}-substituted CCTO phase

Composition	2θ (°)	d (Å)	β (°)	a (Å)	V_{cell} (Å^3)
CCT1	49.209	1.8501	0.289	7.4004	405.30
CCT2	49.259	1.8483	0.283	7.3934	404.15
CCT3	49.308	1.8466	0.312	7.3864	403.00

4.10.2 FTIR analysis

Molecular bands and functional groups attached in the nanocomposites were investigated using FTIR in the range 4000 to 400 cm^{-1}. The FTIR spectra of SrM/CCTO/rGO nanocomposites are presented in **Fig. 4.142**. Characteristics absorption bands of Cs-substituted SrM and Al-substituted CCTO were observed at 446, 551 and 605 cm^{-1} in **Fig. 4.142** (a), (b) and (c), these bands could be attributed to Fe-O stretching vibration in tetrahedral and octahedral sites of the Cs-substituted SrM phase and stretching vibrations of TiO_6 octahedral in the Al-substituted CCTO phase [212][335]. The absorption band occurring at 1527 cm^{-1} could be due to Metal-Oxygen-Metal (M-O-M) bond such as Fe-O-Fe and Co-O-Co whereas that at 2357 cm^{-1} could be attributed to the presence of CO_2 absorbed from the atmosphere [186][187]. The oxygen-containing functional groups in GO and rGO are clearly visible in **Fig. 4.142** (d) and (e) respectively. GO exhibit bands at 1051, 1212, 1405, 1598,

1728 cm^{-1} which respectively corresponds to C-O stretching vibrations of alkoxy, C-O stretching vibrations of epoxy, O-H deformation, C-C vibrations, and C=O bonds [375][4][376]. After reduction, the intensity of the bands were greatly reduced which indicates the removal of some of the oxygen-containing functional groups and the restoration of the carbon basal plane. The band at 1660 cm^{-1} which results from C=C skeletal vibration of sp^2 hybridized un-oxidized graphite was not observed [321].

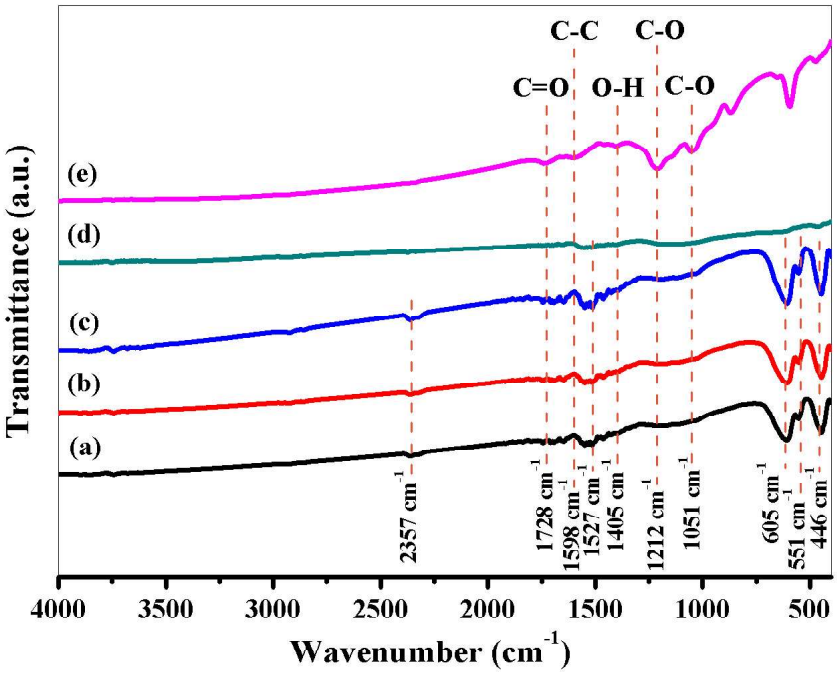

Fig. 4.142 FT-IR spectra for SrM/CCTO/rGO nanocomposites (a) SCR1, (b) SCR2, (c) SCR3, (d) rGO, and (e) GO

4.10.3 Raman spectroscopy

Raman spectroscopy is an extremely useful technique for the study of the extent of structural deformation of carbon based nanomaterials. The Raman spectra of rGO and GO are presented in **Fig. 4.143**, the characteristics D and G bands of GO and rGO are clearly observed. The D and G bands of GO are situated at Raman shift of 1358 and 1604 cm^{-1} respectively, whereas the D and G band of rGO shifted towards lower wavenumber in the Raman shift and are respectively located at Raman shift of 1351 and 1595 cm^{-1}. This shift towards lower Raman shift could be attributed to the destruction of sp^2 bonds between the atoms and the creation of

imperfections in the rGO sheets as a result of oxidation [377]. The presence of D band could be ascribed to out-plane vibration resulting from defects observed at the edges of the structure of the GO and rGO sheets whereas G band is attributed to in-plane vibrations resulting from defects of the sp^2 bonded atoms in the structure of GO and rGO sheets [378]. From the foregoing, we observed that there is a slight shift towards lower wavenumber in the Raman shift of the D and G band of rGO, this could be attributed to charge transfer as a result of interaction of rGO sheets with Cs-substituted SrM and Al-substituted CCTO nanoparticles [9]. Furthermore, the values of I_D/I_G ratio for GO and rGO were found to be 0.97 and 1.07 respectively. The increase in the value of I_D/I_G ratio of rGO compared with that of GO is an indication that rGO has been obtained after reduction of GO [379]. Since the I_D/I_G ratio estimate the extent of the structural defects in the GO and rGO sheets, we can conclude that most of the hydroxyl, carbonyl and carboxyl groups have been remove from the surface of the sheets thereby reducing the structural defects [380]. It is worthy to note that the obtained values of Raman shift for D and G band coupled with the I_D/I_G ratio for both GO and rGO are in close agreement with those obtained by other authors [174][361][381].

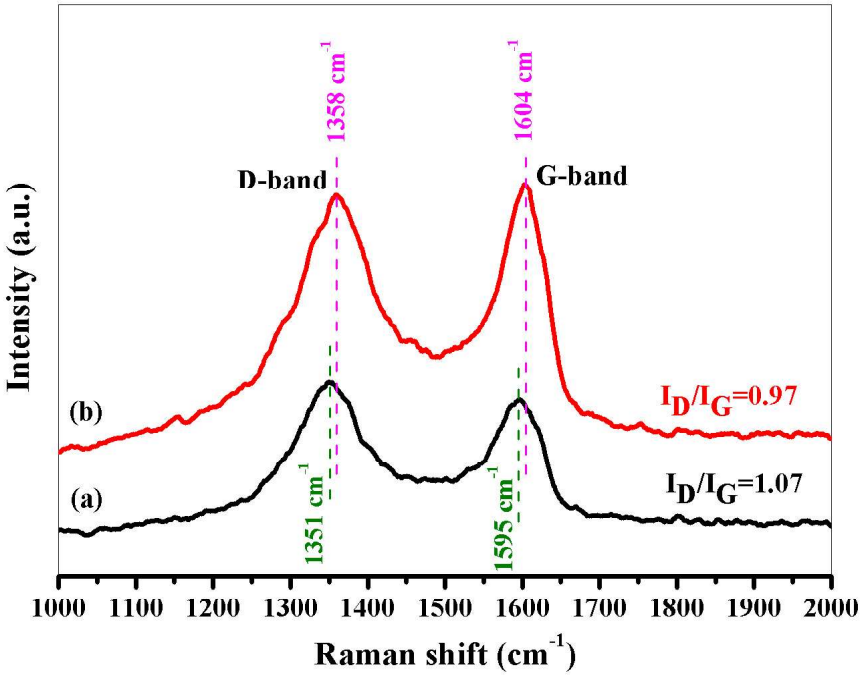

Fig. 4.143 Raman spectra of (a) rGO and (b) GO

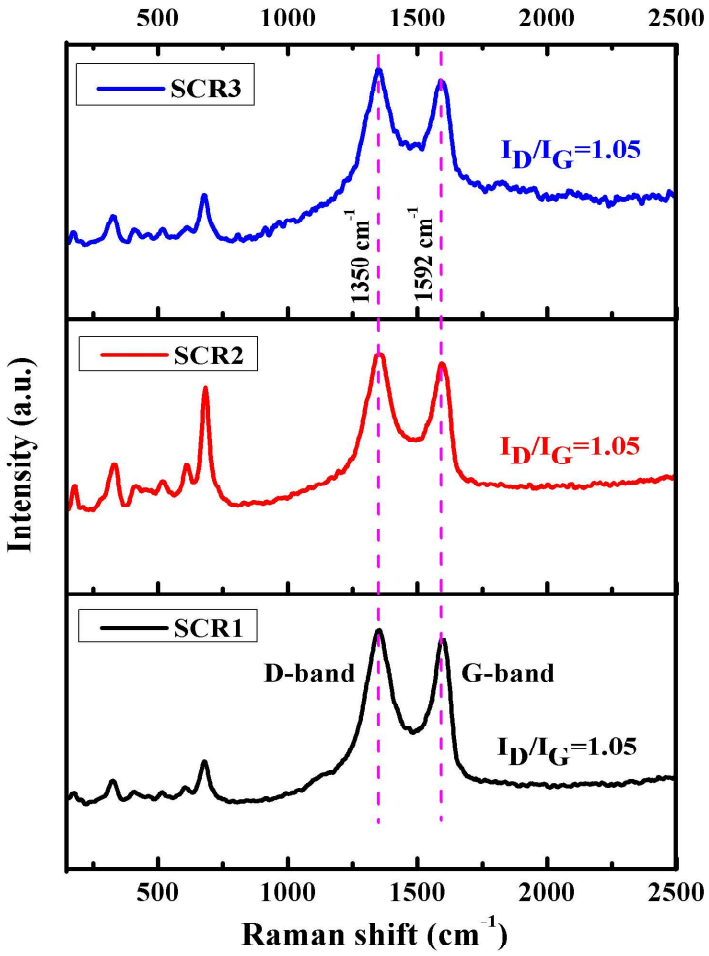

Fig. 4.144 Raman spectra for SrM/CCTO/rGO nanocomposites (a) SCR1, (b) SCR2, and (c) SCR3

The Raman spectra of SrM/CCTO/rGO nanocomposites are presented in **Fig. 4.144**. Vividly, the characteristics Raman shifts of Cs^{3+}-substituted SrM, Al^{3+}-substituted CCTO and rGO are observed. The Raman shifts at 177, 324, 405, 609 and 682 cm^{-1} signify the presence of Cs^{3+}-substituted SrM whereas Al^{3+}-substituted CCTO shows Raman shifts at 460 and 516 cm^{-1}. The D and G bands of rGO were also observed at 1350 and 1592 cm^{-1} respectively, reasons for the presence of these bands have already been given above. In the Cs-substituted SrM phase, vibration of S-block via E_{1g} and E_{2g} symmetry give rise to Raman shifts at 176 and 325 cm^{-1} whereas vibrations of 12k octahedral site, 4f2 octahedral site and 2b bi-pyramidal site through A_{1g} symmetry respectively results in Raman shifts at 405, 609, 682 cm^{-1} [191]. The 450 and 513 cm^{-1} Raman shifts observed in the Al^{3+}-substituted CCTO phase

corresponds toTiO_6 rotation-like mode through A_{1g} and A_{2g} symmetry respectively [166][154]. The observed Raman spectra support not only the purity of the individual nanomaterial in SrM/CCTO/rGO nanocomposites, but also indicates the successful incorporation of Cs-substituted SrM and Al-substituted CCTO on the surfaces of rGO.

4.10.4 Morphology analysis

The Morphology and elemental composition of the prepared nanocomposites were investigated using FESEM, TEM, HRTEM, SAED and EDX. The FESEM micrographs of SrM/CCTO/rGO nanocomposites are presented in **Fig. 4.145** (a), (b), and (c). The presence of the components of the SrM/CCTO/rGO nanocomposites is clearly observed in the FESEM

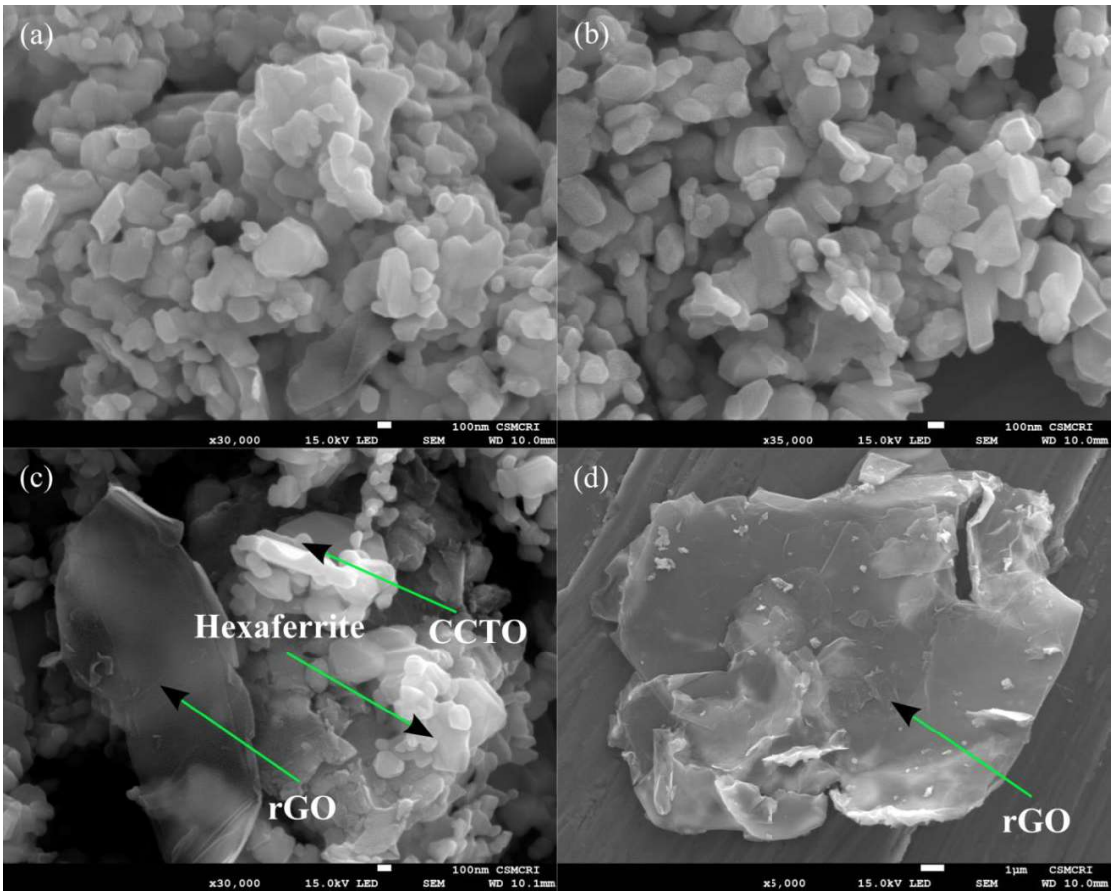

Fig. 4.145 FESEM micrographs of SrM/CCTO/rGO nanocomposites (a) SCR1, (b) SCR2, (c) SCR3, and (d) rGO

micrographs, the SrM and CCTO nanoparticles have been successfully distributed on the surface and between the rGO sheets, this scenario prevent the restacking of the rGO sheets [4]. The rGO sheets are transparent and appear as silky waves with some wrinkles at the

edges (**Fig. 4.145 (d)**)., similar observation was made by P. Liu et al. [21]. The tendency of agglomeration is a direct consequence of enhancement of surface energy and small grain size of the nanoparticles [18]. Agglomeration of the SrM nanoparticles can be observed as result of magnetic dipole interaction with neighbouring SrM nanoparticles [321][200]. Reduction in surface energy and magnetic dipolar interaction prompt the SrM nanoparticles to surround the CCTO nanoparticles and settle at the surface of the rGO sheets [342][332].

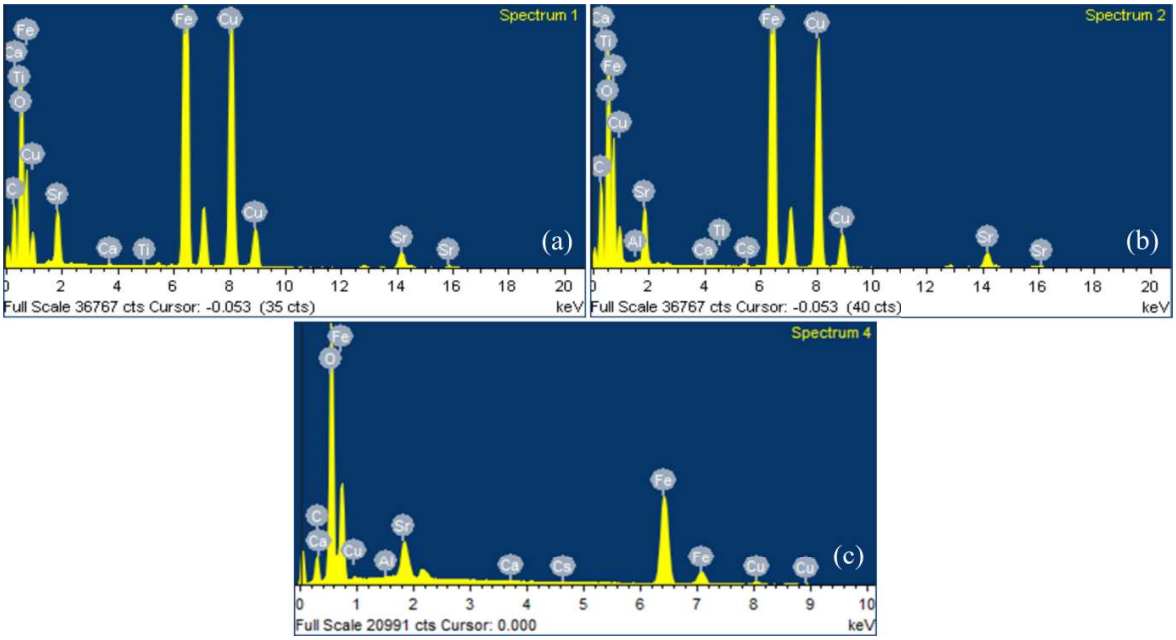

Fig. 4.146 EDX spectra of SrM/CCTO/rGO nanocomposites (a) SCR1, (b) SCR2, and (d) SCR3

The EDX spectra of SrM/CCTO/rGO nanocomposites are presented in **Fig. 4.146** (a), (b), and (c). Clearly, all the substituted elements along with the host elements and rGO are observed, this confirms the stoichiometry of the prepared samples. **Fig. 4.147** (a-j) presents the TEM, HRTEM micrographs and SAED patterns of SrM/CCTO/rGO nanocomposites. Clearly, the TEM images show the presence of hexagonal shaped SrM and cubic shaped CCTO nanoparticles embedded on the surface of the rGO sheets. HRTEM images respectively shows lattice fringes of Cs^{3+}-substituted SrM nanoparticles, Al^{3+}-substituted CCTO nanoparticles, and rGO having size of 0.2629, 0.2613, and 0.3363 nm corresponding to (114), (220), and (002) hkl planes [343]. The SAED pattern shows bright diffraction spots even though it does not show individual diffraction rings of Cs^{3+}-substituted SrM, Al^{3+}-substituted CCTO and rGO sheets. Hence, the SAED patterns confirm the polycrystalline nature of the prepared nanocomposites and that the Cs^{3+}-substituted SrM and Al^{3+}-substituted

CCTO nanoparticles have been successfully assembled on the surface of the rGO sheets. Both the FESEM and TEM micrographs show evidence of the presence nanoparticles of Cs^{3+}-substituted SrM and Al^{3+}-substituted CCTO embedded on the surface rGO sheets.

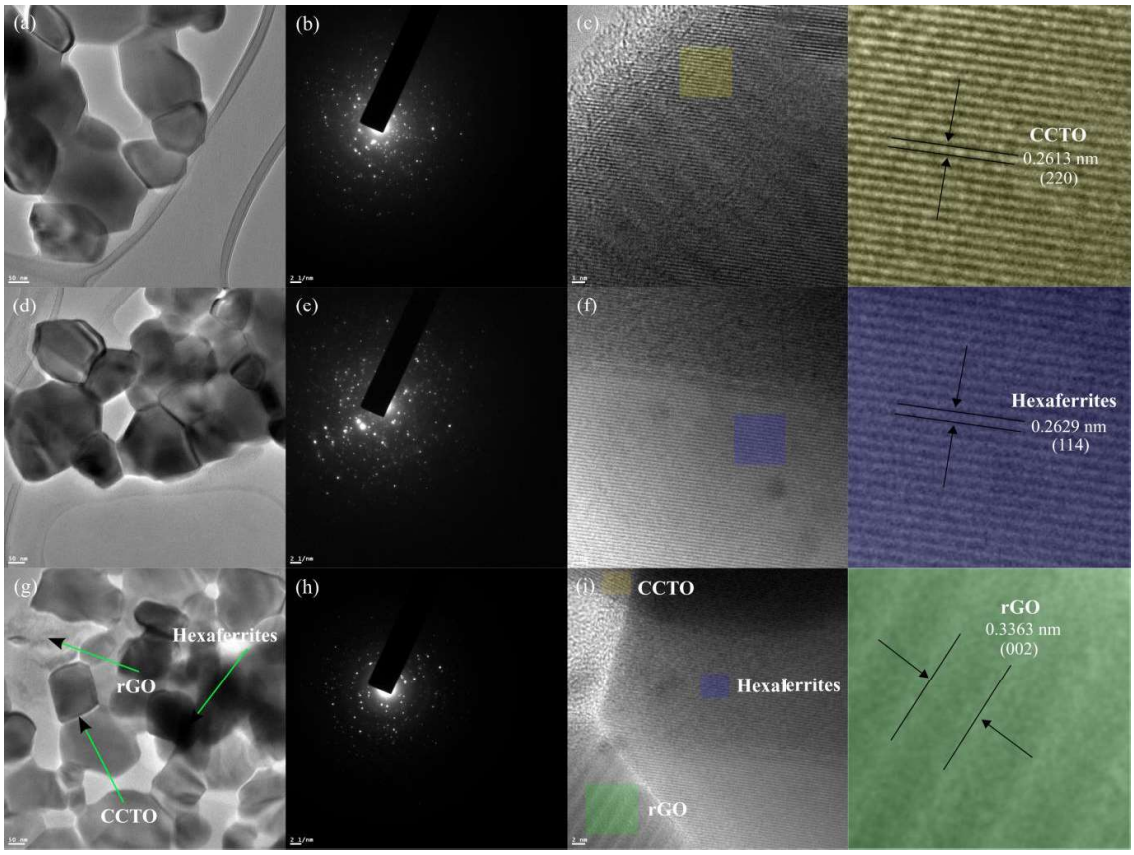

Fig. 4.147 TEM images and SAED patterns of SrM/CCTO/rGO nanocomposites (a-c) SCR1, (d-f) SCR2, and (g-j) SCR3

4.10.5 Optical analysis

The optical analysis of SrM/CCTO/rGO nanocomposite was carried out using UV-visible-NIR spectroscopy in the optical region 234-750 nm. The optical band gap (E_g) was determined via the following formula

$$\alpha h\upsilon = A\left(h\upsilon - E_g\right)^n \tag{4.127}$$

Where α is the absorption, h is the planks constant ($6.6260 \times 10^{-34}\, J.s$), υ is the frequency of incident photon and A is a characteristics constant that depends on n. The values of n varies from 1/2, 3/2, 2 and 3 for indirect allowed, indirect forbidden, direct allowed and direct

forbidden transitions respectively. Changes in absorption with respect to wavelength for SrM/CCTO/rGO nanocomposites are shown in **Fig. 4.148**. The nanocomposites shows absorption peaks at 282, 367, 574 and 728, these absorption peaks results from to $\sigma - \sigma^*$, $n - \sigma^*$, $\pi - \pi^*$, and $n - \pi^*$ transitions respectively. The absorption peak at 367 nm in SCR3 nanocomposite shows hypochromic shift, a hyperchromic shift is also observed at 367 nm in the same nanocomposite. Slight reflections are also observed at 322 and 700 nm. In general, the nanocomposites show absorption in UV region and near Visible light region.

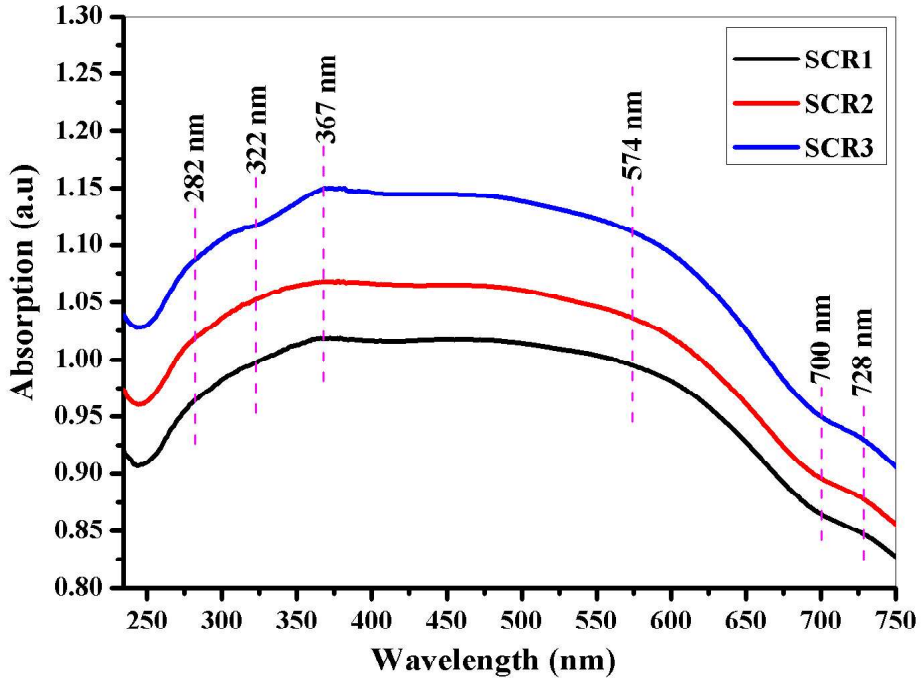

Fig. 4.148 Variation of absorption with wavelength for SrM/CCTO/rGO nanocomposite

Fig. 4.149 (a), (b) and (c) presents the plots of E_g of the SrM/CCTO/rGO nanocomposites. Extrapolation of the linear part of the plots of E_g gives the values of E_g for each of the nanocomposites. The values of E_g for SCR1, SCR2 and SCR3 nanocomposites are respectively 3.39, 3.26 and 3.16 eV; these values are within the range of E_g of semiconductors. The obtained values of E_g of SCR1 is in close agreement with that obtained for MgO nanoflakes ($E_g = 3.46$ eV) [382]. Gallium nitride (p-GaN/n-GaN device) having E_g of 3.5 eV has been used in making nanoscale UV-blue light emitting diodes (LEDs) [163]. UV-blue LEDs are vital for developing high density storage optical disks, colour printers and

image scanners. Also, UV-blue LEDs have been envisioned to pave the way for much higher resolution in television and computer monitors as well as remote sensing and biomedical applications.

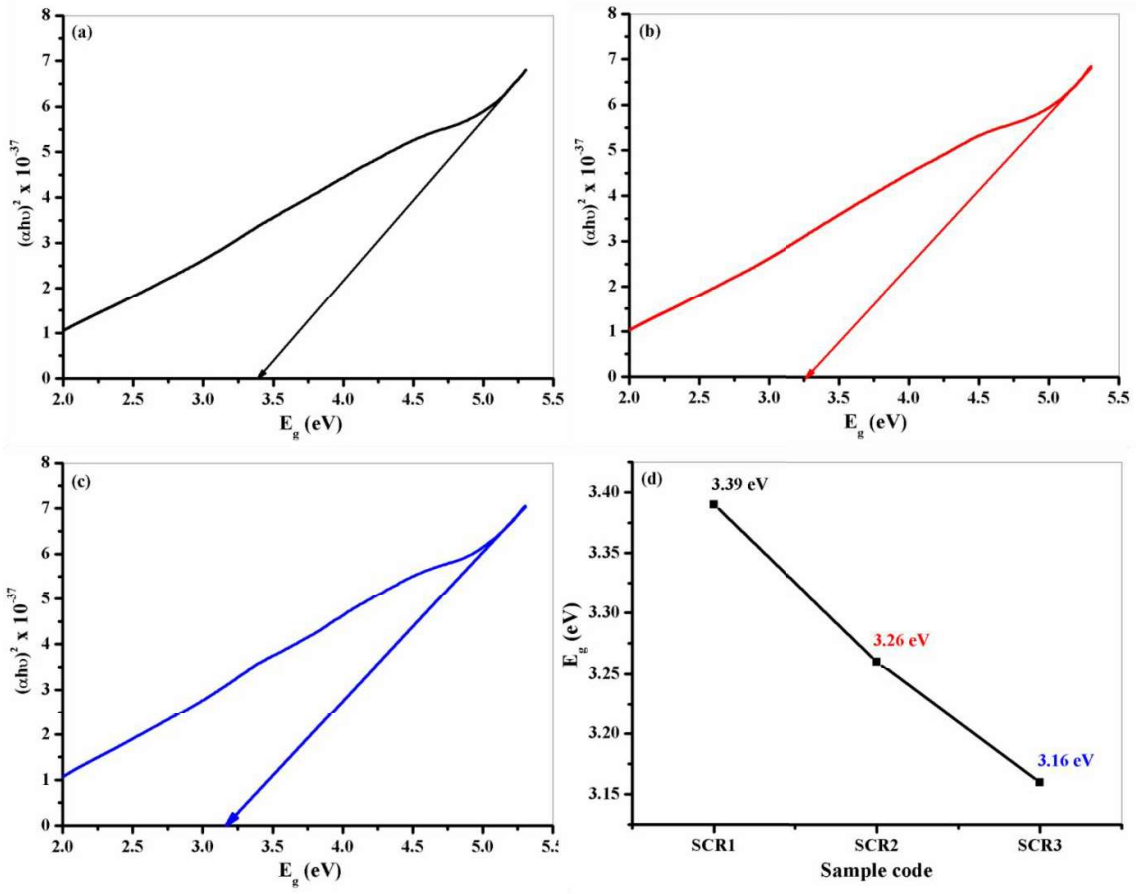

Fig. 4.149 Optical band-gap for SrM/CCTO/rGO nanocomposite (a) SCR1 (b) SCR2 (c) SCR3 and (d) variation of optical band-gap with composition of nanocomposites

It is worthy to note that the absorption spectra (**Fig. 4.148**) of the nanocomposites show good absorption in UV region. Hence, the SrM/CCTO/rGO nanocomposite can be used for UV-blue LED applications. **Fig. 4.149** (d) shows the variation of E_g with composition of the prepared nanocomposites; E_g tend to decrease with change in composition. The decrease in E_g could be attributed to factors such as quantum confinement, crystallite size as well as interaction of SrM and CCTO grains with rGO sheets [174][305][162][186].

4.10.6 Magnetic analysis

Fig. 4.150 presents the M-H hysteresis loop of SrM/CCTO/rGO nanocomposite at room temperature. The prepared nanocomposites exhibit typical ferromagnetic behaviour. Magnetic parameters such as coercivity (H_c), remnant magnetization (M_r), and saturation magnetization (M_s) were determined and presented in **Table 4.29**. The values of H_c, σ_r, and $\sigma_s$were used to calculate the squareness ratio (SR) and anisotropy constant (K) using equation (4.128) and (4.129) respectively [134].

$$SR = \frac{M_r}{M_s} \tag{4.128}$$

$$K = \frac{\mu_0 M_s H_c}{2} \tag{4.129}$$

Where $\mu_0 = 4\pi \times 10^7\ H/M$ is the permeability in vacuum. The obtained values of H_c and M_s are lower compared to the theoretical value ($H_c = 6700$ Oe and $M_s = 74.30$ emu/g) of

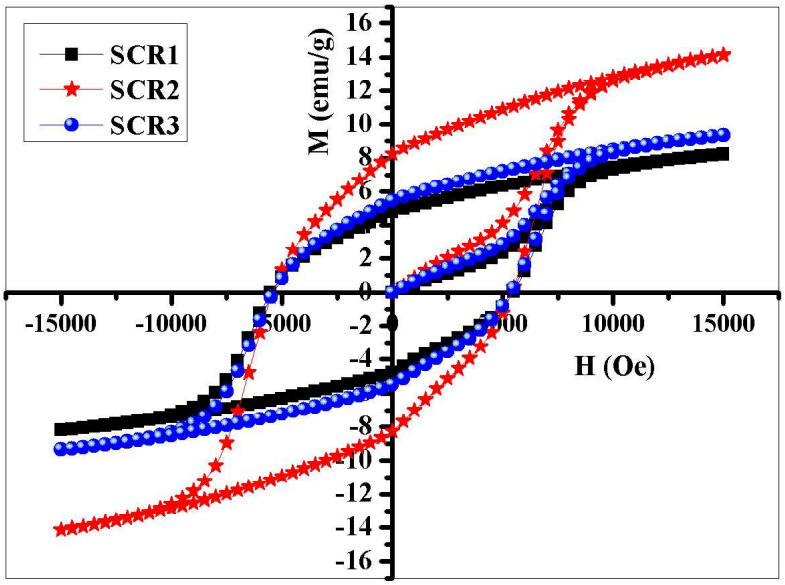

Fig. 4.150 M-H hysteresis loop for SrM/CCTO/rGO nanocomposite

hexaferrites [248]. The lower values M_r and M_s could be attributed to the presence of non-magnetic CCTO and rGO [321][361]. Furthermore, the presence of CCTO phase in the

nanocomposites affects the magnetic properties as a result of non-magnetic nature of CCTO ceramic, M_r decreases from 8.236 to 5.441emu/g while M_s decrease from 14.145 to 9.360 emu/g, this could be due to the presence of lattice defects, interfacial polarization between SrM and CCTO nanoparticles, random orientation of spin at the surface of SrM/CCTO/rGO nanocomposite and weakening of super-exchange interaction as result of presence of CCTO ceramic [342][332]. It has been reported that the nanomaterial with SR greater than 0.5 exhibit single domain [32][254]. It can be observed that the SR of the prepared samples is greater than 0.5 (**Table 4.29**); hence, the prepared nanocomposites are of single domain. The results of the magnetic properties suggest that the method of synthesis in the current study can influence the magnetic properties and consequently the microwave absorption properties of the SrM/CCTO/rGO nanocomposite.

Table 4.29: coercivity (H_c), remnant magnetization (M_r), and saturation magnetization (M_s), squareness ratio (SR), and anisotropy constant (K) for SrM/CCTO/rGO nanocomposite

Sample code	$\boldsymbol{H_c}$ (Oe)	$\boldsymbol{M_r}$ (emu/g)	$\mathbf{M_s}$ (emu/g)	$\boldsymbol{SR}$ ($\boldsymbol{M_r/M_s}$)	$\boldsymbol{K}$ (HA^2/kg)
SCR1	5482.475	4.754	8.206	0.579	2.249
SCR2	5399.177	8.236	14.145	0.582	3.818
SCR3	5376.460	5.441	9.360	0.581	2.516

4.10.7 Microwave absorption analysis

We investigate ε^* and μ^* in order to comprehend the intrinsic factors influencing the microwave absorption properties of the SrM/CCTO/rGO nanocomposite. The electric energy and magnetic energy storage ability of the prepared nanocomposites are respectively determined by the nature of ε' and μ' whereas the ability to dissipate electric and magnetic energy is respectively determined by the values of ε'' and μ'', polarization and resonance relaxation coupled with conduction loss are the main reasons for energy dissipation in an EM wave absorber material [58][15]. The graphs of ε', ε'', μ' and μ'' are respectively presented in **Fig. 4.151 (a), (b), (c) and (d)**, it can be observed that the SrM/CCTO/rGO nanocomposite respectively exhibit values of ε' and ε'' in the range 5.49 to 19.15 and 0.17 to 13.19 over 12.4 to 18 GHz with several resonance peaks. The observed decrease in the values of ε' and ε'' result from the fact that increase in the frequency of the external reverse electric field causes the induction charge phase of the SrM/CCTO/rGO nanocomposite to lag behind the external

applied electric field which in turn causes electromagnetic oscillation, also space charge polarization which results from difference in the values of ε′ decreases with increase in frequency thereby causing a significant reduction in the values of ε′ and ε″ [15]. The extent of polarization process taking place during the experiment and the electrical conductivity of the nanocomposites are as a result of ε′ and ε″ of the nanocomposites respectively [349].

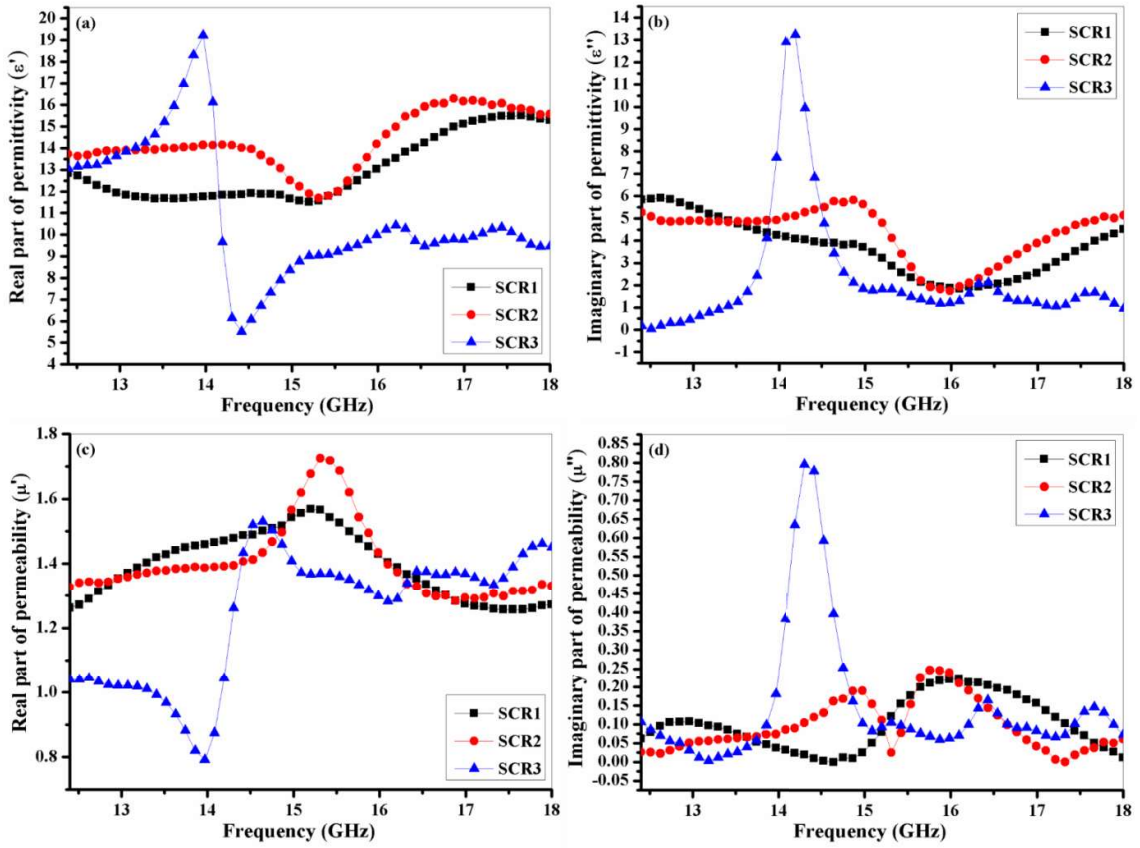

Fig. 4.151 Real part of Complex permittivity (a), imaginary part of Complex permittivity (b), real part of Complex permeability (c) and imaginary part of Complex permeability (d) for SrM/CCTO/rGO nanocomposite

Low values of ε′ results in shortening of the interfacial impedance gap thereby decrease the reflection coefficient of the microwave absorber material [10]. Hence, the microwave absorption properties of an EM wave absorber material also depend on the ε′ values of the material. The values of μ′ and μ″ ranges from 0.79 to 1.72 and 0.02 to 0.79 respectively with several increase and decrease in the form of resonance peaks, the decreasing behaviour of the values of μ′ and μ″ after an increase could be attributed to enhanced skin effects as a result of eddy currents at higher frequencies [383].

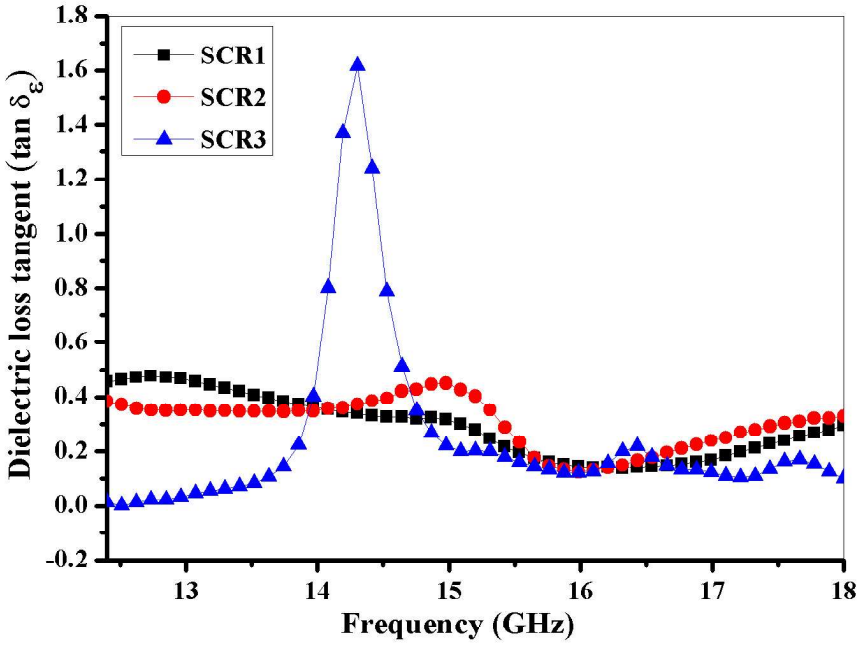

Fig. 4.152 Dielectric tangent loss for SrM/CCTO/rGO nanocomposite

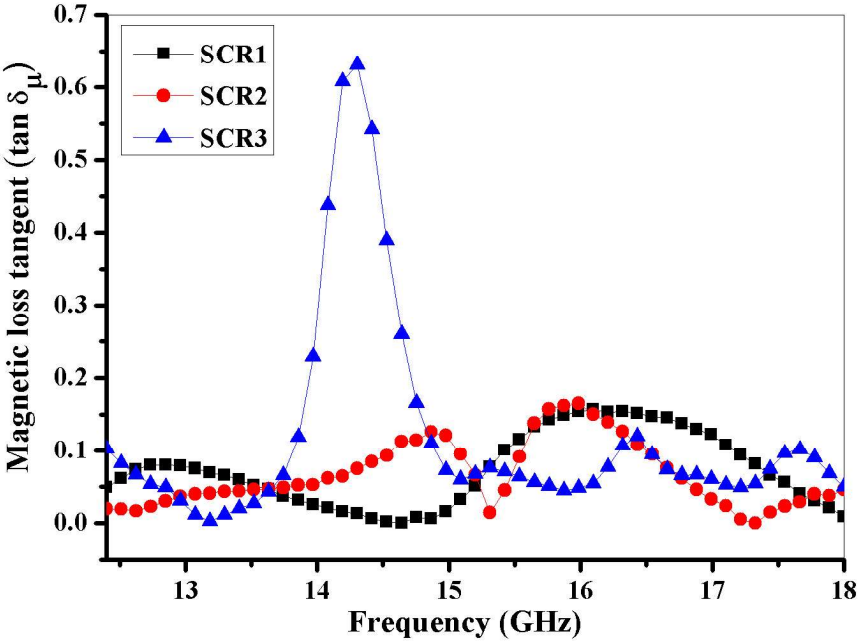

Fig. 4.153 Magnetic tangent loss for SrM/CCTO/rGO nanocomposite

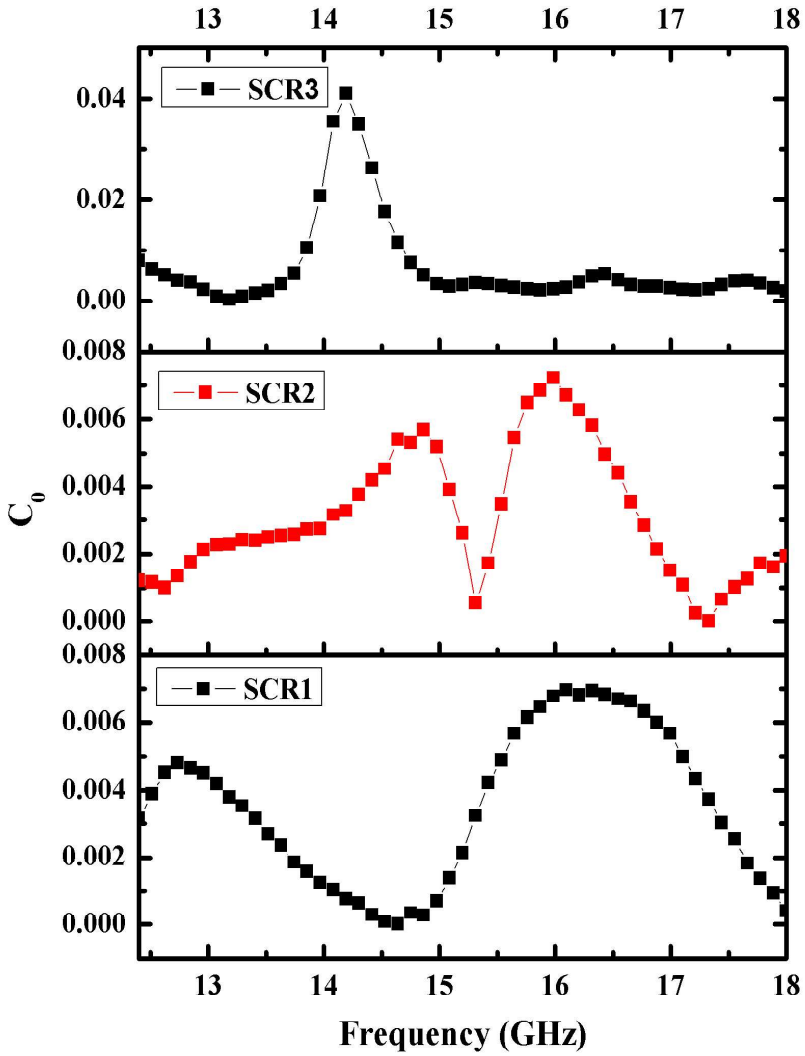

Fig. 4.154 Variation of C_0 with frequency for SrM/CCTO/rGO nanocomposite

The plot of tan δ_ε and tan δ_μ are respectively presented in **Fig. 4.152** and **4.153**. Clearly, the values of tan δ_ε are greater than those of tan δ_μ over the entire frequency range, this indicates that the attenuation of the microwave mainly results from tan δ_ε**.** The observed increased values of tan δ_ε could be ascribed to the presence of defects formed on the surface of rGO by SrM nanoparticles [27]**.** The plot of tan δ_μ vividly shows several resonance peaks over the whole frequency range. In general, these resonance peaks could be due to eddy current effects, magnetic hysteresis loss, domain wall resonance or natural resonance [357]. Domain wall resonance usually occurs in multi domain materials at a frequency range of 1-100 MHz.

However, the analysis of the magnetic properties of the nanocomposites reveals that the nanocomposites exhibit single domain structure. Hence, we can rule out contribution from domain wall resonance. The effects of eddy current can be determined by evaluating **Eqn. 11** and plotting the values of C_0 against frequency (**Fig. 4.154**). According to the skin effect criterion, constant variation of C_0 with frequency signify the contribution of eddy current effects to $\tan\delta_\mu$, since the plot of C_0 against frequency shows variation of C_0 over the whole frequency range, we can conclude from the foregoing that eddy currents effects do not contribute to $\tan\delta_\mu$ [15][17][384]. When the magnetization vector lags behind the applied EM field vector, magnetic hysteresis loss occurs. However, magnetic hysteresis loss is negligible for hexaferrites in frequency range 2 to 18 GHz, therefore we can also conclude that magnetic hysteresis loss does not contribute to $\tan\delta_\mu$ [321]. This left us with natural resonance only, hence we can come to the conclusion that natural resonance is the reason behind $\tan\delta_\mu$ [17]. Another possible contribution to $\tan\delta_\mu$ could be exchange resonance since according to Aharoni's theory, exchange resonance occurs at higher frequencies [16][24].

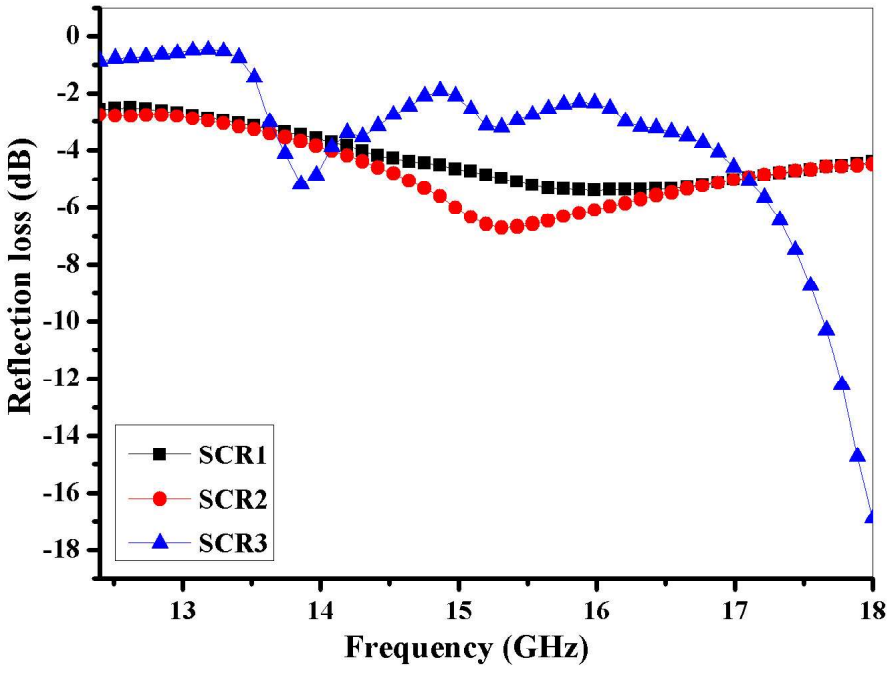

Fig. 4.155 Reflection loss (dB) for SrM/CCTO/rGO nanocomposite

Variation of reflection loss (RL) for SrM/CCTO/rGO nanocomposite is presented in **Fig. 4.155**. The RL is the main parameter that describes the microwave absorption properties. The sample SCR3 shows a maximum reflection loss of -16.0 dB at 18.0 GHz and matching thickness of 2 mm. The obtained microwave absorption could be attributed to attenuation of EM wave and impedance matching. The presence of CCTO phase in the nanocomposites has lowered the H_c of the nanocomposites and also increase the dielectric properties. The conductive properties of the rGO provide the environment for improved hopping of electrons, tunnelling or free band conduction which consequently enhanced the microwave absorption properties of the nanocomposites [174]. Also, the presence of residual functional groups and defects in the rGO sheets favours the absorption of microwaves [385]. The small crystallite size of the SrM nanoparticles increase dipole polarization thereby enhancing the $\tan\delta_\varepsilon$ of the nanocomposites, the presence of multi interfaces in the nanocomposites also serve as polarization centres which vital for high absorption of microwaves [18]. In general, SrM nanoparticles are magnetic loss absorbents and CCTO microparticles are dielectric loss absorbents, the impedance matching between the magnetic and dielectric loss absorbents results in improved microwave absorption.

4.10.8 EMI shielding performance

Fig. 4.156, **4.157**, and **4.158** present the shielding effectiveness for reflection (SE_R), shielding effectiveness for absorption (SE_A), and total shielding effectiveness (SE_T). Usually, ε' and μ' contribute to SE_R and SE_A respectively. At 18.0 GHz, the sample SCR3 shows a maximum SE_R and SE_A value of 24.54 dB and 12.31 dB respectively. All the nanocomposites exhibit good SE_R and SE_A which could be as a result of good impedance matching between the magnetic and dielectric loss absorbents. All the samples show SE_T values above 20 dB, the values of SE_T for the sample SCR1, SCR2, and SCR3 was found to be 23.8 dB at 16.2 GHz, 25.9 dB at 15.3 GHz, and 36.8 dB at 18.0 GHz. The values of SE_T for the sample SCR3 was found to be the highest, this value is higher than other composites (**Table 4.30**).

Table 4.30 Comparison of EMI shielding effectiveness of the SrM/CCTO/rGO nanocomposite with other nanocomposites

Composite	Pellet thickness (t) (mm)	Maximum total shielding effectiveness (SE_T) (dB)	Frequency (GHz)	References
polypropylene/carbon fibre composite foams	3.2	24.9	8-12	[327]
Porous super-hydrophobic polymer/carbon composites	2	28.5	8-12	[368]
core-shell non-woven fabrics covered by reduced graphene oxide	0.27	32.0	8-12	[369]
SrM/CCTO/rGO nanocomposite (SCR3)	3	36.8	18.0	this work

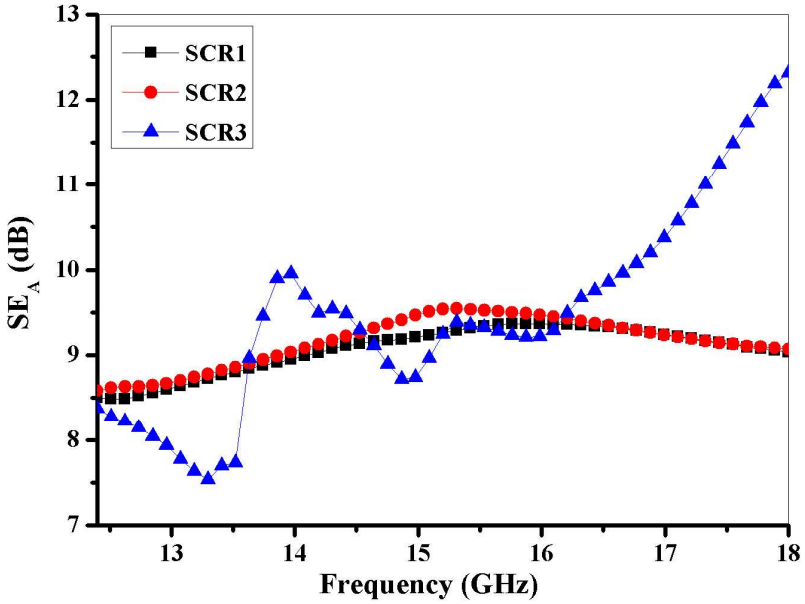

Fig. 4.156 Variation of shielding effectiveness for absorption with frequency for SrM/CCTO/rGO nanocomposite

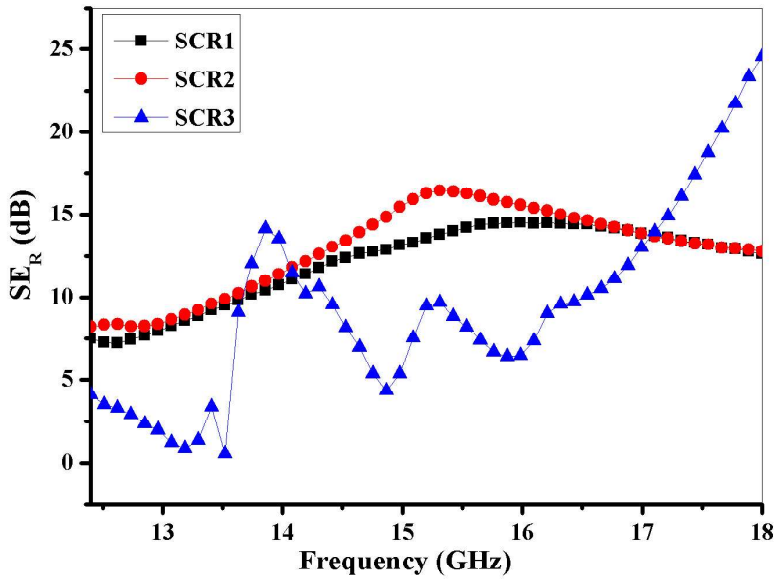

Fig. 4.157 Variation of shielding effectiveness for reflection with frequency for SrM/CCTO/rGO nanocomposite

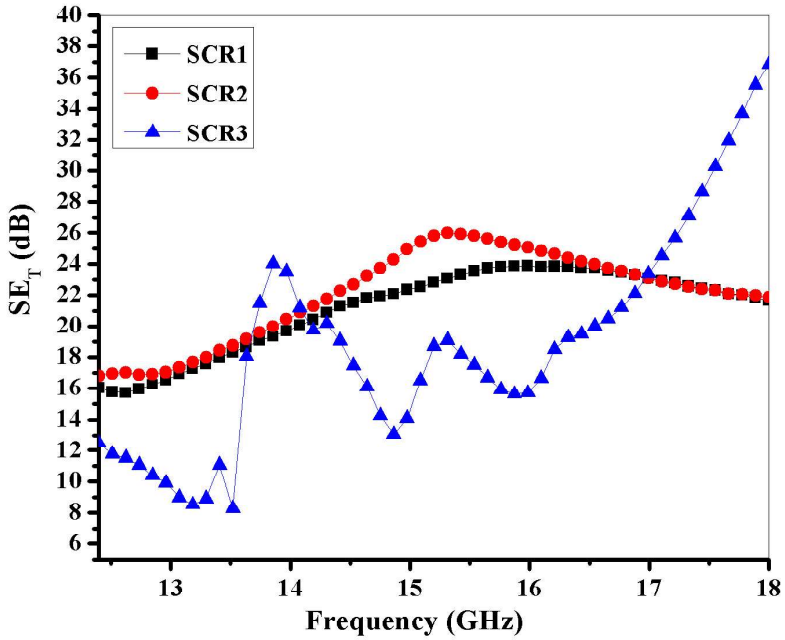

Fig. 4.158 Variation of total shielding effectiveness with frequency for SrM/CCTO/rGO nanocomposite

4.11 Reduced graphene oxide, polyaniline, calcium copper titanate (rGO/PANI/CCTO) nanocomposite

4.11.1 XRD analysis

The XRD patterns of chitosan stabilised rGO/PANI/CCTO nanocomposite are presented in **Fig. 4.159**. The XRD patterns were indexed according to the standard JCPDS card 75-2188and found that the prepared sample exhibit crystalline structure of calcium copper titanate (CCTO) with some traces of secondary phases of calcium titanate ($CaTiO_3$) and copper oxide (CuO). The intensity of these secondary phases has been found to increase with Ce-Ni substitution. The peaks (211), (220), (310), (222), (321), (400), (422), (440), and (620) are major of CCTO whereas (001) is a characteristic peak of PANI.

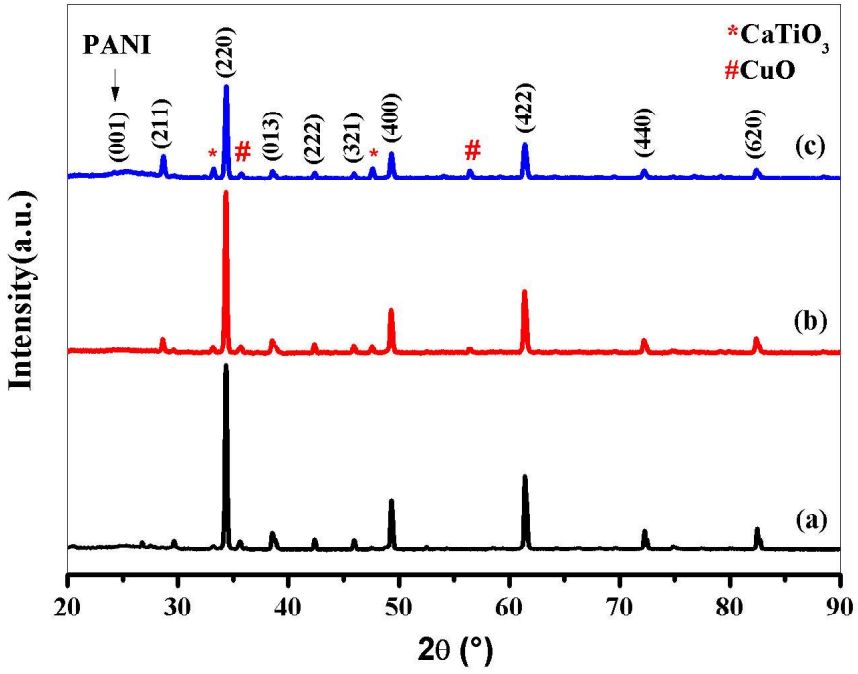

Fig. 4.159 XRD spectra of rGO/PANI/CCTO nanocomposite (a) RPC1, (b) RPC2, and (c) RPC3

4.11.2 FTIR analysis

FTIR spectra of chitosan stabilised rGO/PANI/CCTO nanocomposites are presented in **Fig. 4.160.** The bands at 485 and 604 cm^{-1} gives the idea of the formation of CCTO phase. The main bands of PANI appear at 1582, 1471, 1303, 1129 and 792 cm^{-1}. These bands are due to stretching vibrations of TiO_6 octahedral (Ti-O-Ti) and CuO_4 (Cu-O) in the CCTO structure [335]. The bands at 1582 and 1471 cm^{-1} are attributed to stretching vibration of the benzenoid and quinonoid rings whereas bands at 1303 and 1129 cm^{-1} are due to C=N and C-N stretching vibrations respectively [386]. The bands at 3431 and 3179 cm^{-1} are due to –NH stretching and –OH vibrational modes as a result of absorption of water by PANI. The bands at 1129 and 792 cm^{-1} result from vibrational mode of the N=Q=N stretching mode coupled with aromatic C–H out-of-plane bending of 1,4-dis-ubstituted benzene ring [387]. The band at 2941 cm^{-1} could be attributed to the presence of CO_2 [186]. The characteristics bands of rGO which are 3420 cm^{-1} (–OH), 1728 cm^{-1} (C=O) and 1610 cm^{-1} (C=C) and that of chitosan are not clearly resolved as a result of mixing with other bands of PANI [388].

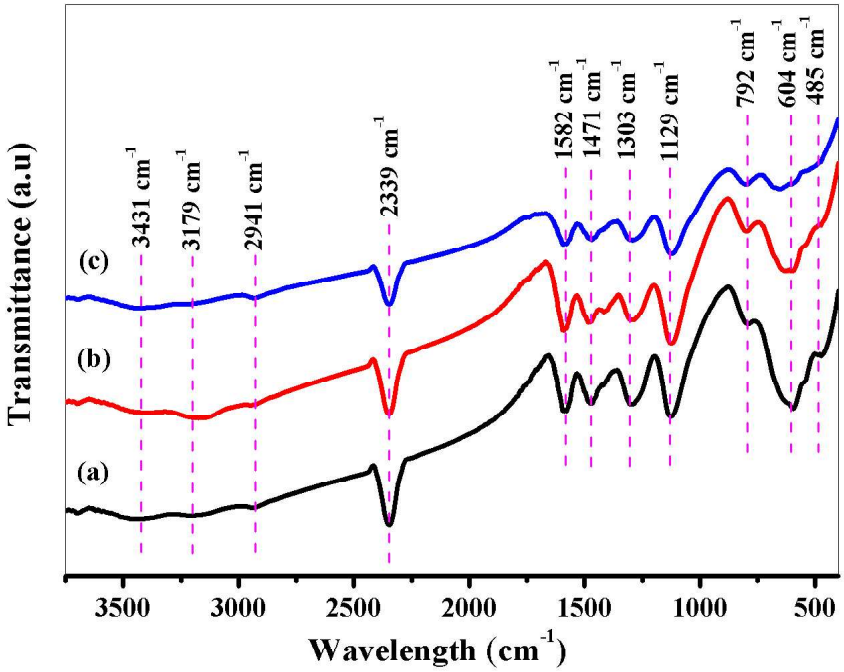

Fig. 4.160 FTIR spectra of rGO/PANI/CCTO nanocomposites (a) RPC1, (b) RPC2 and (c) RPC3

4.11.3 Raman spectroscopy

Raman spectra of chitosan stabilised rGO/PANI/CCTO nanocomposites are presented in **Fig. 4.161.** The characteristics D and G bands of GO at 1595 and 1353 cm^{-1} are clearly observed in **Fig. 4.161**, these bands are attributed to out-plane vibration as a result of presence of defects observed at the edges of the graphene sheets structure and in-plane vibrations of sp^2 bonded atoms in the structure of graphene respectively[378]. The I_D/I_G ratios for GO, rGO and rGO/PANI/$Ca_{0.75}Ce_{0.25}Cu_3Ti_{3.7}Ni_{0.3}O_{12}$ nanocomposite are 0.91, 0.93 and 0.95 respectively. The extent of the reduction of GO to rGO is mostly decided by the D band and the slight increase in the I_D/I_G ratio indicates the extent of reduction of GO to rGO [174].

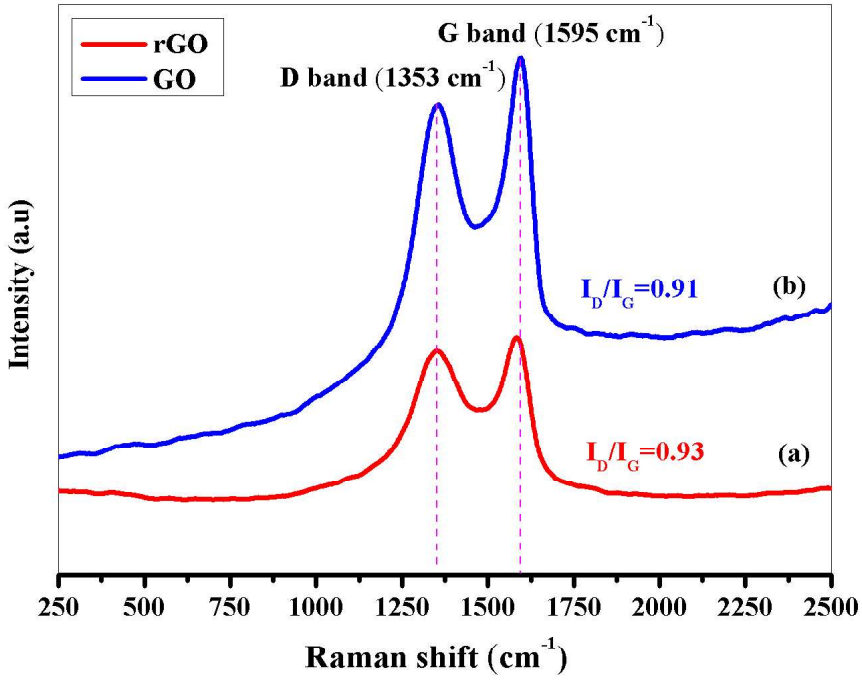

Fig. 4.161 Raman spectra of (a) rGO/PANI/$Ca_{0.75}Ce_{0.25}Cu_3Ti_{3.7}Ni_{0.3}O_{12}$, (b) GO and (c) rGO

4.11.4 Morphology analysis

Fig. 4.162 presents the FESEM micrograph and EDX spectrum of rGO/PANI/$Ca_{0.75}Ce_{0.25}Cu_3Ti_{3.7}Ni_{0.3}O_{12}$ nanocomposite at different magnifications. The as-prepared rGO/PANI/$Ca_{0.75}Ce_{0.25}Cu_3Ti_{3.7}Ni_{0.3}O_{12}$ nanocomposite exhibit rough texture. The FESEM micrographs indicate that the PANI and CCTO nanoparticles have been successfully

distributed on the surface of the rGO sheets. The EDX spectrum shows all the substituted elements of the nanocomposites, this confirms the stoichiometry of the nanocomposites.

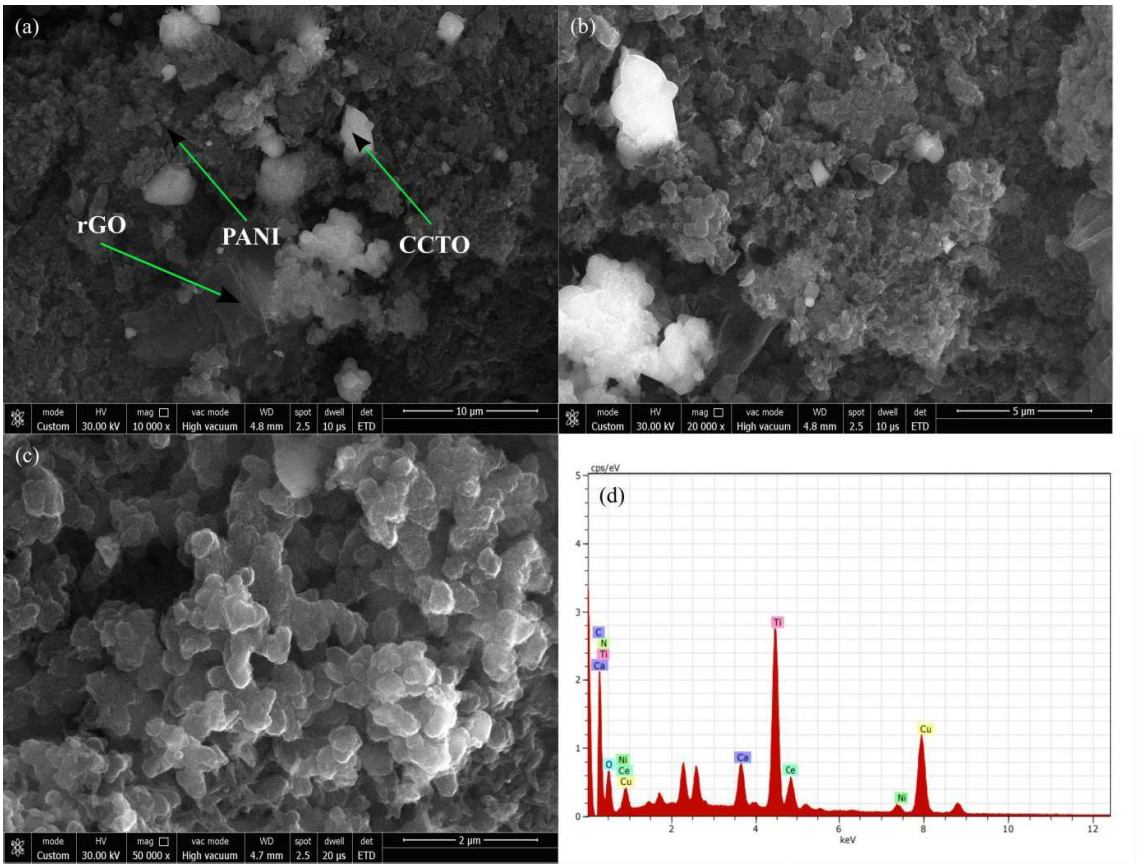

Fig. 4.162 FESEM micrograph and EDX spectrum of rGO/PANI/$Ca_{0.75}Ce_{0.25}Cu_3Ti_{3.7}Ni_{0.3}O_{12}$ nanocomposite (a) 10000 x, (b) 25000 x, (c) 50000 x, and (d) 100000 x magnification (e) EDX spectrum

4.11.5 Dielectric and impedance spectroscopy

The nature of the resistance of the prepared nanocomposite to electric field is determined by the complex permittivity, it is expressed as

$$\varepsilon^* = \varepsilon' - j\varepsilon'' \tag{4.130}$$

Where ε' is the real part of complex permittivity (dielectric constant) and ε'' is the imaginary part of complex permittivity (dielectric loss). Similarly, the complex impedance can be expressed as

$$Z = Z' - jZ'' \tag{4.131}$$

Where Z' and Z'' are the real and imaginary part of complex impedance respectively. The room temperature ε' of the prepared chitosan stabilised rGO/PANI/CCTO nanocomposites are shown in **Fig. 4.163.** The values of ε' for the prepared nanocomposites were determined from the following equation.

$$\varepsilon' = \frac{Z''}{2\pi f C_0 Z^2} \tag{4.132}$$

Where C_0 is the geometrical capacitance and f is the frequency. The behaviour of ε' for the prepared nanocomposites was found to decrease with increase in frequency up to intermediate frequency. The high value of ε' at lower frequencies could be due conductivity of grain boundary and interfacial polarization at the interface of the conductor and insulator whereas lower values of ε' as frequency increases could be attributed to the process of polarization relaxation [174][389]. At higher frequencies, the nanocomposites exhibit frequency independent behaviour. This could be explained on the basis of Maxwell-Wagner relaxation model and Koop's phenomenological theory [272][271]. The RPC1 nanocomposite exhibits the highest dielectric constant (7244).

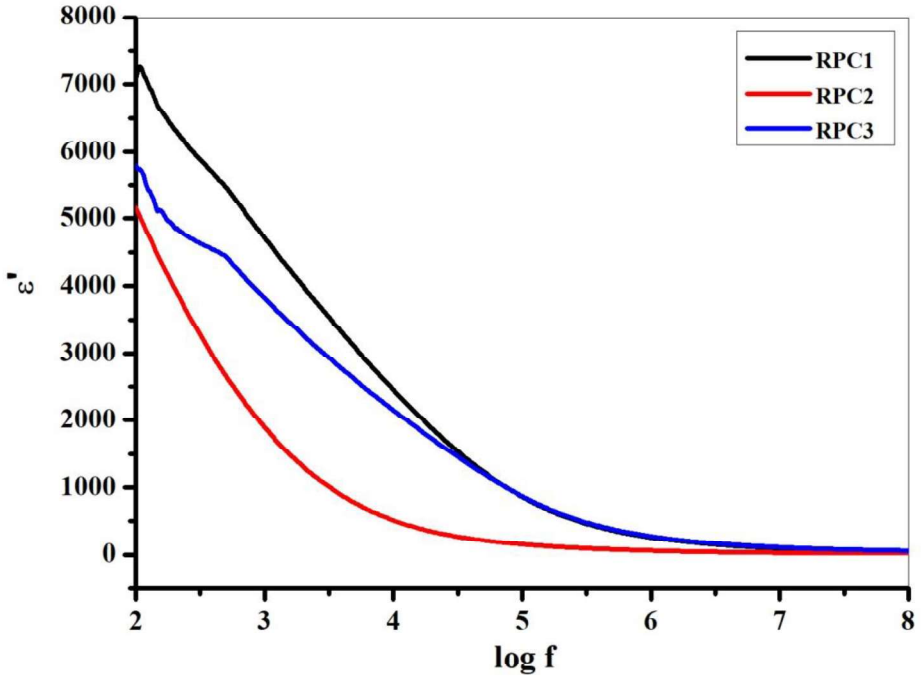

Fig. 4.163 Dielectric constant of rGO/PANI/CCTO nanocomposite

The room temperature dielectric tangent loss ($tan\,\delta$) for the prepared chitosan stabilised rGO/PANI/CCTO nanocomposites are shown in **Fig. 4.164**. The values of $tan\,\delta$ for the prepared nanocomposites were evaluated from the following formula.

$$\tan\delta = \frac{\varepsilon''}{\varepsilon'} \tag{4.133}$$

From **Fig. 4.164**, we can see that $tan\,\delta$ decreases with increase in frequency at lower frequencies as a result of conductivity and interfacial polarization where the frequency independent behaviour observed at intermediate and higher frequencies could be attributed to dipolar relaxation [390].

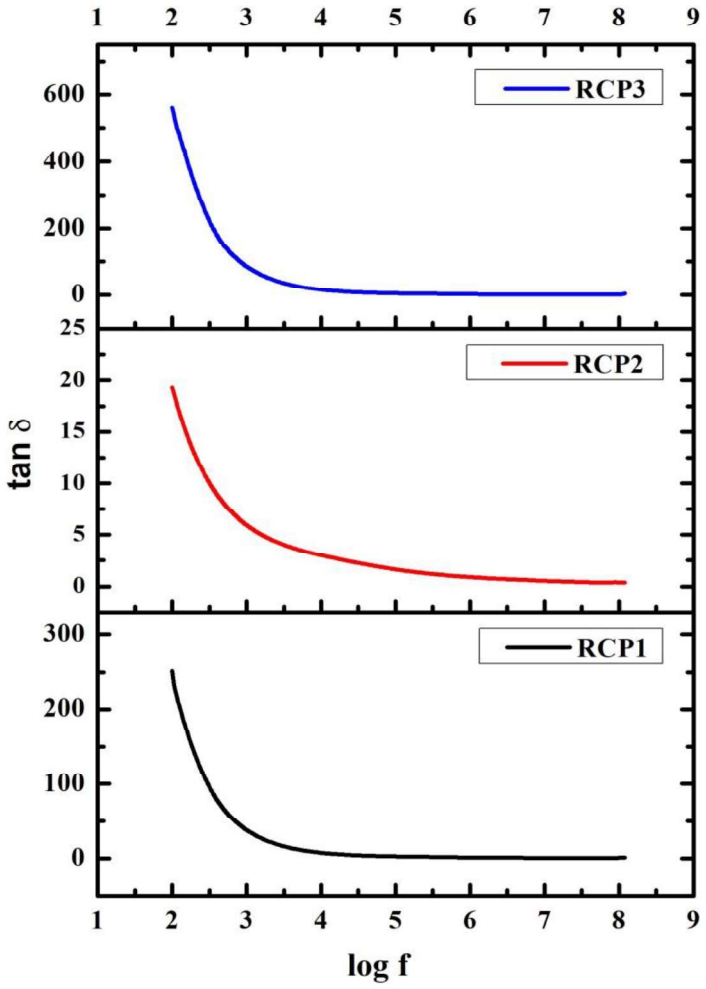

Fig. 4.164 Dielectric tangent loss of rGO/PANI/CCTO nanocomposite

The room temperature variation of AC conductivity (σ_{AC}) with frequency (log f) for the prepared chitosan stabilised rGO/PANI/CCTO nanocomposites are shown in **Fig. 4.165** The values of σ_{AC} for the prepared nanocomposites were determined from the following equation.

$$\sigma_{AC} = 2\pi f \varepsilon'' \varepsilon_0 \tag{4.134}$$

It can be observed that the σ_{AC} is frequency independent at lower and intermediate frequencies. At higher frequencies, the σ_{AC} shows an increasing trend. The RPC3 nanocomposite shows the highest values of Ac conductivity at higher frequencies.

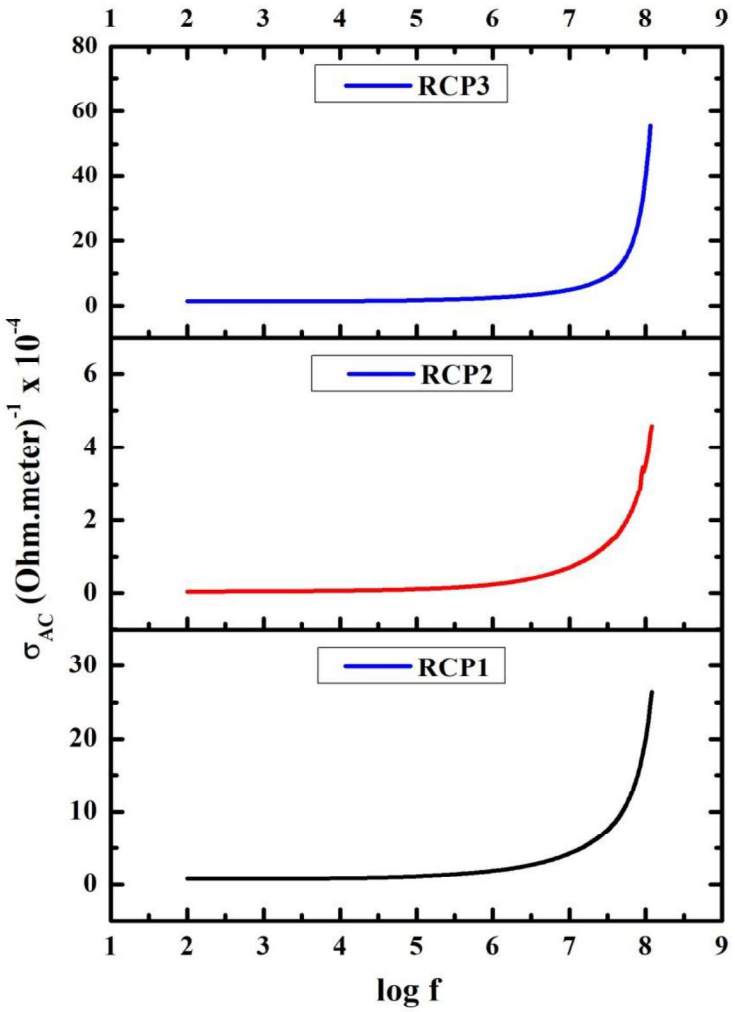

Fig. 4.165 AC conductivity of rGO/PANI/CCTO nanocomposite

4.12 Reduced graphene oxide, strontium hexaferrites, and calcium copper titanate (rGO/SrM/CCTO) nanocomposites

4.12.1 XRD analysis

Fig. 4.166 presents the XRD spectra of biopolymer functionalised rGO/SrM/CCTO nanocomposites. The XRD patterns matched with the standard patterns of hexaferrites (JCPDS no 39-1433) and CCTO (JCPDS no 75-2188). Both Co-substituted SrM and Y-substituted CCTO peaks are respectively identical to the structure of hexaferrites and CCTO with pure and crystalline phases. Secondary phases such as magnetite ($\alpha -Fe_2O_3$), calcium titanate ($CaTiO_3$) and copper oxide (CuO) were absent in the nanocomposites. The peaks with *hkl* values (006), (110), (008), (107), (114), (200), (203), (0010), (205), (206), (1011), (300), (217), (2011), (220), (226), and (317) are major peaks of Co-substituted SrM whereas those with (211), (220), (310), (222), (321), (400), (422), (440), and (620) are major of Y-substituted CCTO.

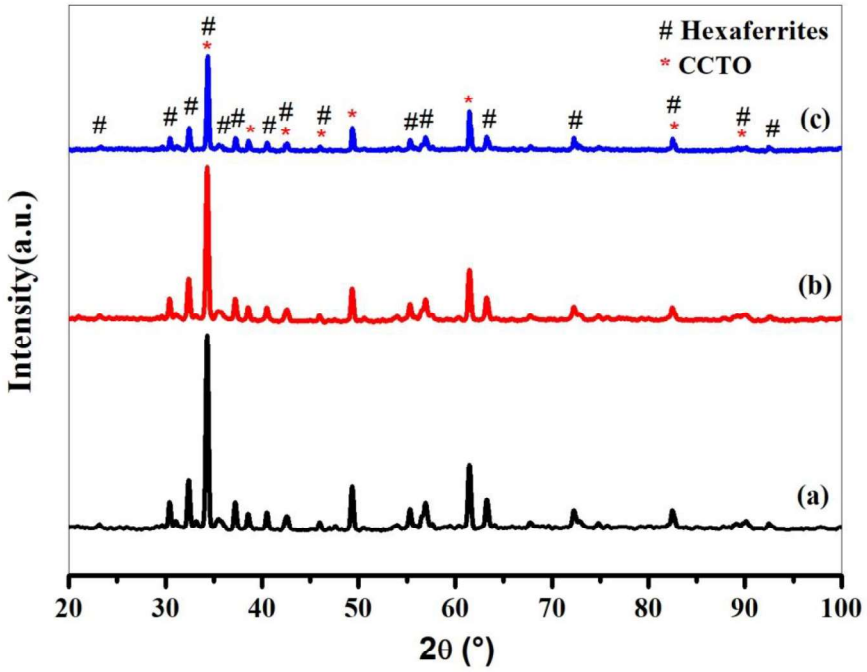

Fig. 4.166 XRD spectra of rGO/SrM/CCTO nanocomposite (a) R1, (b) R2, and (c) R3

4.12.2 FTIR analysis

FTIR analysis was carried in order to study attached functional groups of the nanocomposites**. Fig. 4.167** shows the FTIR spectra of biopolymer functionalised rGO/SrM/CCTO nanocomposite and rGO. The characteristics peaks of Co-substituted SrM and Y-substituted CCTO have been observed at 455 and 616 cm^{-1}. In the Co-substituted SrM structure, these peaks are attributed to stretching vibrations of metal-oxygen bonds whereas the presence of these peaks in the Y-substituted CCTO could be due to stretching vibrations of TiO_6 octahedral (Ti-O-Ti) and CuO_4 (Cu-O) [186][391][392]. These peaks give the idea of the formation of Co-substituted SrM and Y-substituted CCTO phase. Peaks appearing at 1107 cm^{-1} is due to C-O stretching vibrations of alkoxy, 1405cm^{-1} is due O-H deformation, 1607 cm^{-1} C-C vibrations and 3444 cm^{-1} is attributed to O-H stretching vibrations [4]. The peak at 2348 cm^{-1} results from the absorption of CO_2 from the surrounding [9].

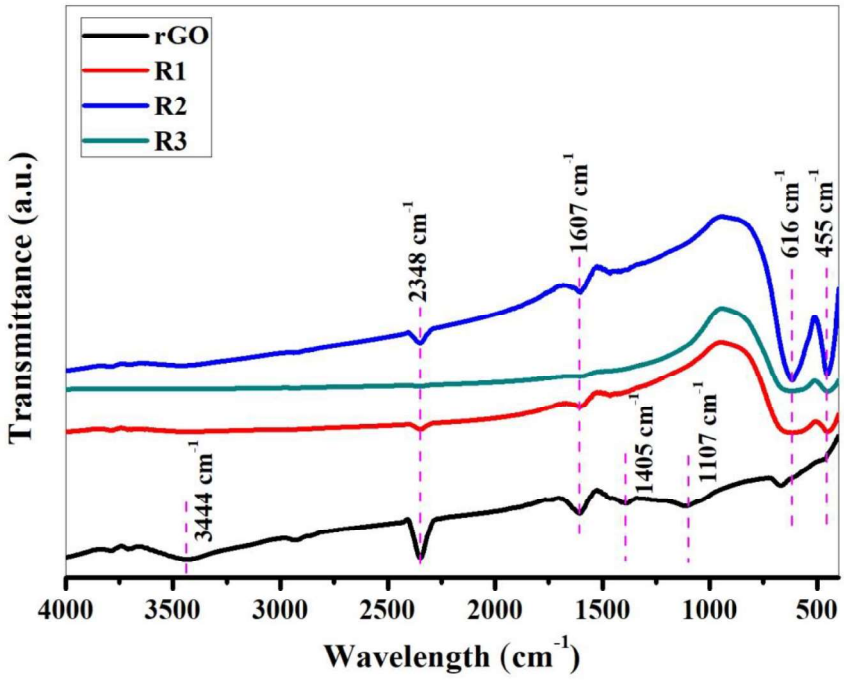

Fig. 4.167 spectra of rGO/SrM/CCTO nanocomposite

4.12.3 Raman spectroscopy

Raman spectroscopy is a powerful non-destructive process to study the degree of ordered or disordered crystal structure of carbon nanomaterials. **Fig. 4.168** presents the Raman spectra of biopolymer functionalised rGO/SrM/CCTO nanocomposites**.** Raman spectra exhibit two broad bands at 1595 and 1353 cm^{-1}; these peaks are the characteristics D and G bands of GO. The D band results from disordered vibrations of sp^3 carbon atoms whereas the G band is attributed to in- plane vibration modes of sp^2 carbon atoms in the 2-dimensional hexagonal lattice of the nanomaterial [5]. The I_D/I_G ratios of GO and rGO are respectively are 0.91, 0.93; the I_D/I_G ratios gives the extent of the reduction of GO to rGO and also the degree of order and disorder of the nanomaterial, the increase observed in the I_D/I_G ratio indicates the extent of reduction of GO to rGO [393].

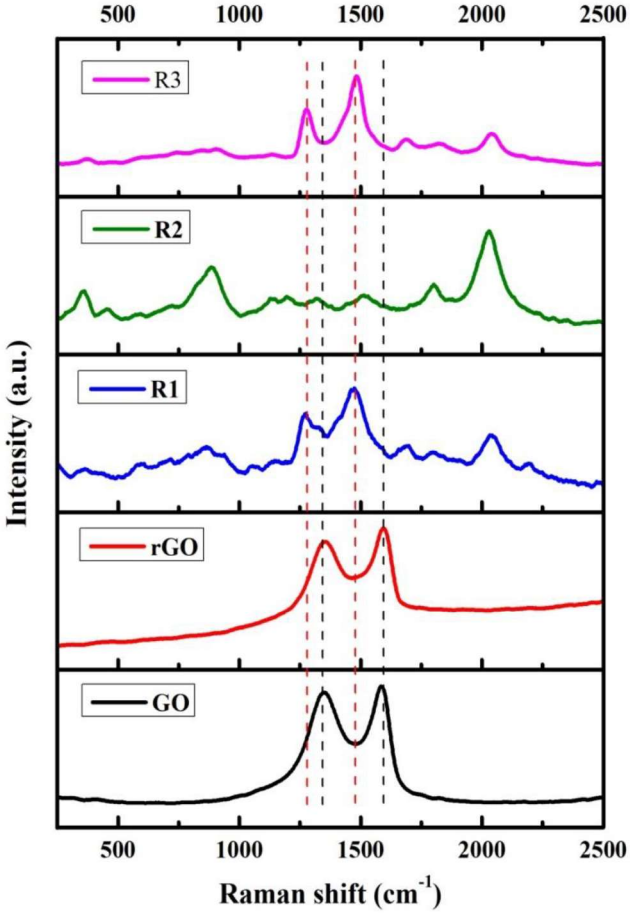

Fig. 4.168 Raman spectra of rGO/SrM/CCTO nanocomposite

4.12.4 Morphology analysis

FESEM micrograph of rGO/SrM/CCTO nanocomposites is shown **Fig. 4.169** (a), (b) and (c). The presence of Co-substituted SrM and Y-substituted CCTO are evident in all the micrographs. The Co-substituted SrM nanoparticles are agglomerated whereas the Y-substituted CCTO nanoparticles are not. The presence of rGO sheets is clearly evident in **Fig. 4.169** (b). The Co-substituted SrM nanoparticles and the Y-substituted CCTO nanoparticles are embedded on the rGO sheets. The Y-substituted CCTO nanoparticles exhibit cubic structure. **Fig. 4.169** (d) shows the EDX spectra rGO/SrM/CCTO nanocomposites. Clearly, stoichiometry of the nanocomposites has been maintained since all the substituted elements are present

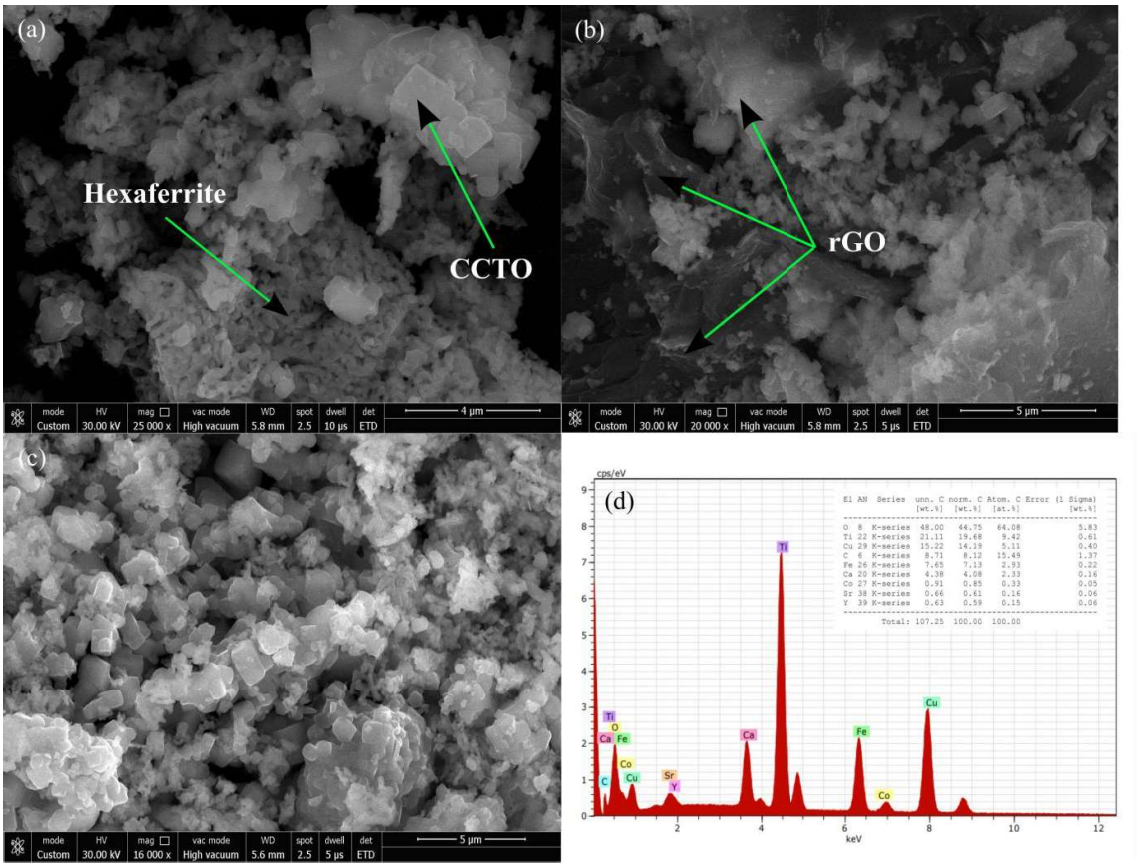

Fig. 4.169 FESEM micrograph and EDX spectra of $SrFe_{11.9}Co_{0.1}O_{19}$/ $CaCu_{2.9}Y_{0.1}Ti_4O_{12}$/rGO

4.12.5 Dielectric and impedance spectroscopy

The dielectric constant and dielectric loss of rGO/SrM/CCTO nanocomposites are presented in **Fig. 4.170** and **4.171** respectively. The values of dielectric constant, dielectric loss and AC conductivity were determined from equation (1), (2), and (3) respectively

$$\varepsilon' = \frac{Z''}{2\pi f C_0 Z^2} \tag{4.135}$$

$$\tan\delta = \frac{\varepsilon''}{\varepsilon'} \tag{4.136}$$

$$\sigma_{AC} = 2\pi f \varepsilon'' \varepsilon_0 \tag{4.137}$$

where Z is the complex impedance, Z'' is the imaginary part of complex impedance, C_0 is the geometrical capacitance, f is the frequency and ε_0 is the permittivity of free space.

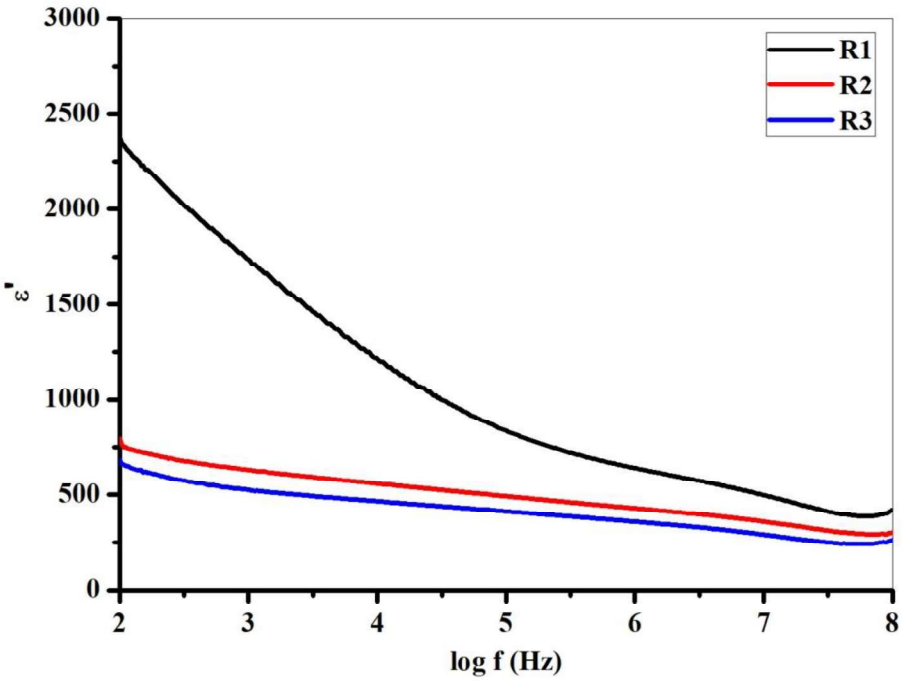

Fig. 4.170 Dielectric constant for rGO/SrM/CCTO nanocomposite

The plot of dielectric constant against frequency is presented in **Fig. 5**. The dielectric constant decreases with increase in frequency throughout the frequency range. The presence of relaxation peaks has not been observed. Conductivity of grain boundary and interfacial polarization at the interface of the conductor and insulator observed are the reason for the

observed high value of ε' at lower frequencies while the polarization relaxation cause the decreased values of ε' as frequency increases [174]. This could be explained on the basis of Maxwell-Wagner relaxation model and Koop's phenomenological theory. The model assumed that the dielectric medium comprises of grains with good conductivity or conductors which are separated by grains with poor conductivity or insulators. When an electric field is applied, the charge carriers can move the grains with little effort; this in turn induces polarization and high dielectric constant.

The plot of dielectric loss versus frequency is shown in **Fig. 4.171**. The dielectric loss is the factor that quantifies the extent of loss in the nanomaterial. The dielectric loss is reasonably low for all the nanocomposites. All the nanocomposites show decreasing behaviour of dielectric loss at low frequency. A broad relaxation peak has been observed in the sample $SrFe_{12}O_{19}$/ $CaCu_3Ti_4O_{12}$/rGO.

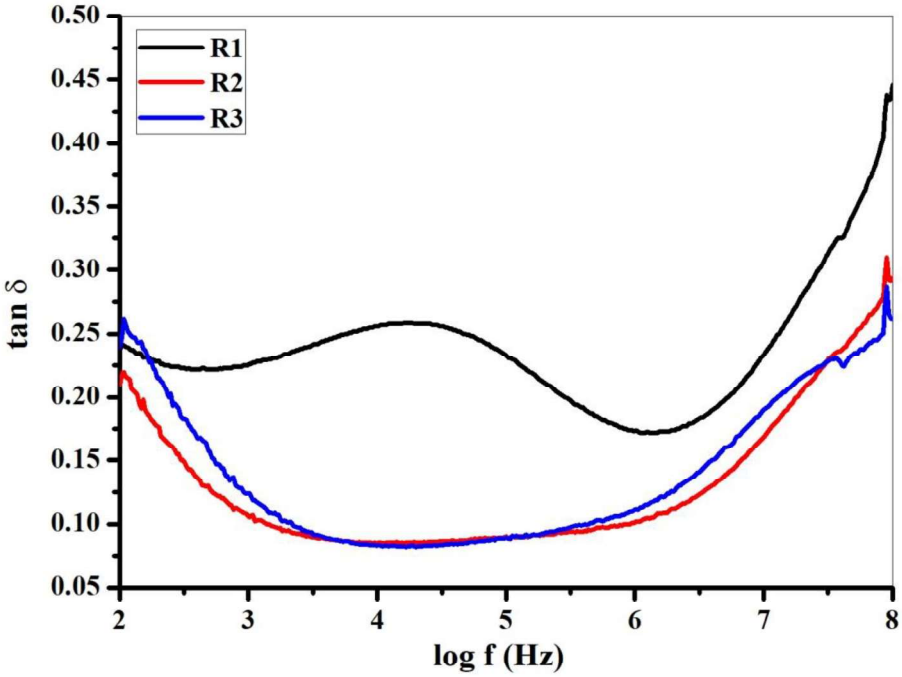

Fig. 4.171 Dielectric loss for rGO/SrM/CCTO nanocomposite

Fig. 4.172 and **Fig. 4.173** presents the AC conductivity and Cole-Cole plot of rGO/SrM/CCTO nanocomposites. The conductivity shows frequency independent behaviour at lower and intermediate frequency. However, there is sudden increase in AC conductivity at higher frequencies, this could be attributed to electron hopping and tunnelling [174]. Cole-

Cole was carried out in order to distinguish between grains and grain boundary effects. The higher frequency region part of the semi-circle of the Cole-Cole plot shows contribution from the grains and is also denoted as grain resistance (R_g) while the lower frequency region shows contribution of the grain boundaries which is called grain boundary resistance (R_{gb}) [276]. From **Fig. 4.173**, we can see that the Cole-Cole plot does not extend to the higher region; hence, we can conclude that most of the contribution to the dielectric properties comes from R_{gb}.

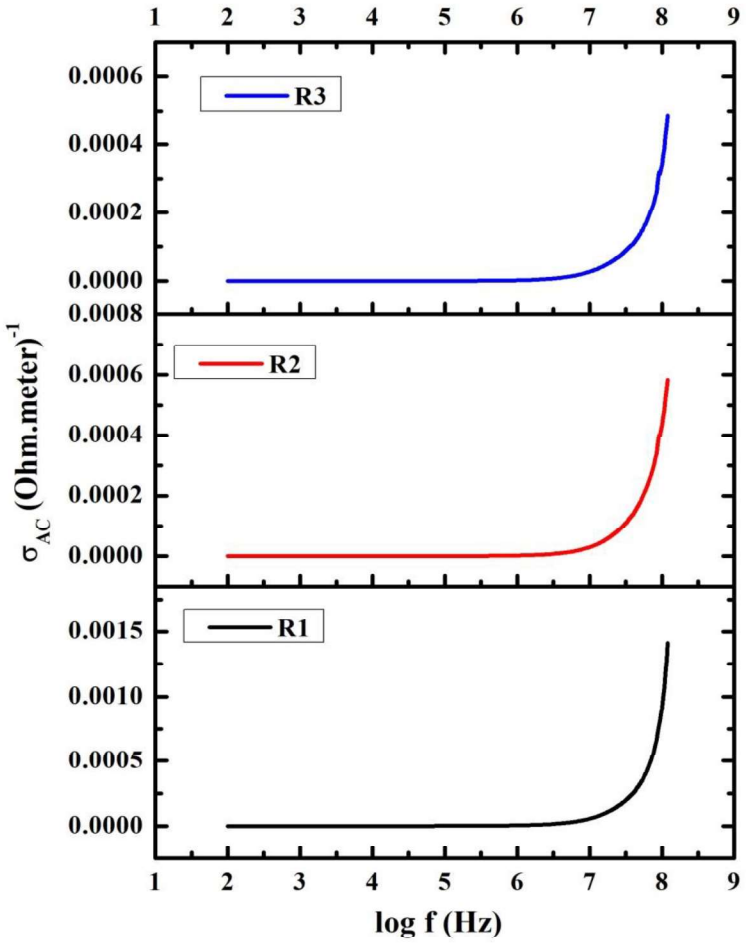

Fig. 4.172 AC conductivity for rGO/SrM/CCTO nanocomposite

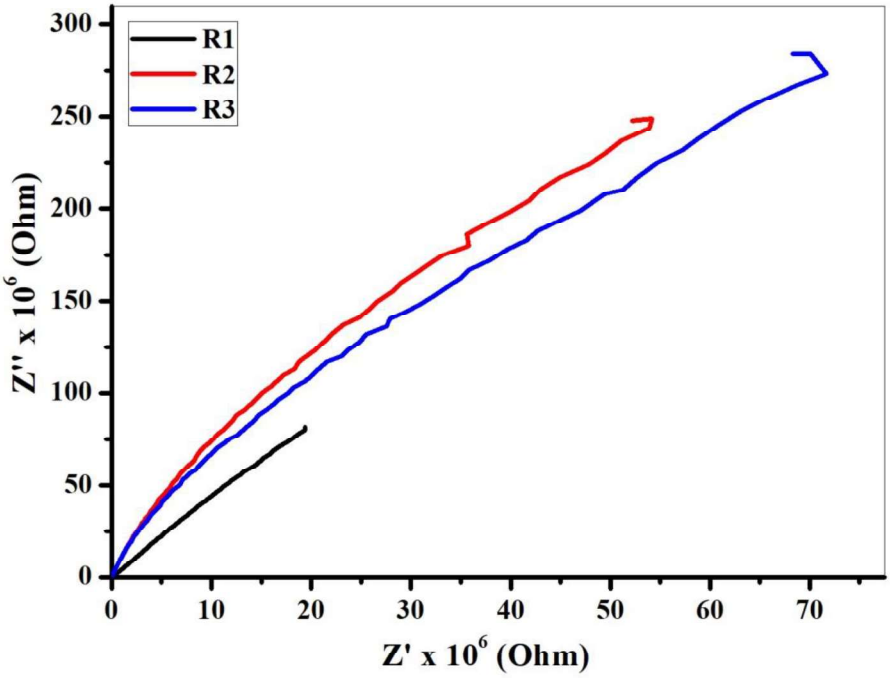

Fig. 4.173 Cole-Cole plot for rGO/SrM/CCTO nanocomposite

Chapter 5

Summary and conclusion

This research has attempted to address some of the challenges faced in the design, synthesis, and characterization of nanocomposites for EMI shielding and microwave absorption. Also, properties such as structural, dielectric, magnetic, and optical properties have also been studied for different nanomaterials. Additionally, Raman and Mössbauer spectroscopy have been carried out in order to understand the site preference and cation distribution in the nanomaterials. The reliability of the sol-gel autocombustion method has been verified as most of the prepared nanomaterials exhibit single phase at reasonable calcination time and duration.

We have successfully employ sol-gel autocombustion method and synthesized Ni^{2+}-La^{3+} substituted CCTO ceramic. The prepared sample was subjected to different characterization techniques in order to understand the evolution of the phase, crystal structure, and morphology as well as dielectric and optical properties with changes in temperature. Our investigation derived the following conclusions. The XRD spectra shows the presence of $CaTiO_3$, CuO, and TiO_2 (anatase phase) secondary phase in the samples with *T1*, *T2*, and *T3*. However, these secondary phases disappear when the sintering temperature was increased to *T4*. Furthermore, the sample with *T4* exhibit greater level of ordered phase and crystal structure as compare to the samples with *T1*, *T2*, and *T3* sequel to the fact it shows the lowest χ^2 values in the Ritveld refinement analysis. We ascribe the lack of ordered phase and crystal structure in the samples with *T1*, *T2*, and *T3* to the presence of the observed secondary phases. We attribute the observed presence of secondary phase in the sample with *T4* in the Raman spectra to the high sensitivity of Raman spectroscopy as compared to XRD. Also, the lack of observed difference in Raman spectra of all the samples could mean that Raman spectroscopy is insensitive to changes in sintering temperature. Our observation shows that the morphology of the prepared Ni^{2+}-La^{3+} substituted CCTO ceramic have propensity for changes in sintering temperature. This is so because the FESEM micrographs shows that particle of the Ni^{2+}-La^{3+} substituted CCTO ceramic starts to resemble the known cubic structure of CCTO ceramic in the sample with *T3* and finally attain this structure in the sample with *T4*. Findings of the XRD analysis regarding the observed hkl values and inter planar spacing were supported by HRTEM and SAED pattern analysis. The absorption spectra shows that changes in temperature affects the electronic structure of the prepared

Ni^{2+}-La^{3+} substituted CCTO ceramic. This claim is most evidently observed in the bathochromic (red) shift (i. e. shifting of the absorption peak towards higher wavelengths region) of the 370 nm absorption peak in the sample with *T2* to the 427 nm absorption peak of the sample with *T3* and finally to the 494 nm absorption peak of the sample with *T4*. The band gap of the prepared Ni^{2+}-La^{3+} substituted CCTO ceramic decrease with increase in sintering temperature, our analysis shows that this behaviour is a consequence of the changes in electronic structure of the Ni^{2+}-La^{3+} substituted CCTO ceramic induced by variation in sintering temperature. We attribute the decrease in dielectric constant with increase in frequency at lower frequency to inter-facial space charge polarization whereas the electronic polarization is the reason behind the dielectric response at higher frequencies. Owing to the presence of $CaTiO_3$, CuO, and TiO_2 in the samples sintered at lower temperature (*T1*, *T2*, and *T3*) and possibly the sample sintered at high temperature (*T4*), we conclude that the dielectric loss in the Ni^{2+}-La^{3+} substituted CCTO ceramic may originate from defects in the CCTO structure, such defects include oxygen vacancies, change in valency of cation, and pores. Also, the synthesized Ni^{2+}-La^{3+} substituted CCTO ceramic shows low frequency resistive nature as a result of dominant grain boundary resistance over grain resistance. In general, our experiment and analysis shows that variation in calcination temperature and the presence of secondary phases ($CaTiO_3$, CuO, and TiO_2) have much effect on the properties of the prepared Ni^{2+}-La^{3+} substituted CCTO ceramic. Additionally, morphology, phase and crystal structure evolution of the synthesized Ni^{2+}-La^{3+} substituted CCTO ceramic depend on sintering temperature.

Pr^{3+}-Co^{2+} substituted CCTO ceramic have been successfully prepared using sol-gel autocombustion technique. The CCTO ceramics show well-defined peaks coupled with single crystalline phase having cubic perovskite structure and space group *Im*-3. Raman spectroscopy was further used to confirm the single phase of the prepared CCTO ceramic. Cubic grains with size in μm and the absence of agglomeration were observed in the morphology of the prepared CCTO ceramics whereas EDX spectra confirm the stoichiometry CCTO ceramics since all the substituted and host cations have been observed. The highest value of E_g (3.88 eV) was observed in the sample J1 whereas the lowest dielectric constant (1920) at 100 Hz was observed in the sample J3. The relaxation peak observed in the sample J4 was explained on the basis of Maxwell-Wagner relaxation process.

Ce^{3+}-Ni^{2+} substituted CCTO have been successfully synthesized and using sol-gel method. The XRD patterns show the presence of $CaTiO_3$ and CuO secondary phase. The morphology shows grains with size in the range 902.4 nm to 1.562 μm. The calculated lattice constant and volume of unit cell are in agreement with literature. All the prepared CCTO ceramics show high dielectric constant and low dielectric loss. The sample K2 shows the highest dielectric constant at lower frequencies as a result of appearance of interfacial polarization.

Al^{3+}-Mn^{2+} substituted strontium hexagonal ferrites have been successfully prepared using sol-gel autocombustion technique. The prepared samples were calcinated at 750 °C, 850 °C, 950 °C and 1050 °C for 5 hours and the effect of variation on the structural, dielectric, optical, and magnetic properties was investigated. XRD patterns shows that the prepared samples exhibit single crystalline phase of hexaferrites with traces of secondary phase (α-Fe_2O_4). The occurrence of this secondary phase could be avoided by making sure that the starting materials are thoroughly mixed, also the small amount of cations should be substituted. The appearance of two peaks between 400 cm^{-1} and 600 cm^{-1} in the FTIR investigation of the prepared samples gives an idea of the formation of hexaferrite. Thermal analysis of the samples shows recrystallization of the sample and a formation temperature of 650 °C. The band gap shows a decreasing behaviour with increase in sintering temperature. High dielectric constant was observed in the samples and the investigation of magnetic parameters indicates that 850 °C is the optimum temperature to obtained high coercivity (6750 Oe) since the coercivity reduces above that temperature. In order to study the effect of variation of composition, we synthesize M-type strontium hexaferrites $Sr_{1-x}Al_xFe_{11.4}Mn_{0.6}O_{19}$ (x=0.0, 0.1, 0.2, and y=0.6) via sol-gel auto combustion technique and calcinated the sample at 950 °C for 5 hours. The prepared sample exhibit low dielectric loss at low frequency (100 Hz). The prepared sample exhibit platelet-like shape which may be useful in high frequency application. The coercivity increases with increase in Al^{3+}-Mn^{2+} concentration. High values of coercivity have been observed in all the samples.

Dy^{3+}-Cr^{2+} substituted barium hexaferrites have been successfully synthesized using sol-gel autocombustion method. The solubility of the cations substituted in the sample can be assumed up to B3 (i.e. x=0.2 and y=0.5) since secondary phase or impurity has not been observed in the XRD patterns. Factors such as quantum confinement and crystallite sizes affect the band gap of the prepared samples. All the prepared samples exhibit dielectric response typical of hexaferrites. The conductivity, dielectric loss as well as dielectric constant of the prepared samples rely on hopping of electrons between Fe^{3+} and Fe^{2+} ions at octahedral

site. Analysis of Cole-Cole plot indicates that the contribution to the dielectric response comes mostly from R_{gb}. It has been observed that under the effect of applied electric field, the relaxation of defects dipoles display decreases with increase in frequency, and consequently, the $\tan\delta$ decreases at the higher frequencies. The Raman spectra show a combination of weak and intense Raman active modes at 175, 197, 287, 320, 405, 516, 615, 675, and 733 cm^{-1} which are in good agreement with pure M-type hexaferrites. Similarly, analysis of Mössbauer spectra indicate that Cr^{3+} ion replaces Fe^{3+} ion at octahedral 12k, 2a, and $4f_2$ site, as well as bipyramidal (2b) sites. The values of H_c, M_r and M_s were found to be in the range 5050.81 to 6047.68 Oe, 20.57 to 34.02 emu/g and 36.00 to 60.69 emu/g respectively. From the magnetic parameters, we can infer that the number of Cr^{3+} ions occupying $4f_2$ crystallographic site is greater than those occupying $12k$ and $2a$ crystallographic sites thereby resulting in increased M_s and M_r and we observed a decrease when they replace Fe^{3+} ions in $12k$ and $2a$ because the net magnetic moment of Cr^{3+} ($3\ \mu_B$) is less than that of Fe^{3+} ($5\ \mu_B$).

Cu^{2+}-Er^{3+} substituted strontium hexaferrites have been prepared using sol-gel autocombustion method. XRD patterns show that the samples exhibit single phase with crystalline peaks and the absence of secondary phase (α-Fe_2O_3). Idea of the formation of hexaferrite was observed in the FTIR spectra by the appearance of peaks between 400 and 600 cm^{-1}. The grains agglomerated are as a result of magnetic interaction with neighbouring grains. Band gap increases a s a result of quantum confinement effects as well as smaller grains. Low dielectric loss coupled with high frequency improvement of dielectric constant was observed in the synthesized samples. Several Raman active modes with varying intensities were observed at 177, 285, 333, 402, 420, 523, 611, 679, and 727 cm^{-1}, these modes corresponds to vibration or rotation of the crystallographic sites in the hexagonal structure. Room temperature magnetization loop shows ferromagnetic behaviour of the prepared samples. The substitution of Cu^{2+}-Er^{3+} result in the decrease of magnetic parameters for all the prepared samples. Our analysis of Mössbauer spectra using the Ligand theory shows that Er^{3+} ion with d^{10} configuration could occupy 12k, $4f_2$, 2a, and 2b site in different proportion.

Pr^{3+}-Co^{2+} substituted strontium hexaferrite have been prepared via sol-gel autocombustion method. XRD patterns show well-defined peaks identical to M-type hexaferrites, secondary phase such as magnetite has not been observed. FESEM micrographs show the formation of larger grains, this usually happens because of the magnetic interaction between the grains. The sample exhibit high values of ε' at lower frequencies, our analysis shows that the presence of oxygen vacancies, grain boundary defects, interfacial dislocation, and the

occurrence of electron hopping between Fe^{3+} to Fe^{2+} could be the reason behind the high observed high values of ε'. Spin rotation coupled with relaxation type dispersion and domain wall motion coupled with resonance type dispersion are the reason behind the evolution of μ'. A reflection loss of -7 dB and maximum value of SE_T value of 27.40 dB for a pellet thickness of 2 mm was observed in the sample S2.

BaM/CCTO nanocomposites have been synthesized via sol gel autocombustion method. XRD patterns and Raman spectra, it has been observed that the BaM/CCTO nanocomposites exhibit pure and crystalline structure. Optical analysis shows that the band gap and crystallite size show similar behaviour with variation in composition of the BaM/CCTO nanocomposites. Eddy current effect and exchange resonance are the main contributors of the magnetic losses of the BaM/CCTO nanocomposites. Dielectric losses are the main contributors to the microwave absorption properties of the BaM/CCTO nanocomposites mainly occur due to dielectric losses. BaMCCTO1 and BaMCCTO4 each having thickness of 3 mm respectively show maximum reflection loss of -22.8 dB (equivalent to 99.47 % absorption of EM wave) with bandwidth of 0.7 GHz and -27.9 dB (equivalent to 99.83 % absorption of EM wave) with bandwidth of 1.7 GHz. In general, a microwave absorber is considered to be efficient and for possible practical application if its reflection loss is less than -10 dB. Hence, the synthesized BaM/CCTO nanocomposites my find practical applications in electronics devices and as microwave absorber. Good attenuation properties were exhibited by all the BaM/CCTO nanocomposites. BaMCCTO4 nanocomposite shows a total shielding effectiveness of 41.8 dB at 16.5 GHz and bandwidth of 4.2GHz, this value corresponds to 99.99 % shielding of EM waves and is above the limit ($SE_T > 20\ dB$). Additionally, it was found o out-performs even nanocomposites of reduced graphene oxide and some polymers earlier reported in literature.

In a preliminary study, we successfully prepare nanocomposites of rGO/PANI/CCTO and rGO/SrM/CCTO. The incorporation of biopolymer (chitosan) is to stabilised reduced graphene oxide (rGO) by ensuring that the RGO sheets do not restack into graphite. XRD patterns indicate the formation of M-type hexaferrites and CCTO phase in the nanocomposites. Raman spectra show the presence of rGO by the appearance of characteristics D and G band. Dielectric constant and loss were determined from the impedance analyser data. The nanocomposites show low value of dielectric loss.

SrM/CCTO/rGO nanocomposite has been successfully synthesized. XRD pattern indicate that the SrM phase, CCTO phase, and rGO have been successfully incorporated together. The intensity of the FTIR peaks decrease after the reduction of the rGO, this indicates that most of the oxygen-containing functional groups have been removed. Furthermore, we can assume the restoration of the carbon basal plane. Interestingly, the I_D/I_G ratio calculated from Raman spectra of GO and rGO also indicates the removal of structural defects and oxygen-containing functional groups such as hydroxyl, carbonyl and carboxyl groups in the rGO sheets. The band gap of the prepared nanocomposite shows a decreasing behaviour with variation in the composition of the prepared nanocomposite, we attribute this observation to factors such as quantum confinement, crystallite size as well as interaction of SrM and CCTO grains with rGO sheets. Investigation of the absorption of microwave by the nanocomposites shows that the dielectric loss is the major contributor to the observed reflection loss. Exchange and natural resonance results in the appearance of magnetic losses. The sample SCR3 shows a minimum reflection loss of -16.0 dB at 18.0 GHz as a result of good impedance matching between the magnetic and dielectric loss absorbents. All the samples show SE_T values above 20 dB at various frequencies, the values of SE_T was found to be 23.8 dB at 16.2 GHz, 25.9 dB at 15.3 GHz, and 36.8 dB at 18.0 GHz for the sample SCR1, SCR2, and SCR3 respectively. The value of SE_T for the sample SCR3 was found is higher than other composite materials reported in literature.

In general, the observed properties of all the prepared samples are in agreement with already published research. Also, most of the properties correlate with certain application. For instance, the band gap of SrM/CCTO/rGO nanocomposite could be used in making nanoscale UV-blue light emitting diodes (LEDs). Most importantly, the EMI shielding and microwave absorption performance of the BaM/CCTO and SrM/CCTO/rGO nanocomposite is remarkably more than that of many nanomaterials and nanocomposites earlier reported in literature.

Future scope

Temperature variation studies are very vital as temperature can rise above room temperature in summer and below room temperature in winter. Hence, there is need to study the performance of nanomaterials and nanocomposites at various temperatures. All the reported data in this thesis was recorded at room temperature. Due to limited access to research equipment, we could not be able to carry out some characterization at low and high

temperature. For instance, magnetic, dielectric, Raman and Mössbauer spectroscopy could be perform while varying the temperature. Additional characterization such as electron paramagnetic resonance (EPR) could be performed in order to further compliment other characterizations. Additionally, single crystals of M-type hexagonal ferrites and CCTO can be grown in order to obtain much purity of the samples.

Bibliography

[1] P. Liu, Y. Huang, Y. Yang, J. Yan, and X. Zhang, "Sandwich structures of graphene@Fe_3O_4@PANI decorated with TiO_2 nanosheets for enhanced electromagnetic wave absorption properties," J. Alloys Compd., **662**, 63–68 (2016).

[2] P. Liu, Y. Huang, L. Wang, M. Zong, and W. Zhang, "Hydrothermal synthesis of reduced graphene oxide–Co_3O_4 composites and the excellent microwave electromagnetic properties," Mater. Lett., **107**, 166–169 (2013).

[3] Y. Wang, Z. Peng, and W. Jiang, "Controlled synthesis of Fe_3O_4@SnO_2/RGO nanocomposite for microwave absorption enhancement," Ceram. Int., **42**, 10682-10689 (2016).

[4] Y. Chen, Y. Li, M. Yip, and N. Tai, "Composites Scien ce and Techn ology Electromagnetic interference shielding efficiency of polyaniline composites filled with graphene decorated with metallic nanoparticles," Compos. Sci. Technol., **80**, 80–86 (2013).

[5] N. Zhang, Y. Huang, M. Zong, X. Ding, S. Li, and M. Wang, "Synthesis of core-shell $ZnFe_2O_4$@SiO_2 hollow microspheres/reduced graphene oxides for a high-performance EM wave absorber," Ceram. Int., **42**, 18879-18886 (2016).

[6] B. Shen, Y. Li, D. Yi, W. Zhai, X. Wei, and W. Zheng, "Strong flexible polymer/ raphene composite films with 3D saw-tooth folding for enhanced and tunable electromagnetic shielding," Carbon, **113**, pp. 55–62 (2017).

[7] M. Zong, Y. Huang, and N. Zhang, "Reduced graphene oxide-$Ni_{0.5}Zn_{0.5}Fe_2O_4$ composite: Synthesis and electromagnetic absorption properties," Mater. Lett., **145**, 115–119 (2015).

[8] W. Song, X. Guan, L. Fan, W. Cao, Q. Zhao, C. Wang, and M. Cao, "Tuning broadband microwave absorption via highly conductive Fe_3O_4/graphene heterostructural nanofillers," Mater. Res. Bull., **72**, 316–323 (2015).

[9] Q. Jia, W. Wang, J. Zhao, J. Xiao, L. Lu, and H. Fan, "Synthesis and characterization of TiO_2/polyaniline/graphene oxide bouquet-like composites for enhanced microwave

absorption performance," J. Alloys Compd., **710**, 717-724 (2017).

[10] Y. Zhang, Y. Huang, H. Chen, Z. Huang, Y. Yang, P. Xiao, Y. Zhou, and Y. Chen, "Composition and structure control of ultralight graphene foam for high-performance microwave absorption," Carbon, **105**, 438–447 (2016).

[11] X. Liu, Y. Chen, C. Hao, J. Ye, R. Yu, and D. Huang, "Graphene-enhanced microwave absorption properties of Fe_3O_4/SiO_2 nanorods," Composites Part A: Applied Science and Mnaufacturing, **89**, 40-46 (2016).

[12] V. Kumar, T. Eren, N. Atar, M. Lüt, C. Parlak, and H. Karimi-maleh, "$CoFe_2O_4$@ TiO_2 decorated reduced graphene oxide nanocomposite for photocatalytic degradation of chlorpyrifos," J. Mol. Liq., **208**, 122–129 (2015).

[13] X. Chen, J. Chen, F. Meng, L. Shan, M. Jiang, and X. Xu, "Hierarchical composites of polypyrrole/graphene oxide synthesized by in situ intercalation polymerization for high efficiency and broadband responses of electromagnetic absorption," Compos. Sci. Technol., **127**, 71–78 (2016).

[14] J. Li, J. Wei, Z. Pu, M. Xu, K. Jia, and X. Liu, "Influence of Fe_3O_4/Fe-phthalocyanine decorated graphene oxide on the microwave absorbing performance," J. Magn. Magn. Mater., **399**, 81–87 (2016).

[15] J. Yan, Y. Huang, X. Chen, and C. Wei, "Conducting polymers-$NiFe_2O_4$ coated on reduced graphene oxide sheets as electromagnetic (EM) wave absorption materials," Synth. Met., **221**, 291–298 (2016).

[16] J. Wang, J. Wang, B. Zhang, Y. Sun, W. Chen, and T. Wang, "Combined use of lightweight magnetic Fe_3O_4-coated hollow glass spheres and electrically conductive reduced graphene oxide in an epoxy matrix for microwave absorption," J. Magn. Magn. Mater., **401**, 209-216 (2015).

[17] Y. Wang, Y. Fu, X. Wu, W. Zhang, Q. Wang, and J. Li, "Synthesis of hierarchical core-shell $NiFe_2O_4$@MnO_2 composite microspheres decorated graphene nanosheet for enhanced microwave absorption performance," Ceram. Int., **43**, 11367–11375 (2017).

[18] P. Liu, Y. Huang, and X. Zhang, "Synthesis, characterization and excellent electromagnetic wave absorption properties of graphene@$CoFe_2O_4$@polyaniline

nanocomposites," Synth. Met., **201**, 76–81 (2015).

[19] P. Liu, Y. Huang, and X. Zhang, "Synthesis, characterization and excellent electromagnetic wave absorption properties of graphene/poly (3,4-ethylenedioxythiophene) hybrid materials with Fe_3O_4 nanoparticles," J. Alloys Compd., **617**, 511–517 (2014).

[20] Y. Wang, X. Wu, W. Zhang, J. Li, C. Luo, and Q. Wang, "Fabrication and enhanced electromagnetic wave absorption properties of sandwich-like graphene@NiO@ PANI decorated with Ag particles," Synth. Met., **229**, 82–88 (2017).

[21] P. Liu, Y. Huang, and X. Zhang, "Synthesis and excellent microwave absorption properties of graphene/polypyrrole composites with Fe_3O_4 particles prepared via a co-precipitation method," Mater. Lett., **129**, 35–38 (2014).

[22] D. Chen, H. Quan, Z. Huang, S. Luo, X. Luo, and F. Deng, "Electromagnetic and microwave absorbing properties of RGO@hematite core–shell nanostructure/PVDF composites," Compos. Sci. Technol., **102**, 126–131 (2014).

[23] Y. Chen, H. Zhang, Y. Huang, Y. Jiang, W. Zheng, and Z. Yu, "Magnetic and electrically conductive epoxy/graphene/carbonyl iron nanocomposites for efficient electromagnetic interference shielding," Compos. Sci. Technol., **118**, 178–185 (2015).

[24] X. Liu, C. Cui, T. Li, A. Xia, and Y. Lv, "Ni@C nanocapsules-decorated $SrFe_{12}O_{19}$ hexagonal nano flakes for high-frequency microwave absorption," J. Alloys Compd., **678**, 234–240, 2016.

[25] M. Zong, Y. Huang, H. Wu, Y. Zhao, Q. Wang, and X. Sun, "One-pot hydrothermal synthesis of RGO/$CoFe_2O_4$ composite and its excellent microwave absorption properties," Mater. Lett., 114, 52–55 (2014).

[26] M. Zong, Y. Huang, H. Wu, Y. Zhao, S. Wang, N. Zhang, and W. Zhang, "Facile synthesis of RGO/Fe_3O_4/Ag composite with high microwave absorption capacity," Mater. Lett., **111**, 188–191 (2013).

[27] H. Zhang, X. Tian, C. Wang, H. Luo, J. Hu, Y. Shen, and A. Xie, "Facile synthesis of RGO/NiO composites and their excellent electromagnetic wave absorption properties," Appl. Surf. Sci., **314**, 228–232 (2014).

[28] P. Liu, Y. Huang, and X. Zhang, "Superparamagnetic $NiFe_2O_4$ particles on poly (3,4-ethylenedioxythiophene)–graphene: Synthesis, characterization and their excellent microwave absorption properties," Compos. Sci. Technol., **95**, 107–113 (2014).

[29] Y. Wang, W. Zhang, C. Luo, X. Wu, and G. Yan, "Superparamagnetic $FeCo@SnO_2$ nanoparticles on graphene- polyaniline : Synthesis and enhanced electromagnetic wave absorption properties," Ceram. Int., **42**, 12496-12502 (2016).

[30] M. Zong, Y. Huang, and N. Zhang, "Reduced graphene oxide-$CoFe_2O_4$ composite : Synthesis and electromagnetic absorption properties," Appl. Surf. Sci., **345**, 272–278 (2015).

[31] M. A. Almessiere, Y. Slimani, H. Güngüne, H. S. El Sayed, and A. Baykal, "AC susceptibility and hyperfine interactions of vanadium substituted barium nanohexaferrites," Ceram. Int., **44**, 17749–17758 (2018).

[32] S. K. Chawla, R. K. Mudsainiyan, S. S. Meena, and S. M. Yusuf, "Sol–gel synthesis , structural and magnetic properties of nanoscale M-type barium hexaferrites $BaCo_xZr_xFe_{(12-2x)}O_{19}$," J. Magn. Magn. Mater., **350**, 23–29 (2014).

[33] I. A. Auwal, H. Güngüne, S. Güner, S. E. Shirsath, M. Sertkol, and A. Baykal, "Structural , magneto-optical properties and cation distribution of $SrBi_xLa_xY_xFe_{12-3x}O_{19}$ (0 . 0 x 0 . 33) hexaferrites," Mterials Research Bulletin, **80**, 263–272 (2016).

[34] R. K. Mudsainiyan, A. K. Jassal, M. Gupta, and S. K. Chawla, "Study on structural and magnetic properties of nanosized M-type Ba-hexaferrites synthesized by urea assisted citrate precursor route," J. Alloys Compd., **645**, 421–428 (2015).

[35] L. Ramajo, R. Parra, J. A. Varela, M. M. Reboredo, M. A. Ramírez, and M. S. Castro, "Influence of vanadium on electrical and microstructural properties of $CaCu_3Ti_4O_{12}/CaTiO_3$," J. Alloys Compd., **497**, 349–353 (2010).

[36] C. Wang, S. Lin, K. Kao, Y. Chen, and S. Weng, "Microstructural and electrical properties of $CaTiO_3$–$CaCu_3Ti_4O_{12}$ ceramics," J. Alloys Compd., **491**, 423–430 (2010).

[37] X. Chen, Q. Zhao, X. Li, and D. Wang, "Enhanced photocatalytic activity of degrading short chain chlorinated paraffins over reduced graphene oxide/$CoFe_2O_4$/Ag

nanocomposite," J. Colloid Interface Sci., **479**, 89–97 (2016).

[38] M. Ahmadipour, M. F. Ain, and Z. A. Ahmad, "A Short Review on Copper Calcium Titanate (CCTO) Electroceramic: Synthesis, Dielectric Properties, Film Deposition, and Sensing Application," Nano-Micro Lett., **8**, 291–311 (2016).

[39] R. C. Pullar, "Hexagonal ferrites : A review of the synthesis , properties and applications of hexaferrite ceramics," Prog. Mater. Sci., **57**, 1191–1334 (2012).

[40] S. K. Chawla, P. Kaur, R. K. Mudsainiyan, S. S. Meena, and S. M. Yusuf, "Effect of Fuel on the Synthesis, Structural, and Magnetic Properties of M-Type Hexagonal $SrFe_{12}O_{19}$ Nanoparticles," J. Supercond. Nov. Magn., **28**, 1589–1599 (2015).

[41] X. Chi, L. Chang, D. Xie, J. Zhang, and G. Du, "Hydrothermal preparation of Co_3O_4/graphene composite as anode material for lithium-ion batteries," Mater. Lett., **106**, 178–181 (2013).

[42] L. Kong, X. Yin, X. Yuan, Y. Zhang, X. Liu, and L. Cheng, "Electromagnetic wave absorption properties of graphene modified with carbon nanotube/poly (dimethyl siloxane) composites," Carbon, **73**, 185–193 (2014).

[43] D. Zhang and W. Zou, "Decorating reduced graphene oxide with Co_3O_4 hollow spheres and their application in supercapacitor materials," Curr. Appl. Phys., **13**, 1796–1800 (2013).

[44] F. Mohd, M. Hashim, I. Ismail, R. Nazlan, and I. Riati, "Recent developments of smart electromagnetic absorbers based polymer-composites at gigahertz frequencies," J. Magn. Magn. Mater., **405**, 197–208 (2016).

[45] O. Acher "Modern microwave magnetic materials : Recent advances and trends," J. Magn. Magn. Mater., **321**, 2033–2034 (2009).

[46] R. E. Camley, Z. Celinski, T. Fal, A. V Glushchenko, A. J. Hutchison, Y. Khivintsev, B. Kuanr, I. R. Harward, V. Veerakumar, and V. V. Zagorodnii, "High-frequency signal processing using magnetic layered structures," J. Magn. Magn. Mater., **321**, 2048–2054 (2009).

[47] Y. Alivov and H. Morkoc, "Microwave ferrites , part 2 : passive components and electrical tuning," Journal of Mterials Science: Materials in Electronics, **20**, 911–952

(2009).

[48] V. G. Harris, A. Geiler, Y. Chen, S. Dae, M. Wu, A. Yang, Z. Chen, P. He, P. V Parimi, X. Zuo, C. E. Patton, M. Abe, O. Acher, and C. Vittoria, "Recent advances in processing and applications of microwave ferrites," J. Magn. Magn. Mater., **321**, 2035–2047 (2009).

[49] M. Pardavi-horvath, "Microwave applications of soft ferrites," J. Magn. Magn. Mater., **215–216**, 171–183 (2000).

[50] Y. Guan, Y. Lin, L. Zou, Q. Miao, M. Zeng, Z. Liu, X. Gao, J. Liu, Y. Guan, Y. Lin, L. Zou, Q. Miao, and M. Zeng, "The effects of Co-Ti co-doping on the magnetic , electrical , and magnetodielectric behaviors of M-type barium hexaferrites The effects of Co-Ti co-doping on the magnetic , electrical , and magnetodielectric behaviors of M-type barium hexaferrites," AIP Adv., **3**, 122115 (2013).

[51] E. S. Alhwaitat, S. H. Mahmood, M. Al-Hussein, O. E. Mohsen, Y. Maswadeh, I. Bsoul, and A. Hammoudeh, "Effects of synthesis route on the structural and magnetic properties of $Ba_3Zn_2Fe_{24}O_{41}(Zn_2Z)$ nanocrystalline hexaferrites," Ceram. Int., **44**, 779-787 (2018).

[52] E. D. Solov, E. V Pashkova, A. E. Perekos, and A. G. Belous, "Structural and Magnetic Properties of $BaFe_{12-2x}Co_xSn_xO_{19}$ Modified M Type Hexaferrites," Inorg. Mater., **48**, 1280–1285 (2012).

[53] T. Kaur, S. Kumar, J. Sharma, and A. K. Srivastava, "Radiation losses in the microwave K_u band in magneto-electric nanocomposites," Beilstein J. Nanotechnol., **6**, 1700–1707 (2015).

[54] T. Kaur, S. Kumar, S. B. Narang, and A. K. Srivastava, "Radiation losses in microwave Ku region by conducting pyrrole/barium titanate and barium hexaferrites based nanocomposites," J. Magn. Magn. Mater., **420**, 336-342 (2016).

[55] Y. Kim and S. Kim, "Magnetic and microwave absorbing properties of Ti and Co substituted M-hexaferrites in Ka-band frequencies (26.5~40 GHz)," Journal of Electroceramics, **24**, 314–318 (2010).

[56] H. Nikmanesh, M. Moradi, G. H. Bordbar, and R. S. Alam, "Synthesis of multi-walled

carbon nanotube/doped barium hexaferrite nanocomposites: An investigation of structural, magnetic and microwave absorption properties," Ceram. Int., **42**, 14342–14349 (2016).

[57] M. Zhang, J. Zheng, L. Liang, F. Jiang, and Y. Wang, "Journal of Magnetism and Magnetic Materials Preparation and microwave absorption properties of Ag-doped $BaTiO_3$ nanocomposites," J. Magn. Magn. Mater., **368**, 198–201 (2014).

[58] S. Iqbal, J. Shah, R. K. Kotnala, and S. Ahmad, "Highly efficient low cost EMI shielding by barium ferrite encapsulated polythiophene nanocomposite," J. Alloys Compd., **779**, 487–496 (2019).

[59] R. C. Pullar, I. K. Bdikin, and A. K. Bhattacharya, "Magnetic properties of randomly oriented BaM , SrM , Co_2-Y , Co_2-Z and Co_2-W hexagonal ferrite fibres," J. Eur. Ceram. Soc., **32**, 905–913 (2012).

[60] B. A Bender and M. J. Pan, "The effect of processing on the giant dielectric properties of $CaCu_3Ti_4O_{12}$," Materials Science and Engineering: B, **117**, 339–347 (2005).

[61] A. Khare, S. S. Yadava, K. D. Mandal, N. K. Mukhopadhyay "Effect of sintering duration on the dielectric properties of $0.9BaTiO_3$–$0.1CaCu_3Ti_4O_{12}$ nanocomposite synthesized by solid state route." Microelectronic Engineering, **164**, 1-6 (2016).

[62] M. A. Subramanian, D. Li, N. Duan, B. A. Reisner, and A. W. Sleight, "High Dielectric Constant in $ACu_3Ti_4O_{12}$ and $ACu_3Ti_3FeO_{12}$ Phases," J. Solid State Chem., vol. **325**, 204, 323–325, (2000).

[63] B. Bochu, M. N. Deschizeaux, and J. C. Joubert, "Synthese et caractbrisation d'une serie de titanates perowskites isotypes de $[CaCu_3](Mn_4)O_{12}$," J. Solid State Chem., **29**, 291–298 (1979).

[64] P. Thomas, K. T. Varughese, K. Dwarakanath, and K. B. R. Varma, "Dielectric properties of Poly (vinylidene fluoride)/$CaCu_3Ti_4O_{12}$ composites," Compos. Sci. Technol., **70**, 539–545 (2010).

[65] S. Kwon, C. C. Huang, M. A. Subramanian, and D. P. Cann, "Effects of cation stoichiometry on the dielectric properties of $CaCu_3Ti_4O_{12}$," J. Alloys Compd., **473**, 433–436 (2009).

[66] B. Rivas-murias, M. Sanchez-Andujar, J. Rivas, and M. A. Senaris-Rodriguez, "Influence of high levels of Nb and Ti doping on the dielectric properties of $CaCu_3Ti_4O_{12}$ type of compounds," Mater. Chem. Phys., **120**, 576–581 (2010).

[67] B. Bochu, J. Chenavas, J. C. Joubert, M. Marezio "High pressure synthesis and crystal structure of a new series of perovskite-like compounds CMn_7O_{12} (C=Na, Ca, Cd, Sr, La, Nd)," Journal of solid state chemistry, **11**, 88–93 (1974).

[68] D. D. L. Chung, "Review Graphite," J. Mater. Sci., **37,** 1475–1489 (2002).

[69] S. V Tkachev, E. Y. Buslaeva, and S. P. Gubin, "Graphene : A Novel Carbon Nanomaterial," Inorg. Mater., **47**, 5–14 (2011).

[70] S. Niyogi, E. Bekyarova, M. E. Itkis, J. L. Mcwilliams, M. A. Hamon, and R. C. Haddon, "Solution Properties of Graphite and Graphene," J. Am. Chem. Soc., **128**, 7720–7721 (2006).

[71] O. Akhavan, "The effect of heat treatment on formation of graphene thin films from graphene oxide nanosheets," Carbon, **48**, 509–519, (2009).

[72] G. Du, X. Wang, L. Zhang, Y. Feng, and Y. Li, "Controllable synthesis of different ZnO architectures decorated reduced graphene oxide nanocomposites," Mater. Lett., **96**, 128–130 (2013).

[73] O. Akhavan, "Photocatalytic reduction of graphene oxides hybridized by ZnO nanoparticles in ethanol," Carbon, **49**, 11–18 (2010).

[74] K. S. Novoselov, A. K. Geim, S. V Morozov, D. Jiang, Y. Zhang, S. V. Dubonos, I. V. Grigorieva, and A. A. Firsov, "Electric Field Effect in Atomically Thin Carbon Films," Science, **306**, 666–669 (2004).

[75] W. S. Hummers and R. E. Offeman, "Preparation of Graphitic Oxide," J. Am. Chem. Soc., **80**, 1339 (1958).

[76] N. I. Kovtyukhova, P. J. Ollivier, B. R. Martin, T. E. Mallouk, S. A. Chizhik, E. V Buzaneva, and A. D. Gorchinskiy, "Layer-by-Layer Assembly of Ultrathin Composite Films from Micron-Sized Graphite Oxide Sheets and Polycations," Chem. Mater., **11**, 771–778 (1999).

[77] J. K. Lee, K. B. Smith, M. Hayner, and H. H. Kung, “Silicon nanoparticles–graphene paper composites for Li ion battery anodes,” chem. commun., **46**, 2025–2027 (2010).

[78] S. Pei and H. Cheng, “The reduction of graphene oxide,” Carbon, **50**, 3210–3228 (2011).

[79] S. V Tkachev, E. Y. Buslaeva, A. V Naumkin, S. L. Kotova, I. V Laure, and S. P. Gubin, “Reduced Graphene Oxide,” Inorg. Mater., **48**, 909–915 (2012).

[80] D. R. Dreyer, S. Park, W. Bielawski, and R. S. Ruoff, “The chemistry of graphene oxide,” Chem. Soc. Rev., **39**, 228–240 (2010).

[81] J. C. Meyer, R. S. Sundaram, A. Chuvilin, S. Kurasch, M. Burghard, K. Kern, and U. Kaiser, “Atomic Structure of Reduced Graphene Oxide Cristina Go,” Nano Lett., **10**, 1144–1148, (2010).

[82] N. Adeela, U. Khan, M. Iqbal, S. Riaz, M. Irfan, H. Ali, K. Javed, I. Bukhtiar, K. Maaz, and S. Naseem, “Structural and magnetic response of Mn substituted Co2 Y-type barium hexaferrites,” J. Alloys Compd., **686**, 1017–1024 (2016).

[83] M. Ahmad, I. Ali, M. U. Islam, and M. U. Rana, “Investigation of Co-Substituted Nanosized Mn_2Y-Hexaferrites Synthesized by Sol-Gel Autocombustion Method,” Journal of Materials Engineering and Performance, **22**, 3909–3915 (2013).

[84] M. Awawdeh, I. Bsoul, and S. H. Mahmood, “Magnetic properties and Mossbauer spectroscopy on Ga , Al , and Cr substituted hexaferrites,” J. Alloys Compd., **585**, 465–473 (2014).

[85] I. Ali, M. Ahmad, and M. S. Awan, “Substitution effects of La^{3+} ions on the structural and magnetic properties of Co_2Y hexaferrites synthesized by sol–gel autocombustion method,” J. sol-gel Sci. Technol., **68**, 141–149 (2013).

[86] T. Kaur, B. Kaur, B. H. Bhat, S. Kumar, and A. K. Srivastava, “Effect of calcination temperature on microstructure, dielectric, magnetic and optical properties of $Ba_{0.7}La_{0.3}Fe_{11.7}Co_{0.3}O_{19}$ hexaferrites,” Phys. B Condens. Matter, **456**, 206–212 (2015).

[87] I. Ali, M. U. Islam, M. S. Awan, and M. Ahmad, “Effects of Heat-Treatment Temperature on the Microstructure , Electrical and Dielectric Properties of M-Type Hexaferrites,” J. Electron. Mater., **43**, 512–521 (2014).

[88] Y. Bai, J. Zhou, Z. Gui, L. Li, and L. Qiao, "The physic properties of Bi–Zn codoped Y-type hexagonal ferrite," J. Alloys Compd., **450**, 412–416 (2008).

[89] I. Ali, M. U. Islam, M. N. Ashiq, I. Sadiq, M. A. Khan, N. Karamat, M. Ishaque, G. Murtaza, I. Shakir, and Z. Ahmad, "Electrical Behavior of Tb-Mn Substituted Y-Type Hexa-ferrites for High-Frequency Applications," Journal of Electronic materials, **44**, 1054–1061 (2015).

[90] I. Ali, M. U. Islam, N. Karamat, A. Iftikhar, and M. Azhar, "Synthesis and magnetic properties of (Eu–Ni) substituted Y-type hexaferrite by surfactant assisted co-precipitation method," J. Magn. Magn. Mater., **385**, 386–393 (2015).

[91] I. Ali, M. U. Islam, M. Naeem, M. A. Iqbal, and M. S. Awan, "Role of Tb–Mn substitution on the magnetic properties of Y-type hexaferrites," J. Alloys Compd., vol. 599, pp. 131–138, 2014.

[92] I. Odeh, H. M. El Ghanem, S. H. Mahmood, S. Azzam, I. Bsoul, and A. Lehlooh, "Dielectric and magnetic properties of Zn-substituted Co 2 Y barium hexaferrite prepared by sol – gel auto combustion method," Phys. B Phys. Condens. Matter, **494**, 33–40 (2016).

[93] Y. Bai, F. Xu, L. Qiao, and J. Zhou, "Effect of Mn doping on physical properties of Y-type hexagonal ferrite," J. Alloys Compd., **473**, 505–508 (2009).

[94] I. Sadiq, I. Ali, E. Rebrov, S. Naseem, M. N. Ashiq, and M. U. Rana, "Nanosized Ce–Zn substituted microwave absorber material for X-band applications," J. Magn. Magn. Mater., **370**, 25–31 (2014).

[95] Z. Yang, Y. Zhang, R. Xiong, and J. Shi, "Effect of sintering in oxygen on electrical conduction and dielectric properties in $CaCu_3Ti_4O_{12}$," Mater. Res. Bull., **48**, 310–314 (2013).

[96] J. Liu, R. W. Smith, and W. Mei, "Synthesis of the Giant Dielectric Constant Material $CaCu_3Ti_4O_{12}$ by Wet-Chemistry Methods," Chem. Mater., **19**, 6020–6024 (2007).

[97] M. Wang, B. Zhang, and F. Zhou, "Preparation and characterization of $CaCu_3Ti_4O_{12}$ powders by non-hydrolytic sol–gel method," J. sol-gel Sci. Technol., **70**, 62–66, 2014.

[98] A. Kumar, N. Kumar, S. Kumar, L. Singh, and K. D. Mandal, "Effect of tantalum

substitutions on microstructures and dielectric properties of calcium copper titanate ($CaCu_3Ti_4O_{12}$) ceramic," Mater. Sci. Eng. B, **177**, 1213–1218 (2012).

[99] A. Kumar, N. Kumar, S. Lee, K. D. Mandal, D. Kumar, and O. Parkash, "Dielectric properties of iron doped calcium copper titanate , $CaCu_{2.9}Fe_{0.1}Ti_4O_{12}$," J. Alloys Compd., **509**, 8901–8906, (2011).

[100] L. Liu, H. Fan, P. Fang, and X. Chen, "Sol–gel derived $CaCu_3Ti_4O_{12}$ ceramics: Synthesis , characterization and electrical properties," Materials Research Bulletin, **43**, 1800–1807 (2008).

[101] L. Liu, H. Fan, P. Fang, and L. Jin, "Electrical heterogeneity in $CaCu_3Ti_4O_{12}$ ceramics fabricated by sol–gel method," Solid State Communications, **142**, 573–576 (2007).

[102] S. Chang, S. Kangning, and C. Pengfei, "Microwave absorption properties of Ce-substituted M-type barium ferrite," J. Magn. Magn. Mater., **324**, 802–805 (2012).

[103] D. C. Marcano, D. V Kosynkin, J. M. Berlin, A. Sinitskii, Z. Sun, A. Slesarev, L. B. Alemany, W. Lu, and J. M. Tour, "Improved Synthesis of Graphene Oxide," ACS Nano, **4**, 4806-4814 (2010).

[104] B. Li, T. Liu, Y. Wang, and Z. Wang, "ZnO/graphene-oxide nanocomposite with remarkably enhanced visible-light-driven photocatalytic performance," J. Colloid Interface Sci., **377**, 114–121 (2012).

[105] X. Liu, L. Pan, T. Lv, and Z. Sun, "Investigation of photocatalytic activities over ZnO–TiO_2–reduced graphene oxide composites synthesized via microwave-assisted reaction," J. Colloid Interface Sci., **394**, 441–444, 2013.

[106] T. Lu, L. Pan, H. Li, G. Zhu, T. Lv, X. Liu, Z. Sun, T. Chen, and D. H. C. Chua, "Microwave-assisted synthesis of graphene – ZnO nanocomposite for electrochemical supercapacitors," J. Alloys Compd., **509**, 5488–5492 (2011).

[107] C. E. Jeyanthi, R. Siddheswaran, P. Kumar, M. K. Chinnu, K. Rajarajan, and R. Jayavel, "Investigation on synthesis , structure , morphology , spectroscopic and electrochemical studies of praseodymium-doped ceria nanoparticles by combustion method," Mater. Chem. Phys., **151**, 22–28 (2015).

[108] J. N. Ding, Y. B. Liu, N. Y. Yuan, G. Q. Ding, Y. Fan, and C. T. Yu, "The influence of

temperature, time and concentration on the dispersion of reduced graphene oxide prepared by hydrothermal reduction," Diam. Relat. Mater., **21**, 11–15 (2012).

[109] C. Xu, X. Shi, A. Ji, L. Shi, C. Zhou, and Y. Cui, "Fabrication and Characteristics of Reduced Graphene Oxide Produced with Different Green Reductants," PLoS One, **10**, 1-15, 2015.

[110] L. Liu, H. Fan, P. Fang, and X. Chen, "Sol-gel derived $CaCu_3Ti_4O_{12}$ ceramics: Synthesis, characterization and electrical properties," Mater. Res. Bull., **43**, 1800–1807 (2008).

[111] A. K. Rai, N. K. Singh, S. K. Acharya, L. Singh, and K. D. Mandal, "Effect of tantalum substitutions on microstructures and dielectric properties of calcium copper titanate ($CaCu_3Ti_4O_{12}$) ceramic," Mater. Sci. Eng. B Solid-State Mater. Adv. Technol., **177**, 1207–1212 (2012).

[112] S. Guillemet-Fritsch, T. Lebey, M. Boulos, and B. Durand, "Dielectric properties of $CaCu_3Ti_4O_{12}$ based multiphased ceramics," J. Eur. Ceram. Soc., **26**, 1245–1257 (2006).

[113] S. Kumar, T. Kaur, S. Kumar, and A. K. Srivastava, "Effect of Heat Treatment on Properties of $Sr_{0.7}Nd_{0.3}Co_{0.3}Fe_{11.7}O_{19}$," J. Supercond. Nov. Magn., **28**, 2935–2940, 2015.

[114] L. Singh, I. W. Kim, B. C. Sin, K. D. Mandal, U. S. Rai, A. Ullah, H. Chung, and Y. Lee, "Dielectric studies of a nano-crystalline $CaCu_{2.90}Zn_{0.10}Ti_4O_{12}$ electro-ceramic by one pot glycine assisted synthesis from inexpensive TiO_2 for energy storage capacitors," RSC Adv., **4**, 52770–52784, 2014.

[115] B. P. Zhu, Z. Y. Wang, Y. Zhang, Z. S. Yu, J. Shi, and R. Xiong, "Low temperature fabrication of the giant dielectric material $CaCu_3Ti_4O_{12}$ by oxalate coprecipitation m ethod," Mater. Chem. Phys., **113**, 746–748 (2009).

[116] L. Singh, U. S. Rai, K. Mandal, B. C. Sin, S. I. Lee, and Y. Lee, "Dielectric, AC-impedance, modulus studies on 0.5BaTiO3·0. 5CaCu3Ti4O12nano-composite ceramic synthesized by one-pot, glycine-assisted nitrate-gel route," Ceram. Int., **40**, 10073–10083 (2014).

[117] S. Sharma, M. M. Singh, U. S. Rai, and K. D. Mandal, "Rationalization of dielectric properties of nano-sized iron doped yttrium copper titanate using impedance and modulus studies," Mater. Sci. Semicond. Process., **31**, 720–727 (2015).

[118] K. D. Mandal, L. Singh, S Sharma, U. S. Rai, and M. M. Singh, "Dielectric and ac impedance studies of nanostructured $CaCu_3Ti_{3.90}Ce_{0.10}O_{12}$ electro-ceramic synthesized by citrate-gel route," Journal of Sol-Gel Science and Technology, **66**, 50-58 (2013).

[119] A. K. Rai, K. D. Mandal, D. Kumar, and O. Parkash, "Characterization of nickel doped CCTO: $CaCu_{2.9}Ni_{0.1}Ti_4O_{12}$ and $CaCu_3Ti_{3.9}Ni_{0.1}O_{12}$ synthesized by semi-wet route," J. Alloys Compd., **491**, 507–512 (2010).

[120] M. J. Abu, J. J. Mohamed, M. F. Ain, and Z. A. Ahmad, "Phase structure, microstructure and broadband dielectric response of Cu nonstoichiometry CaCu3Ti4O12ceramic," J. Alloys Compd., **683**, 579–589 (2016).

[121] J. Mohammed, T. Tekou, T. Carol, H. Y. Hafeez, B. I. Adamu, Y. S. Wudil, Z. I. Takai, S. Kumar, and A. K. Srivastava, "Tuning the dielectric and optical properties of Pr-Co – substituted calcium copper titanate for electronics applications," J. Phys. Chem. Solids, **126**, 85–92 (2019).

[122] A. F. L. Almeida, P. B. A. Fechine, J. C. Góes, M. A. Valente, M. A. R. Miranda, and A. S. B. Sombra, "Dielectric properties of $BaTiO_3$(BTO)-$CaCu_3Ti_4O_{12}$(CCTO) composite screen-printed thick films for high dielectric constant devices in the medium frequency (MF) range," Mater. Sci. Eng. B Solid-State Mater. Adv. Technol., **111**, 113–123 (2004).

[123] T. Li, J. Chen, D. Liu, Z. Zhang, Z. Chen, Z. Li, X. Cao, and B. Wang, "Effect of NiO-doping on the microstructure and the dielectric properties of $CaCu_3Ti_4O_{12}$ceramics," Ceram. Int., **40**, 9061–9067 (2014).

[124] C. Mu, Y. Song, H. Wang, and X. Wang, "Room temperature magnetic and dielectric properties of cobalt doped," J. Appl. Phys., **117**, 17B723 (2015).

[125] F. Amaral, M. Valente, and L. C. Costa, "Synthesis and characterization of calcium copper titanate obtained by ethylenediaminetetraacetic acid gel combustion," Mater. Chem. Phys., **124**, 580–586 (2010).

[126] N. Kolev, R. P. Bontchev, A. J. Jacobson, V. N. Popov, V. G. Hadjiev, A. P. Litvinchuk, and M. N. Iliev, "Raman spectroscopy of $CaCu_3Ti_4O_{12}$," Phys. Rev. B, **66**, 132102 (2002).

[127] J. F. Xu, W. Ji, Z. X. Shen, W. S. Li, S. H. Tang, X. R. Ye, D. Z. Jia, and X. Q. Xin, "Raman Spectra of CuO Nanocrystals," J. Raman Spectrosc., **30**, 413–415 (1999).

[128] M. Pineda, E. Garcla, and J. V Ibarra, "Characterization of zinc oxide and zinc ferrite doped with Ti or Cu as sorbents for hot gas desulphurization," Appl. Surf. Sci., **119**, 1–10 (1997).

[129] S. Rhouma, S. Saîd, C. Autret, S. De Almeida-Didry, M. El Amrani, and A. Megriche, "Comparative studies of pure, Sr-doped, Ni-doped and co-doped $CaCu_3Ti_4O_{12}$ ceramics: Enhancement of dielectric properties," J. Alloys Compd., **717**, 121–126 (2017).

[130] W. Li, T. Zhang, S. Liu, Z. Lu, and R. Xiong, "Decrease in the dielectric loss of $CaCu_3Ti_4O_{12}$ at high frequency by Ru doping," Ceram. Int., **43**, 4366–4371 (2017).

[131] R. Espinoza-gonzález and E. Mosquera, "Influence of micro- and nanoparticles of zirconium oxides on the dielectric properties of $CaCu_3Ti_4O_{12}$," Ceram. Int., **43**, 14659–14665 (2017).

[132] A. Khare, S. S. Yadava, P. Gautam, and A. Kumar, "Dielectric properties of nanocomposite based on bismuth copper titanate," J. Aust. Ceram. Soc., **54**, 139–147, (2017).

[133] J. Mohammed, A. B. Suleiman, Tchouank Tekou Carol T., H. Y. Hafeez, J. Sharma, M. P. K, and K. S. Godara, "Enhanced dielectric and optical properties of nanoscale barium hexaferrites for optoelectronics and high frequency application," Chinese Phys. B, **27**, 128104 (2018).

[134] J. Mohammed, A. B. Suleiman, H. Y. Hafeez, Tchouank Tekou Carol T., J. Sharma, G. R. Bhadu, S. K. Godara, and A. K. Srivastava, "Effect of heat-treatment on the magnetic and optical properties of $Sr_{0.7}Al_{0.3}Fe_{11.4}Mn_{0.6}O_{19}$," Mater. Res. Express, **5**, 086106 (2018).

[135] X. Huang, H. Zhang, M. Wei, Y. Lai, and J. Li, "Effect of semiconductive grain and

microstructure on the dielectric properties of $CaCu_3Ti_4O_{12}$ ceramics with Sr^{2+}doping," J. Alloys Compd., **708**, 1026–1032 (2017).

[136] J. Mohammed, H. Y. Hafeez, Tchouank Tekou Carol T., C. E. Ndikilar, J. Sharma, P. K. Maji, S. K. Godara, and A. K. Srivastava, "Structural, dielectric, and magneto-optical properties of Cu^{2+}-Er^{3+} substituted nanocrystalline strontium hexaferrite," Mater. Res. Express, **6**, 056111 (2019).

[137] J. Mohammed, J. Sharma, S. Kumar, Tchouank Tekou Carol T., and A. K. Srivastava, "Calcination temperature effect on the microstructure and dielectric properties of M-type strontium hexagonal ferrites," AIP Conf. Proceeding, **1860**, 020007, 2017.

[138] L. Singh, U. S. Rai, K. D. Mandal, and N. B. Singh, "Progress in the growth of CaCu3Ti4O12and related functional dielectric perovskites," Prog. Cryst. Growth Charact. Mater., **60**, 15–62, (2014).

[139] S. Jesurani, S. Kanagesan, R. Velmurugan, and T. Kalaivani, "Phase formation and high dielectric constant of calcium copper titanate using sol-gel route," J. Mater. Sci. Mater. Electron., **23**, 668–674 (2012).

[140] S. Jesurani, S. Kanagesan, and K. Ashok, "Microstructure and dielectrical responses of pure and cobalt-doped $CaCu_3Ti_4O_{12}$ ceramics by sol-gel synthesis route," J. Sol-Gel Sci. Technol., **64**, 335–341 (2012).

[141] A. K. Dubey, P. Singh, S. Singh, D. Kumar, and O. Parkash, "Charge compensation, electrical and dielectric behavior of lanthanum doped $CaCu_3Ti_4O_{12}$," J. Alloys Compd., **509**, 3899–3906 (2011).

[142] R. Kashyap, R. K. Mishra, O. P. Thakur, and R. P. Tandon, "Structural, dielectric properties and electrical conduction behaviour of Dy substituted $CaCu_3Ti_4O_{12}$ ceramics," Ceram. Int., **38**, 6807–6813 (2012).

[143] P. Liang, X. Chao, F. Wang, Z. Liu, and Z. Yang, "The Lowered Dielectric Loss and Grain-Boundary Effects in La-doped $Y_{2/3}Cu_3Ti_4O_{12}$ Ceramics," J. Am. Ceram. Soc., **96**, 3883–3890 (2013).

[144] P. Liang, X. Chao, and Z. Yang, "Dielectric response, impedance spectroscopy and scaling behavior of K-doped $Y_{2/3}Cu_3Ti_4O_{12}$ ceramics," Mater. Chem. Phys., **167**, 103–

111 (2015).

[145] P. Liu, Y. Lai, Y. Zeng, S. Wu, Z. Huang, and J. Han, “Influence of sintering conditions on microstructure and electrical properties of $CaCu_3Ti_4O_{12}$ (CCTO) ceramics,” J. Alloys Compd., **650**, 59–64 (2015).

[146] S. Fareed, A. Jamil, M. A. Ra, and F. Sher, “Zinc modified cadmium titanite nanoparticles : Electrical and room temperature methanol sensing properties,” Ceram. Int., **44**, 4751–4757 (2018).

[147] P. Liang, F. Li, X. Chao, and Z. Yang “Effects of Cu stoichiometry on the microstructure, electrical conduction, and dielectric responses of $Y_{2/3}Cu_3Ti_4O_{12}$,” Ceram. Int., **41**, 11314-11322 (2015).

[148] J. Li, R. Jia, L. Hou, L. Gao, K. Wu, and S. Li, “The dimensional effect of dielectric performance in $CaCu_3Ti_4O_{12}$ ceramics: Role of grain boundary,” J. Alloys Compd., **644**, 824–829 (2015).

[149] W. X. Yuan, “Impedance and electric modulus approaches to investigate four origins of giant dielectric constant in $CaCu_3Ti_4O_{12}$ ceramics,” Solid State Sci., **14**, 330–334 (2012).

[150] S. Jesurani, S. Kanagesan, M. Hashim, and I. Ismail, “Dielectric properties of Zr doped $CaCu_3Ti_4O_{12}$ synthesized by sol-gel route,” J. Alloys Compd., **551**, 456–462 (2013).

[151] K. D. Mandal, A. K. Rai, D. Kumar, and O. Parkash, “Dielectric properties of the $Ca_{1-x}La_xCu_3Ti_{4-x}Co_xO_{12}$ system (x=0.10, 0.20 and 0.30) synthesized by semi-wet route,” J. Alloys Compd., **478**, 771–776 (2009).

[152] S. Pongpaiboonkul, D. Phokharatkul, J. H. Hodak, A. Wisitsoraat, and S. K. Hodak, “Chemical Enhancement of H_2S-sensing performances with Fe-doping in $CaCu_3Ti_4O_{12}$ thin films prepared by a sol–gel method,” Sensors Actuators B, **224**, 118–127 (2016).

[153] C. Mu, Y. Song, H. Wang, and X. Wang, “Room temperature magnetic and dielectric properties of cobalt doped,” J. Appl. Phys., **117**, 17B723 (2015).

[154] R. C. Deus, M. R. Silva, J. A. Varela, E. Longo, F. Moura, and A. Z. Sim, “Intense photoluminescence emission at room temperature in calcium copper titanate powders,” Ceram. Int., **39**, 3499–3506 (2013).

[155] S. Jesurani, S. Kanagesan, M. Hashim, and I. Ismail, "Dielectric properties of Zr doped $CaCu_3Ti_4O_{12}$ synthesized by sol–gel route," Adv. Mater. Sci. Eng., **551**, 456-462, (2013).

[156] S. Jesurani, S. Kanagesan, T. Kalaivani, and K. Ashok, "Dielectric properties of Erbium doped $CaCu_3Ti_4O_{12}$ prepared by sol-gel self combustion method," J. Mater. Sci. Mater. Electron., **23**, 692–696 (2012).

[157] H. A. Ardakani, M. Alizadeh, R. Amini, and M. R. Ghazanfari, "Dielectric properties of $CaCu_3Ti_4O_{12}$ improved by chromium/lanthanum co-doping," Ceram. Int., **38**, 4217–4220 (2012).

[158] A. O. Turky, M. M. Rashad, A. M. Hassan, E. M. Elnaggar, and M. Bechelany, "Optical, electrical and magnetic properties of lanthanum strontium manganite $La_{1-x}Sr_xMnO_3$ synthesized through the citrate combustion method," Phys. Chem. Chem. Phys., **19**, 6878–6886 (2017).

[159] M. M. Rashad, A. O. Turky, and A. T. Kandil, "Optical and electrical properties of $Ba_{1-x}Sr_xTiO_3$ nanopowders at different Sr^{2+} ion content," J. Mater. Sci. Mater. Electron., **24**, 9, 3284–3291 (2013).

[160] A. Omar, M. M. Rashad, A. M. Hassan, E. M. Elnaggar, H. Zhao, and M. Bechelany, "Tunable investigation optical, electrical and magnetic behaviors of Gd^{3+} substituted lanthanum strontium manganite $La_{0.5-x}Sr_{0.5}Gd_xMnO_3$ nanopowders facilely synthesized through citrate precursor technique," J. Alloys Compd., **735**, 2175–2181 (2018).

[161] A. O. Turky, M. M. Rashad, Z. I. Zaki, I. A. Ibrahim, and M. Bechelany, "Tuning the optical and dielectric properties of calcium copper titanate $Ca_xCu_{3-x}Ti_4O_{12}$ nanopowders," Optoelectron. Adv. Mater. Rapid Commun., **5**, 18767–18772 (2015).

[162] A. O. Turky, M. M. Rashad, and M. Bechelany, "Tailoring optical and dielectric properties of $Ba_{0.5}Sr_{0.5}TiO_3$ powders synthesized using citrate precursor route," Mater. Des., **90**, 54–59 (2016).

[163] Z. Zhong, F. Qian, D. Wang, and C. M. Lieber, "Synthesis of p-Type Gallium Nitride Nanowires for Electronic and Photonic Nanodevices," nano Lett., **3**, 343–346 (2003).

[164] H. M. Elghanem, S. A. Jawad, J. Aljundi, F. Afaneh, and I. Arafa, "Electrical

properties of macromolecular complexes of coordinated polymers with mixed valence of Co (II), Co (III) and Co (II–III)," Polym. Int., **52**, 1125–1130 (2003).

[165] J. Sebald, S. Krohns, P. Lunkenheimer, S. G. Ebbinghaus, S. Riegg, A. Reller, and A. Loidl, "Colossal dielectric constants: A common phenomenon in $CaCu_3Ti_4O_{12}$ related materials," Solid State Commun., **150**, 857–860 (2010).

[166] F. Amaral, L. C. Costa, M. A. Valente, A. J. S. Fernandes, N. Franco, and E. Alves, "Colossal dielectric constant of poly- and single-crystalline $CaCu_3Ti_4O_{12}$ fibres grown by the laser floating zone technique," Acta Mater., **59**, 102–111 (2011).

[167] S. Jesurani, S. Kanagesan, R. Velmurugan, C. Thirupathi, M. Sivakumar, and T. Kalaivani, "Nanoparticles of the giant dielectric material, calcium copper titanate from a sol-gel technique," Mater. Lett., **65**, 3305–3308 (2011).

[168] F. Amaral, L. C. Costa, and M. A. Valente, "Decrease in dielectric loss of $CaCu_3Ti_4O_{12}$ by the addition of TeO_2," J. Non. Cryst. Solids, **357**, 775–781 (2011).

[169] K. R. Kumar, B. Venkateswarlu, and P. D. Babu, "Neutron Diffraction Studies on the Full Heusler Alloy Co_2FeGe," AIP Conf. Proc., **1447**, 1213–1214 (2012).

[170] T. Kaur, S. Kumar, B. H. Bhat, and A. K. Srivastava, "Enhancement in physical properties of barium hexaferrite with substitution," J. Mater. Res., **30**, 2753–2762 (2016).

[171] L. Singh, U. S. Rai, K. D. Mandal, B. C. Sin, H. Il Lee, H. Chung, and Y. Lee, "Comparative dielectric studies of nanostructured $BaTiO_3$, $CaCu_3Ti_4O_{12}$ and $0.5BaTiO_3 \cdot 0.5CaCu_3Ti_4O_{12}$ nano-composites synthesized by modified sol-gel and solid state methods," Mater. Charact., **96**, 54–62 (2014).

[172] A. Kumar, K. D. Mandal, D. Kumar, and O. Parkash, "Characterization of nickel doped CCTO: $CaCu_{2.9}Ni_{0.1}Ti_4O_{12}$ and $CaCu_3Ti_{3.9}Ni_{0.1}O_{12}$ synthesized by semi-wet route," J. Alloys Compd., **491**, 507–512 (2010).

[173] M. A. Subramanian, D. Li, N. Duan, B. A. Reisner, and A. W. Sleight, "High dielectric constant in $ACu_3Ti_4O_{12}$ and $ACu_3Ti_3FeO_{12}$ phases," J. Solid State Chem., **151**, 323–325 (2000).

[174] R. Bhargava and S. Khan, "Effect of reduced graphene oxide (rGO) on structural,

optical, and dielectric properties of $Mg(OH)_2$/rGO nanocomposites," Adv. Powder Technol., **28**, 2812–2819 (2017).

[175] S. Jesurani, S. Kanagesan, M. Hashim, and I. Ismail, "Dielectric properties of Zr doped $CaCu_3Ti_4O_{12}$ synthesized by sol–gel route," J. Alloys Compd., **551**, 456–462 (2013).

[176] T. B. Adams, D. C. Sinclair, and A. R. West, "Giant Barrier Layer Capacitance Effects in $CaCu_3Ti_4O_{12}$ Ceramics," Adv. Mater., **14**, 1321–1323 (2002).

[177] W. Li, S. Qiu, N. Chen, and G. Du, "Enhanced Dielectric Response in Mg-doped $CaCu_3Ti_4O_{12}$Ceramics," J. Mater. Sci. Technol., **26**, 682–686 (2010).

[178] E. Swatsitang, K. Prompa, and T. Putjuso anagesan, "A novel strategy to improve the thermal stability of dielectric properties and reduce the dielectric loss tangent of $Ca_{1-1.5x}Pr_xCu_3Ti_4O_{12}/TiO_2$ ceramics," Ceram. Int., **45**, 14733-14741 (2019).

[179] L. Liu, H. Fan, P. Fang, and X. Chen, "Sol-Gel Derived $CaCu_3Ti_4O_{12}$ Ceramics : Synthesis , Characterization and Electrical Properties," Mater. Res. Bull., **43**, 1800–1807 (2008).

[180] A. Khare, S. Sundar, K. D. Mandal, and N. K. Mukhopadhyay, "Effect of sintering duration on the dielectric properties of $0.9BaTiO_3$–$0.1CaCu_3Ti_4O_{12}$nanocomposite synthesized by solid state route," Microelectron. Eng., **164**, 1–6 (2016).

[181] L. Singh, I. W. Kim, B. C. Sin, S. K. Woo, S. H. Hyun, K. D. Mandal, and Y. Lee, "Combustion synthesis of nano-crystalline $Bi_{2/3}Cu_3Ti_{2.90}Fe_{0.10}O_{12}$ using inexpensive TiO_2 raw material and its dielectric characterization," Powder Technol., **280**, 256–265 (2015).

[182] A. J. V. Khani, "Influence of Ho substitution on structural , magnetic and microwave absorption properties of PbM-type hexaferrites nanoparticles," J. Mater. Sci. Mater electron, **25**, 244–248 (2014).

[183] V. V Soman, V. M. Nanoti, and D. K. Kulkarni, "Dielectric and magnetic properties of Mg–Ti substituted barium hexaferrite," Ceram. Int., **39**, 5713–5723 (2013).

[184] J. Tang, X. Liu, K. Mehmood Ur Rahman, M. Li, C. Zhang, X. Meng, H. Li, and C. Liu, "Influence of heat treatment temperatures on microstructure and characterization of $BaFe_2^{2+}Fe_{15.6}^{3+}O_{26.4}$ hexaferrite," Journal of Materials Science: Materials in

Electronics, **28**, 12086-12091 (2017).

[185] X. Meng and Y. Ji, "Effect of chemical composition and heat treatment condition on microstructure and magnetic properties of nanocrystalline," J. sol-gel Sci. Technol., **67**, 18–28 (2013).

[186] T. Kaur, S. Kumar, B. Hamid, and B. Basharat, "Effect on dielectric , magnetic , optical and structural properties of Nd–Co substituted barium hexaferrite nanoparticles," Appl. Phys. A, **119**, 1531–1540 (2015).

[187] R. Shams, M. Moradi, M. Rostami, and H. Nikmanesh, "Structural , magnetic and microwave absorption properties of doped Ba-hexaferrite nanoparticles synthesized by co-precipitation method," J. Magn. Magn. Mater., **381**, 1–9 (2015).

[188] S. K. Chawla, R. K. Mudsainiyan, S. S. Meena, and S. M. Yusuf, "Sol-gel synthesis, structural and magnetic properties of nanoscale M-type barium hexaferrites $BaCo_xZr_xFe_{(12-2x)}O_{19}$," J. Magn. Magn. Mater., **350**, 23–29 (2014).

[189] S. M. El-sayed, T. M. Meaz, M. A. Amer, and H. A. El Shersaby, "Magnetic behavior and dielectric properties of aluminum substituted M-type barium hexaferrite," Phys. B Phys. Condens. Matter, **426**, 137–143 (2013).

[190] A. Baykal, I. A. Auwal, S. Güner, and H. Sözeri, "Magnetic and Optical properties of Zn^{2+} ion substituted barium hexaferrites," J. Magn. Magn. Mater., **430**, 29–35 (2017).

[191] T. Kaur, J. Sharma, S. Kumar, and A. K. Srivastava, "Optical and Multiferroic Properties of Gd-Co Substituted Barium Hexaferrite," Cryst. Res. Technol., **52**, 1700098 (2017).

[192] M. A. Malana, R. B. Qureshi, M. N. Ashiq, and M. F. Ehsan, "Synthesis , structural , magnetic and dielectric characterizations of molybdenum doped calcium strontium M-type hexaferrites," Ceram. Int., **42**, 2686–2692 (2016).

[193] Y. Bai, J. Zhou, Z. Gui, and L. Li, "Electrical properties of non-stoichiometric Y-type hexagonal ferrite," J. Magn. Magn. Mater., **278**, 208–213, (2004).

[194] G. M. Turi, "Experimental investigations of the structural transformations induced by the heat treatment in manganese ferrite synthesized by ultrasonic assisted co-precipitation method," Ceram. Int., **42**, 16744–16748 (2016).

[195] Y. Wu, Y. Huang, L. Niu, Y. Zhang, Y. Li, and X. Wang, "Pr^{3+}-substituted W-type barium ferrite: Preparation and electromagnetic properties," J. Magn. Magn. Mater., **324**, 616–621 (2012).

[196] X. Ma, J. Liu, S. Zhu, and H. Shi "Tuning of magnetic properties of aluminium-doped strontium hexaferrite powders," Chinese Physics B., **25**, 126102 (2016).

[197] E. D. Solovyova, E. V Pashkova, V. P. Ivanitski, O. I. V, and A. G. Belous, "M ossbauer and X-ray diffraction study of Co^{2+}–Si^{4+} substituted M-type barium hexaferrite $BaFe_{12-2x}Co_xSi_xO_{19}$," J. Magn. Magn. Mater., **330**, 72–75 (2013).

[198] T. Tchouank Tekou Carol, J. Sharma, J. Mohammed, S. Kumar, and A. K. Srivastava, "Effect of temperature on the magnetic properties of nano-sized M-type barium hexagonal ferrites," AIP Conf. Proc., **1860**, 020008 (2017).

[199] T. Kaur, S. Kumar, H. B. Bhat, and A. K. Srivastava, "Enhancement in physical properties of barium hexaferrite with substitution," J. Mater. Res., **30**, 2753–2762 (2015).

[200] S. Asiri, S. Güner, A. D. Korkmaz, M. Amir, K. M. Batoo, M. A. Almessiere, H. Gungunesf, H. Sözeri, and A. Baykal, "Magneto-optical properties of $BaCr_yFe_{12-y}O_{19}$ ($0.0 \leq y \leq 1.0$) hexaferrites hexaferrites," J. Magn. Magn. Mater., **451**, 463–472 (2018).

[201] A. R. Farhadizadeh, S. A. Seyyed Ebrahimi, and S. M. Masoudpanah, "Magnetic and microwave absorption properties of ZnCo-substituted W-type strontium hexaferrite," J. Magn. Magn. Mater., **382**, 233–236 (2015).

[202] M. Naeem, S. Shakoor, M. Najam-ul-haq, M. Farooq, I. Ali, and I. Shakir, "Structural , electrical , dielectric and magnetic properties of Gd-Sn substituted Sr-hexaferrite synthesized by sol – gel combustion method," J. Magn. Magn. Mater., **374**, 173–178 (2015).

[203] A. Ghasemi, R. Shams, and A. Morisako, "Preparation and magnetic properties of hexagonal barium ferrite films using BaM nanoparticles," Phys. B: Condensed Matter, **403**, 2987–2990 (2008).

[204] H. Z. Wang, Y. N. Hai, B. Yao, Y. Xu, L. Shan, L. Xu, J. L. Tang, and Q. H. Wang, "Tailoring structure and magnetic characteristics of strontium hexaferrite via Al

doping engineering," J. Magn. Magn. Mater., **422**, 204–208 (2017).

[205] V. N. Dhage, M. L. Mane, A. P. Keche, C. T. Birajdar, and K. M. Jadhav, "Structural and magnetic behaviour of aluminium doped barium hexaferrite nanoparticles synthesized by solution combustion technique," Phys. B: Condens. Matter, **406**, 789–793 (2011).

[206] E. Kiani, A. S. H. Rozatian, and M. H. Yousefi, "Structural, magnetic and microwave absorption properties of $SrFe_{12-2x}(Mn_{0.5}Cd_{0.5}Zr)_xO_{19}$ ferrite," J. Magn. Magn. Mater., **361**, 25–29 (2014).

[207] S. Kumar, N. Shimul, K. Nath, A. K. M. A. Hossain, and J. Uddin, "Effect of Zn Doping on Structural and Magnetic Properties of $Ba_4Ni_{2-x}Zn_xFe_{36}O_{60}$ Hexaferrites," J. Supercond. Nov. Magn., **27**, 2655–2662 (2014).

[208] P. Kuruva, P. Reddy, B. Mohammad, and S. Reddigari, "Effect of Ni–Zr codoping on dielectric and magnetic properties of $SrFe_{12}O_{19}$ via sol–gel route," J. Magn. Magn. Mater., **382**, 172–178 (2015).

[209] M. Naeem, M. Javed, M. Najam-ul-haq, P. Hernandez, and A. Mahmood, "Synthesis , magnetic and dielectric properties of Er–Ni doped Sr-hexaferrite nanomaterials for applications in High density recording media and microwave devices," J. Magn. Magn. Mater., **324**, 15–19 (2012).

[210] T. R. Wagner, "Preparation and Crystal Structure Analysis of Magnetoplumbite-Type $BaGa_{12}O_{19}$," J. Solid State Chem., **136**, 120–124 (1998).

[211] A. Baniasadi, A. Ghasemi, A. Nemati, M. Azami, and E. Paimozd, "Effect of Ti–Zn substitution on structural, magnetic and microwave absorption characteristics of strontium hexaferrite," J. Alloys Compd., **583**, 325–328 (2014).

[212] M. Rostami, M. Moradi, R. S. Alam, and R. Mardani, "Characterization of Magnetic and Microwave Absorption Properties of Multi- Walled Carbon Nanotubes/Mn-Cu-Zr Substituted Strontium Hexaferrite Nanocomposites," Mater. Res. Bull., **83**, 379–386 (2016).

[213] S. Supriya, S. Kumar, M. Kar, S. Supriya, S. Kumar, and M. Kar, "Correlation between AC and DC transport properties of Mn substituted cobalt ferrite," J. Appl.

Phys., **120**, 215106 (2016).

[214] J. Kreisel, G. Lucazeau, and H. Vincent, "Raman Study of Substituted Barium Ferrite Single Crystals, $BaFe_{12-2x}Me_xCo_xO_{19}$ (Me=Ir, Ti)," J. Raman Spectrosc., **30**, 115–120, (1999).

[215] J. Kreisel, G. Lucazeau, and H. Vincent, "Raman Spectra and Vibrational Analysis of $BaFe_{12}O_{19}$ Hexagonal Ferrite," J. Solid State Chem., **137**, 127–137 (1998).

[216] S. Kumar, S. Supriya, and M. Kar, "Effect of Sintering Temperature on Electrical Properties of BHF Ceramics Prepared by Modified Sol-Gel Method," Mater. Today Proc., **4**, 5517–5524 (2017).

[217] G. Praveena, R. Tadi, G. Rao, K. N. C. Kumar, and V. Veeraiah, "Investigations on the structural , magnetic and mossbauer properties of cerium doped strontium ferrite," Phys. B: Condens. Matter, **550**, 136–144 (2018).

[218] S. Kumar, S. Supriya, R. Pandey, L. Kumar, R. Kumar, and M. Kar, "Effect of lattice strain on structural and magnetic properties of Ca substituted barium hexaferrite," J. Magn. Magn. Mater., **458**, 30–38 (2018).

[219] N. Velhal, G. Kulkarni, D. Mahadik, and P. Chowdhury, "Effect of Ba^{2+} ion on structural , magnetic and microwave properties of screen printed $Ba_xSr_{1-X}Fe_{12}O_{19}$ thick films," J. Alloys Compd., **682**, 730–737 (2016).

[220] S. Kumar, M. Kumar, S. Supriya, and H. Kumar, "Lattice strain mediated dielectric and magnetic properties in La doped barium hexaferrite," J. Magn. Magn. Mater., **473**, 312–319 (2019).

[221] A. Morel, J. M. Le Breton, J. Kreisel, G. Wiesinger, F. Kools, and P. Tenaud, "Sublattice occupation in $Sr_{1-x}La_xFe_{12-x}Co_xO_{19}$ hexagonal ferrite analyzed by M ossbauer spectrometry and Raman spectroscopy," J. Magn. Magn. Mater., **242–245**, 1405–1407 (2002).

[222] S. Mahadevan, S. B. Narang, and P. Sharma, "Effect of three-step calcination on structural , magnetic and microwave," Ceram. Int., **45**, 9000–9006 (2019).

[223] J. Kreisel, G. Lucazeau, and H. Vincent, "Raman Spectra and Vibrational Analysis of $BaFe_{12}O_{19}$ Hexagonal Ferrite," J. Solid State Chem., **137**, 127–137 (1998).

[224] A. V Trukhanov, V. G. Kostishyn, L. V Panina, S. H. Jabarov, and V. V Korovushkin, "Magnetic properties and Mössbauer study of gallium doped M-type barium hexaferrites," Ceram. Int., **43**, 12822–12827 (2017).

[225] K. Rana, P. Thakur, M. Tomar, V. Gupta, and A. Thakur, "Investigation of cobalt substituted M-type barium ferrite synthesized via co-precipitation method for radar absorbing material in Ku-band (12–18 GHz)," Ceram. Int., **44**, 6370–6375 (2018).

[226] M. A. Almessiere, Y. Slimani, H. S. El Sayed, and A. Baykal, "Structural and magnetic properties of Ce-Y substituted strontium nanohexaferrites," Ceram. Int., **44**, 12511-12519 (2018).

[227] L. Cao, Z. Wang, Z. Ye, Y. Zhang, L. Zhao, Y. Zeng, and D. Ph, "Interface exchange coupling induced enhancements in coercivity and maximal magnetic energy product of $BaFe_{12}O_{19}/Co_3O_4$ nanocomposites," J. Alloys Compd., **715**, 199–205 (2017).

[228] V. Sharma, S. Kumari, and B. K. Kuanr, "Exchange-coupled hard-soft ferrites ; A new microwave material," J. Alloys Compd., **736**, 266–275 (2018).

[229] X. Zhang, Y. Zhang, S. Cao, Z. Yue, and J. Zhang, "$BaFe_{12}O_{19}$ films prepared on Al_2O_3 (0001) by direct current magnetron sputtering," Mater. Lett., **248**, 24-27 (2019).

[230] V. A. P. M. Gazzali, "Effect of divalent cation substitution in the magnetoplumbite structured $BaFe_{12}O_{19}$ system," J. Mater. Sci. Mater electron, **24**, 916–926 (2013).

[231] S. Shannigrahi, W. Q. Au, V. S. Kumar, L. Liu, Z. H. Yang, C. Cheng, C. K. I. Tan, and R. V. Ramanujan "Synthesis and electromagnetic properties of U-type hexaferrites $Ba_4B_2Fe_{36}O_{60}$ (B: Co, Ni, Cu)," Mater. Sci. Eng. B, **325**, 63–68 (2013).

[232] V. Pratap, A. K. Soni, S. Dayal, S. M. Abbas, A. M. Siddiqui, and N. E. Prasad "Electromagnetic and absorption properties of U-type barium hexaferrite-epoxy composites," J. Magn. Magn. Mater., **465**, 540–545 (2018).

[233] O. Heczko and R. Gerber, "Structural , magnetic and magneto-optical properties of $SrFe_{12-x}Al_xO_{19}$ hexaferrite thin films prepared by laser ablation deposition," Thin Solid Films, **358**, 206–214 (2000).

[234] M. N. Ashiq, R. B. Qureshi, M. A. Malana, and M. F. Ehsan, "Fabrication, Structural, Dielectric and Magnetic Properties of Tantalum and Potassium doped M-type

Strontium Calcium Hexaferrites," J. Alloys Compd., **651**, 266-272 (2015).

[235] S. B. Narang, D. Kaur, and K. Pubby, "Structural, dielectric and electrical analysis of $Ba_{2-x}La_{4+2x/3}Ti_8O_{24}$ ceramics system with frequency and temperature," Microw. Opt. Technol. Lett., **58**, 1679–1686 (2016).

[236] A. K. Jassal, R. K. Mudsainiyan, S. K. Chawla, S. B. Narang, and K. Pubby, "Sol-gel route approach and improvisation in physico-chemical , structural , magnetic and electrical properties of $BaCo_{x/2}Zn_{x/2}Fe_{12-2x}O_{19}$ ferrites," J. Magn. Magn. Mater., **447**, 32–41 (2018).

[237] M. N. Ashiq, M. J. Iqbal, and I. H. Gul, "Structural , magnetic and dielectric properties of Zr–Cd substituted strontium hexaferrite ($SrFe_{12}O_{19}$) nanoparticles," J. Alloys Compd., **487**, 341–345 (2009).

[238] P. Thongbai, J. Jumpatam, B. Putasaeng, and T. Yamwong, "Microstructural evolution and Maxwell – Wagner relaxation in $Ca_2Cu_2Ti_{4-x}Zr_xO_{12}$: The important clue to achieve the origin of the giant dielectric behavior," Mater. Res. Bull., **60**, 695–703 (2014).

[239] Z. Lalegani and A. Nemati, "Effects of Ce – Co substitution on structural , magnetic and dielectric properties of M-type barium hexaferrite nanoparticles synthetized by sol–gel auto-combustion route," J. sol-gel Sci. Technol., **68**, 141–149 (2015).

[240] I. Ali, M. U. Islam, M. S. Awan, and M. Ahmad, "Effects of Heat-Treatment Time on the Structural , Dielectric , Electrical , and Magnetic Properties of BaM Hexaferrite," J. Mater. Eng. Perform., **22**, 2104–2114 (2013).

[241] A. Hooda, S. Sanghi, A. Agarwal, and R. Dahiya, "Crystal structure refinement , dielectric and magnetic properties of Ca/Pb substituted $SrFe_{12}O_{19}$ hexaferrites," J. Magn. Magn. Mater., **387**, 46–52 (2015).

[242] B. Want, B. H. Bhat, and B. Z. Ahmad, "Effect of lanthanum substitution on dielectric relaxation, impedance response, conducting and magnetic properties of strontium hexaferrite," J. Alloys Compd., **627**, 78–84 (2014).

[243] K. Pubby, S. K. Chawla, P. Kaur, G. Kaur, and S. Bindra, "Effect of precursors on dielectric properties of Co-Zr doped strontium hexaferrites in 20 Hz–120 MHz frequency range," Ferroelectrics, **505**, 67–73 (2016).

[244] K. Pubby, S. Bindra, and N. S. K. Chawla, "Effect of temperature on dielectric and electrical properties of Co–Zr doped barium hexaferrites prepared by sol–gel method," J. Mater. Sci. Mater. Electron., **27**, 11220-11230 (2016).

[245] E. Roohani, H. Arabi, R. Sarhaddi, and A. Shabani, "Magnetic and Structural Properties of $SrFe_{12-x}Cr_xO_{19}$ Obtained by Sol–Gel Auto-Combustion Method," J. Supercond. Nov. Magn., **31**, 1607–1613 (2018).

[246] V. N. Dhage, M. L. Mane, M. K. Babrekar, C. M. Kale, and K. M. Jadhav, "Influence of chromium substitution on structural and magnetic properties of $BaFe_{12}O_{19}$ powder prepared by sol–gel auto combustion method," J. Alloys Compd., **509**, 4394–4398 (2011).

[247] L. Yadong, R. Liu, Z. Zhang, and C. Xiong, "Synthesis and characterization of nanocrystalline $BaFe_{9.6}Co_{0.8}Ti_{0.8}M_{0.8}O_{19}$ particles," Mater. Chem. Phys., **64**, 256–259 (2000).

[248] P. Kaur, S. K. C. Sukhleen, B. Narang, and K. Pubby, "Effect of Cu-Co-Zr Doping on the Properties of Strontium Hexaferrites Synthesized by Sol-Gel Auto-combustion Method," J. Supercond. Nov. Magn., **30**, 635–645 (2016).

[249] J. V. Khani, G. R. Amiri, and R. Mousarezaei, "Influence of dysprosium addition on the structural , morphological , electrical and magnetic properties of nano-crystalline W-type hexaferrites," Bull. Mater. Sci., **38**, 1–5 (2015).

[250] P. Kaur, S. K. Chawla, S. Bindra, and K. Pubby, "Structural , magnetic and microwave absorption behavior of Co-Zr substituted strontium hexaferrites prepared using tartaric acid fuel for electromagnetic interference suppression," J. Magn. Magn. Mater., **422**, 304–314 (2017).

[251] Q. Fang, H. Cheng, K. Huang, J. Wang, R. Li, and Y. Jiao, "Doping effect on crystal structure and magnetic properties of chromium-substituted strontium hexaferrite nanoparticles," J. Magn. Magn. Mater., **294**, 281–286 (2005).

[252] S. Katlakunta, S. Singh, S. Srinath, M. Bououdina, R. Sandhya, and K. Praveena, "Improved magnetic properties of Cr^{3+} doped $SrFe_{12}O_{19}$ synthesized via microwave hydrothermal route," Mater. Res. Bull., **63**, 58–66 (2015).

[253] M. Zahid, M. U. Islam, M. S. Awan, M. N. Ashiq, S. Naseem, I. Ali, A. Iftikhar, M. Ahmad, and Z. Kamran, "Effect of dysprosium on structural and physical properties of $Ba_2NiCoFe_{12}O_{22}$ Y-type hexaferrites," Journal of the Australian Ceramic Society, **53**, 875-882, (2017).

[254] R. K. Mudsainiyan, S. K. Chawla, and S. S. Meena, "Correlation between site preference and magnetic properties of Co–Zr doped $BaCo_xZr_xFe_{(12-2x)}O_{19}$ prepared under sol–gel and citrate precursor sol–gel conditions," J. Alloys Compd., **615**, 875–881 (2014).

[255] A. Ghasemi, V. Šepelák, X. Liu, and A. Morisako, "The role of cations distribution on magnetic and reflection loss properties of The role of cations distribution on magnetic and reflection loss properties," Journal of Applied Physics, **107**, 09A734 (2010).

[256] A. Baykal, S. Yoku, S. Güner, H. Güngüne, and H. Sözeri, "Magneto-optical properties and Mössbauer Investigation of $Ba_xSr_yPb_zFe_{12}O_{19}$ Hexaferrites," Ceram. Int., **43**, 3475–3482 (2017).

[257] Y. Slimani, A. Baykal, N. Tashkandi, H. Güngüne, S. Guner, H. S. El Sayed, F. Aldakheel, T. A. Saleh, and A. Manikandan, "Substitution e ff ect of Cr^{3+} on hyperfine interactions , magnetic and optical properties of Sr-hexaferrites," Ceram. Int., **44**, 15995–16004 (2018).

[258] J. Le Breton, D. Seifert, J. Töpfer, and L. Lechevallier, "A Mössbauer investigation of $Sr_{1-x}La_xFe_{12}O_{19}$ ($0 \leq x \leq 1$) M-type hexaferrites," Phys. B Phys. Condens. Matter, **470–471**, 33–38 (2015).

[259] R. K. Mudsainiyan, S. K. Chawla, S. S. Meena, N. Sharma, R. Singh, and A. Das, "Cations distribution and magnetic properties of Co–Zr doped $BaCo_xZr_xFe_{(12-2x)}O_{19}$ prepared via citrate precursor sol–gel route," Ceram. Int., **40**, 16617–16626 (2014).

[260] M. A. Almessiere, Y. Slimani, M. Sertkol, M. Nawaz, A. Baykal, and I. Ercan "The impact of Zr substituted Sr hexaferrite: Investigation on structure, optic and magnetic properties," Res. Phys., **13**, 102244 (2015).

[261] K. M. U. Rehman, X. Liu, M. Li, S. Jiang, Y. Wu, C. Zhang, C. Liu, X. Meng, and H. Li, "Synthesization and magnetic properties of $Ba_{1-x}Y_xFe_{12}O_{19}$ hexaferrites prepared by solid-state reaction method," J. Magn. Magn. Mater., **426**, 183–187 (2017).

[262] M. N. Ashiq, M. J. Iqbal, M. Najam-Ul-Haq, P. Hernandez Gomez, and A. M. Qureshi, "Synthesis, magnetic and dielectric properties of ErNi doped Sr-hexaferrite nanomaterials for applications in High density recording media and microwave devices," J. Magn. Magn. Mater., **324**, 15–19 (2012).

[263] A. Bahadur, A. Saeed, S. Iqbal, M. Shoaib, I. Ahmad, M. Saif, M. I. Bashir, W. Hussain, A. Bahadur, A. Saeed, S. Iqbal, M. Shoaib, I. Ahmad, M. Saif, and M. I. Bashir, "Morphological and magnetic properties of $BaFe_{12}O_{19}$ nanoferrite: A promising microwave absorbing material," Ceram. Int., **43**, 7346–7350 (2017).

[264] R. S. Alam, M. Moradi, H. Nikmanesh, J. Ventura, and M. Rostami, "Magnetic and microwave absorption properties of $BaMg_{x/2}Mn_{x/2}Co_xTi_{2x}Fe_{12-4x}O_{19}$ hexaferrite nanoparticles," J. Magn. Magn. Mater., **402**, 20–27 (2016).

[265] S. Liu, K. Wei, Y. Cheng, S. Yan, L. He, and L. Deng, "Structural , magnetic and microwave electromagnetic properties in La- substituted quaternary ferrite," J. Alloys Compd., **791**, 469–476 (2019).

[266] C. Zhao, M. Shen, Z. Li, R. Sun, A. Xia, and X. Liu, "Green synthesis and enhanced microwave absorption property of reduced graphene oxide-$SrFe_{12}O_{19}$ nanocomposites," J. Alloys Compd., **689**, 1037–1043 (2016).

[267] M. A. P. Buzinaro, N. S. Ferreira, F. Cunha, and M. A. Macêdo, "Hopkinson effect , structural and magnetic properties of M-type Sm^{3+}-doped $SrFe_{12}O_{19}$ nanoparticles produced by a proteic sol–gel process," Ceram. Int., **42**, 5865–5872 (2016).

[268] E. S. Zhukova, A. S. Mikheykin, V. I. Torgashev, A. A. Bush, Y. I. Yuzyuk, A. E. Sashin, A. S. Prokhorov, M. Dressel, and B. P. Gorshunov, "Crucial influence of crystal site disorder on dynamical spectral response in artificial magnetoplumbites," **62**, 13–21 (2016).

[269] J. Li, H. Zhang, and Y. Liu, "Phase formation , magnetic properties and Raman spectra of Co–Ti co-substitution M-type barium ferrites," Appl. Phys. A, **119**, 525–532 (2015).

[270] J. Li, H. Zhang, Y. Liu, Q. Li, T. Zhou, and H. Yang "Phase formation, magnetic properties and Raman spectra of Co-Ti co-substitution M-type barium ferrites," Appl. Phys. A, **119**, 525-532 (2015).

[271] K. W. Wagner, “Zur Theorie der unvollkommenen dielektrika.,” Ann. Phys., **345**, 817–855 (1913).

[272] C. G. Koops, “On the dispersion of resistivity and dielectric constant of some semiconductors at audiofrequencies,” Phys. Rev., **83**, 121 (1951).

[273] A. I. Ghoneim, M. A. Amer, T. M. Meaz, and S. S. Attalah, “Dielectric properties of Ti^{4+} substituted $BaFe_{12}O_{19}$ nanoparticles,” Phys. B Phys. Condens. Matter, **507**, 1–12, 2017.

[274] M. J. Iqbal and S. Farooq, “Extraordinary role of Ce–Ni elements on the electrical and magnetic properties of Sr–Ba M-type hexaferrites,” Mater. reserach Bull., **44**, 2050–2055 (2009).

[275] P. Kumar, A. Gaur, and R. K. Kotnala, “Magneto-electric response in Pb substituted M–type barium-hexaferrite,” Ceram. Int., **43**, 1180-1185 (2016).

[276] H. Malik, M. A. Khan, A. Hussain, M. F. Warsi, A. Mahmood, and S. M. Ramay, “Structural, spectral, thermal and dielectric properties of Nd–Ni co-doped Sr–Ba–Cu hexagonal ferrites synthesized via sol-gel auto-combustion route,” Ceram. Int., **44**, 605–612 (2018).

[277] I. Ali, M. U. Islam, M. S. Awan, and M. Ahmad, “Effects of Ga–Cr substitution on structural and magnetic properties of hexaferrite ($BaFe_{12}O_{19}$) synthesized by sol–gel auto-combustion route,” J. Alloys Compd., **547**, 118–125 (2013).

[278] M. Ahmad, F. Aen, M. U. Islam, S. B. Niazi, and M. U. Rana, “Structural , physical , magnetic and electrical properties of La-substituted W-type hexagonal ferrites,” Ceram. Int., **37**, 3691–3696 (2011).

[279] I. A. Auwal, H. Güngüneş, S. Güner, S. E. Shirsath, M. Sertkol, and A. Baykal, “Structural, magneto-optical properties and cation distribution of $SrBi_xLa_xY_xFe_{12-3x}O19$ ($0.0 \leq x \leq 0.33$) hexaferrites,” Mater. Res. Bull., **80**, 263–272 (2016).

[280] A. Baykal, S. Yokuş, S. Güner, H. Güngüneş, and H. Sözeri, “Magneto-optical properties and Mössbauer Investigation of $Ba_xSr_yPb_zFe_{12}O_{19}$ Hexaferrites,” Ceram. Int., **43**, 3475–3482 (2016).

[281] I. A. Auwal, A. Baykal, H. Güngüne, and S. E. Shirsath, "Structural investigation and hyper fi ne interactions of $BaBi_xLa_xFe_{12-2x}O_{19}$," Ceram. Int., **42**, 3380–3387 (2016).

[282] M. A. Almessiere, Y. Slimani, H. Güngüne, S. Ali, A. Baykal, and I. Ercan, "AC susceptibility and hyperfine interactions of Mg-Ca ions co-substituted $BaFe_{12}O_{19}$ nanohexaferrites," Ceram. Int., **45**, 10048-10055 (2019).

[283] J. Sharma, S. Kumar, J. Mohammed, R. Kaur, Tchouank Tekou Carol T., and A. K. Srivastava, "Investigation of structural and magnetic properties of $Ba_{0.3}Gd_{0.7}Co_{0.7}Fe_{11.3}O_{19}$ hexaferrite," AIP Conf. Proceedings, **1860**, 020017 (2017).

[284] I. A. Auwal, A. D. Korkmaz, M. D. Amir, S. M. Asiri, A. Baykal, H. Güngüneş, and S. E. Shirstah, "Mossbauer Analysis and Cation Distribution of Zn Substituted $BaFe_{12}O_{19}$ Hexaferrites," J. Supercond. Nov. Magn., **31**, 151–156 (2018).

[285] M. J. Iqbal and S. Farooq, "Impact of Pr–Ni substitution on the electrical and magnetic properties of chemically derived nanosized strontium–barium hexaferrites," J. Alloys Compd., **505**, 560–567 (2010).

[286] M. A. Almessiere, Y. Slimani, H. Gungunes, A. Manikandan, and A. Baykal, "Investigation of the effects of Tm^{3+} on the structural , microstructural , optical , and magnetic properties of Sr hexaferrites," Results Phys., **13**, 102166 (2019).

[287] A. Ghasemi and V. Sepela, "Correlation between site preference and magnetic properties of substituted strontium ferrite thin films," J. Magn. Magn. Mater., **323**, 1727–1733 (2011).

[288] S. K. Chawla, S. S. Meena, P. Kaur, R. K. Mudsainiyan, and S. M. Yusuf, "Effect of site preferences on structural and magnetic switching prop- erties of CO–Zr doped strontium hexaferrite $SrCo_xZr_xFe_{(12-2x)}O_{19}$," J. Magn. Magn. Mater., **378**, 84–91 (2015).

[289] J. P. Hodges, S. Short, J. D. Jorgensen, X. Xiong, B. Dabrowski, S. M. Mini, and C. W. Kimball, "Evolution of oxygen-vacancy ordered crystal structures in the perovskite series $Sr_nFe_nO_{3n-1}$ (n=2, 4, 8, and ∞), and the relationship to electronic and magnetic properties," J. Solid State Chem. **151**, 190–209 (2000).

[290] A. Awadallah, S. H. Mahmood, Y. Maswadeh, I. Bsoul, M. Awawdeh, Q. I. Mohaidat,

and H. Juwhari, “Structural , magnetic , and Mössbauer spectroscopy of Cu substituted M-type hexaferrites,” Mater. Res. Bull., **74**, 192–201 (2016).

[291] F. van der Woude and G. A. Sawatzky, “Hyperfine Magnetic Fields at Fe57 Nuclei in Ferrimagnetic Spinels,” Phys. Rev. B - Condens. Matter Mater. Phys., **4**, 3159 (1971).

[292] G. V. M. Williams, T. Prakash, J. Kennedy, and S. V Chong, “Spin-dependent tunnelling in magnetite nanoparticles,” J. Magn. Magn. Mater., **460**, 229–233 (2018).

[293] R. K. M. Munish and G. S. K. Chawla, “Self-combustion synthesis of co–zr-doped ba-hexaferrite nanoparticles and their studied physicochemical,” J. Supercond. Nov. Magn., **28**, 3663-3674 (2015).

[294] A. Majeed, M. Azhar, I. Ahmad, M. Niaz, and M. Farooq, “Morphological , Raman , electrical and dielectric properties of rare earth doped X-type hexagonal ferrites,” Phys. B Phys. Condens. Matter, **503**, 38–43 (20169.

[295] X. Chen, N. Thi, M. Hien, K. Han, J. C. Sur, N. H. Sung, B. K. Cho, I. Yang, H. Bafe, and H. Bafe, “Raman studies of spin-phonon coupling in hexagonal $BaFe_{12}O_{19}$,” J. App. Phys., **114**, 013912 (2013).

[296] M. A. P. Buzinaro, M. A. Macêdo, B. F. O. Costa, and N. S. Ferreira, “Disorder of $Fe^{(2)}O_5$ bipyramids and spin-phonon coupling in $SrFe_{12}O_{19}$ nanoparticles,” Ceram. Int., **45**, 13571 - 13574 (2019).

[297] C. Wu, Z. Yu, Y. Yang, K. Sun, J. Nie, Y. Liu, and X. Jiang, “Computational and experimental study on the cation distribution of La-Cu substituted barium hexaferrites,” J. Alloys Compd., **664**, 406–410 (2016).

[298] M. Sharma and S. C. Kashyap, “Improvement in magnetic parameters of polycrystalline barium hexaferrite by nonmagnetic cation substitution and microwave processing,” Ceram. Int., no. February, **45**, 11226-11232 (2019).

[299] W. Abbas, I. Ahmad, M. Kanwal, G. Murtaza, I. Ali, M. Azhar, M. Niaz, and M. Ahmad, “Structural and magnetic behavior of Pr-substituted M-type hexagonal ferrites synthesized by sol – gel autocombustion for a variety of applications,” J. Magn. Magn. Mater., **374**, 187–191 (2015).

[300] Z. Mosleh, P. Kameli, A. Poorbaferani, M. Ranjbar, and H. Salamati, “Structural,

magnetic and microwave absorption properties of Ce-doped barium hexaferrite," J. Magn. Magn. Mater., **397**, 101–107 (2016).

[301] J. F. Wang, C. B. Ponton, and I. R. Harris, "A study of Pr-substituted strontium hexaferrite by hydrothermal synthesis," J. Alloys Compd., **403**, 104–109 (2005).

[302] R. K. Mudsainiyan, A. K. Jassal, M. Gupta, and S. K. Chawla, "Study on structural and magnetic properties of nanosized M-type Ba-hexaferrites synthesized by urea assisted citrate precursor route," J. Alloys Compd., **645**, 421–428 (2015).

[303] J. Kennedy, P. P. Murmu, J. Leveneur, A. Markwitz, and J. Futter, "Applied Surface Science Controlling preferred orientation and electrical conductivity of zinc oxide thin films by post growth annealing treatment," Appl. Surf. Sci., **367**, 52–58 (2016).

[304] A. M. Amanulla, S. K. Jasmine, R. Sundaram, and C. M. Magdalane, "Antibacterial , magnetic, optical and humidity sensor studies of β-$CoMoO_4$-Co_3O_4 nanocomposites and its synthesis and characterization," J. Photochem. Photobiol. B Biol., **183**, 233–241 (2018).

[305] A. O. Turky and I. A. Ibrahim, "Tuning optical and dielectric properties of calcium copper titanate $Ca_xCu_{3-x}Ti_4O_{12}$ nanopowders," RSC Adv., **5**, 18767–18772 (2015).

[306] I. A. Auwal, S. Güner, H. Güngüne, and A. Baykal, "$Sr_{1-x}La_xFe_{12}O_{19}$ ($0.0 \leq x \leq 0.5$) hexaferrites: Synthesis, characterizations , hyperfine interactions and magneto-optical properties," Ceram. Int., **11**, 12995–13003 (2016).

[307] M. Sharma, S. C. Kashyap, and H. C. Gupta, "Effect of Mg–Zr substitution and microwave processing on magnetic properties of barium hexaferrite," Phys. B Phys. Condens. Matter, **448**, 24–28 (2014).

[308] H. Sözeri, H. Deligöz, H. Kavas, and A. Baykal, "Magnetic , dielectric and microwave properties of M – Ti substituted barium," Ceram. Int., **40**, 8645–8657 (2014).

[309] Y. Yang, J. Shao, F. Wang, and D. Huang, "Effects of Pr-Co content on the microstructural and magnetic properties of the Pr-Co substituted M-type strontium hexaferrites," J. Ceram. Process. Res., **18**, 445–450 (2017).

[310] Y. Yang, J. Shao, F. Wang, D. Huang, and K. M. U. Rehman, "Magnetic and microstructural properties of M-type strontium hexaferrites with Pr–ZnAl

substitution," Chinese J. Phys., 56, 468–475 (2018).

[311] S. Ounnunkad, "Improving magnetic properties of barium hexaferrites by La or Pr substitution," Solid State Communications, **138**, 472–475 (2006).

[312] Y. Yang, J. Shao, F. Wang, K. M. U. Rehman, and J. Tang, "Microstructural and magnetic properties of Pr–BiCo co-substituted M-type Sr–Ca hexaferrites," Chinese J. Phys., **56**, 674–682 (2018).

[313] S. B. Narang and K. Pubby, "Electromagnetic Characterization of Co-Ti-Doped Ba-M Ferrite-Based Frequency-Tunable Microwave Absorber in 12.4–40 GHz," J. Supercond. Nov. Magn., **30**, 511–520 (2017).

[314] I. Sadiq, I. Khan, E. V. Rebrov, M. N. Ashiq, S. Naseem, and M. U. Rana, "Structural, infrared, magnetic and microwave absorption properties of rare earth doped X-type hexagonal nanoferrites," J. Alloys Compd., **570**, 7–13 (2013).

[315] Z. Yan and J. Luo, "Effects of Ce-Zn co-substitution on structure , magnetic and microwave absorption properties of nickel ferrite nanoparticles," J. Alloys Compd., **695**, 1185–1195 (2016).

[316] F. M. M. Pereira, M. R. P. Santos, R. S. T. M. Sohn, J. S. Almeida, A. M. L. Medeiros, M. M. Costa, and A. S. B. Sombra, "Magnetic and dielectric properties of the M-type barium strontium hexaferrite ($Ba_xSr_{1-x}Fe_{12}O_{19}$) in the RF and microwave (MW) frequency range," J. Mater. Sci. Mater electron, **20**, 408–417 (2009).

[317] T. Tsutaoka, "Frequency dispersion of complex permeability in Mn-Zn and Ni-Zn spinel ferrites and their composite materials," J. Appl. Phys., **93**, 2789–2796 (2003).

[318] H. Aiping, H. Huahui, F. Zekun, and W. Shilei, "Study on electromagnetic properties of MnZn ferrites with Fe-poor composition," Mater. Chem. Phys., **105**, 303–307 (2007).

[319] J. Qiu, Y. Wang, and M. Gu, "Effect of Cr substitution on microwave absorption of BaFe 12 O 19," Mater. Lett., **60**, 2728–2732 (2006).

[320] S. Salman, S. Afghahi, M. Jafarian, and C. A. Stergiou, "X-band microwave absorbing characteristics of multicomponent composites with magnetodielectric fillers," J. Magn. Magn. Mater., **419**, 386–393 (2016).

[321] J. Luo, P. Shen, W. Yao, C. Jiang, and J. Xu, "Synthesis , Characterization , and Microwave Absorption Properties of Reduced Graphene Oxide/Strontium Ferrite/Polyaniline Nanocomposites," Nanoscale Res. Lett., **11**, 141 (2016).

[322] Y. Wang, H. Guan, C. Dong, X. Xiao, S. Du, and Y. Wang, "Reduced graphene oxide (RGO)/Mn_3O_4 nanocomposites for dielectric loss properties and electromagnetic interference shielding effectiveness at high frequency," Ceram. Int., **42**, 936–942 (2016).

[323] M. H. Al-saleh and U. Sundararaj, "Electromagnetic interference shielding mechanisms of CNT/polymer composites," Carbon, **47**, 1738–1746 (2009).

[324] A. Pratap, P. Garg, F. Alam, K. Singh, R. B. Mathur, R. P. Tandon, A. Chandra, and S. K. Dhawan, "Phenolic resin-based composite sheets filled with mixtures of reduced graphene oxide, α-Fe_2O_3 and carbon fibers for excellent electromagnetic interference shielding in the X-band," Carbon, **50**, 3868–3875 (2012).

[325] T. Kaur, S. Kumar, S. B. Narang, and A. K. Srivastava, "Radiation losses in microwave Ku region by conducting pyrrole/barium titanate and barium hexaferrite based nanocomposites," J. Magn. Magn. Mater., **420**, 336–342 (2016).

[326] A. Pratap, M. Mishra, D. P. Hashim, T. N. Narayanan, P. M. Ajayan, and B. Kumar, "Probing the engineered sandwich network of vertically aligned carbon nanotube–reduced graphene oxide composites for high performance electromagnetic interference shielding applications," Carbon, **85**, 79–88 (2014).

[327] A. Ameli, P. U. Jung, and C. B. Park, "Electrical properties and electromagnetic interference shielding effectiveness of polypropylene/carbon fiber composite foams," Carbon, **60**, 379–391 (2013).

[328] W. Song, M. Cao, M. Lu, S. Bi, and C. Wang, "Flexible graphene/polymer composite films in sandwich structures for effective electromagnetic interference shielding," Carbon, **66**, 67–76 (2013).

[329] M. Hong, W. Choi, K. An, S. Kang, S. Park, Y. Sil, and B. Kim, "Electromagnetic interference shielding behaviors of carbon fibers-reinforced polypropylene matrix composites: II . Effects of filler length control," J. Ind. Eng. Chem., **20**, 3901–3904 (2014).

[330] Y. Zhan, J. Wang, K. Zhang, Y. Li, Y. Meng, and N. Yan, "Fabrication of a fl exible electromagnetic interference shielding Fe_3O_4@reduced graphene oxide/natural rubber composite with segregated network," Chem. Eng. J., **344**, 184–193 (2018).

[331] W. Song, X. Guan, L. Fan, and M. Cao, "Tuning three-dimensional textures with graphene aerogels for ultra-light flexible graphene/texture composites of effective electromagnetic shielding," Carbon, **93**, 151–160 (2015).

[332] A. H. Najafabadi, A. Ghasemi, and R. Mozaffarinia, "Development of novel magnetic-dielectric ceramics for enhancement of reflection loss in X band," Ceram. Int., **42**, 13625–13634 (2016).

[333] K. D. Mandal, A. K. Rai, D. Kumar, and O. Parkash, "Dielectric properties of the $Ca_{1-x}La_xCu_3Ti_{4-x}Co_xO_{12}$ system (x=0.10, 0.20 and 0.30) synthesized by semi-wet route," J. Alloys Compd., **478**, 771–776 (2009).

[334] J. Mohammed, B. F. Abubakar, K. U. Yerima, H. Hamisu, and U. T. Isma, "Biodegradable polymer modified rGO/PANI/CCTO nanocomposites : Structural and dielectric properties," Mater. Today Proc., **5**, 28462–28469 (2018).

[335] P. Thomas, K. Dwarakanath, K. B. R. Varma, and T. R. N. Kutty, "Synthesis of nanoparticles of the giant dielectric material, $CaCu_3Ti_4O_{12}$ from a precursor route.," J. Therm. Anal. Calorim., **95**, 267–272 (2009).

[336] S. Jesurani, S. Kanagesan, R. Velmurugan, and T. Kalaivani, "Phase formation and high dielectric constant of calcium copper titanate using sol–gel route," J. Mater. Sci. Mater electron, **23**, 668–674 (2012).

[337] P. Gautam, A. Khare, S. Sharma, N. B. Singh, and K. D. Mandal, "Characterization of $Bi_{2/3}Cu_3Ti_4O_{12}$ ceramics synthesized by semi-wet," Prog. Nat. Sci. Mater. Int., **26**, 567–571 (2016).

[338] Z. Li, P. Zhao, Z. Wang, X. Xue, and Z. Li, "Dielectric behavior associated with the synergetic microstructure and oxygen vacancies in $CaCu_3Ti_4O_{12}$ ceramics," J. Mater. Sci. Mater. Electron., **27**, 7327–7334 (2016).

[339] X. Huang, H. Zhang, Y. Lai, and J. Li, "The lowered dielectric loss tangent and grain boundary effects in fluorine-doped calcium copper titanate ceramics," Appl. Phys. A,

123, 317 (2017).

[340] R. Espinoza-González and E. Mosquera, "Influence of micro and nanoparticles of zirconium oxides on the dieletric properties of $CaCu_3Ti_4O_{12}$," Ceram. Int., **43**, 14659–14665, 2017.

[341] A. Nautiyal, C. Autret, C. Honstettre, M. El Amrani, S. Roger, B. Negulescu, and A. Ruyter, "Local analysis of the grain and grain boundary contributions to the bulk dielectric properties of $Ca(Cu_{3-y}Mg_y)Ti_4O_{12}$ ceramics: Importance of the potential barrier at the grain boundary," J. Eur. Ceram. Soc., **36**, 1391–1398 (2016).

[342] A. Hojjati-najafabadi, A. Ghasemi, and A. Ghasemi, "Magneto-electric features of $BaFe_{9.5}Al_{1.5}CrO_{19}$-$CaCu_3Ti_4O_{12}$ nanocomposites," Ceram. Int., **43**, 244–249 (2017).

[343] J. Luo, L. Yue, H. Ji, K. Zhang, and N. Yu, "Investigation on the optimization , design and microwave absorption properties graphene oxide nanocomposites," RCS Adv., **5**, 10197-10203 (2018).

[344] J. Iskandar, H. Syafutra, and J. Juansah, "Characterizations of electrical and optical properties on ferroelectric on the annealing time differences and its development as light sensor on satellite technology," Procedia Environ. Sci., **24**, 324–328 (2015).

[345] D. Basandrai, R. K. Bedi, A. Dhami, S. B. Narang, K. Pubby, A. Gupta, and A. K. Srivastava, "Aluminum and chromium substituted Z-type hexaferrites for antenna and microwave absorber applications," J. Sol-Gel Sci. Technol., **85**, 59–65 (2018).

[346] J. Luo, Y. Xu, and H. Mao, "Materials Magnetic and microwave absorption properties of rare earth ions (Sm^{3+}, Er^{3+}) doped strontium ferrite and its nanocomposites with polypyrrole," J. Magn. Magn. Mater., **381**, 365–371 (2015).

[347] J. Lv, S. Zhai, C. Gao, N. Zhou, Q. An, and B. Zhai, "Synthesis of lightweight , hierarchical cabbage-like composites as superior electromagnetic wave absorbent," Chem. Eng. J., **289**, 261–269 (2016).

[348] N. Zhang, Y. Huang, M. Zong, X. Ding, S. Li, and M. Wang, "Synthesis of ZnS quantum dots and $CoFe_2O_4$ nanoparticles co-loaded with graphene nanosheets as an efficient broad band EM wave absorber," Chem. Eng. J., **308**, 214 - 221 (2017).

[349] K. Zhang, X. Gao, Q. Zhang, T. Li, H. Chen, and X. Chen, "Synthesis,

characterization and electromagnetic wave absorption properties of asphalt carbon coated graphene/magnetic $NiFe_2O_4$ modified multi-wall carbon nanotube composites," J. Alloys Compd., **721**, 268–275 (2017).

[350] J. Wang, Y. Sun, W. Chen, T. Wang, R. Xu, J. Wang, J. Wang, Y. Sun, W. Chen, T. Wang, R. Xu, and J. Wang, "Enhanced microwave absorption performance of lightweight absorber based on reduced graphene oxide and Ag-coated hollow glass spheres/epoxy composite," J. Appl. Phys., **117**, 154903 (2015).

[351] T. Wu, K. Lu, C. Peng, Y. Hong, and C. Hwang, "A new method for the preparation of a Fe_3O_4/graphene hybrid material and its applications in electromagnetic wave absorption," Mater. Res. Bull., **70**, 486–493 (2015).

[352] J. Luo, Y. Xu, W. Yao, C. Jiang, and J. Xu, "Synthesis and microwave absorption properties of reduced graphene oxide-magnetic porous nanospheres-polyaniline composites," Compos. Sci. Technol., **117**, 315–321 (2015).

[353] X. Zhang, Y. Huang, X. Chen, and J. Chen, "Hierarchical structures of graphene@$CoFe_2O_4$@SiO_2@TiO_2 nanosheets:Synthesis and excellent microwave absorption properties," Mater. Lett., **158**, 380–383 (2015).

[354] X. Li, S. Yang, J. Sun, P. He, X. Pu, and G. Ding, "Enhanced electromagnetic wave absorption performances of Co_3O_4 nanocube/reduced graphene oxide composite," Synth. Met., **194**, 52–58 (2014).

[355] R. Bera, A. Maitra, S. Paria, S. K. Karan, A. K. Das, A. Bera, S. K. Si, L. Halder, A. De, and B. B. Khatua, "An approach to widen the electromagnetic shielding efficiency in PDMS/ferrous ferric oxide decorated RGO–SWCNH composite through pressure induced tunability," Chem. Eng. J., **335**, 01–509 (2018).

[356] Z. Zhu, X. Sun, G. Li, H. Xue, H. Guo, X. Fan, and X. Pan, "Microwave-assisted synthesis of graphene–Ni composites with enhanced microwave absorption properties in Ku-band," J. Magn. Magn. Mater., **377**, 95–103 (2015).

[357] P. Liu, Z. Yao, and J. Zhou, "Fabrication and microwave absorption of reduced graphene oxide/$Ni_{0.4}Zn_{0.4}Co_{0.2}Fe_2O_4$ nanocomposites," Ceram. Int., **42**, 9241–9249 (2016).

[358] J. Liu, P. Zhang, and X. Zhang, "Synthesis and microwave absorbing properties of La-doped Sr-hexaferrite nanopowders via sol–gel auto-combustion method," Rare Met., **36**, 704–710 (2017).

[359] J. Luo and D. Gao, "Synthesis and microwave absorption properties of PPy/Co nanocomposites," J. Magn. Magn. Mater., **368**, 82–86 (2014).

[360] W. Liu, Q. Shao, G. Ji, X. Liang, Y. Cheng, B. Quan, and Y. Du, "Metal–organic-frameworks derived porous carbon-wrapped Ni composites with optimized impedance matching as excellent lightweight electromagnetic wave absorber," Chem. Eng. J., **313**, 734–744 (2017).

[361] J. Feng, F. Pu, Z. Li, X. Li, X. Hu, and J. Bai, "Interfacial interactions and synergistic effect of CoNi nanocrystals and nitrogen-doped graphene in a composite microwave absorber," Carbon, **104**, 214–225 (2016).

[362] R. Yang, P. M. Reddy, C. Chang, P. Chen, and J. Chen, "Synthesis and characterization of Fe_3O_4/polypyrrole/carbon nanotube composites with tunable microwave absorption properties : Role of carbon nanotube and polypyrrole content," Chem. Eng. J., **285**, 497–507 (2016).

[363] W. Fu, S. Liu, W. Fan, H. Yang, and X. Pang, "Hollow glass microspheres coated with $CoFe_2O_4$ and its microwave absorption property," J. Magn. Magn. Mater., **316**, 54–58 (2007).

[364] J. Mohammed, Tchouank Tekou Carol T., H. Y. Hafeez, D. Basandrai, G. R. Bhadu, S. K. Godara, S. B. Narang, and A. K. Srivastava, "Lightweight SrM/CCTO/rGO nanocomposites for optoelectronics and Ku band microwave absorption," J. Mater. Sci. Mater. Electron., **30**, 4026-4040 (2019).

[365] H. Nikmanesh, M. Moradi, G. H. Bordbar, and R. S. Alam, "Effect of multi dopant barium hexaferrite nanoparticles on the structural, magnetic, and X-Ku bands microwave absorption properties," J. Alloys Compd., **708**, 99–107 (2017).

[366] S. B. Narang, K. Pubby, S. K. Chawla, and P. Kaur, "Origin of Absorption peaks in Reflection Loss spectrum in Ku- frequency band of Co-Zr substituted Strontium Hexaferrites prepared using Sucrose Precursor," J. Magn. Magn. Mater., **426**, 202–205 (2017).

[367] P. Saini, V. Choudhary, B. P. Singh, R. B. Mathur, and S. K. Dhawan, "Polyaniline–MWCNT nanocomposites for microwave absorption and EMI shielding," Mater. Chem. Phys., **113**, 919–926 (2009).

[368] X. Ma, B. Shen, L. Zhang, Y. Liu, and W. Zhai, "Porous superhydrophobic polymer/carbon composites for lightweight and self-cleaning EMI shielding application," Compos. Sci. Technol., **158**, 86–93 (2018).

[369] Y. Yuan, W. Yin, M. Yang, F. Xu, X. Zhao, J. Li, Q. Peng, X. He, S. Du, and Y. Li, "Lightweight , fl exible and strong core-shell non-woven fabrics covered by reduced graphene oxide for high-performance electromagnetic interference shielding," Carbon, **130**, 59–68 (2018).

[370] Y. Chen, Y. Wang, H. Zhang, X. Li, C. Gui, and Z. Yu, "Enhanced electromagnetic interference shielding efficiency of polystyrene/graphene composites with magnetic Fe_3O_4 nanoparticles," Carbon, **82**, 67–76 (2014).

[371] M. R. Eraky, "Electrical conductivity of cobalt–titanium substituted SrCaM hexaferrites," J. Magn. Magn. Mater., **324**, 1034–1039 (2012).

[372] S. E. M. Ghahfarokhi, Z. A. Rostami, and I. Kazeminezhad, "Fabrication of PbFe12O19 nanoparticles and study of their structural, magnetic and dielectric properties.," J. Magn. Magn. Mater., **399**, 130–142 (2016).

[373] S. Jiang and X. Liu, "Synthesis and characterization of $Sr_{12-x}Y_xFe_{12}O_{19}$ hexaferrites prepared by solid-state reaction method," J. Mater. Sci. Mater. Electron., **27**, 12919–12924 (2016).

[374] P. Jing, J. Du, J. Wang, L. Pan, J. Li, and Q. Liu, "Width-controlled M-type hexagonal strontium ferrite ($SrFe_{12}O_{19}$) nanoribbons with high saturation magnetization and superior coercivity synthesized by electrospinning," Sci. Rep., **5**, 15089 (2015).

[375] L. Wang, J. Zhu, H. Yang, F. Wang, Y. Qin, T. Zhao, and P. Zhang, "Fabrication of hierarchical graphene@Fe_3O_4@SiO_2@polyaniline quaternary composite and its improved electrochemical performance," J. Alloys Compd., **634**, 232–238 (2015).

[376] L. Wang, Y. Huang, C. Li, J. Chen, and X. Sun, "Hierarchical composites of polyaniline nanorod arrays covalently-grafted on the surfaces of graphene@Fe_3O_4@C

with high microwave absorption performance," Compos. Sci. Technol., **108**, 1–8, 2015.

[377] R. Bhargava and S. Khan, "Enhanced optical properties of Cu_2O anchored on reduced graphene oxide (rGO) sheets," J. Phys. Condens. Matter, **30**, 335703 (2018).

[378] S. Kellici, J. Acord, J. Ball, and H. S. Reehal, "A single rapid route for the synthesis of reduced graphene oxide with antibacterial activities," RSC Adv., **4**, 14858–14861 (2014).

[379] H. Y. Hafeez, S. K. Lakhera, S. Bellamkonda, G. R. Rao, M. V Shankar, D. W. Bahnemann, and B. Neppolian, "Construction of ternary hybrid layered reduced graphene oxide supported g-C_3N_4-TiO_2 nanocomposite and its photocatalytic production activity," Int. J. Hydrogen Energy, **43**, 3892–3904 (2017).

[380] L. Gan, S. Shang, C. Wah, M. Yuen, S. Jiang, and E. Hu, "Hydrothermal synthesis of magnetic $CoFe_2O_4$/graphene nanocomposites with improved photocatalytic activity," Appl. Surf. Sci., **351**, 140–147 (2015).

[381] T. Huang, M. He, Y. Zhou, S. Li, B. Ding, W. Pan, S. Huang, and Y. Tong, "Solvothermal fabrication of CoS nanoparticles anchored on reduced graphene oxide for high-performance microwave absorption," Synth. Met., **224**, 46–55 (2017).

[382] R. Al-gaashani, S. Radiman, Y. Al-douri, N. Tabet, and A. R. Daud, "Investigation of the optical properties of $Mg(OH)_2$ and MgO nanostructures obtained by microwave-assisted methods," J. Alloys Compd., **521**, 71–76 (2012).

[383] T. Wu, K. Lu, C. Peng, Y. Hong, and C. Hwang, "A new method for the preparation of a Fe3O4/graphene hybrid material and its applications in electromagnetic wave absorption," Mater. Res. Bull., **70**, 486–493, (2015).

[384] K. Zhang, X. Gao, Q. Zhang, T. Li, H. Chen, and X. Chen, "Synthesis, characterization and electromagnetic wave absorption properties of asphalt carbon coated graphene/magnetic $NiFe_2O_4$ modified multi-wall carbon nanotube composites," J. Alloys Compd., **721**, 268–275 (2017).

[385] G. Liu, W. Jiang, D. Sun, Y. Wang, and F. Li, "One-pot synthesis of urchinlike Ni nanoparticles/RGO composites with extraordinary electromagnetic absorption

properties," Appl. Surf. Sci., **314**, 523–529 (2014).

[386] P. S. P. Brush, T. Stability, and S. Property, "Polyaniline-Doped Spherical Polyelectrolyte Brush Nanocomposites with Enhanced Electrical Conductivity, Thermal Stability, and Solubility Property," Polymers, **7**, 1599–1616 (2015).

[387] P. Kharazi, R. Rahimi, and M. Rabbani "Copper ferrite-polyaniline nanocomposite: Structural, thermal, magnetic and dye adsorption properties," Solid State Sciences, **93**, 95–100 (2019).

[388] E. H. Alsharaeh, A. A. Othman, and M. A. Aldosari, "Microwave Irradiation Effect on the Dispersion and Thermal Stability of RGO Nanosheets within a Polystyrene Matrix," Materials, **7**, 5212–5224 (2014).

[389] U. Yaqoob, A. S. M. . I. Uddin, and G. Chung, "The effect of reduced graphene oxide on the dielectric and ferroelectric properties of PVDF–$BaTiO_3$ nanocomposites," RCS Av., **6**, 30747–30754 (2016).

[390] M. Ejaz, V. S. Puli, R. Elupula, S. Adireddy, B. C. Riggs, D. B. Chrisey, and S. M. Grayson, "Core-shell structured poly (glycidyl methacrylate)/$BaTiO_3$ nanocomposites prepared by surface-initiated atom transfer radical polymerization: A novel material for high energy density dielectric storage," J. Mater. Chem., **21**, 5897–5906 (2011).

[391] P. Thomas, K. Dwarakanath, K. B. R. Varma, and T. R. N. Kutty, "Nanoparticles of the giant dielectric material , $CaCu_3Ti_4O_{12}$ from a precursor route.," J. Phys. Chem. Solids, **69**, 2594–2604 (2008).

[392] P. Thomas, K. Dwarakanath, and K. B. R. Varma, "In situ synthesis and characterization of polyaniline–$CaCu_3Ti_4O_{12}$ nanocrystal composites," Synthetic Metals, **159**, 2128–2134 (2009).

[393] G. Liu, W. Jiang, Y. Wang, S. Zhong, D. Sun, J. Liu, and F. Li, "One-pot synthesis of Ag@Fe_3O_4/reduced graphene oxide composite with excellent electromagnetic absorption properties," Ceram. Int., **41**, 4982–4988 (2014).

List of publications

1. **J. Mohammed**, A. B. Suleiman, H. Y. Hafeez, Jyoti Sharma, Tchouank Tekou Carol T., Gopala Ram Bhadu, Sachin Kumar Godara, **A. K. Srivastava**, "Effect of heat-treatment on the magnetic and optical properties of $Sr_{0.7}Al_{0.3}Fe_{11.4}Mn_{0.6}O_{19}$", *Mater. Res. Express*, **5**, 086106 (2018). **Impact Factor: 1.151**
   DOI: 10.1088/2053-1591/aad1e5
   View online**:** https://doi.org/10.1088/2053-1591/aad1e5

2. **J. Mohammed**, A B Suleiman, T. Tchouank Tekou Carol, H. Y. Hafeez, Jyoti Sharma, Pradip K. Maji, Sachin Godara Kumar, **A. K. Srivastava**, "Enhanced dielectric and optical properties of nanoscale barium hexaferrites for optoelectronics and high frequency application", *Chin. Phys. B.*, **27**, 128104 (2018). **Impact Factor: 1.321**
   DOI: 10.1088/1674-1056/27/12/128104
   View online: https://doi.org/10.1088/1674-1056/27/12/128104
3. **J. Mohammed**, T. Tchouank Tekou Carol, H. Y. Hafeez, B. I. Adamu, Y. S. Wudil, Z. I Takai, Sachin Godara Kumar, **A. K. Srivastava**, "Tuning the dielectric and optical properties of Pr-Co–substituted calcium copper titanate for electronics applications", *J. Phys. Chem. Solids*, 127, 85-92 (2019). **Impact Factor: 2.207**
   DOI: 10.1016/j.jpcs.2018.09.034
   View online: https://doi.org/10.1016/j.jpcs.2018.09.034
4. **J. Mohammed**, T. Tchouank Tekou Carol, H. Y. Hafeez, D. Basandrai, Gopala R. Bhadu, Sachin Kumar Godara, S. B. Narang, **A. K. Srivastava**, "Lightweight SrM/CCTO/rGO nanocomposites for optoelectronics and K_u band microwave absorption," *J. Mater. Sci. Mater. Electron.*, **30**, 4026-4040 (2019). **Impact Factor: 2.324**
   DOI: 10.1007/s10854-019-00690-w
   View online: https://doi.org/10.1007/s10854-019-00690-w

5. **J. Mohammed**, Y. Hafeez, Tchouank Tekou Carol T., Chifu E. Ndikilar, Jyoti Sharma, Sachin Kumar Godara, **A. K. Srivastava**, "Structural, dielectric, and magneto-optical properties of Cu^{2+}-Er^{3+}substituted nanocrystalline strontium hexaferrites", *Mater. Res. Express*, **6**, 056111 (2019). **Impact Factor: 1.151**
   DOI: 10.1088/2053-1591/ab063b

View online: https://doi.org/10.1088/2053-1591/ab063b

6. **J. Mohammed**, Tchouank Tekou Carol T., H. Y. Hafeez, D. Basandrai, Gopala Ram Bhadu, Sachin Kumar Godara, S. B. Narang, **A. K. Srivastava**, "Design of Nano-sized Pr^{3+}-Co^{2+} Substituted M-type Strontium Hexaferrites for Optical Sensing and Electromagnetic Interference (EMI) Shielding in K_u Band", *App. Phys. A*.,**125**, 251 (2019). **Impact Factor: 1.604**
   DOI: 10.1007/s00339-019-2545-5
   View online: https://doi.org/10.1007/s00339-019-2545-5

7. **J. Mohammed**, Tchouank Tekou Carol T., H. Y. Hafeez, D. Basandrai, Gopala Ram Bhadu, Sachin Kumar Godara, S. B. Narang, A. K. Srivastava, "Electromagnetic Interference (EMI) Shielding, Microwave Absorption, and Optical Sensing Properties of BaM/CCTO Composites in K_u-band", Results in Physics, (2019). **Impact Factor: 2.147**
   DOI: 10.1007/s00339-019-2545-5
   View online: https://doi.org/10.1007/s00339-019-2545-5

8. Tchouank Tekou Carol T., **J. Mohammed**, Bilal Hamid Bhat, H. Y. Hafeez, Sachin Kumar Godara, **A. K. Srivastava**, "Structural, dielectric, and magneto-optical properties Al-Cr substituted M-type Barium Hexaferrite", *Phys. Status Solidi Appl. Mater. Sci*., **Impact Factor: 1.795**
   Accepted manuscript
   DOI: https://doi.org/10.1002/pssa.201800928
   View online: https://onlinelibrary.wiley.com/doi/abs/10.1002/pssa.201800928

To be communicated papers

1. Phase Structure Evolution, Crystal Structure Refinement, Morphology, and Electro-optical Properties of Heat-Treated $Ca_{0.9}Ni_{0.1}Cu_{2.9}La_{0.1}Ti_4O_{12}$
2. Magnetic, Mossbauer and Raman Spectroscopy of Nanocrystalline Dy^{3+}-Cr^{3+} Substituted Barium Hexagonal Ferrites
3. Cation Distribution and Site Occupancy of Nanoscale Cu^{2+}-Er^{3+} Substituted Strontium Hexagonal Ferrites

4. Magnetic, Mossbauer and Raman Spectroscopy of Nanocrystalline Pr^{3+}-Co^{2+} Substituted M-type Strontium Hexagonal Ferrites

Oral presentation (conference proceedings)

1. **J. Mohammed**, Jyoti Sharma, Sachin Kumar, T. T. Carol Trudel, and **A. K. Srivastava**, "Calcination temperature effect on the microstructure and dielectric properties of M-type strontium hexagonal ferrites" Citation: AIP Conference Proceedings 1860, 020007 (2017)
   DOI: 10.1063/1.4990306
   View online: http://dx.doi.org/10.1063/1.4990306
2. Jyoti Sharma, **J. Mohammed**, T. T. Carol Trudel, and **A. K. Srivastava**, "Effect of rare earth and transition element doping in bismuth multi-ferroic" Citation: AIP Conference Proceedings 1860, 020016 (2017)
   DOI: 10.1063/1.4990315
   View online: http://dx.doi.org/10.1063/1.4990315
3. Jyoti Sharma, **J. Mohammed**, Rajneet Kaur, T. T. Carol Trudel, and **A. K. Srivastava**, "Investigation of structural and magnetic properties of Ba0.3Gd0.7Co0.7Fe11.3O19 Hexaferrite" Citation: AIP Conference Proceedings 1860, 020017 (2017)
   DOI: 10.1063/1.4990316
   View online: http://dx.doi.org/10.1063/1.4990316
4. Tchouank Tekou Carol T., Jyoti Sharma, **J. Mohammed**, Sachin Kumar, and **A. K. Srivastava**, "Effect of temperature on the magnetic properties of nano-sized M-type barium hexagonal ferrites" Citation: AIP Conference Proceedings 1860, 020008 (2017);
   DOI: 10.1063/1.4990307
   View online: http://dx.doi.org/10.1063/1.4990307
5. **J. Mohammed**, Jyoti Sharma, Tchouank Tekou Carol T., U. T. Isma'il, Sachin Kumar, H. Y. Hafeez and A. K. Srivastava, "Structural, dielectric and magnetic properties of Al-Mn substituted nano-sized M-type strontium hexagonal ferrites" ROORKEE
6. Tchouank Tekou Carol T., **J. Mohammed**, Jyoti Sharma, U. T. Isma'il, Sachin Kumar, H. Y. Hafeez and **A. K. Srivastava**, "Structural, dielectric and magnetic

properties of Al-Mn substituted nano-sized M-type strontium hexagonal ferrites" ROORKEE

7. **J. Mohammed**, Isah I. Garba, K.U. Yerima, A. Muhammad, Zulfatu U. F., Mubarak S. Abubakar, Jyoti Sharma, Tchouank Tekou Carol T., Sachin Kumar, and **A. K. Srivastava**, "Structural and Dielectric Properties of Polycrystalline Calcium Copper Titanate (CCTO)" Advanced Manufacturing and Materials Science. Lecture Notes on Multidisciplinary Industrial Engineering. Springer, Cham, 369-378 (2018)
   DOI: 10.1007/978-3-319-76276-0_37
   https://link.springer.com/chapter/10.1007%2F978-3-319-76276-0_37
   Online ISBN: 978-3-319-76276-0
   Print ISBN: 978-3-319-76275-3
8. **J. Mohammed**, B. F. Abubakar, K. U Yerima, H. Hamisu, U. T. Isma'il, A. Muhammad, Zulfatu U. F., A. Abubakar, N. M. Salihu, Mubarak S. Abubakar, Saidu Y., Tchouank Tekou Carol T. and **A. K. Srivastava**, "Biodegradable polymer modified rGO/PANI/CCTO nanocomposites: Structural and dielectric properties", *materials today: proceedings*, 5, 28462-28469 (2018)
   DOI: 10.1016/j.matpr.2018.10.133
   View online: https://doi.org/10.1016/j.matpr.2018.10.133
9. **J. Mohammed**, H. Hamisu, H. A. Daya , K.U. Yerima, A. Muhammad, Mubarak S. Abubakar, Tchouank Tekou Carol T., **A. K. Srivastava** "Structural and Dielectric Properties of Biopolymer Functionalised rGO/SrM/CCTO Nanocomposite" INDORE

International conference attended

1. International Conference on "Recent Advances in Fundamental and Applied Sciences (RAFAS 2016) held at Lovely Professional University, Punjab, India on 25th-26th December 2016.
2. International Conference on Nanotechnology: Ideas, Innovations and Initiatives (ICN:3I-2017) organised by Department of Mechanical & Industrial Engineering and Centre of Nanotechnology, Indian Institute of Technology (IIT) Roorkee, India on December 6-8, 2017
3. International Conference on Advanced Manufacturing and Material Science (ICAMMS 2018), Muthoot Institute of Technology and Science, Kochi, India on 15-16 January, 2018